frontiers | Research Topics

Developments in the lithospheric evolution of the Indo-Pacific region

Edited by
J. Gregory Shellnutt, Meng-Wan Mary Yeh, Manu Prasanth M. P. and Van-Duong Nguyen

Published in
Frontiers in Earth Science

ISSN 1664-8714
ISBN 978-2-8325-3990-3
DOI 10.3389/978-2-8325-3990-3

About Frontiers

Frontiers is more than just an open access publisher of scholarly articles: it is a pioneering approach to the world of academia, radically improving the way scholarly research is managed. The grand vision of Frontiers is a world where all people have an equal opportunity to seek, share and generate knowledge. Frontiers provides immediate and permanent online open access to all its publications, but this alone is not enough to realize our grand goals.

Frontiers journal series

The Frontiers journal series is a multi-tier and interdisciplinary set of open-access, online journals, promising a paradigm shift from the current review, selection and dissemination processes in academic publishing. All Frontiers journals are driven by researchers for researchers; therefore, they constitute a service to the scholarly community. At the same time, the *Frontiers journal series* operates on a revolutionary invention, the tiered publishing system, initially addressing specific communities of scholars, and gradually climbing up to broader public understanding, thus serving the interests of the lay society, too.

Dedication to quality

Each Frontiers article is a landmark of the highest quality, thanks to genuinely collaborative interactions between authors and review editors, who include some of the world's best academicians. Research must be certified by peers before entering a stream of knowledge that may eventually reach the public - and shape society; therefore, Frontiers only applies the most rigorous and unbiased reviews. Frontiers revolutionizes research publishing by freely delivering the most outstanding research, evaluated with no bias from both the academic and social point of view. By applying the most advanced information technologies, Frontiers is catapulting scholarly publishing into a new generation.

What are Frontiers Research Topics?

Frontiers Research Topics are very popular trademarks of the *Frontiers journals series*: they are collections of at least ten articles, all centered on a particular subject. With their unique mix of varied contributions from Original Research to Review Articles, Frontiers Research Topics unify the most influential researchers, the latest key findings and historical advances in a hot research area.

Find out more on how to host your own Frontiers Research Topic or contribute to one as an author by contacting the Frontiers editorial office: frontiersin.org/about/contact

Developments in the lithospheric evolution of the Indo-Pacific region

Topic editors

J. Gregory Shellnutt — National Taiwan Normal University, Taiwan
Meng-Wan Mary Yeh — National Taiwan Normal University, Taiwan
Manu Prasanth M. P. — Institute of Earth Sciences, Academia Sinica, Taiwan
Van-Duong Nguyen — Vietnam Academy of Science and Technology, Vietnam

Citation

Shellnutt, J. G., Yeh, M.-W. M., Manu Prasanth, M. P., Nguyen, V.-D., eds. (2023). *Developments in the lithospheric evolution of the Indo-Pacific region*. Lausanne: Frontiers Media SA. doi: 10.3389/978-2-8325-3990-3

Table of contents

frontiers | Frontiers in Earth Science

TYPE Editorial
PUBLISHED 09 November 2023
DOI 10.3389/feart.2023.1327712

OPEN ACCESS

EDITED AND REVIEWED BY
Michel Grégoire,
UMR5563 Géosciences Environnement Toulouse (GET), France

*CORRESPONDENCE
J. Gregory Shellnutt,
jgshelln@ntnu.edu.tw

RECEIVED 25 October 2023
ACCEPTED 30 October 2023
PUBLISHED 09 November 2023

CITATION
Shellnutt JG, Yeh M-W, Manu Prasanth MP and Nguyen V-D (2023), Editorial: Developments in the lithospheric evolution of the Indo-Pacific region.
Front. Earth Sci. 11:1327712.
doi: 10.3389/feart.2023.1327712

Editorial: Developments in the lithospheric evolution of the Indo-Pacific region

J. Gregory Shellnutt[1]*, Meng-Wan Yeh[1], M. P. Manu Prasanth[2] and Van-Duong Nguyen[3]

[1]Department of Earth Sciences, National Taiwan Normal University, Taipei, Taiwan, [2]Academia Sinica, Institute of Earth Sciences, Taipei, Taiwan, [3]Vietnam Academy of Science and Technology, Institute of Geophysics, Hanoi, Vietnam

KEYWORDS

tectonics, continental crust, geophysics, geochronology, geochemistry

Editorial on the Research Topic
Developments in the lithospheric evolution of the Indo-Pacific region

The Indo-Pacific is a biogeographic region between 30°north and south of the equator that stretches from the Polynesian Islands of the Pacific Ocean in the east to the Indian Ocean in the west (Spalding et al., 2007; Hobbs et al., 2009; Crandall et al., 2019). During the Late Paleozoic to Early Mesozoic (300–200 Ma), the geological development of the Indo-Pacific region was a consequence of the dispersal of Gondwanan cratons and terranes, the destruction of the Tethyan and western Panthalassan (Paleo-Pacific) Oceans, and the subsequent creation of the Indian Ocean (Mann and Taira, 2004; Metcalfe, 2013; Metcalfe, 2017; Hutchinson, 2014; Hall, 2017; Ding and Sun, 2020). The lithotectonic evolution of the Indo-Pacific region involved the collision and accretion of ancient cratons and juvenile terranes between Gondwana and Laurasia and the eruption of continental and oceanic flood basalts. The result of this plate reorganization was the development of the Alpine-Himalaya Orogenic Belt, the Indosinian Orogeny, the Taiwan Orogeny, the New Guinea Orogeny, the initiation of west Pacific volcanic-arc magmatism, the development of marginal sea basins (e.g., South China Sea, Andaman Sea, Sulu Sea, Banda Sea, Sulawesi Sea), formation of energy and mineral resources, and the extrusion of Southeast Asia. Although the tectonic processes that formed Asia are understood within the geodynamic paradigm of plate tectonics, the timing and precise nature of the petrological, geophysical, and structural processes involved in its formation are not well constrained.

Four major tectonic plates of Eurasia, Indo-Australia, Philippine Sea, and Pacific are the main components of the Indo-Pacific region (Hall, 2002). The formation of these plates since the breakup of Pangea involved the closure of the Paleo-Pacific, Paleo-, Meso-, and Neo-Tethys, and amalgamation of a collage of continents and microcontinents such as: the North China, South China, Qiangtang, Lhasa, Baoshan, Sibumasu, Sukhothai, Chanthaburi, and Indochina terranes from West to East respectively (Figure 1; Searle et al., 2012; Sone et al., 2008; Ueno, 2003). Paleogeographic reconstructions indicate the Paleo-Tethys between Laurasia and Gondwana started to close from the Late Carboniferous until the Late Permian and was followed by the separation of the ribbon-like Cimmeria micro-continent from the northern boundary of Gondwana and the formation of the Meso-Tethys (Şengör, 1984, 1987; Metcalfe, 2006; Metcalfe, 2011; Metcalfe, 2013; Seton et al., 2012). The Permian-Triassic Tethyan orogeny formed along the southern Eurasian margin as North China, South China,

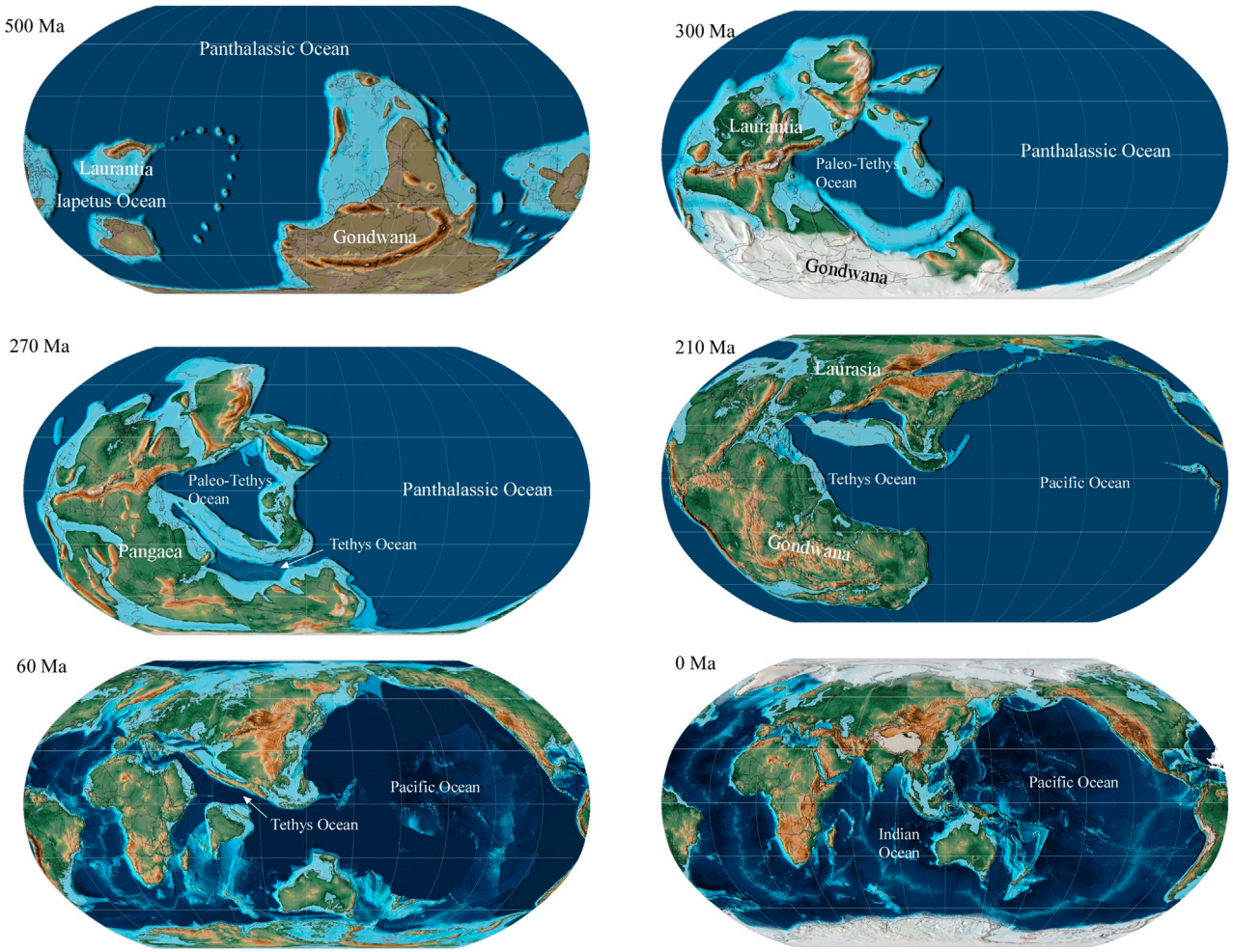

FIGURE 1
Palaeogeographic maps showing the tectonic evolution of Gondwana and Laurasia at 500 Ma, 300 Ma, 270 Ma, 210 Ma, 60 Ma, and present day using GPlates and the base maps of Scotese (2016).

Cathaysia, Indochina, Burma, and Cimmeria terranes amalgamated (Hall, 2002; Metcalfe, 2011; Seton et al., 2012; Metcalfe, 2013; Deng et al., 2014; Hall, 2017; Kapp and Decelles, 2019). The closure of the Meso-Tethys is marked by the Bangong–Nujiang Suture Zone in the central Tibetan Plateau as Qiangtang Terrane and Lhasa Terrane collided together during Cretaceous (Fan et al., 2021). Moreover, the paleo-Pacific continued to subduct under the eastern boundary of the Eurasia plate generating widespread NE-SW trending Cretaceous magmatism. The collision between India and Eurasia marks the closure of Neo-Tethys along the Indus Yarlung Zengbo suture forming the Himalayan orogeny during the Cenozoic time (Mitchell, 1981; Mitchell, 1984; Golognka, et al., 2006; Mitchell et al., 2012).

The Comprehensive Research on East Asia Tectonic Evolution (CREATE) working group was established with a special conference session entitled “Mantle Dynamics and Plate Interactions in East Asia” at the American Geophysical Union Fall Meeting in 1994. The success of the AGU Special Session was the impetus for a formal research initiative that led to a number of seminal papers (i.e., Chung and Jahn, 1995; Lee and Lawver, 1995; Chung et al., 1997; Lo et al., 2002), books (Flower et al., 1998), and journal special issues (Tectonophysics, Journal of Asian Earth Sciences) on the lithotectonic development of East Asia. The goals of the first CREATE project in 1997 were to initiate geoscience research projects with colleagues in China, Hong Kong, and Southeast Asia that related to the Cenozoic collision-extrusion tectonics along the Ailao Shan-Red River fault zone in SE Asia. The Ailao Shan-Red River fault zone is one of the major features responsible for the eastward extrusion of SE Asia after the India-Eurasia collision. Recently, CREATE members have expanded to regions of South Asia, West Asia, and the Indian Ocean and with research interests focusing on the consequences and processes of plate collision, the genesis of juvenile continental crust, and the mechanisms for continental accretion of the well-known Phanerozoic Asian orogenic belts (e.g., Alpine-Himalayan, Indosinian, Yanshanian, Taiwan orogenies).

This Research Topic of Frontiers in Earth Science is a collection of manuscripts focusing on the lithotectonic

evolution of cratons, terranes, and marginal ocean basins of the Indo-Pacific region in celebration of the 25th anniversary of CREATE. The authors use novel methods and analytical techniques in seismology, geochronology, structural geology, and geochemistry to offer robust constraints on the principal tectonomagmatic processes that were operating during the amalgamation of the Tethyan terranes of Gondwana with Eurasia. The papers in this volume encompass research topics related to Precambrian mafic dyke swarms, orocline evolution and tectonic extrusion during the India-Eurasia collision, seismic hazards of Vietnam, volcanic-arc and syn-collisional granite magmatism, and tectonics of the Taiwan Orogeny and propose new views on the lithotectonic development of cratonic India, Indochina, the South China Sea, and the India-Eurasia collision. The contents of the Research Topic are summarized below.

Chiu et al. noticed that the curvature from the eastern Himalayan syntaxis through east Burma to west Yunnan exhibits a unique convex shape toward the mantle wedge, which is different from the concave Baluchistan orocline and the Himalayan orocline. The southeastern stretch of the large-scale curvature of the Himalayan orocline, the Gaoligong orocline, exhibit N-S trend in the northern section and NE-SW trend in the southern section. Based on the reconstructed structural evolution models, five distinct deformation events have been identified, which leads to the proposal that the geometry of the Gaoligong orocline does not reflect a "bended orogeny" but rather an "atypical" orocline.

The Singhbhum craton in eastern India records multiple stages of Precambrian dyke emplacements with contrasting petrogenetic models proposed for their formation. Through field observations, petrography, mineral chemistry, whole rock elemental and Sr-Nd isotope geochemistry Manu Prasanth et al. propose that the ubiquitous continental crustal signature of Precambrian dyke swarms of the Singhbhum craton are best explained by a peridotite source with recycled crustal components, probably in the form of pyroxenites. Furthermore, they point out that crustal recycling in the Singhbhum craton was likely an episodic phenomenon rather than a discrete, single-stage process since the Archean.

Shellnutt et al. explore the Early Cretaceous quartz diorites and diorites from the Snoul pluton of eastern Cambodia, which was emplaced during the subduction of the Paleo-Pacific plate beneath the Indochina terrane. The samples are isotopically distinct from the coeval plutonic rocks of Vietnam from the same tectonic setting, suggesting that there could be a litho-tectonic domain boundary within the southern Indochina terrane.

The Taiwan mountain belt was formed by arc-continent collision followed by the subduction of the South China Sea and subsequent closure of the Luzon forearc. Lo et al. report new zircon U-Pb and amphibole $^{40}Ar/^{39}Ar$ ages from the Shihmen Conglomerate within the uplifted South China Sea turbidite sequence from the Hengchun Peninsula. They propose that a piece of early Miocene South China Sea crust was dynamically metamorphosed at ~13 Ma that led to the formation of an isolated high-relief subaerial mountain range along the Chinese continental margin and is best explained by an obduction event due to stress-strain reorganization of the Manila Trench during initial continental subduction.

Silpa et al. reports whole rock Sm-Nd isotopic compositions along with major and trace element geochemistry of meta-dolerite dykes from the western Dharwar craton. The dykes are proposed to be derived from a depleted subcontinental lithospheric mantle (SCLM) source formed during the Mesoarchean to Neoarchean after komatiitic magma extraction. These widespread dyke swarms are interpreted to be the plumbing system of greenstone belt volcanism in the Western Dharwar craton.

The NW-SE striking Day Nui Con Voi (DNCV) metamorphic massif in northern Vietnam is bounded by the Red River Shear Zone (RRSZ) to the south and continues along strike where it meets the South China Sea (SCS). Dinh et al. document new $^{40}Ar/^{39}Ar$ ages combined with microstructural and petrological analyses to constrain the timing of the left-lateral shearing of the RRSZ. New $^{40}Ar/^{39}Ar$ ages from different structural domains of the DNCV metamorphic massif show a rapid exhumation at 26 to 22 Ma. This extrusion tectonism cannot be considered as the cause for the initial opening of the SCS, rather it can be correlated with the southward ridge jump event of the already opened SCS.

Lee et al. studied the Gongga Shan granite, an intrusion along the Xianshuihe fault in easternmost Tibet. The extensive U-Pb zircon ages of the Gongga Shan granite samples provide evidence for the stepwise partial melting of the crust from 56 Ma to 4 Ma. Furthermore, the zircon U-Pb ages significantly extend the onset of crustal melting and timing of granite formation up to 20 Ma earlier than previously recognized.

Nguyen et al. performed a P- and S-wave travel time seismic tomographic inversion of Luzon Island to constrain the regional lithospheric structure and presented a refined slab tearing model. Their tomographic images indicate contrasting velocity structures across the Philippine Fault, which extends up to 60 km and also confirm the presence of slab-tearing regions extended from the fossilized ridges in the northern Luzon region, creating regional kinematic perturbations.

Lin et al. studied the Lan Sang gneisses from the NW-SE trending Mae Ping shear zone (MPSZ) of Thailand. They used zircon U-Pb geochronology and whole-rock major element analysis to evaluate the magmatic history of the area and found that MPSZ is dominated by Triassic-Jurassic and Eocene-Oligocene thermal events. The spatial and temporal distribution of several Eocene-Oligocene intrusions along the Sibumasu terrane indicates that Neo-Tethyan slab shallowing induced the inward migration of magmatism in the overriding plate.

Author contributions

JS: Conceptualization, Writing–original draft, Writing–review and editing. M-WY: Conceptualization, Writing–original draft, Writing–review and editing. MP: Conceptualization, Writing–original draft, Writing–review and editing. V-DN:

Conceptualization, Writing–original draft, Writing–review and editing.

Funding

The author(s) declare financial support was received for the research, authorship, and/or publication of this article. This project received support from National Science and Technology Council through grant 112-2116-M-003-005-MY2 to JS.

Acknowledgments

We are grateful to the reviewers for providing timely and comprehensive reviews that ensured the efficient handling of the manuscripts. Editorial assistance was provided by Stanislaw Mazur, Claudia Piromallo, Zhong-Hai Li, Shenghong Yang, Changqian Ma, Abderrahmane Bendaoud, Alexander Cruden that handle manuscripts of the guest editors. Finally, we thank Rebecca Thompson, Isabel Pooley, and Kanzis Mattu at Frontiers Media SA for their assistance in the success of this Research Topic.

Conflict of interest

The authors declare that the research was conducted in the absence of any commercial or financial relationships that could be construed as a potential conflict of interest.

Publisher's note

References

Chung, S.-L., and Jahn, B.-M. (1995). Plume-lithosphere interaction in generation of the Emeishan flood basalts at the Permian-Triassic boundary. *Geology* 23, 889–892. doi:10.1130/0091-7613(1995)023<0889:pliigo>2.3.co;2

Chung, S.-L., Lee, T.-Y., Lo, C.-H., Want, P.-L., Chen, C.-Y., Nguyen, T. Y., et al. (1997). Intraplate extension prior to continental extrusion along the Ailao Shan-Red River shear zone. *Geology* 25, 311–314. doi:10.1130/0091-7613(1997)025<0311:ieptce>2.3.co;2

Crandell, E. D., Riginos, C., Bird, C. E., Liggins, L., Tremi, E., Beger, M., et al., and Contributing Members of the Diversity of the Indo-Pacific Network and Gaither, M. R. (2019). The molecular biogeography of the Indo-Pacific: testing hypotheses with multispecies genetic patterns. *Glob. Ecol. Biogeogr.* 28, 943–960. doi:10.1111/geb.12905

Deng, J., Wang, Q., Li, G., Li, C., and Wang, C. (2014). Tethys tectonic evolution and its bearing on the distribution of important mineral deposits in the Sanjiang region, SW China. *Gondwana Res.* 26, 419–437. doi:10.1016/j.gr.2013.08.002

Ding, W., and Sun, Z. (2020). Marginal basins of the NW pacific and eastern Eurasia. *Int. Geol. Rev.* 62, 781–788. doi:10.1080/00206814.2020.1731718

Fan, J. J., Niu, Y., Liu, Y. M., and Hao, Y. J. (2021). Timing of closure of the meso-tethys ocean: constraints from remnants of a 141–135 Ma ocean island within the bangong–nujiang suture zone, Tibetan plateau. *Geol. Soc. Am. Bull.* 133, 1875–1889. doi:10.1130/b35896.1

M. F. J. Flower, S.-L. Chung, C.-H. Lo, and T.-Y. Lee (Editors) (1998). "Mantle Dynamics and Plate Interactions in East Asia," *AGU geodynamic series 27*, 419.

Golonka, J., Gahagan, L., Krobicki, M., Marko, F., and Oszczypko, N. (2006). "Plate-tectonic evolution and paleogeography of the circum-Carpathian region," in *The carpathians and their foreland: geology and hydrocarbon resources*. Editors J. Golonka and F. J. Picha (Tulsa, USA: American Association of Petroleum Geologists Memoir), 11–46.

Hall, R. (2002). Cenozoic geological and plate tectonic evolution of SE Asia and the SW Pacific: computer-based reconstructions, model and animations. *J. Asian Earth Sci.* 20, 353–431. doi:10.1016/s1367-9120(01)00069-4

Hall, R. (2017). Southeast Asia: new views of the geology of the Malay Archipelago. *Annu. Rev. Earth Planet. Sci.* 45, 331–358. doi:10.1146/annurev-earth-063016-020633

Hobbs, J.-P., Frisch, A. J., Allen, G. R., and Van Herwerden, L. (2009). Marine hybrid hotspot at Indo-Pacific biogeographic border. *Bio. Lett.* 5, 258–261. doi:10.1098/rsbl.2008.0561

Hutchinson, C. S. (2014). Tectonic evolution of southeast Asia. *Bull. Geol. Soc. Malays.* 60, 1–18. doi:10.7186/bgsm60201401

Kapp, P., and Decelles, P. (2019). Mesozoic-Cenozoic geological evolution of the Himalayan-Tibetan orogen and working tectonic hypotheses. *Am. J. Sci.* 319, 159–254. doi:10.2475/03.2019.01

Lee, T.-Y., and Lawver, L. A. (1995). Cenozoic plate reconstruction of Southeast Asia. *Tectonophysics* 251, 85–138. doi:10.1016/0040-1951(95)00023-2

Lo, C.-H., Chung, S.-L., Lee, T.-Y., and Wu, G. (2002). Age of the Emeishan flood magmatism and relations to Permian-Triassic boundary events. *Earth Planet. Sci. Lett.* 198, 449–458. doi:10.1016/s0012-821x(02)00535-6

Mann, P., and Taira, A. (2004). Global tectonic significance of the Solomon Islands and Ontong Java Plateau convergent zone. *Tectonophysics* 389, 137–190. doi:10.1016/j.tecto.2003.10.024

Metcalfe, I. (2011). Tectonic framework and phanerozoic evolution of sundaland. *Gondwana Res.* 19, 3–21. doi:10.1016/j.gr.2010.02.016

Metcalfe, I. (2013). Gondwana dispersion and Asian accretion: tectonic and palaeogeographic evolution of eastern Tethys. *J. Asian Earth Sci.* 66, 1–33. doi:10.1016/j.jseaes.2012.12.020

Metcalfe, I. (2017). Tectonic evolution of sundaland. *Bull. Geol. Soc. Malays.* 63, 27–60. doi:10.7186/bgsm63201702

Mitchell, A., Chung, S. L., Oo, T., Lin, T. H., and Hung, C. H. (2012). Zircon U–Pb ages in Myanmar: magmatic–metamorphic events and the closure of a neo-Tethys ocean? *J. Asian Earth Sci.* 56, 1–23. doi:10.1016/j.jseaes.2012.04.019

Mitchell, A. H. G. (1981). Phanerozoic plate boundaries in mainland SE Asia, the himalayas and tibet. *J. Geol. Soc. Lond.* 138, 109–122. doi:10.1144/gsjgs.138.2.0109

Mitchell, A. H. G. (1984). Post-Permian events in the Zangbo "suture" zone, Tibet. *J. Geol. Soc. Lond.* 141, 129–136. doi:10.1144/gsjgs.141.1.0129

Scotese, C. R. (2016). *PALEOMAP PaleoAtlas for GPlates and the PaleoData plotter programs*. PALEOMAP Project. Available at: http://www.earthbyte.org/paleomap–paleaatlas–for-gpates/.

Searle, M. P., Whitehouse, M. J., Robb, L. J., Ghani, A. A., Hutchison, C. S., Sone, M., et al. (2012). Tectonic evolution of the Sibumasu–Indochina terrane collision zone in Thailand and Malaysia: constraints from new U–Pb zircon chronology of SE Asian tin granitoids. *J. Geol. Soc. Lond.* 169, 489–500. doi:10.1144/0016-76492011-107

Seton, M., Müller, R. D., Zahirovic, S., Gaina, C., Torsvik, T., Shephard, G., et al. (2012). Global continental and ocean basin reconstructions since 200Ma. *Earth-Sci. Rev.* 113, 212–270. doi:10.1016/j.earscirev.2012.03.002

Sone, M., and Metcalfe, I. (2008). Parallel tethyan sutures in mainland Southeast Asia: new insights for palaeo-tethys closure and implications for the indosinian orogeny. *C. R. Geosci.* 340, 166–179. doi:10.1016/j.crte.2007.09.008

Spalding, M. D., Fox, H. E., Allen, G. R., Davidson, N., Ferdaña, Z. A., Finlayson, M., et al. (2007). Marine ecoregions of the World: a bioregionalization of coastal and shelf areas. *Biosci* 57, 573–583. doi:10.1641/b570707

Ueno, K. (2003). The Permian fusulinoidean faunas of the Sibumasu and Baoshan blocks: their implications for the paleogeographic and paleoclimatologic reconstruction of the Cimmerian Continent. *Palaeogeogr. Palaeocl.* 193, 1–24. doi:10.1016/s0031-0182(02)00708-3

frontiers | Frontiers in Earth Science

TYPE Original Research
PUBLISHED 11 January 2023
DOI 10.3389/feart.2022.1092823

OPEN ACCESS

EDITED BY
Shenghong Yang,
University of Oulu, Finland

REVIEWED BY
Wei Wang,
China University of Geosciences Wuhan, China
Gaoxue Yang,
Chang'an University, China

*CORRESPONDENCE
M. P. Manu Prasanth,
manu@earth.sinica.edu.tw

SPECIALTY SECTION
This article was submitted to Petrology, a section of the journal Frontiers in Earth Science

RECEIVED 08 November 2022
ACCEPTED 28 December 2022
PUBLISHED 11 January 2023

CITATION
Manu Prasanth MP, Pang K-N, Hari KR, Sahoo BB, Ravindran A and Iizuka Y (2023), Geochemistry of Precambrian dyke swarms in the Singhbhum craton, India: Implications for recycled crustal components in the mantle source. *Front. Earth Sci.* 10:1092823. doi: 10.3389/feart.2022.1092823

Geochemistry of Precambrian dyke swarms in the Singhbhum craton, India: Implications for recycled crustal components in the mantle source

M. P. Manu Prasanth[1]*, Kwan-Nang Pang[1], K. R. Hari[2], Bibhuti Bhusan Sahoo[2,3], Arathy Ravindran[4,5] and Yoshiyuki Iizuka[1]

[1]Institute of Earth Sciences, Academia Sinica, Taipei, Taiwan, [2]School of Studies in Geology and Water Resource Management, Pt. Ravishankar Shukla University, Raipur, India, [3]Central Ground Water Board (CGWB), Northeastern region, Guwahati, India, [4]Institute of Geochemistry and Petrology, ETH Zurich, Zurich, Switzerland, [5]Institute of Geological Sciences, University of Bern, Zurich, Switzerland

The Singhbhum craton, eastern India records multiple stages of emplacement of Precambrian dyke swarms with contrasting petrogenetic models proposed for their formation. In this study, we document elemental and Sr-Nd isotopic data for three major dyke swarms in the southern part of the craton, including the ca. 2.7 Ga Ghatgaon dyke swarm, the Early Proterozoic Keonjhar dyke swarm and the ca. 1.76 Ga Pipilia dyke swarm. Dyke compositions are dominated by basalt and basaltic andesite with minor andesite, showing trace element signatures typical of continental crustal rocks. Age-corrected Nd isotopic data for Ghatgaon (ε_{Ndt} = −4.8 to + 4.6), Keonjhar (ε_{Ndt} = −11.9 to + 3.8), and Pipilia (a single sample with ε_{Ndt} = −8.8) dyke swarms display substantial variations. The lack of magma compositions that could indicate the presence of elevated mantle potential temperature among the rocks suggests melting regime was likely similar to the ambient mantle. The Dy/Yb and Dy/Dy* systematics of the rocks indicates melting occurred between spinel-stable depths and the spinel-garnet transition zone. The dominantly mafic compositions of the rocks and ubiquitous continental crustal trace element signature are best explained by peridotite source with recycled crustal components, probably in the form of pyroxenites. Our new Nd isotopic data, which argue against any simple secular evolution trend invoked in previous studies, indicate that crustal recycling was likely an episodic phenomenon rather than a discrete, single-stage process since the Archean. Geochemical modelling indicates that a sublithospheric mantle source with (10% or less) recycled crustal components satisfactorily explains the trace element variations of the dyke swarms.

KEYWORDS

precambrian, singhbhum craton (India), dyke swarms, mantle melting, crustal recycling

1 Introduction

Giant radiating dyke swarms represent conspicuous extensional structures that are widespread throughout Archean cratons and have been commonly used to reconstruct the rifting history of cratonic blocks (Wilson, 1990; Bleeker and Ernst, 2006; Söderlund et al., 2010). For example, geochronologic and paleomagnetic data for Neoarchean-Paleoproterozoic dyke swarms led to the identification and characterization of several distinct, transient, late Archean super cratons (e.g., Scalvia, Superia and Vaalbara). Although by no means universal, giant

radiating dyke swarms are considered to represent plumbing systems feeding large igneous provinces (LIPs) (Ernst, 2014; Srivastava et al., 2019; Buchan and Ernst, 2021). Dominated by basaltic compositions, the dyke swarms and their volcanic associations have been used to probe mantle source characteristics, conditions of magma genesis and processes of magma differentiation (Huppert et al., 1985; Bédard et al., 2021).

If giant radiating dyke swarms are indeed related to LIPs, then anomalously high mantle potential temperature (T_P) and hence mantle plumes might be implied. However, mantle plumes do not represent a unified explanation even for Phanerozoic LIPs. For example, the Central Atlantic Magmatic Province (CAMP) and North Atlantic Large Igneous Province (NALIP) are explained by internal heating of the upper mantle beneath thick lithosphere as a result of long-term continental insulation (Korenaga, 2004; Coltice et al., 2007; Hole, 2015; Whalen et al., 2015). The magmatism and subsequent rifting events have been ascribed to plate boundary forces associated with the breakup of Pangea (Manu Prasanth et al., 2022). Further, it has been proposed that the mantle sources of NALIP and CAMP contain significant amounts of recycled crustal materials (Korenaga, 2004; Whalen et al., 2015; Marzoli et al., 2018). Such unusually fertile sources could explain the large magma volumes associated with LIPs under ambient mantle thermal regimes (Korenaga, 2004; Coltice et al., 2007). Whether or not that applies to Precambrian dyke swarms, however, has not been explored in sufficient detail.

Precambrian dyke swarms of distinct generations are well preserved in the Singhbhum craton, India. For example, seven distinct groups of dyke swarms are identified based on emplacement ages spanning from Neoarchean to Paleoproterozoic (ca. 2.8–1.7 Ga) and are correlated with dyke swarms in other cratonic masses worldwide (Srivastava et al., 2019). However, the source and magmatic processes responsible for generating the Singhbhum dyke swarms are still controversial, with proposed origins involving a mantle plume (Srivastava et al., 2019), plume-triggered melting of subcontinental lithospheric mantle (SCLM) (Pandey et al., 2021) or interaction between enriched-depleted MORB mantle (DMM) and low degree partial melts of metasomatized SCLM (Adhikari et al., 2021). Here, we document bulk rock geochemical and Sr-Nd isotopic data to explore the mantle source characteristics and melting dynamics of the Neoarchean Ghatgaon dyke swarm (ca. 2.76–2.75 Ga), the Early Paleoproterozoic Keonjhar dyke swarm, and the Paleoproterozoic Pipilia dyke swarm (ca. 1.77 Ga) in the southern part of the Singhbhum craton (Shankar et al., 2018; Dasgupta et al., 2019; Srivastava et al., 2019; Adhikari et al., 2021; Pandey et al., 2021). Based on our new data and published data, we show that the generation of the three sets of dyke swarms most likely involved mantle sources that contain episodically recycled crustal materials.

2 Geological background

The Singhbhum craton, in eastern India, has prolonged sedimentary and magmatic records spanning the Paleoarchean to Neoproterozoic (Olierook et al., 2019). The earliest phase of major crustal growth likely occurred between 3.55 Ga and 3.32 Ga in the Paleoarchean (Upadhyay et al., 2014; Dey et al., 2017; Pandey et al., 2019), manifested in the emplacement of Paleo-Mesoarchean granitoids over two intervals at ~3.45–3.44 Ga and ~3.35–3.34 Ga, and of sodic tonalites and trondhjemites of the older metamorphic group at ~3.45–3.44 Ga. Contemporaneous evolution of older metamorphic group and parts of Iron ore group are noticed at ca. 3.5 to 3.3 Ga (Olierook et al., 2019). The craton also records earliest episode of crustal recycling during the Eoarchean. The Eoarchean detrital zircons record the crustal generation by recycling of Hadean felsic crust formed at ~4.3 to 4.2 Ga and ~3.95 Ga (Sreenivas et al., 2019). There is evidence for a drastic shift from unradiogenic to radiogenic Hf isotope compositions during Paleoarchean and Mesoarchean (~3.5 Ga to 3 Ga), which has been correlated with change in geodynamic regime of the craton (Sreenivas et al., 2019). The craton was stabilized at the end of the Paleoarchean (ca. 3.2 Ga), a period during which potassic granites formed, albeit in a sporadic manner, throughout the craton (Olierook et al., 2019; Pandey et al., 2019; Chaudhuri et al., 2022). The evolved Hf and O isotopic signatures in detrital zircons point out that reworking of existing crust was dominant at 2.67–2.35 Ga (Wang et al., 2022)

The discrete episodes of Precambrian dyke emplacement in Singhbhum craton are correlated with plumbing systems of Precambrian LIPs (Kumar et al., 2017; Srivastava et al., 2019). The Neoarchean to Paleoproterozoic (ca. 2.8–1.7 Ga) dyke swarms of the craton have been divided into seven distinct groups (Srivastava et al., 2019), and are correlated with other cratons to establish the juxtaposition of ancestral cratonic masses, that constitutes Precambrian supercontinents. The earliest dyke swarms known to have emplaced so far are ~2.8 Ga Keshargaria dyke swarm and 2.76–2.75 Ga Ghatgaon dyke swarm, which were correlated to mafic volcanic-intrusive units in the Pilbara and Kapaval Cratons (Kumar et al., 2017; Shankar et al., 2018). Kumar et al. (2017) proposed that at ~2.77 Ga, the Singhbhum, Pilbara, and Kapaval cratons were proximal to each other. Based on the paleomagnetic pole of the 1.75 Ga Pipilia swarm, Shankar et al. (2018) proposed that the Singhbhum, North China, and Baltica cratons were proximal to each other. Moreover, dyke swarms of adjacent eastern Dharwar and Bastar cratons have also been correlated with the Singhbhum dyke swarms (Pandey et al., 2021). Earlier studies named Precambrian mafic dyke swarms of the Singhbhum craton as Newer dolerites. In a recent study, based on the cross-cutting relationships, orientations, and U-Pb and Pb-Pb baddeleyite ages, Srivastava et al. (2019) classified the dyke swarms in the Singhbhum craton into seven groups: 1) NE-SW trending Keshargaria dyke swarm (ca. 2.8 Ga), 2) NNE-SSW to NE-SW-trending Ghatgaon dyke swarm (ca. 2.76–2.75 Ga), 3) NE-SW to ENE-WSW trending Kaptipada dyke swarm (2.26 Ga), 4) early Paleoproterozoic E-W to ENE-WSW Keonjhar dyke swarm, 5) Mid Proterozoic Bhagamunda dyke swarm, 6) WNW-ESE Pipilia dyke swarm (ca. 1.77 Ga), and 7) NS-NNE Barigaon dyke swarm. As indicated above, only four out of seven were radiometrically dated, and others are classified based on the cross-cutting relationship (Srivastava et al., 2019). The focus of this study is the Ghatgaon dyke swarm, the Keonjhar dyke swarm, and the Pipilia dyke swarm (Figure 1), the features of which are described in detail below.

The Ghatgaon dyke swarm is widely distributed throughout the Singhbhum craton and exhibits a general NE-SW trend (Figure 2A). Occurrences of the dykes are more extensive in the southern part of Singhbhum granites, especially north of Bagamunda and south of Pipilia. Apart from the widely distributed NE-SW trending dykes (Srivastava et al., 2019), some dykes exhibit E-W and N-S trends. Samples were collected from Badamahuladiha, Bhimkund, and Dhenkikote regions, which are in the southern part of the craton.

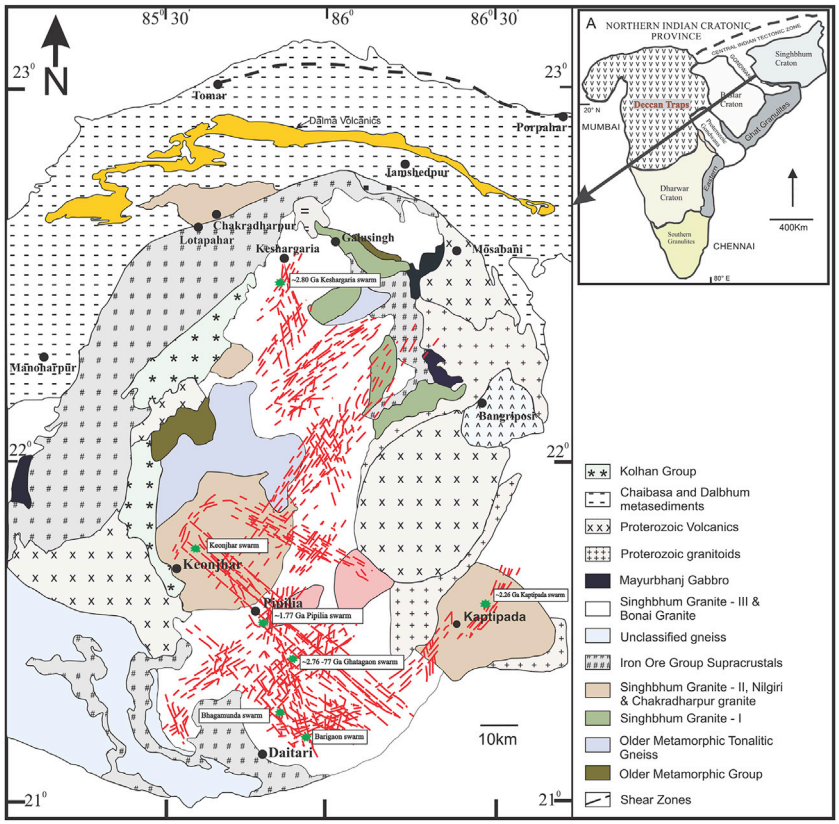

FIGURE 1
Generalized geological map of the Singhbhum craton showing the distribution of major dyke swarms (modified after Kumar et al., 2017; Srivastava et al., 2019).

The Keonjhar dyke swarm is mostly found in the southern part of the Singhbhum granite complex. Most of the Keonjhar dykes are E-W trending (Srivastava et al., 2019), although dykes exhibiting N-S and NE-SW trends could also be identified. Most of the dykes are concentrated in the Keonjhar area (Figure 2D). We collected samples from Dhurpada, Baliaguda and Ghadghadi regions. Srivastava et al. (2019) identified sporadic occurrences of Keonjhar dykes in the northern segment of Singhbhum granites and proposed an overall radiating pattern. The Pipilia dyke swarm is mostly concentrated in the Pipilia region, which is located in the southern part of Singhbhum granites. Srivasatva et al. (2019) proposed a WNW-ESE trend for the Pipilia dykes. According to our field observation, Pipilia dyke swarm exhibit N-S and NW-SE trends. Samples were collected from Pipilia and Dumuria regions. Sampling details and coordinates are given in Table 1.

3 Petrography

Most samples exhibit textures and mineralogy typical of dolerites with ubiquitous clinopyroxene and plagioclase (Figures 2B, C). Relics of olivine are observed in places among the samples. Opaque oxides (mostly Ti-magnetite and minor ilmenite) are also present sporadically. Some samples contain two populations of plagioclase, including those enclosed in the pyroxenes and also as larger zoned crystals. Petrographic observations point to the following crystallization sequence: olivine > clinopyroxene > plagioclase > Fe-Ti oxides > interstitial liquids. Most samples exhibit variable signs of alteration, the plagioclases are often replaced by clay minerals or sericite. Primary olivines, though present in small fractions, are completely replaced by iddingsite or serpentine. Pyroxenes are mostly replaced by chlorites and amphiboles.

4 Analytical methods

4.1 Major and trace element analysis

Bulk rock major and trace element analyses of fine powdered samples were carried out at CSIR-National Geophysical Research Institute, Hyderabad. The major elements were analyzed using XRF (Phillips Axios mAX4), followed by pressed pellet sample preparation technique. The details of the analytical methods, such as instrument calibration, data acquisition, accuracy, and detection limits are provided in Krishna et al. (2016). Trace elements were analyzed using AttoM HR-ICP-MS (Nu Instruments, United Kingdom). 50 mg of finely powdered samples were taken in Savillex® vials and 10 mL of the acid mixture containing HF and HNO_3 (7:3 ratio) was added. Further, the vials were heated at 150°C for 48 h and a clear solution was obtained. 1 mL of $HClO_4$ was added and the sample solutions were dried to form a solid residue. Twenty ml of 1:1 ratio HF and Millipore water mixture was added to the vials and heated at 80°C

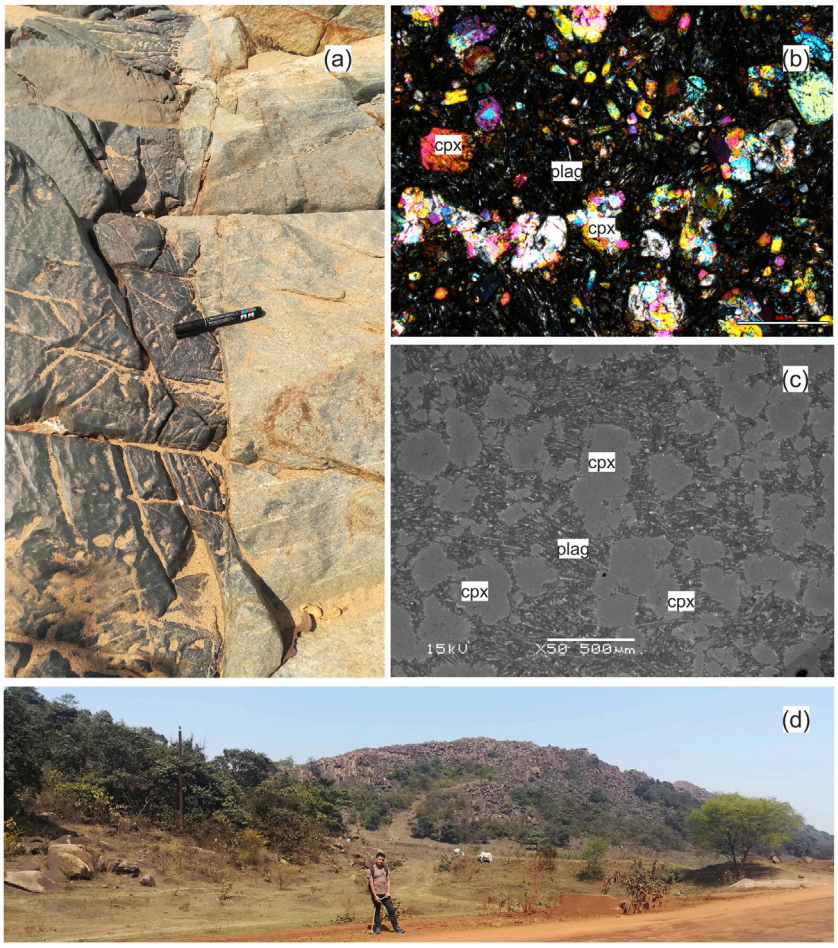

FIGURE 2
Field and petrographic images of the dyke swarms of Singhbhum craton. The field photographs of **(A)** the Ghatgaon dyke swarm shows a cross-cutting relationship with Paleoarchean TTGs and **(D)** the exposure of the Keonjhar dyke swarm in the Dhurpada area. **(B)** Petrographic and **(C)** backscattered images of the Ghatgaon dyke swarm (KD-09) show the clinopyroxene phenocrysts and the groundmass dominantly of plagioclases.

for 1 h. The sample solutions were further transferred to 25 mL conical flasks, and 5 mL of 1 ppm Rh was added as an internal standard. To obtain the optimal total dissolved solids (TDS) level, the sample solution was initially diluted to 250 mL, and 5 mL of the diluted solution is further diluted to 50 mL. The standards UB-N, JP-1 and blank solutions were analyzed along with the samples. The details of the sample digestion method, instrumental parameters, data acquisition, and quality are described in Satyanarayanan et al. (2018).

4.2 Sr-Nd isotopic analysis

Sample preparation for isotopic measurements was carried out at the Institute of Geological Sciences, University of Bern, Switzerland. Around 90 mg of finely powdered sample was spiked with ^{87}Rb-^{84}Sr and ^{149}Sm-^{150}Nd spikes in Savillex® beakers by keeping an empiric error magnification of ~1.5–2 (Stracke et al., 2014). The samples underwent a digestion procedure using concentrated HF, HNO_3 and HCl solutions separately for 2 days each at 120°C. Each step was carried out after drying the samples on a hotplate at low temperatures. After drying the samples, the samples were loaded on DOWEX® AG 50 W-X8 (200–400 mesh) cation columns to separate Rb and Sr The loading reagent was 2.5 M HCl. Rubidium and Sr cuts were collected using 2.5 M HCl with a distinct eluting step in between. Chemical separation of Sm from Nd was done using the procedure outlined by Ravindran et al. (2021).

The Rb and Sr isotopic measurements were done at the Institute of Geological Sciences, University of Bern, Switzerland. The spiked samples were measured for Rb and Sr isotopes on a Thermo Scientific™, Neptune Plus™ multi-collector inductively coupled plasma mass spectrometer (MC-ICP-MS). Dry plasma mode using a Cetac Aridus II desolvation system was used for efficient sample introduction and sensitivity during the measurements on the multi-collector ICPMS. The standards and samples were measured at the same concentration for better accuracy. Background measurements of the washing acid reagent, 0.5 M HNO_3, were subtracted from each measurement of sample and standard solutions. Interferences of ^{84}Kr and ^{86}Kr on ^{84}Sr and 86Sr were monitored and were close to the baseline ($<10^{-5}$ V). Total procedural blanks were < 500 pg that were used for the blank correction of the samples.

The Sr isotopic ratios were corrected for mass bias using exponential law and iteration (Stracke et al., 2014) with a

TABLE 1 Sample details of the dyke swarms of Singhbhum craton.

Sample no.	Area	Trend	Coordinates
Ghatgaon swarm; emplacement age = 2.76–2.75 Ga[1]			
KD-6A	Badamahuladiha	E-W	N21°36′40.1″/E085°39′00.1″
KD-6B	Badamahuladiha	E-W	N21°36′40.1″/E085°39′00.1″
KD-9	Bhimkund	N-S	N21°33′20.1″/E086°01′02.2″
KD-11	Bhimkund	N-S	N21°33′18.5″/E086°01′14.0″
KD-12A	Dhenkikote Toll	NE-SW	N21°31′48.5″/E085°48′29.6″
KD-12B	Dhenkikote Toll	NE-SW	N21°31′48.5″/E085°48′29.6″
KD-13	Dhenkikote 2	NE-SW	N21°32′51.6″/E085°47′50.9″
KD-14	Dhenkikote 2	NE-SW	N21°32′32.5″/E085°47′18.3″
Keonjhar swarm; emplacement age = early Paleoproterozoic[1]			
KD-1A	Dhurpada	E-W	N21°39′18.5″/E085°35′29.4″
KD-1B	Dhurpada	E-W	N21°39′18.5″/E085°35′29.4″
KD-2A	Dhurpada	E-W	N21°39′08.9″/E085°35′07.3″
KD-2B	Dhurpada	E-W	N21°39′08.9″/E085°35′07.3″
KD-4	Baliaguda	NE-SW	N21°39′54.8″/E085°35′17.2″
KD-5	Baliaguda	NE-SW	N21°39′51.8″/E085°35′13.2″
KD-20	Ghadghadi	N-S	N21°37′37.2″/E085°38′18.9″
KD-21	Ghadghadi	N-S	N21°37′34.1″/E085°38′17.3″
Pipilia swarm; emplacement age = 1.77 Ga[2]			
KD-7A	Dumuria	N-S	N21°34′20.1/E085°58′08.2″
KD-7B	Dumuria	N-S	N21°34′20.1″/E085°58′08.2″
KD-15A	Pipilia	NW-SE	N21°34′25.7″/ E085°46′21.06″
KD-15B	Pipilia	NW-SE	N21°34′25.7″/ E085°46′21.06″
16A	Pipilia	NW-SE	N21°34′15.7″/E085°46′28.6″
KD-16B	Pipilia	NW-SE	N21°34′15.7″/E085°46′28.6″
KD-17	Pipilia 2	N-S	N21°34′00.1″/E085°45′13.4″
KD-18	Pipilia 2	N-S	N21°33′58.1″/E085°45′22.5″
KD-19A	Pipilia 2	N-S	N21033′58.1″/E085045′22.5″
KD-19B	Pipilia 2	N-S	N21°33′58.1″/E085°45′22.5″

Age references: 1) Srivastava et al. (2019), 2) Shankar et al. (2014).

normalization ratio of $^{86}Sr/^{88}Sr$ = 0.1194. The NIST standard SRM® 987 yielded $^{87}Sr/^{86}Sr$ = 0.710253 ± 0.000012 (2SD; *n*=8). The Rb isotopic ratios were corrected for mass bias by the standard-sample-standard bracketing method using the exponential law.

Neodymium and Sm isotopes were measured on a Thermo Scientific™, Neptune™ Multi Collector ICPMS at the Institute of Geochemistry and Petrology, ETH Zurich, Switzerland. The same measurement technique used for Rb and Sr isotope measurements was carried out for Nd and Sm isotope measurements. Additionally, apart from using a normalization ratio of $^{146}Nd/^{144}Nd$ = 0.7219, Nd isotope ratios were also internally normalized for instrumental mass bias following Vance and Thirlwall (2002). Standard JNdi yielded an average $^{143}Nd/^{144}Nd$ = .512084 ± 0.000005 (2σ; *n* = 14), with an external reproducibility of 14 ppm.

4.3 Clinopyroxene composition

Analysis of clinopyroxene composition was performed at Institute of Earth Sciences, Academia Sinica, Taiwan. Selected samples were first examined with a scanning electron microscope (JEOL SEM JSM-6360LV) for microtextural observation, qualitative mineral identification, and spotting sites of interest for subsequent electron probe microanalysis (EPMA), which was undertaken by an electron probe micro analyzer (JEOL EPMA JXA-8900 R) equipped with four wavelength dispersive spectrometers (WDS). Secondary electron images and backscattered electron images were used to guide the analysis of the target positions of minerals. For quantitative analysis, a 1 μm beam was used at an acceleration voltage of 15 kV with a beam current of 12 nA. Corrections on the measured X-ray intensities were carried out by oxide-ZAF method using the standard calibration of synthetic standard minerals with various diffracting crystals. The standard minerals analyzed are as follows: wollastonite for Si with TAP crystal, rutile for Ti with PET crystal, corundum for Al (TAP), chromium oxide for Cr (PET), hematite for Fe with LiF crystal, Mn-oxide for Mn (PET), periclase for Mg (TAP), nickel oxide for Ni (LiF), wollastonite for Ca (PET), albite for Na (TAP), apatite for P (PET) and adularia for K(PET). Peak counting for each element and both upper and lower baseline X-rays counted for 10 s and 5 s, respectively. Standards run as unknowns yielded relative standard deviations of < 1% for Si, Na and K, and < 0.5% for other elements. Detection limits were less than 600 ppm for all elements. Analyses were made within the cores of mineral grains to minimize the effects of zonation, alteration and re-equilibration. The results are presented in Supplementary Table S1.

5 Results

5.1 Major and trace element geochemistry

Major and trace element data for samples from the Ghatgaon, Keonjhar and Pipilia dyke swarms are given in Supplementary Table

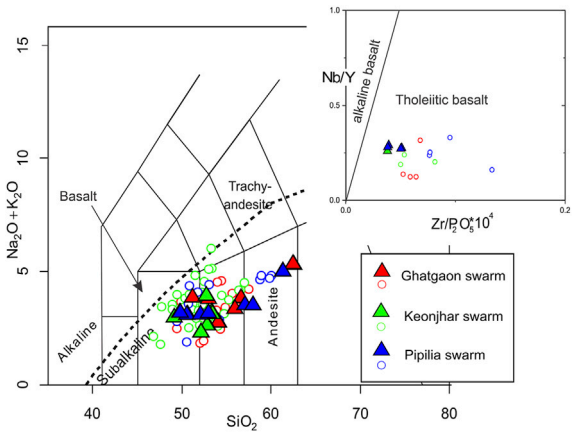

FIGURE 3
Classification of Precambrian dyke swarms of Singhbhum craton on a total alkali *versus* Silica diagram (Le Bas et al., 1986). Three major dyke swarms in the southern part of Singhbhum granite are considered for this study, including Ghatgoan (2.76 Ga), Keonjhar (Early Proterozoic) and Pipilia Swarm (1.77 Ga). Open circles indicate data from previous studies (Dasgupta et al., 2019; Adhikari et al., 2021; Pandey et al., 2021). Solid triangles indicate samples of the present study. The basalt discrimination diagram (inset) between alkaline and tholeiitic basalts is after Winchester and Floyd (1976). The samples plotted in the basalt discrimination diagram are limited to SiO_2 40 to 51 wt%. The dashed line separating alkaline and sub-alkaline compositions on the TAS plot is from Irvine and Baragar (1971).

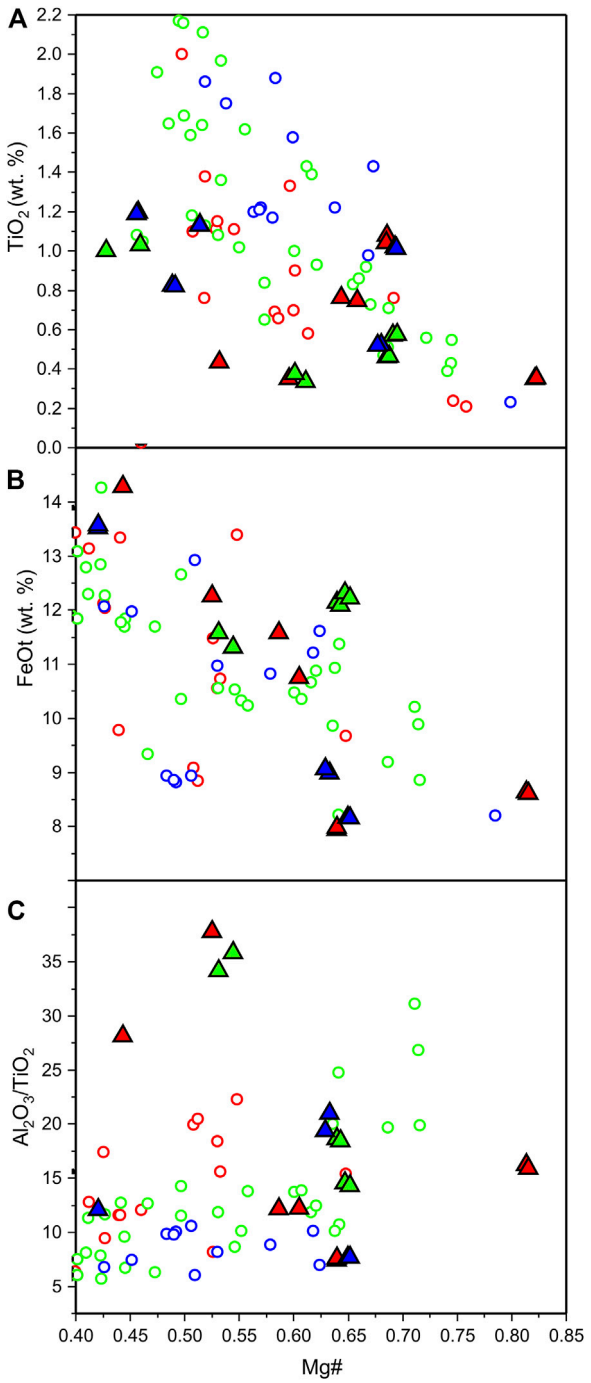

FIGURE 4
The variations of whole rock Mg-number (Mg#) against **(A)** TiO_2, **(B)** FeOt and **(C)** Al_2O_3/TiO_2. The symbols are the same as in Figure 3.

S2. Geochemical variations of the samples range from basalt, basaltic andesite to andesites (Figure 3), showing substantial compositional variations. The samples from Keonjhar exhibit compositional variations from basalt to andesites with 3.7–12.8 wt% MgO and 11.3 to 15.8 wt% FeO_t. Most of the Ghatgaon samples have 6.4 to 9.2 wt% MgO, except two samples (KD-12A, KD-12B) collected from Dhenkikote that have ~21 wt% MgO. Such high MgO is consistent with their cumulate nature. From our data and previous studies (Dasgupta et al., 2019; Adhikari et al., 2021; Pandey et al., 2021) the basalt compositions are filtered out and further plotted into Zr/P_2O_5*10^4 vs. Nb/Y diagram of Winchester and Floyd (1976) to discriminate between alkaline and tholeiitic compositions (Figure 3, inset). The dyke swarms of Ghatgaon, Keonjhar and Pipilia exhibit tholeiitic basalt compositions. A relative compositional variability is observed mainly in Ghatgaon and Pipilia dyke swarms. No systematic trend exists between TiO_2 *versus* Mg# (Figure 4). Variations in Al_2O_3/TiO_2 *versus* Mg# (Figure 4) in relatively less evolved (Mg# >50) lavas indicate moderate degree of partial melting from the mantle source (Nesbitt et al., 1979).

All samples display LREE-enriched patterns in chondrite-normalized variation diagrams (Figure 5). Though the REE patterns of Pipilia swarms are subparallel, the variations in other dyke swarms highlight the differences between the compositional variability of individual dyke swarms. Especially, sample KD-21of Keonjhar dyke swarm exhibit relatively enriched REE patterns (Figure 5C). In the multi-element diagram, compositional variations can be observed in individual dyke swarms, pointing towards a complex petrogenetic relation (Figure 5). Almost all samples exhibit negative Ti anomalies, positive Pb anomalies and negative Nb anomalies (Figure 5). The Ghatgaon samples show negative Y anomalies, whereas the Keonjhar and Pipilia samples exhibit either negative or positive Y anomalies. Negative Sr anomalies relative to Pr and Nd can also be noticed for most of the samples.

5.2 Sr-Nd isotopic compositions

The Sr-Nd isotopic data for nine selected samples with basaltic composition are listed in Table 2, which include four samples from Ghatgaon dyke swarm, four samples from Keonjhar dyke swarm and one sample from the Pipilia dyke swarm. They display large variations. For instance, initial $^{87}Sr/^{86}Sr$ of samples from Keonjhar dyke swarm ranges from .705543 to .707282, and ε_{Ndt} values from -12.0 to + 3.9 (Table 2). The lack of negative correlation between them (Figure 6) indicates the Rb-Sr isotopic system might have been disturbed by post-magmatic processes (e.g., alteration); the Sm-Nd isotopic system is relatively insensitive to such processes. Both positive and negative ε_{Nd} values are evident for the Ghatgaon and Keonjhar samples. In Keonjhar dyke swarm, the sample that exhibits relatively enriched REE patterns (KD-21) also shows an enriched ε_{Ndt} value of -12. A single sample (KD-19A) from the Pipilia dyke swarm yielded an ε_{Nd} value of -8.8.

5.3 Clinopyroxene composition

Due to the altered nature of the samples, representative samples containing fresh clinopyroxene are selected from the three dyke swarms for mineral chemical analysis. The selected samples are from the Keonjhar and Ghatgaon dyke swarms; no Pipilia samples were selected. Clinopyroxene in the Keonjhar samples exhibits mostly augitic compositions ($En_{48-36}Wo_{44-34}Fs_{22-13}$), and are characterized by 51–54 wt% of SiO_2 and 13–17 wt% MgO. Clinopyroxene in the Ghatgaon samples has compositions varying from pigeonite to augite ($En_{50-37}Wo_{36-11}Fs_{44-19}$) (Figure 7A). All analyzed clinopyroxene have relatively low TiO_2. Further, most clinopyroxene compositions plot on or below the equilibrium curve

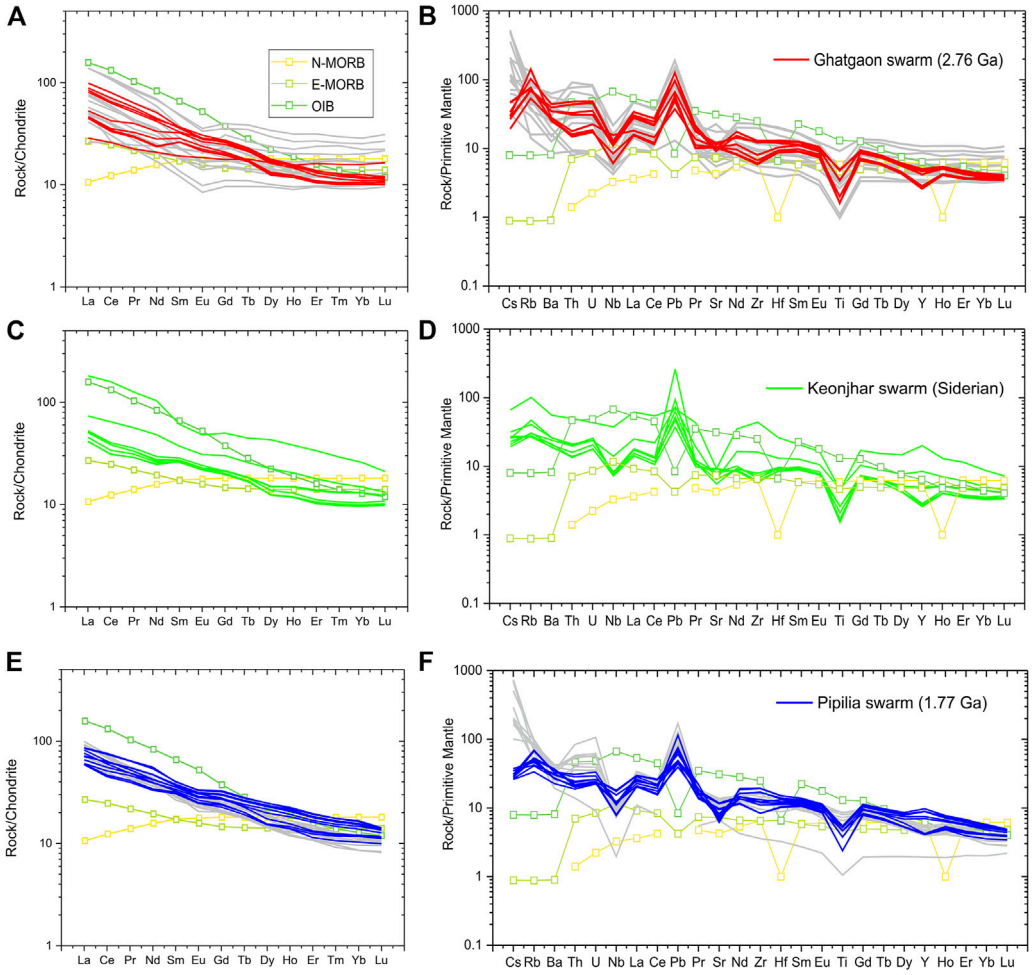

FIGURE 5
Chondrite normalized rare earth element (REE) patterns and primitive mantle normalized multi-element diagram of **(A, B)** Ghatgaon dyke swarm **(C, D)** Keonjhar dyke swarm **(E, F)** Pipilia dyke swarm. Data from the previous studies (grey lines) are also shown for comparison (Adhikari et al., 2021; Pandey et al., 2021). In the primitive mantle normalized diagram, the elements are arranged with increasing incompatibility in mantle rocks from right to left. The normalizing values of chondrite and primitive mantle are from Sun and McDonough (1989).

in the Rhodes diagram (Figure 7B), indicating most clinopyroxene grains formed by equilibrium crystallization. In other words, those grains crystallized from or continually equilibrated with the groundmass that eventually solidified as the framework of the dolerites. Compositional variations in the clinopyroxenes are also exhibit significant overlap with mid-ocean ridge basalts (MORB) and Island arc tholeiites (IAT) (Figure 7C).

6 Discussion

The samples analyzed in this study do not meet the criteria of primitive magmas in equilibrium with mantle peridotites, that is, relatively high Ni (>400–500 ppm), Cr (>1,000 ppm) and Mg# (>70) (Wilson, 1989). Instead, modest values of those geochemical parameters indicate derivation from mantle-derived magmas that underwent differentiation before solidification as the dykes. Below, we focus on three petrogenetic aspects of the dyke swarms that are indicated by available data: the origin of continental crust-like trace element signature, secular variations of Nd isotopes, characteristics of the magma source and conditions of melting.

6.1 Origin of crustal signature

The incompatible trace element patterns of the Singhbhum dykes are markedly different from typical patterns of N-MORB and OIB (Sun and McDonough, 1989). Instead, the patterns of the dykes display strong resemblance to continental crustal rocks (Figure 5). Such a trace element signature is commonly explained by assimilation of continental crustal rocks by mantle-derived magmas during their ascent to the surface, magma derivation from a mantle wedge above a subduction zone or a mantle source already modified by the crustal components. Below, we address these mechanisms in detail.

We have assessed the possibilities of crustal contamination from geochemical signatures (Figure 8A). The Nb and Th ratios have negligible effects on fractional crystallization and mantle melting, therefore the Th/Nb ratios can be used to evaluate the effect of

TABLE 2 Sr and Nd isotope data of the dyke swarms of Singhbhum craton.

Dyke swarm	Sample no	Age (Ma)	Rb (ppm)	Sr (ppm)	$^{87}Rb/^{86}Sr$	$^{87}Sr/^{86}Sr$	± 2 SE	$(^{87}Sr/^{86}Sr)i$	Sm (ppm)	Nd (ppm)	$^{147}Sm/^{144}Nd$	$^{143}Nd/^{144}Nd$	± 2 SE	$(^{143}Nd/^{144}Nd)i$	εNdt
Keonjhar	KD-1A	2400	17.488	196.916	1.1754	0.746291	0.000035	0.705543	4.037	11.465	0.13	0.511398018	0.000008	0.5093	−3.495
Keonjhar	KD-1B	2400							4.037	11.465	0.13	0.5114053	0.000004	0.5093	−3.637
Keonjhar	KD-04	2400	30.152	136.476	1.58044	0.762072	0.00006	0.707282	4.152	12.482	0.1253	0.511705408	0.000007	0.5097	3.868
Keonjhar	KD-21	2400	64.882	196.138	2.01496	0.777065	0.00003	0.707211	9.341	48.261	0.1434	0.511185092	0.000008	0.5089	−11.967
Ghatgaon	KD-6A	2762	46.717	253.881	0.47431	0.722693	0.00001	0.703721	5.036	19.486	0.1334	0.511305377	0.000007	0.5089	−3.515
Ghatgaon	KD-09 (1)	2762	91.724	221.443					4.937	15.577	0.1387	0.511815059	0.000004	0.5093	4.617
Ghatgaon	KD-09	2762	91.724	221.443	1.19683	0.755640	0.00006	0.707767	4.937	15.577	0.1388	0.511816089	0.000005	0.5093	4.577
Ghatgaon	KD-12A	2762	48.566	225.199	2.24309	0.789614	0.00017	0.699892	4.013	11.208	0.1142	0.511441158	0.000007	0.5088	−4.855
Pipilia	KD-19A	1765	26.789	129.793	0.93037	0.742145	0.00002	0.718533	6.093	25.936	0.1458	0.511594628	0.000006	0.5099	−8.856

SE= standard error of the mean; The present-day chondrite values of $^{143}Nd/^{144}Nd = 0.512638$, $^{147}Sm/^{144}Nd = 0.1967$, $^{87}Sr/^{86}Sr = 0.7045$, $^{87}Rb/^{86}Sr = 0.0827$

crustal contamination or mantle source heterogeneity (Tegner et al., 2019). The continental crust has high Th/Nb (0.875; Rudnick and Gao, 2014). The Paleoarchean and Mesoarchean TTGs and Mesoarchean K-rich granitoids of Singhbhum craton also exhibit high Th/Nb (0.786; Upadhyay et al., 2019). In the present study, samples from Ghatgaon dyke swarm (Th/Nb = 0.13–0.44), Keonjhar dyke swarm (Th/Nb= 0.15–0.32) and Pipilia dyke swarm (Th/Nb = 0.15–0.32) exhibit Th/Nb ratios lower than the continental crust, which points out that the contamination from the upper crustal sources is minimal. Further, we have evaluated the role of crustal contamination or possible involvement of recycled components in the source using the Th/Yb and Nb/Yb (Pearce, 2008). The mantle array in the Th/Yb *versus* Nb/Yb diagram represents melts formed from the oceanic mantle sources. Two mixing curves generated between MORB sources (N-MORB and E-MORB) and average continental crust (Rudnick and Gao, 2014) indicate the samples have assimilated 5% to more than 40% crustal components, in which 10%–30% of crustal contamination can explain the Th/Yb and Nb/Yb variations observed in the Pipila and Keonjhar swarms (Figure 8A). The Neoarchean Ghatgaon swarm exhibit assimilation of more than 25% of the crustal components. However, it is unlikely that a sub-alkaline primitive magma assimilates more than 20%–30% of crustal components (Heinonen et al., 2022). Roy et al. (2004) also proposed that variations in $\delta^{18}O$ (avg. + 3.97‰ ± .75‰) of newer dolerite swarms are inconsistent with the incorporation of a large volume of continental crust.

There are several differences in the geochemical and isotopic variations of the dyke swarms that cannot be easily attributed to crustal sources or assimilation of crustal components and/or magma mixing or fractional crystallization alone. The Paleoarchean granitoids of the craton are proposed to be derived from the partial melting of proto-mafic crust at ca. 10–15 kbar (Pandey et al., 2019; Upadhyay et al., 2019), formed from a near chondritic mantle reservoir (Pandey et al., 2019) (ε_{Ndt} = -0.3 to + 2.2 and ε_{Hfi} = -0.3 to + 2.0). The dyke swarms of Singhbhum craton, however, exhibit more enriched Nd isotope values. For example, part of Paleoarchean older metamorphic trondhjemite and Singhbhum granite III which are basement to the Ghatgaon dyke swarm exhibit depleted mantle values (ε_{Ndt} = + 2 .1 to + 4.5; Pandey et al., 2019). However, the Nd isotopes of the Ghatgaon samples show wide variations ($\varepsilon_{Ndt=}$+ 4.6 to -4.8). In the basement of Keonjhar swarm, the Singhbhum granite II exhibits ε_{Ndt} = + 2.7. The ε_{Ndt} values of Keonjhar dyke swarm are -11 to + 3.8. Upadhyay et al. (2019) also noticed that the Paleoarchean-Mesoarchean granites and tonalite–trondhjemite–granodiorites (TTGs) of the craton are derived from a depleted mantle source. If we recalculate the isotopic variations of basement granites it can be a potential contaminant, but it is unlikely that the observed isotopic variability results only from the assimilation of basement granitoids, as the source characteristics of the samples are inconsistent with enriched high-temperature regimes. Moreover, the mantle source characteristics appears to be similar despite their discrete emplacement ages, which points out the isotopically distinct basement granitoids cannot be attributed solely to the compositional variations.

The negative anomalies in Nb, Zr and Hf in the primitive mantle normalized diagrams (Figure 5), relatively high initial $^{87}Sr/^{86}Sr$, and negative ε_{Ndt} values can be correlated with subduction zones (Figure 6) (Zheng, 2019). Also, the clinopyroxene in the Keonjhar and Ghatgaon samples shows significant overlap between the compositional fields of clinopyroxenes from MORB and IAT (Beccaluva et al., 1989) (Figure 7C). However, similar signatures can also be produced from

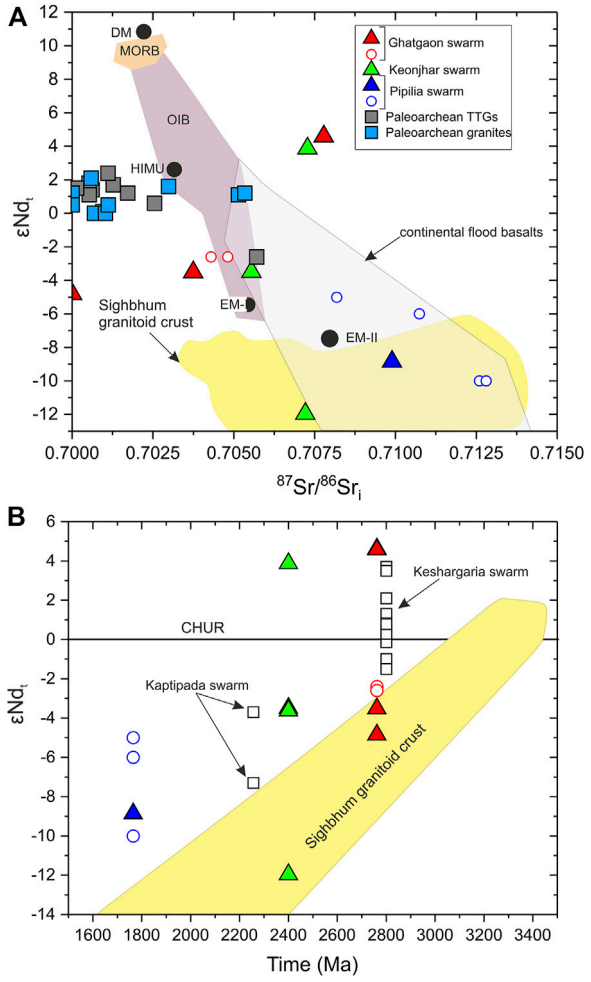

FIGURE 6
(A) Whole-rock $^{87}Sr/^{86}Sr_i$ *versus* ε_{Ndt} variations of Ghatgaon, Keonjhar and Pipilia dyke swarms. The Sr-Nd isotope variation of Paleoarchean TTGs and granites of Singhbhum craton is from Upadhyay et al. (2019). The fields and average values of the depleted mantle (DM), mid-ocean ridge basalts (MORB), ocean island basalts (OIB), OIB with high μ (HIMU), enriched mantle-1 (EM-1), enriched mantle-2 (EM-2) and continental flood basalts are from Dorais et al. (2005). Fields of Singhbhum granitoids represent recalculated values corresponding to the ages of dyke swarms. **(B)** Whole-rock ε_{Ndt} *versus* time (Ma) plot of dyke swarms of Singhbhum craton. The Nd evolution array of the Singhbhum granitoid crust from Pandey et al. (2021). Data from 2800Ma Keshargaria swarm and 2,256 Ma Kaptipada swarm (Pandey et al., 2021) are also shown for comparison.

crustal contamination or crustal components in the source. The age, distribution and cross-cutting relationship of dyke swarms are inconsistent with their origin related to a subduction zone (Figure 8) (Dasgupta et al., 2019; Adhikari et al., 2021; Pandey et al., 2021). The dyke swarms are distributed in an intracratonic regime and the stabilization of the Singhbhum craton occurred during Mesoarchean (Dey et al., 2017; Olierook et al., 2019; Srivastava et al., 2019; Hofmann et al., 2022). The emplacement of these dyke swarms occurred at discrete magmatic episodes from Neoarchean to Mesoproterozoic, and their subparallel distribution and areal extent of more than 100 km are consistent with an intracontinental rift system (Pandey et al., 2021)

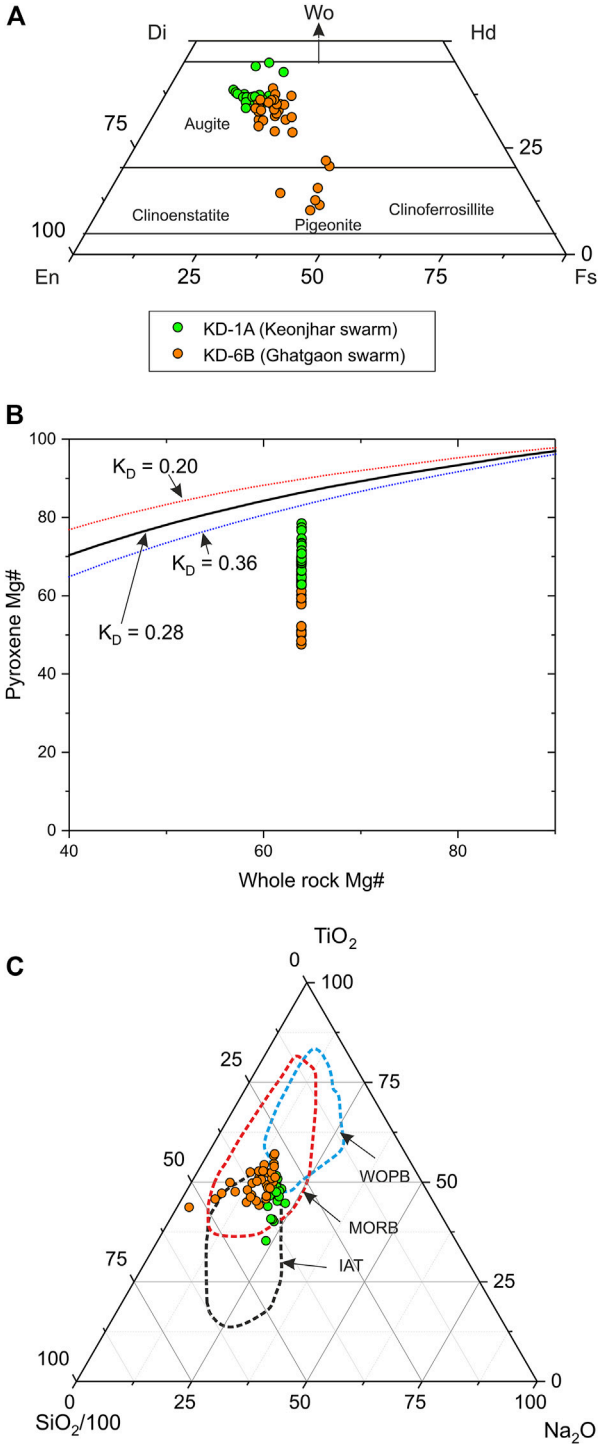

FIGURE 7
Classification of pyroxenes from Ghatgaon and Keonjhar dyke swarms. Most of the pyroxenes plot in the augite field and some from Ghatgaon exhibit distinct compositional variations. **(B)** Mineral rock Fe-Mg equilibrium diagrams for clinopyroxenes. The curves display ranges of equilibrium compositions between mineral and melt for Fe-Mg partition coefficients of .28 ± 0.08 (Putirka, 2008). **(C)** $SiO_2/100$ vs Na_2O vs TiO_2 (Beccaluva et al., 1989) discrimination diagram for clinopyroxenes from the Ghatgaon and Keonjhar dyke swarms. MORB-mid-ocean ridge basalts; IAT-island-arc tholeiites; WOPB-within ocean plate basalts.

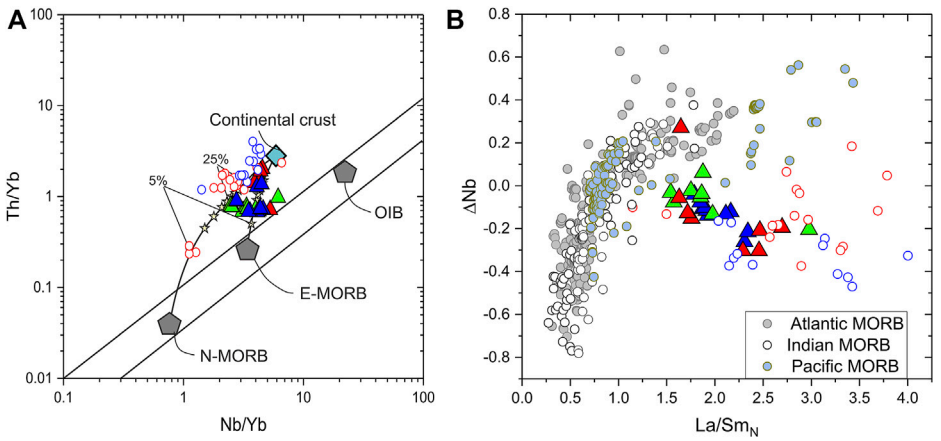

FIGURE 8
The Th/Yb *versus* Nb/Yb variations of the Ghatgaon, Keonjhar and Pipilia dyke swarm. The oceanic mantle array is from Pearce (2008). The average compositions of oceanic mantle end members include depleted mid-ocean ridge basalt or normal mid-ocean ridge basalt (N-MORB), enriched mid-ocean ridge basalt (E-MORB) and ocean island basalt (OIB) (Sun and McDonough, 1989). The average continental crust values are from Rudnick and Gao (2014). Two lines with solid yellow stars illustrate 5%–25% mixing lines of continental crust with N-MORB and E-MORB. **(B)** The ΔNb *versus* La/Sm$_N$ (normalized to primitive mantle; Sun and McDonough 1989). The Singhbhum dykes exhibit La/Sm$_N$ >1, which are consistent with LREE enriched nature (Fitton, 2007), and are compositionally distinct from midoceanic ridge basalts (MORB). The data of Atlantic, Pacific and Indian MORB are from Arevalo Jr and McDonough (2010).

We propose the observed geochemical signatures are most likely to be the characteristics of the mantle source that has incorporated crustal components (Adhikari et al., 2021; Pandey et al., 2021). Evidence for a pre-Neoarchean crustal recycling and subsequent enrichment of DMM mantle source followed by the metasomatism of SCLM has been noticed in the 2.8 Ga Jagannathpur volcanics and Ghatgaon and Keshgaria dyke swarms (Adhikari et al., 2021). Pandey et al. (2021) proposed that subduction-related crustal recycling modified the refractory SCLM. Further episodic plume impingement triggered the partial melting of the enriched SCLM between 2.8 Ga and 1.76 Ga. Moreover, delineation of thick crust under Proterozoic domains is interpreted to be evidence for Neoarchean convergent tectonics in the craton (Mandal, 2017). Recycling of Eoarchean and Paleoarchean crust (Olierook et al., 2019; Sreenivas et al., 2019; Upadhyay et al., 2019) and Mesoarchean and Neoarchean subduction-related magmatism (Mondal et al., 2006; Manikyamba et al., 2015), have been noticed in the Archean tectonic framework of Singhbhum craton. Even though the plate tectonics-related crustal recycling models during Archean are debatable (Hamilton, 2019; Zhu et al., 2021), it is conceivable that either through subduction or through non-plate tectonic modes, like melting of metasomatized lithosphere delaminated from the base of the continental crust (Cousens et al., 2001; Arndt et al., 2009), the earlier crust of Singhbhum craton have been recycled into the mantle. The resulting heterogeneous mantle source(s) can be attributed to the source of dyke swarms of Singhbhum craton (Upadhyay et al., 2014; Olierook et al., 2019; Pandey et al., 2019; Hofmann et al., 2022).

6.2 Source characteristics and melting conditions

Earlier discussion arrived at a view that the mantle source giving rise to the studied Singhbhum dyke swarms acquired a crustal trace element signature. Logical questions that follow are in which part of the mantle did that source reside, and how did it partially melted to yield the magmas that eventually solidified as the dykes. This section addresses issues relevant to geochemical and mineralogical characteristics of the mantle source, and temperature-pressure of partial melting.

First, we employ the parameter ΔNb to examine the relative enrichment and depletion of the mantle source. Calculated as 1.74+ log(Nb/Y) - 1.92 log(Zr/Y), ΔNb is used to express deviation from a reference line (i.e., ΔNb = 0) separating enriched oceanic mantle end-members (E-MORB and OIB) and N-MORB (Fitton, 2007). Fitton (2007) proposed that all N-MORB has ΔNb<0, whereas E-MORB and OIB lavas exhibit ΔNb>0. Figure 8B shows the ΔNb variations of the Gatagaon, Keonjhar and Pipilia dyke swarms. The Ghatgaon and Keonjhar dyke swarms exhibit both positive and negative ΔNb values, whereas the Pipilia dyke swarm exhibit mostly negative ΔNb values. One sample from Ghatgaon (KD-09) exhibits a maximum ΔNb of + 0.27, which means Nb is enriched 2.7 times relative to the ΔNb of zero. Other positive ΔNb values of Ghatgaon dyke swarm range from + 0.04 to + 0.18. One sample from the Keonjhar dyke swarm (KD-05) exhibits + 0.06 ΔNb whereas others exhibit negative ΔNb (-0.2 to -0.5). The variations in the ΔNb values also indicate a heterogeneous mantle source, that has both enriched and depleted components and which is distinct from MORB sources (Figure 8B). Along with ΔNb, elevated La/Sm$_n$ values illustrate high degrees of partial melting or a less depleted source (Figure 8B). Most of the ΔNb values overlap in all three dyke swarms, which again illustrates secular compositional variations (e.g., Pandey et al., 2021) in the mantle source may not be applicable, rather it can be attributed to mantle heterogeneity.

Further, we used the variations in MREE to HREE to evaluate the effects of residual garnet in the source, as garnet prefers HREE relative to MREE. The (Dy/Yb)$_N$ ratios (Davidson et al., 2013), along with (La/Sm)$_N$ ratios have been considered as they reflect the degree of mantle melting (Figure 9) (Tegner et al., 2019). The Keonjhar swarm and Ghatgaon swarms exhibit Dy/Yb of 1.8 and 1.9 (median)

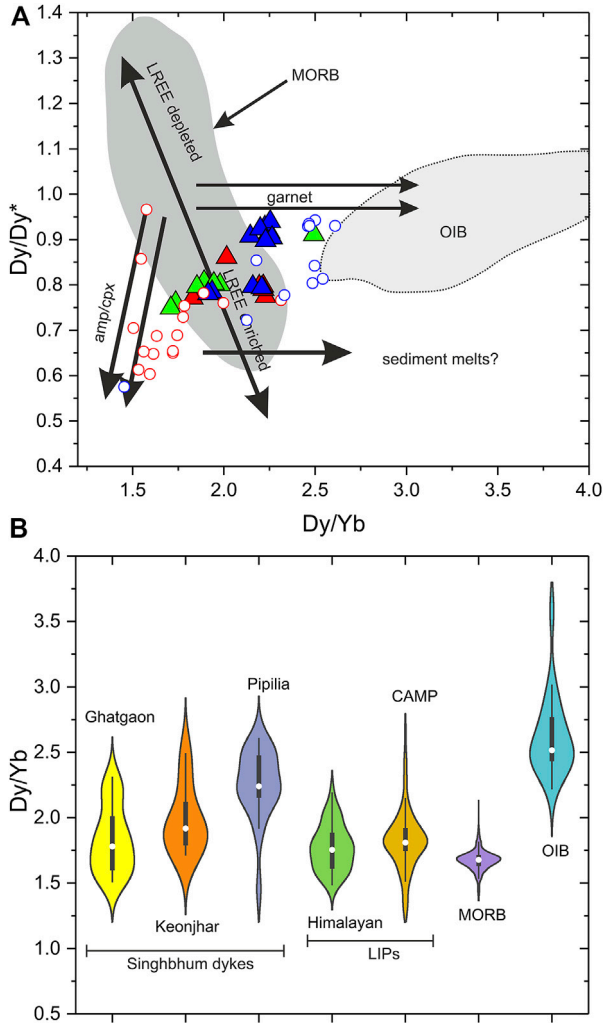

FIGURE 9
(A) Dy/Yb *versus* Dy/Dy* variation (Davidson et al., 2013) of Ghatgaon, Pipilia and Keonjhar dyke swarms. The REE values in the Dy/Dy* calculation are normalized to the values reported in McDonough and Sun (1995). **(B)** Violin plot with box plots inside illustrating the variation of Dy/Yb ratios of Ghatgaon, Keonjhar and Pipilia dyke swarms. Large igneous provinces are sourced from a subduction-modified mantle, which includes the Himalayan magmatic province and CAMP (Data source: Manu Prasanth et al., 2022). The ocean island basalt (OIB) data from Hawaii (from The GEOROC Database: https://georoc.eu/georoc/new-start.asp), and Global MORB variations, which include N-MORB and E-MORB data (Arevalo Jr and McDonough, 2010) are also shown for comparison. White circles inside the box represent mean values.

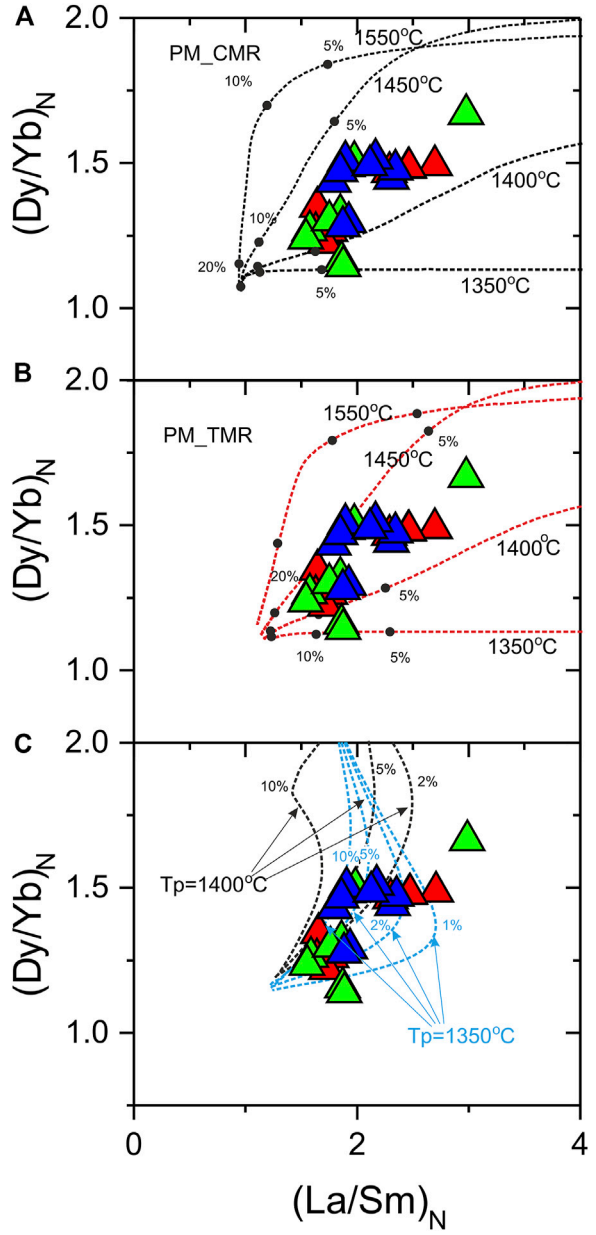

FIGURE 10
$(La/Sm)_N$ *versus* $(Dy/Yb)_N$ of the Ghatagaon, Keonjhar and Pipilia dyke swarms. **(A)** Forward models produced by melting primitive mantle in a columnar melting regime (PM_CMR) (McDonough and Sun, 1995) at mantle potential temperature from 1350°C to 1550°C. **(B)** Forward melting models produced by melting primitive mantle in a triangular melting regime (PM_CMR) (McDonough and Sun, 1995) at the same mantle potential temperatures in **(A)**. Black circles in the melting trajectories represent the degree of melting. **(C)** Forward model melts produced by melting hybrid lithologies of peridotite and pyroxenite (McDonough and Sun, 1995; Pertermann and Hirschmann, 2003). The mantle potential temperature is constrained between 1350°C and 1400°C and the proportions of pyroxenites in the source are indicated in percentage.

whereas the Pipilia swarm exhibit Dy/Yb =2.2. The Dy/Yb variations are slightly higher than MORB values (~1.6) and considerably lower than the OIB values (~2.5) (Figure 9B). The Himalayan magmatic province and CAMP proposed to be derived from a subduction-modified mantle source (Tegner et al., 2019; Manu Prasanth et al., 2022) also show overlap with the Dy/Yb variations of the Ghatgaon, Keonjhar and Pipilia swarms (Figure 10). The Dy/Dy* vs. Dy/Yb (Davidson et al., 2013), relations exhibit LREE enriched field with garnet control on some of the Keonjhar and Pipilia swarms. Most of the Ghatgaon swarm samples exhibit clinopyroxene fractionation (Figure 9A). Some samples from Dhenkikote area of Ghatgaon dyke swarm (KD-12A, KD-12B) possibly stalled at the base of the crust or coalesced into magma chambers as it is evident form their cumulate nature.

The primary magma calculation schemes depend on the addition or removal of olivine (e.g., Herzberg and Asimov, 2015; Lee et al.,

2009) were not able to retrieve realistic thermal and melting conditions as the dyke swarms exhibit fractionation of clinopyroxenes (Figure 4). Therefore, we further explored the mantle melting models using the REEBOX PRO application of Brown and Leshar (2016). This application model the composition of melts produced by lithologically heterogeneous dynamically upwelling mantle. We simulated a range of forward partial melting models of peridotitic and mixed peridotite and pyroxenite source lithologies, using different modes of melting, and variable mantle potential temperatures. The pyroxenites in the model represent recycled crustal domains in the mantle (Figure 9).

For the first two models (Figures 10A, B), we used a pyrolite peridotite source (Sun and McDonough, 1989). In the first model (Figure 10A), we used the columnar melting regime and T_p is constrained between 1350°C to 1550°C, which shows trace element variations can be achieved by 5%–10% partial melting under a T_p of 1400°C to 1,450°C. Two samples from the Keonjhar dyke swarm exhibit melting within the T_p range of 1350°C–1400°C. At 10% of melting (T_p = 1450°C–1350°C) the pressure is 2.4 to 1.3 GPa which indicates melting in the garnet-spinel transition zone and spinel peridotite zone (Su et al., 2010), and also corroborate Dy/Yb variations and both positive and negative anomalies of Y in the primitive mantle normalized diagrams (Figure 5).

In the second model (Figure 10B), we simulated a triangular melting regime with a pyrolite source as the starting composition. Relatively lower T_p (1350°C–1400°C) and 5%–10% of melting can produce compositional variations in some of the Keonjhar dyke swarms. When the T_p increases (1400°C–1450°C), 10%–20% melting is required to produce the compositional variation. Most of the melting took place in the spinel stability field. (Brown and Lesher, 2016).

To address the heterogeneous nature of the mantle source we used combinations of peridotite and pyroxenite under a columnar melting region in the third model. Considering the thick continental lithosphere of the Singhbhum craton and discrete episodes of dyke emplacement, we assumed the columnar melting region is more appropriate (Brown and Lesher, 2016; Tegner et al., 2019). Along with pyrolite peridotite, we also tried modelling with a depleted mantle (Workman and Hart, 2005) with different proportions of pyroxenites. But the melting curves did not follow the observed compositional variations. The results show anhydrous pyrolite peridotite (T_p = 1,350°C and 1,400°C) with 1%–10% pyroxenite (silica-saturated pyroxenite, G2; Pertermann and Hirschmann, 2003) were involved in the petrogenesis.

The SCLM sources combined with convecting asthenospheric regions likely contributed to the wide range of compositions in the dyke swarms of Singhbhum craton (Kamenetsky et al., 2017). The geochemical variations can be compared with LIPs like the Himalayan magmatic province, Central Atlantic Magmatic Province and North Atlantic Magmatic Province (Korenaga, 2004; Coltice et al., 2007; Marzoli et al., 2018; Tegner et al., 2019; Manu Prasanth et al., 2022), as their origins are inconsistent with a deep-seated mantle plume and are proposed to be derived from lithospheric and/or asthenospheric mantle sources with recycled crustal components (Korenaga, 2004; Shellnutt et al., 2021; Manu Prasanth et al., 2022). Narrow zone upwelling of asthenospheric melts associated with the discrete rifting events in the craton might have triggered the melting of the lithospheric mantle domains (Foley, 2008; Tang et al., 2013), which led to the melt generation and emplacement of Ghatgaon, Keonjhar and Pipilia dyke swarms.

6.3 On secular Nd isotopic trends

Pandey et al. (2021) identified a secular Nd isotopic evolution trend for the dyke swarms of Singhbhum craton. In detail, the 2.8 Ga Keshgaria swarm exhibit near chondritic ε_{Ndt} values (-1.0 to + 2.1), whereas younger generations of dyke swarms have progressively more negative values. Such a trend is consistent with a lithospheric mantle source in which crustal materials were incubated since ~2.8–3.0 Ga, and the dyke swarms formed by periodic melt extraction from that source. However, our new data hint complexity beyond a simple, secular Nd isotopic trend. The 2.76 Ga Ghatgaon dyke swarm, which yielded negative ε_{Ndt} (-2.4 to -2.6) values (Pandey et al., 2021), displays a greater range of ε_{Ndt} values from negative to positive (ε_{Ndt} = -4.8 to + 4.6). Also, the Neoarchean-Paleoproterozoic Keonjhar dyke swarm exhibits a similar but more extreme range of ε_{Ndt} values (ε_{Ndt} = -11.9 to + 3.8) (Figure 6). Undoubtedly, at least for the Ghatgaon and Keonjhar dyke swarms, a depleted mantle-like component must also be involved at the time of magma genesis. One way to explain the Nd isotopic range was interaction between asthenosphere and mantle lithosphere that had been previously enriched. However, samples having positive ε_{Ndt} values in this study also show continental crust-like trace element signature as strong as samples having negative ε_{Ndt} values, inconsistent with variable degrees of asthenosphere-lithosphere interaction. An alternative explanation is that the positive ε_{Ndt} values reflect recent mantle enrichment relative to the formation age of the Ghatgaon and Keonjhar dyke swarms. If the secular trend argued by Pandey et al. (2021) tracks evolution of an enriched mantle source formed by recycling of ~2.8–3.0 Ga crustal material, our new data imply that crustal materials younger than that range might also be involved, implying crustal recycling might have been episodic rather than a discrete, single-stage process. In other words, there might be multiple secular trends depending on the age of the recycled material(s). We suggest that this mechanism offers a better explanation for all Nd isotopic data available for the Singhbhum dyke swarms so far.

7 Conclusion

1) The samples from Ghatgaon, Keonjhar and Pipilia dyke swarms are best explained by a mantle source that has recycled crustal components.
2) The petrogenetic modelling indicates dominantly peridotitic source have incorporated pyroxenites through crustal recycling. Partial melting of this hybrid mantle source within the spinel stability field and spinel-garnet transition zones can explain the trace element variability of Ghatgaon, Keonjhar and Pipilia dyke swarms.
3) Thermal regimes inferred from the trace element modelling show that dyke swarms are inconsistent with a mantle plume-related origin and can be comparable with non-plume-related LIPs.
4) Crustal recycling in Singhbhum craton might have been episodic rather than a discrete, single-stage process as proposed by previous studies.

Data availability statement

The original contributions presented in the study are included in the article/Supplementary Material, further inquiries can be directed to the corresponding author.

Author contributions

MM developed the idea, interpreted the data, wrote the manuscript, and created figures. BS, YI and AR contributed to the sample preparation and analysis. K-NP and KRH contributed to the interpretations and manuscript preparation.

Funding

Financial support from the National Science and Technology Council, Taiwan (111-2116-M-001-031 to K-NP) is acknowledged.

Acknowledgments

We are grateful to Amulya Sahoo for their assistance with fieldwork. BS acknowledges a fellowship from CSIR (India) from 2016 to 2018. MM acknowledge the postdoctoral fellowship from the National Science and Technology Council, Taiwan. AR is grateful to Martin Wille and Sukalpa Chatterjee at the University of Bern for their help during isotope measurements. AR is also thankful to Bradley Peters and Jörg Rickli for the JNdi standard and useful comments on the measurement protocol of Sm and Nd isotopes.

Conflict of interest

The authors declare that the research was conducted in the absence of any commercial or financial relationships that could be construed as a potential conflict of interest.

Publisher's note

All claims expressed in this article are solely those of the authors and do not necessarily represent those of their affiliated organizations, or those of the publisher, the editors and the reviewers. Any product that may be evaluated in this article, or claim that may be made by its manufacturer, is not guaranteed or endorsed by the publisher.

Supplementary material

The Supplementary Material for this article can be found online at: https://www.frontiersin.org/articles/10.3389/feart.2022.1092823/full#supplementary-material

References

Adhikari, A., Nandi, A., Mukherjee, S., and Vadlamani, R. (2021). Petrogenesis of Neoarchean (2.80–2.75 Ga) Jagannathpur volcanics and the Ghatgaon and Keshargaria dyke swarms, Singhbhum craton, eastern India: Geochemical, SrNd isotopic and SmNd geochronologic constraints for interaction of enriched-DMM derived magma with metasomatised subcontinental lithospheric mantle. *Lithos* 400, 106373. doi:10.1016/j.lithos.2021.106373

Arevalo, R., Jr, and McDonough, W. F. (2010). Chemical variations and regional diversity observed in MORB. *Chem. Geol* 271, 70–85. doi:10.1016/j.chemgeo.2009.12.013

Beccaluva, L., Macciotta, G., Piccardo, G. B., and Zeda, O. (1989). Clinopyroxene composition of ophiolite basalts as petrogenetic indicator. *Chem. Geol* 77, 165–182. doi:10.1016/0009-2541(89)90073-9

Bédard, J. H., Troll, V. R., Deegan, F. M., Tegner, C., Saumur, B. M., and Evenchick, C. A., (2021). High arctic large igneous province alkaline rocks in Canada: Evidence for multiple mantle components. *J. Petrology* 62, egab042. doi:10.1093/petrology/egab042

Bleeker, W., and Ernst, R. (2006). Short-lived mantle generated magmatic events and their dyke swarms: The key unlocking earth's paleogeographic record back to 2.6 Ga. *Dyke swarms—time markers crustal Evol*, 3–26.

Brown, E. L., and Lesher, C. E. (2016). Reebox PRO: A forward model simulating melting of thermally and lithologically variable upwelling mantle. *Geochem. Geophys. Geosystems* 17, 3929–3968. doi:10.1002/2016gc006579

Buchan, K. L., and Ernst, R. E. (2021). Plumbing systems of large igneous provinces (LIPs) on Earth and Venus: Investigating the role of giant circumferential and radiating dyke swarms, coronae and novae, and mid-crustal intrusive complexes. *Gondwana Res* 100, 25–43. doi:10.1016/j.gr.2021.02.014

Chaudhuri, T., Kamei, A., Das, M., Mazumder, R., and Owada, M. (2022). Evolution of the archean felsic crust of singhbhum craton, india: A reassessment. *Earth-Science Reviews*. 231, doi:10.1016/j.earscirev.2022.104067

Coltice, N., Phillips, B. R., Bertrand, H., Ricard, Y., and Rey, P. (2007). Global warming of the mantle at the origin of flood basalts over supercontinents. *Geology* 35, 391–394. doi:10.1130/g23240a.1

Dasgupta, P., Ray, A., and Chakraborti, T. M. (2019). Geochemical characterisation of the Neoarchaean newer dolerite dykes of the Bahalda region, Singhbhum craton, Odisha, India: Implication for petrogenesis. *J. Earth Syst. Sci* 128, 216–223. doi:10.1007/s12040-019-1228-0

Davidson, J., Turner, S., and Plank, T. (2013). Dy/Dy*: Variations arising from mantle sources and petrogenetic processes. *J. Petrology* 54, 525–537. doi:10.1093/petrology/egs076

Dey, S., Topno, A., Liu, Y., and Zong, K. (2017). Generation and evolution of Palaeoarchaean continental crust in the central part of the Singhbhum craton, eastern India. *Precambrian Res* 298, 268–291. doi:10.1016/j.precamres.2017.06.009

Dorais, M. J., Harper, M., Larson, S., Nugroho, H., Richardson, P., and Roosmawati, N. (2005). A comparison of eastern north America and coastal new england magma suites: Implications for subcontinental mantle evolution and the broad-terrane hypothesis. *Can. J. Earth Sci* 42, 1571–1587. doi:10.1139/e05-056

Ernst, R. E. (2014). *Large Igneous Provinces*. Cambridge University Press. Cambridge, UK

Fitton, J. G. (2007). The OIB paradox, 430. *Special Papers-Geological Society Of America*, 387.

Foley, S. F. (2008). Rejuvenation and erosion of the cratonic lithosphere. *Nat. Geosci* 1, 503–510. doi:10.1038/ngeo261

Hamilton, W. B. (2019). Toward a myth-free geodynamic history of Earth and its neighbors. *Earth-Science Rev* 198, 102905. doi:10.1016/j.earscirev.2019.102905

Heinonen, J. S., Spera, F. J., and Bohrson, W. A. (2022). Thermodynamic limits for assimilation of silicate crust in primitive magmas. *Geology* 50, 81–85. doi:10.1130/g49139.1

Hofmann, A., Jodder, J., Xie, H., Bolhar, R., Whitehouse, M., and Elburg, M. (2022). The Archaean geological history of the Singhbhum Craton, India–a proposal for a consistent framework of craton evolution. *Earth-Science Rev* 228, 103994. doi:10.1016/j.earscirev.2022.103994

Hole, M. J. (2015). The generation of continental flood basalts by decompression melting of internally heated mantle. *Geology* 43, 311–314. doi:10.1130/g36442.1

Huppert, H. E., Stephen, R., and Sparks, J. (1985). Cooling and contamination of mafic and ultramafic magmas during ascent through continental crust. *Earth Planet. Sci. Lett* 74, 371–386. doi:10.1016/s0012-821x(85)80009-1

Irvine, T. N., and Baragar, W. R. A. (1971). A guide to the chemical classification of the common volcanic rocks. *Can. J. earth Sci* 8, 523–548. doi:10.1139/e71-055

Kamenetsky, V. S., Maas, R., Kamenetsky, M. B., Yaxley, G. M., Ehrig, K., and Zellmer, G. F., (2017). Multiple mantle sources of continental magmatism: Insights from "high-Ti" picrites of Karoo and other large igneous provinces. *Chem. Geol* 455, 22–31. doi:10.1016/j.chemgeo.2016.08.034

Korenaga, J. (2004). Mantle mixing and continental breakup magmatism. *Earth Planet. Sci. Lett* 218, 463–473. doi:10.1016/s0012-821x(03)00674-5

Krishna, A. K., Khanna, T. C., and Mohan, K. R. (2016). Rapid quantitative determination of major and trace elements in silicate rocks and soils employing fused glass discs using wavelength dispersive X-ray fluorescence spectrometry. *Spectrochim. Acta Part B At. Spectrosc* 122, 165–171. doi:10.1016/j.sab.2016.07.004

Kumar, A., Parashuramulu, V., Shankar, R., and Besse, J. (2017). Evidence for a neoarchean LIP in the Singhbhum craton, eastern India: Implications to vaalbara supercontinent. *Precambrian Res* 292, 163–174. doi:10.1016/j.precamres.2017.01.018

Le Bas, M., Maitre, R. L., Streckeisen, A., Zanettin, B., and Rocks, I. S. (1986). On the S. of IA chemical classification of volcanic rocks based on the total alkali-silica diagram. *J. petrology* 27, 745–750. doi:10.1093/petrology/27.3.745

Mandal, P. (2017). Lithospheric thinning in the eastern Indian craton: Evidence for lithospheric delamination below the archean Singhbhum craton? *Tectonophysics* 698, 91–108. doi:10.1016/j.tecto.2017.01.009

Manikyamba, C., Ray, J., Ganguly, S., Singh, M. R., Santosh, M., and Saha, A., (2015). Boninitic metavolcanic rocks and island arc tholeiites from the Older Metamorphic Group (OMG) of Singhbhum Craton, eastern India: Geochemical evidence for Archean subduction processes. *Precambrian Res* 271, 138–159. doi:10.1016/j.precamres.2015.09.028

Manu Prasanth, M., Shellnutt, J. G., and Lee, T.-Y. (2022). Secular variability of the thermal regimes of continental flood basalts in large igneous provinces since the Late Paleozoic: Implications for the supercontinent cycle. *Earth-Science Rev* 226, 103928. doi:10.1016/j.earscirev.2022.103928

Marzoli, A., Callegaro, S., Dal Corso, J., Davies, J. H., Chiaradia, M., and Youbi, N., (2018). The central atlantic magmatic province (CAMP): A review. *The Late Triassic World*, 46, 91–125.

McDonough, W. F., and Sun, S.-S. (1995). The composition of the Earth. *Chem. Geol* 120, 223–253. doi:10.1016/0009-2541(94)00140-4

Mondal, S. K., Ripley, E. M., Li, C., and Frei, R. (2006). The Genesis of archaean chromitites from the nuasahi and sukinda massifs in the Singhbhum craton, India. *Precambrian Res* 148, 45–66. doi:10.1016/j.precamres.2006.04.001

Nesbitt, R. W., Sun, S.-S., and Purvis, A. C. (1979). Komatiites; geochemistry and Genesis. *Can. Mineralogist* 17, 165–186.

Olierook, H. K., Clark, C., Reddy, S. M., Mazumder, R., Jourdan, F., and Evans, N. J. (2019). Evolution of the Singhbhum Craton and supracrustal provinces from age, isotopic and chemical constraints. *Earth-Science Rev* 193, 237–259. doi:10.1016/j.earscirev.2019.04.020

Pandey, O. P., Mezger, K., Ranjan, S., Upadhyay, D., Villa, I. M., and Nägler, T. F., (2019). Genesis of the Singhbhum craton, eastern India; implications for archean crust-mantle evolution of the earth. *Chem. Geol* 512, 85–106. doi:10.1016/j.chemgeo.2019.02.040

Pandey, O. P., Mezger, K., Upadhyay, D., Paul, D., Singh, A. K., and Söderlund, U., (2021). Major-trace element and Sr-Nd isotope compositions of mafic dykes of the Singhbhum Craton: Insights into evolution of the lithospheric mantle. *Lithos* 382, 105959. doi:10.1016/j.lithos.2020.105959

Pearce, J. A. (2008). Geochemical fingerprinting of oceanic basalts with applications to ophiolite classification and the search for Archean oceanic crust. *Lithos* 100, 14–48. doi:10.1016/j.lithos.2007.06.016

Pertermann, M., and Hirschmann, M. M. (2003). Partial melting experiments on a MORB-like pyroxenite between 2 and 3 GPa: Constraints on the presence of pyroxenite in basalt source regions from solidus location and melting rate. *J. Geophys. Res. Solid Earth* 108. doi:10.1029/2000jb000118

Putirka, K. D. (2008). Thermometers and barometers for volcanic systems. *Rev. mineralogy Geochem* 69, 61–120. doi:10.2138/rmg.2008.69.3

Ravindran, A., Mezger, K., Balakrishnan, S., and Berndt, J. (2021). Hf-Nd isotopes from ultramafic and mafic rocks in the Western Dharwar Craton, India, record early Archean mantle heterogeneity. *Lithos* 404, 106491. doi:10.1016/j.lithos.2021.106491

Roy, A., Sarkar, A., Jeyakumar, S., Aggrawal, S. K., Ebihara, M., and Satoh, H. (2004). Late archaean mantle metasomatism below eastern Indian craton: Evidence from trace elements, REE geochemistry and Sr—Nd—O isotope systematics of ultramafic dykes. *J. Earth Syst. Sci* 113, 649–665. doi:10.1007/bf02704027

Rudnick, R. L., and Gao, S. (2014). "Composition of the continental crust," in *Treatise on Geochemistry*. Editors H. D. Holland and K. K. Turekian. second edition Elsevier. Netherlands, UK. doi:10.1016/B978-0-08-095975-7.00301-6

Satyanarayanan, M., Balaram, V., Sawant, S. S., Subramanyam, K. S. V., Krishna, G. V., and Dasaram, B., (2018). Rapid determination of REEs, PGEs, and other trace elements in geological and environmental materials by high resolution inductively coupled plasma mass spectrometry. *At. Spectrosc* 39, 1–15. doi:10.46770/as.2018.01.001

Shankar, R., Sarma, D. S., Babu, N. R., and Parashuramulu, V. (2018). Paleomagnetic study of 1765 Ma dyke swarm from the Singhbhum craton: Implications to the paleogeography of India. *J. Asian Earth Sci* 157, 235–244. doi:10.1016/j.jseaes.2017.08.026

Shellnutt, J. G., Ur Rehman, H., and Manu Prasanth, M. P. (2021). Insight into crustal contamination and hydrothermal alteration of the Panjal Traps (Kashmir) from O-isotopes. *Int. Geol. Rev* 64, 1556–1573. doi:10.1080/00206814.2021.1941324

Söderlund, U., Hofmann, A., Klausen, M. B., Olsson, J. R., Ernst, R. E., and Persson, P.-O. (2010). Towards a complete magmatic barcode for the Zimbabwe craton: Baddeleyite U–Pb dating of regional dolerite dyke swarms and sill complexes. *Precambrian Res* 183, 388–398. doi:10.1016/j.precamres.2009.11.001

Sreenivas, B., Dey, S., Rao, Y. B., Kumar, T. V., Babu, E., and Williams, I. S. (2019). A new cache of Eoarchaean detrital zircons from the Singhbhum craton, eastern India and constraints on early Earth geodynamics. *Geosci. Front* 10, 1359–1370. doi:10.1016/j.gsf.2019.02.001

Srivastava, R. K., Söderlund, U., Ernst, R. E., Mondal, S. K., and Samal, A. K. (2019). Precambrian mafic dyke swarms in the Singhbhum craton (eastern India) and their links with dyke swarms of the eastern Dharwar craton southern India. *Precambrian Res* 329, 5–17. doi:10.1016/j.precamres.2018.08.001

Stracke, A., Scherer, E. E., and Reynolds, B. C. (2014). "Application of isotope dilution in geochemistry," in *Treatise on Geochemistry*. Editors H. D. Holland and K. K. Turekian. Second Edition Netherlands, UK: Elsevier, 71–86. doi:10.1016/B978-0-08-095975-7.01404-2

Su, B., Zhang, H., Asamoah, S. P., Qin, K., Tang, Y., and Ying, J., (2010). Garnet-spinel transition in the upper mantle: Review and interpretation. *J. Earth Sci* 21, 635–640. doi:10.1007/s12583-010-0117-x

Sun, S.-S., and McDonough, W. F. (1989). Chemical and isotopic systematics of oceanic basalts: Implications for mantle composition and processes. *Geol. Soc. Lond. Spec. Publ* 42, 313–345. doi:10.1144/gsl.sp.1989.042.01.19

Tang, Y.-J., Zhang, H.-F., Ying, J.-F., and Su, B.-X. (2013). Widespread refertilization of cratonic and circum-cratonic lithospheric mantle. *Earth-Science Rev* 118, 45–68. doi:10.1016/j.earscirev.2013.01.004

Tegner, C., Michelis, S. A., McDonald, I., Brown, E. L., Youbi, N., and Callegaro, S., (2019). Mantle dynamics of the central atlantic magmatic province (CAMP): Constraints from platinum group, gold and lithophile elements in flood basalts of Morocco. *J. Petrology* 60, 1621–1652. doi:10.1093/petrology/egz041

Upadhyay, D., Chattopadhyay, S., Kooijman, E., Mezger, K., and Berndt, J. (2014). Magmatic and metamorphic history of Paleoarchean tonalite–trondhjemite–granodiorite (TTG) suite from the Singhbhum craton, eastern India. *Precambrian Res* 252, 180–190. doi:10.1016/j.precamres.2014.07.011

Upadhyay, D., Chattopadhyay, S., and Mezger, K. (2019). Formation of paleoarchean-mesoarchean Na-rich (TTG) and K-rich granitoid crust of the Singhbhum craton, eastern India: Constraints from major and trace element geochemistry and Sr-Nd-Hf isotope composition. *Precambrian Res* 327, 255–272. doi:10.1016/j.precamres.2019.04.009

Vance, D., and Thirlwall, M. (2002). An assessment of mass discrimination in MC-ICPMS using Nd isotopes. *Chem. Geol* 185, 227–240. doi:10.1016/s0009-2541(01)00402-8

Wang, W., Spencer, C., Pandit, M. K., Wu, Y.-B., Zhao, J.-H., and Zheng, J.-P., (2022). Crustal evolution and tectonomagmatic history of the Indian Shield at the periphery of supercontinents. *Geochimica Cosmochimica Acta* 341, 90–104. doi:10.1016/j.gca.2022.10.040

Whalen, L., Gazel, E., Vidito, C., Puffer, J., Bizimis, M., and Henika, W., (2015). Supercontinental inheritance and its influence on supercontinental breakup: The C entral A tlantic M agmatic P rovince and the breakup of P angea. *Geochem. Geophys. Geosystems* 16, 3532–3554. doi:10.1002/2015gc005885

Wilson, J. F. (1990). A craton and its cracks: Some of the behaviour of the Zimbabwe block from the late archaean to the mesozoic in response to horizontal movements, and the significance of some of its mafic dyke fracture patterns. *J. Afr. Earth Sci. (and the Middle East)* 10, 483–501. doi:10.1016/0899-5362(90)90101-j

Wilson, M. (1989). *Igneous petrogenesis*. Dordrecht, Netherlands: Springer.

Winchester, J. A., and Floyd, P. A. (1976). Geochemical magma type discrimination: Application to altered and metamorphosed basic igneous rocks. *Earth and Planetary Science Letters* 28, 459–469. doi:10.1016/0012-821x(76)90207-7

Workman, R. K., and Hart, S. R. (2005). Major and trace element composition of the depleted MORB mantle (DMM). *Earth and Planetary Science Letters* 231, 53–72. doi:10.1016/j.epsl.2004.12.005

Zheng, Y.-F. (2019). Subduction zone geochemistry. *Geoscience Frontiers* 10, 1223–1254. doi:10.1016/j.gsf.2019.02.003

Zhu, R., Zhao, G., Xiao, W., Chen, L., and Tang, Y. (2021). Origin, accretion, and reworking of continents. *Reviews of Geophysics* 59, doi:10.1029/2019rg000689

frontiers | Frontiers in Earth Science

TYPE Correction
PUBLISHED 08 March 2023
DOI 10.3389/feart.2023.1173153

OPEN ACCESS

APPROVED BY
Frontiers Editorial Office,
Frontiers Media SA, Switzerland

*CORRESPONDENCE
M. P. Manu Prasanth,
manu@earth.sinica.edu.tw

SPECIALTY SECTION
This article was submitted to Petrology, a section of the journal Frontiers in Earth Science

RECEIVED 24 February 2023
ACCEPTED 27 February 2023
PUBLISHED 08 March 2023

CITATION
Manu Prasanth MP, Pang K-N, Hari KR, Sahoo BB, Ravindran A and Iizuka Y (2023), Corrigendum: Geochemistry of Precambrian dyke swarms in the Singhbhum craton, India: Implications for recycled crustal components in the mantle source.
Front. Earth Sci. 11:1173153.
doi: 10.3389/feart.2023.1173153

Corrigendum: Geochemistry of Precambrian dyke swarms in the Singhbhum craton, India: Implications for recycled crustal components in the mantle source

M. P. Manu Prasanth[1]*, Kwan-Nang Pang[1], K. R. Hari[2], Bibhuti Bhusan Sahoo[2,3], Arathy Ravindran[4,5] and Yoshiyuki Iizuka[1]

[1]Institute of Earth Sciences, Academia Sinica, Taipei, Taiwan, [2]School of Studies in Geology and Water Resource Management, Pt. Ravishankar Shukla University, Raipur, India, [3]Central Ground Water Board (CGWB), Northeastern region, Guwahati, India, [4]Institute of Geochemistry and Petrology, ETH Zurich, Zurich, Switzerland, [5]Institute of Geological Sciences, University of Bern, Zurich, Switzerland

KEYWORDS

precambrian, singhbhum craton (India), dyke swarms, mantle melting, crustal recycling

A Corrigendum on
Geochemistry of Precambrian dyke swarms in the Singhbhum craton, India: Implications for recycled crustal components in the mantle source

by Manu Prasanth M. P., Pang K-N, Hari K. R., Sahoo B. B., Ravindran A and Iizuka Y (2023). Front. Earth Sci. 10:1092823. doi: 10.3389/feart.2022.1092823

In the published article, the **Funding** source was not mentioned. The correct **Funding** statement appears below.

Funding

Financial support from the National Science and Technology Council, Taiwan (111-2116-M-001-031 to K-NP) is acknowledged.

The authors apologize for this error and state that this does not change the scientific conclusions of the article in any way. The original article has been updated.

Publisher's note

frontiers | Frontiers in Earth Science

TYPE Original Research
PUBLISHED 25 January 2023
DOI 10.3389/feart.2023.1075043

OPEN ACCESS

EDITED BY
Zhong-Hai Li,
University of Chinese Academy of Sciences, China

REVIEWED BY
Yang Chu,
Institute of Geology and Geophysics (CAS), China
Shengsi Sun,
Northwest University, China

*CORRESPONDENCE
Meng-Wan Yeh,
marywyeh@ntnu.edu.tw

SPECIALTY SECTION
This article was submitted to Structural Geology and Tectonics, a section of the journal Frontiers in Earth Science

RECEIVED 20 October 2022
ACCEPTED 03 January 2023
PUBLISHED 25 January 2023

CITATION
Chiu Y-P, Yeh M-W and Lee T-Y (2023), The atypical Gaoligong orocline: Its geodynamic origin and evolution. *Front. Earth Sci.* 11:1075043. doi: 10.3389/feart.2023.1075043

The atypical Gaoligong orocline: Its geodynamic origin and evolution

Yu-Ping Chiu, Meng-Wan Yeh* and Tung-Yi Lee

Department of Earth Sciences, National Taiwan Normal University, Taipei, Taiwan

Various orocline systems around the India–Eurasia collision zone have long been recognized and studied. Different portions of the India–Eurasia boundaries represent various scales and models of orocline-forming processes, such as the Baluchistan orocline formed by multiple deformation events and the Himalayan orocline formed by a mixture of complex structural mechanisms. The curvature from the eastern Himalayan syntaxis through east Burma to west Yunnan showed a unique convex curvature toward the mantle wedge. This is different from the concave Baluchistan orocline and the Himalayan orocline. The unique geometry of the Gaoligong orocline shows an N-S trend for the northern section and a NE-SW trend for the southern section. This curvature also marks the boundary between the Tengchong and Baoshan blocks along the Santaishan suture in western Yunnan, China. Our structural reconstruction identified five deformation events: 1) D_1 is km-scale upright folding, which only affected the Neoproterozoic meta-sedimentary unit, 2) D_2 recumbent folding, which only developed in the southern section of the Gaoligong orocline, 3) D_3 large-scale gently westward-inclined thrust folding, 4) D_4 right-lateral shear belt, and 5) the D_5 normal faults. Since the D_3 structure is the earliest event that shows penetrative foliation development along the orocline, we consider D_1 and D_2 as pre-orocline-forming events. The geometry of the Gaoligong orocline is controlled by the distribution of the Ordovician basement between the Tengchong and Baoshan blocks. Both north and south sections experienced the same structural evolution since D_3 (a fault-propagation fold system occurred between 40 Ma and 28 Ma), D_4 (steep right-lateral shear belt occurred between 28 Ma and 15 Ma), and D_5 (normal faults after 15 Ma). The curvature first developed as a shovel-like top-to-the-NE thrust plane (S_3) that formed under amphibolite-facies conditions between 40 Ma and 28 Ma. The following deformation events (D_4 and D_5) show orocline parallel foliation development under lower metamorphic conditions, indicating that the curvature of the Gaoligong orocline is not generated by additional rotation along multiple deformation events. However, due to the lack of orocline parallel foliation development for S_3, and the lack of a proper position of the indenter, the Gaoligong orocline cannot be classified as a primary orocline nor a rotational orocline. The curved geometry is an interference pattern of topography relief to the shovel-like thrust plane that developed during D_3. Our new reconstructed structural evolution concludes that the Gaoligong orocline is an "atypical" orocline.

KEYWORDS

orocline, shovel-like thrust plane, Gaoligong, Tengchong block, fault-propagation fold

1 Introduction

For centuries, the two geological features people have noticed are tilted rock layers and curved mountain belts. Since deformation was recognized as the result of bending/distortion of once horizontal strata by Sir James Hall during the 19th century, Alpine geologists had long been using structural reconstruction to delineate the four-dimensional geomorphological

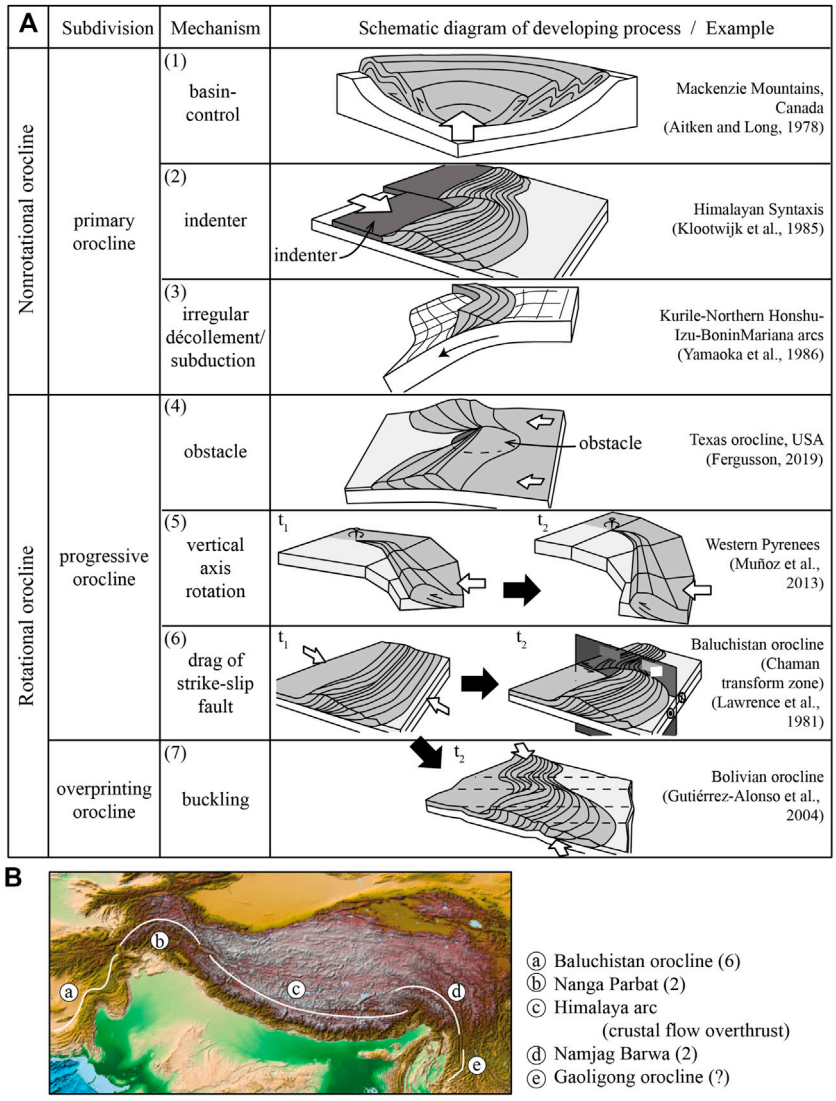

FIGURE 1
(A) Schematic diagrams showing different forming mechanisms and corresponding examples of oroclines. The 3D sketches are modified from Marshak (2005), Hwang et al. (2012), Muñoz et al. (2013),and Bersan et al. (2017). **(B)** ETOPO1 digital relief map around the India–Eurasia collision zone, showing various orocline systems (https://ngdc.noaa.gov/mgg/global/global.html). The numbers mark the type and mechanism that were proposed for its formation by previous studies. No forming mechanism had been proposed for the Gaoligong orocline, from all the orocline systems.

evolution of oroclines through time (Carey, 1955; Sacchi and Cadoppi, 1988; Johnston et al., 2013). They provide windows to understand the complex kinematic interaction system under the evolving stress field of the lithosphere. More research has been conducted over the past decades over numerous oroclines, such as the Alaskan orocline, the Bolivian orocline, the Betic-Rif Belt, the New England orocline, and the Himalayan syntaxes. Recent research interests are more focused on the geodynamic aspects than on the geomorphic/geometric aspects (Bendick and Bilham, 2001; Capitanio et al., 2011; Cawood, 2022).

Several models for primary/non-rotational *versus* progressive/rotational orocline development have been established (Figure 1A; Marshak, 1988; 2005; Weil and Sussman, 2004; Yeh and Bell, 2004; Johnston et al., 2013). The primary/non-rotational orocline reflects the original curvature of the plate boundary without rotation, which is considered to be restricted to thin-skinned thrust belts. The structural characteristic of this subdivision is that only one stage of foliation will develop with different strikes along the orocline. The shape of the primary plate boundary is genetically related to the characteristics of the basin, indenter, or irregularity of basement lithology. The basin-controlled salient (mechanism 1 in Figure 1A) is formed by developing a fold-thrust belt along/within the basin boundary due to uneven sediment thickness (Aitken and Long, 1978; Macedo and Marshak, 1999). For the indentation model (mechanism 2 in Figure 1A), the curvature reflects the geometry of the rigid indenter, such as for the Himalayan syntaxis (Carey, 1955; Klootwijk et al., 1985). The irregularly décollement/subduction model (mechanism 3 in Figure 1A) reflects the heterogeneity in the direction and crustal thickness of décollement/subduction and the variation in the slab thickness (Yamaoka et al., 1986; Macedo and Marshak, 1999; Marshak, 2005; Capitanio et al., 2011).

The progressive/rotational orocline initially forms as a straight mountain belt and is followed by progressive crustal rotation as

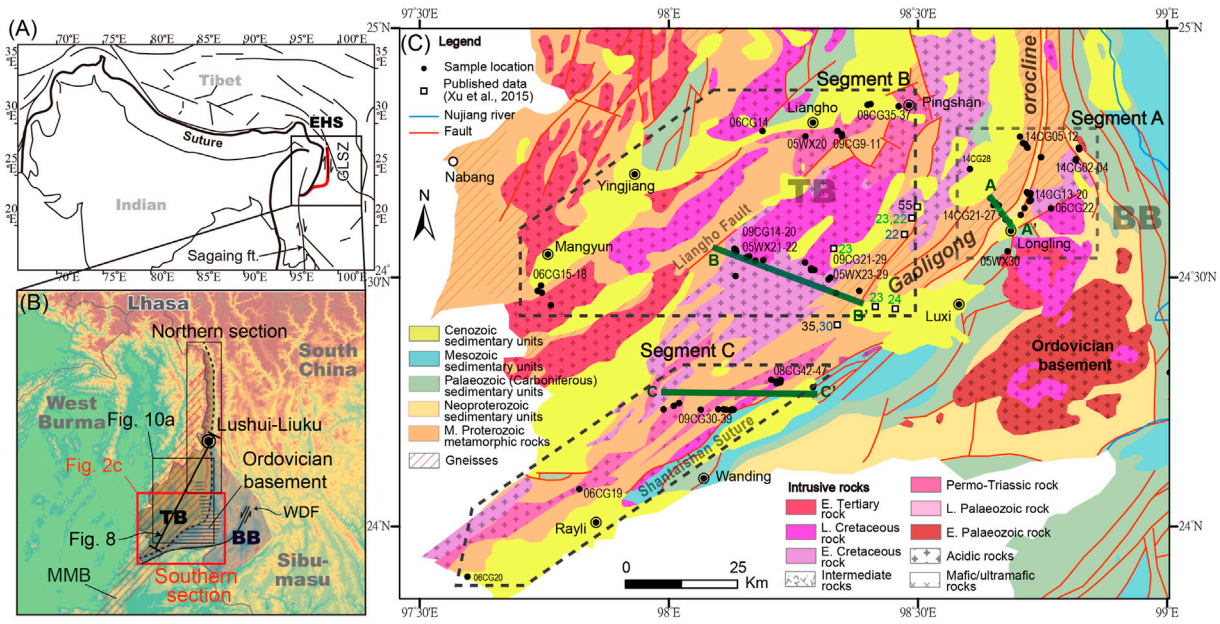

FIGURE 2
Tectonic and geological maps of the study region. **(A)** Sketch diagram showing the general tectonic framework of the oroclines. Most oroclines are convex toward the Indian plate; only the section from EHS to Sagaing fault and the Gaoligong shear zone are convex toward the mantle wedge. The map is modified from Bajolet et al. (2013). **(B)** Topography map with a digital elevation model showing the distribution of the Tengchong block (TB, translucent brown block) and Baoshan block (BB, translucent blue block). The brown hash line marks the Mogok metamorphic block (MMB), and the Ordovician basement is marked by the gray horizontal line (Ye et al., 2020). WDF—Wanding fault. **(C)** Geological map of the Gaoligong orocline showing lithology units, fault distributions, cross-sections, and sample location. The published ages are quoted from Xu et al. (2015). The black number marks the age of zircon U-Pb dating, the blue marks the age of hornblende Ar–Ar dating, and the green marks the age of biotite Ar–Ar dating. The map is modified from BGMRYP (1983), Ma et al. (2014), and Xu et al. (2012).

plate–scale interactions among the crust and lithospheric mantle occur (Johnston et al., 2013). Therefore, the formation of an orocline would accompany multiple deformation events with multiple cross-cutting foliation developments. Three crust rotation styles are further classified as obstacle (mechanism 4 in Figure 1A), vertical axis rotation (mechanism 5 in Figure 1A), and drag of strike-slip fault (mechanism 6 in Figure 1A). The obstacle-produced model (mechanism 4) considers the curvature of a fold-thrust belt and is enhanced as it bends around a strong impeded obstacle such as a seamount (Marshak, 1988; Macedo and Marshak, 1999; Marshak, 2005). The Texas orocline is an example as it is formed by the subduction of a seamount chain (Fergusson, 2019). Both the vertical axis-rotated model and the drag of the strike-slip shearing model (mechanisms 5 and 6) are related to horizontal non-coaxial deformation but under different faulting mechanisms. The vertical axis-rotated model (mechanism 5) was developed based on the detachment/décollement propagating during the vertical axis rotation of the Iberian Peninsula about a pivot in the Western Pyrenees (Carey, 1955). The drag of the strike-slip shearing model (mechanism 6; Marshak, 1988; Macedo and Marshak, 1999) describes the formation of an orocline as a once straight fold-thrust belt that is later sheared into multiple curved fold-thrust belts, such as the Variscan orocline in the Western Alps (Martínez Catalán, 2011) and Chaman transform zone for the Baluchistan orocline in Pakistan (Lawrence et al., 1981).

The overprinting orocline (mechanism 7 in Figure 1A) is formed by alternating the stress direction. As the stress direction of later deformation becomes parallel to the trend of the pre-existing fold-thrust belt, the pre-existing fold-thrust belt is then bent or buckled (Macedo and Marshak, 1999; Marshak, 2005). In the cases of the Bolivian orocline of the Andes (Gutiérrez-Alonso et al., 2004) and the Cantabrian orocline of the Pyrenees (Weil et al., 2001; Gutiérrez-Alonso et al., 2012), the buckling process thickened the curst by adding a strip of oceanic crust into a continental matrix, causing delamination of the lithospheric root under the inner arc region (Gutiérrez-Alonso et al., 2004). A few oroclines were likely affected by multiple mechanisms. The Serra Central Salient of eastern Brazil was formed by a hybrid of non-rotational orocline, followed by vertical axis rotation (Bersan et al., 2017). Another case is the Central Iberian arc that was controlled by progressive and overprinting models (shearing and buckling; Martínez Catalán, 2012).

The Gaoligong orocline is the southeastern stretch of the large-scale curvature of the Himalayan orocline, which marks the general boundary between Eurasia and India plates (Figure 1B). The orocline's shape is generally concave to the subducting plates. As Bajolet et al. (2013) have pointed out, the Himalayan orocline curvature and syntaxes are a unique and present oddity as the curvature is convex toward the subducting plate (India). The Himalayan section shows a concave curvature to the subducting plates and extends from both the western and eastern syntaxes that include the Zagros thrust belt and the Gaoligong orocline. The existence of the Gaoligong orocline has long been recognized, and its structural evolution has been debated for an equally long period (Y.G. Wang et al., 2006a; Song et al., 2010; Eroglu et al., 2013; Xu et al., 2015; Zhang et al., 2017; Chiu et al., 2018). Previous studies mostly focus on reconstructing the detailed evolution of either the northern or the southern section of the Gaoligong orogen, but not the Gaoligong orocline. Furthermore, the structural evolution for the northern and southern sections has not

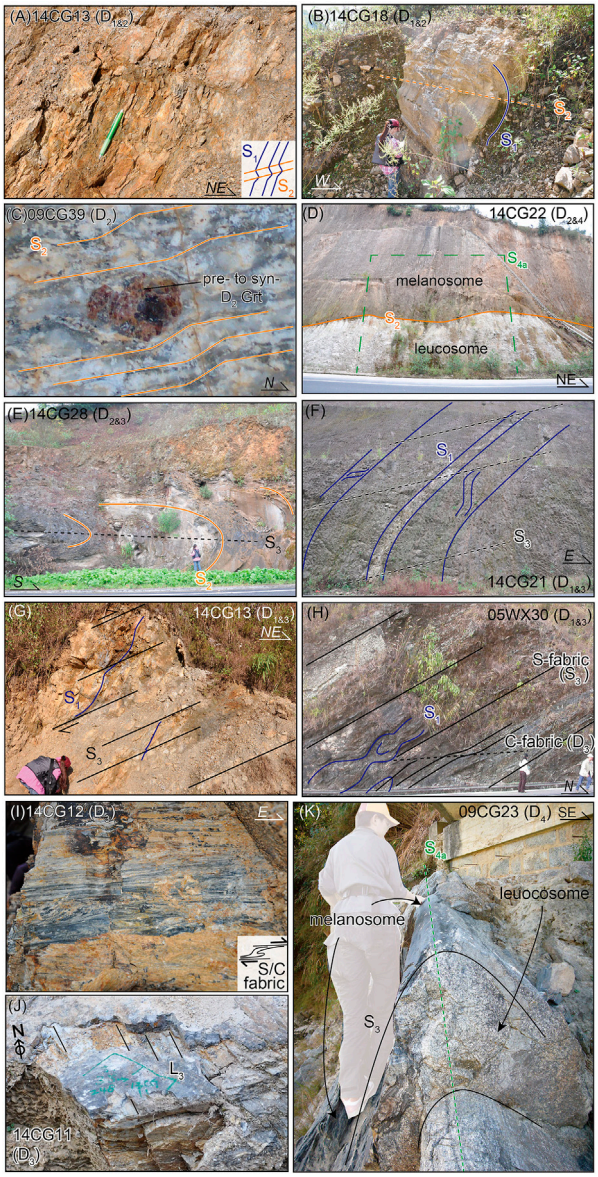

FIGURE 3
Outcrop photos and sketches showing the structural style and fold interference patterns for different deformation events. Photos **(A–D)** are D_2-related structures from low to high strain. Photos **(E–H)** show D_3-related structures with shallow to steep dips and increasing metamorphic grades. **(A)** D_2 N-S-striking sub-horizontal shear plane with the S_1 kink bend. **(B)** Recumbent folds (S_1) with a sub-horizontal fold axial plane (S_2). **(C)** Garnet-bearing mylonitic gneiss showing an N-S-striking sub-horizontal foliation (S_2) under the upper amphibolite to granulite facies. **(D)** Contact between melanosome and leucosome is parallel to the N-S-striking sub-horizontal foliation (S_2), suggesting the migmatization is syn-D_2 under granulite facies. **(E)** D_3 thrust ramp folds forming a NW-SE-striking sub-horizontal fold axial plane (S_3). **(F)** Recumbent folds of slate outcrop with a weakly developed fold axial plane (S_3). **(G)** S_3 fabric showing a thrust sense of shear. **(H)** Outcrop preserving isoclinal D_1 fold with a fold axial plane parallel to the dominant NW-SE-striking SW-dipping matrix foliation (S_3), a penetrative sub-horizontal shear plane **(C)** can be noted to develop at the bottom of the outcrop. **(I)** Mylonite preserves the sense of thrust for the D_3 shear zone. **(J)** N-S-trending L_3 shows on the shear plane of D_3 around the Ordovician basement. **(K)** Outcrop preserving D_3 shear plane folded into the isoclinal D_{4a} fold with NE-SW-striking, NW-dipping fold axial plane (S_{4a}).

been correlated or compared. This is crucial in order to delineate the orocline formation mechanism. For this study, we compare and contrast the structural evolution history of the northern and southern sections to determine the timing and mechanism of the Gaoligong orocline formation.

2 Geological setting

The 20-km wide, 400-km long Gaoligong orocline marks the boundary between the Tengchong and Baoshan blocks (Figures 2A, B). The teleseismic waveform data from temporary broadband seismometers show a difference between the crustal thicknesses of the two blocks. The crust of the Baoshan block (35 km–30 km) is slightly thinner than that of the Tengchong block (35 km–40 km; Zhang and Gao, 2019). The basement of the Tengchong block can further extend southward to the basement of the Mogok metamorphic belt (MMB; Figure 2B; Shi et al., 2011). Both Tengchong and Baoshan blocks are composed of Paleoproterozoic metamorphic and Neoproterozoic sedimentary units (Shi et al., 2011). These blocks are situated at the active volcanic rift setting of the Australian margin of Gondwana before the middle Early Permian (Metcalfe, 1996; Wopfner, 1996; Sone and Metcalfe, 2008; Liu et al., 2009; Liu et al., 2021). At ~500 Ma, the southward-subducted Proto-Tethys slab started to roll back, which induced a back-arc basin formation. The breakoff of the slab around 490 Ma–467 Ma led to basin closure, accompanied by multiple magmatic events (Wang et al., 2013; Zhao et al., 2014; Li et al., 2016; Zhao et al., 2017; Dan et al., 2022). These sedimentary units and the magmatic batholiths composed the Ordovician basement between the Tengchong and Baoshan blocks (Figure 2B; Wang et al., 2013; Zhao et al., 2014; Li et al., 2016; Zhao et al., 2017).

Both Tengchong and Baoshan blocks were individually separated from Gondwana during the Early Permian (Wopfner, 1996; Metcalfe, 2013). They were later sutured together before the Early Cretaceous (Qi et al., 2019). Starting from the Late Cretaceous until the Paleocene, the S-type granites showed a gradual westward younging trend toward the boundary of the Tengchong block (Zhang et al., 2017; Sun et al., 2020). The I-type granitoids intruded along the western margin of the Tengchong block until ~50 Ma, which can be correlated to the Gangdese arc belt as the Neo-Tethys slab subducted beneath Eurasia (Figure 2C; Xu et al., 2012; Ma et al., 2014). The stress regime switched from compression to extension between 53 and 40 Ma. A 53-Ma A_2-type granite extends from the central to western Tengchong block, formed under a back-arc extensional setting (Chen et al., 2015). The magmatic flare-up was likely due to the breakoff of the Neo-Tethys slab and increased the contribution of mantle-derived melts until the emplacement of intraplate-type basaltic dykes at ~40 Ma in the central region of the Tengchong block (Xu et al., 2008; Xie et al., 2016).

The Gaoligong shear zone (GLSZ) and Santaishan suture mark the boundaries between Tengchong and Baoshan blocks. In this study, we defined the N-S trending Gaoligong orogen along the GLSZ as the northern section of the Gaoligong orocline and NE-SW trending region as the southern section (Figure 2B). Chiu et al. (2018) revealed four ductile deformation events for the northern section.

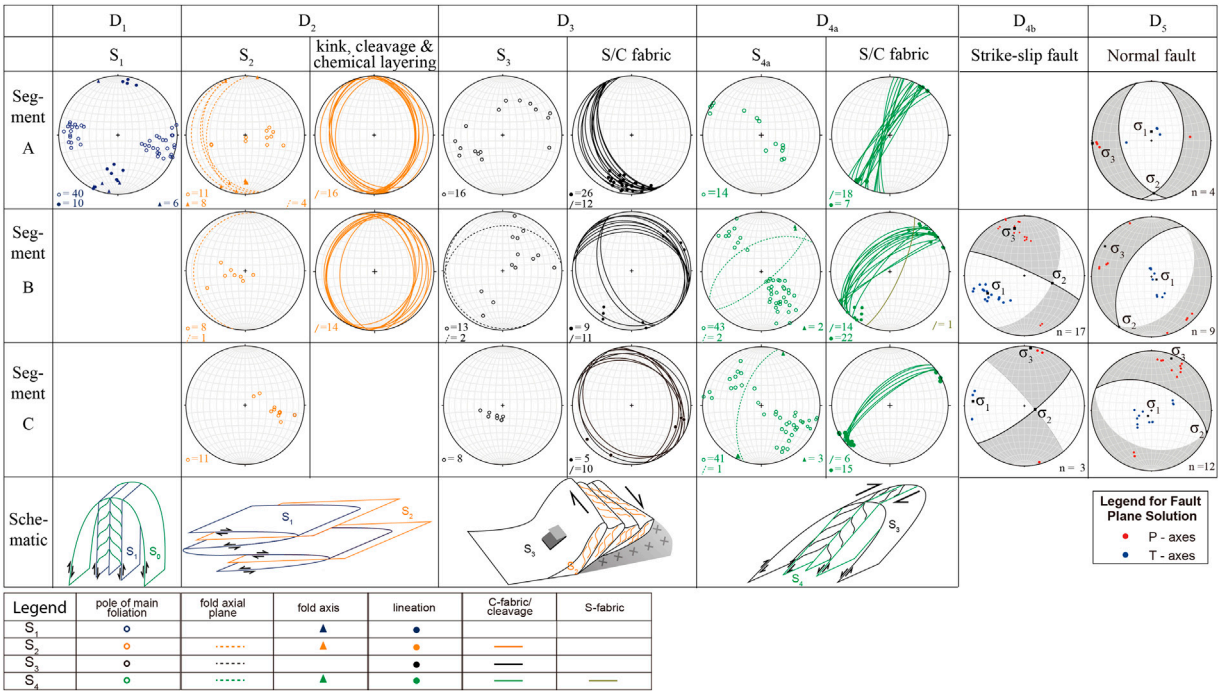

FIGURE 4
Southern hemisphere equal-area projection of field measurements separated according to ductile deformation events from D_1, D_2, D_3, and D_{4a} of three sections A, B, and C. Simplified structural pattern sketches of D_1 to D_4 are provided at the bottom. Various colors mark different foliations. Mylonitic S/C and S/C_1 fabrics are separated from matrix foliation for D_3 and D_{4a}, respectively. Open circles mark the poles of all foliations, solid triangles mark the fold axis, and solid circles mark the mineral stretching lineation. Dash lines mark the fold axial plane, and solid lines mark the cleavages. (B) Fault kinematic solutions of brittle events (D_{4b} and D_5) plotted with equal-area southern hemisphere stereographic projection. The list of field measurement data is provided in Supplementary Table S1.

D_1 formed the WNW-ESE-striking upright folds that are interpreted as resulting from the closure of the Neo-Tethyan ocean during the Early Cretaceous (118 Ma–78 Ma). D_2 caused large-scale eastward thrusting and folding with a top-to-the-N/NE sense of shearing under upper-amphibolite-facies conditions between 50 Ma and 35 Ma. D_3 formed a moderate NE-dipping, NW-SE-striking, and left-lateral shear zone under middle-to-lower-amphibolite-facies metamorphic conditions that accommodated the southeastward extrusion of Indochina around 35 Ma–28 Ma. D_4 caused sub-vertical right-lateral shearing of the GLSZ in the evident N-S trend and retrograded from amphibolite facies into greenschist facies during 28 Ma–15 Ma.

The Gaoligong orocline bends to the NE-SW along the Santaishan suture (Figures 2B, C; Qi et al., 2019). Mitchell et al. (2008) refer to it as the Luxi–Namkham suture and further connects it to the suture of the Paung Laung–Mawchi zone along the Shan boundary. Zhang et al. (2017) reported four ductile deformation events: D_1 is the large-scale top-to-the-east sub-horizontal thrust during 114 Ma–104 Ma. D_2 is an intrusion doming event during 67 Ma–30 Ma. The magmatism caused the migmatization of the host rock and triggered a thrust-fault belt on the top of the dome structure. The contacts between granite, granitic mylonite, mylonite, phyllite, and sedimentary rocks are mostly sub-horizontal, parallel to the flat-laying thrusting detachment (Xu et al., 2015), indicating that major metamorphic layering and differentiation occurred during this event. Minor strike-slip shear belts are developed along both limbs of the dome structure. These strike-slip shear belts are further developed by the following deformation event (D_3) under the right-lateral shear condition that can correspond to the N-S-trending right-lateral shear event (D_4) of the north section (which is D_3 for Zhang et al., 2017; Chiu et al., 2018). By correlating each deformation event to our new data for the southern section and comparing that to the previously studied northern section, we can re-establish a new structural evolution of the southern section of the Gaoligong orocline and delineate which deformation event had caused the formation of the Gaoligong orocline.

3 Results and interpretations

3.1 Reconstructed structural evolution of the southern section of the Gaoligong orocline

Based on cross-cutting relationships observed in the field and oriented thin sections, the succession of four ductile deformation events (D_1, D_2, D_3, and D_{4a}), with D_{4b} marking the ductile-brittle transition event, followed by a brittle deformation (D_5) event, were recognized along the three segments (Figures 3–6). D_1 and D_2 are folding events, while both D_3 and D_{4a} are shearing events with folds of different oriented shear (S/C) fabrics.

3.1.1 D_1

The oldest event, D_1, formed km-scale upright open folds with N-S-striking and sub-vertical axial plane S_1 (between 345°–028°, an

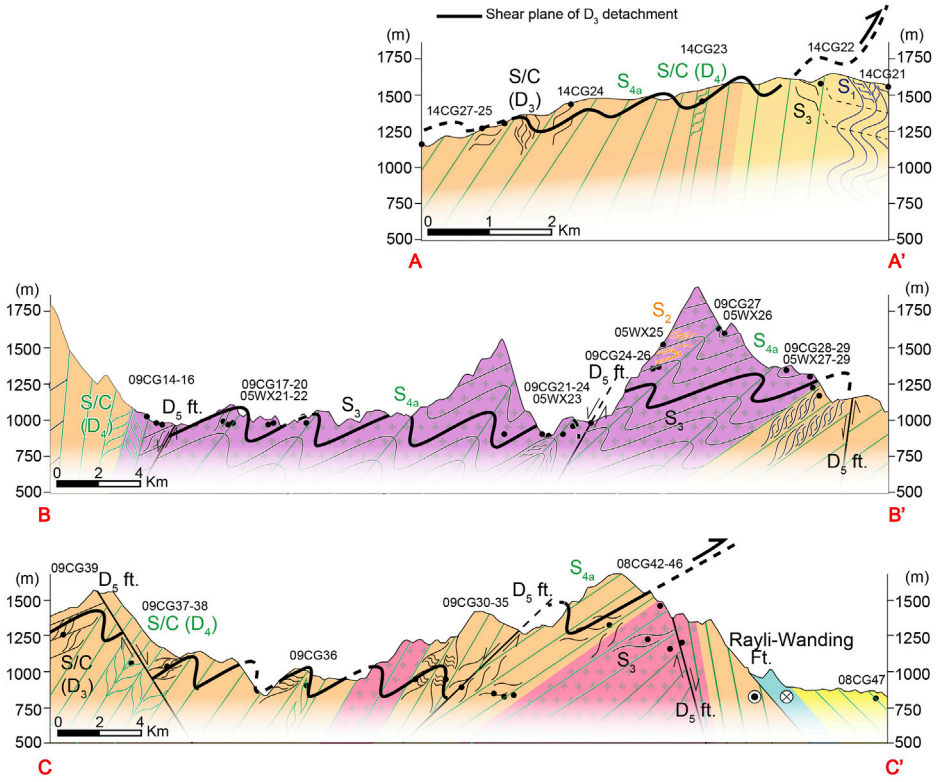

FIGURE 5
Reconstructed cross-sections of **(A,A')**, **(B,B')**, and **(C,C')** segments. The oldest D_1 fold formed the S_1 axial plane (blue lines). D_2 formed the sub-horizontal S_2 foliation and chemical layering (orange lines). D_3 thrust shear folding formed the S_3 fold axial plane (black). The thick black line marks the shear plane of the D_3 fold-thrust belt. The D_4 shear fabrics (green) deformed multiple rock units, and the early stage of D_4 (D_{4a}) folded D_3 thrust shear belts, forming the S_{4a} axial plane (green) and then transformed into brittle deformation (D_{4b}). The latest normal fault (thick gray line), D_5, truncated all ductile fabrics.

average value of 010°; Figures 3A, B; Figure 4; Figure 5). All D_1 structures are observed within the Neoproterozoic meta-sedimentary unit (Figure 5). The S_1 within the meta-sedimentary unit was later deformed by D_2 and D_3 fold axial planes, away from the highly deformed region of the D_3 thrust plane (Figures 3A, B, F). Petrographic analysis shows that the S_1 is defined by mica folia and quartz ribbons with a right-lateral sense of shear (Figure 6A). The grain boundary migration of the quartz ribbon indicates a temperature range >500°C (Figure 6A), and the bulging of feldspar (Figure 6B) further constrains the metamorphic conditions from middle-to-lower amphibolite facies (>600°C; Passchier and Trouw, 1996; Owona et al., 2013).

3.1.2 D_2

D_2 forms meter-scale recumbent folds with the N-S-trending sub-horizontal fold axial plane cleavages (S_2, Figures 3B, 4). Clear metamorphic layering showing a wide range of metamorphic conditions can be observed along different altitude outcrops. Lower-grade metamorphic conditions of brittly kinked mica-bearing D_1-related phyllonite within the meta-sedimentary unit are observed at a higher altitude (~2,000 m; Figure 3A), whereas medium-to-high-grade metamorphism indicated by sillimanite–garnet-bearing mylonitic gneiss is observed for outcrops at lower altitudes (~1,200 m; Figure 3C). Strong metamorphic layering with a segregated quartzo–feldspathic-rich layer and a mica–sillimanite-rich layer can be observed for lower-altitude regions. Furthermore, sub-horizontal N-S-trending leucosome sheets can also be observed at lower-altitude outcrops (Figure 3D), indicating that the metamorphic condition of D_2 could be as high as granulite facies. Even though the melanosome and leucosome have developed S_3 during the later thrusting event, the contact still maintains the characteristics of D_2, which is N-S trending. The vertical variation of metamorphic conditions from high-grade metamorphism at outcrops from 1,000-meter elevation to low-grade metamorphism at outcrops from 2,000-meter elevation showed that a much higher geothermal gradient is required if no structural deformation had occurred to displace rocks. Thrust faults tend to bring deeper rocks up for the hanging wall, whereas normal faults tend to push upper rocks down for the hanging wall. Since most of the outcrops we observed belong to the hanging wall and low-grade metamorphic rocks are observed for higher altitudes, we determined that these recumbent folds should accompany an extensional setting such as normal listric faulting conditions for D_2.

3.1.3 D_3

D_3 is a thrust folding event that reactivated recumbent D_2 folds to form large-scale sub-horizontal to gently westward-inclined folds (Figure 3; Figure 4) along a "listric type" thrust ramp. A dominant top-to-the-NE sense of shear NW-SE-striking, shallow SE dipping S_3 fold axial planes can be noted (Figure 4). The dip (5°–55°) of S_3 foliation showed systematic variation at different altitudes; the higher the elevation, the steeper the dip for S_3 (Figure 5). Concentrated well-developed S-C fabrics are noted for narrow mylonitic belts at lower-altitude outcrops under high-grade metamorphic conditions

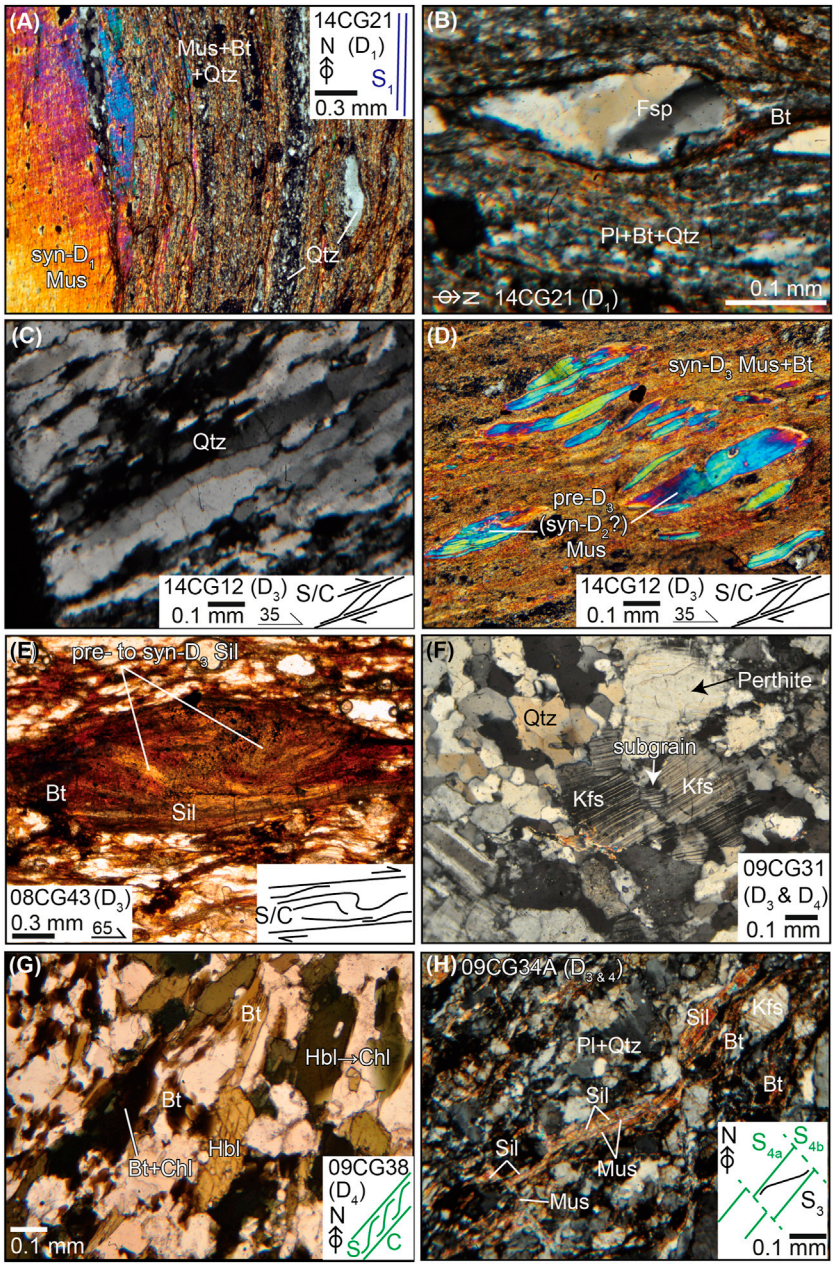

FIGURE 6
Microphotographs illustrating the microstructural and petrological relationship of D_1 to D_4. **(A)** Mylonitic S_1 fabric with a right-lateral sense of shear defined by mica folia and very fine-grained quartz + feldspar aggregates in the ribbon. The deformation mechanism of the relic of quartz ribbon (the left side) is the grain boundary migration. **(B)** Right-lateral sense of shear of D_1 can be indicated by the biotite, which wrapped the pressure shadow of the bulged K-feldspar with undulose extinction. **(C)** Grain boundary migration of quartz was observed from the C-fabric-parallel ribbon with undulose extinction. **(D)** Mylonitic S/C fabric is defined by muscovite + biotite folia and mica fish with a sub-horizontal thrust component. **(E)** Mylonitic S/C fabric is defined by biotite folia. The biotite fish contain folded sillimanite inclusions. **(F)** Microphotograph showing pre- to syn-D_3 subgrain-rotated K-feldspar. **(G)** Mylonitic S/C_1 fabric is defined by chlorite + biotite ± chloritized hornblende with a dextral sense of shear. **(H)** S_3 is defined by sillimanite folia, which are bound by NE-SW-striking S_{4a} foliation defined by fine-grained muscovite and plagioclase and quartz aggregates. Truncation and offsets of both S_3 and S_{4a} by S_{4b} fractures can be noted. Bt, biotite; Chl, chlorite; Fap, feldspar; Hbl, hornblende; Kfs, K-feldspar; Mus, muscovite; Pl, plagioclase; Qtz, quartz; and Sil, sillimanite.

(Figure 3I) along the thrust ramp. The mineral assemblage of muscovite + biotite + sillimanite and quartz ribbons (Figures 6C–E) is observed for the S-C fabric, which is indicative of amphibolite-facies metamorphism (Barrow, 1893). Sub-grain-rotation of feldspar (Figure 6F) indicates a temperature of up to 700°C (Passchier and Trouw, 1996; Owona et al., 2013). This medium-to-high-temperature metamorphism is accompanied by hydrous minerals, such as muscovite, biotite (Figures 6D, E), and hornblende (Figure 6G), which could result in syn-kinematic melting of anatexis (Patino Douce et al., 1990), thus responsible for the thick leucosome of migmatite that appears along the thrust ramp.

Strong strain-partitioning patterns are observed throughout the study region. Older fabrics are better preserved for the less-strained regions as the D_3 C-fabrics are poorly developed, whereas

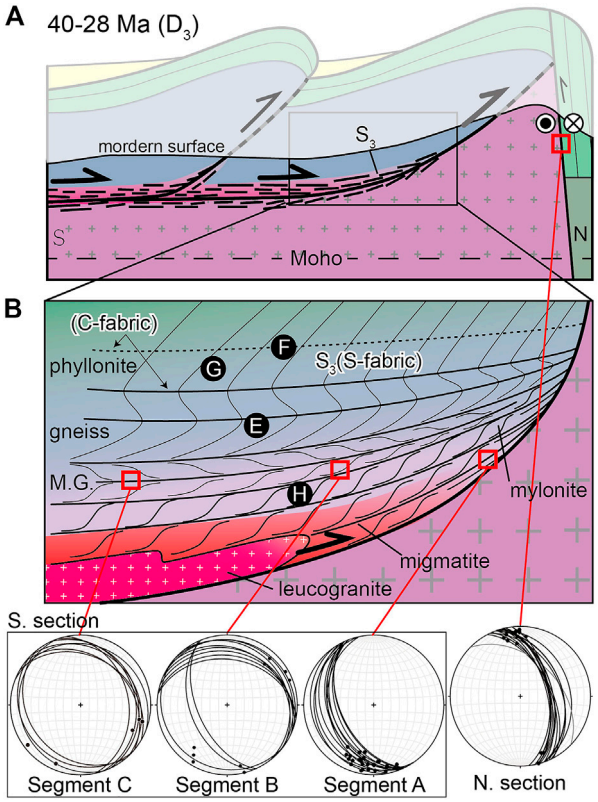

FIGURE 7
Schematic diagram with southern hemisphere equal-area projection stereonet diagram showing geographical distribution of reconstructed S_3 foliation with various dip and metamorphic conditions of the D_3 fold and thrust complex. **(A)** Sub-horizontal to gentle back-limb produces a significant horizontal shearing and folding at higher metamorphic conditions. The steep fore-limb developed the sub-vertical strike-slip fault against the boundary of the Baoshan block as the Ordovician basement prevented stress penetration. **(B)** Schematic diagram showing the structural pattern and relative outcrop altitude labeled as a black circle with text, which correspond to the outcrop photos in Figure 3. The distribution of rock types changed from leucogranite, migmatite, migmatitic gneiss [M. G.], gneiss, and phyllonite toward the top. A higher strain is observed for the lower portion under higher metamorphic conditions. The red square marks the relative position of S_3 foliation measurements, showing sub-horizontal to steep NE-dipping trend.

the S-fabrics are more dominantly observed from the outcrop (Figures 3F–H). Similar to the S_3 fabrics, the upper portion of the fold-thrust belt shows a steeper dip of C-fabrics (40°) than that for the lower portion with a shallower dip of C-fabrics (11°). The curved shear plane cropped out at different elevations from the west at around 800 m–1,000 m of altitude to the east that climbed from ~1,200 m to ~2,000 m (2,075 m is the location of sample 14CG12; the thick black line in Figure 5). A clear spatial pattern of strain condition, structural style, and metamorphic condition can be drawn for the D_3 event. With higher altitude outcrop, less strained low metamorphic grade meta-sedimentary rocks are observed which preserved the older S_1 and S_2 fabrics (Figures 3E–G). In contrast, With lower altitude outcrop, hornblende, gneiss, and mylonitic gneiss rocks are highly strained under medium-to-high-grade metamorphism accompanied by the symmetric sub-horizontal stretching lineation (Figure 7).

3.1.4 D_4

D_4 is a NE-SW-striking steep NW-dipping right-lateral shearing event that can be further divided into two stages: the ductile D_{4a} (Figure 4; Figure 6H) and the brittle D_{4b} (Figure 4). The dip of the shear plane becomes steeper from 45° to 90° from the southwest region toward the northeast region. The D_{4a} right-lateral shearing event accompanied inclined shear folding with NE-SW-striking (22°–55°, the average value is 41.9°; Figure 4), steeply NW-dipping fold axial plane (S_4) under a more ductile regime. This event strongly deformed the earlier fabrics (Figure 3K), including folding the D_3 detachment (the black thick line in Figure 5). Figure 3K shows that the mylonitic melanosome with the D_3 shear sense is folded by the D_4-inclined fold. The S-C_1 shear fabrics are dominated by quartz + biotite + chlorite + tourmaline ± muscovite ± sphene (Figure 6G; Supplementary Table S2) with NE-trending sub-horizontal mineral-stretching lineation L_{4a}. The boudinaged syn-D_2 sillimanite is included in S_4 muscovite (Figure 6H), indicating that a retrograde metamorphism had occurred from D_2 to D_4. This retrograde condition continued to lower greenschist facies according to the chloritization of S_{4a}-parallel biotite and sub-hedral hornblende fragments (Figure 6G). Recrystallized chlorite folia indicate that the D_{4a} shearing event occurred under lower greenschist facies conditions (250°C–400°C).

The lowest temperature of D_4 deformation can be constrained by the development of brittle deformation of D_{4b} (Figure 4). A conjugate fault system of the NE-SW right-lateral and NW-SE left-lateral system was observed and measured (Figure 4; Figure 5; Figure 6H). On the outcrop, the NE-SW right-lateral faults are the dominant fault observed, which is also parallel to the shear plane (C_1) of D_{4a} (Figures 4, 5). The conjugate NW-SE-striking left-lateral fault can also be observed under thin sections as muscovite grains (S_{4b}) truncate the S_{4a} fabric (Figure 6H). The fault kinematic solution results show that the D_{4b} brittle faults formed under a SW-dipping σ_1, E-dipping σ_2, and subhorizontal N- (or S-) trending σ_3 stress regime (Figure 4). Consequently, the NE-SW-striking dextral shearing of the D_4 initially occurred under mid-crustal-level conditions and progressively propagated toward the surface.

3.1.5 D_5

The latest structural features observed are a series of Gaoligong orocline–parallel normal faults (Figure 4) that truncated all ductile fabrics and further rugged the topography (Figure 5). The fault kinematic solution results show sub-vertical σ_1, sub-horizontal N-S trending σ_2, and sub-horizontal E-W trending σ_3 for the formation of these normal faults, and σ_1 and σ_3 exchanged their orientation in the southwest margin of the Tengchong block (Figure 4).

3.2 The correlation of structural evolution among the northern and southern sections

Based on our structural reconstruction, the D_5 normal faults are observed from the northern (Chiu et al., 2018) and southern sections. Although the fault strikes differently among the two sections, the reconstructed fault kinematic analysis and the thermal history are the same for both sections. Xu et al. (2015) obtained the Ar–Ar age plateau of biotite at ca. 23 Ma in the southern section of the Gaoligong orocline (Figure 2C), which is similar to the age in the northern section (Chiu et al., 2018). This indicates that the southern and northern segments have the same thermal history. It should be logical to correlate the

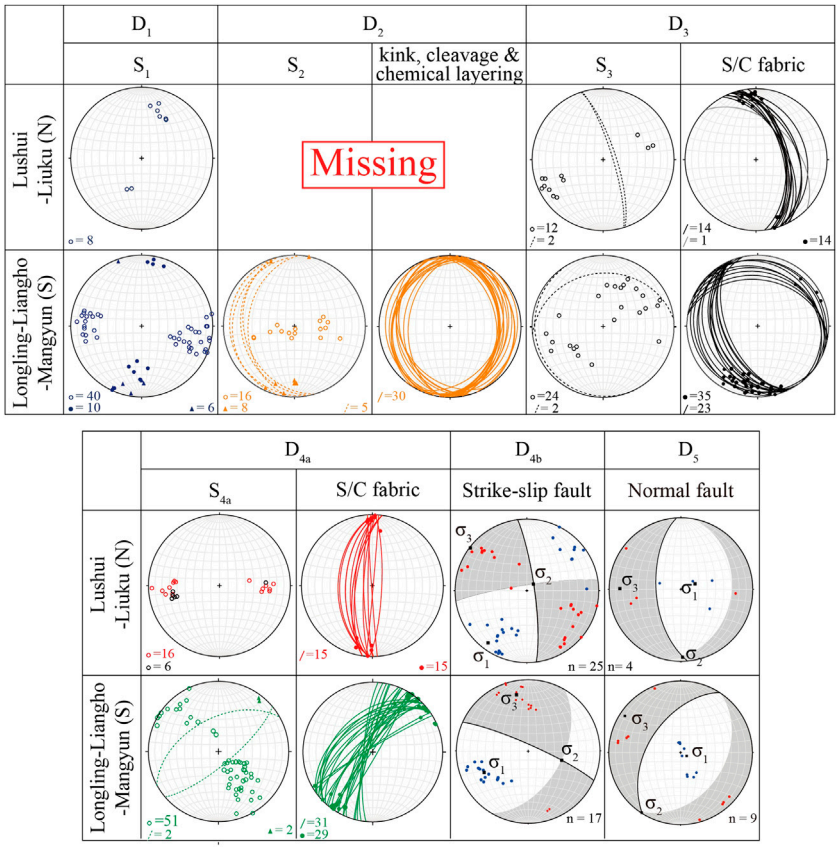

FIGURE 8
Diagram showing southern hemisphere equal-area projection stereonet diagrams of each reconstructed deformation event from both northern (Lushui–Liuku; Chiu et al., 2018) and southern (Longling–Liangho–Mangyun; this study) segments of the Gaoligong orocline. D_3, D_4, and D_5 can be correlated as the same events for both northern and southern sections according to the same structural style and stress pattern. D_2 from the southern section, however, cannot be correlated to any deformation events in the northern section. Therefore, we assume that D_2 only affected the southern section. Although D_1 from both sections shows some similarity in the foliation style, we do not consider the correlation to be formed due to too few data.

same age ranges for D_4 and D_5 as Chiu et al. (2018) suggested. On the premise that the D_4 deformation temperature is close to the closure temperature of the feldspar, Chiu et al. (2018) adopted the younger age of the microcline feldspar as the lower limit of D_4 (15 Ma). The younger age is similar to the start of normal faulting within the Tengchong block (G. Wang et al., 2006). As the fault strikes followed the orocline, the orocline had already formed prior to D_5 (Figure 8). Similar reasoning can be applied to D_4. As D_4 defines the sub-vertical right-lateral strike-slip shear zone developed along the curvature of the Gaoligong orocline, we correlated D_4 from both sections as the same event. This makes D_4 the most dominant right-lateral shearing of the Gaoligong shear belt at this time (28 Ma–15 Ma) and indicates that it was formulated after the formation of the Gaoligong orocline (Figure 8; Chiu et al., 2018).

Unlike D_4 and D_5, D_3 is the first event that did not show structure orientation that follows the trend of the orocline. D_3 in the northern section forms a NW-SE-striking steeply NE dipping thrust belt with a sinistral sense of shear during 35 Ma–28 Ma (Chiu et al., 2018). Although D_3 in the southern section is also a thrusting event, the thrust boundary shows a general NW-SE strike but shallow NE-SW dip direction (Figure 8). A spatial pattern of the steeper dip of the shear plane (C_1) corresponds to the lower metamorphic grade and higher altitude toward the eastern boundary of the Tengchong block as is noted for D_3 (Figure 7B). If we consider the D_3 from the northern and southern sections as the same thrusting event, a shovel-like thrusting plane and curved fold-thrust belt can be recognized that is similar to a fault-propagation fold system (Figure 7A). The various dip directions of the C_1-fabrics can be explained geographically as the northern section marks the footwall of the thrust system. Hence, the NE-dipping steep C_1 foliation observed from the northern section defines the forelimb of the fault propagation fold system (Figure 7A). The shallow-to-moderate dipping C_1 foliations observed from the southern section is equivalent to the flat shear plan to the ramp of this thrust system (Figure 7B).

Other than a spatial pattern between S_3 and C_1 foliations, a spatial pattern can also be observed for the mineral stretching lineation of the mylonites (L_3). Based on Figure 7B, the mineral stretching lineation changed from broad NE-SW plunging to S-plunging and then to N-plunging in mylonitic layers (Figure 3J; Figure 4). This spatial variation in lineation shows the presence of a regional structure along the boundary east of the thrust front which blocked the propagation of strain. Since the D_3 event shows strong spatial variation of foliation, mineral stretching lineation, and metamorphic conditions, we suggest this should be the event that produced the Gaoligong orocline. Recumbent folding under the extensional regime (D_2) is not noted for the northern

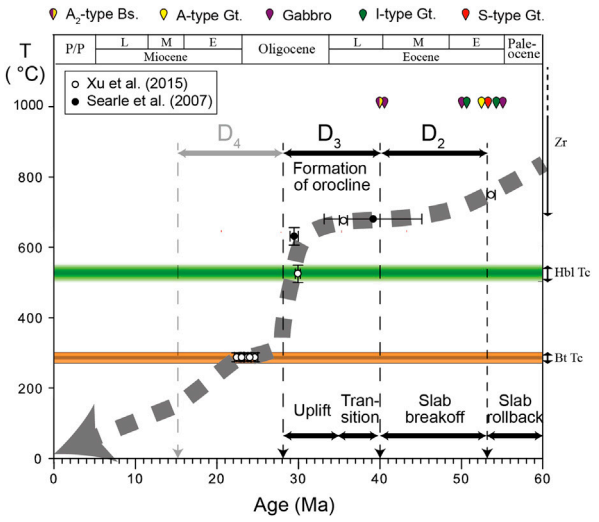

FIGURE 9
Reconstructed cooling path according to published ages and their closure temperature/thermal conditions. The ages are zircon U-Pb dating ages with Ti-in-zircon thermometry, the Ar–Ar ages of hornblende and biotite (Xu et al., 2015), and monazite U-Pb ages with the garnet–biotite geothermometer from the Mogok metamorphic belt (Searle et al., 2007). The different color symbols at 1,000°C mark different magmatic periods of I-type, S-type, A-type, and gabbro in the Tengchong block. Combining the cooling path, the tectonic evolution, and medium-to-high-grade metamorphism conditions for D_2 and D_3, we considered that D_2 occurred during 53–40 Ma when the extensional setting caused the slow cooling of the rock as leucogranite formed. D_3 occurred during 40–28 Ma when the compressional setting produced a thrust fold belt followed by rapid cooling with the uplift, which is D_4. The closure temperatures (T_C) of different minerals used are as follows: T_{CHbl} for hornblende (500°C–550°C; Harrison and McDougall, 1982), T_{CBt} for biotite (275°C–300°C; Harrison et al., 1985); Gt, granite; Bs, basalt; L, late; M, middle; E, early; Paleo, Paleocene; P/P, Pliocene to present.

section. Therefore, we considered the D_2 event as a local event that only occurred in the southern section (Figure 8). Although earlier D_1 events are noted for both sections, insufficient information on neither the structural style nor stress pattern can be used for correlation. Therefore, we only correlate the structural evolution of the whole Gaoligong orocline from D_3 to D_5.

4 Discussion

4.1 The timing of Gaoligong orocline formation

With careful examination of the structural evolution of the Gaoligong orocline, we have revealed that the northern section (Chiu et al., 2018) and the southern section (this study) of the Tengchong block underwent the same structural evolution from D_3 to D_5. With D_4 and D_5 having the same structural trends of the orocline but not D_3, we assigned D_3 to the formulation of the Gaoligong orocline around 40–28 Ma. If we examine the tectonic kinematic setting of the Tengchong block during this time, we can see that the tectonic stress condition changed from extension to compression as the hard collision between India and Eurasia occurred around 40 Ma (Figure 9; Chung et al., 2005; Xu et al., 2008). Before 40 Ma, the Tengchong block was a back-arc setting since 65 Ma due to the rollback of the Neo-Tethys slab (He et al., 2021). This extensional condition continued until slab breakoff occurred around 40 Ma (Xu et al., 2008), making it less likely to form a compressional orocline. The continued northward propagation of the West Burma terrane after 28 Ma (Mitchell, 1993; Gardiner et al., 2018; Morley and Arboit, 2019) is complementary to the further delamination and uplifting of the Tibetan Plateau (Chung et al., 2005). The tectonic strain condition changed to block rotation along the Eastern Himalayan syntaxis and development of N-S-trending dextral shear zones (Chiu et al., 2018). The middle-to-lower-crustal level flow around the Eastern Himalayan syntaxis (Royden et al., 1997; Clark and Royden, 2000; Burchfiel, 2004) is considered as the dominant mechanism for the development of these strike-slip shear zones (D_4). Such a stress condition can reactivate the already deformed thrust plane (S_3) into penetrative shear belts with curvature but not forming a curved shear belt. By comparing the reconstructed structural evolution among the northern and southern sections of

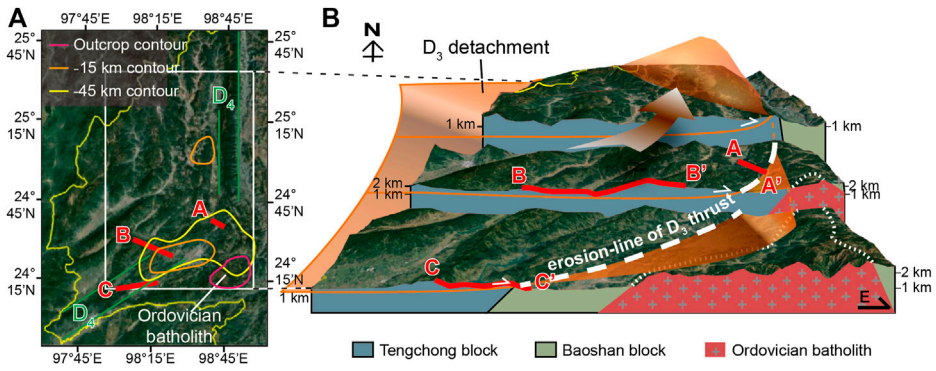

FIGURE 10
Satellite image and 3D-block topography diagram showing major structures and geological units around the Gaoligong orocline. **(A)** Satellite image shows the location of the high-resistivity Ordovician basement (Ye et al., 2020). The red line marks the surface exposure of the Ordovician basement, the orange line marks the boundary at a depth of 15 km, and the yellow line marks the boundary at a depth of 45 km. The green line marks the strike of D_4 shear belts. **(B)** 3D-block diagram showing the curvature of the Gaoligong orocline produced by intersecting the topography surface to the shoveled shape thrust shear plane against the Ordovician batholith.

the Gaoligong orogeny to the regional tectonic evolution, we consider that the formation of the Gaoligong orocline occurred during 40 Ma–28 Ma during a D_3 deformation event.

4.2 Structural geometry influenced by the Ordovician basement

The Tengchong block was accreted to the Baoshan block before the late Cretaceous (Xu et al., 2012; Gardiner et al., 2018). After suturing, these two micro-blocks should have similar structural characteristics as they were under the same tectonic settings: 1) Neo-Tethyan subduction and 2) the India–Eurasia continent–continent collision. However, according to our reconstruction results, the D_3 fold-thrust-belt only developed in the Tengchong block and not in the Baoshan block, suggesting a considerable difference between these two blocks or the presence of some structural barrier to prevent strain from propagating. The Baoshan block is covered by Paleozoic and Mesozoic strata (Akciz et al., 2008) with sporadic intrusion and has a crustal thickness of 30 km–35 km (Zhang and Gao, 2019). On the other hand, the Tengchong block has a relatively thick crust (35 km–40 km) and was repeatedly intruded during 78 Ma–40 Ma (Figure 9; Xu et al., 2008; Xu et al., 2012; Ma et al., 2014; Chen et al., 2015; Xie et al., 2016; Zhang et al., 2017; Zhang and Gao, 2019). The magnetotelluric analysis shows a high-resistivity zone extending through the entire crust beneath the Ordovician basement (Figures 2B and Figure 10; Ye et al., 2020). The collocation of the Tengchong block–Ordovician basement–Baoshan block is similar to the Songpan–Ganzi–Longmenshan–Sichuan basin (Zhao et al., 2012; Wang et al., 2014). Zhao et al. (2012) revealed that the rigid high-resistivity lithosphere blocks the east-directed mid-crustal level flow beneath Longmenshan. Although the tectonic scales of the two localities are different, the concept that an ancient structure, the Proto-Tethys-related Ordovician basement, can stop the strain of D_3 from working on the Baoshan block is consistent between them.

The location of the high-resistivity regions of the Ordovician basement at a depth of 20 km is shown in Figure 10A. The convex shape of the Gaoligong orocline is clear (Ye et al., 2020), but extends beneath the Tengchong block at a depth of middle-to-lower crust (the depth of 15 km and 45 km contours of Figure 10A; Ye et al., 2020). It appears that the Ordovician basement provided a rigid ramp as a footwall for oblique thrusting and resulted in heterogeneous deformation of D_3 in the middle crust (e.g., sample 14CG12; Figure 10B). The Ordovician basement also affected all younger deformation events of the Tengchong block, such as blocking the extension of the N-S-trending GLSZ (red line of Figure 10A) and NE-SW trending D_4 shear zone (green line of Figure 10A). As a response to the accumulated stress (Zhao et al., 2012; Ye et al., 2020), the post-orogeny collapse (D_5) was accompanied by erosion and the development from the south of the Gaoligong mountain to the north after 15 Ma (G. Wang et al., 2006a).

4.3 The formation mechanism of the Gaoligong orocline

The typical formation mechanisms of oroclines can be subdivided into non-rotational (primary) and rotational oroclines (secondary; Figure 1A). According to our reconstruction, no secondary deformation event altered the geometry of the Gaoligong orocline. Thus, we can say that the Gaoligong orocline is more likely to fall within the category of non-rotational (primary) oroclines. The primary orocline is mostly restricted to thin-skinned thrust belts that reflect the plate boundary's original curvature, resulting in one stage of foliation development (e.g., Marshak, 1988; 2005; Weil and Sussman, 2004; Johnston et al., 2013). Based on the lithology distribution, the Gaoligong orocline also marks the boundary between the Tengchong and Baoshan blocks, making it a suitable block setting for developing a non-rotational orocline. In such a case, radial fan foliations that strike parallel to the trend of the orocline should be expected for the syn-orocline-forming event, which would be S/C and S_3 for the Gaoligong orocline. From our field measurements, only NW-SE-striking foliations but not NE-SW-striking foliations are found for the D_3 event. Mechanism 2 is very similar to our reconstructed style, but the indenter, which is the Ordovician basement of the Baoshan block, is situated on the site opposite to the orocline. The wrong geographic position of the indenter and lack of orocline parallel striking foliations argue against the possibility of a primary orocline for the forming mechanism of the Gaoligong orocline. Therefore, we conclude that the Gaoligong orocline is an "atypical" orocline and that the curved geometry along the Tengchong block boundary is a visual effect due to the intersection of the shovel-like thrust belt to the topographically relieved surface.

5 Conclusion

Based on our structural reconstruction, five deformation events were reconstructed for the southern section of the Gaoligong orocline. By correlating the structural evolution between the northern and southern sections, we conclude that the Gaoligong orocline underwent the same deformation event since D_3. All D_4 and D_5 structures show orocline parallel foliation, indicating that they had reused the orocline geometry during deformation. Therefore, the D_4 and D_5 events occurred after the formation of the orocline, leaving D_3 as the most probable candidate for orocline formation during the India–Asia hard collision (40–28 Ma). Since D_4 and D_5 do not show progressive deformation to further develop the curvature of the orocline, we can reject the Gaoligong orocline formed by rotational oroclinal development. Although the thrust belt of D_3 is the major forming mechanism of the Gaoligong orocline, the Ordovician basement behaved as an "indenter" that controlled the geometry of this thrust front. In addition, the radial fan pattern that follows the orocline of the S_3 foliations cannot be observed. Furthermore, according to the primary orocline model, the "indenter" should be situated to the west of the concave orocline, but the Ordovician basement between the Tengchong and Baoshan blocks is situated to the east of the orocline, leading us to reject the hypothesis that the Gaoligong orocline was formed by non-rotational oroclinal development. The geometry of the Gaoligong orocline does not reflect a "bended orogeny," but a visual effect of topography relief over a shovel-like thrusting plane; thus, it is an "atypical" orocline.

Data availability statement

The original contributions presented in the study are included in the article/Supplementary Material; further inquiries can be directed to the corresponding author.

Author contributions

All authors, Y-PC, M-WY, and T-YL, conducted the field study and sample collection of this manuscript together. Y-PC was responsible for sample analysis, structural reconstruction, and manuscript writing. M-WY and T-YL were responsible for data discussion and manuscript editing and revision.

Funding

This study was financially supported by the National Science Council, Taiwan, ROC, under grant numbers National Science Council 102–2116 M003 and NSC 99–2116 M003.

Acknowledgments

We thank Y.Z. Xu and Y.L. Lin for their help in the field. We thank Greg Shellnutt for the final English proofreading.

Conflict of interest

The authors declare that the research was conducted in the absence of any commercial or financial relationships that could be construed as a potential conflict of interest.

Publisher's note

Supplementary material

The Supplementary Material for this article can be found online at: https://www.frontiersin.org/articles/10.3389/feart.2023.1075043/full#supplementary-material

References

Aitken, J. D., and Long, D. G. F. (1978). Mackenzie tectonic arc-Reflection of early basin configuration? *Geology* 6 (10), 626–629. doi:10.1130/0091-7613(1978)6<626:MTAOEB>2.0.CO;2

Akciz, S., Burchfiel, B. C., Crowley, J. L., Jiyun, Y., and Liangzhong, C. (2008). Geometry, kinematics, and regional significance of the chong Shan shear zone, eastern himalayan syntaxis, yunnan, China. *Geosphere* 4, 292–314. doi:10.1130/GES00111.1

Bajolet, F., Replumaz, A., and Lainé, R. (2013). Orocline and syntaxes formation during subduction and collision. *Tectonics* 32 (5), 1529–1546. doi:10.1002/tect.20087

Barrow, G. (1893). On an intrusion of muscovite-biotite gneiss in the south-eastern highlands of scotland, and its accompanying metamorphism. *Quart. J. Geol. Soc. Lond.* 49 (1-4), 330–358. doi:10.1144/GSL.JGS.1893.049.01-04.52

Bendick, R., and Bilham, R. (2001). How perfect is the Himalayan arc? *Geology* 29 (9), 791–794. doi:10.1130/0091-7613(2001)029<0791:HPITHA>2.0.CO;2

Bersan, S. M., Danderfer, A., Lagoeiro, L., and Costa, A. F. O. (2017). The kinematic evolution of the serra central salient, eastern Brazil: A neoproterozoic progressive arc in northern espinhaço fold-thrust belt. *J. South Am. Earth Sci.* 80, 131–148. doi:10.1016/j.jsames.2017.09.013

BGMRYP (1983). *Geological map of yunnan, scale 1:1,000,000 scale*. Kunming: Bureau of Geology and Mineral Resources of Yunnan Province.

Burchfiel, B. C. (2004). 2003 presidential address: New technology; new geological challenges. *GSA Today* 14, 4–10. doi:10.1130/1052-5173(2004)014<4:panngc>2.0.co;2

Capitanio, F. A., Faccenna, C., Zlotnik, S., and Stegman, D. R. (2011). Subduction dynamics and the origin of Andean orogeny and the Bolivian orocline. *Nature* 480, 83–86. doi:10.1038/nature10596

Carey, S. W. (1955). The orocline concept in geotectonics-Part I. *Pap. Proc. - R. Soc. tasman.* 89, 255–288.

Cawood, P. A. (2022). Untangling the history of oroclines and mountain belts. *Natl. Sci. Rev.* 9 (5), nwab211. doi:10.1093/nsr/nwab211

Chen, X. C., Hu, R. Z., Bi, X. W., Zhong, H., Lan, J. B., Zhao, C. H., et al. (2015). Petrogenesis of metaluminous A-type granitoids in the Tengchong–Lianghe tin belt of southwestern China: Evidences from zircon U–Pb ages and Hf–O isotopes, and whole-rock Sr–Nd isotopes. *Lithos* 212-215, 93–110. doi:10.1016/j.lithos.2014.11.010

Chiu, Y. P., Yeh, M. W., Wu, K. H., Lee, T. Y., Lo, C. H., Chung, S. L., et al. (2018). Transition from extrusion to flow tectonism around the Eastern Himalaya syntaxis. *Geol. Soc. Am. Bull.* 130 (9-10), 1675–1696. doi:10.1130/B31811.1

Chung, S. L., Chu, M. F., Zhang, Y. Q., Xie, Y. W., Lo, C. H., Lee, T. Y., et al. (2005). Tibetan tectonic evolution inferred from spatial and temporal variations in post-collisional magmatism. *Earth. Sci. Rev.* 68, 173–196. doi:10.1016/j.earscirev.2004.05.001

Clark, M. K., and Royden, L. H. (2000). Topographic ooze: Building the eastern margin of Tibet by lower crustal flow. *Geology* 28 (8), 703–706. doi:10.1130/0091-7613(2000)028<0703:tobtem>2.3.co;2

Dan, W., Murphy, J. B., Tang, G. J., Zhang, X. Z., White, W. M., and Wang, Q. (2022). Cambrian–Ordovician magmatic flare-up in NE Gondwana: A silicic large igneous province? *GSA Bull.* doi:10.1130/B36331.1

Eroğlu, S., Siebel, W., Danišík, M., Pfänder, J. A., and Chen, F. K. (2013). Multi-system geochronological and isotopic constraints on age and evolution of the Gaoligongshan metamorphic belt and shear zone system in Western Yunnan, China. *J. Asian Earth Sci.* 73, 218–239. doi:10.1016/j.jseaes.2013.03.031

Fergusson, C. L. (2019). Subduction accretion and orocline development in modern and ancient settings: Implications of Japanese examples for development of the New England Orogen of eastern Australia. *J. Geodyn.* 129, 117–130. doi:10.1016/j.jog.2017.11.008

Gardiner, N. J., Searle, M. P., Morley, C. K., Robb, L. J., Whitehouse, M. J., Roberts, N. M. W., et al. (2018). The crustal architecture of Myanmar imaged through zircon U-Pb, Lu-Hf and O isotopes: Tectonic and metallogenic implications. *Gondwana Res.* 62, 27–60. doi:10.1016/j.gr.2018.02.008

Gutiérrez-Alonso, G., Fernández-Suárez, J., and Weil, A. B. (2004). "Orocline triggered lithospheric delamination," in *Orogenic curvature: Integrating paleomagnetic and structural analyses*. Editors A. J. Sussman and A. B. Weil (Colorado: Geological Society of America), 121–131. doi:10.1130/0-8137-2383-3(2004)383[121:OTLD]2.0.CO;2

Gutierrez-Alonso, G., Johnston, S., Weil, A., Pastor-Galán, D., and Fernández-Suárez, J. (2012). Buckling an orogen: The cantabrian orocline. *GSA Today* 22, 4–9. doi:10.1130/GSATG141A.1

Harrison, T. M., Duncan, I., and McDougall, I. (1985). Diffusion of ^{40}Ar in biotite: Temperature, pressure and compositional effects. *Geochim. Cosmochim. Acta* 49 (11), 2461–2468. doi:10.1016/0016-7037(85)90246-7

Harrison, T. M., and McDougall, I. (1982). The thermal significance of potassium feldspar K-Ar ages inferred from age spectrum results. *Geochim. Cosmochim. Ac.* 46 (10), 1811–1820. doi:10.1016/0016-7037(82)90120-X

He, X., Zhou, R., Tan, S., Liu, Z., Wang, G., Jiang, Z., et al. (2021). Late Cretaceous–Eocene magmatism induced by slab rollback and breakoff in the Tengchong terrane, SW China. *Int. Geol. Rev.* 63 (3), 294–316. doi:10.1080/00206814.2019.1709567

Hwang, B. H., Son, M., Kim, J. S., Yang, K., and Kim, J. S. (2012). Cenozoic wrench tectonics and oroclinal bending in SE Korea. *Int. Geol. Rev.* 54 (6), 642–653. doi:10.1080/00206814.2011.562389

Johnston, S. T., Weil, A. B., and Gutiérrez-Alonso, G. (2013). Oroclines: Thick and thin. *Geol. Soc. Am. Bull.* 125, 643–663. doi:10.1130/B30765.1

Klootwijk, C. T., Conaghan, P. J., and McA Powell, C. (1985). The himalayan arc: Large-scale continental subduction, oroclinal bending and back-arc spreading. *Earth Planet. Sci. Lett.* 75 (2), 167–183. doi:10.1016/0012-821X(85)90099-8

Lawrence, R. D., Yeats, R. S., Khan, S. H., Subhani, A. M., and Bonelli, D. (1981). Crystalline rocks of the Spinatizha area, Pakistan. *J. Struct. Geol.* 3 (4), 449–457. doi:10.1016/0191-8141(81)90044-4

Li, G. J., Wang, Q. F., Huang, Y. H., Gao, L., and Yu, L. (2016). Petrogenesis of middle Ordovician peraluminous granites in the Baoshan block: Implications for the early Paleozoic tectonic evolution along East Gondwana. *Lithos* 245, 76–92. doi:10.1016/j.lithos.2015.10.012

Liu, G., Sun, Z., Zi, J., Santosh, M., Zhao, T., Feng, Q., et al. (2021). Proto-Tethys ophiolitic mélange in SW Yunnan: Constraints from zircon U-Pb geochronology and geochemistry. *Geosci. Front.* 12 (5), 101200. doi:10.1016/j.gsf.2021.101200

Liu, S., Hu, R. Z., Gao, S., Feng, C. X., Huang, Z., Lai, S., et al. (2009). U–Pb zircon, geochemical and Sr–Nd–Hf isotopic constraints on the age and origin of early palaeozoic I-type granite from the tengchong–baoshan block, western yunnan province, SW China. *J. Asian Earth Sci.* 36 (2), 168–182. doi:10.1016/j.jseaes.2009.05.004

Ma, L., Wang, Y., Fan, W., Geng, H., Cai, Y., Zhong, H., et al. (2014). Petrogenesis of the early Eocene I-type granites in west Yingjiang (SW Yunnan) and its implication for the eastern extension of the Gangdese batholiths. *Gondwana Res.* 25, 401–419. doi:10.1016/j.gr.2013.04.010

Macedo, J., and Marshak, S. (1999). Controls on the geometry of fold-thrust belt salients. *GSA Bull.* 111 (12), 1808–1822. doi:10.1130/0016-7606(1999)111<1808:COTGOF>2.3.CO;2

Marshak, S. (1988). Kinematics of orocline and arc formation in thin-skinned orogens. *Tectonics* 7 (1), 73–86. doi:10.1029/TC007i001p00073

Marshak, S. (2005). Salients, recesses, arcs, oroclines, and syntaxes - a review of ideas concerning the formation of map-view curves in fold-thrust belts. *AAPG Mem.* 82, 131–156. doi:10.1306/M82813C9

Martínez Catalán, J. R. (2011). Are the oroclines of the Variscan belt related to late Variscan strike-slip tectonics? *Terra nova.* 23, 241–247. doi:10.1111/j.1365-3121.2011.01005.x

Martínez Catalán, J. R. (2012). The Central Iberian arc, an orocline centered in the Iberian Massif and some implications for the Variscan belt. *Int. J. Earth Sci.* 101 (5), 1299–1314. doi:10.1007/s00531-011-0715-6

Metcalfe, I. (2013). Gondwana dispersion and Asian accretion: Tectonic and palaeogeographic evolution of eastern Tethys. *J. Asian Earth Sci.* 66 (0), 1–33. doi:10.1016/j.jseaes.2012.12.020

Metcalfe, I. (1996). Gondwanaland dispersion, Asian accretion and evolution of eastern Tethys. *Aust. J. Earth Sci.* 43 (6), 605–623. doi:10.1080/08120099608728282

Mitchell, A. H. G. (1993). Cretaceous–Cenozoic tectonic events in the Western Myanmar (Burma)–Assam region. *J. Geol. Soc. Lond.* 150 (6), 1089–1102. doi:10.1144/gsjgs.150.6.1089

Mitchell, A. H. G., Hlaing, T., and Oo, T. (2008). "Possible jurassic collision within the Shan-Thai block in central Myanmar: Continuation of the shengza suture in tibet?" in *International conference on tectonics of northwestern Indochina abstract volum*. Editors S. Chantraprasert, O. Limtrakun, and Compilers (Chiang Mai, Thailand), 23–24.

Morley, C. K., and Arboit, F. (2019). Dating the onset of motion on the Sagaing fault: Evidence from detrital zircon and titanite U-Pb geochronology from the North Minwun Basin, Myanmar. *Geology* 47 (6), 581–585. doi:10.1130/G46321.1

Muñoz, J. A., Beamud, E., Fernández, O., Arbués, P., Dinarès-Turell, J., and Poblet, J. (2013). The Ainsa Fold and thrust oblique zone of the central Pyrenees: Kinematics of a curved contractional system from paleomagnetic and structural data. *Tectonics* 32 (5), 1142–1175. doi:10.1002/tect.20070

Owona, S., Ondoa, J. M., and Ekodeck, G. E. (2013). Evidence of quartz, feldspar and amphibole crystal plastic deformations in the paleoproterozoic nyong complex shear zones under amphibolite to granulite conditions (west central african fold belt, SW Cameroon). *J. Geol. Geogr.* 5 (3), 186–201. doi:10.5539/jgg.v5n3p186

Passchier, C. W., and Trouw, R. A. J. (1996). *Microtectonics*. Berlin: Springer-Verlag, 289.

Patiño Douce, A. E., Humphreys, E. D., and Johnston, A. D. (1990). Anatexis and metamorphism in tectonically thickened continental crust exemplified by the Sevier hinterland, Western North America. *Earth Planet. Sci. Lett.* 97, 290–315. doi:10.1016/0012-821x(90)90048-3

Qi, X., Wei, C., Zhang, C., Zhang, S., Hu, Z., and Ji, F. (2019). Southward extension of the bangonghu–nujiang suture: Evidence from early cretaceous intermediate and felsic magmatism in the Gaoligong orogen, China. *J. Asian Earth Sci.* 175, 1–25. doi:10.1016/j.jseaes.2018.09.007

Royden, L. H., Burchfiel, B. C., King, R. W., Wang, E., Chen, Z., Shen, F., et al. (1997). Surface deformation and lower crustal flow in eastern Tibet. *Science* 276, 788–790. doi:10.1126/science.276.5313.788

Sacchi, R., and Cadoppi, P. (1988). Oroclines and pseudo-oroclines. *Tectonophysics* 146 (1), 47–58. doi:10.1016/0040-1951(88)90080-7

Searle, M. P., Noble, S. R., Cottle, J. M., Waters, D. J., Mitchell, A. H. G., Hlaing, T., et al. (2007). Tectonic evolution of the Mogok metamorphic belt, Burma (Myanmar) constrained by U-Th-Pb dating of metamorphic and magmatic rocks. *Tectonics* 26 (3), TC3014. doi:10.1029/2006TC002083

Shi, M. F., Lin, F. C., Li, Z., Ling, X. M., and Shi, H. Z. (2011). Stratigraphic zoning and tectonic events in Indochina and adjacent areas of southwest China. *Geol. China* 38 (5), 1244–1256.

Sone, M., and Metcalfe, I. (2008). Parallel tethyan sutures in mainland southeast asia: New insights for palaeo-tethys closure and implications for the indosinian orogeny. *CR Geosci.* 340 (2–3), 166–179. doi:10.1016/j.crte.2007.09.008

Song, S. G., Niu, Y. L., Wei, C. J., Ji, J. Q., and Su, L. (2010). Metamorphism, anatexis, zircon ages and tectonic evolution of the Gongshan block in the northern Indochina continent- an eastern extension of the Lhasa Block. *Lithos* 120, 327–346. doi:10.1016/j.lithos.2010.08.021

Sun, Z., Dong, G., Santosh, M., Mo, X., Dong, P., Wang, W., et al. (2020). A Late Cretaceous felsic magmatic suite from the Tengchong Block, Western Yunnan: Integrated geochemical and isotopic investigation and implications for Sn mineralization. *Geol. Mag.* 157 (8), 1316–1332. doi:10.1017/S0016756819001493

Wang, G., Wan, J., and Wang, E. (2006a). Extensional collapse of the southern part of the Gaoligong range in the western yunnan, China and its tectonic origin. *Acta Geol. Sin.* 80 (9), 1262–1273. doi:10.3321/j.issn:0001-5717.2006.09.004

Wang, X., Zhang, G., Fang, H., Luo, W., Zhang, W., Zhong, Q., et al. (2014). Crust and upper mantle resistivity structure at middle section of Longmenshan, eastern Tibetan plateau. *Tectonophysics* 619-620, 143–148. doi:10.1016/j.tecto.2013.09.011

Wang, Y. J., Fan, W. M., Zhang, Y. H., Peng, T. P., Chen, X. Y., and Xu, Y. G. (2006b). Kinematics and $^{40}Ar/^{39}Ar$ geochronology of the Gaoligong and Chongshan shear systems, Western Yunnan, China: Implications for early Oligocene tectonic extrusion of SE Asia. *Tectonophysics* 418, 235–254. doi:10.1016/j.tecto.2006.02.005

Wang, Y., Xing, X., Cawood, P. A., Lai, S., Xia, X., Fan, W., et al. (2013). Petrogenesis of early Paleozoic peraluminous granite in the Sibumasu Block of SW Yunnan and diachronous accretionary orogenesis along the northern margin of Gondwana. *Lithos* 182-183, 67–85. doi:10.1016/j.lithos.2013.09.010

Weil, A. B., Van der Voo, R., and Van der Pluijm, B. A. (2001). Oroclinal bending and evidence against the Pangea megashear: The Cantabria-Asturias arc (northern Spain). *Geology* 29 (11), 991–994. doi:10.1130/0091-7613(2001)029<0991:OBAEAT>2.0.CO;2

Weil, A., and Sussman, A. (2004). Classifying curved orogens based on timing relationships between structural development and vertical-axis rotations. *Spec. Pap. Geol. Soc. Am.* 383, 1–17. doi:10.1130/0-8137-2383-3(2004)383[1:CCOBOT]2.0.CO;2

Wopfner, H. (1996). Gondwana origin of the baoshan and Tengchong terranes of West Yunnan. *Geol. Soc. Spec. Publ.* 106 (1), 539–547. doi:10.1144/gsl.sp.1996.106.01.34

Xie, J. C., Zhu, D. C., Dong, G., Zhao, Z., Wang, Q., and Mo, X. (2016). Linking the Tengchong terrane in SW yunnan with the lhasa terrane in southern tibet through magmatic correlation. *Gondwana Res.* 39, 217–229. doi:10.1016/j.gr.2016.02.007

Xu, Y. G., Lan, J. B., Yang, Q. J., Huang, X. L., and Qiu, H. N. (2008). Eocene break-off of the Neo-Tethyan slab as inferred from intraplate-type mafic dykes in the Gaoligong orogenic belt, eastern Tibet. *Chem. Geol.* 255 (3–4), 439–453. doi:10.1016/j.chemgeo.2008.07.016

Xu, Y. G., Yang, Q. J., Lan, J. B., Luo, Z. Y., Huang, X. L., Shi, Y. R., et al. (2012). Temporal–spatial distribution and tectonic implications of the batholiths in the Gaoligong–Tengliang–Yingjiang area, Western Yunnan: Constraints from zircon U–Pb ages and Hf isotopes. *J. Asian Earth Sci.* 53, 151–175. doi:10.1016/j.jseaes.2011.06.018

Xu, Z., Wang, Q., Cai, Z., Dong, H., Li, H., Chen, X., et al. (2015). Kinematics of the Tengchong Terrane in SE Tibet from the late Eocene to early Miocene: Insights from coeval mid-crustal detachments and strike-slip shear zones. *Tectonophysics* 665, 127–148. doi:10.1016/j.tecto.2015.09.033

Yamaoka, K., Fukao, Y., and Kumazawa, M. (1986). Spherical shell tectonics: Effects of sphericity and inextensibility on the geometry of the descending lithosphere. *Rev. Geophys.* 24 (1), 27–53. doi:10.1029/RG024i001p00027

Ye, T., Chen, X., Huang, Q., Zhao, L., Zhang, Y., and Uyeshima, M. (2020). Bifurcated crustal channel flow and seismogenic structures of intraplate earthquakes in western yunnan, China as revealed by three-dimensional magnetotelluric imaging. *J. Geophys. Res. Solid Earth* 125 (9), e2019JB018991. doi:10.1029/2019JB018991

Yeh, M. W., and Bell, T. H. (2004). Significance of dextral reactivation of an E-W transfer fault in the formation of the Pennsylvania orocline, central Appalachians. *Tectonics* 23 (5), TC5009. doi:10.1029/2003TC001593

Zhang, B., Chai, Z., Yin, C. Y., Huang, W. T., Wang, Y., Zhang, J. J., et al. (2017). Intra-continental transpression and gneiss doming in an obliquely convergent regime in SE Asia. *J. Struct. Geol.* 97, 48–70. doi:10.1016/j.jsg.2017.02.010

Zhang, Z., and Gao, Y. (2019). Crustal thicknesses and Poisson's ratios beneath the chuxiong-simao basin in the southeast margin of the Tibetan plateau. *Earth Planet. Sci. Lett.* 3, 69–84. doi:10.26464/epp2019008

Zhao, G., Unsworth, M. J., Zhan, Y., Wang, L., Chen, X., Jones, A. G., et al. (2012). Crustal structure and rheology of the Longmenshan and Wenchuan Mw 7.9 earthquake epicentral area from magnetotelluric data. *Geology* 40 (12), 1139–1142. doi:10.1130/G33703.1

Zhao, S. W., Lai, S. C., Gao, L., Qin, J. F., and Zhu, R. Z. (2017). Evolution of the proto-tethys in the baoshan block along the east Gondwana margin: Constraints from early palaeozoic magmatism. *Int. Geol. Rev.* 59, 1–15. doi:10.1080/00206814.2016.1198994

Zhao, S. W., Lai, S. C., Qin, J. F., and Zhu, R. Z. (2014). Zircon U-Pb ages, geochemistry, and Sr-Nd-Pb-Hf isotopic compositions of the pinghe pluton, southwest China: Implications for the evolution of the early palaeozoic proto-tethys in southeast asia. *Int. Geol. Rev.* 56 (7), 885–904. doi:10.1080/00206814.2014.905998

frontiers | Frontiers in Earth Science

TYPE Original Research
PUBLISHED 06 February 2023
DOI 10.3389/feart.2023.1110568

OPEN ACCESS

EDITED BY
Changqian Ma,
China University of Geosciences Wuhan, China

REVIEWED BY
Fuhao Xiong,
Chengdu University of Technology, China
Anh Nong,
Ho Chi Minh City University of Science, Vietnam
Juliane Hennig-Breitfeld,
Chemostrat Ltd., United Kingdom

*CORRESPONDENCE
J. Gregory Shellnutt,
jgshelln@ntnu.edu.tw

SPECIALTY SECTION
This article was submitted to Petrology, a section of the journal Frontiers in Earth Science

RECEIVED 29 November 2022
ACCEPTED 19 January 2023
PUBLISHED 06 February 2023

CITATION
Shellnutt JG, Ma GS-K, Chan JS-L, Wong JP-M and Wang K-L (2023), Early Cretaceous volcanic-arc magmatism in the Dalat-Kratie Fold Belt of eastern Cambodia: implications for the lithotectonic evolution of the Indochina terrane.
Front. Earth Sci. 11:1110568.
doi: 10.3389/feart.2023.1110568

Early Cretaceous volcanic-arc magmatism in the Dalat-Kratie Fold Belt of eastern Cambodia: implications for the lithotectonic evolution of the Indochina terrane

J. Gregory Shellnutt[1]*, George S.-K. Ma[2], Jacky S.-L. Chan[3], Jean P.-M. Wong[4] and Kuo-Lung Wang[5]

[1]National Taiwan Normal University, Department of Earth Sciences, Taipei, Taiwan, [2]The Chinese University of Hong Kong, Jockey Club Museum of Climate Change, Shatin, NT, Hong Kong SAR, China, [3]ProjecTerra, Hong Kong, Hong Kong SAR, China, [4]The University of Hong Kong, Department of Earth Sciences, Pokfulam, Hong Kong SAR, China, [5]Academia Sinica, Institute of Earth Sciences, Taipei, Taiwan

Mesozoic granitic plutons are found throughout the Indochina terrane of eastern Cambodia and southern Vietnam. The granitic rocks range in age from Early Triassic (240 Ma) to Late Cretaceous (80 Ma) and record distinct tectonomagmatic periods associated with subduction of the Paleotethys and Paleo-Pacific oceans. Samples collected from the Snoul pluton, eastern Cambodia are composed of silicic and intermediate dioritic rocks, and basalt. The quartz diorites and diorites are magnesian, metaluminous, calcic to calc-alkalic, and similar to volcanic-arc granitoids whereas the basaltic rocks are compositionally similar to within-plate basalt. Zircon U-Pb geochronology and Lu-Hf isotopes and whole rock Sr-Nd isotopes show that the silicic rocks are Albian and isotopically juvenile (107.5 ± 0.3 Ma, 109.1 ± 0.4 Ma; $\varepsilon_{Hf}(t)$ = +7.0–+17.0; $^{87}Sr/^{86}Sr_i$ = 0.704313–0.707681; $\varepsilon_{Nd}(t)$ = +3.1–+4.9). Fractional crystallization modeling using a dioritic composition as the parental magma demonstrates that it is possible to generate the quartz diorite compositions under oxidizing (ΔFMQ +1) and hydrous (H_2O = 2 wt%) conditions suggesting that they are consanguineous. The isotopically juvenile nature of the dioritic rocks and their compositional similarity ($SiO_2 \geq 56$ wt%, $Al_2O_3 \geq 15$ wt%, Sr ≥ 400 ppm, Y ≤ 18 ppm, Yb ≤ 1.9 ppm) to adakitic rocks indicates that the parental magmas of the Snoul pluton were likely derived by partial melting of juvenile mafic basement rocks of the Indochina terrane. Moreover, Early Cretaceous plutonic rocks of Cambodia are isotopically distinct from plutonic rocks of similar age and tectonic setting from Vietnam suggesting that there could be a lithotectonic domain boundary within the Southern Indochina terrane. In contrast, the basaltic rocks likely record a temporally distinct period of magmatism associated with Late Cenozoic tensional plate stress.

KEYWORDS

Indochina terrane, volcanic-arc granite, mafic enclaves, Dalat-Kratie Belt, Early Cretaceous

Introduction

The Mesozoic Era was an important time for the lithospheric evolution of South, Southeast, and East Asia (Sone and Metcalfe, 2008; Hall, 2012; Hall, 2017; Wang et al., 2013; Hutchison, 2014; Metcalfe, 2017). During the Triassic to Cretaceous lithotectonic terranes derived from Gondwana (e.g., Qiangtang, West Myanmar, Sibumasu, Indochina) drifted across the Tethyan

oceans and accreted to the southern Eurasian margin and cratons of China (Carter et al., 2001; Metcalfe, 2006; Metcalfe, 2013; Carter and Clift, 2008). Furthermore, the North China Block and South China Block amalgamated and subduction of the Paleo-Pacific plate beneath eastern Eurasia initiated periods of variably intense arc magmatism until the Late Cretaceous (Zhou et al., 2006; Li and Li, 2007; Faure et al., 2008; Lepvrier et al., 2008). Subsequently, during the Cenozoic, the India-Eurasia collision ushered in a period of regional horizontal and vertical tectonics across south and southeast Asia that led to the reorganization and displacement of the accreted terranes (White and Lister, 2012; Bouilhol et al., 2013; Schellart et al., 2019). Moreover, the secession of subduction-related magmatism in the east was followed by a period of crustal relaxation and the development of the proto-South China Sea (Zheng et al., 2019).

Of particular interest is the evolution of the Indochina terrane as it was affected by multiple collisional and accretionary events related to the subduction of the Paleotethys Ocean (Sone and Metcalfe, 2008; Hutchinson, 2014; Metcalfe, 2017; Faure et al., 2018; Wang et al., 2018; Tran et al., 2020; Waight et al., 2021). During the Early Triassic, the Indochina terrane collided and accreted to the South China Block whereas during the Late Triassic it was affected by collision and accretion of the Sukhothai and Sibumasu terranes (Lepvrier et al., 2008; Burrett et al., 2021; Jiang et al., 2021). Furthermore, the Paleo-Pacific plate subducted beneath the Indochina terrane beginning in the Early Cretaceous and was responsible for the generation of widespread Cordilleran Batholiths throughout the Dalat-Kratie Fold Belt of southern Vietnam and eastern Cambodia (Nguyen et al., 2004a; Nguyen et al., 2004b; Shellnutt et al., 2013; Cheng et al., 2019; Hennig-Breitfeld et al., 2021; Nong et al., 2021; Nong et al., 2022). The Dalat-Kratie Fold Belt is composed of Triassic to Cretaceous sedimentary rocks and volcano-plutonic rocks that are overlain by Quaternary basalt (Zaw et al., 2014). The granitic rocks are primarily of Cretaceous (130-75 Ma) ages, although Carboniferous (332 ± 5 Ma), Permian (277 ± 2 Ma), and Triassic (202 ± 0.4 Ma; 238 ± 0.3 Ma; 211 ± 1.7 Ma; 248.9 ± 2.4 Ma) mafic and silicic igneous rocks are also present in the region (Nguyen et al., 2004a; Nguyen et al., 2004b; Shellnutt et al., 2013; Cheng et al., 2019; Hennig-Breitfeld et al., 2021; Kasahara et al., 2021).

The Cretaceous rocks record two distinct periods of granitic magmatism related to the subduction of the Paleo-Pacific plate. The more voluminous, older (130–90 Ma) rocks are attributed to volcanic-arc magmatism and contemporaneous with the Late Yanshanian Orogeny of East Asia whereas the younger (<90 Ma) rocks are correlated with post-collisional magmatism (Nguyen et al., 2004a; Nguyen et al., 2004b; Shellnutt et al., 2013; Cheng et al., 2019; Hennig-Breitfeld et al., 2021; Kasahara et al., 2021). Located within the Dalat-Kratie Fold Belt of eastern Cambodia is the previously unstudied Snoul pluton. Rocks were collected from a surface exposure and mineral exploration drill core. The surface exposure is composed of quartz diorite and diorite whereas the drill core encountered basaltic dykes and dioritic enclaves within the host quartz diorite.

In this paper, we present *in situ* zircon U-Pb geochronology and Hf isotopes, whole rock geochemistry, and whole rock Sr-Nd isotopes of host rocks and enclaves collected from the surface and drill core of the Snoul pluton of eastern Cambodia. The results of this study are used to constrain the age of emplacement and the tectonomagmatic evolution of the host quartz diorite within the context of Mesozoic tectonics of the Indochina terrane. Moreover, we evaluate the relationship between the dioritic and basaltic enclaves to the host rocks in order to assess their petrogenetic relationship.

Geological Background

Present-day Southeast Asia is composed largely of terranes derived from the margin of eastern Gondwana (e.g., Hall, 2012; Hall, 2017; Metcalfe, 2013; Metcalfe, 2017; Usuki et al., 2013). Major terranes include South China, Indochina, Sibumasu, West Burma, East Malay, and West Sumatra (Figure 1) which travelled northwards from the southern hemisphere and accreted to the southern margin of Eurasia. Convergence is still ongoing today, as the Australian plate approaches northward *via* subduction beneath Sumatra, Java, and Timor. The long-term convergence in this region has resulted in multiple episodes of arc magmatism, ocean basin opening and closure, and mountain-building events. The resultant deformation zones and fold belts are important sites of mineral resources such as orogenic gold, porphyry copper, volcanic-hosted massive sulphide, and gemstone deposits (Zaw et al., 2014).

Of the Gondwana-derived fragments, the Indochina Block is one of the largest tectonic units in Southeast Asia, occupying much of Cambodia, Laos, Malaysia, Myanmar, Thailand, and Vietnam (Figure 1; Hutchinson, 2014; Metcalfe, 2017; Nakano et al., 2021). The Indochina Block is bounded to the northeast by the Ailaoshan–Song Ma suture and to the west by the Sukhothai–Chanthaburi arc and the Paleo-Tethys suture. The block is generally divided into several tectonic zones: the Truong Son Fold Belt (Laos and western Vietnam) and Kontum massif (central Vietnam) along its eastern margin, the Loei Fold Belt (western Cambodia, Thailand and eastern Myanmar) along the western margin and the Dalat–Kratie Fold Belt (eastern Cambodia and southern Vietnam) in the south (Hutchinson, 2014; Metcalfe, 2017; Burrett et al., 2021).

The Truong Son Fold Belt is composed of Ordovician–Carboniferous and Neoproterozoic–Silurian sedimentary rocks intruded by Permian-Triassic volcanic and intrusive rocks (Lepvrier et al., 2004; Burnett et al., 2021). The Kontum massif represents a metamorphic core of granulite facies rocks, with Nd depleted mantle model ages of 2.4-1.2 Ga (Lan et al., 2003) and an inherited U–Pb zircon core of 1.4 Ga (Nam et al., 2001). Subsequent deformation and metamorphic overprinting on the Truong Son and Kontum rocks suggests that the accretion of the Indochina Block to the Eurasia margin occurred during the Early Triassic (260-240 Ma; Carter et al., 2001; Lepvrier et al., 2004; Roger et al., 2007). The Loei Fold Belt is composed of a succession of carbonates and metamorphosed tuffaceous rocks, intruded or overlain by Silurian to Late Cenozoic igneous rock (Wang et al., 2018; Burrett et al., 2021; Shi et al., 2021).

The Dalat–Kratie Fold Belt is composed of a Precambrian basement, Triassic–Cretaceous sedimentary rocks, Cretaceous granitic rocks, and Cenozoic intraplate basaltic rocks (Nguyen et al., 2004a; Nguyen et al., 2004b). The Cretaceous granitoids can be subdivided into I-type and A-type (Nguyen et al., 2004a; Nguyen et al., 2004b; Shellnutt et al., 2013; Waight et al., 2021). The more widespread I-type Early Cretaceous granitic batholiths are related to the subduction of the Paleo-Pacific Ocean crust beneath Indochina and contemporaneous with Yanshanian magmatism along the coast of eastern China. The Late Cretaceous A-type granitic rocks that crop out

10.3389/feart.2023.1110568

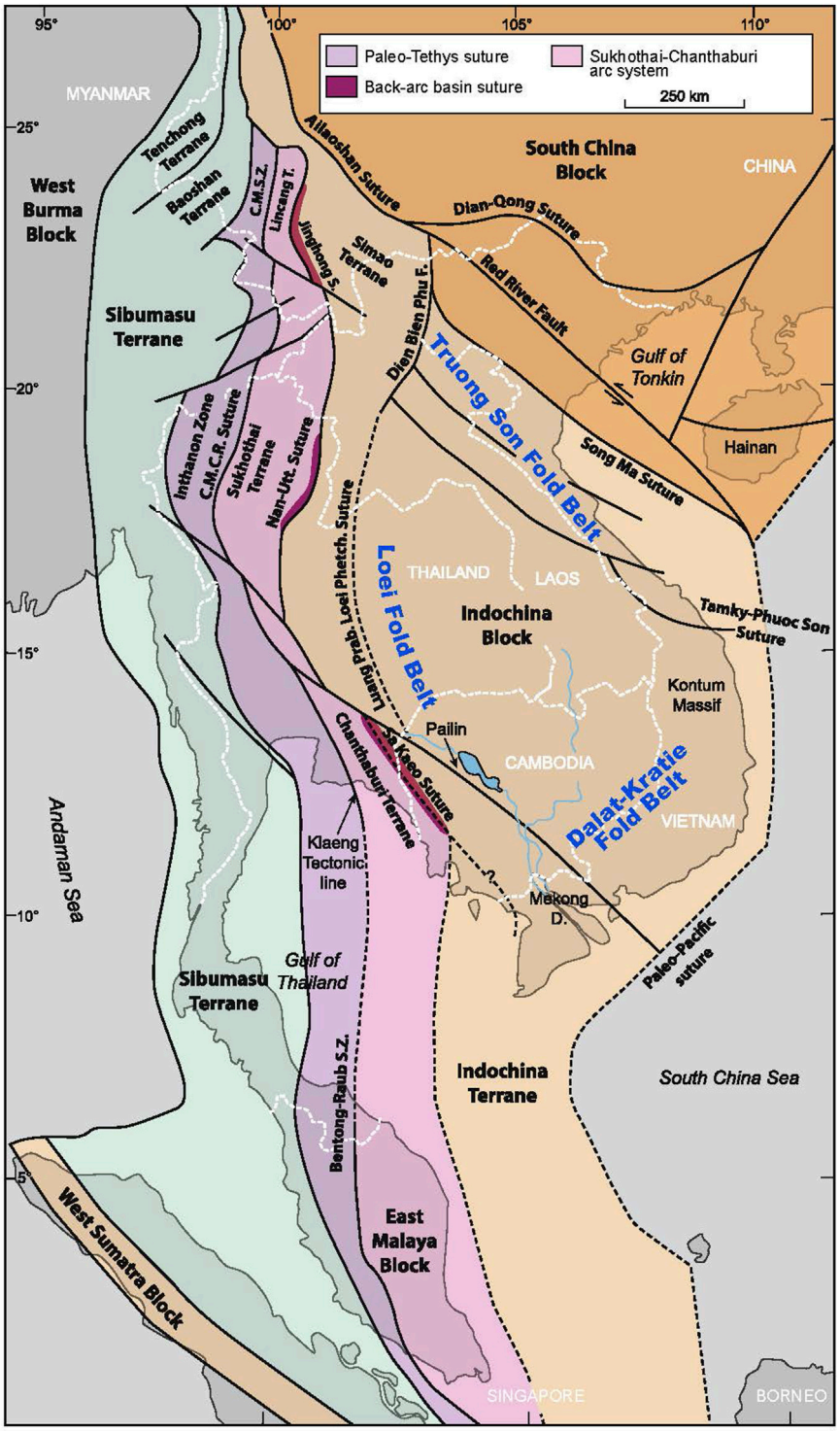

FIGURE 1
Tectonic subdivision of geological terranes of Southeast Asia showing the location of the Dalat-Kratie Fold Belt (modified from Metcalfe, 2017).

in southern Vietnam are interpreted to be related to post-collision extensional stress associated with trench retreat and slab rollback of the Paleo-Pacific Ocean (Zhou et al., 2006; Shellnutt et al., 2013; Cheng et al., 2019; Hennig-Breitfeld et al., 2021; Kasahara et al., 2021; Waight et al., 2021; Nong et al., 2022).

Sample locations

The present study focuses on the granitic rocks and enclaves of the Snoul pluton within the Dalat–Kratie Fold Belt of eastern Cambodia (Figure 2). The Snoul pluton is a newly discovered intrusion of the upper

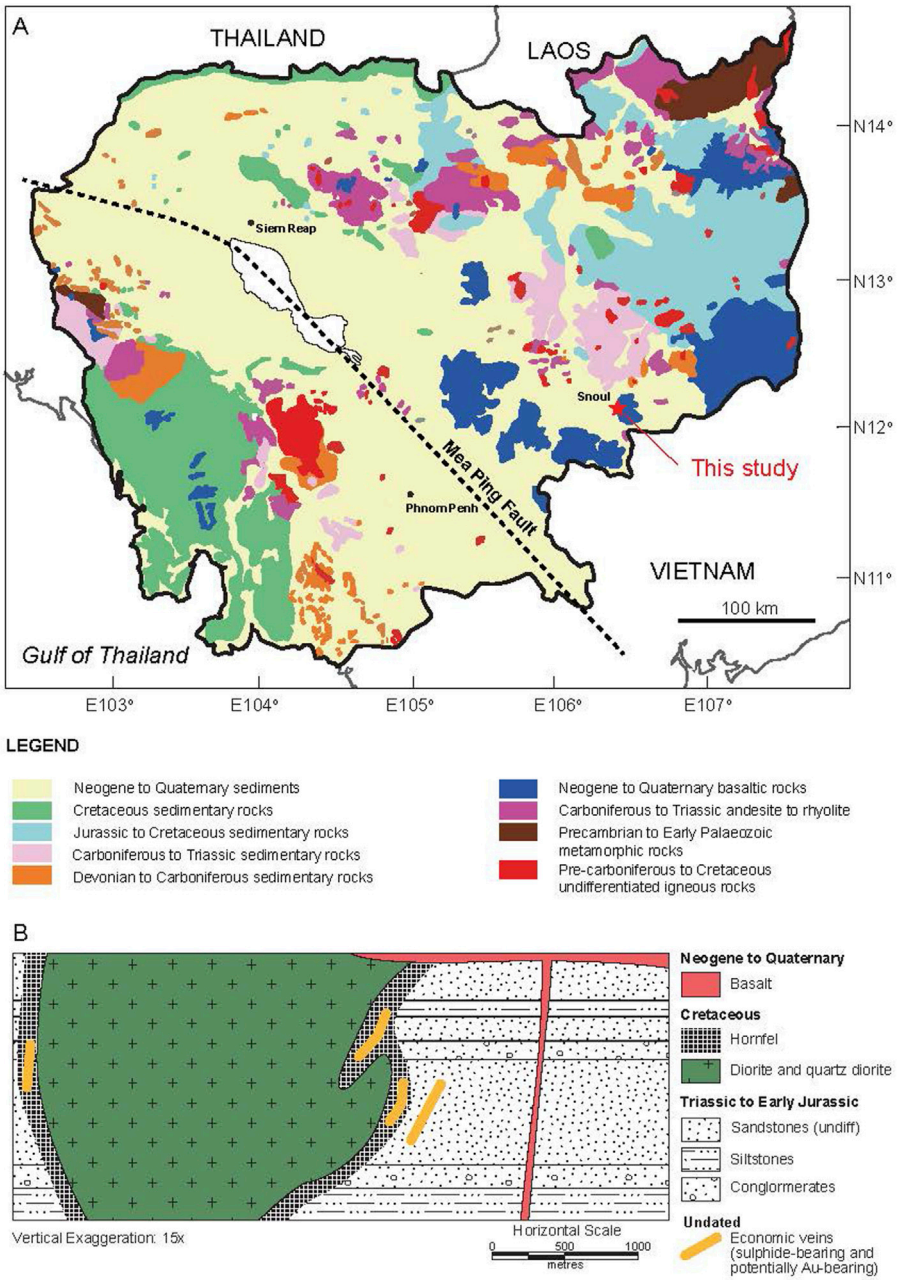

FIGURE 2
(A) Geological map of Cambodia showing the location of the Snoul pluton (modified from Kasahara et al., 2021). **(B)** Schematic cross-section of the region underneath the Snoul pluton (green) highlighting the stratigraphic relationships of various lithological units.

crust that intrudes Triassic–Early Jurassic sandstones, siltstones and conglomerates, although detailed field mapping of the pluton was not possible due to the widespread Quaternary sedimentary cover in the region (Figure 2B). Field occurrences, drill core logging, and geophysical surveys (e.g., airborne magnetic anomalies) were used by local exploration companies to interpret the extent of the pluton which is estimated to be 1.5–2 km in diameter. At least two varieties of quartz diorite were observed in the field, one finer-grained and the other coarser-grained, but with similar mineralogy. The best exposure can be found at 0647977 mE, 1328288 mN and its vicinities, where a fine–medium-grained dioritic body is intruded by aplite and mafic dykes (Figures 3A–C). Most of the samples (A15-series, A17-series) were selected from drill cores provided by Southern Gold (Cambodia) obtained from its 2009 drilling campaign (Figures 3C, D). The drill core samples were split diagonally with one-half taken for this study and the other half retained by Southern Gold (Cambodia). Other samples (O-series) were collected from the few exposed surface outcrops.

Petrography

Quartz diorite

The quartz diorite host rocks (A15.2, A17.1ah, A17.3b, A17-7-HA, A17-14-h, O27b, O52B) were collected from the surface and the drill core. The rocks are coarse grained and granular with the surface

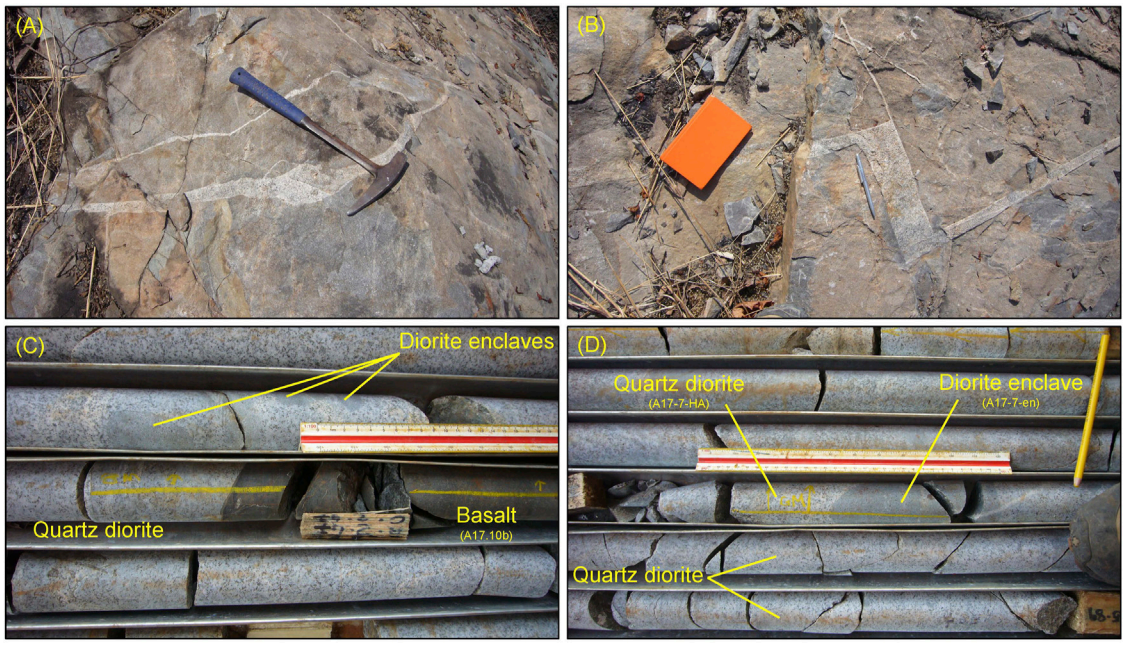

FIGURE 3
Field and drill hole photos of the Snoul pluton. **(A, B)** Fine to medium-grained diorite intruded by a coarse-grained dioritic dyke, demonstrating both **(A)** diffusive and **(B)** brittle, crack-filling fashion of dyking. **(C, D)** Diorite enclaves (irregular- to rounded shape) and basalts in a quartz diorite host rock intersected by drill hole A17 of the Snoul pluton.

samples tending to be more altered than those from the drill core. The rocks are composed of plagioclase (45–50 vol%), amphibole (~35 vol%), quartz (5–15 vol%), biotite (≤5 vol%), and Fe-Ti oxide minerals (≤5 vol %) with accessory amounts (≤1 vol% each) of apatite, zircon, and titanite. Plagioclase is euhedral to subhedral and with straight crystal edges (Figures 4A, B). The larger plagioclase crystals tend to have oscillatory zonation, but the smaller crystals tend to display polysynthetic twinning with a few showing albite twinning. All plagioclase crystals are altered by saussurite, although the extent of alteration can range significantly between different samples. Amphibole (hornblende) is the primary mafic silicate mineral in the rock and is euhedral to anhedral (Figure 4A). Similar to the plagioclase crystals, there are larger (1–3 mm) euhedral crystals (~5 vol%), but most are smaller (<1 mm) and interstitial to the plagioclase. Most of the amphibole crystals are altered by chlorite and/or biotite. The quartz crystals are subrounded and interstitial to the plagioclase and amphibole. The amount of quartz can vary between samples and is typically 5–15 vol%. Euhedral to subhedral biotite is common but its abundance can vary between samples (≤5 vol%). The biotite crystals are tan brown to brown in colour with some crystals having zircon inclusions. Under reflected light, it appears that nearly all of the opaque minerals are magnetite and ilmenite as sulphide minerals were not identified. The opaque minerals are euhedral to subhedral with most having cubic or subrounded shapes (Figure 4A).

Diorite

The diorite rocks (host = A17-8-h, O05c, O20, O27a; enclaves = A17.4b, A17-7-en, A17-8-EN, A17-14-h) were collected from the surface exposure and the drill core. The rocks are phanerocrystalline with some samples having medium to coarse grained textures whereas others are medium to fine grained. In general, the surface samples tend to be more altered than those from the drill core. The mineralogy and textures of the diorites are similar to the quartz diorites, but they have less quartz and biotite (Figures 4C, D). The rocks are primarily composed of plagioclase (50–55 vol%), amphibole (35–40 vol%), and opaque (Fe-Ti oxide minerals) minerals (~5 vol%) with accessory amounts (≤1 vol% each) of quartz, biotite, apatite, zircon, and titanite.

Mafic dykes

The mafic rocks (A15.1b, A17.1b, A17.9, A17.10b) have similar textures and mineralogy and are relatively fresh, but show signs of zeolite facies alteration (Figures 4E, F). The rocks are porphyritic and seriate and composed mostly of plagioclase (50–55 vol%) and clinopyroxene (35–40 vol%) with subordinate amounts of ilmenite/magnetite (5–10 vol%), and olivine (~5 vol%). The plagioclase crystals are mostly euhedral and have lath shapes of similar size. The clinopyroxene (augite) crystals are light brown in colour, subhedral to euhedral in shape. The olivine crystals are euhedral to anhedral (sub-round) and mostly appear as larger phenocrysts. The opaque minerals are euhedral to subhedral with cubic shapes. The basaltic rocks are likely dykes rather than xenoliths as the chilled margin with the host rock was observed (Figures 4G, H). The contact between the quartz diorite host and the basalt is sharp, but there appears to be reaction/transition zone as the contact region changes from brown to dark brown (Figure 4G). The transition zone is aphyric with occasional xenocrysts of quartz and feldspar from the host rock. Farther from the contact, the xenocrysts are absent and the basaltic rock is porphyritic with euhedral to subhedral phenocrysts of olivine and plagioclase microlites (hyalopilitic).

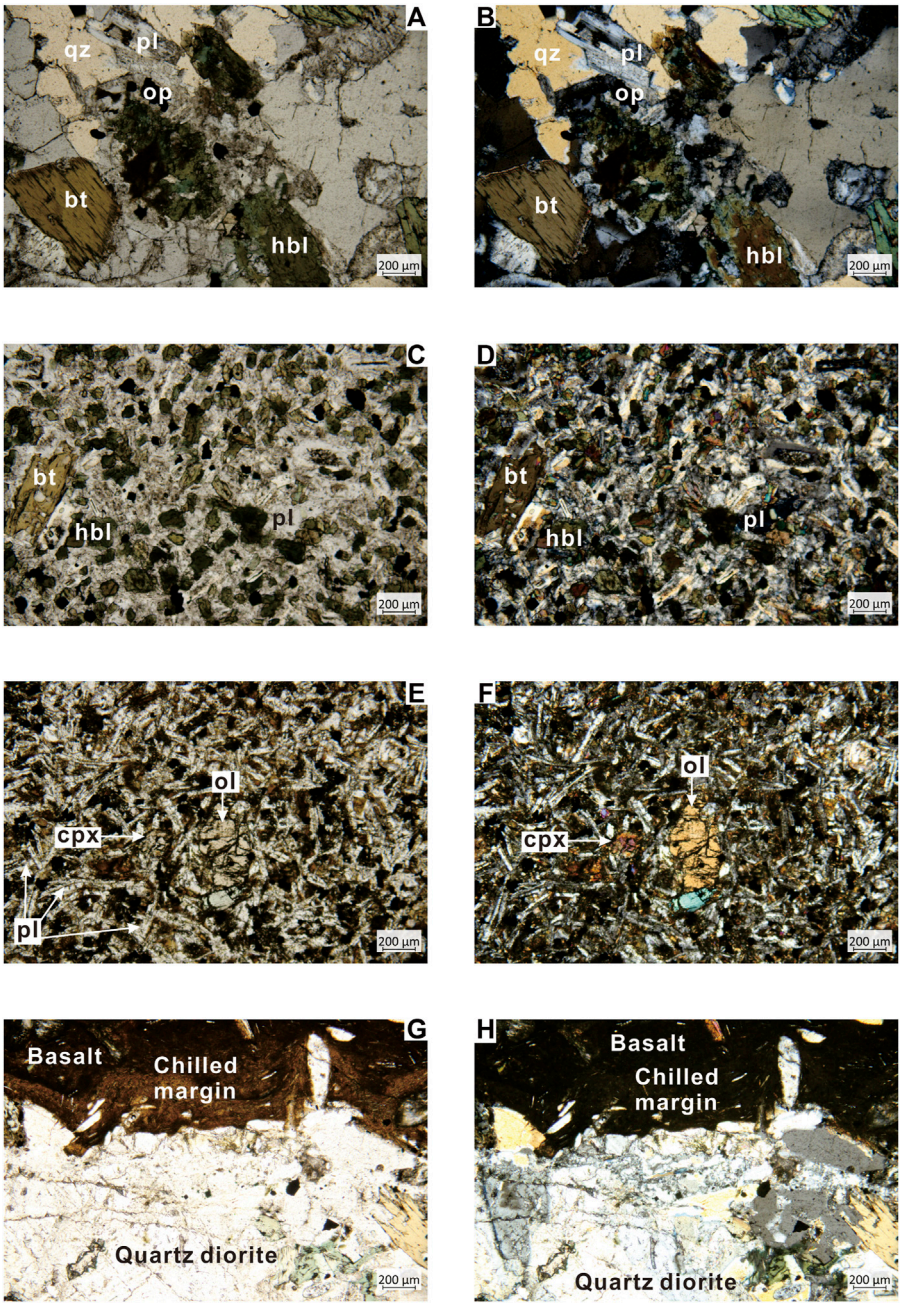

FIGURE 4
Photomicrographs of the rocks of the Snoul pluton. **(A)** Plane polarized light and **(B)** crossed polarized photos of the quartz diorite (A17-3a). **(C)** Plane polarized light and **(D)** crossed polarized photos of a diorite enclave (A17-13). **(E)** Plane polarized light and **(F)** crossed polarized photos of a basaltic rock (A15-1b). **(G)** Plane polarized light and **(H)** crossed polarized photos of the chilled margin between the quartz diorite and basalt. Symbols: qz = quartz, bt = biotite, pl = plagioclase, op = opaque, hbl = hornblende, ol = olivine, cpx = clinopyroxene. Whole rock geochemical data were not measured for samples A17-3a or A17-13.

Materials and Methods

Zircon U-Pb and Lu–Hf isotopic analyses

In situ U-Pb and Lu-Hf isotopic analyses presented in this study were performed using a Nu Plasma HR multi-collector inductively coupled plasma mass spectrometer (MC-ICPMS; Nu Instruments, UK) equipped with an ArF excimer 193 nm laser ablation system (RESOlution M-50, Resonetics LLC, USA), housed at the Department of Earth Sciences, The University of Hong Kong, HKSAR. A modified collector block of the MC-ICPMS contains 12 Faraday collectors and 4 ion counting detectors dispersed on the low mass side of the array, allowing simultaneous acquisition of ion signals ranging from mass ^{204}Pb to ^{238}U. A spot diameter of 30 μm, pulse rate of 6 Hz and energy density of 15 J/cm^2 were used. Ablation time was 40 s, resulting in pits 20–30 microns deep. Instrument parameters can be referred to Xia et al. (2011). The standard zircon 91500 (Wiedenbeck et al., 1995) and GJ-1 (Jackson et al., 2004) were used for calibration. Off-line data reduction was performed by

the software *ICPMSDataCal. Version 7.2* (Liu et al., 2010). Ages were calculated using ISOPLOT/Excel version 3.6 (Ludwig, 2008). The results are presented in Supplementary Tables S1, S2 where the isotopic ratios and ages are given with 1 sigma error.

The zircon Hf isotopes were analyzed on the same spots as those with a concordant U-Pb age. The Hf isotopic data reported in this study were obtained with a beam diameter of 55 μm, pulse rate of 6 Hz and energy density of 15 J/cm^2. Each analytical spot was subjected to 40 ablation cycles, resulting in pits 30–40 μm deep. Atomic masses 172 to 179 were simultaneously measured in static-collection mode. Isobaric interference of ^{176}Yb on ^{176}Hf was corrected against the ^{176}Yb/^{172}Yb ratio of 0.5886 (Chu et al., 2002). Interference of ^{176}Lu on ^{176}Hf was corrected by measuring the intensity of the interference-free ^{175}Lu isotope and using a recommended ^{176}Lu/^{175}Lu ratio of 0.02655 (Machado and Simonetti, 2001). External calibration was made by measuring zircon standard 91,500 (^{176}Hf/^{177}Hf = 0.282275 ± 0.000011) for the unknown samples during the analyses to evaluate the reliability of the analytical data and GJ-1 has been used for monitoring the data quality which yielded a weighted mean ^{176}Hf/^{177}Hf ratio of 0.282008 ± 0.000001 (Supplementary Table S3).

The measured ^{176}Lu/^{177}Hf and ^{176}Lu/^{177}Hf ratios and a^{176}Lu decay constant of 1.865 x 10^{-11}a^{-1} as reported by Scherer et al. (2001) were used to calculate the initial ^{176}Hf/^{177}Hf ratios. Calculations of $\varepsilon_{Hf}(t)$ values were based on the chondritic values of ^{176}Hf/^{177}Hf and ^{176}Lu/^{177}Hf as reported by Blichert-Toft and Albarède (1997). The mantle extraction model age (T_{HfDM}) was calculated using the measured ^{176}Lu/^{177}Hf of the zircon, but this only provides a minimum age for the source material of the magma from which the zircon crystallized. Therefore, "crustal" model ages T_{Hfc} were calculated (Supplementary Table S3), which assume that the parental magma of the zircons was produced from average continental crust, but was ultimately derived from the depleted mantle. A ratio of 0.015 most realistically reflects the ^{176}Lu/^{177}Hf ratio of our samples.

Wavelength dispersive X-ray fluorescence

Three grams (3.0000 ± 0.0005 g) of each sample was added to a ceramic crucible of known mass (+lid) and placed in an oven at 105°C for 3 h. After the initial heating step, the powders were cooled to ambient temperature inside a desiccator for ~15 min before they were weighed. The samples were then baked to peak temperature at 900°C (held for 10 min) in a high temperature furnace before cooling. The samples were then cooled in a desiccator until reaching ambient temperature. Each sample was weighed for a final time and the loss on ignition was calculated from the masses obtained from the low and high temperature cycles. Six grams (6.0000 ± 0.0005 g) of lithium metaborate was added to each sample (0.6000 ± 0.0005 g) at a ratio of 10:1 and fused to produce a glass disc using a Claisse M4 fluxer. The major elements were measured by wave-length dispersive X-ray fluorescence using Panalytical Axios^{mAX} at the XRF Laboratory, Department of Earth Sciences, National Taiwan Normal University. Standard reference materials measured during the study include: BIR-1a, BCR-2, and AVG-2a (Supplementary Table S4).

Inductively coupled plasma mass spectrometry

Trace elements were measured using an Agilent 7500cx inductively coupled plasma mass spectrometer (ICP-MS) at National Taiwan University, Taipei, Taiwan. Approximately 50–100 mg of each sample powder was dissolved in a Teflon beaker using a combination of HF, HNO_3, and HCl. Each sample was heated in closed beakers with HF and HNO_3 for at least 48 h and then dried. After drying, 2 mL of 6 N HCl was added to each sample and then left to dry. This step was followed by the addition of 2 mL of 1 N HCl to each sample then the solution was centrifuged. The supernatant was extracted and then placed into a new beaker. If solid residue remained in the beaker after extraction, then the procedure was repeated until the powder was fully digested. Samples were diluted using 2% HNO_3 and an Rh and Bi spike was added for the internal standard. The standard reference materials measured for the trace elements of this study are AGV-2 (andesite), BCR-2 (basalt), and DNC-1 (dolerite) (Supplementary Table S4).

Thermal ionization mass spectrometry

Whole rock Sr and Nd isotopes were measured at the Institute of Earth Sciences, Academia Sinica, Taipei (Supplementary Table S5). Approximately 75 mg of sample powder was dissolved using a mixture of HF and HNO_3 at 120°C for 48 h, then taken to dryness followed by dissolution in 2 mL 4 N HCl. Separation and purification of Sr and Nd were achieved using a 3-column technique. The first column was contained 0.2 mL Sr spec resin (manufactured by Eichron Industries, Inc.) to collect the Sr fraction using HNO_3 as eluent. The elution was then passed through the second column containing 2.5 mL cation exchange resin (Bio Rad AG50W-X8, 100–200 mesh) to isolate the rare Earth elements using HCl as eluent. The third column used for Nd separation contained 1 mL Ln-B25-A (Eichrom) resin, covered on top by a thin layer of anion exchange resin (Bio Rad AG1-X8, 200–400 mesh), using HCl as eluent.

Strontium was loaded on a single Ta filament and compositional analysis was performed using 7-collector Finnigan MAT-262 thermal ionization mass spectrometer in dynamic mode. Neodymium loaded on a double Re filament and the isotopic measurement was analyzed using 9-collector Thermo Fisher Scientific Triton thermal ionization mass spectrometer with static mode for automatic run. The isotopic ratios were corrected for mass fractionation by normalizing to ^{86}Sr/^{88}Sr = 0.1194 and ^{146}Nd/^{144}Nd = 0.7219. At the time of analysis, the NBS-987 Sr standard yielded an average value of ^{87}Sr/^{86}Sr = 0.710249 with a long-term reproducibility of 0.000045 (2σ) and the JMC Nd standard gave an average of ^{143}Nd/^{144}Nd = 0.511813 with a long-term reproducibility of 0.000009.

Results

In situ zircon U-Pb ages

Twenty-six zircons were analyzed from sample O05c (diorite). Zircon grains range in size from ~50 μm to ~300 μm in length and have euhedral (prismatic to equant) to subhedral (fragmented to sub-round) shapes. Nearly all zircons show igneous (oscillatory) zonation whereas very few have core-rim structures (Corfu et al., 2003). All zircons yielded ages that were 92% concordant or better, however we only select zircons with ≥97% concordance to interpret their emplacement age (Supplementary Table S1). The ^{206}Pb/^{238}U ages revealed a bimodal distribution of ~111 Ma and ~107 Ma. Five

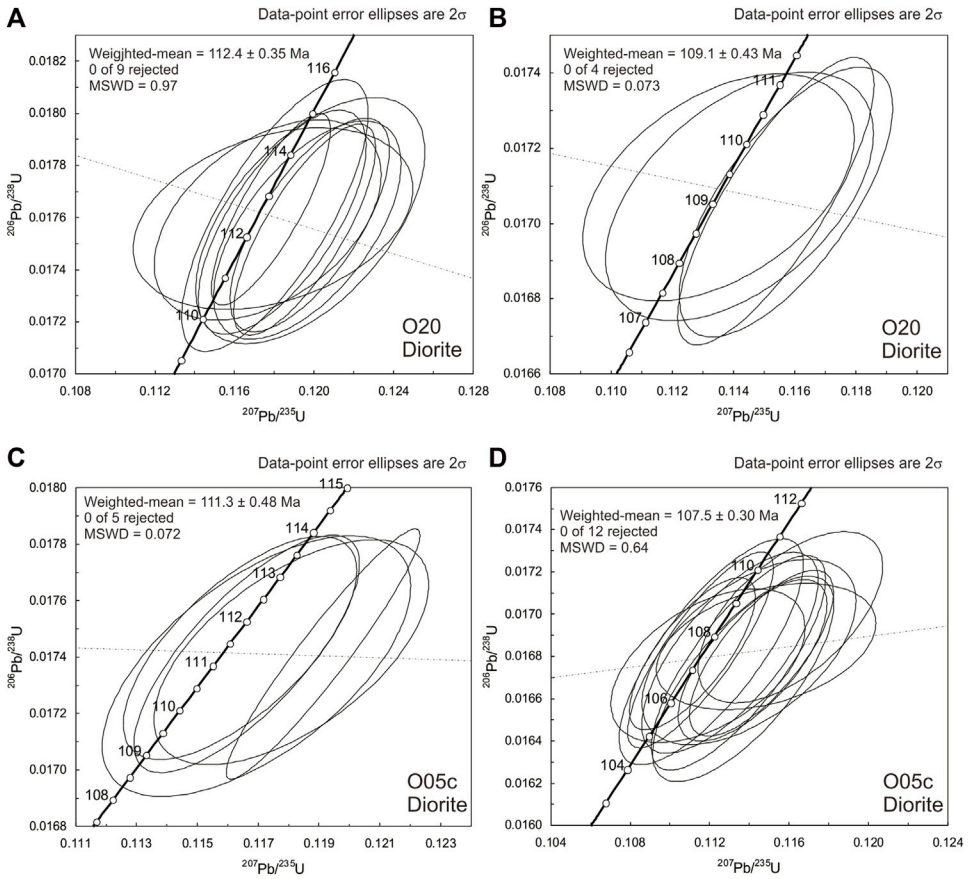

FIGURE 5
(A) Concordia diagram with the weighted-mean age of the older (inherited) population of zircon U-Pb data from sample O20. **(B)** Concordia diagram with the weighted-mean age of the younger population (emplacement age) of zircon U-Pb data from sample O20. **(C)** Concordia diagram with the weighted-mean age of the older (inherited) population of zircon U-Pb data from sample O05c. **(D)** Concordia diagram with the weighted-mean age of the younger (emplacement age) population of zircon U-Pb data from sample O05c.

zircons yielded an intercept age of 111.3 ± 1.8 Ma and weighted-mean $^{206}Pb/^{238}U$ age of 111.3 ± 0.5 Ma which we interpret as an inheritance age (Figure 5A). The majority of zircons (12) yielded an intercept age of 107.4 ± 1.0 Ma and weighted-mean $^{206}Pb/^{238}U$ age of 107.5 ± 0.3 Ma which we interpret as the emplacement age (Figure 5B). The older group of zircons (~111 Ma) do not show significantly different internal structures (i.e., core-rim structures) nor are their crystal shapes significantly different from the younger (~107 Ma) group of zircons.

Thirty-eight zircons were analyzed from sample O20 (diorite), however only twenty-six zircons with ≥97% concordance are considered for the emplacement ages (Supplementary Table S2). Zircon grains range in size from ~40 μm to ~400 μm in length and have euhedral (prismatic to equant) to subhedral (fragmented to sub-round) shapes. The zircons are morphological similar to those from sample O05c. The $^{206}Pb/^{238}U$ ages range from ~106 Ma to ~577 Ma with the majority (9) of ages around ~112 Ma. The nine zircons yielded an intercept age of 112.6 ± 1.4 Ma with a weighted-mean age of 112.4 ± 0.4 (Figure 5C). Four zircons with ≥97% concordance yielded an intercept age of 109.2 ± 1.3 Ma and weighted-mean $^{206}Pb/^{238}U$ age of 109.1 ± 0.4 Ma which we interpret as the emplacement age as they are within the uncertainty of the ages of O05c (Figure 5D). The inherited zircons with ≥97% concordance are mostly Carboniferous to Permian (258–335 Ma), but there are single zircon ages of ~106 Ma, ~114 Ma, ~118 Ma, and ~577 Ma. Much like sample O20, there does not appear to be significantly different internal structures or crystal shapes between the two groups of Cretaceous zircons. However, the older inherited zircons (i.e., >250 Ma) tend to have irregular to rounded shapes.

In situ zircon Hf isotopes

Hafnium isotopes were measured on the same zircon spot locations as the U-Pb ages of samples O20 and O05c. Not all zircons could be analyzed for Hf isotopes due to the limited amount of material left after ablation for U-Pb dating. The dataset can be found in the Supplementary Table S3. The depleted mantle lines in Figure 6 are defined by present-day $^{176}Hf/^{177}Hf = 0.28325$ and $^{176}Lu/^{177}Hf = 0.0384$ (Griffin et al., 2000).

The magmatic zircons (12) from sample O20 yielded initial $^{176}Hf/^{177}Hf(t)$ ratios from 0.283048 to 0.283186 with $\varepsilon_{Hf}(t)$ values ranging from +12.1 to +17.0. The meaningful T_{DM1} ages range from 123 Ma to 291 Ma whereas the T_{DM2} ages range from 141 Ma to 543 Ma. In comparison, the inherited (296–335 Ma) zircons (5) have initial $^{176}Hf/^{177}Hf(t)$ ratios from 0.282675 to 0.283025 and $\varepsilon_{Hf}(t)$ values ranging

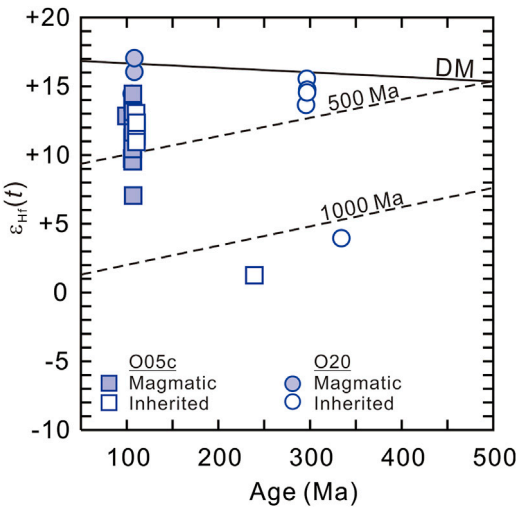

FIGURE 6
Zircon Hf isotopic evolution of the diorites (O05c, O20) from the Snoul pluton. The evolution curves (dashed lines) are calculated assuming Lu/Hf crustal value of 0.015 (Griffin et al., 2004; Chauvel et al., 2008). DM = depleted mantle.

from +3.9 to +15.5. The T_{DM1} ages range from 313 Ma to 813 Ma whereas the T_{DM2} ages range from 341 Ma to 1,490 Ma.

Twenty-two magmatic zircons from sample O05c yielded initial $^{176}Hf/^{177}Hf(t)$ ratios from 0.282904 to 0.283113 with corresponding $\varepsilon_{Hf}(t)$ values from +7.0 to +14.4. The T_{DM1} ages range from 194 Ma to 493 Ma whereas the T_{DM2} ages range from 319 Ma to 1,040 Ma. There is one inherited zircon (240 Ma). It has an initial $^{176}Hf/^{177}Hf(t)$ ratio of 0.282657 and $\varepsilon_{Hf}(t)$ value of +1.2 and T_{DM1} and T_{DM2} ages of 830 Ma and 1,688 Ma.

Major and trace elemental geochemistry

The SiO_2 contents of the host rocks range from ~55.7 to ~71.6 wt% with nearly all ANCK values (mol. $Al_2O3/[mol. CaO+Na_2O+K_2O]$) between 0.87 and 1.01 and alkali-alumina (mol. [Na+K]/mol. Al) values <1 (Figures 7A, B). According to the scheme of Frost et al. (2001), the rocks classify as magnesian (FeOt/FeOt+MgO = 0.65–0.71) and calcic (Figures 7C, D). Magnesian, metaluminous, calcic rocks are considered to be typical of the outboard portions of Cordilleran Batholiths (i.e., volcanic-arc granites). Sample A15.2 has very low Na_2O and K_2O contents and consequently has a very high ANCK value (~1.9). However, this sample is altered and it is likely that the alkali metals were mobilized (L.O.I. = 3.21 wt%). Nonetheless, for the exception of A15.2, all rocks are sodic (K_2O/Na_2O = 0.28–0.71) and their Mg# ([mol Mg/(mol Mg+tFe^{2+})]× 100) are 42.1–49.4 (Figures 7E, F). The loss on ignition (L.O.I.) values, for the exception of A15.2, are ≤0.51 wt% and indicate that the rocks did not undergo significant post-emplacement hydrothermal/deuteric alteration.

The host rocks have uniformly low concentrations of transition metals (Sc = 5.4–16.8 ppm), V = 93.6–170.6 ppm, Cr = 6–19 ppm, Co = 8.5–16.3 ppm, Ni = 4–8 ppm, Cu = 4.9–34.7 ppm, Zn = 16.7–55.3 ppm). The large ion lithophile element (LILE) concentrations are more variable (Rb = 0.9–84.9 ppm, Sr = 77–679 ppm, Cs = 0.12–2.3 ppm, Ba = 34–538 ppm). Similar to the LILE, the high field strength elements are variable (Zr = 22–108 ppm, Nb = 3.1–4.8 ppm, Y = 9.3–23.5 ppm, Hf = 0.78–2.68 ppm, Ta = 0.27–0.37 ppm, Th = 2.6–6.4 ppm, U = 1.1–1.9 ppm). The mid-ocean ridge basalt normalized incompatible patterns of the rocks are broadly similar, although there is some variability in the Rb–Ba and Hf–Zr concentrations (Figure 8A). All rocks have similar chondrite normalized rare Earth element patterns (Figure 8B). The rocks are light rare Earth element (REE) enriched with high La_N/Sm_N (1.9–3.3) and flat to bowl shaped middle to heavy REEs (Gd_N/Yb_N = 1.1–1.6) patterns. The Eu/Eu* values [$2*Eu_N/(Sm_N+Gd_N)$] are 0.93–1.09.

The four dioritic enclaves have intermediate compositions with SiO_2 ranging from 54.8–57.6 wt% and Na_2O+K_2O wt% equal to 5.2–5.6 wt% (Figure 7A). The enclaves are metaluminous, magnesian, and alkali-calcic (Figures 7B–D). The Fe_2O_3t ranges from 7.5–8.9 wt% and MgO from 3.9–5.0 wt% with the Mg# ranging from 46.6–53.6. The TiO_2 (0.65–0.68 wt%) and MnO (<0.25 wt%) contents are low and the CaO is ~7.5–7.8 wt%. The transition metals decrease with increasing SiO_2 contents, although some elements have limited variability (Sc = 14.1 and 21.9 ppm, V = 190 and 195 ppm, Cr = 18 and 38 ppm, Co = 16 and 17.5 ppm, Ni = 10 and 12 ppm, Cu = 22.4, and 38.4 ppm, Zn = 38.9–44.5 ppm). The mid-ocean ridge ocean basalt normalized incompatible element patterns are similar to the host rocks with enriched patterns of Cs, Rb, Ba, Th, and U with a depletion of Nb and relatively flat La–Nd patterns and flat but lower concentrations of Hf–Y with a positive anomaly of Sm (Figure 8C). The enclaves have light REE-enriched patterns with $(La/Yb)_N$ and $(La/Sm)_N$ ratios of 4.9–5.0 and 2.4. The rocks do not have negative Eu anomalies with Eu/Eu* ratios from 0.97–0.98 (Figure 8D). Furthermore, the rocks tend to have bowl shape patterns as the middle rare Earth elements (Dy–Er) are flat and the heavy rare Earth elements (Tm–Lu) are slightly higher.

The four basaltic rocks have SiO_2 ranging from 48.7–50.6 wt% and Na_2O+K_2O wt% equal to 4.2–5.4 wt% (Figure 7A). There is a distinct SiO_2 gap between the basaltic (~50.5 wt%) rocks and dioritic (~54.8 wt%) enclaves (Figures 7A, F). The basalts are mildly alkaline with alkalis (Na_2O+K_2O) increasing with increasing SiO_2 contents. The Fe_2O_3t ranges from 9.6–11.2 wt% and MgO from 4.9–9.1 wt% with the Mg# ranging from 50.1–61.7. The TiO_2 (1.5–1.6 wt%) and MnO (<0.20 t.%) contents are low. The Al_2O_3 ranges from 15.3–18.2 wt%, and CaO from 9.4–10.6 wt%. The transition metals generally decrease with increasing SiO_2 contents, although some elements have limited variability (Sc = 7.9–10.1 ppm, V = 219–224 ppm, Cr = 16–354 ppm, Co = 28.7–48.9 ppm, Ni = 24–205 ppm, Cu = 45.1–58.6 ppm, Zn = 81.5–111.7 ppm). The mid-ocean ridge ocean basalt normalized incompatible element patterns show low Cs and Rb concentrations and declining concentrations from Ba to Y (Figure 8E). The basalts have chondrite normalized light REE-enriched patterns with $(La/Yb)_N$ and $(La/Sm)_N$ ratios between 11.2 and 13.2 and 2.7–3.1. The rocks do not have significant negative Eu anomalies with Eu/Eu* ratios from 0.93–0.96 (Figure 8F).

Sr-Nd isotope geochemistry

Five samples were selected for Sr and Nd isotopic analysis (Supplementary Table S5). The initial isotopic ratios of the diorites and quartz diorites were calculated based on the U-Pb ages of this study (107 Ma) whereas the initial isotopic ratios of the basaltic rocks are thought to be contemporaneous with the adjacent Neogene–Quaternary volcanic rocks and an age of 10 Ma was

10.3389/feart.2023.1110568

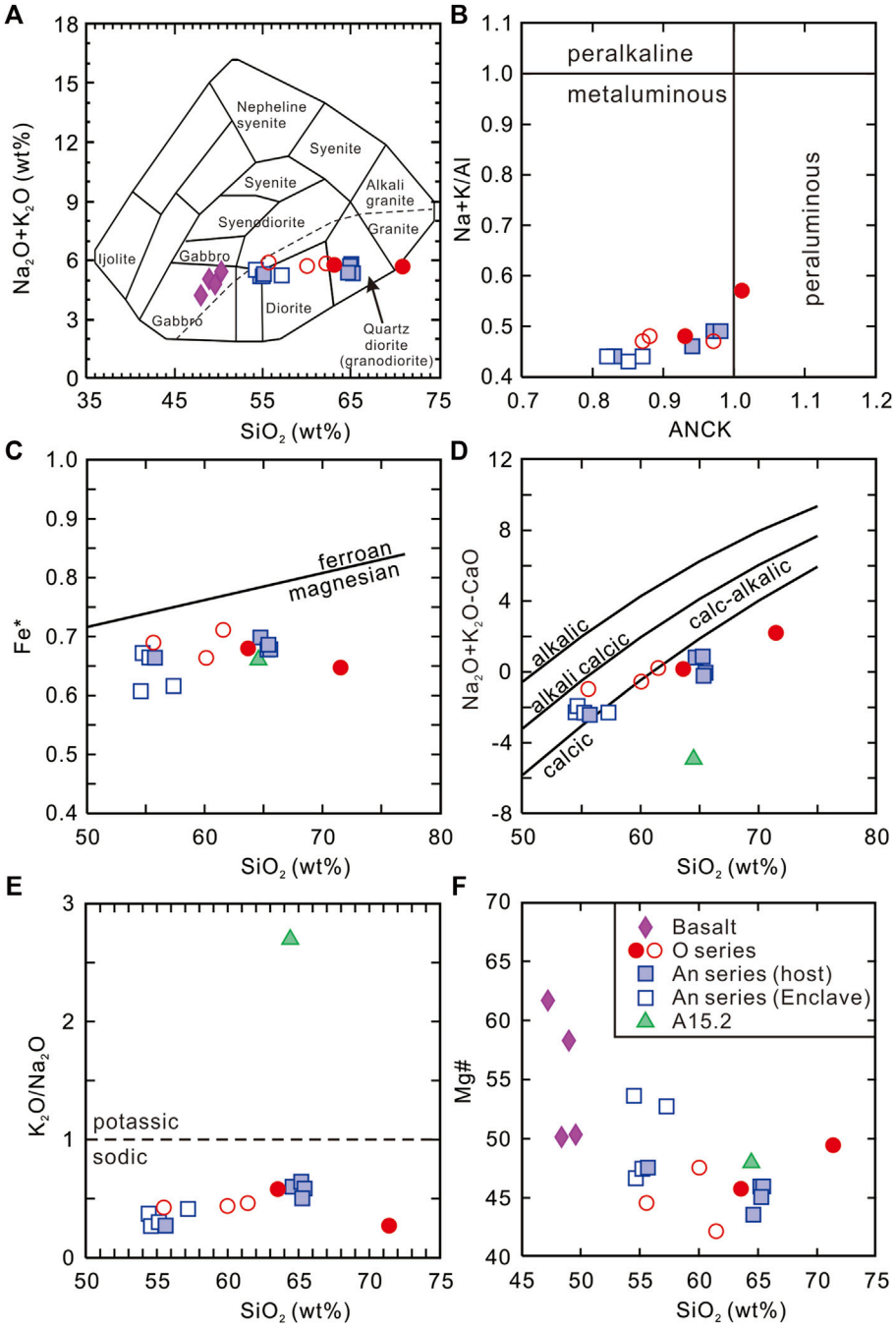

FIGURE 7
Chemical classification of the rocks from the Snoul pluton. **(A)** $Na_2O + K_2O$ (wt%) vs. SiO_2 (wt%) classification of rocks (Cox et al., 1979). **(B)** Alkali index (mol. Na + K/mol. Al) versus aluminum saturation index (ASI = mol. Al/mol. Ca + Na + K). Classification of the quartz dioritic and dioritic rocks using **(C)** the Fe* [(FeOt/(FeOt + MgO)] value and **(D)** the modified alkali-lime index ($Na_2O + K_2O$-CaO) vs. SiO_2 (wt%) of Frost et al. (2001). **(E)** K_2O/Na_2O vs. SiO_2 showing the sodic nature of the rocks. **(F)** Mg# vs. SiO_2 (wt%) of the mafic and silicic rocks from the Snoul pluton.

assumed (Nguyen and Flower, 1998). The initial $^{87}Sr/^{86}Sr$ ratios of the granitic rocks range from 0.704313 to 0.707681 (Figure 9). The initial $^{143}Nd/^{144}Nd$ ratios range from 0.512660 to 0.512750 for the granitic samples. Their $\varepsilon_{Nd}(t)$ values, using $^{147}Sm/^{144}Nd$ of 0.1967 and a $CHUR_{today}$ value of 0.512638, correspond to +3.1– +4.9 (Figure 9). The depleted mantle model ages (T_{DM}) range from 598 Ma to 847 Ma. The lone basalt sample has an initial $^{87}Sr/^{86}Sr$ ratio of 0.703978, an $\varepsilon_{Nd}(t)$ value of +4.2, and T_{DM} age of 513 Ma.

Discussion

Age of the Snoul pluton and its regional correlation

The zircon U-Pb geochronology results of the surface rocks yielded Albian ages (O05c = 107.5 ± 0.3 Ma; O20 = 109.1 ± 0.4 Ma). Moreover, sample O20 has inherited zircons that range in

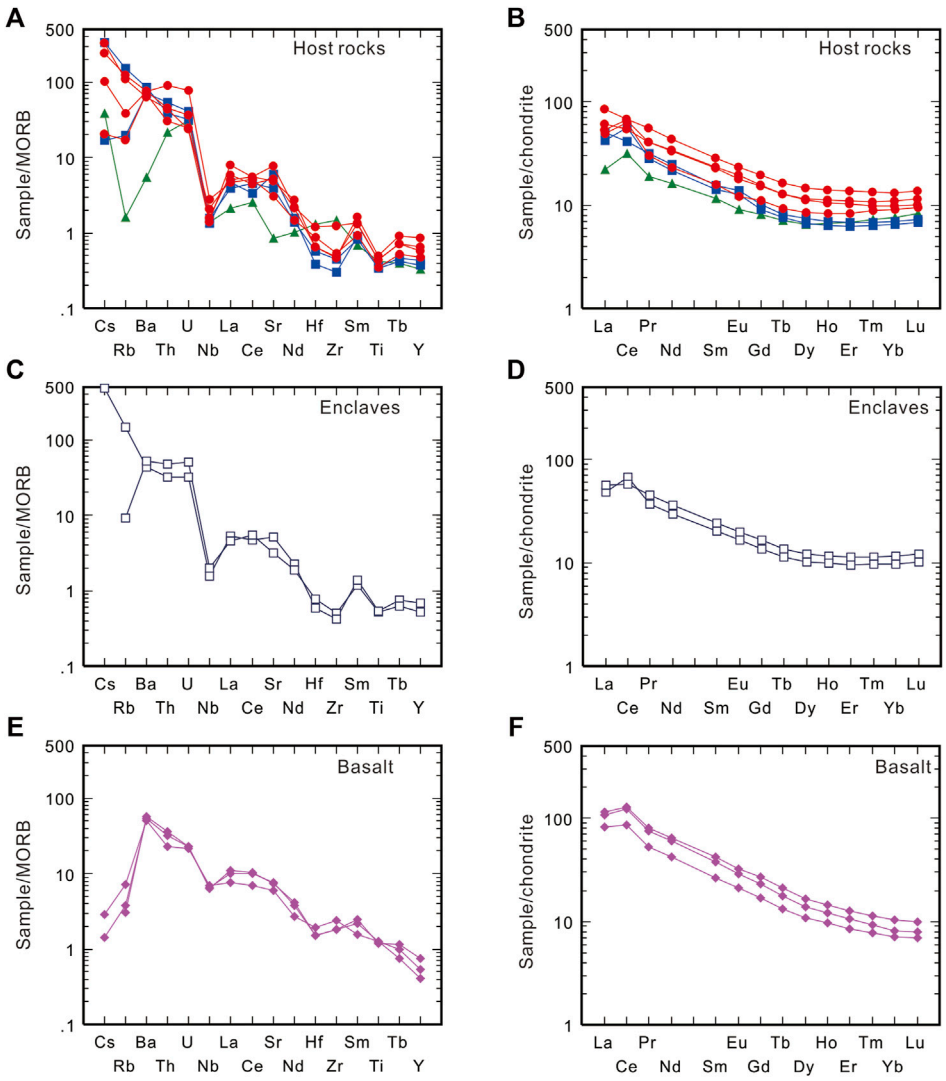

FIGURE 8
Mid-ocean ridge basalt (MORB) normalized incompatible element of the **(A)** host quartz dioritic and dioritic rocks, **(C)** the dioritic enclaves, and **(E)** the basaltic rocks. Chondrite normalized rare Earth element diagrams of the **(B)** host quartz dioritic and dioritic rocks, **(D)** the dioritic host rocks, and **(F)** the basaltic rocks. Mid-ocean ridge basalt and chondrite normalizing values of Sun and McDonough (1989). Symbols of the Snoul pluton are the same as in Figure 7.

age from Late Ediacaran (~577 Ma) to Early Cretaceous (~118 Ma) whereas sample O05c has one early Triassic zircon (~240 Ma). The zircon ages of the diorites from this study are contemporaneous with Early Cretaceous granitic magmatism throughout the Dalat-Kratie Fold Belt of Vietnam and Cambodia (Nguyen et al., 2004a; Shellnutt et al., 2013; Breitfeld et al., 2020; Hennig-Breitfeld et al., 2021; Kasahara et al., 2021; Nong et al., 2021; Nong et al., 2022). Specifically, they correlate to a period of subduction-related (130–90 Ma) magmatism along the western margin of the Paleo-Pacific Ocean (Taylor and Hayes, 1983; Metcalfe, 2006; Yang, 2013; Hennig-Breitfeld et al., 2021; Waight et al., 2021).

Farther north along the SE coast of China, the Early Cretaceous period of arc-magmatism is referred to as the Late Yanshanian Orogen and is typified by I-type granite magmatism with subordinate S-type granite magmatism (Zhou et al., 2006; Li et al., 2012; Li et al., 2014; Dong et al., 2018; Shellnutt et al., 2020a; Suga and Yeh, 2020). From a geodynamic point of view, the Early Cretaceous Eurasian margin arc-magmatism is related to subduction of Paleo-Pacific oceanic crust (Maruyama et al., 1997; Yang, 2013; Wu et al., 2022).

Inherited zircons are more common in sample O20 whereas there was only one identified in O05c (~240 Ma). Sample O20 has the most inherited zircons (22) and a clear Paleozoic population (335–296 Ma) and one Late Ediacaran zircon (~577 Ma). There are eleven inherited zircons with a slightly older age range (112–118 Ma) than the weighted-mean ages of the diorite. We interpret these inherited zircons as being derived from an older period of spatially associated subduction-related magmatism as they have similar Hf isotopic values ($\varepsilon_{Hf}(t)$ = +13.2– +16.8) as the emplacement age zircons ($\varepsilon_{Hf}(t)$ = +12.1– +17.0). Moreover, the inherited Early Cretaceous (112–118 Ma) ages overlap with reported rock ages throughout the Dalat-Kratie Fold Belt of Vietnam and Cambodia (Nguyen et al., 2004a; Shellnutt et al., 2013; Hennig-Breitfeld et al., 2021; Kasahara et al., 2021; Nong et al., 2021). The Late Paleozoic (335–296 Ma) inherited zircons are contemporaneous with Middle Carboniferous

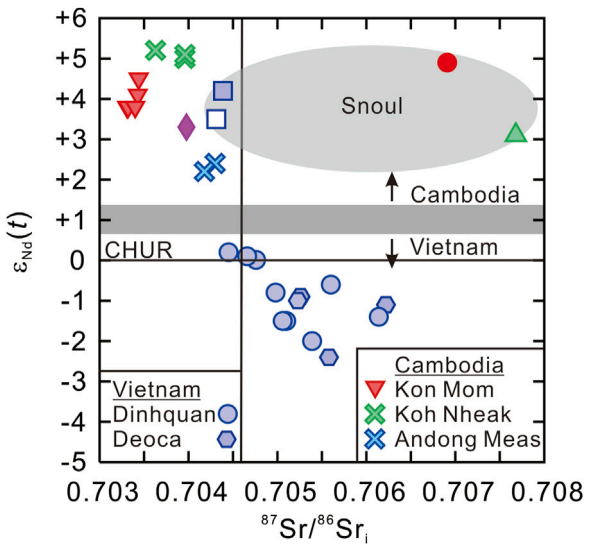

FIGURE 9
Sr-Nd isotopic data from the dioritic and quartz dioritic rocks of the Snoul pluton. Additional data from the Aptian-Albian volcanic-arc granites from southern Vietnam and eastern Cambodia (Nguyen et al., 2004a; Shellnutt et al., 2013; Cheng et al., 2019). Symbols of the Snoul pluton are the same as in Figure 7.

(336 ± 3 Ma) to Permian (267 ± 3 Ma) mafic and silicic rocks known throughout Indochina. The magmatic rocks may be related to an earlier period of subduction of the Paleotethys and back-arc extension prior to the amalgamation between the Sukhothai and Indochina terranes or subduction of the Paleo-Pacific plate (Hall and Sevastjanova, 2012; Burrett et al., 2014; 2021; Wang et al., 2018; Cheng et al., 2019; Kasahara et al., 2021; Shi et al., 2021; Waight et al., 2021; Breitfeld et al., 2022).

The Triassic zircon of O05c is contemporaneous with rocks in Cambodia as Cheng et al. (2019), Kasahara et al. (2021) and Waight et al. (2021) reported zircon U-Pb ages from 201.88 ± 0.36 Ma to 238.21 ± 0.31 Ma. The Triassic magmatism in Cambodia is interpreted to be related to subduction and back-arc extension associated with Paleotethys subduction along the western margin of the amalgamated Sukhothai-Indochina terranes (Sone and Metcalfe, 2008; Kasahara et al., 2021; Waight et al., 2021). Moreover, there is Triassic magmatism throughout Vietnam that may be related to subduction of the Paleo-Pacific plate (Hennig-Breitfeld et al., 2021).

Petrogenesis of the Snoul pluton, enclaves, and basaltic rocks

Tectonomagmatic discrimination of the quartz diorites, diorites, and basaltic rocks

The host rocks are geochemically (magnesian, metaluminous, calcic) similar to granitic rocks that are typical of the outboard portions of Cordilleran Batholiths or volcanic-arcs (Frost et al., 2001). Moreover, the rocks do not exceed CIPW normative corundum of 1% (Chappell and White, 2001) and their data fall within the fields of volcanic-arc or I-type granites in the tectonomagmatic discrimination diagrams of Pearce et al. (1984), Whalen et al. (1987), and Whalen and Hildebrand (2019)

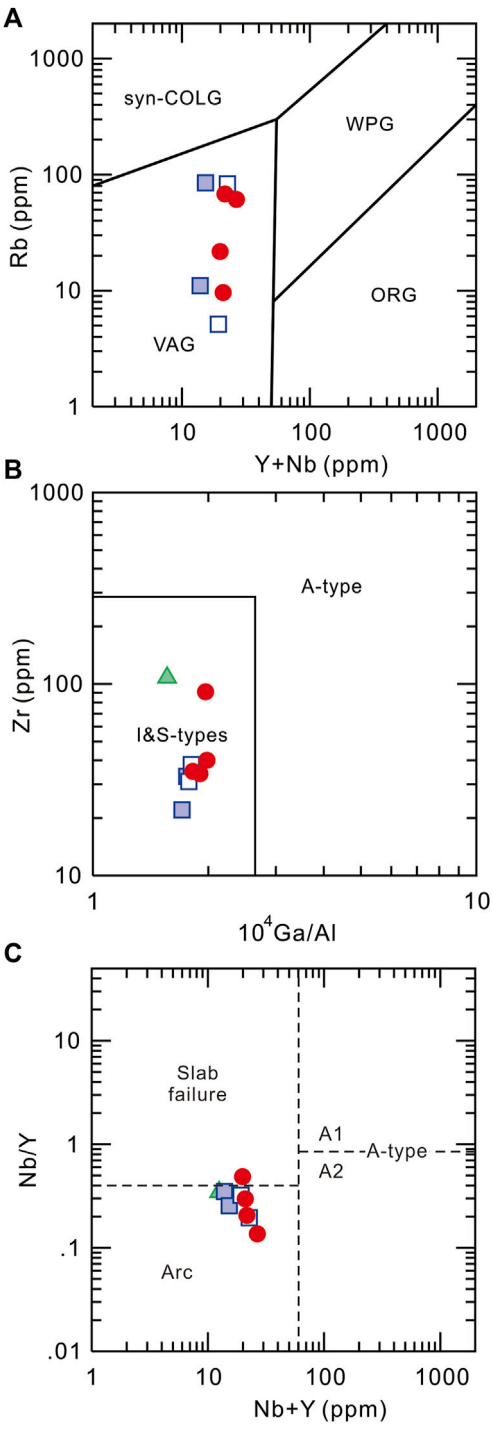

FIGURE 10
Tectonomagmatic discrimination of the dioritic and quartz dioritic rocks of the Snoul pluton of **(A)** Pearce et al. (1984), **(B)** Whalen et al. (1987), and **(C)** Whalen and Hildebrand (2019). Symbols of the Snoul pluton are the same as in Figure 7.

(Figure 10). The emplacement ages and location of the rocks are consistent with other volcanic-arc rocks in the eastern portion of the Dalat-Kratie belt of Vietnam and more broadly with the period of Late Yanshanian magmatism along the eastern margin of Eurasia (Nguyen et al., 2004a; Nguyen et al., 2004b; Shellnutt et al., 2013; Cheng et al., 2019; Hennig-Breitfeld et al., 2021; Kasahara et al., 2021).

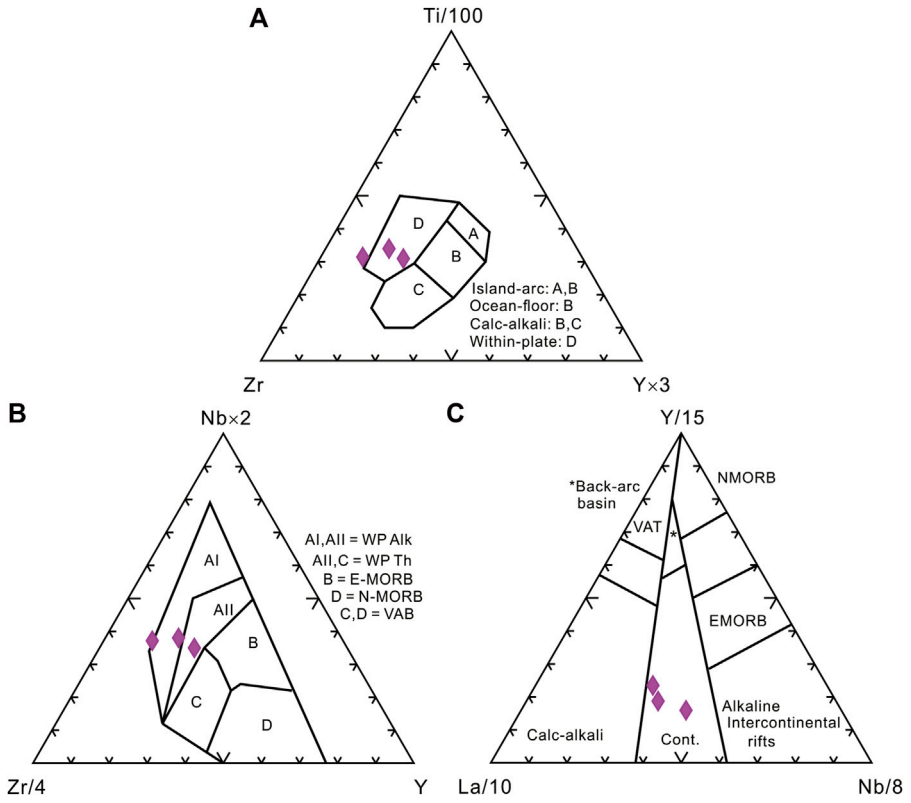

FIGURE 11
Tectonomagmatic discrimination of the basaltic rocks using the schemes of **(A)** Pearce and Cann (1973), **(B)** Meschede (1986), and **(C)** Cabanis and Lecolle (1989). WP Alk = within-plate alkaline basalt; WP Th = within-plate tholeiitic basalt; E-MORB = enriched mid-ocean ridge basalt; N-MORB = normal mid-ocean ridge basalt; VAB = volcanic-arc basalt; VAT = volcanic-arc tholeiite.

The dioritic (A17.4b, A17-7-en, A17-8-EN, A17.11b) enclaves (SiO_2 = 54–57 wt%) are chemically similar to the host diorites (A17-8-h, O05c, O20, O27a) as they are magnesian and metalumiunous, but tend to be calc-alkalic to calcic rather than calcic. The difference between calcic and calc-alkalic rocks, according to Frost et al. (2001), is that calc-alkalic rocks are representative of the main portions of Cordilleran Batholiths rather than the outboard portions. The subtle distinction between the enclaves and the host diorite may not be meaningful as it is likely that the two rock types are petrogenetically related whereby the enclaves are representative of the parental arc magmas of the quartz diorites. The petrogenetic relationship between the enclaves and host rock will be discussed later. Nevertheless, the enclaves fall within the volcanic-arc and I-type fields of Pearce et al. (1984), Whalen et al. (1987), and Whalen and Hildebrand (2019) and correspond to the ACG (amphibole-rich, calc-alkaline) granitoids of Barbarin (1999) (Figure 10).

The basaltic rocks are compositionally similar to transitional to mildly alkaline basalt (Figures 7A, 11). Petrographically, the rocks are not composed of cumulus minerals and their Eu/Eu* values (0.93–0.96) are close to unity. The Eu/Eu* values do not indicate significant fractionation or accumulation of plagioclase. In other words, the mafic rocks do not appear to be restites and the chilled margin texture is indicative of an intrusive contact rather than a xenolith. The application of three tectonomagmatic discrimination diagrams consistently show that the rocks plot as within-plate basalt typical of continental rift settings rather than convergent margin settings (Figure 11). The classification of the basaltic rocks as 'within-plate' is supportive of their intrusive nature (i.e., dyke) as they would be younger, but also likely correlative to the adjacent Neogene–Quaternary Phuoc Long flood basalt province (Nguyen and Flower, 1998; An et al., 2017).

Magma evolution of the silicic system

The quartz diorite and dioritic rocks are compositionally similar (magnesian, metaluminous) and show chemical evolution trends of major elements (decrease of TiO_2, Al_2O_3, Fe_2O_3t, MgO, CaO, Na_2O, and an increase of K_2O) against SiO_2 that may be indicative of magma compositional evolution. Moreover, the Sr-Nd isotopes of the host rocks ($^{87}Sr/^{86}Sr_i$ = 0.704389–0.707681; $\varepsilon_{Nd}(t)$ = +3.1– +4.9) are similar to the enclave ($^{87}Sr/^{86}Sr_i$ = 0.704313; $\varepsilon_{Nd}(t)$ = +3.5) and all rocks have similar chondrite normalized La/Yb (2.9–7.2) and Gd/Yb (1.1–1.6) ratios, low Nb/U (1.9–4.1), and high primitive mantle normalized Th/Nb (6.3–15.0) ratios. Consequently, it is possible that the diorites or enclave may be representative of the parental or earlier magma composition of the quartz diorites.

In order to evaluate the petrological relationship between the quartz diorites and the diorites we apply Rhyolite-MELTS (version 1.0.2) fractional crystallization modeling (Gualda et al., 2012). We select sample A17.11b (enclave) as the starting composition as it has the highest MgO content (~4.2 wt%), the second highest Ni (10 ppm) content, lowest Sr (282 ppm) content, and the second highest Mg# (52.7) of all the dioritic rocks. The starting conditions are not quantitatively constrained, however given that the rock is similar to

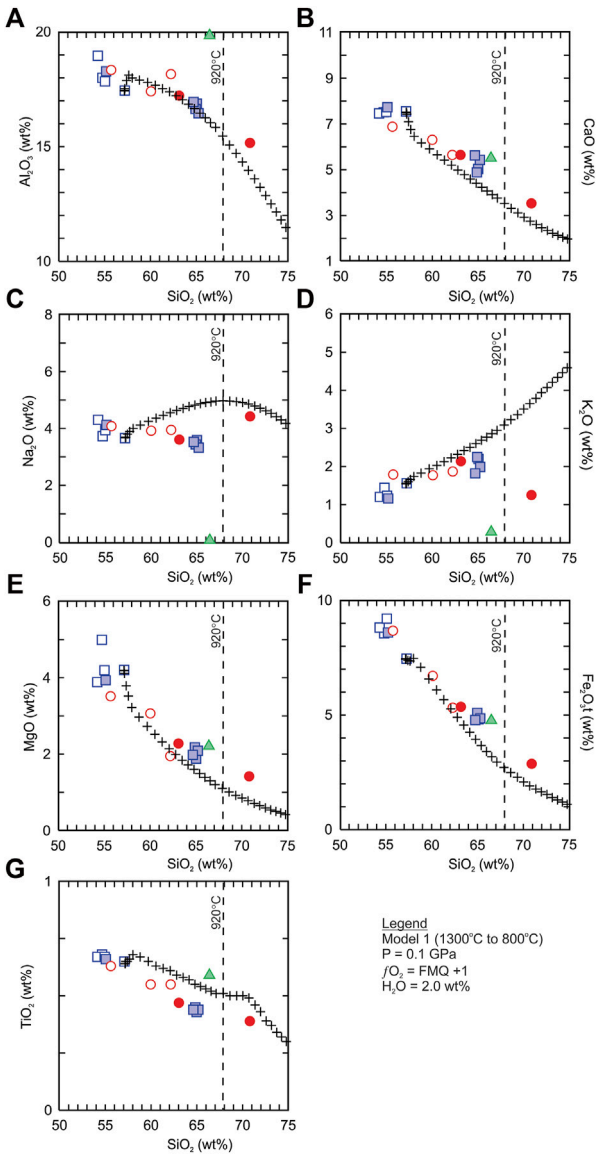

FIGURE 12
The results of hydrous fractional crystallization of the Snoul pluton at 0.1 GPa and fO_2 = ΔFMQ +1. **(A)** Al_2O_3 (wt%), **(B)** CaO (wt%), **(C)** Na_2O (wt%), **(D)** K_2O (wt%), **(E)** MgO (wt%), **(F)** Fe_2O_3t (wt%), and **(G)** TiO_2 (wt%) vs. SiO_2 (wt%). The residual silicic liquids compositions are at 10°C intervals. The complete modeling results are in online Supplementary Table S6. All data are normalized to 100%. Symbols of the Snoul pluton are the same as in Figure 7.

volcanic arc granite, we select conditions that are typical of convergent margin magma systems (Supplementary Table S6). The relative oxidation state is set to one log unit above the fayalite-magnetite-quartz buffer (ΔFMQ +1) as magnesian and calcic-calc alkalic rocks from arc settings tend to be associated with oxidizing conditions (Frost et al., 2001; Arculus, 2003). The initial water content was set to 2 wt% as most mafic arc magmas contain 2–6 wt% water content (Plank et al., 2013). The pressure of crystallization is set to 0.1 GPa (~3.7 km) which is indicative of the upper crust location of the pluton.

The residual liquid model curve is shown in Figure 12 with the complete results available in online Supplementary Supplementary Table S6. The liquid compositions are shown at 10°C intervals and the starting temperature was set to 1,300°C. The liquidus temperature is 1090°C when clinopyroxene ($Wo_{40}En_{47}Fs_{13}$) crystallizes. The compositional range of the silicic system is generated from ~1090°C to ~880°C. At 880°C, ~59% of the total magma system crystallized with ~41% liquid remaining. The fractionated assemblage from the liquidus temperature to 880°C is: clinopyroxene (1090°C–930°C), orthopyroxene (1070°C–880°C), plagioclase (1070°C–880°C), Fe-Ti (titanomagnetite) spinel (1050°C–910°C, 880 °C), and ilmenite (880 °C). The proportions, relative to the total solid, and compositional ranges of the fractionated minerals at 880°C are: clinopyoxene ($Wo_{40-30}En_{47-52}Fs_{13-18}$) = ~15.8%, orthopyroxene = 13.6%, plagioclase (An_{74-36}) = 61.9%, spinel (titanomagnetite) = 8.6%, and ilmenite = 0.02%.

The compositional variability of the rocks can be explained primarily by crystal fractionation (~90%) of clinopyroxene, orthopyroxene, and plagioclase, although Na_2O tends to be ~1 wt% higher for rocks with 63–67 wt% SiO_2 until matching the high SiO_2 sample (Figure 12). The fractionating mineral assemblage is consistent with the decrease in Sc, Ni, Co, and Sr concentration with increasing SiO_2 content of the rocks. However, two quartz diorites (A17.1ah and A17.3b) have Eu/Eu* values greater than one suggesting that Eu may have increased in the magma system before the onset of feldspar fraction or that the rocks are composed of cumulus plagioclase. Alternatively, the higher Eu/Eu* values could be related to a high magmatic oxidation state as this would favour Eu^{3+} which does not partition as readily into feldspar as Eu^{2+} (Cicconi et al., 2022). Nevertheless, the model shows good agreement from the intermediate rocks to the diorites indicating that they may represent a cogenetic magma that developed in the upper crust under hydrous and oxidizing conditions. We cannot eliminate the possibility that crustal contamination or other syn/post-emplacement processes affected the system as inherited zircons were identified, but only that crystal fractionation was the primary process of magma differentiation.

Magma source

The fractional crystallization modeling and Sr-Nd isotopes are supportive of a cogenetic origin of the diorites and quartz diorites of the Snoul pluton. Moreover, it is likely that the diorites are similar to the original parental magma. The Sr-Nd-Hf isotopes ($^{87}Sr/^{86}Sr_i$ = 0.704313 and 0.706909; $\varepsilon_{Nd}(t)$ = +3.5 and +4.9; $\varepsilon_{Hf}(t)$ = +7.0– +17.0) of the diorites rocks are moderately depleted and indicative of either a juvenile crustal source or a depleted mantle source that was enriched by subduction-related or crustal materials (i.e., melt and/or fluids). That is, the parental magma may have been derived by partial melting of juvenile mafic crust (Defant and Drummond, 1990; Rapp and Watson, 1995; Rapp et al., 1999; Moyen, 2009; Castillo, 2012), by partial melting of a pyroxenitic mantle source (Kogiso et al., 2004; Straub et al., 2008; Straub et al., 2011), or was derived by mixing between a basaltic magma and a crustal melt.

We do not think that the parental magma of the dioritic rocks (SiO_2 = 54–61 wt%) was derived by mixing between a basaltic magma and crustal magma as the Eu/Eu* values are 0.97–0.98 and the Ni concentration is ≤12 ppm. It is unlikely that mixing between an isotopically enriched upper crustal melt with a primitive arc basalt could yield a hybrid composition that has such a high Eu/Eu* value and low Ni concentration. Furthermore, average middle and lower crust compositions of Rudnick and Gao (2014) have relatively high Ni

content (33–88 ppm) and high Eu/Eu* values (>0.95) and thus any melt composition derived from either would be insufficient to drive Ni contents lower than 12 ppm while increasing the SiO_2 content by 3–5 wt% and maintaining an $\varepsilon_{Nd}(t)$ values greater than +3. Therefore, it is likely that the dioritic rocks are either derived by melting of a pyroxenitic mantle source or partial melting of a subducted oceanic slab or juvenile lower crust.

Silicic magma (SiO_2 = 55–65 wt%) may be generated by direct melting of 'reaction pyroxenite' peridotite (Straub et al., 2008; Straub et al., 2011). However, these magmas tend to have high Mg# (>55) and Ni > 50 ppm as they inherit the high MgO and FeO ratio of the original peridotite mantle (Baker et al., 1994; Straub et al., 2011). The melts also tend to have TiO_2 > 0.7 wt% (Kogiso et al., 2004). The dioritic rocks have Ni ≤ 12 ppm, Mg# of 42.1–53.6, and TiO_2 < 0.7 wt%. In comparison, adakitic melts generated by melting of subducted slab tend to have SiO_2 ≥ 56 wt%, Al_2O_3 ≥ 15 wt%, MgO <3 wt% (rarely >6 wt%), Sr ≥ 400 ppm, Y ≤ 18 ppm, Yb ≤ 1.9 ppm, Sr/Y > 40, and Ni < 50 ppm (Defant and Drummond, 1990; Castillo, 2012). The diorites of this study, in particular samples O20 and O27a, are somewhat similar to adakitic rocks as they have SiO_2 = 54.8–61.8 wt%, Al_2O_3 > 17.5 wt%, MgO ≤5 wt%, Sr = 282–679 ppm, Y = 14.6–23.5 ppm, Yb = 1.65–2.20 ppm, and Sr/Y = 18.5–41.9, but they do not fit perfectly within the low-SiO_2 or high-SiO_2 adakite groupings of Martin et al. (2005). The moderately depleted isotopic compositions and Late Neoproterozoic to Paleozoic Nd and Hf depleted mantle model ages imply the rocks are derived from juvenile crust whereas their negative primitive mantle normalized anomalies of Nb are consistent with continental crust generated at an arc setting. Although we cannot be more certain on the exact nature of the source for the parental magmas, we conclude that it is either mafic, juvenile, arc-related lower crust of the Indochina terrane or the upper subducted Paleo-Pacific oceanic crust. If the former is true, then it offers an explanation for the distinct change in the source composition of the contemporaneous Aptian-Albian volcanic-arc rocks across the Dalat zone as granitic rocks to the east are isotopic different ($^{87}Sr/^{86}Sr_i$ = 0.70444–0.71188; $\varepsilon_{Nd}(t)$ = −2.4- +0.2) (Figure 9).

Magma evolution of the mafic system

The origin of the basaltic rocks is likely different from the silicic system as they are compositionally similar to within-plate basalt rather than arc basalt. The basaltic rocks have similar primitive mantle normalized and chondrite normalized incompatible elemental patterns suggesting that they are petrogenetically related. Specifically, the rocks have modest negative Nb anomalies and very similar light rare Earth element enriched patterns (Figures 8E, F). The compositions are not primary as their Mg# (50.1–61.7) and MgO (4.88–9.11 wt%) and Ni (24–205) contents are evolved. Sample A17.10b is the most primitive, but the CaO (9.40–10.65 wt%) contents are low and Fe_2O_3t (9.57–11.21 wt%) contents are high. The low Mg# and CaO and absence of negative Eu/Eu* (0.93–0.96) indicates that the rocks underwent fractionation of mafic silicate minerals (e.g., olivine, clinopyroxene) with minimal plagioclase fractionation.

The results of fractional crystallization modeling using Rhyolite-MELTS and a starting composition similar to sample A17.10b with a pressure of 0.1 GPa, initial water content of 1.25 wt%, and fO_2 at the Ni-NiO (ΔFMQ +0.7) buffer is shown in Figure 13 (Supplementary Table S6). The results indicate that fractionation of olivine (8.2 vol%), clinopyroxene (12.8 vol%), plagioclase (2.2 vol%), and spinel (0.85 vol %) from 1,260–1,090°C with ~75.1 vol% liquid remaining can explain the chemical variability of the basaltic rocks (Figure 13). Moreover, the high La/Yb_N (11.2–13.2) and Tb/Yb_{PM} (1.9–2.2) ratios indicate that the mantle source was garnet bearing and had a minimum depth of melting of 60–70 km which is similar to estimates for the Neogene–Quaternary flood basalts of Southeast Asia (Nguyen and Flower, 1998; Wang et al., 2002).

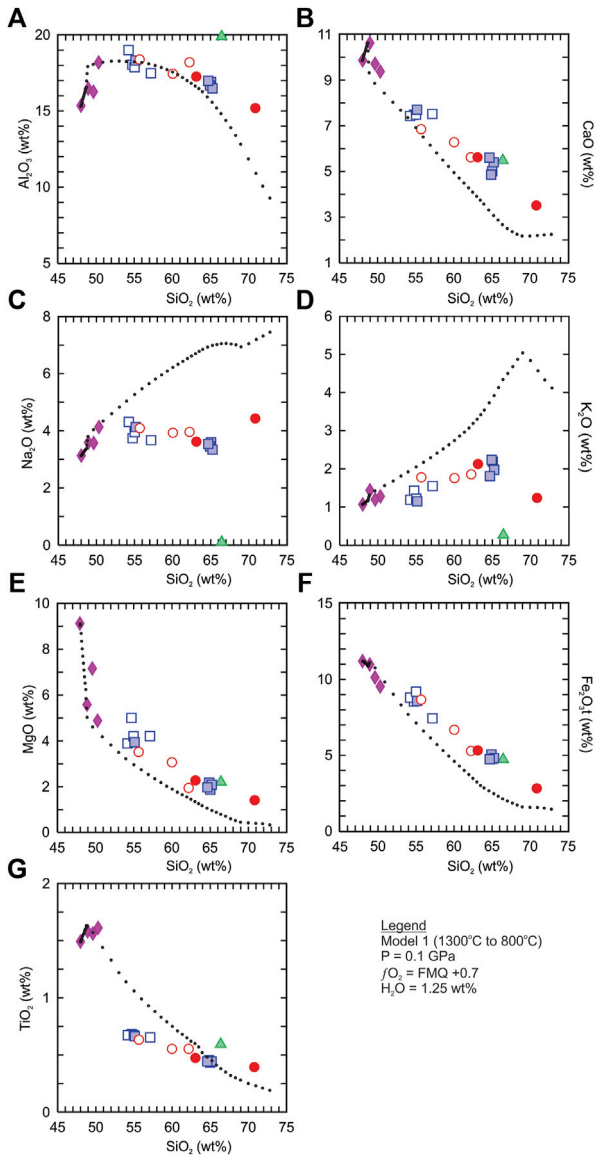

FIGURE 13
The results of hydrous fractional crystallization of the basaltic rocks from the Snoul pluton at 0.1 GPa and fO_2 = ΔFMQ +0.7. **(A)** Al_2O_3 (wt%), **(B)** CaO (wt%), **(C)** Na_2O (wt%), **(D)** K_2O (wt%), **(E)** MgO (wt%), **(F)** Fe_2O_3t (wt%), and **(G)** TiO_2 (wt%) vs. SiO_2 (wt%). The residual silicic liquids compositions are at 10°C intervals. The complete modeling results are in online Supplementary Table S6. All data are normalized to 100%. Symbols of the Snoul pluton are the same as in Figure 7.

The most extensive eruption of within-plate alkaline basalt across SE Asia occurred during the Late Cenozoic (<10 Ma) with correlative rocks identified in eastern Cambodia (Flower et al., 1993; Nguyen and Flower, 1998; Fedorov and Koloskov, 2005; An et al., 2017; Zhao et al., 2021). If we assume an emplacement age of 10 Ma for the basaltic

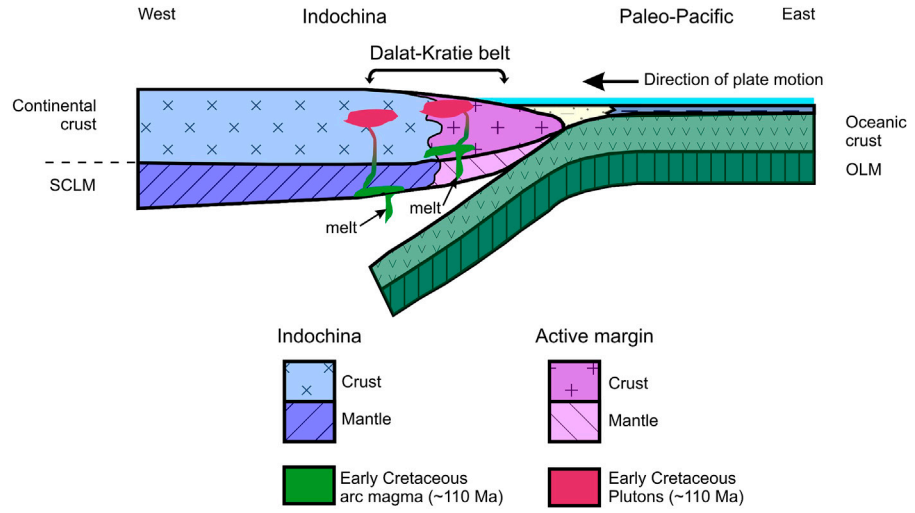

FIGURE 14
Conceptual model for the genesis of the Cretaceous (130-90 Ma) volcanic-arc granites of the Dalat-Kratie belt. Subduction of the Paleo-Pacific plate beneath the Indochina terrane belt generates arc magmas that may be derived from the subducted slab, lower crust, or from mixed crustal/mantle sources. The granitic plutons closer (purple region) to arc front are more likely to be isotopically enriched whereas those located farther (blue region) from the arc front are more likely to be isotopically juvenile. It is possible that the isotopic differences are an intrinsic feature of the Indochina terrane and that there may exist a domain boundary within the southeast Indochina terrane.

rocks of this study then the initial Sr-Nd ratios ($^{87}Sr/^{86}Sr_i$ = 0.703978; $\varepsilon_{Nd}(t)$ = +4.2) are indicative of a moderately depleted source. It is likely that the basaltic rocks of this study were emplaced during a period of regional tensional plate stress and that their source (i.e., garnet-spinel bearing peridotite) may be indicative of the lithospheric mantle in this part of the Indochina terrane.

Migration of the continental-arc or discovery of a terrane boundary?

Many continental and island arcs show evidence of magmatic migration over time (e.g., Lesser Antilles, Andes, Sunda) that is thought to be related to changes in the subducting plate dynamics (Kay et al., 2005; He and Xu, 2012; Allen et al., 2019; Lai et al., 2021). The Late Mesozoic granites of eastern China are an example of secular variation of granitic batholiths in a convergent margin regime as magmatism changed from one of sinistral strike-slip compression during the Jurassic to an active continental margin during the Early Cretaceous (Zhou et al., 2006; Dong et al., 2018). The Cretaceous granitic batholiths of eastern China show chemo-temporal transition from subduction-related Cordilleran-type batholiths during the Early Cretaceous (130–100 Ma) to extension-related A-type granitic batholiths during the Late Cretaceous (<90 Ma) (Zhou and Li, 2000; Zhou et al., 2006; Li et al., 2012). Correlative with the Late Yanshanian granites of eastern China are the Early Cretaceous granitic batholiths of the southern Indochina terrane (Nguyen et al., 2004a; Nguyen et al., 2004b; Shellnutt et al., 2013).

The reported ages of the Dalat-Kratie granites are mostly between ~120 Ma and ~80 Ma and show a chemical transition from Cordilleran I-type granites to post-collisional (A-type) granites over time (Nguyen et al., 2004a; Nguyen et al., 2004b; Shellnutt et al., 2013; Hennig-Breitfeld et al., 2021). Although there is a compositional transition from I-type granite to A-type granite, there does not appear to be a spatial correlation as the older I-type granites (120-115) geographically overlap with the younger I-type granites (110-90 Ma) and the A-type granites (<90 Ma) (Nguyen et al., 2004a; Nguyen et al., 2004b; Shellnutt et al., 2013; Cheng et al., 2019; Kasahara et al., 2021; Hennig-Breitfeld et al., 2021; Waight et al., 2021; Nong et al., 2022). However, there is a distinct change in the Sr-Nd isotopic compositions of the I-type granites in Cambodia compared to the granites of similar age in Vietnam (Figure 9).

The precise reason for the isotopic change is not clear, but it must be related to the parental magma source. Consequently, there are two possibilities: 1) there is a change in the lithospheric composition of each region, or 2) there were differences in the amount of isotopically enriched components in the genesis of the parental magmas. If the parental magmas of the I-type granites of each region are derived primarily by lithospheric melting then the western region must be isotopically juvenile compared to the eastern region. This could imply that there is a heretofore unseen lithotectonic boundary between the two regions (c.f., Dijkstra and Hatch, 2018). Alternatively, it could reflect differences in the amount of enriched material (e.g., fluids, melts) originating either from subducted sediment or crustal melts that is incorporated into the parental magmas whether they are derived from the mantle or subducted slab. That is, there was more enriched material involved in the genesis of the granitoids from Vietnam than the granitoids from Cambodia.

We cannot be certain which of the two scenarios is more likely, although we tend to favour the possibility that there is a domain boundary between eastern Cambodia and southern Vietnam (Figure 14). The western region of the Dalat-Kratie belt in Vietnam and Cambodia is referred to as the Srepok-Tay Nam Bo orogenic belt (c.f., Hennig-Brietfeld et al., 2021). Consequently,

it is possible that the Srepok-Tay Nam Bo orogenic belt and the Dalat-Kratie belt are compositionally and tectonically distinct regions of the Indochina terrane. Our preferred interpretation is based on the fact that the Carboniferous-Permian (343–253 Ma) inherited zircons from the Late Cretaceous (86.6 ± 1.6 Ma) Ankroet "A-type" granite of Vietnam have negative $\varepsilon_{Hf}(t)$ values (−10.2– −3.3; Shellnutt et al., 2013) whereas the Carboniferous-Permian (335–296 Ma) inherited zircons from the Snoul pluton have positive $\varepsilon_{Hf}(t)$ values (+3.9– +15.5). Furthermore, the single Triassic (249 ± 5 Ma, 1σ) inherited zircon from Ankroet has a highly negative $\varepsilon_{Hf}(t)$ value (−17.2) whereas in the Snoul pluton the Early Triassic (240 Ma) inherited zircon has near chondritic value $\varepsilon_{Hf}(t)$ values (+1.2). Thus, the Hf isotopes of the inherited Paleozoic zircons and the whole rock Sr-Nd isotopes indicate that the isotopic differences between the two regions are likely to be an intrinsic feature of the Indochina lithosphere that predates the Cretaceous (e.g., Shellnutt et al., 2020b). Therefore, it possible that the lithosphere of the southern Indochina terrane is composed of distinct lithotectonic domains.

Conclusion

The quartz diorites and diorites of the Snoul pluton are compositionally similar to volcanic-arc granitoids. The rocks were emplaced during the Early Cretaceous (107.5 ± 0.3 Ma, 109.2 ± 0.4 Ma) subduction of the Paleo-Pacific plate beneath the Indochina terrane. The whole rock Sr-Nd isotopes show that the host rocks ($^{87}Sr/^{86}Sr_i$ = 0.704389–0.707681; $\varepsilon_{Nd}(t)$ = +3.1– +4.9) are similar to the enclave ($^{87}Sr/^{86}Sr_i$ = 0.704313; $\varepsilon_{Nd}(t)$ = +3.5) and indicate that they are part of the same magmatic system.

Fractional crystallization modeling under oxidizing (ΔFMQ +1), hydrous (H_2O = 2 wt%), and low pressure (p = 0.1 GPa) conditions shows that it is possible that the dioritic rocks are representative of the parental magma composition of the system. Moreover, some of the diorites are compositionally similar to adakitic rocks which may suggest that they were originally derived by partial melting of juvenile mafic crust of the Indochina terrane. If this is true, then it may explain the isotopic change in granitic rocks from enriched Sr-Nd values in Vietnam to moderately depleted values in Cambodia.

The basaltic rocks represent a different magmatic system as they are compositionally similar to within-plate basalt rather than volcanic-arc basalt. Fractional crystallization modeling using the most primitive basalt as the parental composition can explain the chemical variability within the basaltic rocks. The Sr-Nd isotopic values are moderately depleted and are similar to host intrusion. We think that it is likely that the basaltic rocks are contemporaneous with the Neogene–Quaternary flood basalts of SE Asia and petrogenetically unrelated to the Snoul pluton.

Data availability statement

The original contributions presented in the study are included in the article/Supplementary Material, further inquiries can be directed to the corresponding author.

Author contributions

GM and JC conceived of the study and collected the samples. JS, GM, and JW wrote the manuscript. JW measured the zircon U-Pb and Hf isotopes, K-LW assisted with the whole rock Sr-Nd isotopes and whole rock trace elements, and JS measured the whole rock major elements. All authors contributed to the manuscript, read, and approved the submitted version.

Funding

This project received support from the National Science and Technology Council (Taiwan) through grant 111-2116-M-003-006.

Acknowledgments

We thank Fu-Lung Wang and Robert Hsieh for their help during sample preparation and analytical work and Southern Gold (Cambodia) for sample provision.

Conflict of interest

The authors declare that the research was conducted in the absence of any commercial or financial relationships that could be construed as a potential conflict of interest.

Publisher's note

Supplementary material

The Supplementary Material for this article can be found online at: https://www.frontiersin.org/articles/10.3389/feart.2023.1110568/full#supplementary-material

References

Allen, R. W., Collier, J. S., Stewart, A. G., Henstock, T., Goes, S., Rietbrock, A., et al. (2019). The role of arc migration in the development of the esser Antilles: new tectonic model for the enozoic evolution of the eastern aribbean. *Geology* 47, 891–895. doi:10.1130/G46708.1

An, A.-R., Choi, S. H., Yu, Y., and Lee, D.-C. (2017). Petrogenesis of ate enozoic basaltic rocks from southern Vietnam. *Lithos* 272-273, 192–204. doi:10.1016/j.lithos.2016.12.008

Arculus, R. J. (2003). Use and abuse of the terms calcalkaline and calcalkalic. *J. Petrol* 44, 929–935. doi:10.1093/petrology/44.5.929

Baker, M. B., Grove, T. L., and Price, R. (1994). Primitive basalts and andesites from the Mt. Shasta region, N. California: roducts of varying melt fraction and water content. *Contrib. Mineral. Petrol.* 118, 111–129. doi:10.1007/BF01052863

Barbarin, B. (1999). A review of the relationships between granitoid types, their origins and their geodynamic environments. *Lithos* 46, 605–626. doi:10.1016/S0024-4937(98)00085-1

Blichert-Toft, J., and Albarede, F. (1997). The Lu-Hf isotope geochemistry of chondrites and the evolution of the mantle-crust system. *Earth Planet. Sci. Lett.* 148, 243–258. doi:10.1016/S0012-821X(97)00040-X

Bouilhol, P., Jagoutz, O., Hanchar, J. M., and Dudas, F. O. (2013). Dating the India-Eurasia collision through arc magmatic records. *Earth Planet. Sci. Lett.* 366, 163–175. doi:10.1016/j.epsl.2013.01.023

Breitfeld, H. T., Davies, L., Hall, R., Armstrong, R., Forster, M., Lister, G., et al. (2020). Mesozoic aleo-acific subduction beneath SW orneo: U-Pb geochronology of the chwaner granitoids and the inoh metamorphic group. *Front. Earth Sci.* 8, 568715. doi:10.3389/feart.2020.568715

Breitfeld, H. T., Hennig-Breitfeld, J., Boudagher-Fadel, M., Schmidt, W. J., Meyer, K., Reinprecht, J., et al. (2022). Provenance of Oligocene-Miocene sedimentary rocks in the Cuu Long and Nam Con Son basins, Vietnam and early history of the Mekong River. *Int. J. Earth Sci* 111, 1773–1804.

Burrett, C., Udchachon, M., and Thassanapak, H. (2021). The Truong Son, oei-hetchabun, and Kontum erranes in Indochina: rovenance, rifting, and collisions. *Front. Earth Sci.* 9, 603565. doi:10.3389/feart.2021.603565

Burrett, C., Zaw, K., Meffre, S., Lai, C. K., Khositanont, S., Chaodumrong, P., et al. (2014). The configuration of reater Gondwana–Evidence from LA ICPMS, U–Pb geochronology of detrital zircons from the alaeozoic and esozoic of Southeast Asia and China. *Gondwana Res* 26, 31–51. doi:10.1016/j.gr.2013.05.020

Cabanis, B., and Lecolle, M. (1989). Le diagramme La/10–Y/15–Nb/8: n outil pour la discrimination des series volcanique et la mise en evidence des processus de melange et/ou de contamination crustale. *Acad. Sci. Ser. II* 309, 2023–2029.

Carter, A., and Clift, P. D. (2008). Was the Indosinia orogeny a Triassic mountain building or a thermotectonic reactivation event? *C. R. Geosci.* 340, 83–93. doi:10.1016/j.crte.2007.08.011

Carter, A., Roques, D., Bristow, C., and Kinny, P. (2001). Understanding esozoic accretion in outheast Asia: ignificance of riassic thermotectonism (ndosinian orogeny) in Vietnam. *Geology* 29, 211–214. doi:10.1130/0091-7613(2001)029<0211:UMAISA>2.0.CO;2

Castillo, P. R. (2012). Adakite petrogenesis. *Lithos* 134-135, 304–316. doi:10.1016/j.lithos.2011.09.013

Chappell, B. W., and White, J. R. (2001). Two contrasting granite types: 25 years later. *Aust. J. Earth Sci.* 48, 489–499. doi:10.1046/j.1440-0952.2001.00882.x

Chauvel, C., Lewin, E., Carpentier, M., Arndt, N. T., and Marini, J.-C. (2008). Role of recycled oceanic basalt and sediment in generating the Hf-Nd mantle array. *Nat. Geosci.* 1, 64–67. doi:10.1038/ngeo.2007.51

Cheng, R., Uchida, E., Katayose, M., Yarimizu, K., Shin, K.-C., Kong, S., et al. (2019). Petrogenesis and tectonic setting of ate aleozoic to ate esozoic igneous rocks in Cambodia. *J. Asian Earth Sci.* 185, 104046. doi:10.1016/j.jseaes.2019.104046

Chu, N. C., Taylor, R. N., Chavagnac, V., Nesbitt, R. W., Boella, R. M., Milton, J. A., et al. (2002). Hf isotope ratio analysis using multi-collector inductively coupled plasma mass spectrometry: n evaluation of isobaric interference corrections. *J. Anal. At. Spect.* 17, 1567–1574. doi:10.1039/B206707B

Cicconi, M. R., Le Losq, C., Henderson, G. S., and Neuville, D. R. (2021). "The redox behaviour of rare elements," in *Magma edox eochemistry*. Editors R. Moretti and D. R. Neuville (New York, USA: American Geophysical Union Geophysical Monograph), 381–398.

Corfu, F., Hanchar, J. M., Hoskin, P. W. O., and Kinny, P. (2003). Atlas of zircon textures. *Rev. Mineral. Geochem.* 53, 469–500. doi:10.2113/0530469

Cox, K. G., Bell, J. D., and Pankhurst, R. J. (1979). *The interpretation of igneous rocks*. London, UK: George Allen and Unwin Ltd, 450.

Defant, M. J., and Drummond, M. S. (1990). Derivation of some modern arc magmas by melting of young subducted lithosphere. *Nature* 347, 662–665. doi:10.1038/347662a0

Dijkstra, A., and Hatch, C. (2018). Mapping a hidden terrane boundary in the mantle lithosphere with lamprophyres. *Nat. Comm.* 9, 3770. doi:10.1038/s41467-018-06253-7

Dong, S., Zhang, Y., Li, H., Shi, W., Xue, H., Li, J., et al. (2018). The anshan orogeny and late esozoic multi-plate convergence in ast-Asia–Commemorating 90th years of the "Yanshan Orogeny". *Sci. China Earth Sci.* 61, 1888–1909. doi:10.1007/s11430-017-9297-y

Faure, M., Lin, W., Monié, P., and Meffre, S. (2008). Palaeozoic collision between the North and South China blocks, Triassic intracontinental tectonics, and the problem of the ultrahigh-pressure metamorphism. *C. R. Geosci.* 340, 139–150. doi:10.1016/j.crte.2007.10.007

Faure, M., Nguyen, V. V., Hoai, L. T. T., and Lepvrier, C. (2018). Early aleozoic or arly-iddle riassic collision between the South China and Indochina locks: he controversy resolved? Structural insights from the on um massif (entral Vietnam). *J. Asian Earth Sci.* 166, 162–180. doi:10.1016/j.jseaes.2018.07.015

Fedorov, P. I., and Koloskov, A. V. (2005). Cenozoic volcanism of southeast Asia. *Petrology* 13, 352–380. doi:10.1038/s41598-018-20712-7

Flower, M. F. J., Nguyen, H., Nguyen, T. Y., Nguyen, X. B., McCabe, R. J., and Harder, S. H. (1993). Cenozoic magmatism in Indochina: ithosphere extension and mantle potential temperature. *Geol. Soc. Malays Bull.* 33, 211–222. doi:10.7186/bgsm33199316

Frost, B. R., Barnes, C. G., Collins, W. J., Arculus, R. J., Ellis, D. J., and Frost, C. D. (2001). A geochemical classification for granitic rocks. *J. Petrol.* 42, 2033–2048. doi:10.1093/petrology/42.11.2033

Griffin, W. L., Belousova, E. A., Shee, S. R., Pearson, N. J., and O'Reilly, S. Y. (2004). Archean crustal evolution in the northern ilgarn raton: U–Pb and Hf-isotope evidence from detrital zircons. *Precambrian Res.* 131, 231–282. doi:10.1016/j.precamres.2003.12.011

Griffin, W. L., Pearson, N. J., Belousova, E., Jackson, S. E., van Achterbergh, E., O'Reilly, S. Y., et al. (2000). The Hf isotope composition of cratonic mantle: LAM-MC-ICPMS analysis of zircon megacrysts in kimberlites. *Geochim. Cosmochim. Ac.* 64, 133–147. doi:10.1016/S0016-7037(99)00343-9

Gualda, G. A. R., Ghiorso, M. S., Lemons, R. V., and Carley, T. L. (2012). Rhyolite-MELTS: modified calibration of MELTS optimized for silica-rich, fluid-bearing magmatic systems. *J. Petrol.* 53, 875–890. doi:10.1093/petrology/egr080

Hall, R. (2012). Late urassic-enozoic reconstructions of the Indonesian region and the Indian cean. *Tectonophysics* 570-570, 1–41. doi:10.1016/j.tecto.2012.04.021

Hall, R., and Sevastjanova, I. (2012). Australian crust in Indonesia. *Aust. J. Earth Sci.* 59, 827–844. doi:10.1080/08120099.2012.692335

Hall, R. (2017). Southeast Asia: ew views of the geology of the Malay rchipelago. *Annu. Rev. Earth Planet. Sci.* 45, 331–358. doi:10.1146/annurev-earth-063016-020633

He, Z.-Y., and Xu, X.-S. (2012). Petrogenesis of the ate anshanian mantle-derived intrusions in southeastern China: esponse to the geodynamics of aleo-Pacific plate subduction. *Chem. Geol.* 328, 208–221. doi:10.1080/08120099.2012.692335

Hennig-Breitfeld, J., Breitfeld, H. T., Sang, D. Q., Vinh, M. K., Long, T. V., Thirlwall, M., et al. (2021). Ages and character of igneous rocks of the Da Lat zone in SE Vietnam and adjacent offshore regions (Cuu long and Nam Con Son basins). *J. Asian Earth Sci.* 218, 104878. doi:10.1016/j.jseaes.2021.104878

Hutchinson, C. S. (2014). Tectonic evolution of southeast Asia. *Bull. Geol. Soc. Malays* 60, 1–18. doi:10.1016/j.jseaes.2021.104878

Jackson, S. E., Pearson, N. J., Griffin, W. L., and Belousova, E. A. (2004). The application of laser ablation-inductively coupled plasma-mass spectrometry to *in situ* U–Pb zircon geochronology. *Chem. Geol.* 211, 47–69. doi:10.1016/j.chemgeo.2004.06.017

Jiang, H., Li, W.-Q., Zhao, K.-D., Zhang, D., and Jiang, S.-Y. (2021). Middle riassic diorites from the Loei Fold Belt, NE Thailand: etrogenesis and tectonic implications in the context of aleotethyan subduction. *Lithos* 382-383, 105955. doi:10.1016/j.lithos.2020.105955

Kasahara, N., Niki, S., Uchida, E., Yarimizu, K., and Cheng, R. (2021). Zircon U-Pb chronology on plutonic rocks from northeastern Cambodia. *Heliyon* 7, e06752. doi:10.1-16/j.heliyon.2021.e06752

Kay, S. M., Godoy, E., and Kurtz, A. (2005). Episodic arc migration, crustal thickening, subduction erosion, and magmatism in the south-central Andes. *Geol. Soc. Am. Bull.* 117, 67–88. doi:10.1130/B25431.1

Kogiso, T., Hirschmann, M. M., and Pertermann, M. (2004). High-pressure partial melting of mafic lithologies in the mantle. *J. Petrol.* 45, 2407–2422. doi:10.1093/petrology/egh057

Lai, Y.-M., Chung, S.-L., Ghani, A. A., Murtadha, S., Lee, H.-Y., and Chu, M.-F. (2021). Mid-Miocene volcanic migration in the westernmost Sunda arc induced by India-Eurasia collision. *Geology* 49, 713–717. doi:10.1130/G48568.1

Lan, C.-Y., Chung, S.-L., Long, T. V., Lo, C.-H., Lee, T.-Y., Mertzman, S. A., et al. (2003). Geochemical and Sr-Nd isotopic constraints from the Kontum massif, central Vietnam on the crustal evolution of the Indochina block. *Precambrian Res.* 122, 7–27. doi:10.1016/S0301-9268(02)00205-X

Lepvrier, C., Maluski, H., Tich, V. V., Leyreloup, A., Thi, P. T., and Vuong, N. V. (2004). The arly riassic ndosinian orogeny in Vietnam (Truong Son elt and Kontum assif); implications for the geodynamic evolution of Indochina. *Tectonophysics* 393, 87–118. doi:10.1016/j.tecto.2004.07.030

Lepvrier, C., Nguyen, V. V., Maluski, H., Phan, T. T., and Tich, V. V. (2008). Indosinian tectonics in Vietnam. *C. R. Geosci.* 340, 94–111. doi:10.1016/j.crte.2007.10.005

Li, Z.-X., Li, X.-H., Chung, S.-L., Lo, C.-H., Xu, X., and Li, W.-X. (2012). Magmatic switch-on and switch-off along the South China continental margin since the ermian: ransition from an ndean-type to a estern acific-type plate boundary. *Tectonophysics* 532-535, 271–290. doi:10.1016/j.tecto.2012.02.011

Li, Z.-X., and Li, X.-H. (2007). Formation of the 1300-km-wide intracontinental orogeny and post-orogenic magmatic province in esozoic outh China: flat-slab subduction model. *Geology* 35, 179–182. doi:10.1130/G23193A.1

Li, Z., Qiu, J.-S., and Yang, X.-M. (2014). A review of the geochronology and geochemistry of ate anshanian (retaceous) plutons along the ujian coastal area of southeastern China: mplications for magma evolution related to slab break-off and rollback in the retaceous. *Earth-Sci. Rev.* 128, 232–248. doi:10.1016/j.earscirev.2013.09.007

Liu, Y. S., Gao, S., Hu, Z. C., Gao, C. G., Zong, K. Q., and Wang, D. B. (2010). Continental and oceanic crust recycling-induced melt-peridotite interactions in the rans-orth China rogen: U-Pb dating, Hf isotopes and trace elements in zircons from mantle xenoliths. *J. Petrol.* 51, 537–571. doi:10.1093/petrology/egp082

Ludwig, K. R. (2008). *Isoplot 3.6; A eochronology oolkit for icrosoft xcel*. Berkeiey, CA, USA: Berkeley Geochronology Center, 77.

Machado, N., and Simonetti, A. (2001). "U–Pb dating and Hf isotopic composition of zircons by laser ablation-MC-ICP-MSA,". Editor P. Sylvester, 29, 121–146. *Laser Earth Sci Princ Appl Course Assoc. Canada*. doi:10.1016/j.rgg.2016.01.013

Martin, H., Smithies, R. H., Rapp, R., Moyen, J.-F., and Champion, D. (2005). An overview of adakite, tonalite-trondhjemite-quartz diorite (TTG), and sanukitoid: elationships and some implications for crustal evolution. *Lithos* 79, 1–24. doi:10.1016/j.lithos.2004.04.048

Maruyama, S., Isozaki, Y., Kimura, G., and Terabayashi, M. (1997). Paleogeographic maps of the Japanese slands: late tectonic synthesis from 750 Ma to the present. *Isl Arc.* 6, 121–142. doi:10.1111/j.1440-1738.1997.tb00043.x

Meschede, M. (1986). A methods of discriminating between different types of mid-ocean ridge basalts and continental tholeiites with the Nb–Zr–Y diagram. *Chem. Geol.* 83, 207–218. doi:10.1016/0009-2541(86)90004-5

Metcalfe, I. (2013). Gondwana dispersion and sian accretion: ectonic and palaeogeographic evolution of eastern ethys. *J. Asian Earth Sci.* 66, 1–33. doi:10.1016/j.jseaes.2012.12.020

Metcalfe, I. (2006). Palaeozoic and esozoic tectonic evolution and palaeogeography of East sian crustal fragments: he Korean eninsula in context. *Gondwana Res* 9, 24–46. doi:10.1016/j.gr.2005.04.002

Metcalfe, I. (2017). Tectonic evolution of undaland. *Bull. Geol. Soc. Malays* 63, 27–60. doi:10.7186/bgsm63201702

Moyen, J.-F. (2009). High Sr/Y and La/Yb ratios: he meaning of the "adakitic signature. *Lithos* 112, 556–574. doi:10.1016/j.lithos.2009.04.001

Nakano, N., Osanai, Y., Owada, M., Binh, P., Hokada, T., and Kaiden, H. (2021). Evolution of the Indochina block from its formation to amalgamation with Asia: constraints from protoliths in the Kontum Massif, Vietnam. *Gondwana Res* 90, 47–62.

Nam, T. N., Sano, Y., Terada, K., Toriumi, M., Van Quynh, P., and Dung, L. T. (2001). First SHRIMP U–Pb zircon dating of granulites from the Kontum massif (Vietnam) and tectonothermal implications. *J. Asian Earth Sci.* 19, 77–84. doi:10.1016/S1367-9120(00)00015-8

Nguyen, H., and Flower, M. (1998). Petrogenesis of enozoic basalts from Vietnam: mplication for origins of a 'diffuse igneous province. *J. Petrol.* 39, 369–395. doi:10.1093/petroj/39.3.369

Nguyen, T. T. B., Satir, M., Siebel, W., and Chen, F. (2004a). Granitoids in the Dalat zone, southern Vietnam: ge constraints on magmatism and regional geological implications. *Int. J. Earth Sci.* 93, 329–340. doi:10.1007/s00531-004-0387-6

Nguyen, T. T. B., Satir, M., Siebel, W., Vennemann, T., and Long, T. V. (2004b). Geochemical and isotopic constraints on the petrogenesis of granitoids from the Dalat zone, southern Vietnam. *J. Asian Earth Sci.* 23, 467–482. doi:10.1016/j.jseaes.2003.06.001

Nong, A. T. Q., Hauzenberger, C. A., Fallhofer, D., Skrzypek, E., and Dinh, S. Q. (2022). Geochemical and zircon U-Pb geochronological constraints on late Mesozoic Paleo-Pacific subduction-related volcanism in southern Vietnam. *Mineral. Petrol.* 116, 349–369. doi:10.1007/s00710-022-00785-z

Nong, A. T. Q., Hauzenberger, C. A., Gallhofer, D., and Dinh, S. Q. (2021). Geochemistry and zircon U-Pb geochronology of ate esozoic igneous rocks from SW ietnam-SE Cambodia: mplications for episodic magmatism in the context of the aleo-acific subduction. *Lithos* 390-391, 106101. doi:10.1016/j.lithos.2021.106101

Pearce, J. A., and Cann, J. R. (1973). Tectonic setting of basic volcanic rocks determined using trace element analyses. *Earth Planet. Sci. Lett.* 19, 290–300. doi:10.1016/0012-821X(73)90129-5

Pearce, J. A., Harris, N. B. W., and Tindle, A. G. (1984). Trace element discrimination diagrams for the tectonic interpretation of granitic rocks. *J. Petrol.* 25, 956–983. doi:10.1093/petrology/25.4.956

Plank, T., Kelley, K. A., Zimmer, M. M., Hauri, E. H., and Wallace, P. J. (2013). Why do mafic arc magmas contain ~4 wt% water on average? *Earth Planet. Sci. Lett.* 364, 168–179. doi:10.1016/j.epsl.2012.11.044

Rapp, R. P., Shimizu, N., Norman, M. D., and Applegate, G. S. (1999). Reaction between slab-derived melts and peridotite in the mantle wedge: xperimental constraints at 3.8 GPa. *Chem. Geol.* 160, 335–356. doi:10.1016/S0009-2541(99)00106-0

Rapp, R. P., and Watson, E. B. (1995). Dehydration melting of metabasalt at 8–32 kbar: mplications for continental growth and crust–mantle recycling. *J. Petrol.* 36, 891–931. doi:10.1038/s41467-022-34343-0

Roger, F., Maluski, H., Leyreloup, A., Lepvrier, C., and Thi, P. T. (2007). U–Pb dating of high temperature metamorphic episodes in the Kon Tum Massif (Vietnam). *J. Asian Earth Sci.* 30, 565–572. doi:10.1016/j.jseaes.2007.01.005

Rudnick, R. L., and Gao, S. (2014). Composition of the continental crust. *Treatise Geochem.* 4, 1–51.

Schellart, W. P., Chen, Z., Strak, V., Duarte, J. C., and Rosas, F. M. (2019). Pacific subduction control on Asian continental deformation including Tibetan extension and eastward extrusion tectonics. *Nat. Comm.* 10, 4480. doi:10.1038/s41467-019-12337-9

Scherer, E., Munker, C., and Mezger, K. (2001). Calibration of the utetium-afnium lock. *Science* 293, 683–687. doi:10.1016/0016-7037(95)00038-2

Shellnutt, J. G., Lan, C.-Y., Long, T. V., Usuki, T., Yang, H.-J., Mertzman, S. A., et al. (2013). Formation of retaceous ordilleran and post-orogenic granites and their microgranular enclaves from the Dalat zone, southern Vietnam: ectonic implications for the evolution of outheast Asia. *Lithos* 182-183, 229–241. doi:10.1016/j.lithos.2013.09.016

Shellnutt, J. G., Nguyen, D. T., and Lee, H.-Y. (2020b). Resolving the origin of the Seychelles microcontinent: nsight from zircon geochronology and Hf isotopes. *Precambrian Res.* 343, 105725. doi:10.1016/j.precamres.2020.105725

Shellnutt, J. G., Vaughan, M. W., Lee, H.-Y., and Iizuka, Y. (2020a). Late Jurassic leucogranites of Macau (SE China): record of crustal recycling during the arly anshanian rogeny. *Front. Earth Sci.* 8, 311. doi:10.3389/feart.2020.00311

Shi, M., Khin, Z., Liu, S., Xu, B., Meffre, S., Cong, F., et al. (2021). Geochronology and petrogenesis of arboniferous and riassic volcanic rocks in NW Laos: mplications for the tectonic evolution of the Loei Fold Belt. *J. Asian Earth Sci.* 208, 104661. doi:10.1016/j.jseaes.2020.104661

Sone, M., and Metcalfe, I. (2008). Parallel ethyan sutures in mainland southeast Asia: new insight for alaeo-ethys closure and implications for the ndosinian orogeny. *C. R. Geosci.* 340, 166–179. doi:10.1016/j.crte.2007.09.008

Straub, S. M., Gomez-Tuena, A., Stuart, F. M., Zellmer, G. F., Espinasa-Perena, R., Cai, Y., et al. (2011). Formation of hybrid arc andesites beneath thick continental crust. *Earth Planet. Sci. Lett.* 303, 337–347. doi:10.1016/j.epsl.2011.01.013

Straub, S. M., LaGatta, A. B., Martin-Del Pozzo, A. L., and Langmuir, C. H. (2008). Evidence from high-Ni olivines for a hybridized peridotite/pyroxenite source for orogenic andesites from the central Mexican volcanic belt. *Geochem. Geophys. Geosys.* 9, Q03007. doi:10.1029/2007GC001583

Suga, K., and Yeh, M.-W. (2020). Secular variation of arly retaceous granitoids in yushu, SW Japan: he role of mélange rocks as a possible magma source. *Front. Earth Sci.* 8, 95. doi:10.3389/feart.2020.00095

Sun, S. S., and McDonough, W. F. (1989). "Chemical and isotopic systematics of oceanic basalts: mplications for mantle composition and processes," in *Magmatism in the cean asins*. Editors A. D. Saunders and M. J. Norry (Bath, UK: Geological Society of London Special Publication), 313–435.

Taylor, B., and Hayes, D. E. (1983). "Origin and history of the South China Sea basin," in *The ectonic and eological volution of Southeast sian eas and slands: Part 2*. Editor D. Hayes (New York, USA: American Geophysical Union Geophysical Monograph), 23–56.

Tran, T. V., Faure, M., Nguyen, V. V., Bui, H. H., Fyhn, M., Nguyen, T. Q., et al. (2020). Neoproterozoic to arly riassic tectono-stratigraphic evolution of Indochina and adjacent areas: review with new data. *J. Asian Earth Sci.* 191, 104231. doi:10.1016/j.jseaes.2020.104231

Usuki, T., Lan, C.-Y., Wang, K.-L., and Chiu, H.-Y. (2013). Linking the Indochina block and Gondwana during the arly aleozoic: Evidence from U–Pb ages and Hf isotopes of detrital zircons. *Tectonophysics* 586, 145–159. doi:10.1016/j.tecto.2012.11.010

Waight, T., Fyhn, M. B. W., Thomsen, T. B., Tran, V. T., Nielsen, L. H., Abatzis, I., et al. (2021). Permian to retaceous granites and felsic volcanics from SW Vietnam and S Cambodia: mplications for tectonic development of Indochina. *J. Asian Earth Sci.* 219, 104902. doi:10.1016/j.seaes.2021.104902

Wang, K., Plank, T., Walker, J. D., and Smith, E. I. (2002). A mantle melting profile across the Basin and Range, SW USA. *J. Geophys. Res.* 107. doi:10.1029/2001JB000209

Wang, Y., Fan, W., Zhang, G., and Zhang, Y. (2013). Phanerozoic tectonics of the South China lock: ey observations and controversies. *Gondwana Res* 23, 1273–1305. doi:10.1016/j.gr.2012.02.019

Wang, Y., Qian, X., Cawood, P. A., Liu, H., Feng, Q., Zhao, G., et al. (2018). Closure of the ast aleotethyan cean and amalgamation of the eastern immerian and southeast Asia continental fragments. *Earth-Sci. Rev.* 186, 195–230. doi:10.1016/j.earscirev.2017.09.013

Whalen, J. B., Currie, K. L., and Chappell, B. W. (1987). A-ype granites: eochemical characteristics, discrimination and petrogenesis. *Contrib. Mineral. Petrol.* 95, 407–419. doi:10.1007/BF00402202

Whalen, J. B., and Hildebrand, R. S. (2019). Trace element discrimination of arc, slab failure, and A-type granitic rocks. *Lithos* 348-349, 105179. doi:10.1016/j.lithos.2019.105179

White, L. T., and Lister, G. S. (2012). The collision of India with Asia. *J. Geodyn.* 56-57, 7–17. doi:10.1016/j.jog.2011.06.006

Wiedenbeck, M., Allé, P., Corfu, F., Griffin, W. L., Meier, M., Oberli, F., et al. (1995). Three atural ircon tandards for U-Th-Pb, Lu-Hf, race element and REE nalyses. *Geostand. Newslett.* 19, 1–23. doi:10.1111/j.1751-908X.1995.tb00147.x

Wu, J., Lin, Y.-A., Flament, N., Wu, J. T.-J., and Liu, Y. (2022). Northwest Pacific-Izanagi plate tectonics since Cretaceous times from Pacific mantle structure. *Earth Planet. Sci. Lett.* 583, 117445. doi:10.1016/j.epsl.2022.117445

Xia, X., Sun, M., Geng, H., Sun, Y., Wang, Y., and Zhao, G. (2011). Quasi-simultaneous determination of U-Pb and Hf isotope compositions of zircon by excimer laser-ablation multiple-collector ICPMS. *J. Anal. At. Spect.* 26, 1868–1871. doi:10.1039/C1JA10116A

Yang, Y.-T. (2013). An unrecognized major collision of the khotomorsk lock with East Asia during the ate retaceous, constraints on the plate reorganization of the orthwest acific. *Earth-Sci. Rev.* 126, 96–115.

Zaw, K., Meffre, S., Lai, C.-K., Burrett, C., Santosh, M., Graham, I., et al. (2014). Tectonics and metallogeny of mainland Southeast Asia – a review. *Gondwana Res* 26, 5–30. doi:10.1016/j.gr.2013.10.010

Zhao, D., Toyokuni, G., and Kurata, K. (2021). Deep mantle structure and origin of enozoic intraplate volcanoes in Indochina, ainan and South China Sea. *Geophys. J. Int.* 225, 572–588. doi:10.1093/gji/ggaa605

Zheng, H., Sun, X., Wang, P., Chen, W., and Yue, J. (2019). Mesozoic tectonic evolution of the roto-South China Sea: perspective from radiolarian pa`leobiogeography. *J. Asian Earth. Sci.* 179, 35–55. doi:10.1016/j.jseaes.2019.04.009

Zhou, X. M., and Li, W. X. (2000). Origin of ate esozoic igneous rocks in southeastern China: mplications for lithosphere subduction and underplating of mafic magmas. *Tectonophysics* 326, 269–287. doi:10.1016/S0040-1951(00)00120-7

Zhou, Z., Sun, T., Shen, W., Shu, L., and Niu, Y. (2006). Petrogenesis of esozoic granitoids and volcanic rocks in outh China: response to tectonic evolution. *Episodes* 29, 26–33. doi:10.18814/epiiugs/2006/v29i1/004

frontiers | Frontiers in Earth Science

TYPE Original Research
PUBLISHED 09 May 2023
DOI 10.3389/feart.2023.1153003

OPEN ACCESS

EDITED BY
J. Gregory Shellnutt,
National Taiwan Normal University, Taiwan

REVIEWED BY
John Greenough,
University of British Columbia, Canada
Boris Belyatsky,
A.P. Karpinsky Russian Geological Research Institute, Russia

*CORRESPONDENCE
A. S. Silpa,
silpa@riko.shimane-u.ac.jp

RECEIVED 28 January 2023
ACCEPTED 28 April 2023
PUBLISHED 09 May 2023

CITATION
Silpa AS, Satish-KumarM, Takahashi T and Kamei A (2023), Sm-Nd isotopic constraints on the metadolerite dykes from Western Dharwar Craton, Southern India: implications on the evolution of Archean subcontinental lithospheric mantle.
Front. Earth Sci. 11:1153003.
doi: 10.3389/feart.2023.1153003

Sm-Nd isotopic constraints on the metadolerite dykes from Western Dharwar Craton, Southern India: implications on the evolution of Archean subcontinental lithospheric mantle

A. S. Silpa[1]*, M. Satish-Kumar[2], T. Takahashi[2] and A. Kamei[1]

[1]Department of Earth Science, Interdisciplinary Faculty of Science and Engineering, Shimane University, Matsue, Japan, [2]Department of Geology, Faculty of Science, Niigata University, Niigata, Japan

Introduction: Metadolerite dykes in the Western Dharwar Craton represent the oldest generation of mafic dyke swarms in the craton. The emplacement of these dykes after a period of crust building activity and komatiite volcanism, helps to understand the evolution of Subcontinental Lithospheric Mantle (SCLM) and Archean dynamics.

Methods: We report whole rock major, trace element geochemistry and Sr-Nd isotope characteristics for this weakly metamorphosed suite of dykes. Remnant igneous textures and mineralogy are well preserved.

Results: The trace and rare earth element concentrations and an overall flat pattern suggests depleted mantle source for these dykes. Three groups are primarily identified: Group one with initial $^{87}Sr/^{86}Sr$ ratios varying between 0.70041 and 0.70102, Group two dykes and Group three dykes with initial ratios 0.70045–0.70154, and 0.70041–0.70153 respectively. Group one dykes show a good Rb-Sr isochron relationship and an errorchron age of ca. 3,003 ± 102 Ma is obtained. The initial $^{143}Nd/^{144}Nd$ ratios varies from 0.508,245 to 0.509,172. The epsilon Nd values are mostly negative, ranging between −12 and +5. Group one and two show an epsilon Nd value ranging between −1 and +5 and 0.1 to +5 respectively and group three varies between −0.5 and −12.

Discussion: The geochemical characteristics suggest that the group one dykes are derived from a homogenous depleted SCLM source, group two formed by a lower degree of partial melting of a source mantle with enriched components. Group three may have formed from a progressively enriched group one source. All these dykes can be considered as exposed remnants of feeders for the greenstone volcanism in the Western Dharwar Craton.

KEYWORDS

Metadolerite dykes, mafic dyke swarms, Western Dharwar Craton (India), Archean subcontinental lithospheric mantle, Sr-Nd isotope systematics

1 Introduction

The geotectonic framework of the early earth is considerably different from present day owing to the high mantle temperatures, early crust-mantle differentiation, large mantle convection and crustal recycling processes (Hoffman and Ranalli, 1988; Armstrong, 1991; Bowring and Housh, 1995; Brown et al., 1995). The formation of continental crust in the Archean and recycling back into the mantle drastically changed the nature and composition of subcontinental lithospheric mantle (SCLM) in the Archean itself (Hawkesworth et al., 2010; Dhuime et al., 2012; Johnson et al., 2019). While these early formed crusts are limited in their distribution as present-day Archean cratonic nuclei, they preserve excellent records of the Archean dynamics including continental growth, episodic mafic magmatism, continental rifting, and breakup of protocontinents with associated production of Large Igneous Provinces (LIPs) (Bleeker, 2003; Ernst et al., 2005; Ernst and Bleeker., 2010). One of the key features of such Archean cratons is the regional scale mafic dyke swarms which are principal constituents of several ancient supercontinents or supercratons (Ernst and Buchan, 2001; Bleeker, 2003; Bleeker and Ernst, 2006; French and Heaman, 2010 and the references therein). Such episodes are often correlated with major Large Igneous Provinces (LIPs), the magmatic events during which large volumes of mantle generated materials are emplaced within a short period of time. The giant mafic dyke swarms in the Archean cratons are thought to be the exposed remnants of deeply eroded LIPs (Coffin and Eldholm, 1991; Coffin and Eldholm, 1994; Ernst, 2014) and they provide crucial information regarding the nature and composition of the subcontinental lithospheric mantle during its formation.

Precambrian mafic dyke swarms are common within Archean cratons and the Dharwar Craton of southern India is one such craton where dyke swarms of varying generations and dimensions are present (Figure 1). These dykes intrude

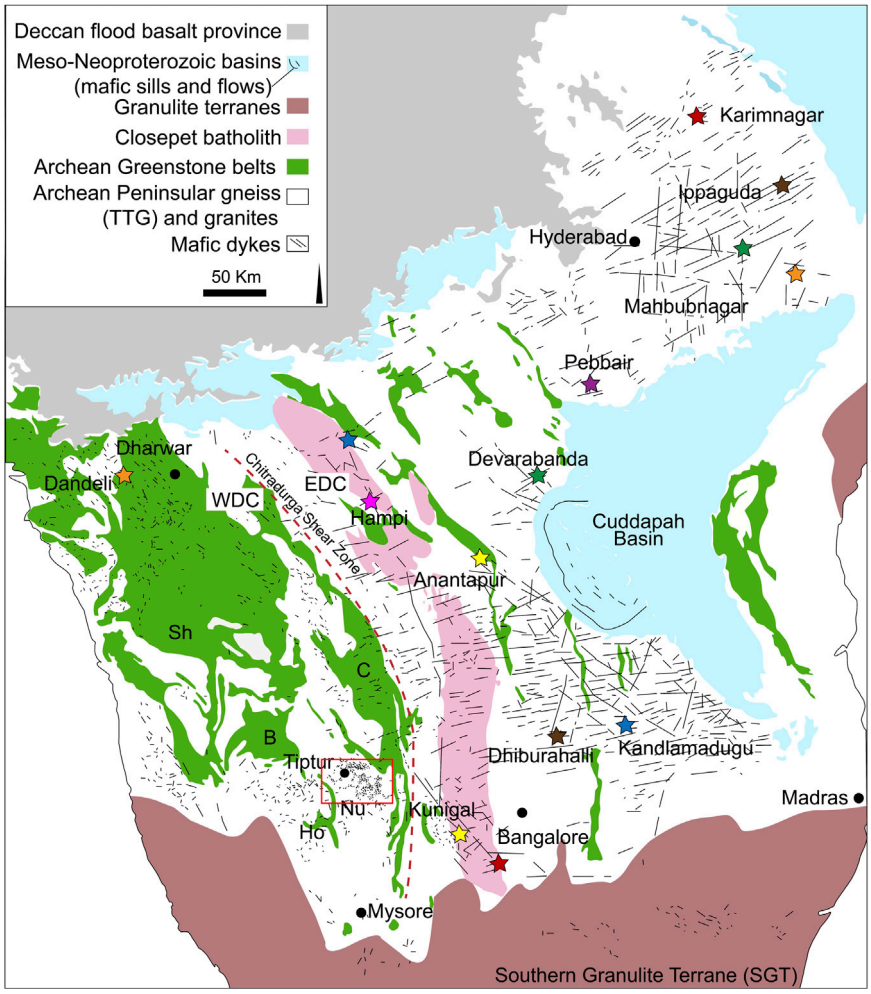

FIGURE 1
Simplified geological map of Dharwar craton showing the distribution of mafic dykes (modified after French and Heaman, 2010). Traditional classification of Dharwar craton is marked as WDC and EDC, Greenstone belts are: Sh- Shimoga; C- Chitradurga; B-Bababudan; Nu- Nuggihalli; Ho-Holenarsipur. Areal extent of recognized mafic dyke swarms after Söderlund et al. (2019) are marked with the same-colored stars. Tiptur swarm is the major dyke swarm in the Western Dharwar Craton, and area of the current study is marked as the red box.

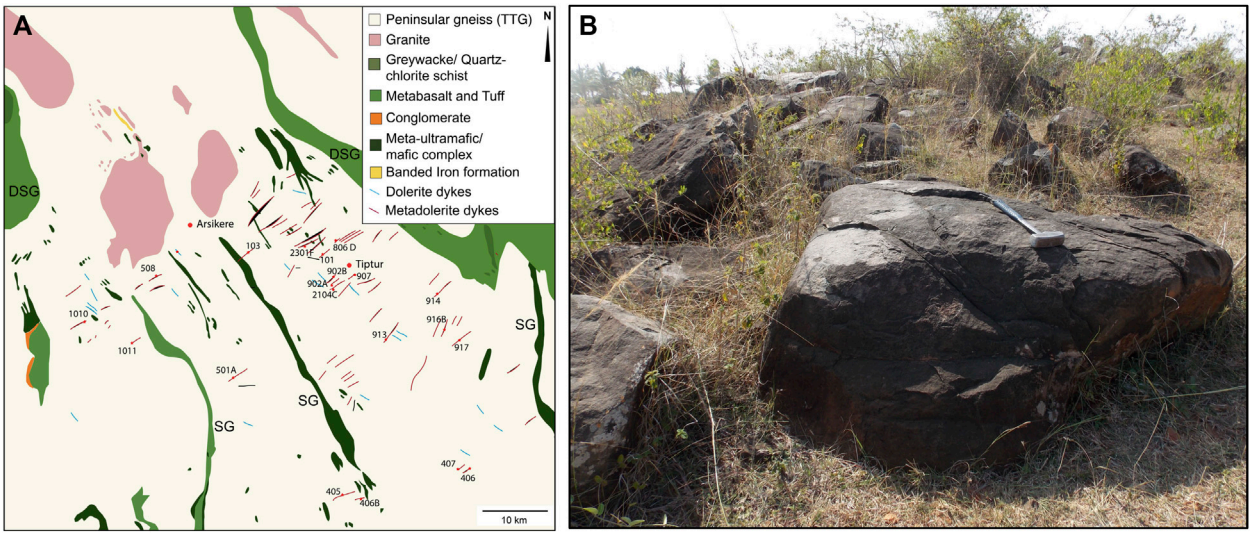

FIGURE 2
(A) Simplified geologic map of Tiptur area showing the distribution of dykes (modified from Geological Survey of India quadrangle map, 1994) and sampling locations **(B)** typical field occurrence of a NE-SW trending metadolerite dykes as extended hill. SG, Sargur group; DSG, Dharwar supergroup.

basement gneisses and supracrustal rocks and are especially prominent in the Eastern Dharwar Craton (~2.37 to ~1.79 Ga) (Chatterjee and Bhattacharji, 2001; French and Heaman, 2010; Srivastava et al., 2014; Srivastava et al., 2015; Rai et al., 2019; Pandey and Paul, 2022, and the references therein). The Western Dharwar Craton on the other hand is characterized by the abundance of greenstone belts and ultramafic volcanics including komatiites (Jayananda et al., 2008; Patra et al., 2021; Ravindran et al., 2021 and the references therein) and coexisting mafic dykes. Such widespread volcanic activity succeeding large scale crust building activity has led to the development of heterogeneous depleted mantle reservoirs beneath the Western Dharwar craton in the Mesoarchean (Jayananda et al., 2008; Jayananda et al., 2018; Jayananda et al., 2022). The formation and evolution of subcontinental lithospheric mantle during the Archean is complicated by the subduction of early formed oceanic crust and plume activities (Rudnick et al., 1998; Stern, 2005; Cawood et al., 2013; Jayananda et al., 2015; Bédard, 2018; Jayananda et al., 2018; Hawkesworth and Jaupart, 2021). The fact that the mantle temperatures were high during the Archean (Choukroune et al., 1995; Monteux et al., 2020), makes it much more difficult to understand the behavior of SCLM during Archean. The mafic dyke swarms in the Western Dharwar craton are also peculiar in that they occur as elongate hills with the surrounding rocks deeply eroded. Unmetamorphosed dolerite dykes (Rb-Sr errorchron age ~2.7 Ga; Silpa et al., 2021) have been reported from the Western Dharwar Craton along with older metamorphosed dykes showing remnants of igneous textures and mineralogy (Silpa and Satish-Kumar, 2018; Rai et al., 2019). Considering the dykes are typically the remnants of large-scale volcanism (Halls et al., 2000; Ernst and Buchan, 2001; Halls et al., 2007) the metamorphosed dykes are thought to be the feeders of the widespread greenstone volcanism in Western Dharwar Craton (WDC). These older dykes restricted to WDC, termed as metadolerite dykes (Silpa and Satish-Kumar, 2018) are considered in the present study. We report their Sm-Nd isotopic compositions along with major, trace and rare earth element geochemistry to understand the mantle source characteristics and early evolution of Archean subcontinental lithospheric mantle (SCLM).

2 Geological background

The Dharwar craton (DC) of southern India is one of the oldest and well-preserved cratonic blocks in India and is traditionally divided into two major units based on the crustal thickness, age, and lithological characteristics as Western Dharwar Craton (WDC) and Eastern Dharwar Craton (EDC) (Jayananda et al., 2000; Gupta et al., 2003; Ramakrishnan and Vaidyanathan, 2008). The shear zone to the east of Chitradurga Greenstone belt is considered the boundary between these two blocks (Jayananda et al., 2006). Recent studies divide the craton into three blocks (Western, Central and Eastern blocks) based on the age, thermal and accretionary histories, separated by major shear zones (Peucat et al., 2013; Jayananda et al., 2018; Jayananda et al., 2020). Similar to other Archean cratons of the world, Dharwar craton is predominantly composed of tonalite-trondhjemite-granodiorite (TTG) type gneisses, volcano-sedimentary greenstone belts and calc-alkaline to potassic granitoid rocks (Peucat et al., 2013; Jayananda et al., 2018; Swami Nath and Ramakrishnan, 1981 and the references therein). The western block is regarded as the oldest part of the craton and consists of TTG type gneisses known as Peninsular gneiss (c. 3.4–3.2 Ga), two generations of greenstone belts: older

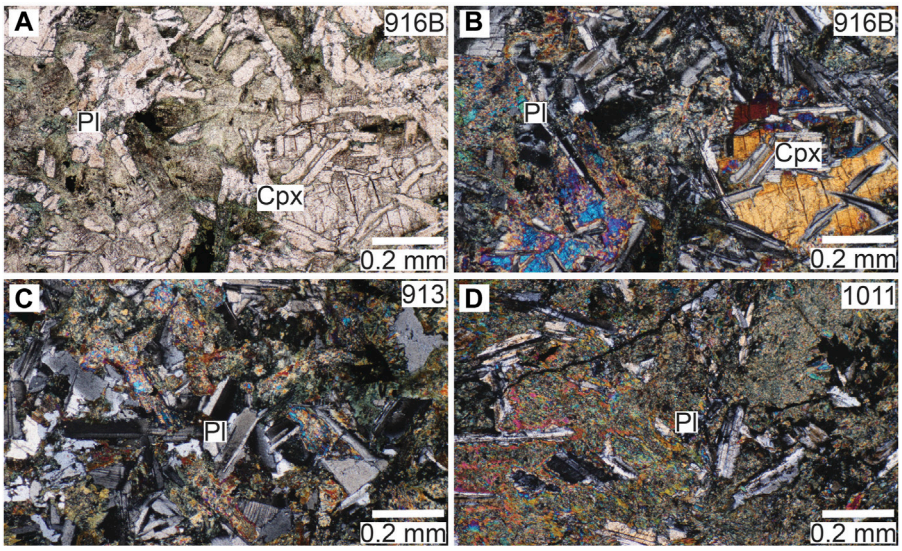

FIGURE 3
Photomicrographs of metadolerite dykes showing **(A)** remnant igneous textures, chief minerals **(B)** clinopyroxene **(C)** plagioclase and **(D)** amphibole. Detailed descriptions are given in the text.

c. 3.35–3.10 Ga Sargur Group and younger c. 2.9–2.6 Ga Dharwar Supergroup and high potassic plutons (Swami Nath and Ramakrishnan, 1981; Jayananda et al., 2008; Ramakrishnan and Vaidyanathan, 2008; Mukherjee et al., 2012; Jayananda et al., 2015). The central block consists of older TTGs (c. 3.23–2.96 Ga) along with younger transitional TTGs (c. 2.7–2.6 Ga), linear greenstone belts and calc-alkaline granitoids. In contrast to these two blocks, the eastern block is composed of younger transitional TTGs (c. 2.7–2.5 Ga) and thin belts of greenstone sequences along with calc-alkaline plutons (Jayananda et al., 2000; Dey et al., 2012; Jayananda et al., 2018).

The entire craton is profusely intruded by Archean to early Proterozoic mafic dyke swarms (Figure 1). Distinct mafic magmatic events between ~2.37 and ~1.79 Ga are recognized especially in the Eastern Dharwar Craton and are well defined by several researchers and are related to the presence of ancient LIPs. They include the most widespread ~2.37 Ga giant radiating Bangalore dyke swarm, globally correlated 2.22 Ga dyke swarm, 450 km long N-S trending 2.21 Ga Andhra-Karnataka Long Dyke (AKLD), and the 1.79 Ga Pebbair swarm (Chatterjee and Bhattacharji, 2001; Halls et al., 2007; French et al., 2008; French and Heaman, 2010; Kumar et al., 2012a; Kumar et al., 2012b; Belica et al., 2014; Srivastava et al., 2014; Srivastava et al., 2015; Nagaraju et al., 2018a; Nagaraju et al., 2018b; Rai et al., 2019; Söderlund et al., 2019; Pandey and Paul, 2022, and the references therein). Only limited data are available for the mafic dyke swarms in the Western Dharwar Craton. Previous researchers recognized three main dyke swarms in the WDC, concentrated towards the southern part of the craton (Murthy et al., 1987; Radhakrishna and Joseph, 1993; Meert and Pandit, 2015). However, recent studies on the mafic dyke swarms of WDC reported dykes that are exclusive to the Western Dharwar Craton along with younger generations of dykes that are geochemically coherent to the ~2.37 Ga dykes of the EDC (Silpa and Satish-Kumar, 2018; Rai et al., 2019; Yadav et al., 2020; Silpa et al., 2021; Silpa et al., 2021; Pandey and Paul., 2022). Unmetamorphosed dykes that preserve pristine igneous textures and mineralogy including ~2.7 Ga (Rb-Sr errorchron age) olivine dolerite dykes (Silpa et al., 2021a; Silpa et al., 2021b.) and older metamorphosed dykes with remnants of igneous textures and mineralogy are recognized in the Western Dharwar Craton (Silpa and Satish-Kumar, 2018; Rai et al., 2019).

Mafic dykes are abundantly distributed in the southern part of the Western Dharwar Craton in the major swarm called Tiptur swarm. The dykes can be generally classified as younger dolerite dykes that are mostly trending in NW-SE direction and the older NE-SW trending metadolerite dykes (Silpa and Satish-Kumar, 2018). This study focuses on the metadolerite dykes (Figure 2A) that are predominantly NE-SW in orientation. They normally occur as boulders or continuous hillocks (Figure 2B) extending a few meters to hundreds of meters in length. They rarely preserve any chilled margin and cross cutting relationship with the surrounding rocks owing to its prolonged exposure. In hand specimen the dykes are slightly greenish in color, lack visible plagioclase laths. In contrast the younger dolerite dykes have observable laths and are dark black in color and in places preserve contact relations with country rocks.

3 Materials and methods

Multiple samples were collected from 21 representative metadolerite dyke locations and petrographic thin sections were prepared. For geochemical analysis, thin slabs were cut, cleaned, and pulverized in an agate ball mill. The major elements and selected trace element concentrations were measured by using the X-ray Fluorescence Spectrometer (XRF) facility (Rigaku RIX 3000). Trace and rare earth elements were analyzed using the Inductively Coupled Plasma Mass Spectrometer (Agilent 7500a) facility

TABLE 1 The whole rock major oxides, trace and rare-earth element geochemical compositions of the studied metadolerite dykes from the Tiptur area, Western Dharwar Craton, southern India.

	Group 1						
Sample no.	806D	907	916	101	103	1010	1011
Major element geochemistry							
SiO_2	50.06	50.09	50.78	49.81	50.12	50.02	50.04
TiO_2	1.09	0.99	0.99	1.11	1.01	1.09	1.07
Al_2O_3	15.90	15.53	15.00	15.43	15.42	14.75	15.58
FeO*	11.55	11.49	11.71	12.10	11.28	12.40	11.25
MnO	0.21	0.20	0.21	0.21	0.19	0.20	0.19
MgO	7.51	8.03	7.93	8.00	8.32	7.89	8.18
CaO	11.37	11.62	11.32	11.18	11.51	11.30	11.64
Na_2O	2.07	1.85	1.89	1.89	1.87	1.98	1.78
K_2O	0.18	0.14	0.11	0.21	0.22	0.30	0.20
P_2O_5	0.07	0.06	0.06	0.07	0.06	0.06	0.07
LOI	0.85	0.49	0.40	1.03	1.00	0.83	0.71
Total	100.85	100.49	100.40	101.03	101.00	100.83	100.71
Mg#	39	41	40	40	42	39	42
Trace and rare earth element geochemistry							
Li	9.0	5.2	3.1	5.1	5.4		13.7
B		2			1		1
Sc	38.9	35.0	37.3	42.4	37.2		38.6
V	293	271	293	320	284		299
Cr	187	264	268	249	240		315
Co	54	54	57	63	59		61
Cu	111	95	125	95	142		110
Zn	113	95	103	119	83		94
Ga	16.37	16.67	16.84	18.99	16.91		18.15
Ge	1.4	1.8	1.8	2.4	1.8		2.2
Rb	3.5	4.0	8.0	4.4	5.1		2.0
Sr	112.9	108.8	95.9	98.2	107.1		114.5
Y	21	21	23	23	21		22
Zr	56.8	50.0	52.7	61.2	52.3		57.2
Nb	3.14	2.87	2.74	2.30	3.05		3.07
Cd	0.14	0.33	0.38	0.29	0.35		0.25
Cs	0.016	0.219	0.712	0.044	0.130		0.039
Ba	30	20	25	29	14		25
La	3.34	3.32	3.32	3.50	3.01		3.79
Ce	9.16	8.69	8.56	9.35	8.10		9.56
Pr	1.42	1.38	1.39	1.51	1.32		1.51
Nd	6.9	7.1	7.2	8.1	6.8		7.7
Sm	2.28	2.15	2.42	2.44	2.17		2.47
Eu	0.891	0.821	0.885	0.874	0.825		0.904
Gd	2.79	2.87	3.09	3.10	3.00		3.17
Tb	0.54	0.53	0.57	0.60	0.51		0.57
Dy	3.35	3.03	3.37	3.42	3.15		3.39
Ho	0.714	0.757	0.812	0.839	0.746		0.773
Er	2.06	2.14	2.57	2.59	2.31		2.40
Tm	0.35	0.33	0.36	0.36	0.32		0.33
Yb	1.87	1.81	2.07	1.95	1.78		1.78
Lu	0.306	0.311	0.373	0.371	0.315		0.317
Hf	1.6	1.3	1.4	1.5	1.3		1.5
Ta	0.183	0.175	0.178	0.191	0.157		0.198
W	12.7	10.9	14.3	9.9	9.7		11.0
Pb	2	1	1	2	2		1
Th	0.33	0.24	0.24	0.28	0.23		0.25
U	0.101	0.075	0.077	0.058	0.058		0.062

(Continued on following page)

TABLE 1 (*Continued*) The whole rock major oxides, trace and rare-earth element geochemical compositions of the studied metadolerite dykes from the Tiptur area, Western Dharwar Craton, southern India.

	Group 1						
Sample no.	806D	907	916	101	103	1010	1011
Ratios used for discrimination diagrams							
Nb/Yb	1.68	1.58	1.33	1.18	1.72		1.72
Th/Yb	0.18	0.13	0.12	0.14	0.13		0.14
Zr/Yb	30.41	27.61	25.51	31.31	29.47		32.09
TiO_2/Yb	0.58	0.55	0.48	0.57	0.57		0.60
Zr/Y	2.64	2.43	2.33	2.63	2.51		2.59
(La/Lu) N	1.17	1.15	0.95	1.01	1.02		1.28
Nb/Y	0.15	0.14	0.12	0.10	0.15		0.14
Th/Nb	0.09	0.09	0.06	0.07	0.06		0.06
(La/Sm) N	1.46	1.55	1.37	1.43	1.38		1.54
(Sm) N	2.28	2.15	2.42	2.44	2.17		2.47
Zr/Nb	18.07	17.42	19.23	26.57	17.16		18.65
Nb/Th	9.60	11.78	11.22	8.35	13.37		12.15

	Group 2				
Sample no.	914	902B	902A	917	913
Major element geochemistry					
SiO_2	52.90	50.98	51.14	53.26	53.61
TiO_2	1.36	1.72	1.59	1.25	0.71
Al_2O_3	13.73	14.05	14.40	14.16	14.37
FeO*	13.02	13.93	13.08	11.93	11.07
MnO	0.20	0.23	0.23	0.19	0.20
MgO	5.81	5.88	6.20	6.32	6.78
CaO	10.30	10.54	10.65	10.43	10.99
Na_2O	2.24	2.31	2.38	2.08	1.84
K_2O	0.33	0.25	0.23	0.30	0.32
P_2O_5	0.10	0.12	0.11	0.09	0.11
LOI	0.93	0.59	0.57	0.91	0.48
Total	100.93	100.59	100.57	100.91	100.48
Mg#	31	30	32	35	38
Trace and rare earth element geochemistry					
Li	7.6	7.2	13.0	4.3	8.6
B	2	4	117	0	2
Sc	30.8	39.7	35.8	31.0	41.1
V	350	379	367	304	229
Cr	19	138	162	65	81
Co	59	50	63	46	50
Cu	68	121	131	38	80
Zn	102	136	145	98	85
Ga	21.33	19.54	17.80	20.47	13.70
Ge	2.3	2.1	1.7	2.2	1.6
Rb	2.6	5.5	5.3	5.7	5.9
Sr	195.1	112.9	119.8	174.1	110.3
Y	26	36	31	27	26
Zr	88.2	103.1	70.3	78.8	73.8
Nb	3.93	6.41	5.38	3.75	4.39
Cd	0.50	0.25	0.25	0.34	0.26
Cs	0.034	0.064	0.015	0.069	0.197
Ba	30	36	34	43	84
La	6.91	7.06	5.62	9.61	11.91
Ce	16.64	18.47	14.91	13.71	24.07
Pr	2.43	2.90	2.34	3.05	3.36
Nd	11.8	14.5	11.4	14.6	14.1

(Continued on following page)

TABLE 1 (*Continued*) The whole rock major oxides, trace and rare-earth element geochemical compositions of the studied metadolerite dykes from the Tiptur area, Western Dharwar Craton, southern India.

Group 2					
Sample no.	914	902B	902A	917	913
Sm	3.53	4.11	3.71	4.21	3.17
Eu	1.282	1.422	1.205	1.408	0.840
Gd	4.23	5.21	4.64	4.67	3.32
Tb	0.77	0.95	0.76	0.81	0.58
Dy	4.30	5.36	4.68	4.39	3.57
Ho	0.966	1.297	1.080	0.941	0.845
Er	2.72	3.66	3.01	2.85	2.86
Tm	0.36	0.55	0.51	0.36	0.41
Yb	1.98	3.06	3.02	1.91	2.47
Lu	0.334	0.495	0.418	0.330	0.443
Hf	2.2	2.6	1.7	2.0	1.7
Ta	0.258	0.395	0.326	0.228	0.262
W	10.0	11.7	12.7	7.5	10.4
Pb	3	2	3	2	2
Th	0.96	0.54	0.44	0.84	1.23
U	0.228	0.132	0.139	0.155	0.253
Ratios used for discrimination diagrams					
Nb/Yb	1.98	2.09	1.78	1.96	1.78
Th/Yb	0.49	0.18	0.15	0.44	0.50
Zr/Yb	44.49	33.70	23.28	38.65	30.94
TiO_2/Yb	0.69	0.56	0.52	0.65	0.29
Zr/Y	3.34	2.88	2.24	2.77	2.91
(La/Lu) N	2.22	1.53	1.44	3.12	2.88
Nb/Y	0.15	0.18	0.17	0.14	0.17
Th/Nb	0.17	0.09	0.07	0.18	0.23
(La/Sm) N	1.96	1.72	1.51	2.28	3.75
(Sm) N	3.53	4.11	3.71	4.21	3.17
Zr/Nb	22.43	16.09	13.06	19.69	17.37
Nb/Th	4.09	11.89	12.23	4.44	3.58

Group 3									
Sample no.	405	406B	407	406	2502	501A	2301F	2104C	508
Major element geochemistry									
SiO_2	50.44	50.99	51.49	50.24	52.10	50.07	52.55	54.58	50.07
TiO_2	1.15	0.49	1.21	1.00	2.09	1.11	1.05	0.95	1.09
Al_2O_3	14.93	10.78	14.78	15.40	13.27	15.39	13.71	14.87	15.49
FeO*	12.76	11.02	11.97	11.68	15.28	11.67	12.30	10.77	11.80
MnO	0.21	0.19	0.23	0.20	0.24	0.20	0.20	0.18	0.20
MgO	6.98	15.02	6.84	7.64	4.41	7.67	6.59	5.03	7.60
CaO	11.01	9.42	11.21	11.68	8.67	11.52	11.42	9.14	11.44
Na_2O	2.20	1.64	1.94	1.93	2.56	2.04	1.78	3.79	1.96
K_2O	0.23	0.38	0.25	0.16	1.10	0.26	0.32	0.59	0.27
P_2O_5	0.08	0.07	0.09	0.07	0.28	0.08	0.08	0.09	0.08
LOI	1.01	0.84	1.47	0.59	0.86	0.78	1.62	1.13	0.88
Total	101.01	100.84	101.47	100.59	100.86	100.78	101.62	101.13	100.88
Mg#	35	58	36	40	22	40	35	32	39

(Continued on following page)

TABLE 1 (*Continued*) The whole rock major oxides, trace and rare-earth element geochemical compositions of the studied metadolerite dykes from the Tiptur area, Western Dharwar Craton, southern India.

Group 3									
Sample no.	405	406B	407	406	2502	501A	2301F	2104C	508
Trace and rare earth element geochemistry									
Li	15.1	7.0	8.6	22.6	10.8	11.0	4.2	9.6	13.3
B	4	7	9	3	19	−11	−7	8	42
Sc	33.9	27.3	37.0	34.3	33.5	39.2	36.0	38.0	32.0
V	281	280	341	325	354	320	320	282	313
Cr	172	221	164	219	406	295	261	326	223
Co	46	54	51	62	66	59	59	61	59
Cu	118	144	168	126	109	144	151	143	121
Zn	90	87	104	108	97	104	100	103	88
Ga	15.25	15.21	16.94	16.45	17.65	17.07	16.88	15.71	16.60
Ge	1.6	1.6	1.9	1.8	2.0	1.9	1.8	1.5	1.8
Rb	3.1	3.6	2.7	3.9	5.4	2.8	2.0	5.1	2.5
Sr	84.2	91.9	80.1	91.6	130.5	114.6	98.3	93.0	109.2
Y	25	22	30	27	21	23	22	19	23
Zr	36.8	42.9	26.6	37.5	42.3	44.7	45.5	42.5	44.5
Nb	2.83	2.36	3.09	3.44	2.66	3.05	2.69	2.58	2.81
Cd	0.07	0.11	0.07	0.16	0.10	0.31	0.15	0.17	0.05
Cs	0.066	0.070	0.036	0.020	0.034	0.053	0.027	0.072	0.105
Ba	23	18	18	30	20	36	19	31	22
La	3.37	2.79	4.11	3.73	4.49	3.12	2.97	2.87	3.09
Ce	8.75	7.53	9.70	9.96	10.95	8.51	7.94	7.58	7.78
Pr	1.41	1.26	1.67	1.64	1.62	1.44	1.28	1.21	1.28
Nd	6.8	6.3	8.6	8.3	7.8	7.0	6.6	6.0	6.7
Sm	2.26	2.29	3.09	2.88	2.83	2.40	2.33	2.00	2.42
Eu	0.816	0.814	0.973	0.962	0.862	0.831	0.793	0.686	0.822
Gd	3.39	2.86	4.09	3.69	3.53	3.36	3.13	2.70	3.34
Tb	0.56	0.50	0.66	0.64	0.56	0.56	0.52	0.48	0.55
Dy	3.66	3.24	4.47	4.15	3.30	3.30	3.17	2.80	3.26
Ho	0.858	0.734	1.016	0.954	0.709	0.752	0.725	0.654	0.774
Er	2.36	2.23	2.87	2.71	1.90	2.11	2.01	1.83	2.17
Tm	0.39	0.34	0.44	0.43	0.27	0.32	0.33	0.28	0.36
Yb	2.45	2.07	2.60	2.51	1.69	2.03	1.96	1.74	2.02
Lu	0.375	0.313	0.417	0.408	0.224	0.274	0.286	0.238	0.301
Hf	1.0	1.2	0.8	1.1	1.2	1.2	1.2	1.1	1.2
Ta	0.204	0.136	0.202	0.236	0.137	0.202	0.154	0.138	0.191
W	11.2	18.3	12.0	17.5	19.3	18.8	18.2	35.9	11.8
Pb	2	1	2	3	2	12	2	2	2
Th	0.32	0.23	0.30	0.29	0.62	0.23	0.20	0.21	0.23

(Continued on following page)

TABLE 1 (*Continued*) The whole rock major oxides, trace and rare-earth element geochemical compositions of the studied metadolerite dykes from the Tiptur area, Western Dharwar Craton, southern India.

Group 3									
Sample no.	405	406B	407	406	2502	501A	2301F	2104C	508
U	0.073	0.056	0.085	0.088	0.138	0.069	0.063	0.055	0.054
Ratios used for discrimination diagrams									
Nb/Yb	1.19	1.15	1.14	1.37	1.57	1.50	1.37	1.48	1.39
Th/Yb	0.12	0.13	0.11	0.12	0.36	0.11	0.10	0.12	0.11
Zr/Yb	10.24	14.98	20.69	14.94	25.00	21.98	23.17	24.35	21.98
TiO_2/Yb	0.47	0.47	0.24	0.40	1.24	0.54	0.53	0.55	0.54
Zr/Y	0.88	1.50	1.97	1.39	2.02	1.93	2.07	2.18	1.94
(La/Lu) N	0.96	0.95	1.06	0.98	2.15	1.22	1.11	1.29	1.10
Nb/Y	0.10	0.11	0.11	0.13	0.13	0.13	0.12	0.13	0.12
Th/Nb	0.08	0.06	0.10	0.07	0.16	0.06	0.06	0.07	0.05
(La/Sm) N	1.33	1.49	1.22	1.30	1.58	1.30	1.27	1.43	1.27
(Sm) N	3.09	2.26	2.29	2.88	2.83	2.40	2.33	2.00	2.42
Zr/Nb	8.59	13.01	18.18	10.91	15.89	14.65	16.87	16.46	15.80
Nb/Th	10.21	8.80	10.38	11.81	4.31	13.08	13.69	12.49	12.25

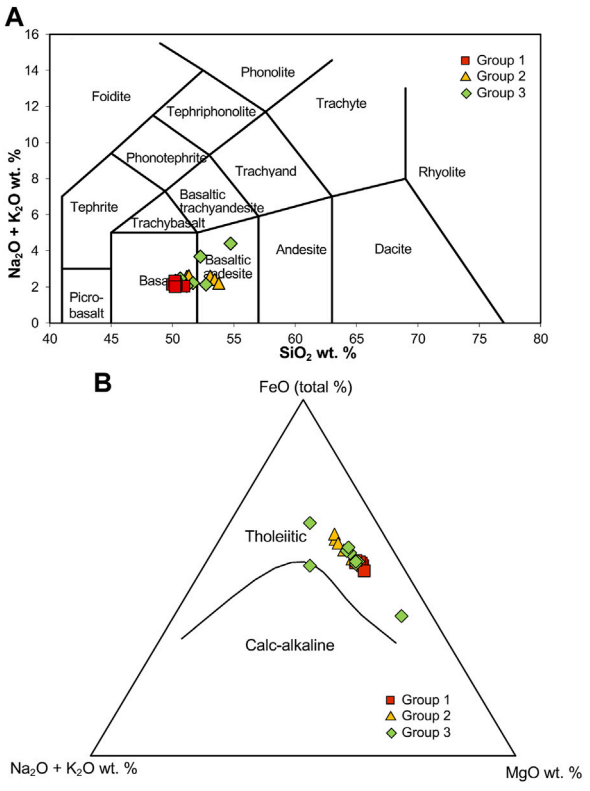

FIGURE 4
(A) Total Alkali versus Silica (TAS) diagram (after Le Maitre, 2002) showing the general classification of dykes as basalt to basaltic andesite in composition and **(B)** tholeiitic in the AFM (alkali, Fe, and Mg oxides) ternary diagram (after Irvine and Baragar, 1971).

housed at the Department of Geology, Faculty of Science, Niigata University.

Glass beads were prepared from the powdered samples for whole rock geochemical analysis using XRF. The powdered samples were dried in a muffle furnace for 6 hours at > 900°C to calculate the Loss on Ignition (LOI) of the samples. The dried sample powders were then mixed with anhydrous lithium tetraborate (LiB_4O_7) and lithium metaborate ($LiBO_2$) flux (2:1 ratio). The mixture was fused into a glass bead in a platinum crucible. The geochemical compositions were measured using the prepared glass beads with JB-1b (basalt) as the standard. The detailed analytical procedure is given in Takahashi and Shuto (1997). For ICP-MS analysis, sample preparation used the acid digestion method of Yokoyama et al., 1999. Sample powder weighing 0.1 g was taken in a Teflon vial and completely dissolved by adding hydrofluoric acid (HF), nitric acid (HNO_3), and perchloric acid ($HClO_4$) in step with heating and evaporating in a fume hood. The sample was then diluted with HNO_3, and trace and rare earth element concentrations measured by ICP-MS following the analytical procedure of Senda et al. (2014). Internal standards were ^{115}In, ^{185}Re and ^{209}Bi, the USGS standards BHVO2 and W-2a were used for drift correction and calibration and the external standard used was JB-2 (basalt).

The Rb-Sr and Sm-Nd isotope measurements employed cation exchange chromatography with a two-step column separation technique (Hamamoto et al., 2000; Takahashi et al., 2009). The sample preparation procedure was carried out in a clean room facility (class 100 laminar flow hood and class 10,000 clean room) at the Faculty of Science, Niigata University to prevent any contamination. Initial sample digestion was done by adding hydrofluoric acid (HF), nitric acid (HNO_3), and hydrochloric acid (HCl). Sr and the REE

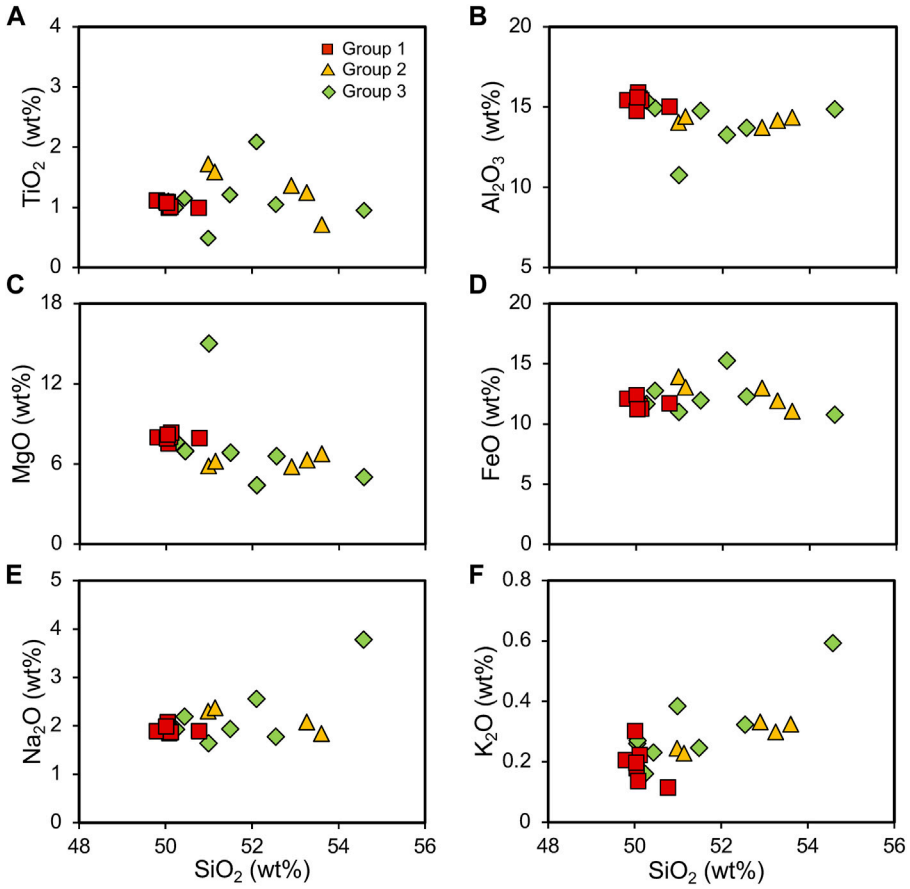

FIGURE 5
The Harker variation diagrams of SiO_2 versus the major oxides, **(A)** TiO_2, **(B)** Al_2O_3, **(C)** MgO, **(D)** FeO, **(E)** Na_2O and **(F)** K_2O for the metadolerite dykes. Group 1 is mostly clustered whereas groups 2 and 3 are showing variations in their distribution.

were separated using AG50W-X8 resin during the first column separation. The separation and purification of Sr and Nd were done using a second column. In the second column separation for Sr, Sr spec. resin was used, and Nd separated from the other REE by ion-exchange chromatographic technique, using α-hydroxy isobutyric acid (HIBA) as the eluent. Purified Sr was loaded on a degassed rhenium filament with Ta activator on either side of Sr. The isotope ratios were measured using Thermal Ionization Mass Spectrometer (TIMS) MAT 262. Subsequently, the purified Nd was loaded onto the filament and measured by TIMS. NIIST 987 was used as the standard for Sr measurements and the mean ratio was 0.710,221 ± 0.00002 (SD, n = 11). The standard used for Nd was JNdi-1 which gave a mean ratio of 0.512,046 ± 0.000025 (SD, n = 8).

4 Results

4.1 Petrography

The dykes in the current study are chiefly composed of plagioclase, clinopyroxene and amphibole along with opaque phases. Even though the medium to fine-grained plagioclase shows varying degrees of alteration, lath shapes are distinguishable (Figures 3A–D) and show remnant ophitic textures. Clinopyroxene is mostly subhedral to anhedral, medium to coarse-grained and locally altered along the grain boundaries (Figures 3A, B). Amphibole exhibit a light green color under plane polarized light and long slender needles of hornblende are commonly observed (Figure 3A). Minor biotite and chlorite were observed in a few thin sections. The opaque minerals are mostly pyrrhotite, pyrite and chalcopyrite (Silpa and Satish-Kumar, 2022). Despite low-temperature metamorphism, remnants of the original mineralogy and original igneous textures (eg., ophitic texture; Figures 3C, D) are well preserved and hence we termed these rocks metadolerites.

4.2 Geochemistry

The whole rock geochemical compositions (see Table 1) of metadolerite dykes from the Tiptur area show an SiO_2 content varying between 49.8 and 54.57 wt%, indicating their general mafic nature. In the Total Alkali versus Silica (TAS) diagram (Figure 4A; Le Maitre, 2002) most samples fall in sub-alkaline field. They range in composition from basalt to basaltic andesite and are mostly

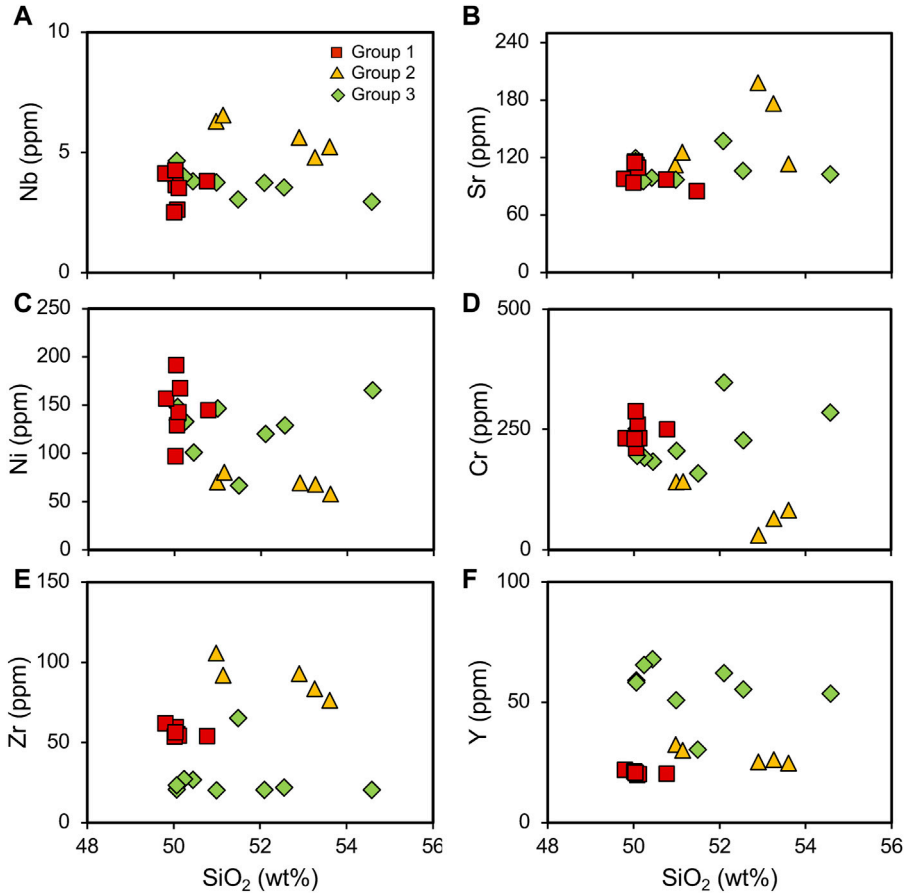

FIGURE 6
Binary geochemical variation diagrams of SiO_2 versus **(A)** Nb, **(B)** Sr, **(C)** Ni, **(D)** Cr, **(E)** Zr, and **(F)** Y. The three groups are showing distinct trends.

tholeiitic (Figure 4B; Irvine and Baragar, 1971). Major, trace, and rare earth element distributions of the studied dykes indicate the presence of three different groups, hereafter referred as group 1, 2, and 3.

The SiO_2 content ranges from 49.8 to 50.77 wt%, for group one dykes, 50.98 to 53.6 wt% for group two dykes and 50.06 to 54.57 wt% for group three dykes. The Mg# (MgO/(MgO+FeO) *100) are low and varies from 22 to 42 except for one sample showing a value of 57. Major oxides like Al_2O_3 have a concentration varying between 10.77 and 15.9 wt%. MgO content for group one varies from 7.51 to 8.32 wt%, group two from 5.81 to 6.77 wt% and group three from 4.41 to 15.02 wt%. FeO varies between 10.77 and 15.27 wt%, K_2O and Na_2O varies from 0.11 to 1.1 wt% and 0.18 to 0.23 wt% respectively. In the basic Harker-type discrimination diagrams, Group one samples are mostly clustered in their distribution (See Figures 5A–F). The SiO_2 versus the major oxides for group 2 samples show a slight negative correlation for MgO (Figure 5C) and groups 2 and 3 exhibit a positive correlation for K_2O (Figure 5F). Other major oxides like and TiO_2 (Figure 5A), Al_2O_3 (Figure 5B) and FeO (Figure 5D) doesn't show much variation in their distributions; group 1 is mostly clustered and group 2 and 3 show a linear trend.

Geochemical composition of key trace and rare earth elements are also presented in Table 1. Concentrations of compatible elements like Ni varies from 58 ppm to 191 ppm and Cr varies from 30 to 348 ppm. Large Ion Lithophile Elements (LILE) like Rb and Sr ranges between 3.8 and 11.3 and 84.7, and 198.5 ppm respectively. High Field Strength Elements (HFSE) Zr and Nb are showing concentrations from 20.2 to 105.7 ppm and 2.5 to 6.6 ppm respectively. La ranges from 2.78 to 11.91 ppm, Sm and Nd ranges from 2 to 4.2 ppm and 6.01–14.63 ppm respectively. Other key elements like Th, Y, and Lu show concentrations ranging from 19 to 67.78 ppm, 0.19–1.22 ppm and 0.22–0.49 ppm respectively.

Harker variation diagrams for SiO_2 versus trace elements appear in Figures 6A–F. A generally clustered pattern is observed for group 1 dykes except for Ni. Group 2 shows a slight positive correlation for Sr (Figure 6B), a negative correlation for Ni and Cr (Figures 6C, D) and the highest concentrations for Zr (Figure 6E). A slight positive trend can be identified for Ni and Cr for group 3 dykes, and they show a high Y. Binary plot of Mg# versus compatible and incompatible elements are shown in Figures 7A–D. Distinctly different patterns are observed for the three groups of dykes.

Primitive mantle and chondrite normalized (Sun and McDonough, 1989) multi-element spidergrams were constructed using the obtained rare earth element concentrations. A general depleted pattern with a very nominal LILE enrichment was observed in the primitive mantle normalized multi-element spider Gram

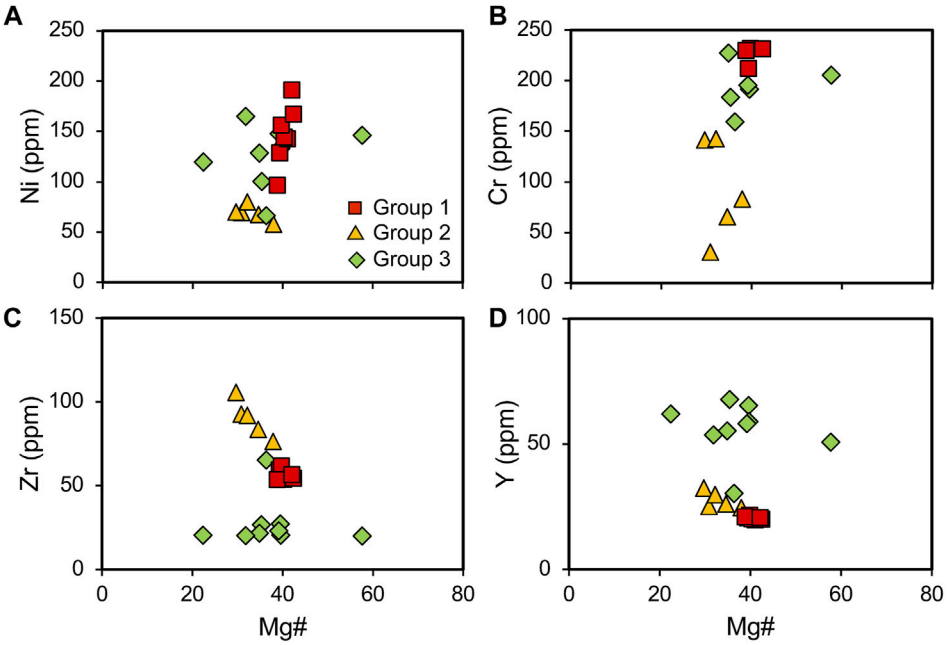

FIGURE 7
Bivariate plots of Mg# versus main trace elements **(A)** Ni, **(B)** Cr, **(C)** Zr and **(D)** Y. Similar to Figure 6, the three genetic groups can be identified.

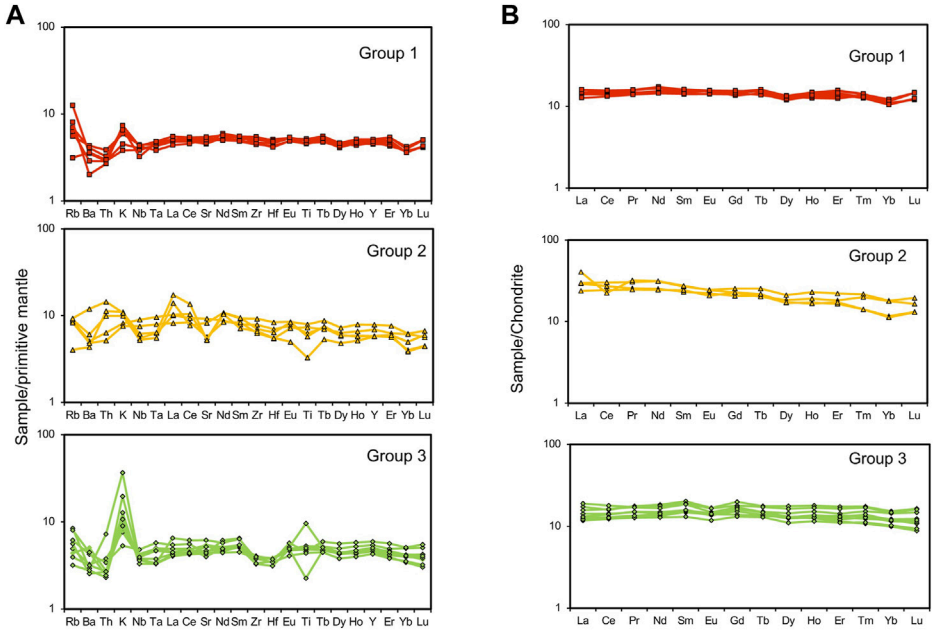

FIGURE 8
(A) The primitive mantle-normalized multi-element diagram of the metadolerite dykes. Group 1 dykes show a general depleted pattern with a very nominal LILE enrichment, a Sr and Ti negative anomalies and slight Nb negative anomaly are observed for group two dykes and group three exhibits a negative anomaly for Zr and Hf and slight Sr negative anomaly. **(B)** Chondrite-normalized rare earth element spidergram of three groups of metadolerite dykes showing distinct patterns. Normalizing values are from Sun and McDonough (1989).

(Figure 8A). Group one and two show a slight positive anomaly for K whereas a strong positive anomaly is observed for group three. Group two exhibits Sr and Ti negative anomalies and slight negative anomaly for Nb. Group three shows a negative anomaly for Zr and Hf and slight Sr negative anomaly. In the chondrite normalized REE diagram (Figure 8B) a general flat pattern is observed for all the

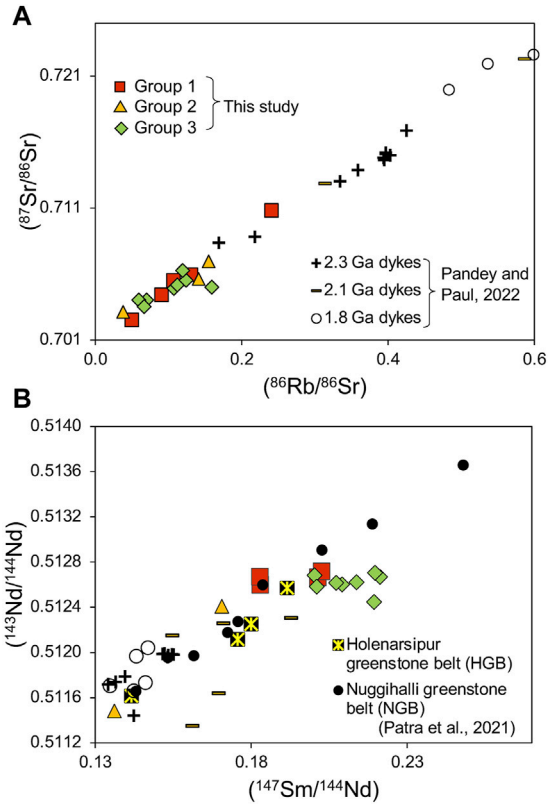

FIGURE 9
(A) Rb-Sr isotope evolution and **(B)** Sm-Nd isotope evolution diagrams for the studied metadolerites. The samples from the present study are compared with younger dykes (sample details are in Pandey and Paul. (2022)) and ca. 2.9 Ga intrusive mafic-ultramafic rocks from Nuggihalli greenstone belt (NGB) and Holenarsipur greenstone belt (HGB) (Patra et al., 2021) of Western Dharwar craton.

dykes. Group two dykes show a slight enrichment of LREE whereas a flat LREE and a slight negative Eu anomaly is shown by group 3 dykes.

4.3 Sr-Nd isotope geochemistry

Sr and Nd isotopic ratios are plotted in Figures 9A, B with data in Table 2. The measured $^{87}Sr/^{86}Sr$ isotope ratio varies from 0.70251 to 0.71080. For further calculations, the $^{87}Rb/^{86}Sr$ value of CHUR is taken as 0.0839 and the present $^{87}Sr/^{86}Sr$ ratio of the reservoir is taken as 0.7045 (DePaolo and Wasserburg, 1976) and the age is tentatively fixed as 2,900 Ma. The initial $^{87}Sr/^{86}Sr$ ratios calculated for 2,900 Ma varies between 0.70041 and 0.70102, for group one dykes, 0.70045 to 0.70154 for group two dykes, and 0.70041 to 0.70153 for group three dykes. Group one dykes show a good Rb-Sr isochron relationship and an errorchron age of ca. 3,003 ± 102 Ma. Measured $^{143}Nd/^{144}Nd$ ratios vary from 0.51148 to 0.512,719. The $^{147}Sm/^{144}Nd$ of CHUR is taken as 0.1967 and $^{143}Nd/^{14}4Nd$ of CHUR at present is taken as 0.51238 (DePaolo and Wasserburg, 1976) and the initial $^{143}Nd/^{144}Nd$ ratio varies from 0.508,245 to 0.509,172 for the age of 2,900 Ma. The epsilon Nd values are mostly negative, ranging between −12 and +5. Group one and two shows an epsilon Nd value ranging between −1 and +5 and 0.1 to +5 respectively and group three varies between −0.5 and −12.

5 Discussion

The dykes are weakly metamorphosed due to the overprinting of regional metamorphism at around 2.5 Ga in the Dharwar craton. However, low loss on ignition (LOI) values around 1wt% and preservation of primary igneous minerals and textures support minimal post magmatic alteration. Group 1 dykes are tholeiitic basalts whereas group two and three are basaltic to basaltic andesite in nature (Figure 4A). The petrography as well as the geochemical characteristics indicate that the three groups are not co-genetic and thus probably derived from different mantle sources.

5.1 Petrogenesis

The major oxides in the Harker variation diagram (Figure 5) do not show any significant variations for group one indicating the derivation from the same source. Groups two and three exhibit wide distribution for SiO_2. Indicating progressive partial melting of the source. This combined with trace element concentrations (Figures 6, 7) suggest the derivation of the three groups of dykes from distinct source mantle characteristics. The rare earth element concentrations with respect to primitive mantle for group one and threr suggest the derivation from a depleted source (Figure 8). On the other hand, group two has negative anomalies for Nb, Ta, Sr, and Ti and an enrichment of LREE in the chondrite normalized pattern suggesting the derivation from a slightly enriched source. In the case of group three, the trace and rare earth element concentrations indicate a depleted source and the negative anomalies for Zr, Hf indicative of a higher degree of melting of the source mantle. The positive K anomaly on the other hand is probably due to crustal contamination or the source modification by recycling of subducted crust. Th and Nb are useful in understanding crustal contamination and/or assimilation the presence of crustal input by subduction. Th and Nb are also immobile during lower grade metamorphism (Pearce, 2008) and are ideal proxies for the weakly metamorphosed dykes in the current study. Ti-Yb on the other hand is a proxy for melting depth (Pearce, 2008). Incompatible element (Th/Yb vs. Nb/Yb) ratio diagram is constructed (Figure 10A) on which crustal input proxy (Th/Nb) follows a diagonal trend as marked (Pearce et al., 2021). Most of the studied dykes falls in MORB-OPB-OIB array. Group one is mostly concentrated between MORB and OPB, probably indicating a primary mantle source. Groups two and three plot close to MORB and extend towards IAB array. A few of the samples that plot between OPB and CAB suggest the modification of mantle derived source due to interaction with crustal components. This could be evidence of crustal contamination or a signature of a subducted crustal input in the source. However, in the Zr/Yb-Nb/Yb ratio diagram group two dykes translate to an enriched source and fall within the

10.3389/feart.2023.1153003

TABLE 2 Rb-Sr and Sm-Nd isotopic data of metadolerite dykes from the Tiptur area, Western Dharwar craton.

	Sample no.	Rb(ppm)	Sr(ppm)	$^{87}Rb/^{86}Sr$	$(^{87}Sr/^{86}Sr)0$ Ma	$(^{87}Sr/^{86}Sr)TMa$
Group 1	806D	3.54	112.89	0.0907	0.704412	0.700601
	907	4.03	108.85	0.1070	0.705521	0.701024
	916	7.98	95.87	0.2409	0.710808	0.700680
	101	4.44	98.23	0.1307	0.705953	0.700458
	1011	1.99	114.45	0.0502	0.702519	0.700410
Group 2	914	2.57	195.14	0.0381	0.703144	0.701542
	902B	5.52	112.86	0.1414	0.706538	0.700593
	913	5.91	110.30	0.1550	0.706968	0.700451
Group 3	405	3.13	84.16	0.1075	0.704928	0.700410
	406B	3.57	91.91	0.1123	0.705175	0.700454
	406	3.93	91.60	0.1240	0.705531	0.700316
	2502	5.38	130.50	0.1192	0.706273	0.701261
	501A	2.78	114.58	0.0702	0.704036	0.701085
	2301F	2.02	98.33	0.0594	0.704036	0.701537
	2104C	5.12	93.04	0.1592	0.705025	0.698333
	508	2.51	109.16	0.0666	0.703547	0.700747

Sample no.	Sm (ppm)	Nd (ppm)	$^{147}Sm/^{144}Nd$	$(^{143}Nd/^{144}Nd)$ 0 Ma	$(^{143}Nd/^{144}Nd)TMa$	εNd tMa
806D	2.28	6.85	0.2014	0.512666	0.508810	−1.2
907	2.15	7.10	0.1829	0.512601	0.509100	4.4
916	2.42	7.21	0.2026	0.512720	0.508841	−0.6
101	2.44	8.07	0.1828	0.512672	0.509172	5.9
1011						
914						
902B	4.11	14.54	0.1707	0.512408	0.509141	5.2
913	3.17	14.07	0.1362	0.511484	0.508877	0.1
405	2.26	6.82	0.2004	0.512683	0.508846	−0.5
406B	2.29	6.25	0.2213	0.512669	0.508431	−8.7
406	2.88	8.31	0.2092	0.512601	0.508597	−5.4
2502	2.83	7.79	0.2194	0.512447	0.508245	−12.4
501A	2.40	6.99	0.2073	0.512616	0.508647	−4.5
2301F	2.33	6.59	0.2139	0.512623	0.508528	−6.8
2104C	2.00	6.01	0.2010	0.512583	0.508733	−2.8
508	2.42	6.66	0.2197	0.512705	0.508497	−7.4

intra-oceanic arc and subduction zone enrichment area (Figure 10B). Group three on the other hand shows a wide distribution for Zr and minimal variation for Nb. According to Pearce and Peate (1995), when Zr and Nb are added to a homogenous mantle source from a subducting slab, such a vertical trend is observed. It is possible to assume that the trace element concentrations reflect the source mantle modification due to subduction rather than crustal contamination. Geochemical compositions are also affected by the depth and degree of melting of the source mantle. The tectonomagmatic discrimination diagram based on Ti-Yb and Nb-Yb (Pearce, 2008) are useful in understanding the magma genesis and evolution. In Figure 10C, all of the samples in groups one and three plot within the main OPB array

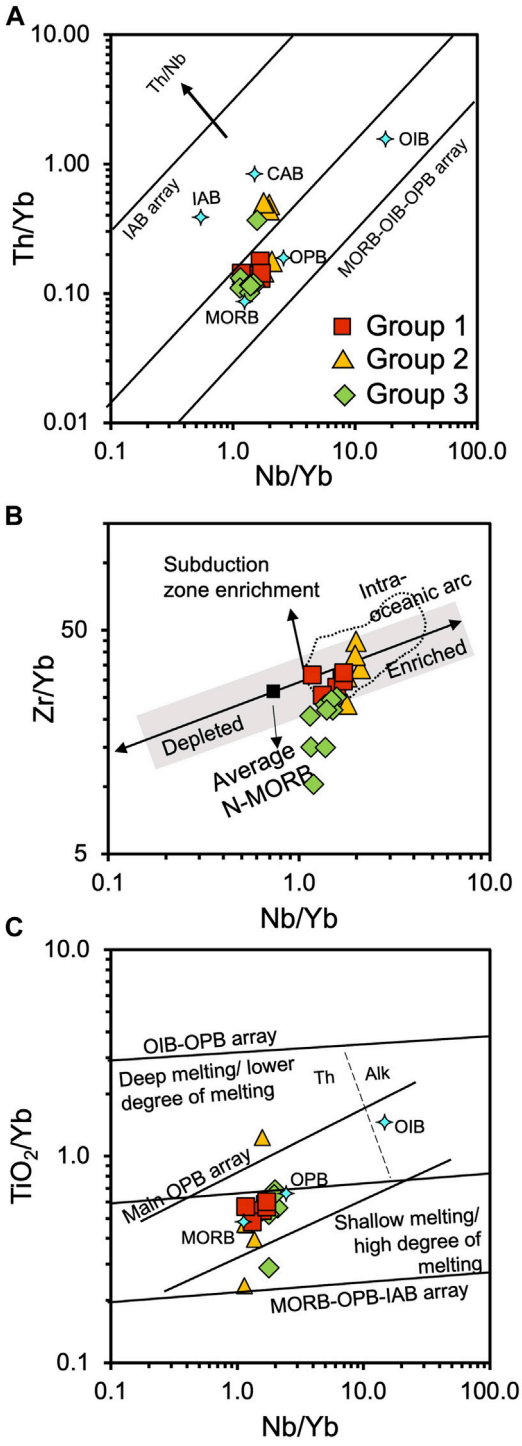

FIGURE 10
(A) Immobile incompatible element ratio diagram of Th/Yb vs. Nb/Yb (after Pearce et al., 2021), discrimination diagrams based on **(B)** TiO_2-Yb and Nb-Yb (Pearce, 2008), and **(C)** Zr- Yb and Nb-Yb (modified after Pearce et al., 2021).

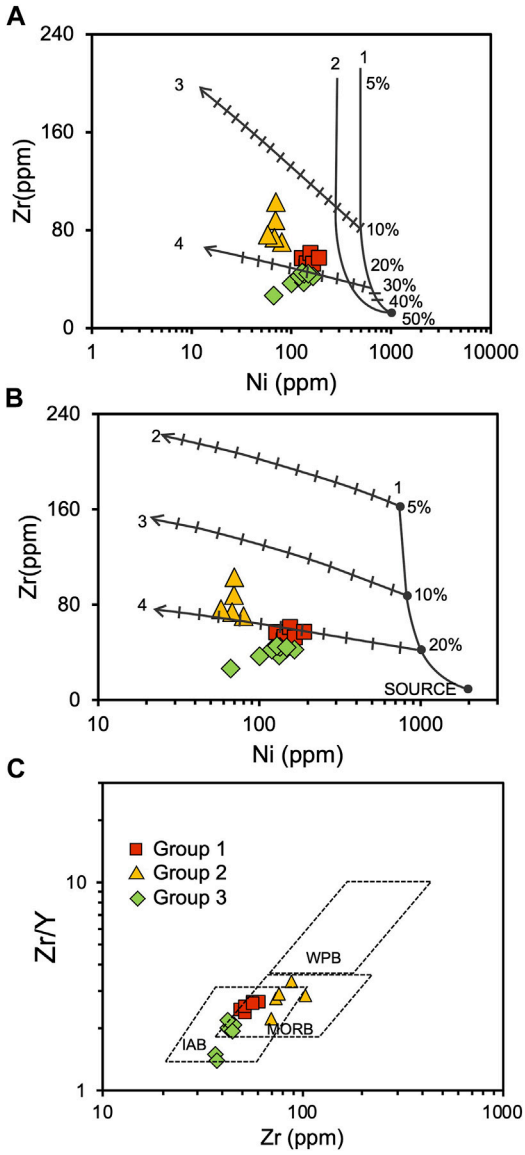

FIGURE 11
Petrogenetic models based on Zr and Ni abundances **(A)** after Rajamani et al. (1985). Curves 1 and 2 are calculated batch melting curves at 1850°C, 50 kb and 1,575°C, 25 kb respectively, and percentages of melting are marked. Curves 3 and 4 are olivine fractionation trends at 1 atm with an increment of 5% at each mark. **(B)** Modified after Condie et al. (1987). A lherzolite mantle with the compositions of Ni=2,000 ppm and Zr=11 ppm is considered as the source and a batch melting curve 1 at 1,500°C, and 1 atm is calculated with olivine fractionation curves at 2, 3, and 4. **(C)** Discrimination diagram of Zr versus Zr/Y to distinguish the tectonic environment of formation (after Pearce and Norry, 1979).

between MORB and OPB compositions. They show shallow melting (low pressure) or high degree of melting of the source. The difference in trace element characteristics of groups one and three seen in Figures 10A, B could result from of different evolution histories of the similar mantle sources. Group two dykes on the other hand are derived from an enriched mantle source with varying degrees of melting.

A petrogenetic modelling based on the trace elements Ni and Zr after Rajamani et al. (1985) is attempted to understand the extent of melting and fractionation (Figure 11A). A mantle source with Ni concentration of 2,000 ppm and Zr of 7.8 ppm, batch melting curves 1 and 2 at 1,850°C, 50 kb and 1,575°C, 25 kb, respectively is

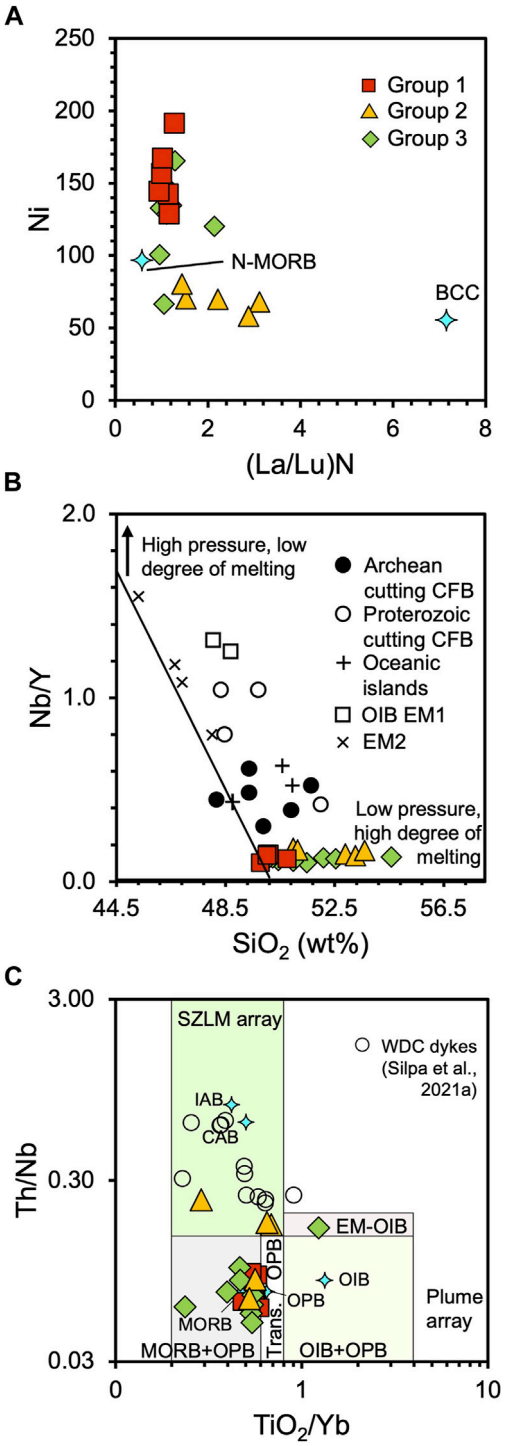

FIGURE 12
(A) Concentration of compatible trace element Ni (ppm) against Chondrite normalized (Sun and McDonough, 1989) La/Lu ratio. N-MORB value is from Gale et al. (2013) and bulk continental crust (BCC) is from Rudnick and Gao (2003). **(B)** SiO_2 (wt%) vs. Nb/Y ratios for understanding the depth and degree of melting. Diagonal line indicates primitive basalts. Comparison with continental flood basalts (CFB) cutting Archean and Proterozoic lithosphere, oceanic islands with tholeiitic compositions such as Hawaii and Iceland and normal oceanic island basalts (OIB) with enriched mantle component (EM1) and enriched mantle 2 (EM2) (after Greenough and McDivitt, 2018). **(C)** Variation diagram of TiO_2/Yb and Th/Nb for understanding crustal input and melting processes (after Pearce et al., 2021). MORB, (*Continued*)

FIGURE 12 (Continued)
OIB and OPB (oceanic plateau basalts) values are from Pearce (2008) and IAB (island arc basalts) and CAB (continental arc basalts) values are from Pearce and Peate (1995). SZLM-subduction modified mantle.

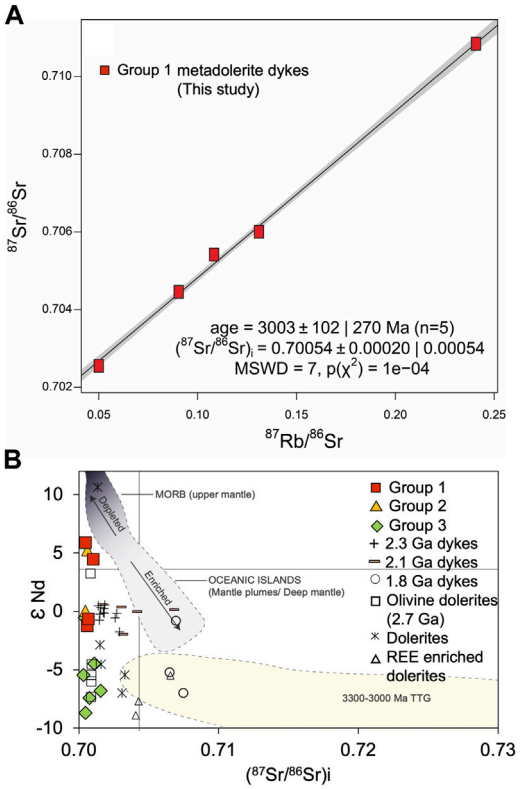

FIGURE 13
(A) Rb-Sr isochron diagram for the group one metadolerites constructed using IsoplotR. An errorchron age ca. 3,003 ± 102 Ma (MSWD =7) and initial $^{87}Sr/^{86}Sr$ ratio of 0.70054 was obtained. **(B)** εNd vs. $^{87}Sr/^{86}Sr$ (initial) ratio diagram to understand the source characteristics of the studied dykes. The dykes from the present study are compared with younger dykes from Western Dharwar Craton. Olivine dolerites, dolerites and REE enriched dolerites from Silpa et al. (2021) and 2.3, 2.1, and 1.8 Ga dykes' data are from Pandey and Paul. (2022) and TTG field is from Jayananda et al. (2018).

considered. Curves 3 and 4 are olivine fractionation trends at 1 atm with an increment of 5% at each mark. The dykes from the current study fall near the batch melting curve with a moderately high percentage of olivine fractionation. According to this model, group one dykes are derived from a melt generated by around 20% batch melting of a depleted mantle and ~25% olivine fractionation. Group three might have originated from a similar source with a higher degree of melting. Group two on the other hand is derived from a completely different source generated by around 15% batch melting of a depleted mantle source and a higher percentage of olivine fractionation. This result is further confirmed with a petrogenetic

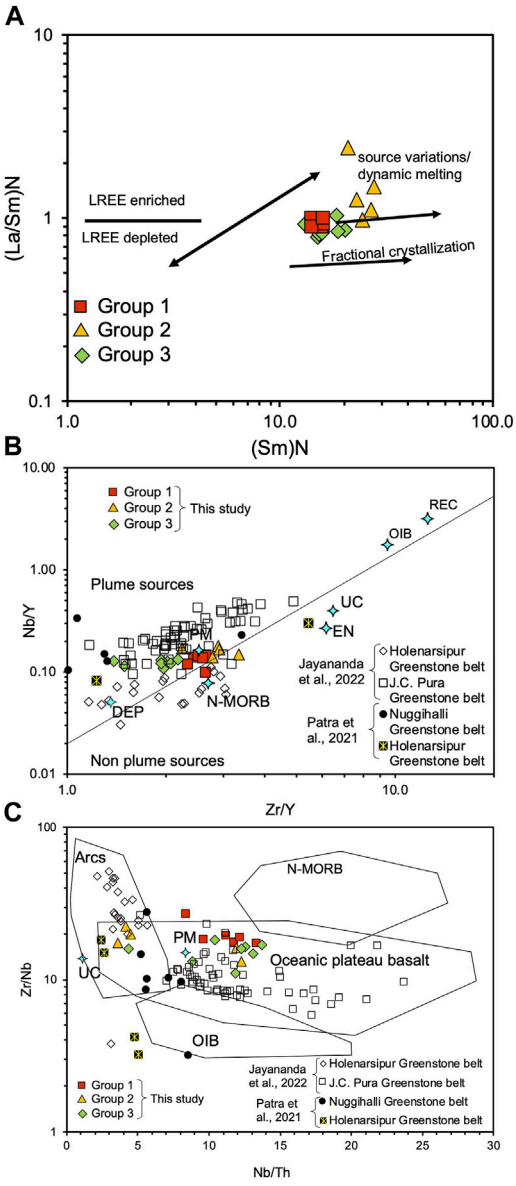

FIGURE 14
(A) Variation trends of chondrite normalized La/Sm vs. Sm, showing the role of source variation and fractional crystallization in the magmatic evolution of studied dykes. Diagrams showing mantle compositional components and various tectonic settings: **(B)** Nb/Y versus Zr/Y (after Condie, 2005) plot indicating primitive mantle to depleted mantle sources for the studied dykes. Compared with the greenstone belts from Western Dharwar Craton (Patra et al., 2021; Jayananda et al., 2022). **(C)** Zr/Nb versus Nb/Th plot (after Condie, 2005) showing oceanic plateau for group one and three, arc to oceanic plateau for group two dykes. PM, primitive mantle; DM, depleted mantle; ARC, arc related volcanics; N-MORB, normal ocean ridge basalt; OIB, oceanic island basalt; DEP, deep depleted mantle; EN, enriched component; REC, recycled components.

model by Condie et al. (1987). If a lherzolite mantle with 2,000 ppm of Ni and 11 ppm of Zr is considered as the source, a batch melting curve 1 at 1,500°C and 1 atm can be defined in which olivine fractionation curves are at 2, 3, and 4 (Figure 11B). It is evident that the group one dykes are derived from a 20% batch melting of a depleted lherzolite mantle source whereas a similar source with more than 25% melting is responsible for the group three dykes. Group two, however, is formed from a source with a lower degree of melting and a higher degree of olivine fractionation. In order to clarify the nature of the source magma, tectonic discrimination diagram based on Zr and Y (Pearce and Norry, 1979) is considered. In Figure 11C, most of the dykes are plotted in the IAB-MORB transition area, except for some group three samples that fall within the IAB field. Even though this can be interpreted as the arc tectonic setting (Srivastava et al., 2014), absence of significant negative anomalies for Nb-Ta suggest the derivation from a source modified by metasomatized mantle.

The Mg# of the studied dykes are lower (Figure 7) and suggestive of distinct fractionation histories for the three groups of dykes. Mg# does not show much variation for group one, probably indicating a quick emplacement after the extraction of the parent melt or a lack of significant fractional crystallization. The SiO_2 and Zr trends also (Figure 6) suggest the same. Groups two and three exhibit either significant fractionation or a higher degree of melting of the source. The calculated atomic Mg# ((Mg/(Mg+0.9Fet) atomic)) for the samples are <0.4 indicating a highly differentiated source. The enrichment of light rare earth element (LREE) and fractional crystallization trends are examined by Ni vs. chondrite normalized La/Lu ratio diagram (Figure 12A). Groups one and three exhibit normal fractional crystallization trends of primary magma. Group two dykes plot between average N-MORB value (Gale et al., 2013) and BCC (Rudnick et al., 2003) and has a varying LREE indicating a source enrichment. The source mantle is further characterized by Nb/Y vs. SiO_2 plot (Figure 12B) and is compared with other continent flood basalts cross-cutting Archean and Proterozoic lithospheric units (Greenough and McDivitt, 2018). All the dykes show a low pressure or a shallow derivation of the source, and higher degree of melting. Group one dykes plot close to primitive basalt line. SiO_2 increases for Group two and three however, there is no variation in Nb/Y. Such a signature coincides with the previous interpretation of compositional difference within the original mantle source. This modification of the source due to subduction or degree of melting is further correlated by the relationship between Th/Nb and TiO_2/Yb (Pearce et al., 2021). In Figure 12C, group one and three dykes exhibit a composition between MORB and OPB. Group three also shows enriched components, probably due to the increasing degrees of melting. Group two trends towards subduction-modified lithospheric mantle (SZLM) array which supports the recycling of subducted crust in its source mantle. The metadolerite dykes are compared with the younger (2.7 Ga and younger) dolerite dykes from WDC, all of which follow SZLM array. The petrogenesis of younger dolerite dykes suggest that they are derived from a depleted MORB like mantle source (DMM) which is modified by the addition of subducted oceanic crustal components (Silpa et al., 2021). This also leads us to conclude that the group two dykes have ancient, subducted components in its source.

The geochemical evolution of mantle beneath Western Dharwar craton during the Archean can be tracked by reliable isotopic systems like Rb-Sr and Sm-Nd isotopes (Figures 9A, B). The group one dykes in the current study gives a Rb-Sr errorchron age of ca. 3,003 ± 102 Ma (Figure 13A). The dykes in the current study are compared with the spatially

associated greenstone belts of the Western Dharwar craton with similar ages since they are considered to be the conduits for the continental volcanism. Drury et al. (1983) has reported Sm-Nd whole rock age of 3,020± 230 Ma for the metavolcanics in the Dharwar supergroup. Similarly, an age of 2,934± 88 Ma is reported for the Holenarasipur and Nugihalli mafic volcanics in the Sargur supra crustals (Patra et al., 2021) that are proximal to the current study area. The initial $^{143}Nd/^{144}Nd$ ratios calculated range from 0.50879 to 0.50887, which is very close to the initial ratios of 0.508,245–0.509,172 obtained for the samples in the current study. Jayananda et al. (2022) reported similar imprecise age of 3,043 ± 428 Ma and an initial $^{143}Nd/^{144}Nd$ ratio of 0.50876 ± 0.00037 for the greenstone volcanics from the eastern block of Holenarsipur belt. The published ages around 3,000 Ma have significant overlap between oldest lithologic units of Dharwar Supergroup and the youngest units of Sargur group of metavolcanics (Patra et al., 2021). The similarities between these mafic volcanics and the studied metadolerites are due to the fact that the Archean to early Proterozoic mafic rocks are derived from depleted mantle sources (DePaolo and Wasserburg, 1981; Jahn et al., 1987). The εNd values (Figure 13B) of group one and two dykes are close to zero to +5 indicating heterogeneous depleted SCLM reservoirs beneath the Dharwar craton. εNd values shown by group three range from −12 to −0.4 and the initial Sr isotope ratios of 0.70041–0.70153. The large variation in Nd and minimal scatter in Sr ratios suggest that the Rb-Sr and Sm-Nd systems were in isotopic equilibrium and rule out the possibilities of any external factors affecting the mantle source. This along with the lower Th/Nb ratios and LREE concentrations are suggestive of a mantle source enriched by subducted crustal components and little effect of crustal contamination. Based on the whole rock geochemical characteristics including the isotopic ratios, is it evident that the metadolerite dykes in the current study are derived from varying degrees of melting of a depleted sub-continental lithospheric mantle beneath Archean Dharwar craton. The group two dykes, however, has an enriched component possibly derived from the subduction of oceanic slab in the original source mantle.

5.2 Geodynamic implications

Archean geodynamics are poorly constrained and highly debated due to the large volumes of crustal extraction, the drastic changes in the temperature and composition of the mantle, the formation of continental crust and episodic large-scale volcanic activity (Ernst and Buchan, 2001; Smithies et al., 2003; Ernst et al., 2013; Dhiume et al., 2015, and the references therein). The Archean crust was mafic in nature before 3,200–3,000 Ma (Tang et al., 2016). The extraction of komatiites and komatiite-basalts has led to the removal of MgO from the mantle and resulted in the decrease in MgO and Ni around 3000 Ma (Condie, 1993; Herzberg et al., 2010; Keller and Schoene, 2012; Keller and Schoene, 2018). This compositional change is also attributed to the decrease in mantle potential temperatures (Windley et al., 2021). The formation of extensive oceanic crust from Paleoarchean to komatiites and microcontinents made of TTGs, towards the end of 3000 Ma has significantly depleted the SCLM. Oceanic subduction and related metasomatization of the mantle by recycled crust was predominant during that time (Halla et al., 2009; Dhiume et al., 2015; Halla et al., 2017). However, during the Mesoarchean to Neoarchean the melting source changed from hydrated oceanic lithosphere to variously enriched mantle wedge. This resulted in abundance of melts and fluids derived from heterogeneously enriched mantle (Halla et al., 2009; Windley et al., 2021). This transition in the mantle composition is also evident from the greenstone volcanics and associated mafic dykes. The differences in the source or the melting conditions of the studied dykes are analyzed using rare earth element concentrations (Figure 14A). Group one dykes do not show much variation in degree of melting or fractional crystallization. This leads us to conclude that rapid emplacement of a depleted mantle source resulted in the formation of Group one dykes. The formation of group two dykes can be explained by either of the following two scenarios: 1) Source variation or 2) a dynamic melting with no influence of fractional crystallization. The melting of a source over a range of depths (pressures) is defined as dynamic melting (Elliot et al., 1991; Pearce and Peate, 1995) and usually regarded as a process between batch melting and fractional crystallization. Dynamic melting process usually has high MgO, high Fe, Na, and low K (Pearce and Peate, 1995). The pressure and depth of melting proxy SiO_2 vs. the degree of melting proxy Nb/Y diagram (Figure 12B; modified after Greenough and McDivitt, 2018) support shallow depth of melting for all the dykes. Given the mantle temperature and composition of SCLM during Mesoarchean to Neoarchean, source variation is the most plausible explanation. Group three on the other hand is showing a slight trend towards source variation which might have been derived from higher degree of melting. This, combined with the results from the petrogenetic modelling (Figures 11A, B) leads to the conclusion that they might have derived from a mantle source similar to group one dykes with a higher percentage of melting that lead to progressive enrichment of the source. The greenstone belts in the Western Dharwar craton are comparable to the neighboring metadolerites due to the similarity in the geochemical characteristics, especially Sr and Nd isotope compositions. To further examine the geochemical coherence and the mantle source constraints, trace element ratios Nb/Y, Zr/Y, Zr/Nb and Nb/Th (Figures 14B, C) are constructed. Similar to the greenstone belts from the previous studies (Patra et al., 2021; Jayananda et al., 2022), metadolerite dykes from the current study indicate primitive mantle to MORB source reservoirs in the trace element ratio diagram Zr/Y versus Nb/Y (Figure 14B). In the Nb/Th versus Zr/Nb plot, most of the dykes plots in the oceanic plateau basalts, Group one dykes are plotting close to primitive mantle whereas Group two and three are following an arc trend (Figure 14C). The greenstone volcanics are showing oceanic plateau and arc to oceanic plateau signatures and are thought to be represent oceanic crust related to subduction accretion processes (Patra et al., 2021). Such processes are

argued to be common during the Archean and preservation of subduction signatures in Archean greenstone belts has been reported by earlier studies (Smithies et al., 2003; Jayananda et al., 2008; Patra et al., 2021 and the references there in). The metadolerites reported here also represent an SZLM with subducted crustal signatures as well as depleted SCLM that was present beneath the Archean Dharwar craton.

6 Conclusion

The metadolerite dykes in the current study are derived from a depleted SCLM source during the Mesoarchean to Neoarchean after komatiitic magma extraction. Compositionally three groups are identified. Group one is thought to be derived from a depleted mantle source, emplaced at ca. 3,003 ± 102 Ma. Group two dykes are compositionally distinct and are progressively enriched, possibly by the addition of subducted oceanic crustal components. Group three dykes are geochemically similar to group one dykes; however, they show a gradual evolution of the source owing to increasing degree of melting. The dykes in the current study have geochemical similarities with the neighboring greenstone belts and it is possible to infer that were the conduits of the widespread greenstone volcanism in the Western Dharwar Craton.

Data availability statement

The original contributions presented in the study are included in the article/supplementary material, further inquiries can be directed to the corresponding author.

Author contributions

ASS conducted the field work and geochemical analysis. MS-K supported the entire research, during field work, analysis, and discussion of the results. TT supported the geochemical analysis of samples. AK contributed to the interpretation of the results. All authors contributed to the article and approved the submitted version.

Funding

This study was supported by the Grant-in-Aid for Scientific Research on Innovative Areas. MS-K acknowledges KAKENHI research grants from the Ministry of Education, Culture, Sports, Science and Technology, Japan (Nos. JP15H05831 and 20KK0081) and partial support through JSPS KAKENHI grant numbers JP23340155 and JP25302008. For field work support the authors acknowledge JSPS grant for Japan-India Science Cooperative Programs (lead by TT 2019-20).

Acknowledgments

The authors thank the guest editor for an efficient editorial handling of the manuscript and the reviewers for their valuable comments which helped in improving the manuscript to a large extent. ASS acknowledges Japanese Government (Monbukagakusho) scholarship for PhD program at Niigata University. We also express our sincere thanks Ms. Rikako Nohara for the help rendered during the geochemical analysis of dykes at Niigata University. Prof. Sajeev, Dr. Thanooja, and S. Kiran are thanked for the help rendered during field studies in Dharwar craton.

Conflict of interest

The authors declare that the research was conducted in the absence of any commercial or financial relationships that could be construed as a potential conflict of interest.

Publisher's note

References

Armstrong, R. L. (1991). The persistent myth of crustal growth. *Aust. J. Earth Sci.* 38 (5), 613–630. doi:10.1080/08120099108727995

Bédard, J. H. (2018). Stagnant lids and mantle overturns: Implications for Archaean tectonics, magma Genesis, crustal growth, mantle evolution, and the start of plate tectonics. *Geosci. Front.* 9 (1), 19–49. doi:10.1016/j.gsf.2017.01.005

Belica, M. E., Piispa, E. J., Meert, J. G., Pesonen, L. J., Plado, J., Pandit, M. K., et al. (2014). Paleoproterozoic mafic dyke swarms from the Dharwar craton; paleomagnetic poles for India from 2.37 to 1.88 Ga and rethinking the Columbia supercontinent. *Precambrian Res.* 244, 100–122. doi:10.1016/j.precamres.2013.12.005

Bleeker, W., and Ernst, R. E. (2006). "Short-lived mantle generated magmatic events and their dyke swarms: The key unlocking earth's paleogeographic record back to 2.6 Ga," in *Dyke swarms – time markers of crustal evolution*. Editors E. Hanski, S. Mertanen, T. Rämö, and J. Vuollo (London: Taylor and Francis), 3–26.

Bleeker, W. (2003) The late archean record: A puzzle in ca. 35 pieces *Lithos* 71 (2-4), 99–134. doi:10.1016/j.lithos.2003.07.003

Bowring, S. A., and Housh, T. (1995). The Earth's early evolution. *Science* 269 (5230), 1535–1540. doi:10.1126/science.7667634

Brown, M., Rushmer, T., and Sawyer, E. W. (1995). Introduction to special section: Mechanisms and consequences of melt segregation from crustal protoliths. *J. Geophys. Res. Solid Earth* 100 (B8), 15551–15563. doi:10.1029/95jb01253

Cawood, P. A., Hawkesworth, C. J., and Dhuime, B. (2013). The continental record and the generation of continental crust. *Bulletin* 125 (1-2), 14–32. doi:10.1130/b30722.1

Chatterjee, N., and Bhattacharji, S. (2001). Petrology, geochemistry and tectonic settings of the mafic dikes and sills associated with the evolution of the Proterozoic Cuddapah Basin of south India. *J. Earth Syst. Sci.* 110 (4), 433–453. doi:10.1007/bf02702905

Choukroune, P., Bouhallier, H., and Arndt, N. T. (1995). Soft lithosphere during periods of Archaean crustal growth or crustal reworking. *Geol. Soc. Lond. Spec. Publ.* 95 (1), 67–86. doi:10.1144/gsl.sp.1995.095.01.05

Coffin, M. F., and Eldholm, O. (1994). Large igneous provinces: Crustal structure, dimensions, and external consequences. *Rev. Geophys.* 32 (1), 1–36. doi:10.1029/93rg02508

Coffin, M. F., and Eldholm, O. (1991). *Large igneous provinces: JOI/USSAC workshop report*. Austin TX, USA: Institute of Geophysics, University of Texas, 79.

Condie, K. C., Bobrow, D. J., and Card, K. D. (1987). Geochemistry of precambrian mafic dykes from the southern superior province of the Canadian shield. *Geol. Assoc. Can.* 34, 95–108. Special Paper.

Condie, K. C. (1993). Chemical composition and evolution of the upper continental crust: Contrasting results from surface samples and shales. *Chem. Geol.* 104 (1-4), 1–37. doi:10.1016/0009-2541(93)90140-e

Condie, K. C. (2005). High field strength element ratios in archean basalts: A window to evolving sources of mantle plumes? *Lithos* 79 (3-4), 491–504. doi:10.1016/j.lithos.2004.09.014

DePaolo, D. J., and Wasserburg, G. J. (1976). Nd isotopic variations and petrogenetic models. *Geophys. Res. Lett.* 3 (5), 249–252. doi:10.1029/gl003i005p00249

Dey, S., Pandey, U. K., Rai, A. K., and Chaki, A. (2012). Geochemical and Nd isotope constraints on petrogenesis of granitoids from NW part of the eastern dharwar craton: Possible implications for late archaean crustal accretion. *J. Asian Earth Sci.* 45, 40–56. doi:10.1016/j.jseaes.2011.09.013

Dhuime, B., Hawkesworth, C. J., Cawood, P. A., and Storey, C. D. (2012). A change in the geodynamics of continental growth 3 billion years ago. *Science* 335 (6074), 1334–1336. doi:10.1126/science.1216066

Dhuime, B., Wuestefeld, A., and Hawkesworth, C. J. (2015). Emergence of modern continental crust about 3 billion years ago. *Nat. Geosci.* 8 (7), 552–555. doi:10.1038/ngeo2466

Drury, S. A., Holt, R. W., Van Clasteren, P. C., and Beckinsale, R. D. (1983). Sm-Nd and Rb-Sr ages for Archaean rocks in Western Karnataka, south India. *J. Geol. Soc. India* 24 (9), 454–459.

Elliott, T. R., Hawkesworth, C. J., and Grönvold, K. (1991). Dynamic melting of the Iceland plume. *Nature* 351 (6323), 201–206. doi:10.1038/351201a0

Ernst, R., and Bleeker, W. (2010). Large igneous provinces (LIPs), giant dyke swarms, and mantle plumes: Significance for breakup events within Canada and adjacent regions from 2.5 Ga to the Present. This article is one of a selection of papers published in this special issue on the the theme *lithoprobe—parameters, processes, and the evolution of a continent*.Lithoprobe contribution 1482. Geological Survey of Canada contribution 20100072. *Can. J. Earth Sci.* 47 (5), 695–739. doi:10.1139/e10-025

Ernst, R. E., Bleeker, W., Söderlund, U., and Kerr, A. C. (2013). Large Igneous Provinces and supercontinents: Toward completing the plate tectonic revolution. *Lithos* 174, 1–14. doi:10.1016/j.lithos.2013.02.017

Ernst, R. E., and Buchan, K. L. (Editors) (2001). *Mantle plumes: Their identification through time* (United States: Geological Society of America).

Ernst, R. E., Buchan, K. L., and Campbell, I. H. (2005). Frontiers in large igneous province research. *Lithos* 79 (3-4), 271–297. doi:10.1016/j.lithos.2004.09.004

Ernst, R. E. (2014). *Large igneous provinces*. United Kingdom: Cambridge University Press.

French, J. E., Heaman, L. M., Chacko, T., and Srivastava, R. K. (2008). 1891–1883 Ma southern bastar–cuddapah mafic igneous events, India: A newly recognized large igneous province. *Precambrian Res.* 160 (3-4), 308–322. doi:10.1016/j.precamres.2007.08.005

French, J. E., and Heaman, L. M. (2010). Precise U–Pb dating of paleoproterozoic mafic dyke swarms of the dharwar craton, India: Implications for the existence of the neoarchean supercraton sclavia. *Precambrian Res.* 183 (3), 416–441. doi:10.1016/j.precamres.2010.05.003

Gale, A., Dalton, C. A., Langmuir, C. H., Su, Y., and Schilling, J. G. (2013). The mean composition of ocean ridge basalts. *Geochem. Geophys. Geosystems* 14 (3), 489–518. doi:10.1002/ggge.20038

Greenough, J. D., and McDivitt, J. A. (2018). Earth's evolving subcontinental lithospheric mantle: Inferences from LIP continental flood basalt geochemistry. *Int. J. Earth Sci.* 107, 787–810. doi:10.1007/s00531-017-1493-6

Gupta, S., Rai, S. S., Prakasam, K. S., Srinagesh, D., Bansal, B. K., Chadha, R. K., et al. (2003). The nature of the crust in southern India: Implications for precambrian crustal evolution. *Geophys. Res. Lett.* 30 (8). doi:10.1029/2002gl016770

Halla, J., van Hunen, J., Heilimo, E., and Hölttä, P. (2009). Geochemical and numerical constraints on Neoarchean plate tectonics. *Precambrian Res.* 174 (1-2), 155–162. doi:10.1016/j.precamres.2009.07.008

Halla, J., Whitehouse, M. J., Ahmad, T., and Bagai, Z. (2017). Archaean granitoids: An overview and significance from a tectonic perspective. *Geol. Soc. Lond. Spec. Publ.* 449 (1), 1–18. doi:10.1144/sp449.10

Halls, H. C., Kumar, A., Srinivasan, R., and Hamilton, M. A. (2007). Paleomagnetism and U–Pb geochronology of easterly trending dykes in the dharwar craton, India: Feldspar clouding, radiating dyke swarms and the position of India at 2.37 Ga. *Precambrian Res.* 155 (1-2), 47–68. doi:10.1016/j.precamres.2007.01.007

Halls, H. C., Li, J., Davis, D., Hou, G., Zhang, B., and Qian, X. (2000). A precisely dated Proterozoic palaeomagnetic pole from the North China craton, and its relevance to palaeocontinental reconstruction. *Geophys. J. Int.* 143 (1), 185–203. doi:10.1046/j.1365-246x.2000.00231.x

Hamamoto, T., Yuhara, M., Miyazaki, M., Fukase, H., Kondo, T., Ikawa, J., et al. (2000). *Rb, Sr, Sm and Nd separation from rocks, minerals and natural water using ion-exchange resin*. Niigata: Science Report Niigata University, Search E. Geology, 49–58.15

Hawkesworth, C., and Jaupart, C. (2021). Heat flow constraints on the mafic character of Archean continental crust. *Earth Planet. Sci. Lett.* 571, 117091. doi:10.1016/j.epsl.2021.117091

Hawkesworth, C. J., Dhuime, B., Pietranik, A. B., Cawood, P. A., Kemp, A. I., and Storey, C. D. (2010). The generation and evolution of the continental crust. *J. Geol. Soc.* 167 (2), 229–248. doi:10.1144/0016-76492009-072

Herzberg, C., Condie, K., and Korenaga, J. (2010). Thermal history of the Earth and its petrological expression. *Earth Planet. Sci. Lett.* 292 (1-2), 79–88. doi:10.1016/j.epsl.2010.01.022

Hoffman, P. F., and Ranalli, G. (1988). Archean oceanic flake tectonics. *Geophys. Res. Lett.* 15 (10), 1077–1080. doi:10.1029/gl015i010p01077

Irvine, T. N., and Baragar, W. R. A. (1971). A guide to the chemical classification of the common volcanic rocks. *Can. J. earth Sci.* 8 (5), 523–548. doi:10.1139/e71-055

Jayananda, M., Aadhiseshan, K. R., Kusiak, M. A., Wilde, S. A., Sekhamo, K. U., Guitreau, M., et al. (2020). Multi-stage crustal growth and neoarchean geodynamics in the eastern dharwar craton, southern India. *Gondwana Res.* 78, 228–260. doi:10.1016/j.gr.2019.09.005

Jayananda, M., Chardon, D., Peucat, J. J., and Capdevila, R. (2006). 2.61 Ga potassic granites and crustal reworking in the Western dharwar craton, southern India: Tectonic, geochronologic and geochemical constraints. *Precambrian Res.* 150 (1-2), 1–26. doi:10.1016/j.precamres.2006.05.004

Jayananda, M., Chardon, D., Peucat, J. J., and Fanning, C. M. (2015). Paleo-to mesoarchean TTG accretion and continental growth in the Western dharwar craton, southern India: Constraints from SHRIMP U–Pb zircon geochronology, whole-rock geochemistry and Nd–Sr isotopes. *Precambrian Res.* 268, 295–322. doi:10.1016/j.precamres.2015.07.015

Jayananda, M., Guitreau, M., Aadhiseshan, K. R., Miyazaki, T., and Chung, S. L. (2022). Origin of the oldest (3600–3200 Ma) cratonic core in the western dharwar craton, southern India: Implications for evolving tectonics of the archean earth. *Earth-Science Rev.* 236, 104278. doi:10.1016/j.earscirev.2022.104278

Jayananda, M., Kano, T., Peucat, J. J., and Channabasappa, S. (2008). 3.35 Ga komatiite volcanism in the Western dharwar craton, southern India: Constraints from Nd isotopes and whole-rock geochemistry. *Precambrian Res.* 162 (1-2), 160–179. doi:10.1016/j.precamres.2007.07.010

Jayananda, M., Moyen, J. F., Martin, H., Peucat, J. J., Auvray, B., and Mahabaleswar, B. (2000). Late archaean (2550–2520 Ma) juvenile magmatism in the eastern dharwar craton, southern India: Constraints from geochronology, Nd–Sr isotopes and whole rock geochemistry. *Precambrian Res.* 99 (3-4), 225–254. doi:10.1016/s0301-9268(99)00063-7

Jayananda, M., Santosh, M., and Aadhiseshan, K. R. (2018). formation of archean (3600–2500 Ma) continental crust in the dharwar craton, southern India. *Earth-Science Rev.* 181, 12–42. doi:10.1016/j.earscirev.2018.03.013

Johnson, T. E., Kirkland, C. L., Gardiner, N. J., Brown, M., Smithies, R. H., and Santosh, M. (2019). Secular change in TTG compositions: Implications for the evolution of Archaean geodynamics. *Earth Planet. Sci. Lett.* 505, 65–75. doi:10.1016/j.epsl.2018.10.022

Keller, B., and Schoene, B. (2018). Plate tectonics and continental basaltic geochemistry throughout Earth history. *Earth Planet. Sci. Lett.* 481, 290–304. doi:10.1016/j.epsl.2017.10.031

Keller, C. B., and Schoene, B. (2012). Statistical geochemistry reveals disruption in secular lithospheric evolution about 2.5 Gyr ago. *Nature* 485 (7399), 490–493. doi:10.1038/nature11024

Kumar, A., Hamilton, M. A., and Halls, H. C. (2012a). A Paleoproterozoic giant radiating dyke swarm in the Dharwar Craton, southern India. *Geochem. Geophys. Geosystems* 13 (2). doi:10.1029/2011gc003926

Kumar, A., Nagaraju, E., Besse, J., and Rao, Y. B. (2012b). New age, geochemical and paleomagnetic data on a 2.21 Ga dyke swarm from south India: Constraints on Paleoproterozoic reconstruction. *Precambrian Res.* 220, 123–138. doi:10.1016/j.precamres.2012.08.001

Le Maitre, R. W. (Editor) (2002). *Igneous rocks: A classification and glossary of terms* (United Kingdom: Cambridge University Press), 236.

Meert, J. G., and Pandit, M. K. (2015). *The archaean and proterozoic history of peninsular India: Tectonic framework for precambrian sedimentary basins in India*, 43. London: Geological Society, 29–54.1

Monteux, J., Andrault, D., Guitreau, M., Samuel, H., and Demouchy, S. (2020). A mushy Earth's mantle for more than 500 Myr after the magma ocean solidification. *Geophys. J. Int.* 221 (2), 1165–1181. doi:10.1093/gji/ggaa064

Mukherjee, R., Mondal, S. K., Frei, R., Rosing, M. T., Waight, T. E., Zhong, H., et al. (2012). The 3.1 Ga Nuggihalli chromite deposits, Western Dharwar craton (India): Geochemical and isotopic constraints on mantle sources, crustal evolution and implications for supercontinent formation and ore mineralization. *Lithos* 155, 392–409. doi:10.1016/j.lithos.2012.10.001

Murthy, Y. G. K., Babu Rao, V., Guptasarma, D., Rao, J. M., Rao, M. N., and Bhattacharji, S. (1987). Tectonic, petrochemical and geophysical studies of mafic dyke swarms around the Proterozoic Cuddapah basin, South India. *Mafic dyke swarms* 34, 303–316.

Nagaraju, E., Parashuramulu, V., Babu, N. R., and Narayana, A. C. (2018b). A 2207 Ma radiating mafic dyke swarm from eastern Dharwar craton, Southern India:

Drift history through Paleoproterozoic. *Precambrian Res.* 317, 89–100. doi:10.1016/j.precamres.2018.08.009

Nagaraju, E., Parashuramulu, V., Kumar, A., and Sarma, D. S. (2018a). Paleomagnetism and geochronological studies on a 450 km long 2216 Ma dyke from the Dharwar craton, southern India. *Phys. Earth Planet. Interiors* 274, 222–231. doi:10.1016/j.pepi.2017.11.006

Pandey, O. P., and Paul, D. (2022). Secular evolution of the subcontinental lithospheric mantle beneath Indian cratons: Insights from geochemistry and geochronology of the Precambrian mafic dykes. *Lithos* 422, 106729. doi:10.1016/j.lithos.2022.106729

Patra, K., Giri, A., Anand, R., Balakrishnan, S., and Dash, J. K. (2021). Dharwar stratigraphy revisited: New age constraints on the 'oldest' supracrustal rocks of Western dharwar craton, southern India. *Int. Geol. Rev.* 63 (12), 1450–1470. doi:10.1080/00206814.2020.1775138

Pearce, J. A., Ernst, R. E., Peate, D. W., and Rogers, C. (2021). LIP printing: Use of immobile element proxies to characterize Large Igneous Provinces in the geologic record. *Lithos* 392, 106068. doi:10.1016/j.lithos.2021.106068

Pearce, J. A. (2008). Geochemical fingerprinting of oceanic basalts with applications to ophiolite classification and the search for Archean oceanic crust. *Lithos* 100 (1-4), 14–48. doi:10.1016/j.lithos.2007.06.016

Pearce, J. A., and Norry, M. J. (1979). Petrogenetic implications of Ti, Zr, Y, and Nb variations in volcanic rocks. *Contributions mineralogy petrology* 69 (1), 33–47. doi:10.1007/bf00375192

Pearce, J. A., and Peate, D. W. (1995). Tectonic implications of the composition of volcanic arc magmas. *Annu. Rev. Earth Planet. Sci.* 23 (1), 251–285. doi:10.1146/annurev.ea.23.050195.001343

Peucat, J. J., Jayananda, M., Chardon, D., Capdevila, R., Fanning, C. M., and Paquette, J. L. (2013). The lower crust of the dharwar craton, southern India: Patchwork of archean granulitic domains. *Precambrian Res.* 227, 4–28. doi:10.1016/j.precamres.2012.06.009

Radhakrishna, T., and Joseph, M. (1993). Proterozoic paleomagnetism of the south Indian shield and tectonic constraints. *Geol. Soc. India Memoirs* 26, 321–336.

Rai, A. K., Srivastava, R. K., Samal, A. K., and Sesha Sai, V. V. (2019). Geochemistry, petrogenesis, and geodynamic implications of NE–SW to ENE–WSW trending P alaeoproterozoic mafic dyke swarms from southern region of the Western Dharwar Craton. *Geol. J.* 54 (5), 3493–2869. doi:10.1002/gj.3493

Rajamani, V., Shivkumar, K., Hanson, G. N., and Shirey, A. S. (1985). Geochemistry and petrogenesis of amphibolites, kolar schist belt, south India: Evidence for komatiitic magma derived by low percentages of melting of the mantle. *J. Petrology* 26 (1), 92–123. doi:10.1093/petrology/26.1.92

Ramakrishnan, M., and Vaidyanathan, R. (2008). *Geology of India*. Bangalore: Geological Society of India, 556.

Ravindran, A., Mezger, K., Balakrishnan, S., and Berndt, J. (2021). Hf-Nd isotopes from ultramafic and mafic rocks in the Western Dharwar Craton, India, record early Archean mantle heterogeneity. *Lithos* 404, 106491. doi:10.1016/j.lithos.2021.106491

Rudnick, R. L., Gao, S., Holland, H. D., and Turekian, K. K. (2003). Composition of the continental crust. *crust* 3, 1–64.

Rudnick, R. L., McDonough, W. F., and O'Connell, R. J. (1998). Thermal structure, thickness and composition of continental lithosphere. *Chem. Geol.* 145 (3-4), 395–411. doi:10.1016/s0009-2541(97)00151-4

Senda, R., Kimura, J. I., and Chang, Q. (2014). Evaluation of a rapid, effective sample digestion method for trace element analysis of granitoid samples containing acid-resistant minerals: Alkali fusion after acid digestion. *Geochem. J.* 48 (1), 99–103. doi:10.2343/geochemj.2.0280

Silpa, A. S., and Satish-Kumar, M. (2018). Dyke swarms in the dharwar craton: A key to understanding the late archean to early proterozoic cratonic correlations. *J. Indian Inst. Sci.* 98 (4), 365–378. doi:10.1007/s41745-018-0090-4

Silpa, A. S., and Satish-Kumar, M. (2022). Multiple sulfur isotope geochemistry of the Precambrian mafic dykes and komatiites in the Dharwar Craton, Southern India: Evidence for crustal recycling and enrichment in the subcontinental lithospheric mantle. *Lithosphere* 2022, 4679300. doi:10.2113/2022/4679300

Silpa, A. S., Satish-Kumar, M., and Takahashi, T. (2021a). Sr-Nd isotopic study of dolerite dykes in the Western Dharwar craton, southern India: Implications for the evolution of the subcontinental lithospheric mantle in late Archean. *Lithos* 388, 106023. doi:10.1016/j.lithos.2021.106023

Silpa, S. A., Satish-Kumar, M., Takazawa, E., and Sajeev, K. (2021b). Trace and rare Earth element geochemistry of clinopyroxene in mafic dykes from Western Dharwar craton, southern India. *J. Mineralogical Petrological Sci.* 116 (2), 108–112. doi:10.2465/jmps.201130c

Smithies, R. H., Champion, D. C., and Cassidy, K. F. (2003). Formation of Earth's early Archaean continental crust. *Precambrian Res.* 127 (1-3), 89–101. doi:10.1016/s0301-9268(03)00182-7

Söderlund, U., Bleeker, W., Demirer, K., Srivastava, R. K., Hamilton, M., Nilsson, M., et al. (2019). Emplacement ages of paleoproterozoic mafic dyke swarms in eastern dharwar craton, India: Implications for paleoreconstructions and support for a~ 30° change in dyke trends from south to north. *Precambrian Res.* 329, 26–43. doi:10.1016/j.precamres.2018.12.017

Srivastava, R. K., Jayananda, M., Gautam, G. C., Gireesh, V., and Samal, A. K. (2014). Geochemistry of an ENE–WSW to NE–SW trending~ 2.37 Ga mafic dyke swarm of the eastern Dharwar craton, India: Does it represent a single magmatic event? *Geochemistry* 74 (2), 251–265. doi:10.1016/j.chemer.2013.07.007

Srivastava, R. K., Samal, A. K., and Gautam, G. C. (2015). Geochemical characteristics and petrogenesis of four Palaeoproterozoic mafic dike swarms and associated large igneous provinces from the eastern Dharwar craton, India. *Int. Geol. Rev.* 57 (11-12), 1462–1484. doi:10.1080/00206814.2014.938366

Stern, R. J. (2005). Evidence from ophiolites, blueschists, and ultrahigh-pressure metamorphic terranes that the modern episode of subduction tectonics began in Neoproterozoic time. *Geology* 33 (7), 557–560. doi:10.1130/g21365.1

Sun, S. S., and McDonough, W. F. (1989). Chemical and isotopic systematics of oceanic basalts: Implications for mantle composition and processes. *Geol. Soc. Lond. Spec. Publ.* 42 (1), 313–345. doi:10.1144/gsl.sp.1989.042.01.19

Swami Nath, J., and Ramakrishnan, M. (1981). Early Precambrian supracrustals of southern Karnataka. *Memoirs Geol. Surv. India* 112, 350.

Takahashi, T., Hirahara, Y., Miyazaki, T., Vaglarov, B. S., Chang, Q., Kimura, J. I., et al. (2009). Precise determination of Sr isotope ratios in igneous rock samples and application to micro-analysis of plagioclase phenocrysts. *JAMSTEC Rep. Res. Dev.* 2009, 59–64.

Takahashi, T., Shuto, K., and Iho, S. (1997). Differentiation of myeloid cells and 1,25-dihydroxyvitamin D3. *Rigaku J.* 28, 25–33. doi:10.3109/10428199709068268

Tang, M., Chen, K., and Rudnick, R. L. (2016). Archean upper crust transition from mafic to felsic marks the onset of plate tectonics. *Science* 351 (6271), 372–375. doi:10.1126/science.aad5513

Windley, B. F., Kusky, T., and Polat, A. (2021). Onset of plate tectonics by the Eoarchean. *Precambrian Res.* 352, 105980. doi:10.1016/j.precamres.2020.105980

Yadav, P., Sarma, D. S., and Parashuramulu, V. (2020). Pb-Pb baddeleyite ages of mafic dykes from the Western dharwar craton, southern India: A window into 2.21–2.18 Ga global mafic magmatism. *J. Asian Earth Sci.* 191, 104221. doi:10.1016/j.jseaes.2019.104221

Yokoyama, T., Makishima, A., and Nakamura, E. (1999). Evaluation of the coprecipitation of incompatible trace elements with fluoride during silicate rock dissolution by acid digestion. *Chem. Geol.* 157 (3-4), 175–187. doi:10.1016/s0009-2541(98)00206-x

frontiers | Frontiers in Earth Science

TYPE Original Research
PUBLISHED 09 May 2023
DOI 10.3389/feart.2023.1118520

OPEN ACCESS

EDITED BY
Stanislaw Mazur,
Institute of Geological Sciences, Polish Academy of Sciences, Poland

REVIEWED BY
Sreehari Lakshmanan,
Shimane University, Japan
Thembiso O. Basupi,
Botswana International University of Science and Technology, Botswana

*CORRESPONDENCE
Chih-Tung Chen,
chihtung@ncu.edu.tw,
kthomasch@gmail.com

RECEIVED 07 December 2022
ACCEPTED 18 April 2023
PUBLISHED 09 May 2023

CITATION
Lo Y-C, Chen C-T, Lo C-H, Chung S-L and Yeh M-W (2023), Record of short-lived "orogen" on Eurasian continental margin by South China Sea obduction preserved in Taiwan collision.
Front. Earth Sci. 11:1118520.
doi: 10.3389/feart.2023.1118520

Record of short-lived "orogen" on Eurasian continental margin by South China Sea obduction preserved in Taiwan collision

Yun-Chieh Lo[1], Chih-Tung Chen[2]*, Ching-Hua Lo[1], Sun-Lin Chung[1,3] and Meng-Wan Yeh[4]

[1]Department of Geosciences, National Taiwan University, Taipei, Taiwan, [2]Department of Earth Sciences, National Central University, Taoyuan, Taiwan, [3]Institute of Earth Sciences, Academia Sinica, Taipei, Taiwan, [4]Department of Earth Sciences, National Taiwan Normal University, Taipei, Taiwan

The Taiwan mountain belt is the result of an arc-continent collision following the total subduction of the South China Sea and subsequent closure of the Luzon forearc, a process important in the accretionary growth of continents. Due to the oblique convergence, the southern tip of Taiwan Island is experiencing incipient collision, which is key to observing the oceanic-continental subduction transition. Within the monotonous turbidite extensively exposed on the Hengchun Peninsula as an uplifted Manila Trench accretionary wedge, the Shihmen Conglomerate, as a few intercalated lenses of coarse mafic pebbles, represents a dramatic change in sediment provenance and the causal tectonic event. New zircon U-Pb and amphibole $^{40}Ar/^{39}Ar$ ages are obtained from sediments, including sands and mafic pebbles that are either gabbro or foliated amphibolite. The 22–24 Ma zircon crystallization ages confirm the South China Sea origin of the mafic clasts, while the much younger 13 ± 2 Ma amphibole $^{40}Ar/^{39}Ar$ isochron ages from foliated amphibolites suggest a later thermal-tectonic event other than seafloor metamorphism. The amphibole $^{40}Ar/^{39}Ar$ ages overlap with the biostratigraphic age (~11–14 Ma), indicating that the mafic source rocks were exhumed and eroded in a high-relief topography immediately after metamorphism. Detrital zircon U-Pb ages from a sandy layer within the conglomerate are also mostly identical to those from the mafic pebbles. Since the paleocurrent of the Shihmen Conglomerate was similar to that of the neighboring turbidites, which were derived from major rivers draining the southeastern Chinese continent, the provenance of the mafic pebbles and sands was best explained as an isolated subaerial mountain on the Eurasian continental margin with a very limited temporal and spatial extent, as the detrital products are poorly distributed. The most likely cause of the ephemeral mountain was the obduction of the South China Sea onto the Eurasian continental margin when the latter first impinged on the Philippine Sea Plate at the Manila Trench, where the gabbroic oceanic crust was uplifted and exhumed, followed by dynamic metamorphism along the basal thrust.

KEYWORDS

Eurasian continental margin, South China Sea, Taiwan mountain belt, ophiolite obduction, zircon U-Pb dating, $^{40}Ar/^{39}Ar$ dating

1 Introduction

Arc-continent collisions are an integral part of the accretionary growth of continents (Sengor et al., 1993; Jahn et al., 2000) and have crucial and varying effects on the tectonic evolution of continental margins (Ryan and Dewey, 2019). One of the key questions is how an initially subducted continental margin can affect the state and configuration of the subduction zone and the overall convergent plate boundary, as increased roughness of the subduction interface is known to heighten the friction of the subduction megathrust (Lallemand et al., 2018; Tan et al., 2022). Coupling changes along the subduction interface may propagate laterally or across the ocean basin to influence continent-ocean transition (COT) tectonics, including faulting and ophiolite obduction (Searle et al., 2022). Within the complex geodynamics of the Indo-Pacific and eastern Eurasia region, the active Taiwan mountain belt serves as a natural laboratory for studying arc-continent collision processes (Byrne et al., 2011) under a well-defined tectonic framework (Figure 1, inset) that allows synchronous observation of orogenesis from initiation in the south to the final stage in the north due to oblique convergence (Suppe, 1988). Near the southern end of the island, the uplifted accretionary wedge as the Hengchun Peninsula sits on the transition from oceanic subduction to collision (Shyu et al., 2005; Figure 1); the tectonic regime change is documented in local geological structures (Chang et al., 2003) and may also be reflected in sedimentological variations within the off-scraped South China Sea marine sequence. One such anomaly is the occurrence of puzzling conglomerates composed almost exclusively of coarse mafic pebbles (Chen et al., 1985; Sung, 1991), indicating the presence of former ophiolitic mountain ranges in the periphery of the South China Sea (Pelletier and Stephan, 1986). How such a transient "mountain building" event was generated would shed light on the impact of continental subduction on the subduction zone dynamics and tectonic evolution of the COT and is therefore worthy of detailed investigation.

The Taiwan mountain belt is the result of active oblique convergence between the Eurasian and Philippine Sea plates (Suppe, 1988; Teng, 1990) and began with subduction of the Eurasian continental margin along the Manila Trench followed by the collision of the Luzon Arc (Malavieille et al., 2002) (Figure 1, inset). Prior to the orogeny at ~15 Ma (evidenced by the onset of Luzon Arc volcanism; Song and Lo, 2002; Lai et al., 2018), the Manila Trench began to receive the South China Sea, which was formed along slowly spreading ridges (Chung and Sun, 1992) from ~37 to 15 Ma (Briais et al., 1993; Yeh et al., 2010). The Hengchun Ridge formed above the trench is an accretionary prism composed of the fault-folded South China Sea marine sequence and becomes larger and subaerial as the Hengchun Peninsula in the north, where the South China Sea is completely consumed and the continental margin enters the subduction zone. The exposed Late Miocene pelagic turbidite sequence accreted to the accretionary wedge is collectively termed the Mutan Formation, and lenses of meta-mafic conglomerates are found intercalated in its lower part and called the Shihmen Conglomerate (Chen et al., 1985; Figure 1).

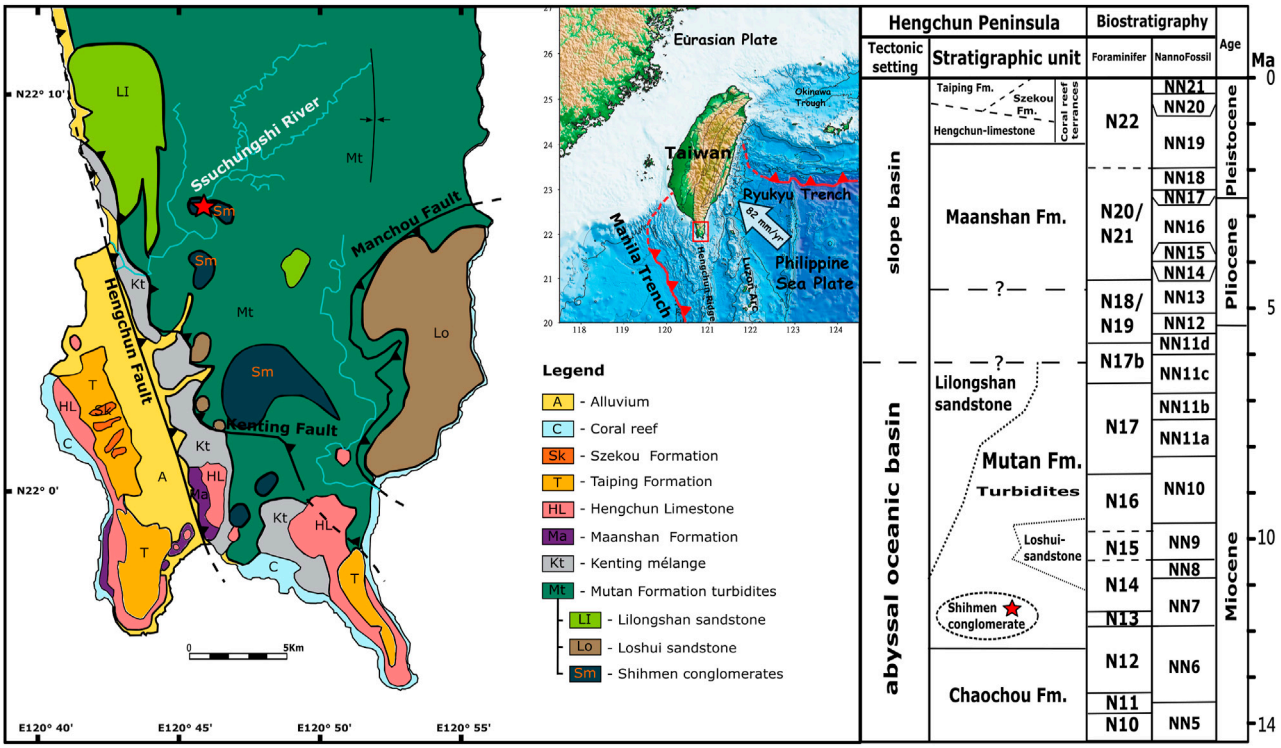

FIGURE 1
Geological map of the Hengchun Peninsula and tectonic framework of Taiwan. The red star marks the outcrop of the Shihmen Conglomerate along the Sschungchi River. The geologic map and stratigraphic column were modified from Sung (1991) and Zhang et al. (2014). Biostratigraphic ages are from Denne (2017).

How these rounded and well-sorted, sometimes intensely foliated mafic pebbles were generated and deposited in the deep basin of the northern South China Sea has intrigued researchers with hypotheses including an emergent oceanic crust (Page and Lan, 1983; Zhang et al., 2022), a reworking of obducted ophiolites (Pelletier and Stephan, 1986), temporary uplift and collapse of seamounts (Tian et al., 2019) or eastward deep-water transport (Cui et al., 2021; Meng et al., 2021). A crucial missing key to resolving the provenance and tectonic origin of the Shihmen Conglomerate lies in exact chronological constraints on the formation and metamorphism of the gabbroic protolith and is addressed here by applying zircon U-Pb dating analysis for both pebbles and matrix sands and amphibole $^{40}Ar/^{39}Ar$ dating analysis for foliated amphibolitic meta-gabbro pebbles. The acquired ages are incorporated into the local stratigraphic and tectonic framework, suggesting a temporary fringe mini-orogen resulting from the South China Sea obduction onto the Eurasian continental margin in response to the incipient collision of the Manila subduction system to the north, where the Taiwan orogen initially began.

2 Geologic setting and sample description

The Hengchun Peninsula at the southernmost tip of Taiwan Island represents the youngest segment of the orogenic system due to the oblique plate convergence (Suppe, 1988; Shyu et al., 2005; Figure 1, inset). Fault-folded Late-Miocene turbidites of the Mutan Formation with N-S structural grains (Sung, 1991; Chang et al., 2003; 2009a) comprise the main hilly terrane of the peninsula as a southern extension of the Backbone Range, and are bounded to the west and southwest by the Kenting mélange, a paleo-subduction channel relict of the Manila Trench (Lu and Hsu, 1992; Chang et al., 2003; Figure 1). Both the Mutan Formation and the Kenting mélange outcrop east of the active sinistral-reversal Hengchun Fault; the small plain of the Hengchun Basin in the immediate footwall and the uplifted West Hengchun Tableland of Quaternary limestone reefs further west make up the rest of the peninsula (Figure 1), demonstrating westward propagation of the trench/deformation front and widening and thickening of the accretionary wedge (Chang et al., 2003; Lin et al., 2009). To the north, further exhumation leads to exposure of the slate Lushan Formation, the low-grade metamorphosed pelagic South China Sea deposits, in the Backbone Range (Chen et al., 1983; Beyssac et al., 2007).

The Mutan Formation is composed of deep-sea fan turbidite sequences with shale-sandstone alternations (Hu and Tsan, 1984; Figure 1) of planktic foraminiferal biozones N14–17 (Chang, 1964) and southeastern mainland China continent provenance as indicated by sandstone lithology, paleocurrent, and detrital zircon dating data (Pelletier and Stephan, 1986; Chang et al., 2003; Zhang et al., 2014; Tsai et al., 2020). Several lenticular bodies of coarser deposits, including the Shihmen Conglomerate, Lilongshan Sandstone, Shihtzutou Sandstone, and Loshui Sandstone, are intercalated within the Mutan turbidite as products of major submarine channels draining from the slope of the Chinese continental margin (Pelletier and Stephan, 1986; Sung, 1991; Chang et al., 2003). While the Mutan turbidite and the other lenticular units are of continental provenance, the Shihmen Conglomerate stands out with dominant rounded mafic clasts including gabbro, basalt and diabase, and foliated amphibolite, supplemented by minor granitic gneiss, siliceous schist, quartz vein and marble/limestone, representing erosional products of emergent oceanic crust (Page and Lan, 1983). The age of deposition of the Shihmen Conglomerate has been constrained at ~11–14 Ma from biostratigraphic records (NN6; Chi, 1982; ~N14; Sung, 1991). Previous attempts to date mafic pebbles from the Ssuchungshi Gorge outcrop of the Shihmen Conglomerate have all yielded early Miocene results, including K-Ar dating of amphibolite amphiboles (22–23 Ma, Pelletier and Stephan, 1986) and zircons from both gabbro (23.78 ± 0.41, Meng et al., 2021; 23.73 ± 0.69 Ma; Cui et al., 2021) and amphibolite (24.2 ± 1.1 Ma, Tian et al., 2019) pebbles, within the age range of the South China Sea spreading. Therefore, the Shihmen Conglomerate signified a dramatic change in the provenance environment along the Eurasian continental margin, such as an obduction event (Pelletier and Stephan, 1986), while others speculated that the site of obduction was the accretionary wedge (Page and Lan, 1983) or rifted continental sliver (Suppe, 1988) along the southeastern side of the South China Sea.

The most accessible outcrop of the Shihmen conglomerate is along the Sschungchi River at the ancient Shihmen ("Rock Gate") battlefield. The sampled roadside outcrop (E 120.76118, N 22.11190) is about 40 m wide and ~100 m high, exposing sub-vertical conglomerate beds that trend NW-SE and dip steeply to the west, consistent with the neighboring Mutan turbidite (Figures 2A,B). The conglomerate content is dominated by rounded and sub-rounded pebbles of gabbro and foliated amphibolite and minor siliceous and chloritic schist and quartz vein; pebble diameters vary from 1 to 15 cm and sometimes reach ~30 cm (Figure 2C). Coarse sands make up the matrix in addition to occasional concordant sandstone beds (Figure 2D). To unravel the tectonic characteristics of the provenance, foliated amphibolite pebbles, plutonic gabbro pebbles, and sands from the intercalated sandy layer (Figures 2C–E) were sampled for zircon U-Pb and amphibole $^{40}Ar/^{39}Ar$ dating analyses. The ages obtained were then correlated with regional seafloor spreading and plate convergence histories for a comprehensive geodynamic interpretation.

Sample 1202A is a collection of more than 5 kg of fresh, sub-rounded, foliated amphibolite pebbles 10–20 cm in diameter collected from the conglomerate outcrop. The sampled pebbles exhibit strong penetrating amphibolitic foliation with mm-thick repeating amphibole and plagioclase bands throughout or in part of the pebbles (Figure 2E). Under the microscope, the cleavage domain is mainly composed of smaller (lengths less than 300 μm) aligned amphibole grains with minor opaques, and the adjacent plagioclase layers are of larger grain size (up to 0.5 mm in diameter) with twinning and interlobular boundaries (Figure 3A). Ductile shear deformation during recrystallization is evident in the metamorphic paragenesis of lineated amphiboles and the interlobate recrystallizing (grain boundary migration) plagioclase grains (Figure 3A) and may have persisted into post-recrystallization brittle-ductile states as evidenced by albite twinning in plagioclase (Figure 3A). The protolith of the

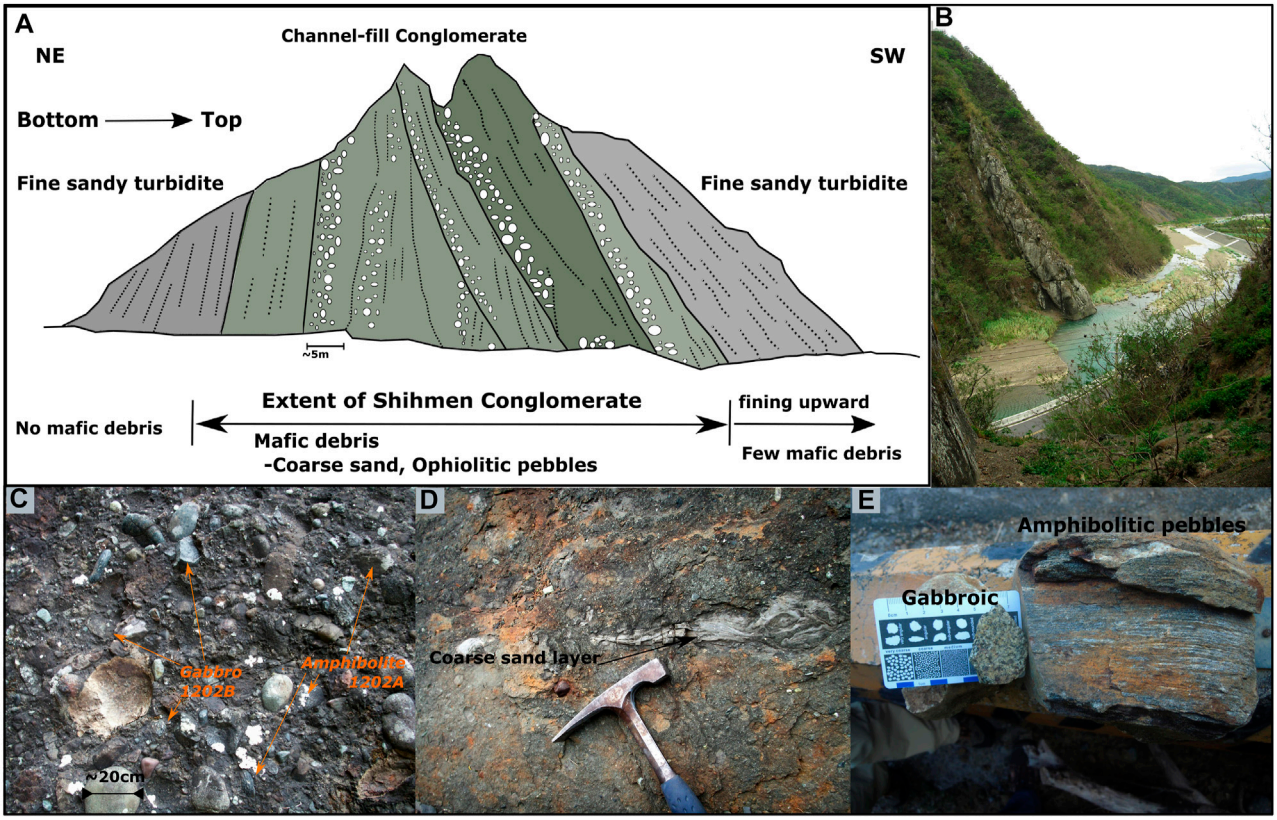

FIGURE 2
Field observations of the Shihmen Conglomerate: **(A)** Sketch of the outcrop of the Shihmen Conglomerate across the Sschungchi River from the sampled roadside outcrop, showing conglomerate layers composed of Few mafic pebbles/ophiolitic sands and pebbles conformably intercalated into mid-late Miocene turbidites of the Mutan Formation; **(B)** Photo of the outcrop illustrated in **(A)**; **(C)** Close-up photo of the conglomerate formation, field of view ~1 m; **(D)** concordant sandy layer within the conglomerate formation; **(E)** samples of plutonic gabbro and foliated amphibolite pebbles from the conglomerate formation.

foliated amphibolites is probably gabbro, as some of the pebbles preserve relict pyroxene (Figure 3A) and display plutonic texture where not foliated, as indicated by geochemical analyses (Page and Lan, 1983; Pelletier and Stephan, 1986). Both zircon and amphibole are separated for dating analyses.

Sample 1202B is a collection of more than 5 kg of fresh, sub-rounded gabbro pebbles, 10–20 cm in length, collected from the conglomerate outcrop (Figure 2C). The pebbles exhibit a phaneritic plutonic texture with interlocking euhedral tabular plagioclase crystals and mostly anhedral pyroxene grains (Figure 3B). Some of the pyroxene grains have been substituted by amphibole, but the replacement is rather minor and does not yield sufficient amphibole grains for $^{40}Ar/^{39}Ar$ dating analysis. Zircon is extracted for U-Pb dating to determine the crystallization age of the gabbro, which indicates the timing of ocean crust formation.

Sample 1202C is a sandstone sample from a ~20 cm-thick concordant sandy layer within the conglomerate (Figure 2). The medium-coarse sandy layer is monotonous without pebbles or grading texture and consists of 0.1–1 mm rounded grains of mostly greenish mafic clasts (Figure 3C). Zircon is separated for U-Pb ages to resolve the provenance of the sandy deposits.

3 Geochronological analyses

3.1 U-Pb dating

Zircons from each sample were separated using conventional magnetic and heavy-liquid methods. After separation, zircon grains with crystal lengths >60–200 μm were linearly mounted with epoxy resin and then polished to expose the interior grains for U-Pb dating. Prior to U-Pb analysis, cathodoluminescence (CL) images were taken at the Institute of Earth Sciences, Academia Sinica, Taiwan. CL pictures help to locate analytical spots by examining the internal structures of individual zircon grains and avoiding inclusions during analysis. *In-situ* laser ablation inductively coupled plasma mass spectrometry (LA-ICP-MS) U-Pb dating was performed using an Agilent 7500s quadrupole ICP-MS coupled with a 193 nm Analyte G2 excimer laser ablation system housed at the Department of Geosciences, National Taiwan University. The beam size of the laser ablation pits is ~30 μm in diameter. Measured U-Th-Pb isotope ratios were calculated using the GLITTER 4.4 (GEMOC) software, and calibration was performed using the zircon standard GJ-1 aged at 608.5 ± 0.4 Ma (Jackson et al., 2004). Zircon 91,500 (1065 ±

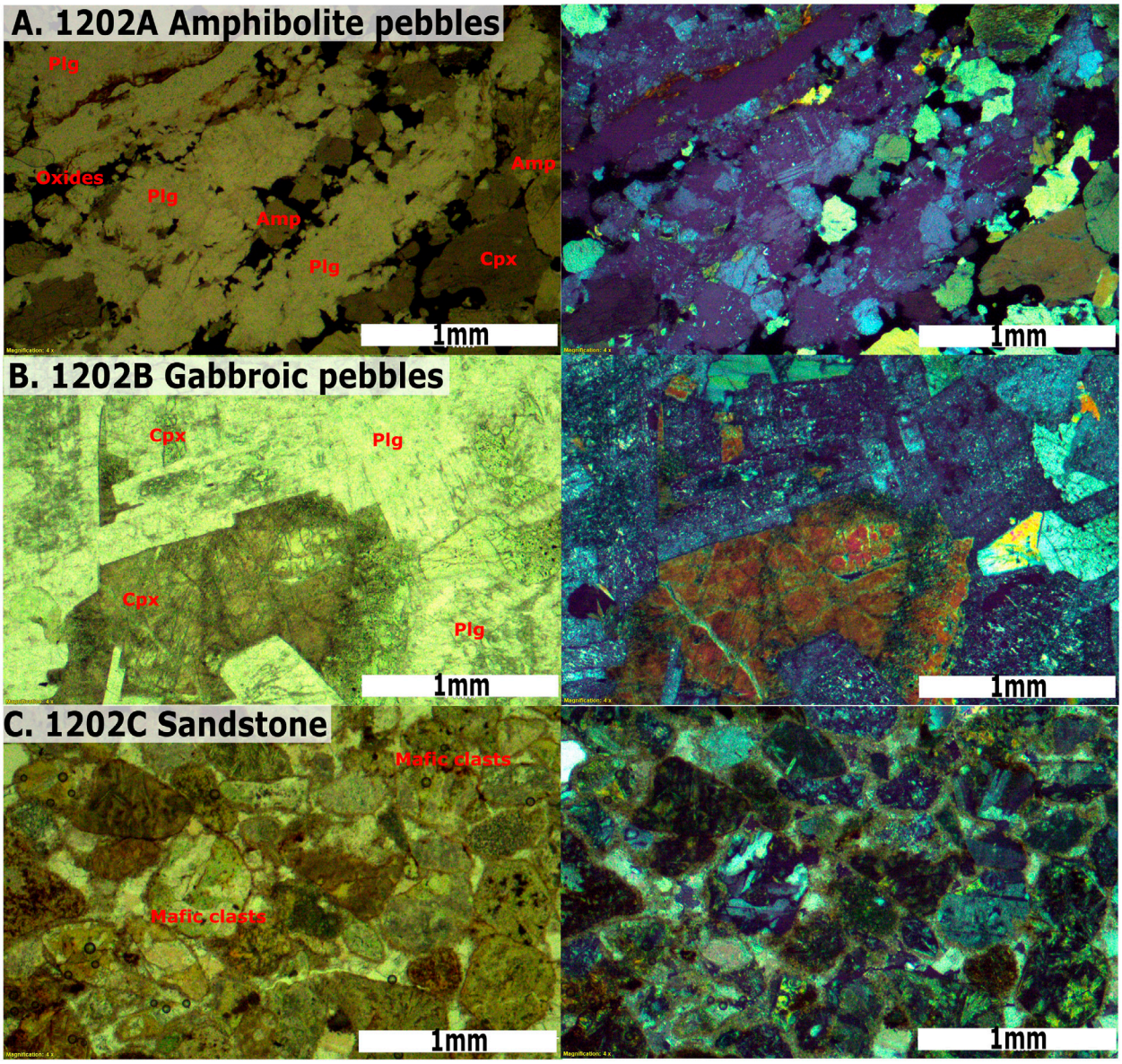

FIGURE 3
Photomicrographs of the analyzed samples (planar and cross-polarized light for the left and right, respectively): **(A)** Foliated amphibolite pebbles (sample 1202A); **(B)** Gabbroic pebbles (sample 1202B); **(C)** Sandstone (sample 1202C) from a concordant sandy layer within the conglomerate composed of coarse sub-rounded mafic clasts. The white scale bar is 1 mm in length. Plg: plagioclase; Amp: amphibole; Cpx: clinopyroxene; Qtz: quartz.

0.4 Ma; Wiedenbeck et al., 1995) and Plešovice (337.1 ± 0.4 Ma; Sláma et al., 2008) were analyzed as secondary standards for data quality control in each analysis cycle. Operating conditions and analytical procedures followed (Chiu et al. 2009). Common lead in zircons was corrected with the lead correction function proposed by Andersen (2002), and weighted mean U-Pb ages and Concordia plots were then conducted using Isoplot 4.15. (Ludwig, 2008). For U-Pb ages <50 Ma, $^{206}Pb/^{238}U$ ages are chosen without consideration of concordance due to the low U concentration of mafic samples and the imprecision of ^{207}Pb measurements for such young zircons using the LA-ICPMS method (Gehrels et al., 2008; Spencer et al., 2016).

3.2 $^{40}Ar/^{39}Ar$ dating

For $^{40}Ar/^{39}Ar$ dating, samples and standards were cleaned with an ultrasonic bath in acetone, alcohol, and deionized water, respectively, and then dried. Approximately 250 mg of amphibole separated from amphibolite pebbles was packaged and irradiated along with standards in the VT-C position of the Tsing-Hua Open-Pool Reactor (THOR) at Tsing-Hua University, Taiwan. Fish Canyon Sanidine (FCs) standard of 28.10 ± 0.04 Ma (Spell and McDougall, 2003) was used to monitor the neutron flux, and the J-value of 0.0047937 ± 0.000025 at the 1-sigma level was obtained from the analyses of FCs adjacent to the sample.

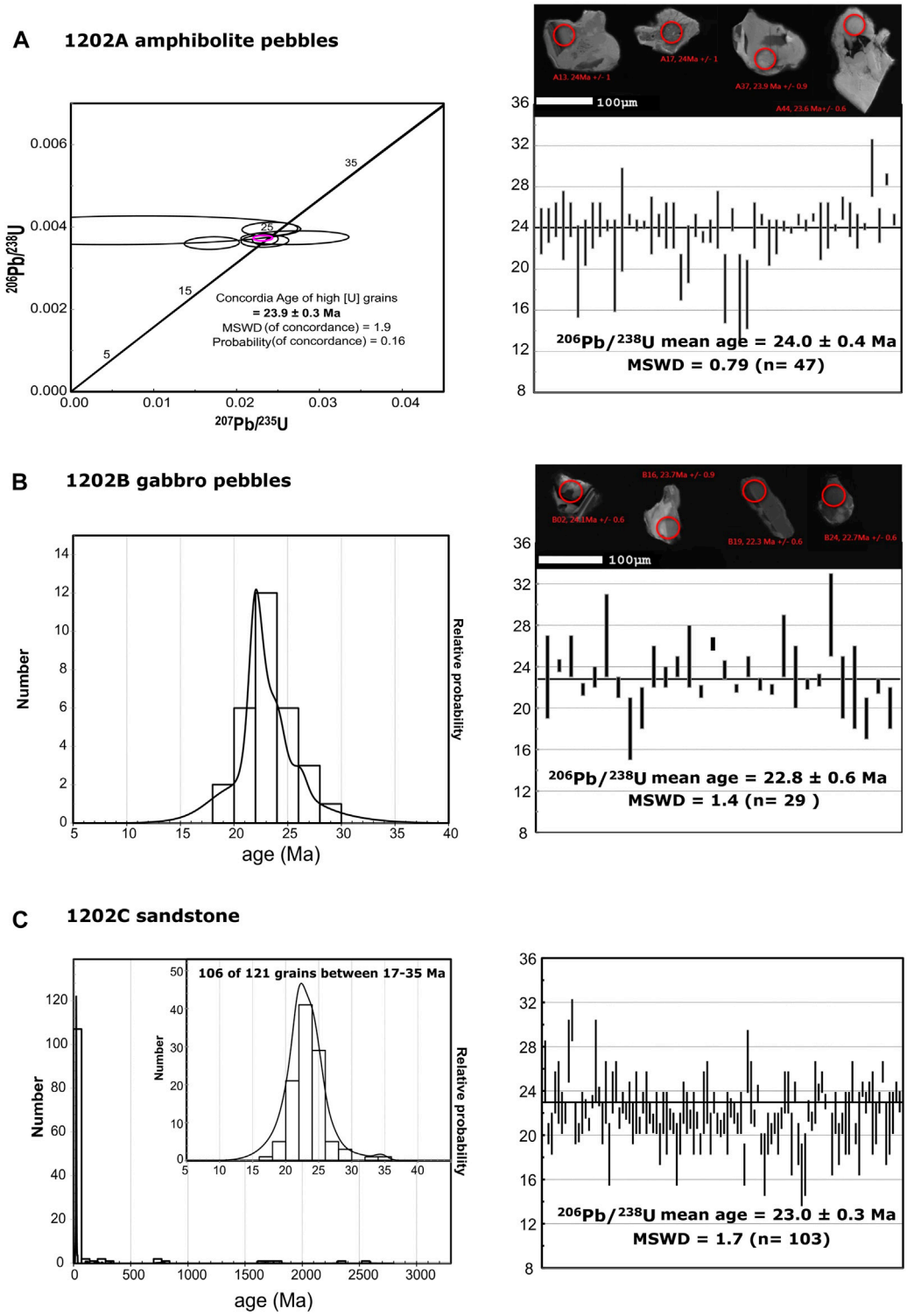

FIGURE 4
Zircon U-Pb dating results: **(A)** Sample 1202A of amphibolite pebbles yields a weighted mean age of 24.0 ± 0.4 Ma, shown in the red circle; **(B)** $^{206}Pb/^{238}U$ ages of sample 1202B of gabbroic pebbles fall between 18 and 29 Ma with a weighted mean age of 22.8 ± 0.6 Ma; **(C)** 88% of the detrital zircons in the concordant sandy layer of sample 1202C show $^{206}Pb/^{238}U$ ages of 17–35 Ma with a weighted mean of 23.0 ± 0.3 Ma.

The sample was loaded (without any other sample or standard) into an ultra-high vacuum laser chamber and baked at 150°C for over 24 h to remove atmospheric contamination prior to analysis. Argon was extracted using the single-grain total fusion method with a Synrad 48–1 CO_2 laser fusion system attached to a VG3600 mass spectrometer at National Taiwan Normal

University (NTNU). Before isotopic analysis, the sample gas was purified by a Ti-sponge for 3 min and then by two getters (one kept at 450 C and the other at room temperature) for 5 min to remove active gases (e.g., CO_2, H_2O, CH_4). Detailed instrumental and analytical procedures are outlined in Lo et al. (2002). Data processing, including peak intensity regression and corrections for blanks, mass spectrometer discrimination, isotopic decay, and neutron-induced interference reactions, was performed using the ArArCALC software of Koppers (2002). The atmospheric argon ratio of 298.56 ± 0.31 was suggested by Lee et al. (2006). Isochron and weighted mean age re-statistics were obtained using IsoplotR (Vermeesch, 2018). Uncertainties in ages were reported as one standard deviation, taking into account errors in J-values, standard mineral ages, and isotopic interference factors.

3.3 Dating results

3.3.1 U-Pb zircon geochronology

Zircons from the foliated amphibolite pebbles (1202A) appeared as transparent and colorless, occurring as truncated to prismatic crystals with sharp facets and some rounded terminations. Grain lengths ranged from ~100 to 300 μm with aspect ratios ranging from 1:1 to 3:1. A total of 51 zircon grains were analyzed and the U-Pb age results were concentrated in the 21–25 Ma interval, yielding a weighted mean age of 24.0 ± 0.4 Ma (MSWD = 0.79, n = 47), with high U-content grains that could have a Concordia age of 23.9 ± 0.3 Ma (MSWD = 1.9) (Figure 4A, and Supplementary Table S1 for detailed data). Most zircon crystals showed oscillatory zoning, but only one large zircon grain was found possessing a 34 Ma inherited core and a 23.8 Ma rim overgrowth; no other inherited cores or visible rim growth were found. Uranium concentrations in the zircons range from 20 to 1847 ppm, with most grains <200 ppm. The younger cluster had a lower U content and higher age uncertainty. All analyses yielded Th/U values >0.1 (0.19–1.38) implying a magmatic origin for all dated zircons (Williams and Claesson, 1987; Vavra et al., 1996; Hoskin and Black, 2000; Hartmann and Santos, 2004).

Zircons from gabbroic pebbles (1202B) appeared as euhedral to subhedral, generally colorless and transparent, and equivalent to long columnar grains with lengths of ~80–200 μm and aspect ratios ranging from 4:1 to 1:1. All U-Pb dating results fall between 18 and 29 Ma with a single major peak and a weighted mean age of 22.8 ± 0.6 Ma (MSWD = 1.4) (Figure 4B; Supplementary Table S2). The wide range of U contents (30–1942 ppm) with all Th/U values >0.1 (0.16–1.61) also suggested a magmatic origin of zircon crystallization.

A total of 121 zircon grains, ranging in length from ~50 to 250 μm, were recovered from the sandstone (1202C). Most of the U-Pb dating results fell in the 17–34.5 Ma age range (106 of 121, 88%) with a weighted mean age of 23.0 ± 0.3 Ma (MSWD = 1.7, n= 103), and the remainder had ages ranging from 100 to 2600 Ma (14 of 121, 12%) (Figure 4C; Supplementary Table S3). Most grains yielded ages in the 17–34.5 Ma age range and exhibited low uranium contents of <150 ppm, with Th/U values >0.1 (0.05–1.89, only 2 grains <0.1).

3.3.2 $^{40}Ar/^{39}Ar$ amphibole geochronology

Amphiboles from the foliated amphibolite pebbles (1202A) yielded apparent $^{40}Ar/^{39}Ar$ ages between 10.8 and 24.3Ma with a weighted mean age of 14.9 ± 0.7Ma for the main cluster (Figure 5B; Supplementary Table S4), while the uncertainty for individual analyses was high, up to ~20%, due to the low K content and high Ca/K ratios. Excess argon was found in a few analyses of apparent ~24 Ma results, so the inverse isochron age of 13.3 ± 2.0 Ma with a $^{40}Ar/^{36}Ar$ intercept of 302.0 ± 4.1 from the younger main cluster was preferred (Figure 5B).

4 Discussion

4.1 Provenance of sediments

To determine how the ophiolite-dominated Shihmen Conglomerate was intercalated with pelagic turbidites from the South China Sea, the provenance properties of the pebbles have to be investigated. The data reported here can elucidate key provenance characteristics of the pebbles, such as the parent rock affinities, formation ages, and thermal-metamorphic history for amphibolitic clasts. Both plutonic gabbro and foliated amphibolite pebbles yielded similar U-Pb zircon crystallization ages of 22–24 Ma (Figures 4A,B), indicating that the dated gabbro was the protolith of the foliated amphibolites. The age results are consistent with geochemical analyses indicating a common ocean ridge tholeiite origin for both the gabbroic and amphibolite clasts (Page and Lan, 1983; Pelletier and Stephan, 1986). The gabbro crystallization age is similar to that reported by Wang et al. (2012) and falls within the time span of South China Sea spreading (~37 - ~15 Ma; Taylor and Hayes, 1983; Briais et al., 1993; Yeh et al., 2010), therefore the South China Sea crust should be the common source of these mafic materials since the oceanic crust of the westernmost Philippine Sea plate has been interpreted as either Eocene (~50–~40 Ma: Karig et al., 1975; Sibuet et al., 2002) or Cretaceous (~130–~120 Ma: Deschamps et al., 2000; Queano et al., 2007), ruling out the upper Manila Trench plate as a possible source. The dating results are also consistent with previous attempts to analyze these mafic pebbles (Pelletier and Stephan, 1986; Tian et al., 2019; Cui et al., 2021; Meng et al., 2021), and they also concur with the paleocurrent analyses pointing to Eurasian-side sources instead of the overriding plate (Chang et al., 2003).

4.2 Metamorphism of the amphibolite pebbles

The cause of metamorphism on the foliated amphibolite could be inferred from the $^{40}Ar/^{39}Ar$ amphibole ages. Since the turbidite sequence exposed on the Hengchun Peninsula is not metamorphosed with a maximum peak temperature <200°C as suggested by vitrinite reflectance constraints (Zhang et al., 2016), the K-Ar isotope system of amphibole, with much higher closure temperatures (~490–578°C, Harrison, 1982), must have remained closed during subduction to accretionary wedge stages. The obtained isochron age of 13.3 ± 2.0 Ma, roughly 10 million years younger than the gabbro crystallization age from zircon U-Pb dating, also rules out

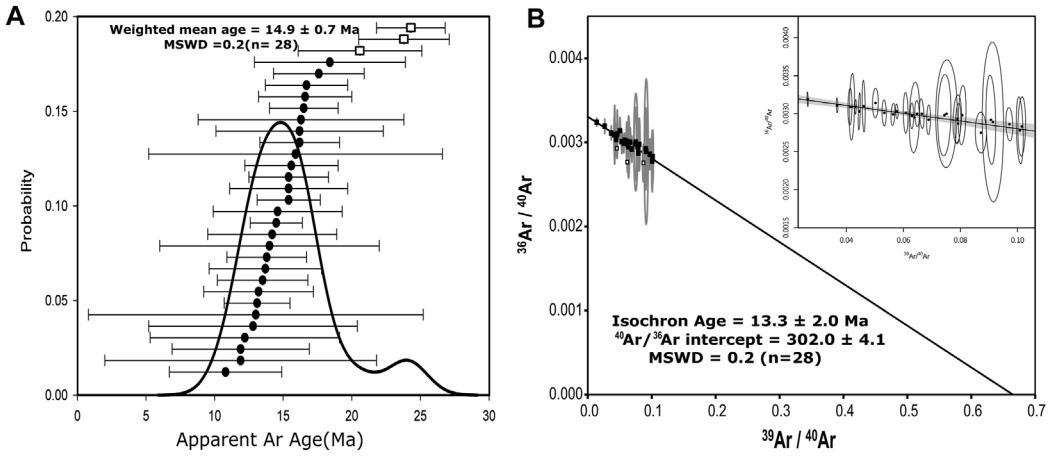

FIGURE 5
Results of laser-fusion $^{40}Ar/^{39}Ar$ dating for amphibole from sample 1202A foliated amphibolite pebbles: **(A)** Distribution of apparent ages showing a main cluster (excluding those in the square) with a weighted mean age of 14.9 ± 0.7 Ma; **(B)** inverse isochron plot yielding a $^{40}Ar/^{39}Ar$ intercept age of 13.3 ± 2.0 Ma with a $^{40}Ar/^{36}Ar$ initial value of 302.0 ± 4.1 for the main cluster. The inset displays the data distribution in detail.

sub-seafloor metamorphism as the main source, which typically occurs immediately after oceanic lithosphere formation along mid-ocean ridges with proximal heating and generally produces extensive veining and sulfide deposits indicative of intense fluid-rock interactions (Frost and Frost, 2014). The foliated amphibolite pebbles are mostly vein-free and exhibit significant ductile shearing as the aligned amphibole crystals and dynamically recrystallizing albite grains (Figures 3A,B), which is characteristic of tectonic deformation along the major shear zone rather than metasomatic seafloor metamorphism. The $^{40}Ar/^{39}Ar$ amphibole ages record either amphibole paragenesis of both metamorphism and shearing or cooling during the subsequent exhumation. These would indicate that part of the 22–24 Ma gabbroic oceanic crust that is the source of the Shihmen Conglomerate must have been dynamically metamorphosed at ~13 Ma or slightly earlier.

4.3 Tectonic implications

The occurrence of both gabbro and foliated amphibolite as rounded pebbles up to boulder sizes, together with other mafic clasts, indicates that a portion of the South China Sea crust was not only subaerial but must have possessed high relief to generate the torrential dumping of these coarse deposits into the South China Sea basin (Pelletier and Stephan, 1986). Detrital zircon U-Pb ages from the concordant sandy interlayer (23.0 ± 0.3 Ma, Figure 4C) are almost identical to those from the gabbroic (22.8 ± 0.6 Ma, Figure 4B) and foliated amphibolite pebbles (24.0 ± 0.4 Ma, Figure 4A), demonstrating that this ophiolitic source of the South China Sea ages produced both coarse pebbles and sands. The mafic magmatic origin of the dated zircon crystals from both pebbles and sandstones is also indicated by the low U content, which is mostly less than 100 ppm or even less than 10 ppm. The age spectrum of the Shihmen sands contrasts dramatically with normal sandstones of the Mutan Formation (Figure 6A) which are dominated by various pre-Cenozoic zircon populations of the southeastern Chinese continent, including Yenshanian (200–65 Ma), Indosinian (250–200 Ma) and Luliangian (1900–1700 Ma) ages, with extremely rare Tertiary (<50 Ma) results (Zhang et al., 2014; Tsai et al., 2020). The turbidite layers adjacent to or in the periphery of the Shihmen deep-sea fan yield zircon populations (Figure 6B; Tsai et al., 2020; Meng et al., 2021) as diluted mixtures between Shihmen sands (Figure 6C) and normal Mutan sands (Figure 6A). Taking into account the inference from paleocurrent analyses that the sediment transport and source directions for the entire Mutan Formation were from the southeastern Chinese continent (Chang et al., 2003), the provenance of the Shihmen Conglomerate would be an ephemeral isolated rugged mountain composed exclusively of South China Sea ophiolite on the Eurasian continental margin, and the sediment routing system would be separated from the major rivers and their offshore extensions that drained the other common Mutan turbidites (Figure 7B). The tentatively postulated short-lived mountain building was most likely an obduction of the South China Sea crust onto the Eurasian continental margin at ~13 Ma (Figure 7B); the lower-crustal gabbroic rocks along and near the basal thrust were dynamically recrystallized to foliated amphibolite in a metamorphic sole-like fashion (Searle et al., 2022; profile B-2 in Figure 7B) in the hanging-wall; both the upthrust gabbro and amphibolite, with minor other mafic lithologies, created a high-relief topography and delivered coarse detritus eastward to form deep-sea channel and fan turbidite deposits that are intercalated with normal Mutan sediments during the mid-Miocene at ~11–13 Ma (Sung, 1991, profile B-2 in Figure 7B). Another possibility is that the amphibolite was generated during subduction metamorphism of the South China Sea slab, and a portion of it was extruded back into the shallow crust and amalgamated with the obducting ophiolite sequence. The predominance of gabbroic lithologies in the pebbles may be due to the slow-spreading nature of the South China Sea crust (Chung and Sun, 1992; Briais et al., 1993).

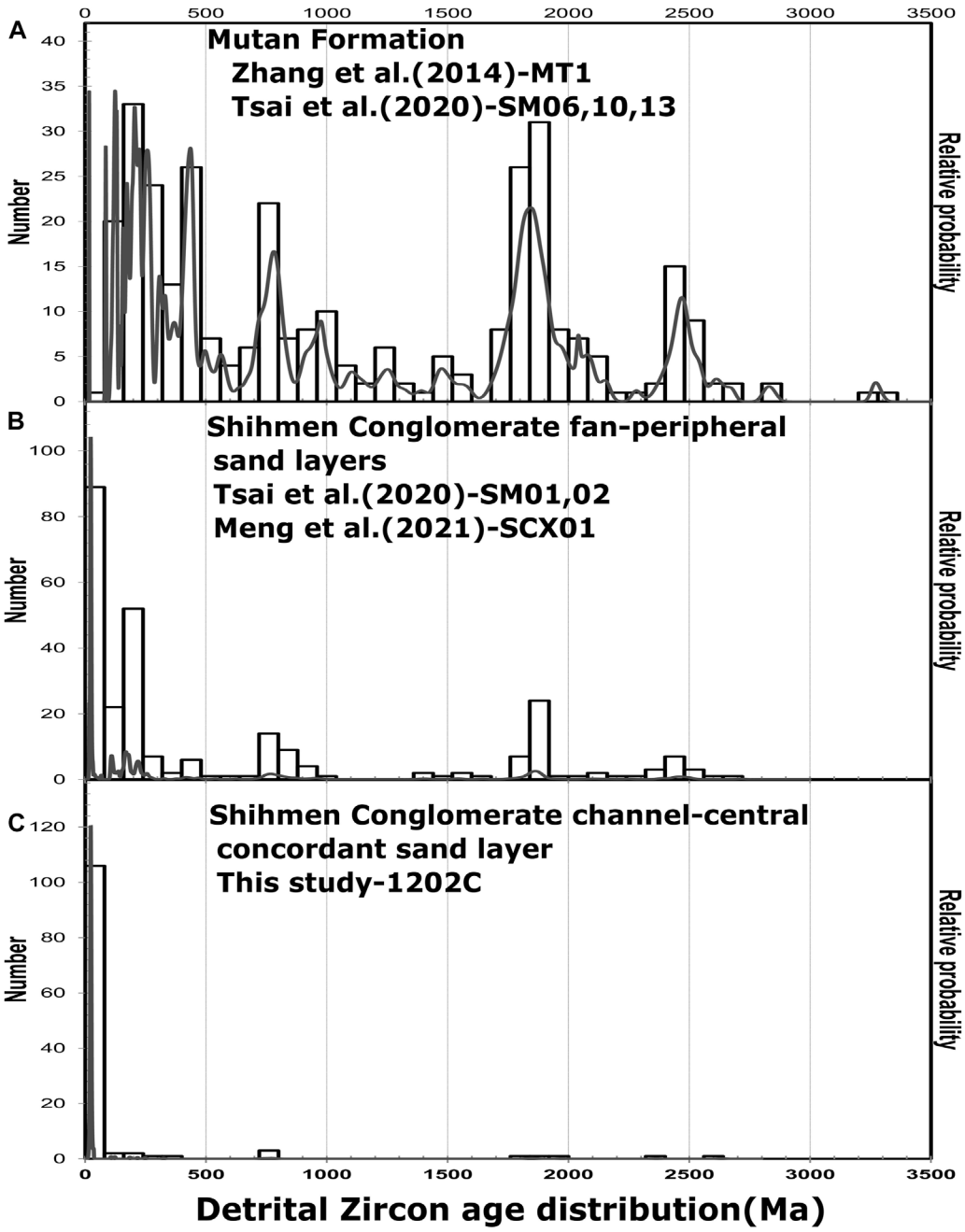

FIGURE 6
Detrital zircon age distribution diagrams for **(A)** common South China Sea turbidite sandstone of the Mutan Formation (Zhang et al., 2014; Tsai et al., 2020); **(B)** Turbidite sandstone adjacent to the Shihmen Conglomerate (Tsai et al., 2020; Meng et al., 2021); and **(C)** sandy layer within the Shihmen Conglomerate of sample 1202C.

The mechanism of the brief South China Sea obduction proposed above can be elucidated by the temporal relationships with tectonic events in the Manila subduction system and the Taiwan collisional orogeny. Immediately after seafloor spreading, the South China Sea was subducted under the Philippine Sea Plate along the Manila Trench since at least 15 Ma, as evidenced by the earliest arc magmatism (Lai et al., 2018; Figure 7A). The first continental subduction at the Manila Trench, which probably took place near present-day northern Taiwan due to the oblique configuration between the trench and the COT (Suppe, 1988; Figure 7B), was estimated to be around 13 Ma (Chen et al., 2019) and was likely 11–9 Ma in central Taiwan, as inferred from the onset of blueschist retrograde cooling (Lo and Yui, 1996; Lo et al., 2020). The date of the obduction in question was close to these estimates of the initial impingement of the continent on the Manila Trench, which would induce major changes in the mechanical boundary conditions of the plate boundary (Malavieille and Trullenque, 2009) to cause the

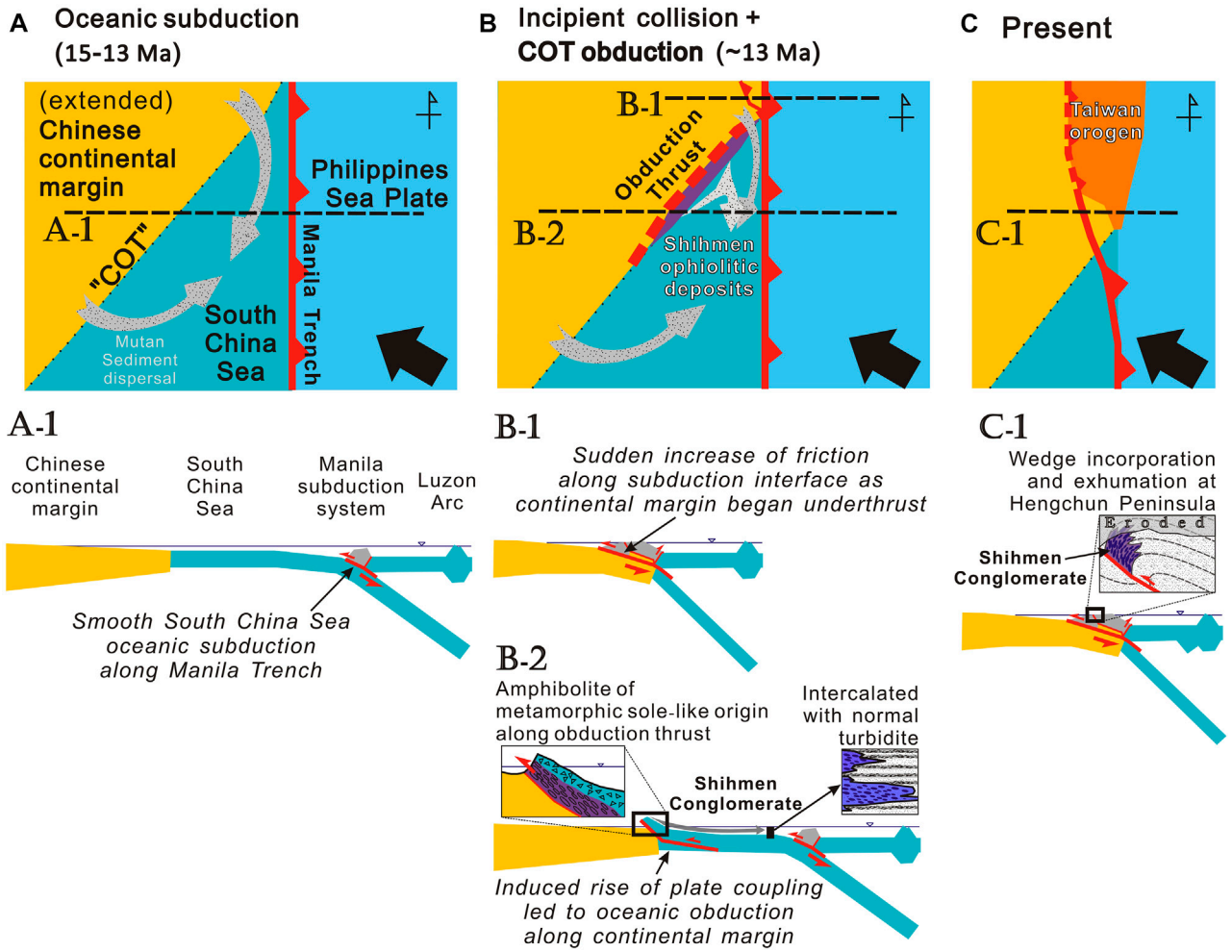

FIGURE 7
Conceptualartoon depicting the tentative tectonic evolution of the Manila subduction system **(A)** before and **(B)** after the initial impingement of the Chinese continental margin at ~13 Ma, and the present configuration **(C)**. Profile A-1: normal oceanic subduction of the South China Sea slab. Profile B-1: initial subduction of the Chinese continental margin in the north, due to the oblique configuration between the trench and COT orientations, leading to a dramatic increase in roughness and friction along the subduction interface and a widening of the deformation zone. Profile B-2: south of the site of impingement of the Chinese continental margin on the Manila Trench, the sudden increase in friction and coupling along the subduction interface induced partitioning of shortening strain within the downgoing plate to the COT, causing obduction of the South China Sea crust onto the continental margin with dynamic metamorphism along the deeper part of the obduction thrust, and deposition of the Shihmen Conglomerate within the South China Sea turbidite sequence. Profile C-1: Shihmen Conglomerate as part of the Mutan Formation was incorporated into the Hengchun Ridge accretionary wedge during Manila subduction and is now exhumed on the Hengchun Peninsula due to the onset of continental subduction at this latitude.

trench jump as the convergent strain was partitioned away from the trench itself (Chang et al., 2009b). Such mechanical transformation lies in the different frictional properties and seismic coupling of the subduction zone and is controlled by the roughness of the incoming seafloor (Lallemand et al., 2018), particularly the presence of cover-basement irregularities such as seamounts (Tan et al., 2022). Greater roughness is expected for the incorporation of continental crust with rugged topography and the cover-basement interface of the continental margin, causing strain partitioning from the subduction interface to a larger area, eventually leading to mountain building (Chang et al., 2009b; Malavieille et al., 2021). For an obliquely subducting oceanic slab such as the South China Sea, the initial arrival of the Eurasian continental margin at the Manila Trench in the north would locally increase plate coupling and interface friction (profile B-1 of Figure 7B); a sudden interruption of subduction would divert a portion of the plate convergence to the COT southwestward as one of the major structural weaknesses within the descending plate, resulting in the simultaneous obduction of the South China Sea onto the Eurasian continental margin (Figure 7B). The hypothesized obduction would be short-lived, as the strain reorganization described above is transient in nature; therefore, the Shihmen Conglomerate has a rather limited temporal occurrence, no later than ~11 Ma. The Shihmen Conglomerate, as part of the South China Sea sedimentary succession (the Mutan Formation), was then incorporated into the accretionary wedge of the Manila subduction system and is now exhumed on the Hengchun Peninsula (Figure 7C).

5 Concluding remarks

The active arc-continent collision of the Taiwan mountain belt provides valuable insights into the evolution and growth of the East Asian continent, particularly the transition from oceanic to continental subduction. Due to oblique convergence, southernmost Taiwan is the youngest in orogenic history to record such a transition in both structures and stratigraphy. For the mafic-dominated Shihmen Conglomerate within the uplifted South China Sea turbidite sequence outcropping on the Hengchun Peninsula, new geochronological constraints indicate that a piece of early Miocene South China Sea crust dynamically metamorphosed at ~13 Ma, forming an isolated high-relief subaerial mountain range along the Chinese continental margin. This ephemeral mountain building of ophiolitic materials is best explained by an obduction event due to stress-strain reorganization of the Manila Trench during initial continental subduction. Such dramatic yet transient phenomena reveal the hidden tectonic complications in oceanic-continental subduction transitions, with important implications for the geodynamic evolution of continental margins.

Data availability statement

The original contributions presented in the study are included in the article/Supplementary Material, further inquiries can be directed to the corresponding author.

Author contributions

Y-CL: field investigation, sample preparation, experiment, data analysis, scientific discussion, manuscript writing. C-TC: conceptualization, project planning, field investigation, data curation, scientific discussion, manuscript writing, funding acquisition C-HL: conceptualization, project planning, data curation, scientific discussion, manuscript writing, funding acquisition. S-LC: experiment, data curation, scientific discussion M-WY: experiment, data curation, scientific discussion.

Funding

This work was financially supported by grants from the National Science and Technology Council, Taiwan, R.O.C. to C-HL (111-2116-M-002-043- and 110-2116-M-002-029-) and C-TC (111-2116-M-008-019- and 108-2628-M-008-002-MY2).

Acknowledgments

The authors are indebted to Hao-Tsu Chu for their invaluable knowledge and guidance on Hengchun geology and Taiwan tectonics.

Conflict of interest

The authors declare that the research was conducted in the absence of any commercial or financial relationships that could be construed as a potential conflict of interest.

The handling editor MP declared a shared affiliation with the author SLC at the time of review.

Publisher's note

All claims expressed in this article are solely those of the authors and do not necessarily represent those of their affiliated organizations, or those of the publisher, the editors and the reviewers. Any product that may be evaluated in this article, or claim that may be made by its manufacturer, is not guaranteed or endorsed by the publisher.

Supplementary material

The Supplementary Material for this article can be found online at: https://www.frontiersin.org/articles/10.3389/feart.2023.1118520/full#supplementary-material

References

Andersen, T. (2002). Correction of common lead in U-Pb analyses that do not report ^{204}Pb. *Chem. Geol.* 192, 59–79. doi:10.1016/s0009-2541(02)00195-x

Beyssac, O., Simoes, M., Avouac, J.-P., Farley, K. A., Chen, Y. G., Chan, Y. C., et al. (2007). Late Cenozoic metamorphic evolution and exhumation of Taiwan. *Tectonics* 26, TC6001. doi:10.1029/2006tc002064

Briais, A., Patriat, P., and Tapponnier, P. (1993). Updated interpretation of magnetic anomalies and seafloor spreading stages in the south China sea: Implications for the tertiary tectonics of southeast asiafloor spreading stages in the South China sea: Implications for the tertiary tectonics of southeast asia. *J. Geophys. Res.* 98, 6299–6328. doi:10.1029/92jb02280

Byrne, T., Chan, Y.-C., Rau, R.-J., Lu, C.-Y., Lee, Y.-H., and Wang, Y.-J. (2011). "The arc-continent collision in Taiwan," in *Arc-continent collision: The making of an orogen, Frontiers in earth sciences*. Editors D. Brown and P. Ryan (Heidelberg: Springer), 211–243.

Chang, C.-P., Angelier, J., and Huang, C.-Y. (2009b). "Evolution of subduction indicated by melanges in Taiwan," in *Subduction zone geodynamics*. Editors S. Lallemand and F. Funiciello (Berlin: Springer), 207–225.

Chang, C.-P., Angelier, J., Lee, T.-Q., and Huang, C.-Y. (2003). From continental margin extension to collision orogen: Structural development and tectonic rotation of the Hengchun peninsula, southern Taiwan. *Tectonophysics* 361, 61–82. doi:10.1016/s0040-1951(02)00561-9

Chang, C.-P., Angelier, J., and Lu, C.-Y. (2009a). Polyphase deformation in a newly emerged accretionary prism: Folding, faulting and rotation in the southern Taiwan mountain range. *Tectonophysics* 466, 395–408. doi:10.1016/j.tecto.2007.11.002

Chang, L.-S. (1964). A biostratigraphic study of the tertiary in the Hengchun Peninsula, Taiwan, based on smaller foraminifera (I: Northern Part). *Proceeding Geol. Soc. China* 7, 48–62.

Chen, C.-H., Chu, H.-T., Liou, J. G., and Ernst, W. G. (1983). *Explanatory notes for the metamorphic facies map of Taiwan*. Taiwan: Special Publication of Central Geological Survey, 1–3.

Chen, W.-S., Cheng, Y.-M., and Huang, C.-Y. (1985). Geology of the Hengchun peninsula, southern taiwan. *Ti-Chih* 6, 47–74.

Chen, W.-S., Yeh, J.-J., and Syu, S.-J. (2019). Late Cenozoic exhumation and erosion of the Taiwan orogenic belt: New insights from petrographic analysis of foreland basin sediments and thermochronological dating on the metamorphic orogenic wedge. *Tectonophysics* 750, 56–69. doi:10.1016/j.tecto.2018.09.003

Chi, W.-R. (1982). The calcareous nannofossils of the Lichi Melange and the Kenting Melange, and their significance in the interpretation of plate tectonics of the Taiwan region. *Ti-Chih* 4, 99–112.

Chiu, H.-Y., Chung, S.-L., Wu, F.-Y., Liu, D., Liang, Y.-H., Lin, I.-J., et al. (2009). Zircon U-Pb and Hf isotopic constraints from eastern Transhimalayan batholiths on the precollisional magmatic and tectonic evolution in southern Tibet. *Tectonophysics* 477, 3–19. doi:10.1016/j.tecto.2009.02.034

Chung, S.-L., and Sun, S.-S. (1992). A new genetic model for the East taiwan ophiolite and its implications for dupal domains in the northern hemisphere. *Earth Planet. Sci. Lett.* 109, 133–145. doi:10.1016/0012-821x(92)90079-b

Cui, Y., Shao, L., Yu, M., and Huang, C. (2021). Formation of Hengchun accretionary prism turbidites and implications for deep-water transport processes in the northern South China sea. *Acta Geol. Sin.* 95, 55–65. doi:10.1111/1755-6724.14640

Denne, R. A. (2017). "Biostratigraphy," in *Encyclopedia of petroleum geoscience. Encyclopedia of earth sciences series*. Editor R. Sorkhabi (Heidelberg: Springer), 20.

Deschamps, A., Monié, P., Lallemand, S., Hsu, S. K., and Yeh, K. Y. (2000). Evidence for early cretaceous oceanic crust trapped in the philippine Sea plate. *Earth Planet. Sci. Lett.* 179, 503–516. doi:10.1016/s0012-821x(00)00136-9

Frost, B. R., and Frost, C. D. (2014). *Essentials of igneous and metamorphic petrology*. New York, USA: Cambridge University Press, 303.

Gehrels, G. E., Valencia, V. A., and Ruiz, J. (2008). Enhanced precision, accuracy, efficiency, and spatial resolution of U-Pb ages by laser ablation-multicollector-inductively coupled plasma –mass spectrometry. *Geochem. Geophys. Geosystems* 9, Q03017. doi:10.1029/2007gc001805

Harrison, T. M. (1982). Diffusion of ^{40}Ar in hornblende. *Contributions Mineralogy Petrology* 78, 324–331. doi:10.1007/bf00398927

Hartmann, L. A., and Santos, J. O. S. (2004). Predominance of high Th/U, magmatic zircon in Brazilian Shield sandstones. *Geology* 32, 73–76. doi:10.1130/g20007.1

Hoskin, P. W. O., and Black, L. P. (2000). Metamorphic zircon formation by solid-state recrystallization of protolith igneous zircon. *J. Metamorph. Geol.* 18, 423–439. doi:10.1046/j.1525-1314.2000.00266.x

Hu, H.-N., and Tsan, S.-F. (1984). *Structural study of the slate formation along the South link railroad, taiwan*. Taiwan: Special Publication of Central Geological Survey, 25–43.

Jackson, S. E., Pearson, N. J., Griffin, W. L., and Belousova, E. (2004). The application of laser ablation inductively coupled plasma mass spectrometry to *in-situ* U–Pb zircon geochronology. *Chem. Geol.* 211, 47–69. doi:10.1016/j.chemgeo.2004.06.017

Jahn, B.-M., Wu, F., and Chen, B. (2000). Granitoids of the central asian orogenic belt and continental growth in the phanerozoic. *Trans. R. Soc. Edinb. Earth Sci.* 91, 181–193. doi:10.1017/s0263593300007367

Karig, D. E., Ingle, J. C., Bouma, A. H., Ellis, C. H., Haile, N., Koizumi, I., et al. (1975). *Nitial reports of the deep sea drilling project*. in *I*. Washington, D.C.: U.S. Government Printing Office, 972.

Koppers, A. A. P. (2002). ArArCALC-software for ^{40}Ar/^{39}Ar age calculations. *Comput. Geosci.* 28, 605–619. doi:10.1016/s0098-3004(01)00095-4

Lai, Y.-M., Chu, M.-F., Chen, W.-S., Shao, W.-Y., Lee, H.-Y., and Chung, S.-L. (2018). Zircon U-Pb and Hf isotopic constraints on the magmatic evolution of the Northern Luzon Arc. *Terr. Atmos. Ocean. Sci.* 29, 149–186. doi:10.3319/tao.2017.08.29.01

Lallemand, S., Peyret, M., van Rijsingen, E., Arcay, D., and Heuret, A. (2018). Roughness characteristics of oceanic seafloor prior to subduction in relation to the seismogenic potential of subduction zones. *Geochem. Geophys. Geosystems* 19, 2121–2146. doi:10.1029/2018gc007434

Lee, J. Y., Marti, K., Severinghaus, J. P., Kawamura, K., Yoo, H. S., Lee, J. B., et al. (2006). A redetermination of the isotopic abundances of atmospheric Ar. *Geochimica Cosmochimica Acta* 70, 4507–4512. doi:10.1016/j.gca.2006.06.1563

Lin, A. T., Yao, B., Hsu, S. K., Liu, C. S., and Huang, C. Y. (2009). Tectonic features of the incipient arc-continent collision zone of Taiwan: Implications for seismicity. *Tectonophysics* 479, 28–42. doi:10.1016/j.tecto.2008.11.004

Lo, C. H., Chung, S. L., Lee, T. Y., and Wu, G. Y. (2002). Age of the Emeishan flood magmatism and relations to Permian-Triassic boundary events. *Earth Planet. Sci. Lett.* 198, 449–458. doi:10.1016/s0012-821x(02)00535-6

Lo, C. H., and Yui, T. F. (1996). ^{40}Ar/^{39}Ar dating of high-pressure rocks in the Tananao basement complex, Taiwan. *J. Geol. Soc. China* 39, 13–30.

Lo, Y. C., Chen, C. T., Lo, C. H., and Chung, S. L. (2020). Ages of ophiolitic rocks along plate suture in Taiwan orogen: Fate of the South China Sea from subduction to collision. *Terr. Atmos. Ocean. Sci.* 31, 383–402. doi:10.3319/tao.2019.06.19.01

Lu, C.-Y., and Hsu, K. J. (1992). Tectonic evolution of the Taiwan mountain belt. *Pet. Geol. Taiwan* 27, 21–46.

Ludwig, K. R. (2008). *User's manual for isoplot/ex: A geochronological toolkit for microsoft excel*. Canterbury: Department of Computer Science University of Canterbury, 206–207.

Malavieille, J., Dominguez, S., Lu, C. Y., Chen, C. T., and Konstantinovskaya, E. (2021). Deformation partitioning in mountain belts: Insights from analogue modelling experiments and the taiwan collisional orogen. *Geol. Mag.* 158, 84–103. doi:10.1017/s0016756819000645

Malavieille, J., Lallemand, S. E., Dominquez, S., Deschamps, A., Lu, C. Y., Liu, C. S., et al. (2002). "Arc-continent collision in Taiwan: New marine observation and tectonic evolution," in *Geology and geophysics of an Arc-Continent collision* (USA: Geological Society of America Special Paper), 189–213.

Malavieille, J., and Trullenque, G. (2009). Consequences of continental subduction on forearc basin and accretionary wedge deformation in SE Taiwan: Insights from analogue modeling. *Tectonophysics* 466, 377–394. doi:10.1016/j.tecto.2007.11.016

Meng, X., Shao, L., Cui, Y., Zhu, W., Qiao, P., Sun, Z., et al. (2021). Sedimentary records from Hengchun accretionary prism turbidites on Taiwan Island: Implication on late Neogene migration rate of the Luzon subduction system. *Mar. Petroleum Geol.* 124, 104820. doi:10.1016/j.marpetgeo.2020.104820

Page, B. M., and Lan, C. Y. (1983). *The Kenting Mélange and its record of tectonic events*. China: Memoir of Geological Society of China, 227–248.

Pelletier, B., and Stephan, J. F. (1986). Middle Miocene deduction and late Miocene beginning of collision registered in the Hengchun Peninsula: Geodynamic implications for the evolution of Taiwan. *Tectonophysics* 125, 133–160. doi:10.1016/0040-1951(86)90011-9

Queano, K. L., Ali, J. R., Milsom, J., Aitchison, J. C., and Pubellier, M. (2007). North Luzon and the Philippine Sea Plate motion model: Insights following paleomagnetic, structural, and age-dating investigations. *J. Geophys. Res.* 112, B05101. doi:10.1029/2006jb004506

Ryan, P. D., and Dewey, J. F. (2019). The Ordovician Grampian Orogeny, western Ireland: Obduction versus "bulldozing" during arc-continent collision. *Tectonics* 38, 3462–3475. doi:10.1029/2019TC005602

Searle, M., Rioux, M., and Garber, J. M. (2022). One line on the map: A review of the geological history of the semail thrust, Oman-uae mountains. *J. Struct. Geol.* 158, 104594. doi:10.1016/j.jsg.2022.104594

Sengor, A. M. C., Natal'in, B. A., and Burtman, V. S. (1993). Evolution of the Altaid tectonic collage and Palaeozoic crustal growth in Eurasia. *Nature* 346, 299–307. doi:10.1038/364299a0

Shyu, J. B. H., Sieh, K., and Chen, Y. G. (2005). Tandem suturing and disarticulation of the Taiwan orogen revealed by its neotectonic elements. *Earth Planet. Sci. Lett.* 233, 167–177. doi:10.1016/j.epsl.2005.01.018

Sibuet, J. C., Hsu, S.-K., Le Pichon, X., Le Formal, J. P., Reed, D., Moore, G., et al. (2002). East asia plate tectonics since 15 Ma: Constraints from the taiwan region. *Tectonophysics* 344, 103–134. doi:10.1016/s0040-1951(01)00202-5

Sláma, J., Košler, J., Condon, D. J., Crowley, J. L., Gerdes, A., Hanchar, J. M., et al. (2008). Plešovice zircon — a new natural reference material for U–Pb and Hf isotopic microanalysis. *Chem. Geol.* 249, 1–35. doi:10.1016/j.chemgeo.2007.11.005

Song, S. R., and Lo, H. J. (2002). Lithofacies of volcanic rocks in the central Coastal Range, eastern Taiwan: Implications for island arc evolution. *J. Asian Earth Sci.* 21, 23–38. doi:10.1016/s1367-9120(02)00003-2

Spell, T. L., and McDougall, I. (2003). Characterization and calibration of ^{40}Ar/^{39}Ar dating standards. *Chem. Geol.* 198, 189–211. doi:10.1016/s0009-2541(03)00005-6

Spencer, C. J., Kirkland, C. L., and Taylor, R. J. M. (2016). Strategies towards statistically robust interpretations of *in situ* U-Pb zircon geochronology. *Geosci. Front.* 7, 581–589. doi:10.1016/j.gsf.2015.11.006

Sung, Q. (1991). Geologic map and the explanatory text for the Hengchun peninsula, geologic map of taiwan. *Scale* 1, 50000.

Suppe, J. (1988). Tectonics of arc-continent collision on both sides of the South China sea: Taiwan and mindoro. *Acta Geol. Taiwanica* 26, 1–18.

Tan, H., Gao, X., Wang, K., Gao, J., and He, J. (2022). Hidden roughness of subducting seafloor and implications for megathrust seismogenesis: Example from northern Manila Trench. *Geophys. Res. Lett.* 49, e2022GL100146. doi:10.1029/2022gl100146

Taylor, B., and Hayes, D. E. (1983). "Origin and history of the South China Sea basin," in *The tectonic and geologic evolution of southeast asian seas and islands: Part 2*. Editor D. E. Hayes (China: Geophysical Monograph Series), 23–56.

Teng, L. S. (1990). Geotectonic evolution of late Cenozoic arc-continent collision in Taiwan. *Tectonophysics* 183, 57–76. doi:10.1016/0040-1951(90)90188-e

Tian, Z. X., Yan, Y., Huang, C. Y., Zhang, X. C., Liu, H. Q., Yu, M. M., et al. (2019). Geochemistry and geochronology of the accreted mafic rocks from the Hengchun peninsula, southern taiwan: Origin and tectonic implicationsfic crocks from the Hengchun peninsula, southern taiwan: Origin and tectonic implications. *J. Geophys. Res. Solid Earth* 124, 2469–2491. doi:10.1029/2018jb016562

Tsai, C. H., Shyu, J. B. H., Chung, S.-L., and Lee, H. Y. (2020). Miocene sedimentary provenance and paleogeography of the Hengchun Peninsula, southern Taiwan: Implications for tectonic development of the Taiwan orogen. *J. Asian Earth Sci.* 194, 104032. doi:10.1016/j.jseaes.2019.104032

Vavra, G., Gebauer, D., Schmidt, R., and Compston, W. (1996). Multiple zircon growth and recrystallization during polyphase Late Carboniferous to Triassic metamorphism in granulites of the Ivrea Zone (southern Alps): An ion microprobe (SHRIMP) study. *Contributions Mineralogy Petrology* 122, 337–358. doi:10.1007/s004100050132

Vermeesch, P. (2018). IsoplotR: A free and open toolbox for geochronology. *Geosci. Front.* 9, 1479–1493. doi:10.1016/j.gsf.2018.04.001

Wang, K. L., Lo, Y. M., Chung, S. L., Lo, C. H., Hsu, S. K., Yang, H. J., et al. (2012). Age and geochemical features of dredged basalts from offshore SW Taiwan: The coincidence of intra-plate magmatism with the spreading South China Sea. *Terr. Atmos. Ocean. Sci.* 23, 657–669. doi:10.3319/tao.2012.07.06.01(tt)

Wiedenbeck, M., Alle, P., Corfu, F., Grin, W. L., Meier, M., Oberli, F., et al. (1995). Three natural zircon standards for U-Th-Pb, Lu-Hf, trace element and REE analyses. *Geostand. Newsl.* 19, 1–23. doi:10.1111/j.1751-908x.1995.tb00147.x

Williams, I. S., and Claesson, S. (1987). Isotopic evidence for the Precambrian provenance and Caledonian metamorphism of high grade paragneisses from the Seve Nappes, Scandinavian Caledonides. II Ion microprobe zircon U–Th–Pb. *Contributions Mineralogy Petrology* 97, 205–217. doi:10.1007/bf00371240

Yeh, Y. C., Sibuet, J. C., Hsu, S. K., and Liu, C. S. (2010). Tectonic evolution of the northeastern south China sea from seismic interpretation. *J. Geophys. Res.* 115, B06103. doi:10.1029/2009JB006354

Zhang, X., Cawood, P. A., Huang, C. Y., Wang, Y., Yan, Y., Santosh, M., et al. (2016). From convergent plate margin to arc-continent collision: Formation of the Kenting Melange, Southern Taiwan. *Gondwana Res.* 38, 171–182. doi:10.1016/j.gr.2015.11.010

Zhang, X., Yan, Y., Dilek, Y., Chen, W. H., and Shan, Y. (2022). Mid-Miocene uplift and tectonic-sedimentary evolution of the Taiwan accretionary prism: Constraints from sedimentary records in the Hengchun Peninsula, southern Taiwan. *Mar. Petroleum Geol.* 147, 105994. doi:10.1016/j.marpetgeo.2022.105994

Zhang, X., Yan, Y., Huang, C. Y., Chen, D., Shan, Y., Lan, Q., et al. (2014). Provenance analysis of the Miocene accretionary prism of the Hengchun Peninsula, southern Taiwan, and regional geological significanceficance. *J. Asian Earth Sci.* 85, 26–39. doi:10.1016/j.jseaes.2014.01.021

frontiers | Frontiers in Earth Science

TYPE Original Research
PUBLISHED 13 July 2023
DOI 10.3389/feart.2023.1125279

OPEN ACCESS

EDITED BY
Alexander Cruden,
Monash University, Australia

REVIEWED BY
Nguyen Van Vuong,
VNU University of Science, Vietnam
Muhammad Afiq Md Ali,
University of Malaysia Terengganu, Malaysia

*CORRESPONDENCE
Meng-Wan Yeh,
marywyeh@ntnu.edu.tw

RECEIVED 16 December 2022
ACCEPTED 25 May 2023
PUBLISHED 13 July 2023

CITATION
Dinh T-H, Yeh M-W, Lee T-Y, Kunk MJ, Wintsch RP and McAleer R (2023), Extrusion tectonism of Indochina reassessed: constraints from $^{40}Ar/^{39}Ar$ geochronology from the Day Nui Con Voi metamorphic massif, Vietnam. *Front. Earth Sci.* 11:1125279. doi: 10.3389/feart.2023.1125279

Extrusion tectonism of Indochina reassessed: constraints from $^{40}Ar/^{39}Ar$ geochronology from the Day Nui Con Voi metamorphic massif, Vietnam

Thi-Hue Dinh[1], Meng-Wan Yeh[2]*, Tung-Yi Lee[2], Michael J. Kunk[3], Robert P. Wintsch[4] and Ryan McAleer[3]

[1]Department of Earth Sciences, National Central University, Taoyuan City, Taiwan, [2]Department of Earth Sciences, National Taiwan Normal University, Taipei City, Taiwan, [3]U.S. Geological Survey, Florence Bascom Geoscience Center, Reston, VA, United States, [4]Department of Earth and Environmental Sciences, Wesleyan University, Middletown, CT, United States

The extrusion tectonic model for the southeastern margin of the Himalayan orogeny links the crustal shear activity along the Red River Shear Zone (RRSZ) to the opening of the South China Sea (SCS). The Day Nui Con Voi (DNCV) metamorphic massif in northern Vietnam strikes NW-SE, is bounded by the RRSZ to the south and continues along the strike where it meets the SCS. The DNCV is thus a critical area to document thermotectonic history in order to advance our understanding of the tectonic evolution of Indochina extrusion and its relationship to the opening of the SCS. Our new $^{40}Ar/^{39}Ar$ data combined with microstructural and petrological analyses constrained the timing of the left-lateral shearing of the RRSZ and revealed the thermal evolution of the DNCV metamorphic massif. Three ductile deformation events were observed. D_1 formed NNW-SSE striking upright folds under granulite to upper amphibolite facies conditions. D_2 was a horizontal to sub-horizontal folding event that occurred at amphibolite facies conditions. D_3 was a doming event that formed NW-SE striking up-right folds bounded by left-lateral shearing mylonite belts along the two limbs. The S/C fabrics were defined by muscovite fish, quartz + albite + K-feldspar aggregates, and muscovite folia. The D_3 doming event exhumed the DNCV metamorphic massif from amphibolite facies conditions to the lower greenschist facies conditions. The $^{40}Ar/^{39}Ar$ ages obtained from amphibole (~26 Ma), phlogopite (~25 Ma), muscovites (~24-23 Ma), biotite (~25-23 Ma), and K-feldspars (~25-22 Ma) from different structural domains of the DNCV metamorphic massif indicated a rapid exhumation ~26–22 Ma. We interpreted this as the time period for the D_3 event, with the onset of left-lateral shearing occurring around 24 Ma based on ages obtained from syn-kinematic muscovites. This age was much younger than the initiation of sea-floor spreading of the SCS (since 32 Ma) but coincided with the age for the ridge jump event in the SCS. Based on these new data, we proposed that extrusion tectonism cannot be the cause for the initial opening of the SCS. Rather, the extrusion of the Indochina block was temporally correlative with the southward ridge jump event of the already opened SCS.

KEYWORDS

Red River Shear Zone (RRSZ), Day Nui Con Voi (DNCV), South China Sea (SCS), $^{40}Ar/^{39}Ar$ geochronology, tectonic evolution

1 Introduction

The potential oil and gas reserves in the South China Sea (SCS) have attracted much research into the formation and evolution of the SCS over the past few decades (e.g., Dung et al., 2012; Hall, 2002; Sun, 2016; Tapponnier et al., 1982; tapponnier et al., 1986; Taylor and Hayes, 1980; Mai et al., 2018; Ye et al., 2018). To explain how the SCS was formed, many tectonic models have been proposed, such as the back-arc extension model (e.g., Karig, 1971; Avraham and Uyeda, 1983; Mai et al., 2018), the indentation-extrusion model (e.g., Tapponnier et al., 1982; tapponnier et al., 1986), and the subduction of the proto-SCS model (e.g., Hall, 1997; Hall, 2009; Longley, 1997; Morley, 2002). Among them, the indentation-extrusion model has received the most attention. In this model, the southeastward extrusion of the Indochina block accommodated by left-lateral movement along the RRSZ was considered the cause for the opening of the SCS (Figure 1A) (Tapponnier et al., 1982; tapponnier et al., 1986). The key supporting evidence to the indentation-extrusion model is the contemporaneity between the left-lateral movement along the RRSZ (ca. 35 to 17 Ma, Leloup and Kienast, 1993; Zhang and Schärer, 1999) and the sea-floor spreading in the SCS (ca. 32 to 15.5 Ma, Briais et al., 1993; Lee and Lawver, 1995). Various methods were applied to constrain the timing of the left-lateral movement in the RRSZ. Absent in this model, however, is a significant consideration of driving forces for plate movements. Based on Wilson cycle, a continental crust must first be thinned for rifting to take place. Strike-slip motion on steeply dipping and relatively narrow fault zones does not provide enough structural softening to significantly lower the strength of the continental crust outside of the shear belt, and so will not, by itself, initiate regional crustal thinning. Furthermore, the density of the continental crust is approximately 2.7 g/cm^3, much less dense than the oceanic crust, which is approximately 3.0 g/cm^3 (e.g., Christopherson et al., 2009). Because of its relatively lower density, the light and buoyant continental crust is unlikely to be the causal mechanism to push and open a new oceanic crust (Girdler, 1965). Additionally, Mai et al. (2018) conducted a temporal and geographical reconstruction of Cretaceous and Cenozoic magmatism within the SE margin of Eurasia with the isochrones of major basins within the SCS, and concluded: 1) the rollback of the paleo-pacific sea plate is the main crustal thinning mechanism along the southeastern boundary of Eurasia, and 2) the 3,000 km long north dipping subduction belt of Neo-Tethys stretching from Burma–Andaman block to Sumatra should be a more plausible candidate for the opening of the SCS.

Initial geochronologic research suggested left-lateral activity on the RRSZ from ~35–17 Ma; almost exactly coincident with sea-floor spreading in the SCS. In brief, U-Pb and ^{40}Ar/^{39}Ar ages between 35 and 17 Ma were obtained for zircon, monazite,

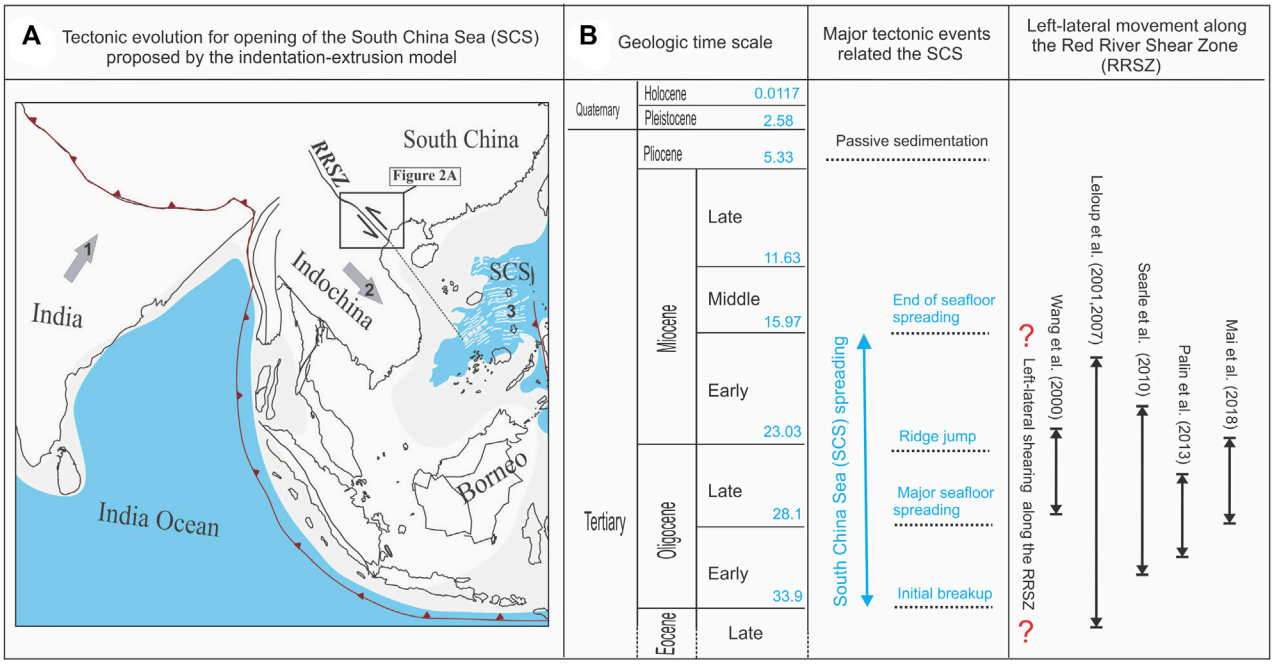

FIGURE 1
(A) Stretch map shows the time sequence following the indentation-extrusion model (Tapponnier et al., 1982; 1986), indicated by the India-Eurasia collision first, then by the southeastward extrusion of the Indochina block along the RRSZ, and finally by the opening of the SCS. The numbers represent the order of tectonic events. Black rectangles indicate the location of northern Vietnam (Figure 2A). **(B)** Schematic diagram showing major tectonic events related to the opening of the South China Sea (SCS) and the proposed timing of left-lateral movement along the Red River Shear Zone (RRSZ) from a previous study. The shearing was constrained from ca. 27–22 Ma (^{40}Ar-^{39}Ar data; Wang et al., 2000); 35–17 Ma (U-Pb and ^{40}Ar-^{39}Ar data; Leloup et al., 2001; 2007); 32–22 Ma (structural and geochronological data; Searle et al., 2010); 31–25 Ma (geochronological and petrological data; Palin et al., 2013); 28–23 Ma (tectonic reconstructions; Mai et al., 2018).

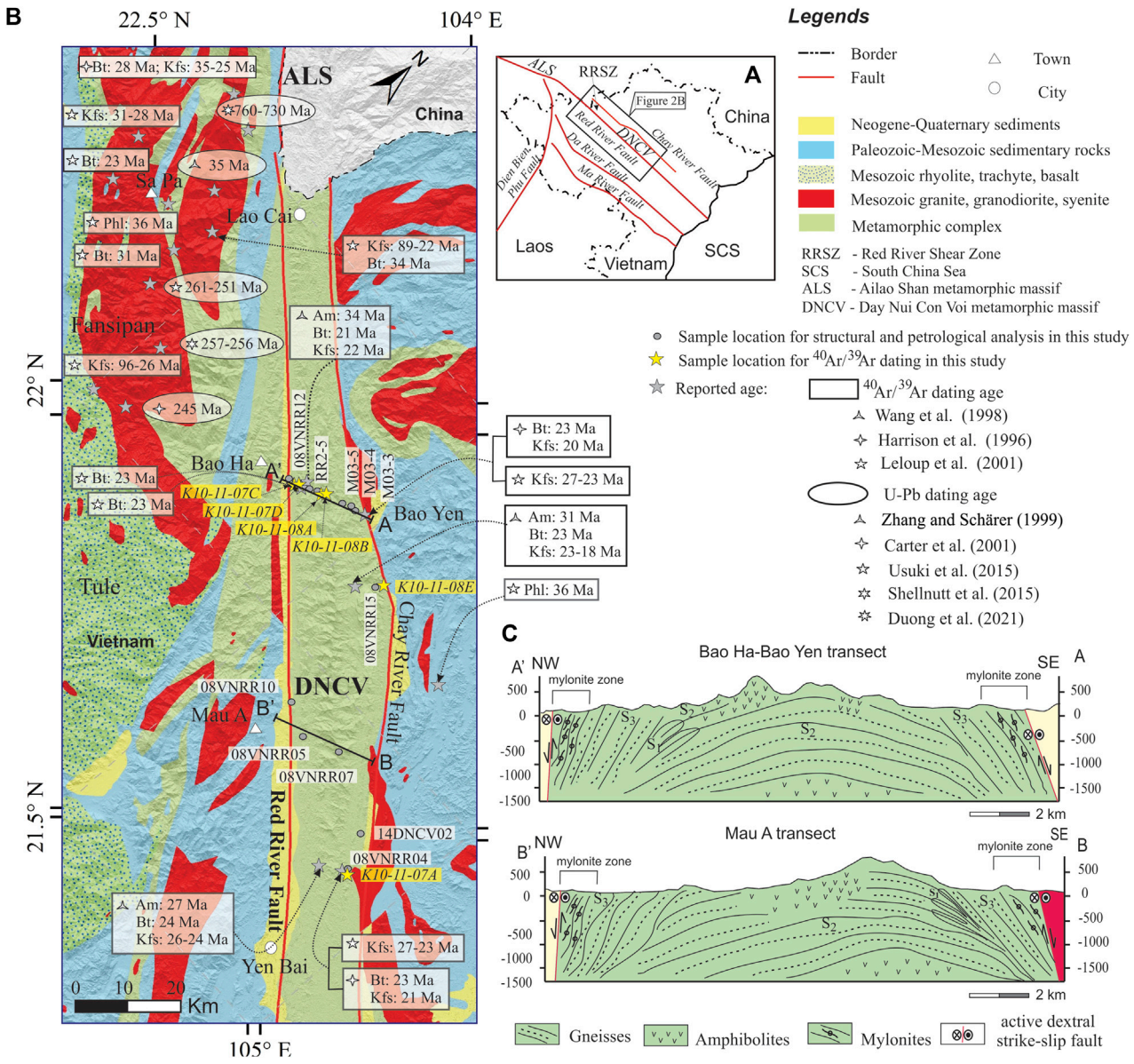

FIGURE 2
(A) Tectonic sketch showing the location of major strike-slip faults (red lines) in northwestern Vietnam and the location of the study area (black rectangle). **(B)** Geological map (Modified from 1:1,500,000 geological map, General Geological Department of Vietnam, 1983) with previously reported $^{40}Ar/^{39}Ar$ ages and U-Pb zircon ages within Day Nui Con Voi massif and surrounding areas. **(C)** Two cross-sections of the Bao Yen- Bao Ha and Mau A transects across the Day Nui Con Voi massif show different deformation events. S_1 is the fold axial plane of the oldest deformation event (D_1). The second deformation event (D_2) folded the S_1 axial plane, forming the S_2 fold axial plane. This plane was folded and deformed by a later deformation event (D_3), represented by the S_3 fold axial plane.

hornblende, biotite, and titanite from granitic rocks near the shear zone (Leloup and Kienast, 1993; Zhang and Schärer, 1999; Leloup et al., 2001; Leloup et al., 2007). However, later studies by Wang et al. (2000), Searle (2006), and Searle et al. (2010) pointed out that most of the granitic rocks are pre-kinematics and so U/Pb zircon ages provide only a maximum age for the initiation of left-lateral motion on the RRSZ. Additionally, recent studies (Junlai et al., 2020; Gou et al., 2021; Li et al., 2021) concluded that these granitic melts were formed as a product of the crustal collapse of the thickened crustal lithosphere and that this magmatism may have helped to weaken the lithosphere, facilitating the initiation of movement along the RRSZ. In other words, these dated granitic rocks were emplaced prior to the tectonic extrusion of the Indochina block. The crystallization age of those magmas should not be conflated with the timing of left-lateral movement along the RRSZ.

Different time ranges for motion on the RRSZ have been proposed by different authors, such as ca. 32–22 Ma by Searle et al. (2010), ca. 31–25 Ma by Palin et al. (2013), ca. 27–22 Ma by Wang et al. (2000), and ca. 28–23 Ma by Mai et al. (2018), as

presented in Figure 1B. Clearly, debates remain over the actual timing of the left-lateral movement along the RRSZ, and the mechanism for extrusion of the Indochina block and its linkage to the opening of the SCS need further examination. This study re-examines the timing of left-lateral movement along the RRSZ by sampling across the DNCV metamorphic massif, which is critical for assessing the true temporal and kinematic relationship of extrusion of the Indochina block and tectonic evolution of the SCS.

2 Geological background

The RRSZ is one of the largest strike-slip shear zones in SE Asia, stretching from the southeastern corner of the Tibetan plateau to the SCS (Figure 1). There is a sequence of granitic rocks and four metamorphic massifs distributed along and near the RRSZ. Zircon U-Pb dating studies indicated at least three generations for granitic rocks within and surrounding the shear zone (Figure 2). The first generation occurred at ca. 760-730 Ma (Duong et al., 2021) and produced partial melting of surrounding rocks during the Neoproterozoic Jinning orogeny. The second generation of granitic rocks crystallized at ca. 261–245 Ma (Carter et al., 2001; Usuki et al., 2015; Shellnutt et al., 2020) and may relate to magmatism during the Permian-Triassic Indosinian orogeny. The third generation is represented by granitic rocks with zircon U-Pb ages of ca. 35 Ma (Zhang and Schärer, 1999). This Late Eocene magmatism is related to the India-Eurasia collision event. The four metamorphic massifs distributed along the RRSZ are the Xuelong Shan, Diancang Shan, the Ailao Shan massifs in China, and the DNCV in Vietnam. The metamorphic massifs display gneiss dome-like structures, with medium to high-grade gneiss and amphibolite within their cores bounded by low-grade schist and mylonite belts along both limbs (Yeh et al., 2008; 2014; Wu et al., 2017; Liu et al., 2020).

The DNCV metamorphic massif is in the southeastern most segment of the RRSZ and strikes in an NW-SE direction. It is approximately 30 km wide and more than 250 km long, extending from Lao Cai to Viet Tri city, in northern Vietnam. At its northern extent (near Lao Cai city), the DNCV metamorphic massif is a gneiss dome structure and nearly connects to the Ailao Shan metamorphic massif (Figure 2). The southern portion is covered by Neogene-Quaternary sediments in the south near the city of Viet Tri. The DNCV metamorphic massif is bounded by two steep normal faults of the Red River Fault along the SW limb and the Chay River Fault along the NE limb (Leloup et al., 1995) (Figure 2). The DNCV metamorphic massif is composed mainly of amphibolite, mylonite, garnet-biotite-sillimanite gneiss, garnet-biotite gneiss, two mica-garnet schists with garnet, and small lenses of marble. Petrological and geothermal-barometric studies indicated that two main periods of metamorphism and deformation occurred in the DNCV metamorphic massif (Nam et al., 1998; Yeh et al., 2008). The first period relates to the peak metamorphism, and reached upper amphibolite facies condition with calculated temperature and pressure ranges of 650–830°C and 5–9 kbar, respectively (Nam et al., 1998; Gilley et al., 2003; Anczkiewicz et al., 2007; Khoi et al., 2016). The second period of metamorphism and deformation occurred in greenschist facies with a peak temperature of ~480°C and <3 kbar (Nam et al., 1998) as a result of retrograde processes. The high-grade metamorphism was initially considered to be synchronous with left-lateral shearing along the RRSZ resulting from shear heating (Leloup et al., 2007). Yeh et al. (2008) deciphered three deformation events accompanied by regional metamorphism under the mid-crustal level since the Triassic Indosinian orogeny. However, other than the establishment of these deformation events are pre-left lateral shearing (Yeh et al., 2008; Yeh et al., 2014; Searle et al., 2010). The actual timing of these upright folding (D_1), recumbent folding (D_2), and gneiss doming (D_3) events is uncertain. Existing and new geochronologic and thermochronologic data need to be interpreted within the context of this newly deciphered structural and metamorphic evolution.

3 Materials and methods

Microstructural and petrological analyses were carried out from the oriented thin sections by using optical and cathodoluminescence (CL) petrography at the Department of Earth Sciences, National Taiwan Normal University. Electron microscopy was carried out by using a Camera SX-50 electron microprobe to determine characteristic mineral assemblages and microstructural evidence for the sequence of deformation events. CL images were taken using a Leica DM LP petrographic microscope equipped with CITL CCL8200mk3 CL stage under an acceleration potential of 12 kV, a beam current of 700 A, and an exposure time of 30 s. Based on cross-cutting relationships observed from the field and the oriented thin sections, different deformation events occurring in the study area were distinguished and a relative structural history was reconstructed. Within the context of this detailed microstructural and petrological analysis, $^{40}Ar/^{39}Ar$ dating of different minerals was also carried out. Thirteen samples of mineral separates from different lithologies, including biotite gneiss, amphibolite, schist, and mylonite (Table 1), were analyzed using the $^{40}Ar/^{39}Ar$ furnace step-heating method on either a VG MM 1200b or MAP 216 mass spectrometer at the U.S. Geological Survey argon dating laboratory, Reston, Virginia, following procedures stated in Haugerud and Kunk (1988) and Kunk et al. (2005). The samples were crushed and ground in the jaw crusher and disk mill, respectively. The minerals of interest were then concentrated to an optical purity of >99% via standard magnetic and density separation techniques. Aliquots of the separates were packaged in high-purity copper and then irradiated in the TRIGA reactor (GSTR) at the U.S. Geological Survey, Denver, Colorado for 20 MWh along with Fish Canyon Tuff sanidine (28.201 ± 0.046 Ma; Kuiper et al., 2008) as the monitor mineral, or for 40 MWh (1 of 14 samples) along with MMHB hornblende (527 Ma; Schmitz, 2012). Following irradiation, the mineral packets were incrementally heated in a low-blank furnace for 10–15 min per heating step, with schedules varying between 10 and 16 steps.

Data reduction was accomplished using an updated version of Ar-Ar* (Haugerud and Kunk, 1988) or MassSpec (Deino, 2014), the decay constants of Min et al. (2000), and atmospheric argon isotopic abundances of Lee et al. (2006). A plateau age was calculated here when three or more contiguous steps agreed at 2σ and

TABLE 1 Sample list and age summaries obtained from mineral separates of different samples with lithology and location information (indicates does not meet all criteria for age plateau. Criteria not meet are in italics.).**

Sample no.	Lithology	Location		Dated minerals	LabID	Min age (Ma)	Max age (Ma)	Plat age (Ma)	2 sigma	^{39}Ar %	Steps	MSWD	Integ age (Ma)	Isoch age (Ma)	Prefe-rred Age (Ma)	Instrument
		Lon (E)	Lat (N)													
K10-11-07A	Amphibolite	104.911°	21.797°	Biotite	73KD57	24.7	26.4	24.9**	0.2	94.8	10	3.5	24.9	Na	24.7	VG1200
K10-11-07A1	Leucogranitic dyke			Biotite	28KD59	23.3	26.6	25.0	0.4	99.9	10	0.99	26.4	24.9	25.0	MAP216
				K-Feldspar	107KD57	23.0	27.2	Na					26.2	Na	23.0	VG1200
K10-11-07A2	Biotite +Garnet Augen Gneiss			K-Feldspar	30KD57	22.7	27.6	24.6	0.2	61.2	3	1.5	25.0	23.3	24.6	MAP216
K10-11-07A3	Phlogopite bearing Marble			Phlogopite	46KD57	24.7	26.2	25.0	0.2	99.8	17	1.3	25.3	25.0	25.0	MAP216
K10-11-07C	K-feldspar vein	104.360°	22.180°	Muscovite	92KD57	23.88	24.87	24.3	0.2	100	18	1.0	24.4	24.3	24.3	MAP216
				K-feldspar	97KD57	21.5	25.8	Na					24.6	Na	21.45	VG1200
K10-11-07C1	Phyllite			Muscovite	44KD57	22.6	37.2	24.5	0.2	82.3	9	1.6	24.1	24.3	24.5	MAP216
K10-11-07D	Muscovite bearing Mylonite	104.359°	22.180°	K-feldspar	28KD57	22.3	39.2	Na					31.6	Na	23.0	MAP216
K10-11-08A	Amphibolite	104.367°	22.181°	Amphibole	126KD57	26.5	27.8	26.6	0.1	56.9	2		27.3	Na	26.5	VG1200
K10-11-08B	Muscovite bearing Pegmatitic vein	104.394°	22.196°	Muscovite	100KD57	22.9	25.3	23.3	0.2	73.1	7	2.31	23.5	23.1	23.3	MAP216
				K-feldspar	104KD57	23.7	38.9	Na					29.6	Na	23.7	MAP216
K10-11-08B1B	Garnet+sillimanite+biotite Mylonite			Biotite	88KD57	22.8	35.8	Na					25.4	Na	22.8	MAP216
K10-11-08E	Muscovite bearing Mylonite	104.585°	22.174°	Muscovite	102KD57	22.4	24.8	23.5	0.3	99.9	16	0.9	23.4	23.3	23.5	MAP216

10.3389/feart.2023.1125279

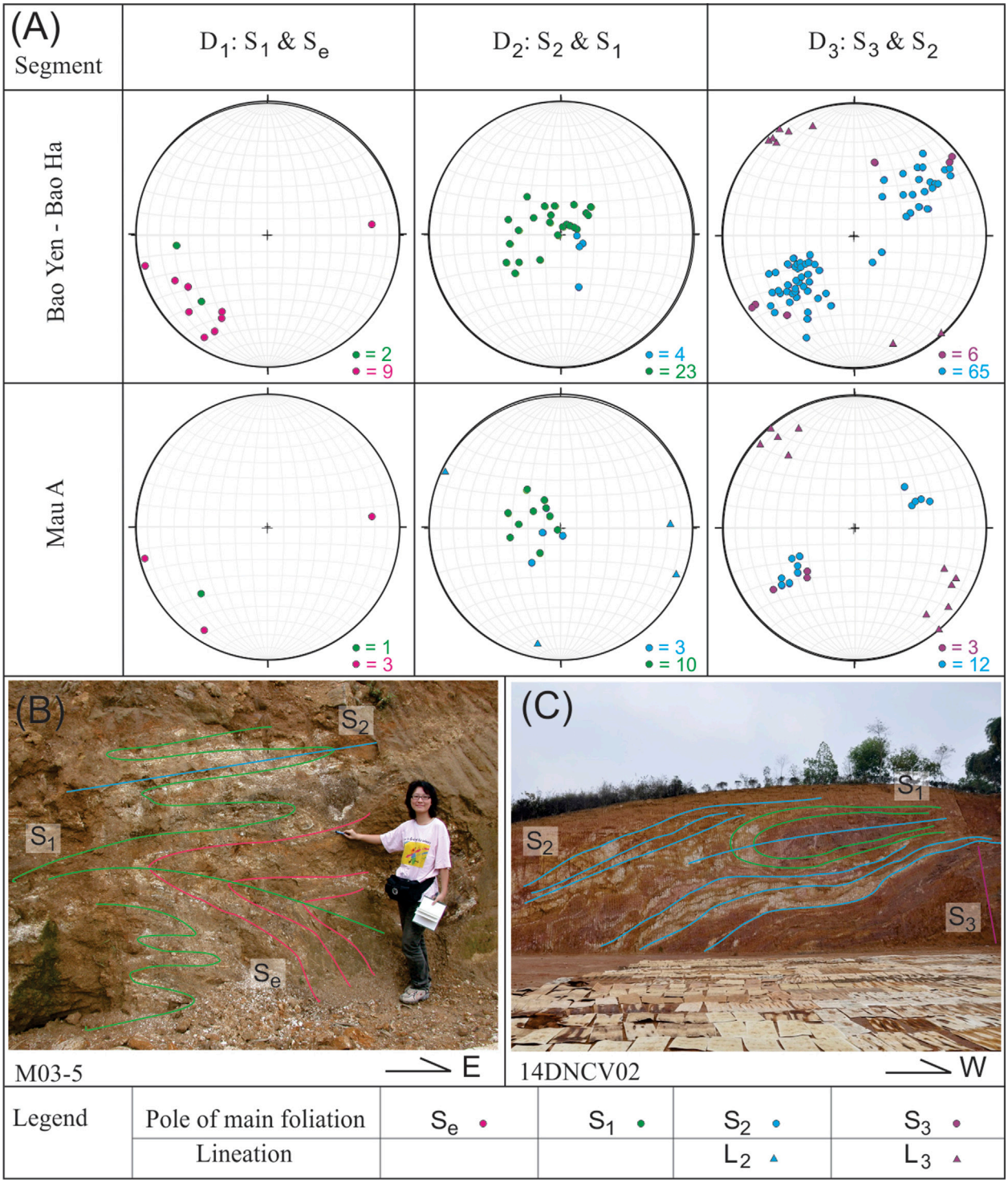

FIGURE 3
(A) Equal area stereographic projections (S hemisphere) of poles to S_e, S_1, S_2, S_3 foliation planes and lineation corresponding to different deformation events D_1, D_2, D_3 from the Bao Yen-Bao Ha and Mau A transects and field photos showing relationship of different deformations in the outcrops M03-5 **(B)** and 14DNCV02 **(C)**.

included >60% of the ^{39}Ar. In several instances, age spectra were "flat" but did not meet the above statistical criteria. In these cases, a preferred weighted average age was used and the relevant statistics are reported in Table 1. Production rates for reactor-induced interfering isotopes were those listed by Cassel et al. (2009). Errors in preferred ages included analytical errors in analysis, decay factor uncertainties, measured atmospheric or calculated initial $^{40}Ar/^{36}Ar$ ratios, the irradiation parameter J, the

10.3389/feart.2023.1125279

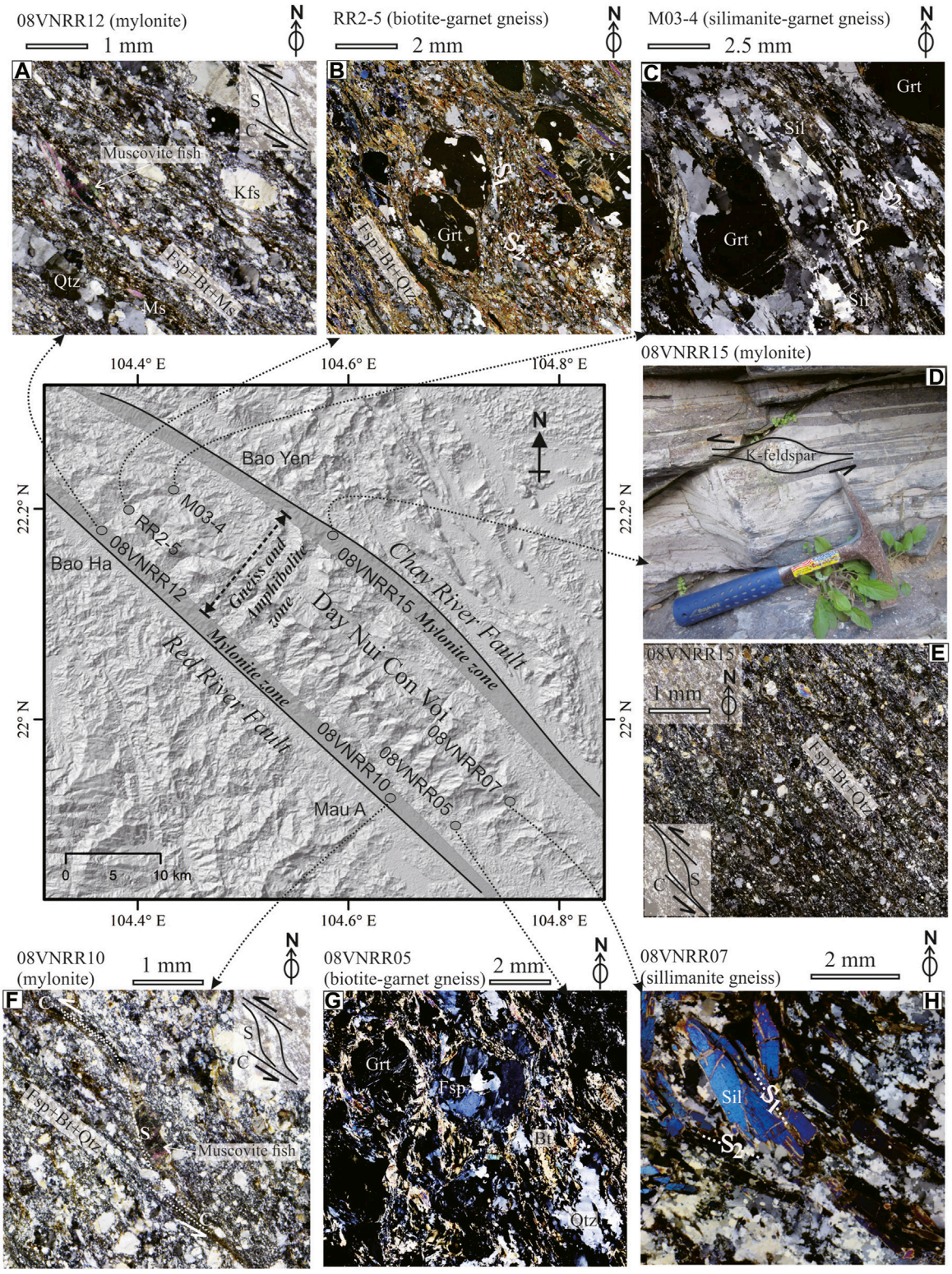

FIGURE 4
Shaded relief map showing dome-like structure with boundary mylonitic zones and sample location for petrological analysis. Representative field photographs and related microphotographs illustrate different metamorphic conditions presented by different rock types changing from the core to the rims of the Day Nui Con Voi metamorphic massif. The dominant rocks in the core of the massif are gneiss with foliation defined by the orientation of quartz ribbon, feldspar, mica folia, and sillimanite (RR2-5, M03-4, 08VNRR05, 08VNRR07) **(B, C, G, H)**. Garnet porphyroblasts are wrapped and truncated by all matrix foliation **(B, C, G)**. The dominant rock type is mylonite and phyllite for both limbs of the massif **(A, D, E, F)**. As represented in samples 08VNRR10, 08VNRR12, 08VNRR15 showing fine-sized grains of quartz, feldspar, and muscovite defining S/C fabrics. Mineral abbreviations: Bt- biotite; Fsp- feldspar; Kfs- K-feldspar; Grt- garnet; Ms- muscovite; Qtz- quartz; Sil- sillimanite.

production ratios of the various reactors that induced argon-producing reactions, and the uncertainty in the age of the monitor mineral. Additional data reduction parameters as well as complete isotopic data can be found in the Supplementary Tables and in the work by Dinh et al. (2023).

General guidelines for $^{40}Ar/^{39}Ar$ age data reporting that were described by Schaen et al. (2020) were followed. A relatively high diffusion rate through multi-domains is a common feature for argon systems at the middle and lower crust level. That makes the determination of closure temperatures of obtained $^{40}Ar/^{39}Ar$ ages a challenging issue for minerals that went through stable or slowly cooled thermal conditions such as in the case of plutonic or metamorphic rocks. By assuming the cooling pattern was linear and monotonic, we estimated the bulk closure temperatures using Eq. 1 (Dodson, 1973; Schaen et al., 2020).

$$T_c = \frac{E}{R\ln\left(AD_oRT_c/a^2E\left(dT/dt\right)\right)} \quad (1)$$

Where E is the activation energy, R is the gas constant, and A is a numeral constant that depends on the model geometry that represents the best diffusion of ^{40}Ar within the mineral. Values of 55, 27, or 8.7 for diffusion from a sphere, cylinder, or plane sheet can be assigned respectively. D_0 is a pre-exponential constant in the Arrhenius equation, a is the diffusion size, and dT/dt is the assumed cooling rate. As Lovera et al. (1991) pointed out, a smaller diffusion size (a) than grain size should be utilized if subgrains are observed. Therefore, we utilized an assumed diffusion domain size (a) of 100 μm, and a rapid cooling rate from 50°C/Ma to 100°C/Ma to gain the maximum and minimum bulk cooling temperature ranges.

4 Results and interpretations

4.1 Reconstructed structural and petrological evolution of the DNCV metamorphic massif

In order to determine the structural and metamorphic history of the DNCV metamorphic massif, two mapping transects across the width of the DNCV metamorphic massif were made. These transects are here termed the Bao Ha - Bao Yen transect and the Mau A transect (Figures 2, 3). Each transect records the same general structural history, and so observations from both transects were included when discussing the composite history of the DNCV metamorphic massif. The core region of the DNCV metamorphic massif mainly consists of garnet + biotite + sillimanite gneiss with interlayered amphibolite. The foliations are horizontal to sub-horizontal and recumbent folds are common. Petrographically, the foliations are well-defined by the aligned sillimanite, biotite, and quartz ribbons (Figures 4B, C, G, H). The matrix foliation becomes steeper toward the margins of the DNCV metamorphic massif resulting in a dome-like structure. The two limbs of the massif are characterized by mylonite zones that range from 10 to 200 m in width. Both margins display well-defined S/C fabrics that are typically defined by muscovite fish with a left-lateral sense of shear, and biotite folia and quartz and feldspar aggregates (Figures 4A, D, E, F). Three ductile deformation events were reconstructed through our field and microstructural analyses and are discussed in more detail below.

4.1.1 D_1 deformation event

The oldest deformation event, D_1, formed centimeter to meter scale NNW-SSE striking upright folds that folded the pre-existing metamorphic layering (S_e). These F_1 folds have a sub-vertical to steep NE dipping axial plane (S_1). The hinges of the centimeter to meter scale upright F_1 folds that were truncated by sub-horizontal foliation (S_2) were observed in a few outcrops. Almost all of them were refolded and deformed by later deformations (e.g., Figure 3B). The reported orientation of S_1 was based on the rare examples where F_1 folds appeared largely unaffected by later deformation events. In thin sections, the S_1 foliation was defined by the alignment of sillimanite and biotite within the cleavage domain, and quartz and feldspar aggregates defined the microlithon domain for gneiss samples (Figures 4B, C, G, 5C). Garnet porphyroblasts were observed within the microlithon domain and were wrapped and/or truncated by all matrix foliations, suggesting garnet growth occurred pre-to syn-D_1 (Figures 5A, C). The mineral assemblage of quartz, K-feldspar, biotite, garnet, and sillimanite was commonly referred to as a granulite facies assemblage (Froese, 1973). Myrmekite was also commonly observed. In the CL image (Figure 5B), K-feldspar appears dark blue against pale green myrmekite growth, which is parallel to S_1 foliation (Figures 5A, B). The development of pre-to post-plagioclase myrmekite suggests that the D_1 deformation event occurred at a high temperature of more than 550°C (e.g., Wirth and Voll, 1987; Cesare et al., 2002). The mineral assemblage of sillimanite, biotite, quartz, and feldspars along with the pre-to syn-D_1 growth of garnet suggests that the following reaction likely occurred:

Garnet + K-feldspar +Liquid → Biotite + Sillimanite + quartz (Froese, 1973).

This further constrained the temperature of the D_1 deformation event from granulite facies to upper amphibolite facies (800°C–650°C).

4.1.2 D_2 deformation event

The D_2 deformation event was associated with sub-horizontal to inclined folds that were centimeters to a few meters in scale and had a horizontal axial plane (S_2, Figures 3B, C). The poles of folded S_1 foliations and S_2 fold axial planes are marked by green and blue circles, respectively, as shown in Figure 3A. The blue triangles mark the mineral stretching lineation, show a general ESE-WNW trend, and plunge shallowly (<10°) to the ESE and WNW. Microstructural and petrological analyses indicated that the S_2 foliation was well-defined by sillimanite and biotite folia, quartz, and feldspar (Figures 5A, C, D, 6A). Quartz commonly forms ribbons and finer grains with irregular grain boundaries and undulose extinction (Figures 5A, C, 6A). Euhedral sillimanite and subhedral biotite were in textural equilibrium and had long axes parallel to the S_2 foliation (Figure 5D). Muscovite, which is only present in pegmatites, is was texturally late, and appeared to replace K-feldspar. These observations indicated muscovite was absent in the D_2 assemblage (e.g., Figure 5A). Mineral assemblages of sillimanite + biotite + high deformed quartz and feldspar suggested that the D_2

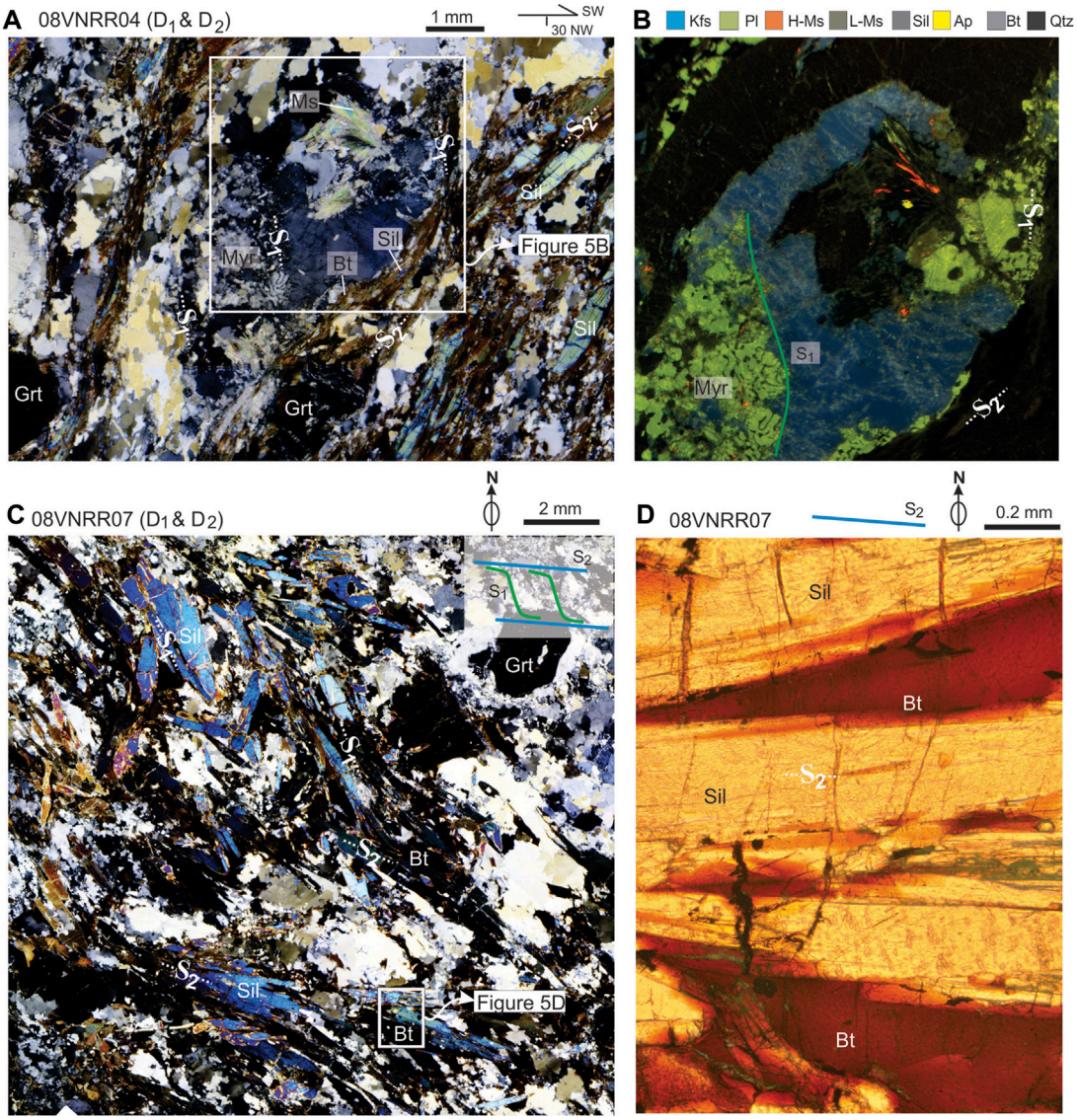

FIGURE 5
Microphotographs and cathodoluminescence (CL) images illustrate the microstructural and petrological relationship of D_1 and D_2 deformation events. **(A)** The XZ plane of sample 08VNRR04 striking SW and dipping towards NW at 30° shows quartz + feldspar + myrmekite aggregated microlithon domain and biotite + sillimanite aligned cleavage domain showing the cross-cutting relationship of S_1 and S_2 foliations. All garnets are rounded and truncated by S_1 and S_2 indicating a pre-to-syn- D_1 deformation event. **(B)** CL image shows that myrmekite extensively developed at the boundary of K-feldspar parallel to S_1 foliation. The blue color represents K-feldspar, and the green represents plagioclase and myrmekite. **(C)** Horizontal thin section of sample 08VNRR07 pointing to the top presents a cross-cutting relationship between S_1 and S_2 foliations. Both S_1 and S_2 are defined by plagioclase, K-feldspar, biotite, quartz, and sillimanite. **(D)** The straight boundary between sillimanite and biotite parallel to S_2 foliation indicates the syn-tectonic growth of sillimanite during the D_2 event. Abbreviations: Bt-biotite; Kfs- K-feldspar; Pl-plagioclase; Grt-garnet; Ms-muscovite; H-Ms- high temperature muscovite; L-Ms- low temperature muscovite Qtz-quartz; Sil-sillimanite; Ap-apatite; Myr-myrmekite.

deformation event happened between upper to lower amphibolite facies (500°C–650°C) condition.

4.1.3 D_3 deformation event

The latest ductile deformation event, D_3, formed the kilometer scale open to tight antiformal dome structure across the DNCV (Figure 2B). The orientation of D_3 fabrics is shown in Figure 3. The poles of folded S_2 foliations are marked by blue circles, whereas the purple circles mark the pole of NW-SE striking NE steep dipping S_3 fold axial planar cleavages. The purple triangles mark the mineral stretching lineation that is parallel to the long axis (NW-SE) of the DNCV massif (Figure 3A). Mylonite zones are strongly developed along both limbs of the DNCV metamorphic massif with dominant left-lateral shear sense indicators including asymmetrical pressure shadows around feldspar augen (Figure 4D), as well as mylonitic S-C fabrics with mica-fishes (Figures 4A, 6B). The orientation of the C plane of the mylonitic S/C fabrics was parallel to the S_3 fold axial plane, and no cross-cutting relationship could be observed between mylonitic fabrics and the D_3 fabrics under both macro and micro scales (Figures 4A, 6C), indicating that the mylonite zones developed

10.3389/feart.2023.1125279

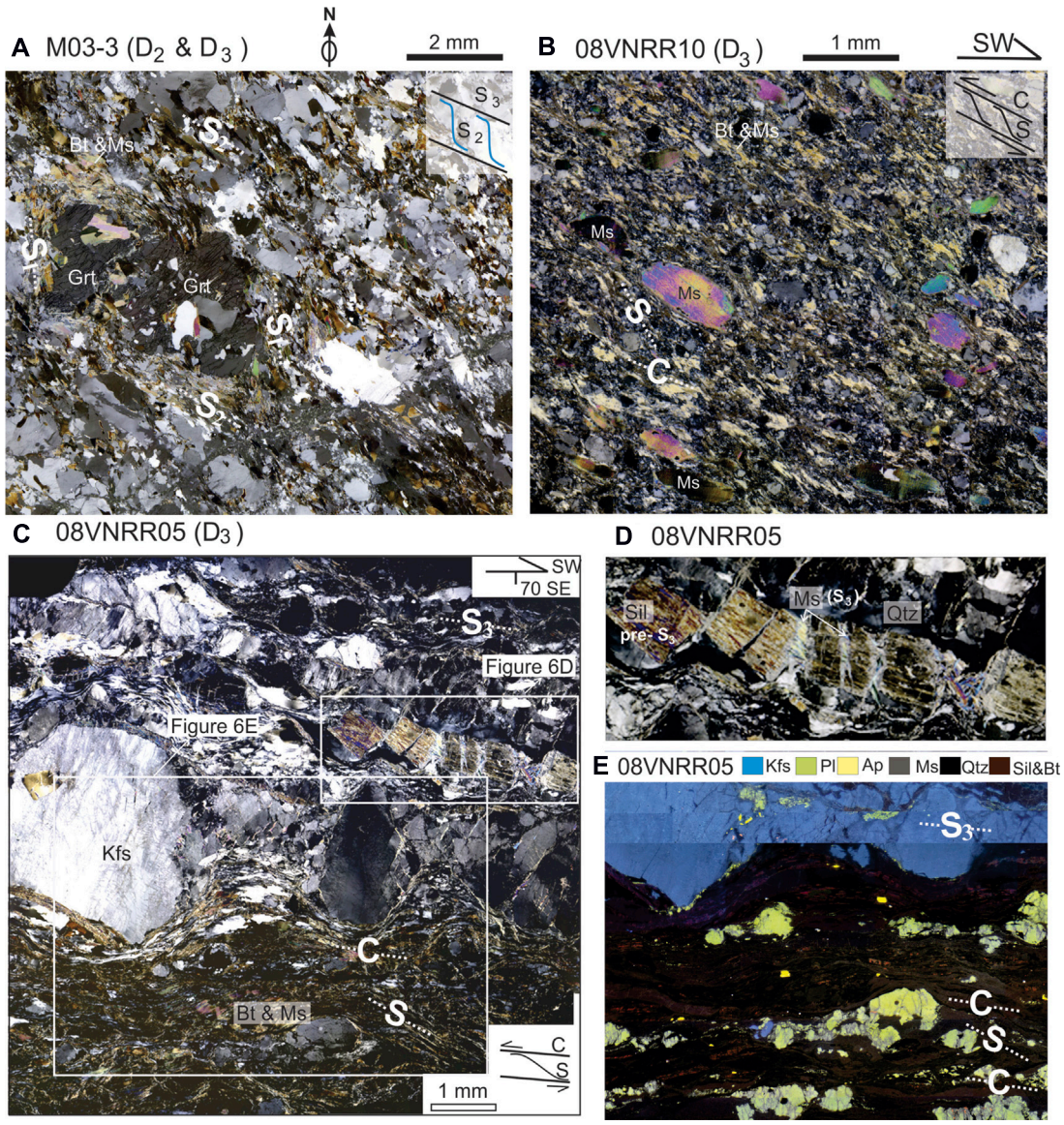

FIGURE 6
Cross-polarized and cathodoluminescence (CL) microphotographs illustrate the microstructural and petrological relationship of D_2 and D_3 deformation events. **(A)** Horizontal thin section of sample M03-3 with the north pointing to the top showing the cross-cutting relationship of S_2 and S_3 foliations. All garnets are truncated by S_2 foliation defined by the orientation of deformed muscovite and biotite with a left-lateral sense of shear. S_3 foliation is indicated by the elongation of muscovite + biotite+ quartz and feldspar. **(B)** Vertical thin section striking to SW of mylonite sample 08VNRR10 showing S-C fabrics with a left-lateral sense of shear. Muscovite fishes are truncated by C fabrics indicating muscovite fish grew pre-to syn-D_3 event. **(C)** XZ plane of sample 08VNRR05 with SW striking, 70° SE dipping showing coarse-grained feldspar phenocrysts with S-C fabrics with left-lateral shearing indicator. Boudinaged sillimanite also indicated a left-lateral sense of shear. The C- plane is defined by muscovite, biotite, elongated quartz, and feldspar ribbon. The S- plane is defined by oriented muscovite and biotite. **(D)** The enlarged image shows the brittle deformation of sillimanite and infilling of new-growth muscovite in sillimanite fractures. **(E)** CL image showing strain localization likely resulting from different grain sizes and chemical reactions. While, in the upper part, K-feldspar has a large grain size with brittle deformation, the lower part mostly presents recrystallization and ductile deformation of fine-grained plagioclase. Abbreviations: Bt-biotite; Kfs- K-feldspar; Pl-plagioclase; Grt-garnet; Ms-muscovite; Qtz-quartz; Sil-sillimanite; Ap-apatite.

contemporaneously with the D_3 doming event. Compared to the core regions that are mainly composed of gneiss and amphibolite interlayers, the mylonite regions have much finer grain size and narrower microlithon domains than the cleavage domain (Figure 4) and strongly developed C fabrics. The shearing fabric (S) was defined by the alignment of coarse-grained muscovite fish and feldspar augens, and fine-grained sillimanite, biotite, plagioclase, K-feldspar, and quartz aggregates. The shear band cleavage (C) was defined by the alignment of fine-grained muscovite and biotite (Figures 4, 6B). As stated above, muscovite was rarely observed for garnet sillimanite-bearing gneiss. On the contrary, muscovite was an abundant mineral commonly observed within mylonite.

The previously described high-grade mineral assemblages that include orthoclase, garnet, and sillimanite were relics from the D_1

10.3389/feart.2023.1125279

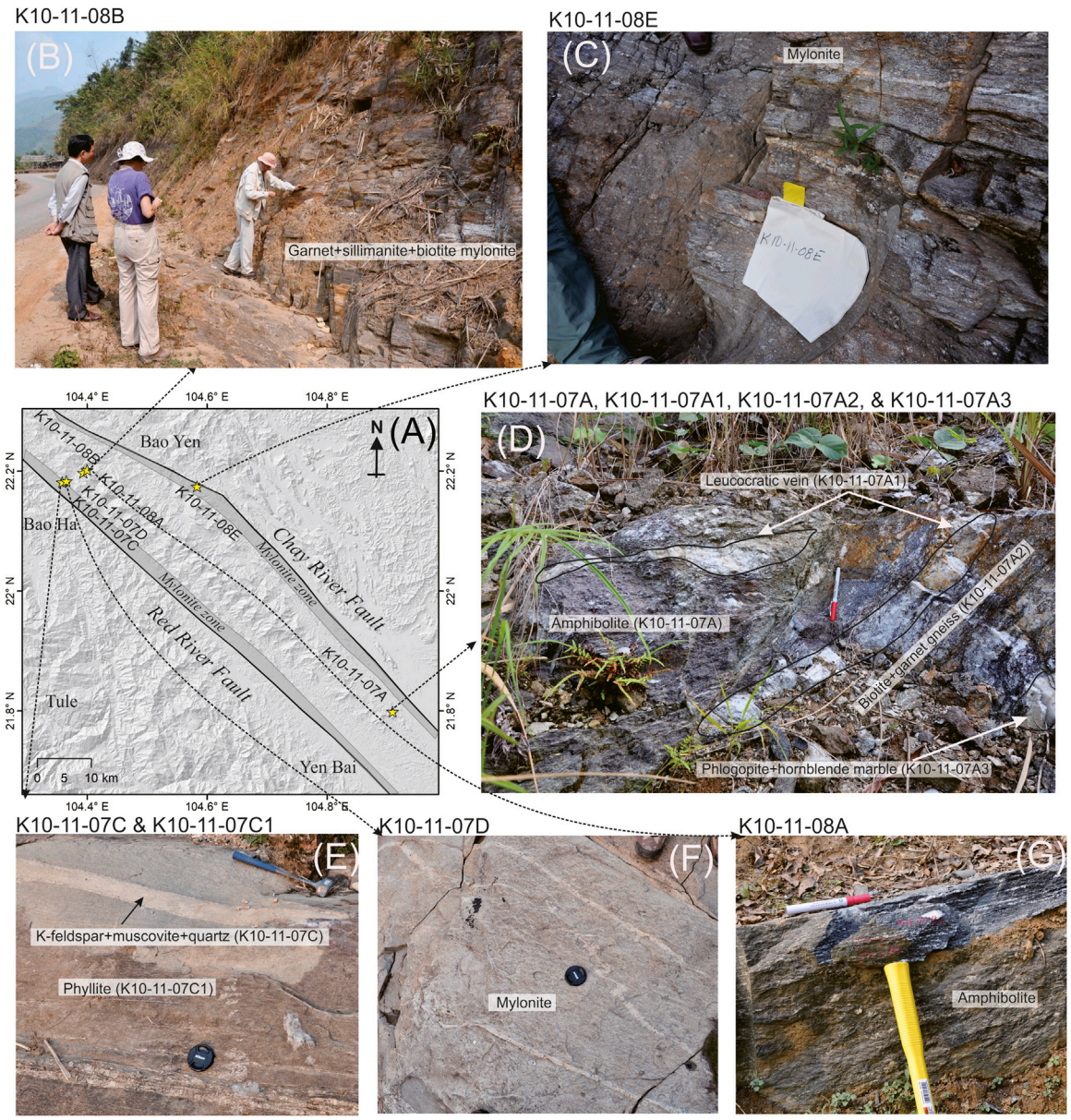

FIGURE 7
(A) Shaded relief map and the field photos showing sample locations for ^{40}Ar-^{39}Ar analysis. **(B)** Sample K10-11-08B showing minerals of garnet, sillimanite, biotite in mylonite, was collected in the inner part of the DNCV metamorphic massif. **(C)** Sample K10-11-08E was separated from the mylonite zone in the eastern portion of the DNCV metamorphic massif. **(D)** Sample K10-11-07A located in the inner part of the DNCV metamorphic massif shows different structural domains and rock types with amphibolite (K10-11-07A), leucocratic vein (K10-11-07A1), gneiss (K10-11-07A2), and marble (K10-11-07A3). **(E)** K-feldspar vein (K10-11-07C) and phyllite (K10-11-07C1) were separated in almost the same location near the rims of the DNCV metamorphic massif. **(F)** Sample K-10-11-07D was separated from the mylonite zone in the western portion of the DNCV metamorphic massif. **(G)** Sample K10-11-08A was collected in the amphibolite in the inner core of the DNCV metamorphic massif. More detail about dating results have been shown in Figure 8 and Table 1.

and D_2 that did not grow during the D_3. They all showed clear evidence of brittle fracturing and/or boudinage (Figure 6C, E) in an orientation consistent with D_3 deformation. The neck of sillimanite boudinage was filled with quartz and muscovite with a basal plane parallel to the direction of extension. This further indicated the syn-D_3 growth of muscovite and the brittle deformation condition of high-grade minerals. The cathodoluminescence microphoto (Figure 6E) of a mylonitic sample showed a relict K-feldspar porphyroclast, but a near absence of K-feldspar in the finer-grained and well-foliated muscovite-rich domain. This microstructural pattern suggests that the following retrograde metamorphic reaction was likely responsible for foliation development and microtextural softening of the rock during deformation:

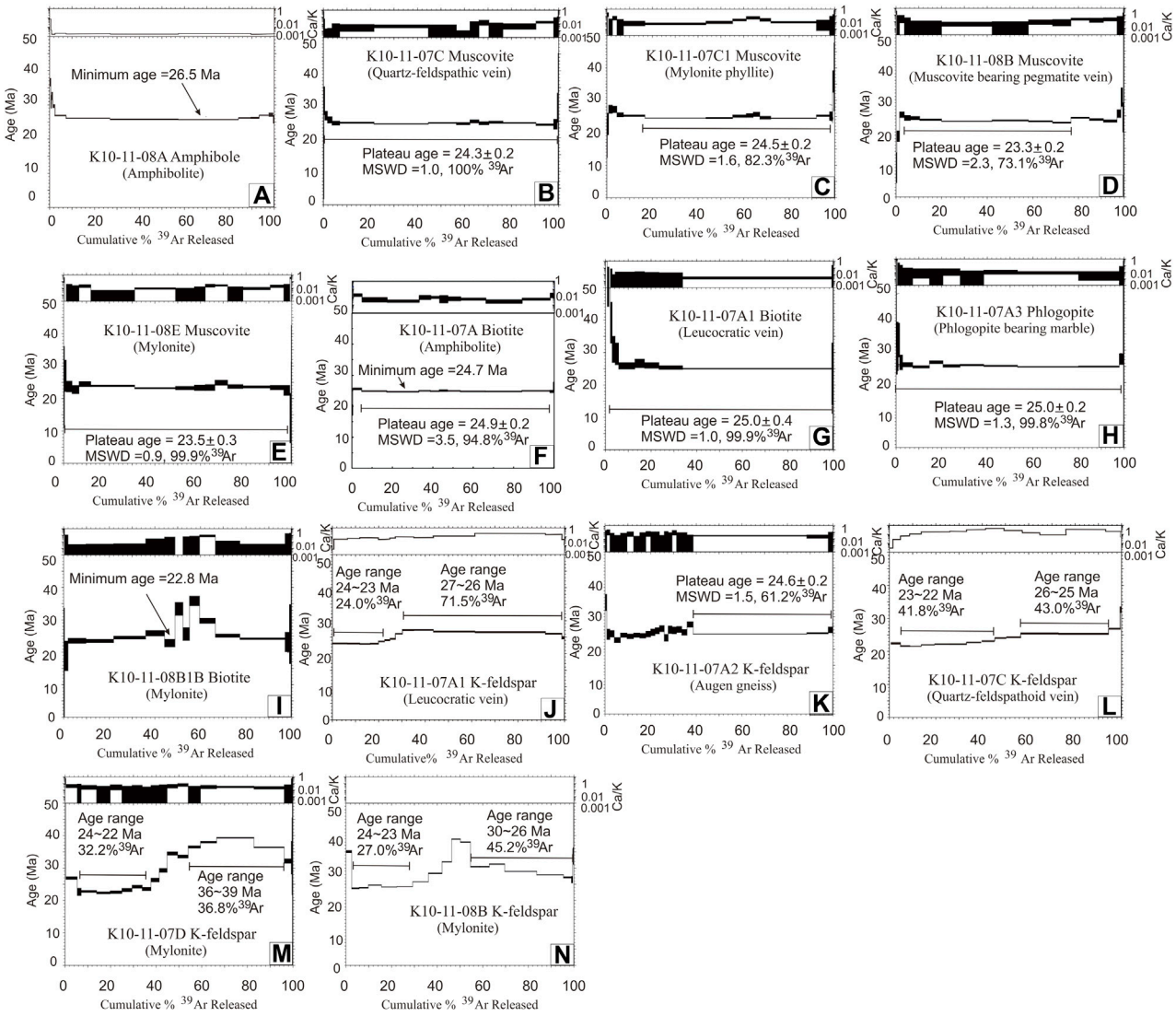

FIGURE 8
^{40}Ar-^{39}Ar step heating age spectra of **(A)** amphibole; **(B–E)** muscovite; **(F,G,I)** biotite; **(H)** phlogopite; and **(J–N)** K-feldspars separated from the DNCV metamorphic massif.

3K-feldspar + 2H+ + → Muscovite + 6SiO2 + 2K+

This coexistence of biotite in textural equilibrium with muscovite in the S_3 foliation indicates that the D_3 event occurred above the biotite isograd (400°C; Spear et al., 1999). The brittle fracture of sillimanite and plagioclase within the muscovite-rich domain (Figures 6D, E) suggests the left-lateral shearing of the RRSZ continued from the greenschist facies conditions (400°C–500°C) until brittle deformation condition.

4.2 $^{40}Ar/^{39}Ar$ geochronology results

As described above, the DNCV metamorphic massif is composed of numerous rock types that went through at least three stages of ductile deformations including prograde granulite facies metamorphism (D_1) and retrograde greenschist facies deformation associated with left-lateral motion (D_3). Of these, the timing of the D_3 event is most relevant to motion on the RRSZ, tectonic escape, and opening of the SCS. Therefore, in order to constrain the relevant post-peak-metamorphism history of the DNCV metamorphic massif, $^{40}Ar/^{39}Ar$ step-heating experiments were performed on 14 mineral separates (one amphibole, four muscovites, three biotite, one phlogopite, and five K-feldspars) from different structural and lithological domains across the DNCV metamorphic massif. There was one amphibole separate from the amphibolite interlayer sample (K10-11-08A) that preserved D_2 structures from the core region of the DNCV metamorphic massif (Figure 7), as well as four muscovite separates from the two mylonitic zones (eastern mylonite: K10-11-08E; western mylonitic phyllite: K10-11-07C1, and quartz-feldspathic vein: K10-11-07C) and the high strain belt within the core region (Sil + Bt + Gt gneiss: K10-11-08B; Figure 7). In addition, there were three biotite separates from the north and south outcrops within the core

TABLE 2 Estimated bulk closure temperatures for Amphibole, Phlogopite, Muscovite, Biotite, and K-feldspar with an assumed diffusion dimension of 100 μm for assumed cooling rate from 50 °C/Ma to 100°C/Ma (Schaen et al. (2020)).

Assumed cooling rate (°C/ Ma)	Tc Amphibole (°C) Spherical	Tc Phlogopite (°C) Cylindrical	Tc Muscovite (°C) Spherical	Tc Biotite (°C) Cylindrical	Tc K-feldspar (Orthoclase) (°C) Spherical
Do m^2/s	2.40E-06	7.50E-05	2.00E-03	1.50E-06	9.80E-07
E (kJ)	268	242	264	186	183
A	55	27	55	27	55
50	539	417	416	339	299
60	543	420	418	342	302
70	546	422	421	344	304
80	549	424	423	346	306
90	551	426	424	347	308
100	553	428	426	349	309

region of the DNCV metamorphic massif (Figure 7). K10-11-08B1B came from the same Sil + Bt + Gt gneiss K10-11-08B outcrop with muscovite, K10-11-07A and K10-11-07A1 came from the amphibolite and leucogranite vein within the same outcrop. The one phlogopite separate came from the marble layer of the same outcrop (K10-11-07A3) as well. Five K-feldspar separates (K10-11-07A1, K10-11-07A2, K10-11-07C, K10-11-07D, and K10-11-08B) from different rock types were collected from five outcrops with different structural domains across the DNVC metamorphic massif (Table 1; Figure 7). Argon isotopic data and K/Ca vs. cumulative % ^{40}Ar plots are presented graphically in Figure 8, and preferred ages are reported for each sample in Tables 1, 3–7. Complete isotopic data for each step-heating experiment can be found in Supplementary Appendix S5 and in the associated data released by Dinh et al. (2023). In this study, calculated values for the closure temperature of the dated minerals used the Arrhenius parameters summarized by Schaen et al. (2020). Estimated closure temperatures for amphibole, phlogopite, muscovite, biotite, and K-feldspar (orthoclase) are presented in Table 2 In this table, all closure temperatures were calculated by using an assumed diffusion domain size of 100 μm and a rapid cooling rate of 50°C/Ma to 100°C/Ma consistent with age data.

4.2.1 Amphibole

Amphibole was separated from an amphibolite interlayer (K10-11-08A) in the core region of the DNCV metamorphic massif (Figure 7). The amphibolite layer was composed of dominantly amphibole and plagioclase and preserved D_2 structures. Amphibole grains were optically unzoned and appeared unaltered. A step-heating experiment on an aliquot of amphibole yielded a relatively flat age spectrum and a preferred age of 26.6± 0.1 Ma. The purity of the mineral separate was confirmed by the uniform Ca/K ratios.

4.2.2 Muscovite

Four samples were collected for ^{40}Ar/^{39}Ar analysis of muscovite. These samples came from the DNCV core as well as the east and west-bounding D_3 shear zones (Figure 7). Sample K10-11-08B was from a muscovite-bearing pegmatitic vein in the core of the DNCV and near the dated amphibolite sample K10-11-08A. The vein crosscut a D_2 Grt+Sil+Bt gneiss but was deformed, indicating it was a late D_2 pegmatite. The sample yielded a plateau age of 23.3 ± 0.2 Ma. Sample K10-11-08E was a mylonitic phyllite from the eastern D_3 mylonite zone. The dominant foliation was defined by muscovite fish + quartz and plagioclase aggregates. Muscovite separated from this sample yielded a plateau age of 23.5 ± 0.3 Ma. Samples K10-11-07C and K10-11-07C1 were from the same outcrop within the western D_3 mylonitic zone. K10-11-07C1 was a mylonitic phyllite with a dominant foliation defined by muscovite fish + quartz and plagioclase aggregates. Sample K10-11-07C was from a Ksp + Qz+ Ms vein that crosscut the phyllite at a low angle (Figure 7E), suggesting that this vein was syn-S3. These two samples yielded nearly identical plateau ages of 24.3 ± 0.2 Ma and 24.5 ± 0.2 Ma.

4.2.3 Biotite and phlogopite

Three samples were collected for ^{40}Ar/^{39}Ar analysis of biotite and one sample for phlogopite. All four samples were from the core of the DNCV where D_3 deformation was limited. Three samples came from the same outcrop in the southeastern portion of the DNCV metamorphic massif. Here biotite+garnet gneiss, amphibolite, and phlogopite marble were interlayered and folded forming F2 folds. Leucocratic veins were also present and were parallel to S2 (Figure 7D). Biotite was separated from both the amphibolite (K10-11-07A), the leucocractic vein (K10-11-07A1), and phlogopite was separated from the marble (K10-11-07A3). The three samples yielded plateau ages of 24.9 ± 0.2 Ma, 25.0 ± 0.4 Ma, and 25.0 ± 0.2 Ma, respectively, and were in general agreement. The fourth sample, K10-11-08B1B, was from farther north, but was also situated within the central portion of the DNCV, and again preserved sub-horizontal S_2 fabrics (Figure 7). The sample was a D_2 mylonite with an S_2 foliation defined by Sil+Bt and garnet also present in the assemblage. The sample yielded a disturbed age spectrum with several anomalously old age steps at approximately 50% of the ^{39}Ar release. However, most of the spectrum yielded ages between 22.8 and 25.6 Ma and a total gas age of 25.4 Ma, in agreement with the other data. The cause(s) of the older age steps in this sample was unknown. No chloritization of biotite was observed in the thin section or the

separated biotite grains, so we suggested the presence of minor excess argon and that 25.4 Ma was the maximum age of the sample.

4.2.4 K-feldspar

Five samples were collected for $^{40}Ar/^{39}Ar$ analysis of K-feldspar. Samples K10-11-07A1 and K10-11-07A2 were from the core in the southern part of the DNCV metamorphic massif. Sample K10-11-07A1 was an S_2-parallel leucocratic vein and sample K10-11-07A2 was a biotite+ K-feldspar +garnet. Sample K10-11-07A1 yielded a climbing age spectrum with low-temperature steps yielding an age of ~23 Ma and high-temperature steps yielding an age of ~26.5 Ma. K10-11-07A2 yielded a similar spectrum with low-temperature steps yielding an age of ~24 Ma and high-temperature steps yielding a plateau age of 24.6 ± 0.2 Ma. Sample K10-11-08B was from the core of the northern portion of the DNCV and samples K10-11-07C and K10-11-07D were from the western margin of the DNCV (Table 1; Figure 7). Sample K10-11-08B was a mylonite and yielded a hump shape spectrum with low-temperature steps yielding an age of ~24 Ma, intermediate-heating steps yielding an age of ~38 Ma, and high-temperature steps yielding an age of ~28 Ma. Sample K10-11-07C was from a quartz-feldspathoid vein located within the D_3 western mylonite zone and had an S/C mylonitic fabric. The sample yielded a climbing age spectrum with low and high-temperature steps yielding ages of ~22 Ma and 25.5 Ma, respectively. Sample K10-11-07D was from a mylonitic phyllonite from the same outcrop and yielded a climbing age spectrum with low-temperature steps yielding an age of ~22 Ma and high-temperature steps yielding a significantly older age of 39 Ma.

4.3 Interpretation of $^{40}Ar/^{39}Ar$ ages

The $^{40}Ar/^{39}Ar$ method has been widely utilized to reconstruct the cooling history, and to constrain the timing of exhumation in various paths of the RRSZ (Wang et al., 1998; Wang et al., 2000; Leloup et al., 2001). As noted above, the RRSZ is a poly-deformed belt with evidence for deformation and associated metamorphic reaction from granulite to the greenschist facies conditions. Therefore, critical to the interpretation of the isotopic ages is the petrologic and structural context of the dated minerals. The mineralogy and structural relationships for amphibolite sample K10-11-08A indicated the dated amphibole grains grew at upper amphibolite facies conditions (>550°C) during D_2, and published work from samples in the same belt yielded peak temperatures of >600°C (Palin et al., 2013). Therefore, we interpreted the $^{40}Ar/^{39}Ar$ system to record the time of cooling through the closure temperature for the diffusion of argon in amphibole at 26.6± 0.1 Ma. This also provided a minimum age constraint on D_2 deformation that pre-dated D_3 of the DNCV metamorphic massif. Muscovite, biotite, and K-feldspar ages were only slightly younger, suggesting rapid cooling (50–100°C/km) through and following amphibole closure-resulting in an amphibole closure temperature of ~540–550°C (Schaen et al., 2020).

In both the core and marginal shear zones of the DNCV metamorphic massif, the muscovite was retrograde, forming folia that truncated higher-grade assemblages (Figure 6A), and/or replaced minerals from the higher-grade assemblage (Figures 5A, 6C, D). Important for the interpretation of the $^{40}Ar/^{39}Ar$ data was the temperature at which these fabric-forming retrograde reactions occurred. In both sample K10-11-07C1 and sample K10-11-08E, the mylonitic D_3 foliation was defined by muscovite and biotite in apparent textural equilibrium. This indicated deformation occurred above the biotite isograd (~400°C) and the brittle fracture of both sillimanite (Figure 6D) and feldspars (Figure 6C) during D_3 suggested a temperature of < ~500°C for D_3 (e.g., Fossen, 2016). In other words, D_3 occurred at ~400–500°C. The calculated closure temperature for muscovite was ~415–425°C, and so we interpreted the similar plateau ages of all samples (24.5-23.3 Ma, Tables 1, 3–7) as cooling ages. These ages could also be growth ages, but due to the rapid cooling rate of the samples, in either interpretation, the geologic conclusions are very similar. These data either constrain the timing of the upper greenschist facies D_3 deformation and mylonite formation to 26.6-23.3 Ma or directly date the growth of mylonite-defining fabrics at 24.5–23.3 Ma.

All biotite (five biotite and one phlogopite) samples yielded similar ages of ~25.4-24.9 Ma. For the reasons given above, we interpreted all ages as cooling ages though 340–350°C and 420–430°C, respectively. In general, the biotite ages were expected to be younger than both phlogopite and muscovite ages due to the biotite's lower closure temperature. However, we observed that biotite ages overlapped with phlogopite ages but were slightly older than most muscovite ages. In as much, as the muscovite and biotite samples were not from identical outcrops and were similar in age, we interpreted the older biotite ages to reflect local differences in cooling rate in this complex structural region. We also could not rule out a minor component of excess argon in biotite as is commonly observed (e.g., Kelley, 2002).

The interpretation of the K-feldspar data was somewhat more complicated, as mineralogically and microstructurally K-feldspars are complicated, and no consensus exists in the geochronology community on the interpretation of K-feldspar degassing data (e.g., Harrison and Lovera, 2014; Villa, 2014). In this research, we interpreted the high-temperature step ages of step-heating experiments to reflect the time of cooling through ~300–310°C (Table 2), and the low-temperature steps to reflect the time of cooling through ~250-150°C (Harrison and McDougall, 1982), and/or recrystallization. Three samples, of which two were from the DNCV core (K10-11-07A1 and K10-11-07A2) and one was from a Qz-Ksp-Ms vein (K10-11-07C) in the western shear zone, yielded nearly identical age spectra with low-temperature steps yielding ages of ~24.0-21.5 Ma and high-temperature steps yielding ages of ~27-25 Ma. The high-temperature ages overlapped with the ages of biotite from the same samples. These values were again consistent with rapid cooling through K-feldspar closure-concomitant with D_3 deformation. Two samples from mylonitic rocks yielded different ages. Sample K10-11-08B from a D_3 shear zone yielded a humped-shaped spectrum with "intermediate age maxima," a feature common in K-feldspar from highly deformed rocks but that is poorly understood (Lovera et al., 2002). Interestingly the low and high-temperature steps yielded similar ages to the other three samples—and we suggested they were broadly consistent. Sample K10-11-07D from the western mylonite yielded a low-temperature age of ~22 Ma, but an anomalously high-temperature age of ~39 Ma. We interpreted this older age to reflect local post-D_3-mylonite vertical displacements within the

TABLE 3 $^{40}Ar/^{39}Ar$ dating result of Amphibole, sample K10-11-08A.

Sample No	Mineral dated		Rock type			Longitude		Latitude
K10-11-08A	Amphibole		Amphibolite			104.36749		22.18094
K10-11-8A Amphibole 126KD57			J = 0.004817			wt. = 205.1 mg		
Temperature (°C)	^{39}Ar(% total)	Radiogenic yield (%)	$^{39}Ar_K$ (moles)	$^{40}Ar^*/^{39}Ar_K$	Ca/K	Cl/K	Age (Ma)	Error (Ma)
700	0.0	−673.7	9.91E-17	36.355	***	***	295.4	320.9
900	0.1	24.2	3.84E-13	27.134	4.4307	0.2000	224.9	4.2
1,000	0.5	73.6	8.40E-14	4.309	2.2467	0.0044	37.6	0.6
1,050	0.3	67.4	4.83E-14	3.639	5.7372	0.0060	31.8	1.0
1,075	0.5	78.1	8.17E-14	3.837	8.0128	0.0046	33.5	0.6
1,100	1.0	83.8	1.31E-13	3.486	7.9681	0.0033	30.5	0.3
1,125	4.9	92.8	5.42E-13	3.170	7.3964	0.0023	27.7	0.1
1,150	19.7	94.5	2.06E-12	3.075	7.6982	0.0025	26.9	0.1
1,175	30.2	96.6	3.05E-12	3.039	7.8003	0.0025	26.6	0.1
1,200	26.7	98.1	2.65E-12	3.029	7.5529	0.0023	26.5	0.1
1,225	5.4	92.8	5.77E-13	3.081	7.5415	0.0027	27.0	0.1
1,250	3.7	91.2	4.03E-13	3.088	7.9051	0.0028	27.0	0.1
1,275	4.2	93.6	4.57E-13	3.175	7.7519	0.0025	27.8	0.1
1,300	2.0	90.9	2.21E-13	3.197	7.7821	0.0030	28.0	0.3
1,350	0.6	79.9	7.76E-14	3.034	7.6511	0.0040	26.6	0.6
1,450	0.3	53.5	5.44E-14	3.174	7.7160	0.0068	27.8	0.9
1,650	0.1	7.7	4.11E-13	20.109	7.2464	0.2500	169.2	15.3
1,650	0.0	8.1	1.66E-13	36.672	4.0225	0.5000	297.8	25.7
Plateau age= 26.55 ± 0.1 (Ma)							Integrated age= 27.3 (Ma)	

10.3389/feart.2023.1125279

TABLE 4 $^{40}Ar/^{39}Ar$ dating results of Muscovite.

Muscovite K10-11-07C								
Sample No	Mineral dated		Rock type			Longitude		Latitude
K10-11-07C	Muscovite		K-feldspar vein close to phyllite			104.35962		22.18013
K10-11-07C Muscovite 92KD57			J = 0.004921			wt. = 2.75 mg		
Temperature (°C)	^{39}Ar (% total)	Radiogenic yield (%)	$^{39}Ar_K$ (moles)	$^{40}Ar^*/^{39}Ar_K$	Ca/K	Cl/K	Age (Ma)	Error (Ma)
600	0.2	1.6	5.26E-16	1.381	0.317	0.0191	12.4	10.8
700	0.4	38.7	9.80E-16	3.474	−0.060	0.0004	31.0	4.2
800	1.3	70.6	3.05E-15	2.970	−0.037	0.0005	26.6	1.4
850	1.9	59.7	4.42E-15	2.832	−0.024	0.0007	25.3	0.9
900	3.3	59.8	7.89E-15	2.722	−0.006	0.0006	24.4	0.6
950	14.5	74.7	3.45E-14	2.735	0.004	0.0004	24.5	0.2
1,000	23.1	91.6	5.50E-14	2.700	0.005	0.0003	24.2	0.1
1,050	12.0	95.2	2.87E-14	2.727	0.003	0.0003	24.4	0.2
1,100	5.7	89.8	1.36E-14	2.698	−0.008	0.0000	24.1	0.3
1,150	3.8	88.3	9.12E-15	2.781	0.006	0.0002	24.9	0.5
1,200	4.2	87.5	9.95E-15	2.723	0.020	0.0004	24.4	0.5
1,250	5.9	82.6	1.41E-14	2.752	0.003	0.0005	24.6	0.4
1,300	14.1	92.9	3.37E-14	2.723	0.005	0.0003	24.4	0.1
1,350	7.5	93.6	1.80E-14	2.669	0.017	0.0004	23.9	0.3
1,450	1.4	81.4	3.31E-15	2.684	0.040	0.0002	24.0	1.5
1,650	0.4	48.3	9.86E-16	3.236	−0.012	0.0012	28.9	4.4
1,650	0.1	7.4	2.19E-16	1.331	−0.230	0.0066	12.0	20.3
1,650	0.1	4.6	1.32E-16	1.531	−0.111	0.0122	13.7	31.5
Plateau age= 24.31± 0.18 (Ma)							Integrated age= 24.4 (Ma)	
Muscovite K10-11-07C1								
Sample No	Mineral dated		Rock type			Longitude		Latitude
K10-11-07C1	Muscovite		Phyllite			104.35962		22.18013
K10-11-07C1 Muscovite 44KD57			J = 0.004819 ± 0.50%					
Temperature (°C)	^{39}Ar (% total)	Radiogenic yield (%)	$^{39}Ar_K$ (moles)	$^{40}Ar^*/^{39}Ar_K$	Ca/K	Cl/K	Age (Ma)	Error (Ma)
600	0.3	10.7	6.21E-16	2.032	0.094	0.0109	18.1	5.9
700	0.6	45.6	1.13E-15	2.540	0.161	0.0032	22.6	3.3
800	1.5	78.6	2.81E-15	3.053	−0.005	0.0010	27.2	1.3
850	1.9	82.1	3.53E-15	3.051	0.053	0.0000	27.2	1.0
900	3.0	72.8	5.47E-15	2.855	0.007	0.0003	25.4	0.7
950	9.4	67.7	1.72E-14	2.830	0.009	0.0004	25.2	0.3
1,000	26.6	78.4	4.86E-14	2.744	0.006	0.0003	24.4	0.1
1,050	11.9	91.5	2.17E-14	2.739	0.011	0.0004	24.4	0.2
1,100	5.9	87.2	1.08E-14	2.815	0.024	0.0003	25.1	0.4
1,150	3.0	77.0	5.50E-15	2.836	0.049	0.0004	25.3	0.6

(Continued on following page)

TABLE 4 (*Continued*) $^{40}Ar/^{39}Ar$ dating results of Muscovite.

Muscovite K10-11-07C1								
Sample No	Mineral dated		Rock type			Longitude		Latitude
1,200	2.9	76.0	5.38E-15	2.882	0.045	0.0005	25.7	0.7
1,250	4.8	60.0	8.73E-15	2.756	0.024	0.0006	24.6	0.5
1,300	20.0	85.9	3.64E-14	2.742	0.010	0.0003	24.4	0.1
1,350	5.7	92.9	1.04E-14	2.831	0.011	0.0005	25.2	0.3
1,450	1.4	72.6	2.55E-15	2.819	0.036	0.0001	25.1	1.3
1,650	0.6	38.6	1.06E-15	4.025	0.060	0.0007	35.7	3.4
1,650	0.2	8.8	3.81E-16	4.187	0.331	0.0041	37.2	10.5
1,650	0.1	10.4	1.45E-16	9.328	−0.076	−0.0062	81.8	27.0
Plateau age= 24.5 ± 0.2							Integrated age= 24.9 (Ma)	
Muscovite K10-11-08B								
Sample No	Mineral dated		Rock type			Longitude		Latitude
K10-11-08B	Muscovite		Pegmatitic feldspar vein with muscovite			104.39417		22.19635
K10-11-08B Muscovite 100KD57			J = 0.004916± 0.50%			wt. = 2.98 mg		
Temperature (°C)	^{39}Ar (% total)	Radiogenic yield (%)	$^{39}Ar_K$ (moles)	$^{40}Ar^*/^{39}Ar_k$	Ca/K	Cl/K	Age (Ma)	Error (Ma)
600	0.5	2.6	1.32E-15	0.990	0.251	0.0124	8.9	4.6
700	1.2	38.1	2.80E-15	2.084	0.018	0.0020	18.7	1.7
800	2.1	64.1	5.14E-15	2.831	0.041	0.0016	25.3	0.9
850	2.6	78.3	6.20E-15	2.715	0.006	0.0007	24.3	0.8
900	4.0	77.8	9.68E-15	2.715	−0.006	0.0006	24.3	0.5
950	9.7	77.9	2.34E-14	2.656	0.005	0.0009	23.7	0.2
1,000	22.1	92.1	5.33E-14	2.601	0.005	0.0009	23.3	0.1
1,050	15.9	96.0	3.84E-14	2.631	0.004	0.0010	23.5	0.1
1,100	10.6	91.8	2.54E-14	2.600	0.010	0.0011	23.2	0.2
1,150	8.1	86.5	1.96E-14	2.558	0.011	0.0015	22.9	0.2
1,200	8.1	90.7	1.94E-14	2.720	0.023	0.0014	24.3	0.2
1,250	6.2	86.4	1.49E-14	2.664	0.019	0.0009	23.8	0.4
1,300	6.0	88.6	1.44E-14	2.609	0.023	0.0008	23.3	0.4
1,350	1.6	88.8	3.93E-15	2.866	0.009	0.0008	25.6	1.2
1,450	0.7	90.6	1.70E-15	3.438	−0.055	−0.0008	30.7	2.9
1,650	0.5	36.9	1.14E-15	2.738	0.056	0.0007	24.5	4.5
1,650	0.1	4.6	1.32E-16	4.081	0.571	0.0207	36.4	38.3
1,650	0.0	6.2	7.10E-17	7.896	0.453	−0.0291	69.7	70.8
Plateau age= 23.3± 0.2 (Ma)							Integrated age= 23.5 (Ma)	
Muscovite K10-11-08E								
Sample No	Mineral dated		Rock type			Longitude		Latitude
K10-11-08E	Muscovite		Mylonite			104.58536		22.17402
K10-11-08E Muscovite 102KD57			J = 0.004889 ± 0.50%			wt. = 2.79 mg		

(Continued on following page)

TABLE 4 (*Continued*) $^{40}Ar/^{39}Ar$ dating results of Muscovite.

Temperature (°C)	^{39}Ar (% total)	Radiogenic Yield (%)	$^{39}Ar_k$ (moles)	$^{40}Ar^*/^{39}Ar_k$	Ca/K	Cl/K	Age (Ma)	Error (Ma)
600	0.4	3.1	9.13E-16	2.643	0.209	0.0116	23.5	12.6
700	0.9	37.4	1.98E-15	3.036	−0.060	0.0009	27.0	4.9
800	2.5	66.1	5.61E-15	2.659	0.019	0.0004	23.6	1.7
850	3.2	63.9	7.26E-15	2.550	0.007	0.0002	22.7	1.3
900	5.2	59.8	1.18E-14	2.742	0.021	0.0002	24.4	0.8
950	19.1	71.5	4.36E-14	2.687	0.001	0.0001	23.9	0.2
1,000	17.9	88.1	4.09E-14	2.595	0.008	0.0002	23.1	0.2
1,050	8.3	83.5	1.90E-14	2.604	0.003	0.0002	23.2	0.5
1,100	4.8	76.3	1.09E-14	2.616	0.003	0.0004	23.3	0.9
1,150	4.2	73.5	9.68E-15	2.627	0.023	0.0003	23.4	1.0
1,200	5.6	48.6	1.28E-14	2.791	0.025	0.0004	24.8	0.8
1,250	6.6	61.7	1.52E-14	2.661	0.007	0.0003	23.7	0.6
1,300	12.0	81.1	2.73E-14	2.644	0.009	0.0003	23.5	0.3
1,350	6.0	81.4	1.37E-14	2.619	0.019	0.0002	23.3	0.7
1,450	2.6	59.1	6.00E-15	2.523	0.016	0.0000	22.4	1.5
1,650	0.5	13.5	1.21E-15	1.565	0.317	0.0017	13.9	7.7
1,650	0.1	−12.4	1.78E-16	−2.323	0.782	0.0021	−20.9	52.2
1,650	0.0	−21.8	9.76E-17	−6.064	−1.713	−0.0045	−55.1	97.6
Plateau age= 23.5± 0.3 (Ma)							Integrated age= 23.4 (Ma)	

western mylonite zone. In this scenario, sample K10-11-07D was in the lower greenschist facies (~250–300°C) during incipient D_3 deformation at ~25 Ma. This resulted in the recrystallization of some feldspar during D_3 (22 Ma) but also the preservation of relict (pre-D_3) ^{40}Ar in K-feldspar porphyroclast.

4.4 Reconstructed cooling path and timing structural events of the DNCV

Based on our structural, petrological, and geochronological data, and the interpretations aforementioned we reconstructed a cooling path for the DNCV metamorphic massif (Figure 9). All phlogopite, muscovite, and biotite ages were interpreted as cooling ages (see above) and were plotted with ±25°C error bars on the closure temperatures reported in Table 2. K-feldspar high-temperature steps ages were plotted with a closure temperature of ~300–310°C and the low-temperature step ages were plotted at ~250–150°C, recognizing that recrystallization also played a role in the argon systematics. Three different cooling paths were reconstructed for different lithology units as they went through different paths. For the amphibolite and garnet-biotite-sillimanite gneiss within the core of the DNCV dome, the timing and peak temperature conditions could be linked via our new amphibole, phlogopite, muscovite, biotite, and K-feldspar ages within the core region. The amphibole cooling ages reported by Wang et al. (1998) and the timing of peak metamorphism from Palin et al. (2013) were also combined with our reconstructed cooling path (dashed green line in Figure 9B). The thermal evolution of the core of the DNCV dropped from 700°C to 550°C around 32 Ma, but remained within 540°C–550°C from 32 Ma until 26 Ma. The core further uplifted to 410°C–430°C condition during 26–24 Ma followed by further uplifting till ~200°C condition during 23 Ma. Similarly, by combining all muscovite and K-feldspar ages within the mylonite zones, a steep cooling path from 410 to 430°C condition starting from 24 Ma until ~200°C condition during 22 Ma was indicated (gray solid line in Figure 9B). Although we did not collect any samples from the deformed Eocene leucogranite bodies, we reconstructed a third cooling path for these magmatic units based on previously reported ages (Harrison et al., 1996; Leloup et al., 2001; Palin et al., 2013). We observed a rapid cooling path from 800°C to 350°C around 34 Ma followed by stable conditions of 350°C to 300°C between 34 and 24 Ma followed by a rapid cooling to ~200°C condition during 22 Ma (red dash line in Figure 9B).

The timing of D_1 to D_3 corresponded to the reconstructed cooling paths that were allocated according to the estimated metamorphic conditions and observed structural styles. As our petrography and structural results indicated, the D_1 occurred under granulite facies with compressional conditions. Therefore, we linked the timing of D_1 to before 32 Ma but after the youngest magmatism that intruded the DNCV (35 Ma; Zhang and Schärer, 1999). Although the Permian-Triassic Indosinian orogeny is the most dominant magmatic

TABLE 5 $^{40}Ar/^{39}Ar$ dating result of Biotite.

Biotite K10-11-07A								
Sample No	Mineral dated		Rock type			Longitude		Latitude
K10-11-07A	Biotite		Amphibolite			104.91108		21.79692
K10-11-07A Biotite 73KD57			J = 0.004845 ± 0.5 %			wt. = 18.3 mg		
Temperature (°C)	^{39}Ar (% total)	Radiogenic yield (%)	$^{39}Ar_K$ (moles)	$^{40}Ar^*/^{39}Ar_K$	Ca/K	Cl/K	Age (Ma)	Error (Ma)
600	0.1	5.5	2.68E-15	6.245	0.9910	0.1429	55.5	2.4
700	0.4	30.4	8.90E-15	2.094	0.2084	0.0132	18.8	0.9
800	4.4	56.4	1.13E-13	2.857	0.0190	0.0087	25.6	0.1
850	12.4	85.4	3.21E-13	2.779	0.0055	0.0068	24.9	0.1
900	15.9	95.1	4.09E-13	2.752	0.0033	0.0065	24.7	0.1
950	5.7	95.1	1.47E-13	2.791	0.0107	0.0071	25.0	0.1
1,000	4.4	95.8	1.13E-13	2.776	0.0097	0.0065	24.9	0.1
1,050	4.1	95.7	1.05E-13	2.796	0.0087	0.0066	25.0	0.1
1,100	6.3	95.6	1.63E-13	2.787	0.0072	0.0063	25.0	0.1
1,150	12.5	95.0	3.21E-13	2.767	0.0058	0.0064	24.8	0.1
1,200	17.9	95.2	4.62E-13	2.764	0.0031	0.0065	24.8	0.1
1,250	13.9	95.6	3.58E-13	2.788	0.0057	0.0065	25.0	0.1
1,300	1.7	88.5	4.46E-14	2.763	0.0206	0.0066	24.8	0.2
1,350	0.3	75.8	8.83E-15	2.944	0.0809	0.0081	26.4	0.7
1,450	0.0	19.7	4.51E-16	4.414	0.5231	0.0263	39.4	11.6
1,650	0.0	11.5	4.53E-16	5.673	0.0685	0.0769	50.5	10.6
1,650	0.0	9.5	1.02E-16	16.101	2.4795	0.2000	139.7	60.7
No plateau age							Integrated age = 24.9 (Ma)	
Biotite K10-11-07A1								
Sample No	Mineral dated		Rock type			Longitude		Latitude
K10-11-07A1	Biotite		Leucocratic dyke			104.91108		21.79692
K10-11-07A1 Biotite 28KD59			J = 0.009363 ± 0.0000468			wt. = 0.5 mg		

(Continued on following page)

10.3389/feart.2023.1125279

TABLE 5 (*Continued*) $^{40}Ar/^{39}Ar$ dating result of Biotite.

Temperature (°C)	^{39}Ar (% total)	Radiogenic yield (%)	$^{39}Ar_K$ (moles)	$^{40}Ar^*/^{39}Ar_K$	Ca/K	Cl/K	Age (Ma)	Error (Ma)
600	0.2	2.0	6.34E-16	2.249	1.8822	0.1142	38.1	45.2
700	0.2	38.7	6.10E-16	7.542	1.6513	0.2070	124.6	32.6
850	0.6	51.5	2.32E-15	4.509	0.9254	0.1128	75.5	9.0
900	0.6	69.8	2.32E-15	3.121	−0.0051	0.0158	52.6	8.5
925	0.6	122.9	2.19E-15	3.946	−0.1774	0.0078	66.3	9.0
950	0.8	85.0	3.18E-15	2.311	−0.0339	0.0070	39.1	6.4
975	1.3	74.7	4.90E-15	1.822	−0.0538	0.0051	30.9	4.1
1,000	1.6	72.4	6.25E-15	1.741	−0.0279	0.0048	29.5	3.3
1,100	7.1	45.5	2.68E-14	1.519	0.0119	0.0093	25.8	1.0
1,150	4.3	80.4	1.63E-14	1.565	0.0082	0.0181	26.6	1.3
1,200	6.3	78.9	2.40E-14	1.530	0.0075	0.0181	26.0	0.9
1,250	10.4	71.6	3.93E-14	1.487	0.0078	0.0111	25.3	0.6
1,350	65.4	89.7	2.48E-13	1.466	0.0030	0.0467	24.9	0.1
1,450	0.6	34.7	2.14E-15	1.369	0.0981	0.4174	23.3	9.6
1,650	0.1	11.3	1.99E-16	5.747	−0.7250	0.6764	95.7	103.0
1,650	0.0	9.0	1.43E-17	50.917	11.7876	0.1244	712.3	1,000.3
Plateau age = 25.0 ± 0.4 (Ma)							Integrated age = 26.4 Ma	
Biotite K10-11-08B1B								
Sample No	Mineral dated		Rock type			Longitude		Latitude
K10-11-08B1B	Biotite		Garnet + sillimanite + biotite + mylonite			104.39417		22.19635
K10-11-8B1B Biotite 88KD57			J = 0.004841 ± 0.0000242			wt. = 0.93 mg		
Temperature (°C)	^{39}Ar (% total)	Radiogenic yield (%)	$^{39}Ar_K$ (moles)	$^{40}Ar^*/^{39}Ar_K$	Ca/K	Cl/K	Age (Ma)	Error (Ma)
600	0.5	0.9	3.36E-16	1.607	0.485	0.0247	14.4	19.1
700	1.5	24.2	1.02E-15	2.110	−0.027	0.0055	18.9	4.6
800	7.9	68.6	5.32E-15	2.625	−0.020	0.0077	23.5	0.8

(Continued on following page)

10.3389/feart.2023.1125279

TABLE 5 (*Continued*) $^{40}Ar/^{39}Ar$ dating result of Biotite.

Biotite K10-11-08B1B								
Sample No	Mineral dated		Rock type			Longitude		Latitude
850	12.3	88.6	8.27E-15	2.624	−0.011	0.0081	23.5	0.5
900	13.9	95.4	9.39E-15	2.736	−0.010	0.0082	24.5	0.5
950	8.3	98.7	5.62E-15	2.885	0.001	0.0080	25.8	0.9
1,000	4.6	84.4	3.09E-15	2.542	−0.004	0.0082	22.8	1.3
1,050	3.4	111.2	2.26E-15	3.730	−0.130	0.0072	33.3	2.0
1,100	2.9	81.7	1.98E-15	2.851	−0.007	0.0080	25.5	2.0
1,150	4.5	92.8	3.01E-15	4.011	−0.003	0.0098	35.8	1.5
1,200	7.0	93.5	4.69E-15	3.320	0.076	0.0084	29.7	0.9
1,250	10.7	76.1	7.24E-15	2.802	−0.005	0.0083	25.1	0.6
1,300	19.7	92.3	1.33E-14	2.695	−0.005	0.0078	24.1	0.3
1,350	2.0	68.8	1.33E-15	2.581	0.078	0.0066	23.1	3.0
1,450	0.6	54.9	4.33E-16	2.858	−0.102	0.0082	25.6	9.2
1,650	0.1	13.6	4.58E-17	11.909	−1.639	0.0252	104.3	81.5
1,650	0.0	8.8	2.30E-17	10.576	−1.489	−0.0008	92.9	160.2
1,650	0.0	−4.3	2.27E-17	−4.543	7.483	0.0483	−41.4	178.8
No plateau age								Integrated age = 25.4 Ma

10.3389/feart.2023.1125279

TABLE 6 $^{40}Ar/^{39}Ar$ dating result of Phlogopite.

Phlogopite K10-11-07A3								
Sample No	Mineral dated		Rock type			Longitude		Latitude
K10-11-07A3	Phlogopite		Marble + amphibole+ phlogopite			104.91108		21.79692
K10-11-07A3 Phlogopite 46KD57			J = 0.004904± 0.50 %			wt.= 2.6 mg		
Temperature (°C)	^{39}Ar (% total)	Radiogenic yield (%)	$^{39}Ar_K$ (moles)	$^{40}Ar^*/^{39}Ar_K$	Ca/K	Cl/K	Age (Ma)	Error (Ma)
600	0.2	−0.1	3.75E-16	−0.126	0.456	0.0327	−1.1	23.2
700	0.2	27.2	4.82E-16	5.158	0.433	0.0029	45.7	14.9
800	0.4	44.6	8.82E-16	3.429	0.755	0.0010	30.5	8.0
850	0.4	64.2	9.26E-16	3.494	−0.023	0.0015	31.1	7.5
900	0.6	60.4	1.32E-15	3.716	0.050	0.0013	33.0	5.2
950	1.3	57.0	3.03E-15	2.933	0.029	0.0017	26.1	2.3
1,000	4.4	60.7	1.04E-14	2.857	0.021	0.0011	25.5	0.7
1,050	7.3	78.6	1.72E-14	2.777	0.015	0.0012	24.8	0.4
1,100	5.9	93.6	1.39E-14	2.940	0.015	0.0009	26.2	0.5
1,150	7.4	89.6	1.75E-14	2.814	0.017	0.0012	25.1	0.4
1,200	10.6	74.4	2.48E-14	2.844	0.005	0.0012	25.4	0.3
1,250	14.6	74.2	3.45E-14	2.822	0.011	0.0011	25.2	0.2
1,300	26.8	87.8	6.30E-14	2.787	0.008	0.0011	24.8	0.1
1,350	17.8	91.8	4.20E-14	2.792	0.006	0.0010	24.9	0.2
1,450	1.7	77.7	4.10E-15	3.046	0.014	0.0008	27.1	1.7
1,650	0.2	27.6	5.86E-16	4.829	0.008	0.0024	42.8	12.1
1,650	0.1	31.5	1.71E-16	6.188	−0.117	0.0017	54.7	39.8
1,650	0.0	15.7	6.26E-17	6.284	0.385	−0.0226	55.5	109.6
Plateau Age = 25 ± 0.2 (Ma)								Integrated age= 25.3 (Ma)

10.3389/feart.2023.1125279

TABLE 7 $^{40}Ar/^{39}Ar$ **dating results of K-feldspar.**

K-feldspar K10-11-07A1								
Sample No	Mineral dated		Rock type			Longitude		Latitude
K10-11-07A1	K-feldspar		Leucocratic dyke			104.91108		21.79692
K10-11-07A1 K-feldspar 107KD57			J = 0.004806 ± 0.5 %			wt. = 27.9 mg		
Temperature (°C)	^{39}Ar (% total)	Radiogenic yield (%)	$^{39}Ar_K$ (moles)	$^{40}Ar^*/^{39}Ar_K$	Ca/K	Cl/K	Age (Ma)	Error (Ma)
700	0.6	27.8	3.39E-14	11.235	0.2326	0.0345	97.9	6.5
750	5.8	89.2	3.15E-13	2.669	0.0225	0.0003	23.7	0.1
800	5.3	95.0	2.89E-13	2.666	0.0188	0.0002	23.7	0.1
850	4.5	95.2	2.45E-13	2.585	0.0155	***	23.0	0.1
900	3.4	94.9	1.87E-13	2.645	0.0167	0.0002	23.5	0.1
950	2.7	93.4	1.46E-13	2.685	0.0232	0.0002	23.9	0.1
1,000	2.3	89.8	1.23E-13	2.698	0.0215	0.0004	24.0	0.1
1,050	2.4	87.0	1.29E-13	2.788	0.0170	0.0004	24.8	0.1
1,100	3.0	82.1	1.64E-13	2.924	0.0125	0.0007	26.0	0.1
1,150	4.9	77.9	2.65E-13	3.065	0.0133	0.0009	27.2	0.1
1,200	8.4	81.2	4.56E-13	3.063	0.0145	0.0008	27.2	0.1
1,250	17.8	85.9	9.68E-13	2.995	0.0107	0.0005	26.6	0.1
1,300	30.3	87.6	1.64E-12	2.965	0.0057	0.0004	26.3	0.1
1,350	7.1	87.1	3.86E-13	2.909	0.0071	0.0006	25.9	0.1
1,400	1.1	86.5	5.81E-14	2.832	0.0232	0.0007	25.2	0.2
1,450	0.3	82.5	1.34E-14	2.921	0.0897	0.0012	26.0	0.9
1,650	0.2	60.7	9.44E-15	2.765	0.0159	0.0029	24.6	0.9
1,650	0.0	7.2	9.97E-17	8.226	5.2743	0.1667	72.2	80.1
No Plateau age							Integrated age= 26.2 (Ma)	
K-feldspar K10-11-07A2								
Sample No	Mineral dated		Rock type			Longitude		Latitude
K10-11-07A2	K-Feldspar		Biotite+Garnet+ augen Feldspar			104.91108		21.79692
K10-11-07A2 K-feldspar 30KD57			J = 0.00478 ± 0.50%			wt. = 2.8 mg		
Temperature (°C)	^{39}Ar (% total)	Radiogenic yield (%)	$^{39}Ar_K$ (moles)	$^{40}Ar^*/^{39}Ar_K$	Ca/K	Cl/K	Age (Ma)	Error (Ma)
600	0.2	25.0	4.60E-16	10.374	−0.388	0.0153	90.0	13.6
700	0.8	63.5	2.44E-15	3.901	0.021	0.0020	34.4	2.5
750	1.2	91.9	3.55E-15	2.778	0.135	0.0005	24.5	1.7
800	2.0	97.7	6.04E-15	2.802	0.013	0.0004	24.8	1.0
850	2.6	90.9	7.88E-15	2.573	−0.018	0.0006	22.7	0.8
900	2.9	97.1	8.70E-15	2.743	0.032	0.0005	24.2	0.7
950	3.0	95.8	8.85E-15	2.705	0.061	0.0001	23.9	0.7
1,000	2.8	88.9	8.32E-15	2.743	−0.017	0.0004	24.2	0.7
1,050	2.5	86.6	7.60E-15	2.724	0.035	0.0005	24.1	0.8
1,100	2.1	92.0	6.44E-15	2.788	0.073	0.0004	24.6	0.9
1,150	1.9	93.2	5.68E-15	2.844	0.044	0.0006	25.1	1.0
1,200	2.1	92.4	6.17E-15	2.900	0.044	0.0005	25.6	0.9
1,250	2.1	95.2	6.28E-15	2.978	−0.021	0.0005	26.3	0.9

(Continued on following page)

TABLE 7 (*Continued*) $^{40}Ar/^{39}Ar$ dating results of K-feldspar.

K-feldspar K10-11-07A2								
Sample No	Mineral dated		Rock type			Longitude		Latitude
1,275	1.7	87.5	5.20E-15	2.656	0.057	0.0004	23.5	1.1
1,300	1.7	92.0	5.11E-15	2.937	0.016	0.0004	25.9	1.1
1,325	2.0	86.5	5.86E-15	2.917	0.097	0.0002	25.8	1.1
1,350	2.2	86.6	6.67E-15	2.942	0.030	0.0007	26.0	1.0
1,375	2.4	86.2	7.21E-15	2.847	0.030	0.0004	25.1	0.9
1,400	2.6	66.6	7.84E-15	3.127	−0.009	0.0000	27.6	0.9
1,450	49.9	86.8	1.50E-13	2.783	0.027	0.0003	24.6	0.1
1,550	9.4	87.5	2.83E-14	2.814	0.025	0.0002	24.9	0.2
1,650	1.9	77.4	5.77E-15	2.933	0.038	0.0008	25.9	1.0
Plateau Age = 24.6 ± 0.2							Integrated age= 25 (Ma)	
K-feldspar K10-11-07C								
Sample No	Mineral dated		Rock type			Longitude		Latitude
K10-11-07C	K-feldspar		K-feldspar vein close to phyllite			104.35962		22.18013
K10-11-07C K-feldspar 97KD57			J = 0.004831± 0.5 %			wt. = 27.26 mg		
Temperature (°C)	^{39}Ar(% total)	Radiogenic yield (%)	$^{39}Ar_K$ (moles)	$^{40}Ar^*/^{39}Ar_K$	Ca/K	Cl/K	Age (Ma)	Error (Ma)
700	0.7	16.5	2.06E-14	11.619	0.3206	0.0667	101.6	1.1
750	4.8	69.8	1.39E-13	2.494	0.0357	0.0013	22.3	0.1
800	4.1	83.5	1.20E-13	2.398	0.0386	0.0007	21.5	0.1
850	4.1	87.9	1.20E-13	2.409	0.0353	0.0005	21.5	0.1
900	4.8	90.7	1.38E-13	2.454	0.0266	0.0002	22.0	0.1
950	5.7	92.0	1.66E-13	2.514	0.0259	0.0002	22.5	0.1
1,000	6.2	90.7	1.79E-13	2.514	0.0266	0.0003	22.5	0.1
1,050	6.2	91.1	1.79E-13	2.564	0.0212	0.0002	22.9	0.1
1,100	6.0	88.9	1.74E-13	2.612	0.0187	0.0003	23.4	0.1
1,150	6.3	80.6	1.83E-13	2.686	0.0184	0.0006	24.0	0.1
1,200	7.4	71.8	2.14E-13	2.738	0.0215	0.0011	24.5	0.1
1,250	16.6	65.4	4.84E-13	2.842	0.0284	0.0017	25.4	0.1
1,300	21.8	69.8	6.35E-13	2.863	0.0135	0.0014	25.6	0.1
1,350	3.6	68.2	1.06E-13	2.892	0.0174	0.0017	25.8	0.1
1,400	1.4	62.5	3.97E-14	3.023	0.0364	0.0025	27.0	0.3
1,450	0.4	58.9	1.06E-14	3.054	0.0370	0.0029	27.3	0.9
1,650	0.1	33.6	2.51E-15	3.702	0.1850	0.0112	33.0	4.3
1,650	0.0	11.9	6.16E-17	25.328	5.0327	0.2500	214.7	118.0
No Plateau age							Integrated age= 24.6 (Ma)	
K-feldspar K10-11-07D								
Sample No	Mineral dated		Rock type			Longitude		Latitude
K10-11-07D	K-feldspar		Muscovite mylonite			104.35852		22.17977
K10-11-07D K-feldspars 28KD57			J = 0.004778 ± 0.50%			wt.= 2.8 mg		
Temperature (°C)	^{39}Ar (% total)	Radiogenic Yield (%)	$^{39}Ar_K$ (moles)	$^{40}Ar^*/^{39}Ar_k$	Ca/K	Cl/K	Age (Ma)	Error (Ma)
600	0.5	37.7	1.42E-15	13.931	0.305	0.0094	119.9	4.5
700	5.0	89.0	1.38E-14	3.035	0.045	0.0004	26.8	0.4

(Continued on following page)

TABLE 7 (*Continued*) $^{40}Ar/^{39}Ar$ dating results of K-feldspar.

K-feldspar K10-11-07D								
Sample No	Mineral dated		Rock type			Longitude		Latitude
750	1.8	95.2	4.85E-15	2.559	0.003	0.0003	22.6	1.2
800	6.8	96.4	1.89E-14	2.566	0.029	0.0004	22.7	0.3
850	5.8	96.1	1.60E-14	2.524	0.013	0.0003	22.3	0.4
900	5.2	89.7	1.45E-14	2.544	0.034	0.0002	22.5	0.4
950	4.5	94.3	1.25E-14	2.623	0.009	0.0004	23.2	0.5
1,000	4.2	98.0	1.17E-14	2.738	0.017	0.0005	24.2	0.5
1,050	3.9	92.7	1.08E-14	2.658	−0.006	0.0004	23.5	0.5
1,100	3.6	95.2	9.95E-15	2.967	0.015	0.0003	26.2	0.6
1,150	3.5	91.4	9.74E-15	3.312	0.020	0.0006	29.2	0.6
1,200	4.6	75.2	1.26E-14	3.906	0.045	0.0007	34.4	0.5
1,250	4.7	83.1	1.31E-14	3.806	0.060	0.0006	33.5	0.4
1,275	5.3	89.7	1.47E-14	4.131	0.013	0.0005	36.4	0.4
1,300	7.1	93.7	1.96E-14	4.312	0.032	0.0005	37.9	0.3
1,325	16.4	95.4	4.53E-14	4.461	0.029	0.0006	39.2	0.1
1,350	13.3	96.0	3.69E-14	4.122	0.022	0.0006	36.3	0.2
1,375	2.9	93.8	8.14E-15	3.643	0.018	0.0007	32.1	0.7
1,400	0.4	74.5	1.12E-15	3.761	0.168	0.0019	33.1	5.1
1,450	0.2	44.7	4.77E-16	3.811	0.074	0.0007	33.6	11.8
1,550	0.1	51.9	3.85E-16	6.602	0.185	−0.0004	57.8	14.9
1,650	0.0	11.1	8.97E-17	4.795	5.170	0.0312	42.1	67.5
No Plateau age							Integrated age= 31.6 (Ma)	
K-feldspar K10-11-08B								
Sample No	Mineral dated		Rock type			Longitude		Latitude
K10-11-08B	K-feldspar		Pegmatic feldspar vein with muscovite			104.39417		22.19635
K10-11-08B K-feldspars 104KD57						J = 0.004807 ± 0.50%		
Temperature (°C)	^{39}Ar (%total)	Radiogenic yield (%)	$^{39}Ar_k$ (moles)	$^{40}Ar^*/^{39}Ar_k$	Ca/K	Cl/K	Age (Ma)	Error (Ma)
600	0.2	86.4	1.32E-15	70.896	0	0.0031	544.6	5.3
700	2.5	90.4	1.92E-14	3.947	0	−0.0001	35.0	0.3
750	3.2	96.9	2.43E-14	2.661	0	−0.0001	23.7	0.2
800	4.2	99.0	3.25E-14	2.682	0	0.0000	23.8	0.1
850	5.7	99.4	4.37E-14	2.775	0	0.0001	24.7	0.1
900	6.8	97.1	5.17E-14	2.704	0	0.0000	24.0	0.1
950	7.2	98.8	5.47E-14	2.722	0	0.0000	24.2	0.1
1,000	6.9	99.2	5.27E-14	2.892	0	0.0000	25.7	0.1
1,050	6.1	99.0	4.64E-14	3.193	0	−0.0001	28.3	0.1
1,100	4.4	98.9	3.35E-14	3.584	0	0.0000	31.8	0.1
1,150	3.8	97.0	2.94E-14	4.388	0	0.0000	38.9	0.2
1,200	4.5	89.2	3.41E-14	4.282	0	0.0000	37.9	0.2
1,250	4.0	89.9	3.10E-14	3.419	0	0.0000	30.3	0.2
1,275	4.3	91.4	3.31E-14	3.420	0	−0.0001	30.3	0.2

(Continued on following page)

TABLE 7 (*Continued*) $^{40}Ar/^{39}Ar$ dating results of K-feldspar.

K-feldspar K10-11-08B								
Sample No	Mineral dated		Rock type			Longitude		Latitude
1,300	6.7	93.6	5.11E-14	3.513	0	0.0000	31.2	0.2
1,325	14.2	92.4	1.09E-13	3.255	0	0.0000	28.9	0.1
1,350	12.0	91.3	9.19E-14	3.138	0	0.0000	27.9	0.1
1,375	3.4	90.2	2.63E-14	3.039	0	−0.0001	27.0	0.2
1,400	0.5	84.7	3.93E-15	2.970	0	−0.0006	26.4	1.0
1,450	0.3	103.0	2.25E-15	3.841	0	0.0001	34.0	1.9
1,550	0.2	74.4	1.61E-15	3.790	0	−0.0002	33.6	2.6
1,650	0.0	32.3	3.68E-16	8.229	0	−0.0046	72.2	11.3
1,650	0.0	28.4	7.00E-17	31.919	0	−0.0056	265.4	61.5
No Plateau age							Integrated age= 29.6 (Ma)	

event that produced the majority of granitic rocks in northern Vietnam (Carter et al., 2001; Usuki et al., 2015; Shellnutt et al., 2020) and provided a more suitable kinematic condition for D_1, it is unlikely that the high-grade metamorphic condition remained from the Permian-Triassic time until the Eocene. Without the cross-cutting relationship of granite introducing into the D_1 structure nor the D_1 structure deforming these Eocene leucogranites, the actual timing of D_1 cannot be distinguished and, with our current data, we can only suggest that it occurred before 32 Ma. The stable thermal condition under amphibolite facies between 26 and 32 Ma coincided with the sub-horizontal folding. Hence, we allocated this time period to D_2 with an estimated cooling rate of ~25°C/Ma. The retrograde evolution from amphibolite facies to the greenschist facies between 26–22 Ma was considered to be the timing of D_3, with an estimated cooling rate of ~100°C/Ma. The timing of shear belt development was defined between 24 and 22 Ma as the cooling path for mylonitic rocks. Brittle deformation occurred after 22 Ma, with an estimated cooling rate of ~10°C/Ma, which is similar to the static denudation (≤10°C/Ma; Costa et al., 1993). If we convert the cooling rate to rock exhumation rate by assuming an average continental geotherm of 25°C/km (Criss, 2020), D_2 uplifted the DNCV metamorphic massif from 30-28 km to 20-18 km with an uplifting rate of 1.2 mm/year, and D_3 uplifted the DNCV massif from ~20 km to ~8 km with an uplifting rate of 3 mm/year. The uplifting rate of 1–3 mm/year was not fast compared to the average uplifting rate of orogenic belts, which is 4–10 mm/year. Instead, it nearly fell within the average denudation rate of ca 2–5 mm/year for the tropical regions for the time scale over tens of million years (Regard et al., 2016). Therefore, the cooling path that we reconstructed was a feasible one, and the "rapid cooling" could correspond to the D_3 up-right doming accompanied by tropical fast denudation rather than to the strike-slip shearing-induced uplifting.

5 Discussion

5.1 Comparison of $^{40}Ar/^{39}Ar$ data with previous works

The $^{40}Ar/^{39}Ar$ system can be a thermochronometer and/or a geochronometer. In a poly-deformed geologic setting, and/or a setting where deformation and mineral growth continue over a wide temperature range, it is possible that multiple age groups from the same phase can be obtained. We also plotted previously reported $^{40}Ar/^{39}Ar$ ages (Harrison et al., 1996; Wang et al., 1998; Leloup et al., 2001) in Figure 9. Our results were broadly consistent with Wang et al. (1998) as nearly all data points fell along the reconstructed cooling curve. Harrison et al. (1996) and Leloup et al. (2001) showed quite different results (older and wider age ranges) that were unlikely compatible with our proposed cooling path. Due to the strain partitioning, the structure preserved within different portions of the DNCV metamorphic massif was heterogeneous. However, that did not greatly vary the ages of the same mineral that passes through the closure temperature, and the youngest age of the same mineral separates marked the timing for passing through the closure age. No distinct variation for the cooling pattern was noticed between the north outcrop *versus* the southern outcrop within the DNCV. The granitic rocks further away from the DNCV massif might have contributed to the wider age range reported by Leloup et al. (2001). Searle et al. (2006) pointed out that these granitic rocks were formed pre-shearing, and had nothing to do with left-lateral shearing along the RRSZ. Hence, the $^{40}Ar/^{39}Ar$ ages obtained from these granitic rocks may not provide timing for shearing. All our samples were collected within different structural domains including the mylonite belts along the DNCV massif, making a more reliable reconstruction of the geochronological-thermal evolution.

5.2 Newly constrained timing of left lateral shearing along the RRSZ

Multiple structural events within the DNCV metamorphic massif were reported by numerous studies (e.g., Ankczkiewicz et al., 2007; Yeh et al., 2008). Different interpretations have been given to explain what type of deformation event is syn-shearing. Our petrological and structural reconstruction indicated three ductile deformation events. The granulite facies to upper amphibolite facies centimeter to meter scale NNW-SSE striking upright D_1 folds formed prior to 32 Ma. This D_1 event can be linked to the peak metamorphism as previously published studies noted (e.g., Nam et al., 1998; Gilley et al., 2003; Khoi et al., 2016). Wang and Burchfiel

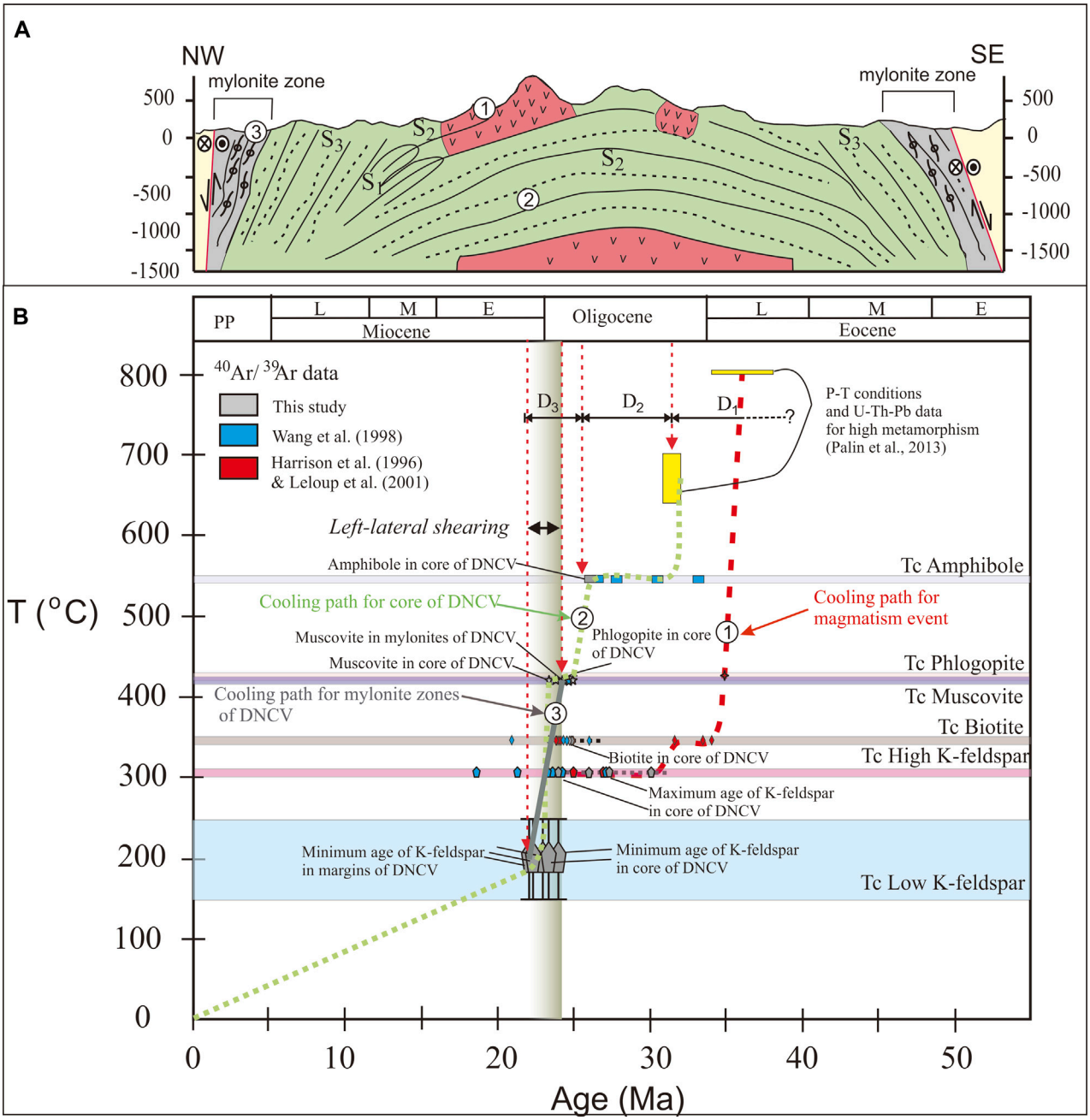

FIGURE 9
Reconstructed cooling paths of different lithological units within the Day Nui Con Voi metamorphic massif based on our age results and published data (Harrison et al., 1996; Wang et al., 1998; Leloup et al., 2001; Palin et al., 2013). **(A)** Cross section indicating the three lithological units that are used for cooling path reconstruction. The green region represents the metamorphic complex core, and the red region represents the Eocene leucogranites that are deformed by D_2. The gray region represents the mylonitic belts. **(B)** The reconstructed cooling paths of the Eocene leucogranite rocks (red dashed line), metamorphic complex core (green dashed line), and mylonitic belts (gray solid line). The yellow box represents data from Palin et al. (2013) for high-temperature deformation of the DNCV metamorphic massif. Rectangle, 4-branch star, 5-branch star, and rhombus indicate $^{40}Ar/^{39}Ar$ data of amphibole, phlogopite, muscovite, and biotite, respectively. Pentagon and pentagon with bar represent high- and low-temperature K-feldspar, respectively. The estimated closure temperatures of different minerals are Tc of amphibole: ~540–550°C; Tc of phlogopite: ~420–430°C; Tc of muscovite: ~415–425°C; Tc of biotite: ~340–350°C; Tc of High K-feldspar (orthoclase): ~300–310°C (Table 2); and Tc of Low K-feldspar: ~150–250°C (Harrison and McDougall, 1982).

(1997) and Jolivet et al. (2001) suggested crustal thickening with regional shortening structures that occurred in southeastern China and northern Vietnam result from the India and Eurasia collision during the Eocene to Early Oligocene. The mechanism of crustal thickening with regional shortening structures is suggested to have caused the lithology units to reach the granulite facies condition and anatexis melting of the over thickened crust. The emplacement of Eocene leucogranite was further supported by Zhang and Scharer (1999).

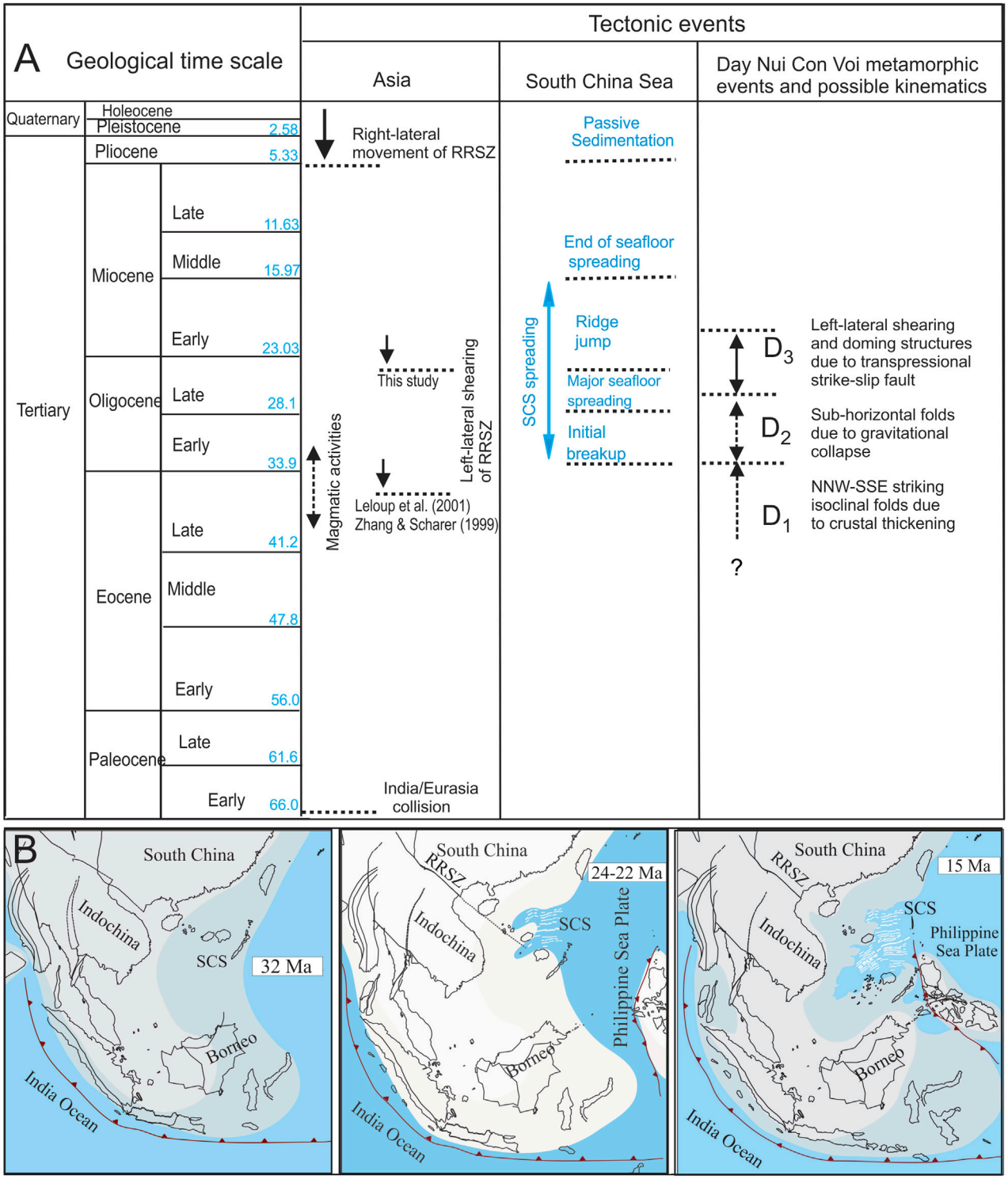

FIGURE 10
(A) Reconstructed timing of tectonic events occurring in Asia since the Cenozoic time as compiled from our data and published research (Taylor and Hayes, 1980; Tapponnier et al., 1982; 1986; Briais et al., 1993; Lee and Lawver, 1995; Zhang and Schärer, 1999; Leloup et al., 2001; Li et al., 2014). **(B)** Paleogeographic reconstruction shows the timing relationship between the opening of the SCS and the movement of the RRSZ (Modified from Mai et al., 2018). The sea-floor spreading of the SCS started around 32 Ma at the northwest sub-basin. The spreading ridge jumped into the southwestward direction at around 24 Ma, which is temporally consistent with the onset movement of the RRSZ. The opening of the SCS ended at around 15 Ma.

The amphibolite facies meter-scale subhorizontal D_2 folds occurred during 32-26 Ma. Similar structures were also observed by Jolivet et al. (2001) in the DNCV metamorphic massif and by Zhang et al. (2021) in the Diancang Shan metamorphic massif. Jolivet et al. (2001) indicated the horizontal structures observed in the DNCV metamorphic massif had been formed due to sub-

horizontal shear doming. Yeh et al. (2008), on the other hand, further explained the subhorizontal shear folding due to gravitational collapsing instead of shear doming. Changing to gravitational collapse after crustal thickening is a common phenomenon in most mountainous regions, such as: in the Alps and Himalaya mountain ranges (Burov, 2010), and in the Fansipan mountain range of northern Vietnam (Dinh et al., 2022). We considered the DNCV metamorphic massif to be no exception, that the thickened crust of the massif started to collapse during D_2. The collapse of the thickened mountain ranges caused the maximum principal stress (σ_1) to change direction from horizontal to vertical, and formed the horizontal folding structures as observed in the D_2 deformation event. The stable thermal condition under amphibolite facies, with little cooling/ up-lifting, is expressed in our reconstructed cooling path. Such stress setting is not suitable for triggering left-lateral shearing event; thus, we do not consider D_2 to be a syn-shearing event.

The D_3 doming event under green schist facies during ~26–22 Ma was considered to be a syn-shearing event. Petrological and microstructural analyses indicated that the D_3 deformation event occurred under greenschist facies conditions with muscovite fish bearing mylonite. The muscovite fish and other shear sense indicators all showed a left-lateral sense of shear. The same orientation of the shear plan of the S/C fabrics and the S_3 fold axial plane indicated that these fabrics were formed under the same deformation event. The temperature ranges of greenschist facies nearly overlapped the closure temperatures in the argon system for amphibole, muscovite, biotite, phlogopite, and K-feldspar (Table 2). This allowed us to provide better constraints on the timing, rate, and duration of the D_3 event. As the closure temperature of the amphibole was consistent with the upper limit of the inferred temperature for the D_3 event, the minimum age of the amphibole (ca. 26 Ma) was used to constrain the onset timing of the D_3 deformation event. The minimum age of K-feldspar (ca. 22 Ma) could be used to provide the termination time of the D_3 event. Although the reconstructed cooling path indicated relatively rapid cooling since 26 Ma, and duration time for the D_3 event of ~26–22 Ma, our microstructural and petrological analyses of mylonite showed syn-shearing growth of muscovite. The cooling ages of muscovite (~24 Ma), thus, was marked as the upper bound of the initiation of the left-lateral shearing activity. The termination of the left-lateral shearing was marked as the mylonites had passed the brittle-ductile transition condition, marked by the youngest age of K-feldspar (~22 Ma). Thus, the timing for left-lateral shearing was further constrained from ~24 Ma to ~22 Ma.

Previous studies linked our D_2 and D_3 together (Jolivet et al., 2001; Anczkiewicz et al., 2007; Viola and Anczkiewicz, 2008) by suggesting a transtensional kinematic condition to form the sub-horizontal folds that were later sheared into a dome via transtension This extensional setting created the space for high-grade metamorphic and magmatic rocks from the lower crustal portion to be uplifted to form the core of the dome. Hence, according to their reconstructed structural evolution, the youngest magmatism within the DNCV (Eocene to Early Oligocene; e.g., Chung et al., 1997) was syn-shearing. Zhang and Schärer (1999) and Leloup et al. (2001) constrained the timing for the onset of left-lateral shearing along the RRSZ to be around 35 Ma by dating the undeformed granitic rocks from the Fansipan massif, 10 km away from the RRSZ. A wide distribution of undeformed Late Eocene granitic rocks with ages ranging from around 39 to 30 Ma was reported across the Tibetan Plateau, Yunnan, and Vietnam regions (e.g., Chung et al., 1997; Junlai et al., 2020; Gou et al., 2021; Li et al., 2021). This geographical distribution further contradicted the hypothesis that these magmatism events were syn-transtensional shearing. On the contrary, these magmatism events corresponded to our D_1 granulite facies metamorphism as the thickened crust started to stretch and extend. Geochemical data of Chung et al. (1997) and Gou et al. (2021) revealed these magmas originated from collapsing of the thickened crust within plate following the India-Eurasia collision. However, the proposed transtension shearing was not the forming mechanism for our D_3 event as a transtensional basin rather than a dome would have been expected in such a case. We agree with Yeh et al. (2008) that a transpressional condition with sub-horizontal compression along with an oblique component of strike-slip movement further compressed the high-grade metamorphic rocks from the middle crustal level to the upper crystal level. The tectonic transition from the D_2 gravitational collapse to D_3 left-lateral transpressional shearing can be explained by the interaction between tectonics and surface processes. Gravitational collapse likely occurred in the high mountainous area as a result of gravitational potential energy that produced the vertical maximum principle stress (σ_1). After some time, the mountain heights would be reduced due to the effect of surface processes, particularly erosion. Under the intense impact of the erosional process, together with continued crustal shortening in the Indochina block in response to the oblique collision between the India and Eurasia block, the direction of maximum principle stress (σ_1) will switch from vertical to horizontal. In this scenario, the transpressional tectonic setting would likely occur, which could result in the D_3 structures observed in the DNCV metamorphic massif.

5.3 Tectonic implications of the evolution of the DNCV metamorphic massif

Structural styles are fundamentally controlled by regional tectonic settings. Thus, structural changes are a direct reflection of the change in the tectonic setting. Vietnam is situated between the Tibetan plateau and the SCS, which means the structural evolution would be influenced by the Cenozoic India Eurasia collision and the Cenozoic opening of the SCS. The geodynamics of the thickened continental crust within and around the Tibetan Plateau would also affect the structural activities of many oblique regions such as in SE Asia. Following the India-Eurasia collision, the extrusion of the SE Asia continental crust away from India during the Tertiary induced many large-scale strike-slip faults (Tapponnier et al., 1982; tapponnier et al., 1986). Among the strike-slip faults, the RRSZ fault is considered one of the most significant geological structures in SE Asia. Left-lateral strike-slip movement along the RRSZ has been widely regarded as a tectonic mechanism for the opening of the SCS as supported by the indentation extrusion model (Tapponnier et al., 1982; tapponnier et al., 1986). If the indentation

extrusion tectonism is corrected, tectonic events/deformation of the whole process will be in accordance with the time sequence for the opening of SCS as shown in Figure 1A.

Based on data from our study and the published research of others, we have reconstructed the temporal relationship of tectonic events that occurred in Asia (Figure 10). The onset of sea-floor spreading in the SCS was suggested to be around 32 Ma at the northwest sub-basin (Briais et al., 1993; Lee and Lawver, 1995). The ridge jumped southwestward around 24 Ma (Li et al., 2014). The spreading of the SCS ended at around 15 Ma (Taylor and Hayes, 1980; Briais et al., 1993). By assuming the undeformed 39 to 30 Ma granitic rocks as the anatexial product of the syn-shearing activity, this shearing activity was considered to cause the opening of the SCS as the Indochina block extruded (Jolivet et al., 2001; Leloup et al., 2001; Anczkiewicz et al., 2007; Viola and Anczkiewicz, 2008). Our new constrained age of ~24–22 Ma for the shear activity suggested otherwise. The SCS had opened before the initiation of the left-lateral shear activity of the RRSZ. The formation of the protolith of our D_1 gneiss fabrics, which formed under granulite facies prior to 32 Ma, can be linked to crustal thinning due to back arc extension and subduction of Neotethys as the SCS opened (e.g., Karig, 1971; Mai et al., 2018). These granulite facies metamorphism and wide-spread regional leucogranitic magmatism played a critical role in crustal weakening before the strike-slip movement (e.g., Chung et al., 1997; Junlai et al., 2020; Gou et al., 2021; Li et al., 2021). As the SCS further rifted, the continental crust was further thinned. Yeh et al. (2008) reported the sub-horizontal fold (D_2) with the sense of shear of a top to NW and bottom to SW sense of shear along the sub-horizontal folds (D_2). The rapid cooling following the D_2 sub-horizontal folding with retrograde metamorphism reflects this crustal thinning condition. Based on our reconstructed cooling paths of leucogranite and the core of the DNCV, the continental crust of northern Vietnam has been thermally weakened by the Eocene magmatism followed by crustal stretching and thinning due to gravitational collapsing prior to the development of mylonite belts that initiated movement along the RRSZ.

Our interpretation of ~24–22 Ma for the left-lateral movement of the RRSZ matches the southwestward ridge jumping event of the SCS (e.g., Karig, 1971; Mai et al., 2018). Kinematically, it would be difficult for a low-density continental crust to "push" a dense oceanic crust. Therefore, it is unlikely that the left-lateral movement along the RRSZ triggered the southwestward ridge jump in the SCS. On the contrary, the continental crust moved along with the oceanic crust as the ridge jumped. In such a case, a northwestward younging trend should be expected for the initiation age of the RRSZ as the shear activity propagated from the oceanic crust to the continental crust. In other words, if the RRSZ was a result of southeastward extrusion as proposed by the indentation extrusion model (Tapponnier et al., 1982; tapponnier et al., 1986), the shear zone should have developed and propagated from the SW corner of the Tibetan plateau toward the SCS. Initiation age is expected to be older for the northwestern-most metamorphic complex, such that Diancang Shan is older than Ailao Shan that, inturn, is older than the DNCV metamorphic massif. Leloup et al. (2001) showed different cooling histories preserved from different portions of the RRSZ. The reported initiation age within the southeastern part of the Ailao Shan massif was between 21–17 Ma (Harrison et al., 1996; Leloup et al., 2001), and that for the Diancang Shan massif was between 23–17 Ma (Yeh et al., 2014; Zhang et al., 2021), which are slightly younger than what we proposed for the DNCV. If the initiation timing is correct, that further supports that the left-lateral shearing propagated from Vietnam northwestward toward southwestern Tibet, and the extrusion of Indochina coincided with the ridge jumping event rather than the opening event of the SCS.

6 Conclusion

The $^{40}Ar/^{39}Ar$ ages obtained from amphibole (~26 Ma), phlogopite (~25 Ma), muscovites (~24-23 Ma), biotite (~25-23 Ma), and K-feldspars (~25-22 Ma) collected from different structural domains of the DNCV metamorphic massif showed a rapid exhumation between ~26–22 Ma. By incorporating microstructural, petrological, and thermochronological evolution, a temporal-thermal-deformation history was reconstructed. The oldest deformation event D_1 formed NNW-SSE striking vertical axial-plane folds. The mineral assemblage of quartz, K-feldspar, biotite, garnet, and sillimanite indicated metamorphic conditions from granulite facies to upper amphibolite facies possibly occurred before 32 Ma. The second deformation event D_2 relates to sub-horizontal to inclined folds. Mineral assemblages of sillimanite + biotite + high deformed quartz and feldspar suggested that the D_2 deformation event happened between upper to lower amphibolite facies (~650°C–500°C) conditions, possibly during ~32–26 Ma. The last ductile deformation event D_3 was a large-scale doming event associated with left-lateral transpressional shearing. The new precipitation of muscovite and albite within the mylonite belts indicated a greenschist facies metamorphic condition had occurred during shearing. The cooling age of syn-shearing muscovite (~24 Ma) marked the upper bound of the initiation of the left-lateral shear activity. The youngest K-feldspar age (~22 Ma) indicated the termination of the ductile shearing activity as the deformation condition had passed the brittle-ductile transition. This age (~24–22 Ma) coincided with the age of the ridge jump event rather than the initial rifting event in the SCS. Thus, the extrusion tectonism had not caused the initial opening of the SCS. Rather, the SE extrusion of Indochina coincided with the southward ridge jump of the SCS.

Data availability statement

The original contributions presented in the study are included in the article/Supplementary Material, further inquiries can be directed to the corresponding author.

Ethics Statement

Written informed consent was obtained from the individual(s) for the publication of any potentially identifiable images or data included in this article.

Author contributions

The samples were collected by M-WY, T-YL, MK, and RW. Argon analysis are conducted by MK, and RM. Data are

processed by T-HD and M-WY. The MS is mainly composed by T-HD, M-WY, and T-YL. All authors contributed to the article and approved the submitted version.

Funding

Ministry of Science and Technology (MOST) of Taiwan. This research was supported by the Ministry of Science and Technology (MOST) of Taiwan under project numbers: NSC 99-2116-M-003 -005 - and NSC 100-2116-M-003 -002.

Acknowledgments

We thank Prof. H. S. Mii, Department of Earth Sciences of the National Taiwan Normal University, Taiwan for providing equipment for cathodoluminescence analyses. Any use of trade, firm, or product names was for descriptive purposes only and does not imply endorsement by the U.S. Government.

Conflict of interest

The authors declare that the research was conducted in the absence of any commercial or financial relationships that could be construed as a potential conflict of interest.

Publisher's note

Supplementary material

The Supplementary Material for this article can be found online at: https://www.frontiersin.org/articles/10.3389/feart.2023.1125279/full#supplementary-material

References

Anczkiewicz, R., Viola, G., Müntener, O., Thirlwall, M. F., Villa, I. M., and Quong, N. Q. (2007). Structure and shearing conditions in the day Nui Con Voi massif: Implications for the evolution of the Red River Shear zone in northern Vietnam. *Tectonics* 26. doi:10.1029/2006TC001972

Ben-Avraham, Z., and Uyeda, S. (1983). Entrapment origin of marginal seas. *Geodyn. West. Pacific-Indonesian Reg.* 11, 91–104.

Briais, A., Patriat, P., and Tapponnier, P. (1993). Updated interpretation of magnetic anomalies and seafloor spreading stages in the south China Sea: Implications for the Tertiary tectonics of Southeast Asia. *J. Geophys. Res. Solid Earth* 98, 6299–6328. doi:10.1029/92JB02280

Burov, E. (2010). *New Frontiers in integrated solid Earth Sciences*. Berlin, Germany: Springer. doi:10.1007/978-90-481-2737-5

Carter, A., Roques, D., Bristow, C., and Kinny, P. (2001). Understanding mesozoic accretion in southeast Asia: Significance of triassic thermotectonism (indosinian orogeny) in Vietnam. *Geology* 29, 211214. doi:10.1130/0091-7613(2001)029<0211:UMAISA>2.0.CO;2

Cassel, E. J., Calvert, A. T., and Graham, S. A. (2009). Age, geochemical composition, and distribution of Oligocene ignimbrites in the northern Sierra Nevada, California: Implications for landscape morphology, elevation, and drainage divide geography of the Nevadaplano. *Int. Geol. Rev.* 51 (7-8), 723–742.

Cesare, B., Marchesi, C., and Connolly, J. A. D. (2002). Growth of myrmekite coronas by contact metamorphism of granitic mylonites in the aureole of Cima di Vila, Eastern Alps, Italy. *J. Metamorph. Geol.* 20, 203–213. doi:10.1046/j.0263-4929.2001.00351.x

Christopherson, R. W., Byrne, M.-L., and Aitken, A. E. (2009). *Geosystems: An introduction to physical geography*. Saddle River, New Jersey: Pearson/Prentice Hall Upper.

Chung, S.-L., Lee, T.-Y., Lo, C.-H., Wang, P.-L., Chen, C.-Y., Yem, N. T., et al. (1997). Intraplate extension prior to continental extrusion along the Ailao Shan-Red River shear zone. *Geology* 25, 311. doi:10.1130/0091-7613(1997)025<0311:IEPTCE>2.3

Costa, S., Maluski, H., and Lardeaux, J.-M. (1993). 40Ar-39Ar chronology of variscan tectono-metamorphic events in an exhumed crustal nappe: The monts du Lyonnais complex (massif central, France). *Chem. Geol.* 105, 339–359.

Criss, R. E. (2020). "Chapter 6 - thermal models of the continental lithosphere," in *Heat transport and energetics of the Earth and rocky planets* (Amsterdam, Netherlands: Elsevier), 151–174.

Deino, A. L. (2014). Users manual for Mass Spec v. 7.961. Berkeley Geochronology Center Special Publication 3, 130.

Dinh, T. H., Chan, Y. C., and Chen, C. T. (2022). Extensional tectonics and basement uplift of the fansipan and tule mountain ranges in northern Vietnam. *Front. Earth Sci.* 9, 1–18. doi:10.3389/feart.2021.741670

Dinh, T.-H., Yeh, M.-W., Lee, T.-Y., Kunk, M. J., Wintsch, R. P., McAleer, R. J., et al. (2023). 40Ar/39Ar isotopic data from the Day Nui Con Voi metamorphic massif. *U. S. Geological Survey Data Release*. doi:10.5066/P95TMTH2

Dodson, M. H. (1973). Closure temperature in cooling geochronological and petrological systems. *Contributions Mineralogy Petrology* 40 (3), 259–274.

Dung, P. T., Hoa, T. T., Anh, T. T., Van Hieu, T., Ly, V. H., Ching-Ying, L., et al. (2012). New data of Ye Yen Sun granite complex in Phan Si Pan uplift. *Sci. Earth* 34 (3), 193–204.

Duong, V. H., Trinh, P. T., Nguyen, T. D., Piestrzyski, A., Nguyen, D. C., Pieczonka, J., et al. (2021). Cu-Au mineralization of the sin quyen deposit in north Vietnam: A product of cenozoic left-lateral movement along the Red River Shear zone. *Ore Geol. Rev.* 132, 104065. doi:10.1016/j.oregeorev.2021.104065

Fossen, H. (2016). *Structural geology*. Cambridge, United Kingdom: Cambridge University Press.

Froese, E. (1973). The assemblage quartz–K feldspar–biotite–garnet–sillimanite as an indicator of–T conditions. *Can. J. Earth Sci.* 10, 1575–1579.

Gilley, L. D., Harrison, T. M., Leloup, P. H., Ryerson, F. J., Lovera, O. M., and Wang, J.-H. (2003). Direct dating of left-lateral deformation along the Red River shear zone, China and Vietnam. *J. Geophys. Res. Solid Earth* 108. doi:10.1029/2001JB001726

Girdler, R. W. (1965). The formation of new oceanic crust. *Philos. Trans. R. Soc. Lond. Ser. A, Math. Phys. Sci.* 258, 123–136.

Gou, Q., Qian, X., Wang, Y., Wang, Y., Zhang, Y., and Wang, Y. (2021). Eocene-oligocene crustal thickening-collapse of the eastern Tibetan plateau: Evidence from the potassic granitoids in SW China. *Lithosphere* 2021, 1–34. doi:10.2113/2021/3343655

Hall, R. (2002). Cenozoic geological and plate tectonic evolution of SE Asia and the SW pacific: Computer-based reconstructions, model and animations. *J. Asian Earth Sci.* 20, 353–431. doi:10.1016/S1367-9120(01)00069-4

Hall, R. (1997). Cenozoic plate tectonic reconstructions of SE Asia. *Geol. Soc. Lond. Spec. Publ.* 126, 11–23.

Hall, R. (2009). Southeast Asia's changing palaeogeography. *Blumea-Biodiversity, Evol. Biogeogr. Plants* 54, 148–161.

Harrison, T. M., Leloup, P. H., Ryerson, F. J., Tapponnier, P., Lacassin, R., and Chen, W. (1996). Diachronous initiation of transtension along the ailao Shan-Red River Shear zone, yunnan and Vietnam. *World Reg. Geol.*, 208–226.

Harrison, T. M., and Lovera, O. M. (2014). The multi-diffusion domain model: Past, present and future. *Geol. Soc. Lond. Spec. Publ.* 378 (1), 91–106.

Harrison, T. M., and McDougall, I. (1982). The thermal significance of potassium feldspar K-Ar ages inferred from 40Ar39Ar age spectrum results. *Geochim. Cosmochim. Acta* 46, 1811–1820.

Haugerud, R. A., and Kunk, M. J. (1988). ArAr*; a computer program for reduction of 40Ar-39Ar data. *U.S. Geological Survey Open-file Report* 88–261, 67. doi:10.3133/OFR88261

Jolivet, L., Beyssac, O., Goffé, B., Avigad, D., Lepvrier, C., Maluski, H., et al. (2001). Oligo-Miocene midcrustal subhorizontal shear zone in Indochina. *Tectonics* 20, 46–57. doi:10.1029/2000TC900021

Junlai, L., Xiaoyu, C., Tang, Y. B., Song, Z., and Wang, W. (2020). The Ailao Shan–Red River shear zone revisited:Timing and tectonic implications. *Bull. Geol. Soc. Am.* 132, 1165–1182. doi:10.1130/b35220.1

Karig, D. E. (1971). Origin and development of marginal basins in the Western Pacific. *J. Geophys. Res.* 76, 2542–2561. doi:10.1029/JB076i011p02542

Kelley, S. (2002). Excess argon in K–Ar and Ar–Ar geochronology. *Chem. Geol.* 188 (1-2), 1–22.

Khoi, N. N., Hauzenberger, C. A., Tuan, D. A., Hager, T., Van Nam, N., and Duong, N. T. (2016). Mineralogy and petrology of gneiss hosted corundum deposits from the Day Nui Con Voi metamorphic range, Ailaoshan-Red River shear zone (North Vietnam). *J. Mineralogy Geochem.* 193 (2), 161.

Kuiper, K. F., Deino, A., Hilgen, F. J., Krijgsman, W., Renne, P. R., Wijbrans, J. R., et al. (2008). Synchronizing rock clocks of Earth history. *science* 320 (5875), 500–504.

Kunk, M. J., Wintsch, R. P., Naeser, C. W., Naeser, N. D., Southworth, C. S., Drake, A. A., et al. (2005). Contrasting tectonothermal domains and faulting in the Potomac terrane, Virginia-Maryland - discrimination by 40Ar/39Ar and fission-track thermochronology. *Bull. Geol. Soc. Am.* 117, 1347–1366. doi:10.1130/B25599.1

Lee, J.-Y., Marti, K., Severinghaus, J. P., Kawamura, K., Yoo, H.-S., Lee, J. B., et al. (2006). A redetermination of the isotopic abundances of atmospheric. *Ar. Geochim. Cosmochim. Acta* 70, 4507–4512.

Lee, T.-Y., and Lawver, L. A. (1995). Cenozoic plate reconstruction of southeast Asia. *Tectonophysics* 251, 85–138. doi:10.1016/0040-1951(95)00023-2

Leloup, P. H., Arnaud, N., Lacassin, R., Kienast, J. R., Harrison, T. M., Trong, T. T. P., et al. (2001). New constraints on the structure, thermochronology, and timing of the Ailao Shan-Red River shear zone, SE Asia. *J. Geophys. Res. Solid Earth* 106, 6683–6732. doi:10.1029/2000JB900322

Leloup, P. H., and Kienast, J.-R. (1993). High-temperature metamorphism in a major strike-slip shear zone: The ailao Shan—red River, people's republic of China. *Earth Planet. Sci. Lett.* 118, 213–234. doi:10.1016/0012-821X(93)90169-A

Leloup, P. H., Lacassin, R., Tapponnier, P., Schärer, U., Zhong, D., Liu, X., et al. (1995). The ailao Shan-Red River Shear zone (yunnan, China), tertiary transform boundary of Indochina. *Tectonophysics* 251, 3–84. doi:10.1016/0040-1951(95)00070-4

Leloup, P. H., Tapponnier, P., Lacassin, R., and Searle, M. P. (2007). Discussion on the role of the Red River Shear zone, yunnan and Vietnam, in the continental extrusion of SE Asia. *J. Geol. Soc. Lond.* 164, 12531260. doi:10.1144/0016-76492007-065

Li, C-F., Xu, X., Lin, J., Sun, Z., Zhu, J., Yao, Y., et al. (2014). Ages and magnetic structures of the South China Sea constrained by deep tow magnetic surveys and IODP Expedition 349. *Geochem. Geophys. Geosystems* 15, 4958–4983. doi:10.1002/2014GC005567

Li, J., Cao, S., Neubauer, F., Cheng, X., Wang, H., and Genser, J. (2021). Structure and spatial-temporal relationships of Eocene-Oligocene potassic magmatism linked to the Ailao Shan-Red River shear zone and post-collisional extension. *Lithos* 396–397, 106203. doi:10.1016/j.lithos.2021.106203

Liu, J., Chen, X., Tang, Y., Song, Z., and Wang, W. (2020). The Ailao ShanRed River shear zone revisited: Timing and tectonic implications. *Geol. Soc. Am. Bull.* 132 (5-6), 1165–1182.

Longley, I. M. (1997). The tectonostratigraphic evolution of SE Asia. *Geol. Soc. Lond. Spec. Publ.* 126, 311–339.

Lovera, O. M., Grove, M., and Harrison, T. M. (2002). Systematic analysis of K-feldspar 40Ar/39Ar step heating results II: Relevance of laboratory argon diffusion properties to nature. *Geochimica Cosmochimica Acta* 66 (7), 1237–1255.

Lovera, O. M., Richter, F. M., and Harrison, T. M. (1991). Diffusion domains determined by 39 Ar released during step heating. *J. Geophys. Res.* 96, 2057. doi:10.1029/90JB02217

Mai, H. A., Chan, Y. L., Yeh, M. W., and Lee, T. Y. (2018). Tectonic implications of Mesozoic magmatism to initiation of Cenozoic basin development within the passive South China Sea margin. *Int. J. Earth Sci.* 107, 1153–1174. doi:10.1007/s00531-017-1537-y

Min, K., Mundil, R., Renne, P. R., and Ludwig, K. R. (2000). A test for systematic errors in 40Ar/39Ar geochronology through comparison with U/Pb analysis of a 1.1–Ga rhyolite. *Geochim. Cosmochim. Acta* 64, 73–98.

Morley, C. K. (2002). A tectonic model for the Tertiary evolution of strike–slip faults and rift basins in SE Asia. *Tectonophysics* 347, 189–215.

Nam, T. N., Toriumi, M., and Itaya, T. (1998). P-T-t paths and post-metamorphic exhumation of the Day Nui Con Voi shear zone in Vietnam. *Tectonophysics* 290, 299–318. doi:10.1016/S0040-1951(98)00054-7

Palin, R. M., Searle, M. P., Waters, D. J., Parrish, R. R., Roberts, N. M. W., Horstwood, M. S. A., et al. (2013). A geochronological and petrological study of anatectic paragneiss and associated granite dykes from the Day Nui Con Voi metamorphic core complex, North Vietnam: Constraints on the timing of metamorphism within the Red River shear zone. *J. Metamorph. Geol.* 31, 359–387. doi:10.1111/jmg.12025

Regard, V., Carretier, S., Boeglin, J., Ndam Ngoupayou, J., Dzana, J., Bedimo Bedimo, J., et al. (2016). Denudation rates on cratonic landscapes: Comparison between suspended and dissolved fluxes, and 10Be analysis in the Nyong and Sanaga River basins, South Cameroon. *Earth Surf. Process. Landforms* 41, 1671–1683.

Schaen, A. J., Jicha, B. R., Hodges, K. V., Vermeesch, P., Stelten, M. E., Mercer, C. M., et al. (2020). Interpreting and reporting 40 Ar / 39 Ar geochronologic data. *Geol. Soc. Am. Bull.* 133 (3–4), 461–487. doi:10.1130/B35560.1/5084442/b35560.pdf

Schmitz, M. D. (2012). "Radiogenic isotope geochronology," in *The geologic time scale 2012*. Editors F. M. Gradstein, J. G. Ogg, M. D. Schmitz, and G. M. Ogg (Boston, Massachusetts: Elsevier), 115–126. doi:10.1016/B978-0-444-59425-9.00006-8

Searle, M. P. (2006). Role of the Red River Shear zone, yunnan and Vietnam, in the continental extrusion of SE Asia. *J. Geol. Soc. Lond.* 163, 1025–1036. doi:10.1144/0016-76492005-144

Searle, M. P., Yeh, M.-W., Lin, T.-H., and Chung, S.-L. (2010). Structural constraints on the timing of left-lateral shear along the Red River Shear zone in the ailao Shan and Diancang Shan ranges, yunnan, SW China. *Geosphere* 6, 316–338. doi:10.1130/GES00580.1

Shellnutt, J. G., Pham, T. T., Denyszyn, S. W., Yeh, M. W., and Tran, T. A. (2020). Magmatic duration of the Emeishan large igneous province: Insight from northern Vietnam. *Geology* 48, 457–471. doi:10.1130/G47076.1

Spear, F. S., Kohn, M. J., and Cheney, J. T. (1999). P-T paths from anatectic pelites. *Contrib. Mineral. Pet* 134, 17–32. doi:10.1007/s004100050466

Sun, W. (2016). Initiation and evolution of the South China sea: An overview. *Acta Geochim.* 35, 215–225. doi:10.1007/s11631-016-0110-x

Tapponnier, P., Peltzer, G., and Armijo, R. (1986). On the mechanics of the collision between India and Asia. *Geol. Soc. Lond. Spec. Publ.* 19, 113–157. doi:10.1144/GSL.SP.1986.019.01.07

Tapponnier, P., Peltzer, G., Le Dain, A. Y., Armijo, R., and Cobbold, P. (1982). Propagating extrusion tectonics in Asia: New insights from simple experiments with plasticine. *Geology* 10, 611–616. doi:10.1130/0091-7613(1982)10<611:PETIAN>2.0

Taylor, B., and Hayes, D. E. (1980). *The tectonic evolution of the South China Basin*. Washington, D.C., United States: American Geophysical Union AGU, 89–104. doi:10.1029/GM023p0089

Usuki, T., Lan, C.-Y., Tran, T. H., Pham, T. D., Wang, K.-L., Shellnutt, G. J., et al. (2015). Zircon U–Pb ages and Hf isotopic compositions of alkaline silicic magmatic rocks in the Phan Si Pan-Tu Le region, northern Vietnam: Identification of a displaced Western extension of the Emeishan Large Igneous Province. *J. Asian Earth Sci.* 97, 102–124. doi:10.1016/J.JSEAES.2014.10.016

Villa, I. M. (2014). Diffusion of Ar in K-feldspar: Present and absent. *Geol. Soc. Lond. Spec. Publ.* 378 (1), 107–116.

Viola, G., and Anczkiewicz, R. (2008). Exhumation history of the Red River shear zone in northern Vietnam: New insights from zircon and apatite fission-track analysis. *J. Asian Earth Sci.* 33, 78–90. doi:10.1016/j.jseaes.2007.08.006

Wang, E., and Burchfiel, B. C. (1997). Interpretation of Cenozoic tectonics in the right-lateral accommodation zone between the Ailao Shan shear zone and the eastern Himalayan syntaxis. *Int. Geol. Rev.* 39, 191219. doi:10.1080/00206819709465267

Wang, P. L., Lo, C. H., Lee, T. Y., Chung, S. L., Lan, C. Y., and Yem, N. T. (1998). Thermochronological evidence for the movement of the ailao Shan-Red River Shear zone: A perspective from Vietnam. *Geology* 26, 887–890. doi:10.1130/0091-7613(1998)026<0887:TEFTMO>2.3

Wang, P.-L., Lo, P.-H., Chung, S. L., Lee, T.-Y., Lan, C.-Y., Thang, T. V., et al. (2000). Onset timing of left-lateral movement along the Ailao ShanRed River Shear Zone: 40Ar/39Ar dating constraint from the Nam Dinh Area, northeastern Vietnam. *J. Asian Earth Sci.* 18 (3), 281–292. Elsevier. Available at:https://www.sciencedirect.com/science/article/pii/S1367912099000644 (Accessed October 23, 2018).

Wirth, R., and Voll, G. (1987). Cellular intergrowth between quartz and sodium-rich plagioclase (myrmekite) - an analogue of discontinuous precipitation in metal alloys. *J. Mat. Sci.* 22, 1913–1918. doi:10.1007/BF01132916

Wu, W., Liu, J., Zhang, L., Qi, Y., and Ling, C. (2017). Characterizing a middle to upper crustal shear zone: Microstructures, quartz c-axis fabrics, deformation temperatures and flow vorticity analysis of the northern Ailao Shan-Red River shear zone, China. *J. Asian Earth Sci.* 139, 95–114.

Ye, Q., Mei, L., Shi, H., Camanni, G., Shu, Y., Wu, J., et al. (2018). The Late Cretaceous tectonic evolution of the South China Sea area: An overview, and new perspectives from 3D seismic reflection data. *Earth-Science Rev.* 187, 186–204. doi:10.1016/j.earscirev.2018.09.013

Yeh, M.-W., Lee, T.-Y., Lo, C.-H., Chung, S.-L., Lan, C.-Y., and Anh, T. T. (2008). Structural evolution of the day Nui Con Voi metamorphic complex: Implications on the development of the Red River Shear zone, northern Vietnam. *J. Struct. Geol.* 30, 1540–1553. doi:10.1016/J.JSG.2008.08.007

Yeh, M. W., Wintsch, R. P., Liu, Y. C., Lo, C. H., Chung, S. L., Lin, Y. L., et al. (2014). Evidence for cool extrusion of the north Indochina block along the ailao Shan Red River Shear zone, a Diancang Shan perspective. *J. Geol.* 122, 567–590. doi:10.1086/677263

Zhang, B., Chen, S. Y., Wang, Y., Reiners, P. W., Cai, F. L., Speranza, F., et al. (2021). Crustal deformation and exhumation within the India-Eurasia oblique convergence zone: New insights from the Ailao Shan-Red River shear zone. *GSA Bull* doi:10.1130/b35975.1

Zhang, L.-S., and Schärer, U. (1999). Age and origin of magmatism along the Cenozoic Red River shear belt, China. *Contrib. Mineral. Pet.* 134, 67–85. doi:10.1007/s004100050469

frontiers | Frontiers in Earth Science

TYPE Original Research
PUBLISHED 14 August 2023
DOI 10.3389/feart.2023.1176937

OPEN ACCESS

EDITED BY
Shuangshuang Chen,
Sun Yat-sen University, China

REVIEWED BY
Gaoxue Yang,
Chang'an University, China
Anh Nong,
Ho Chi Minh City University of Science, Vietnam

*CORRESPONDENCE
Yuan-Hsi Lee,
leeyuanhsi@gmail.com

†PRESENT ADDRESS
Kristen L. Cook,
IRD, ISTerre, Université Grenoble Alpes, Grenoble, France

RECEIVED 01 March 2023
ACCEPTED 24 July 2023
PUBLISHED 14 August 2023

CITATION
Lee Y-H, Cook KL, Tan X-B, Chu M-F, Chiu H-Y, Li Q-L, Shellnutt JG and Xu X-W (2023), U-Pb ages of Gongga Shan granite, western Sichuan and its implication to the tectonic evolutions of eastern Tibet.
Front. Earth Sci. 11:1176937.
doi: 10.3389/feart.2023.1176937

U-Pb ages of Gongga Shan granite, western Sichuan and its implication to the tectonic evolutions of eastern Tibet

Yuan-Hsi Lee[1]*, Kristen L. Cook[2,3†], Xi-Bin Tan[4,5], Mei-Fei Chu[2], Han-Yi Chiu[2], Qui-Li Li[6], J. Gregory Shellnutt[7] and Xi-Wei Xu[4]

[1]Department of Earth and Environmental Sciences, National Chung-Cheng University, Minxiong, Taiwan, [2]Department of Geosciences, National Taiwan University, Taipei, Taiwan, [3]German Research Center for Geosciences, GFZ Potsdam, Potsdam, Germany, [4]Institute of Geology, China Earthquake Administration, Beijing, China, [5]State Key Laboratory of Earthquake Dynamics, Institute of Geology, China Earthquake Administration, Beijing, China, [6]Institute of Geology and Geophysics, Chinese Academy of Sciences, Beijing, China, [7]Department of Earth Sciences, National Taiwan Normal University, Taipei, Taiwan

The eastern margin of the Tibetan Plateau has given rise to much debate about mechanisms of plateau uplift and evolution and, in particular, the role of the lower crust in crustal thickening. Knowledge of the middle to lower crust conditions is critical for evaluating various models of crustal deformation, but data on crustal evolution through time are lacking. Here, we turn to the Gongga Shan granite, an intrusion along the Xianshuihe fault in easternmost Tibet that directly records local Cenozoic crustal conditions. We present 124 U-Pb samples from the Gongga Shan granite (GSG) that prove that the crust has been stepwise producing partial melt from 56 Ma to 4 Ma. According to the age distribution, the GSG can be separated into four major groups with ages of 4–10 Ma, 12–20 Ma, 25–40 Ma, and 43–56 Ma. Combining the timing information with geophysics and low-temperature thermochronology data, we suggest that events younger than 10 Ma may indicate the onset of recent crustal channel flow in the middle to lower crust. In contrast, the youngest 4 Ma ages indicate the ongoing partial melting of the middle crust. The 12–20 Ma events could be related to an earlier stage of crustal channel flow, consistent with the regional large-scale crustal channel flow in central Tibet.

KEYWORDS

Gongga Shan granite, eastern Tibet, magmatism, U-Pb dating, crustal channel flow

1 Introduction

The Tibetan plateau results from the collision between the India Plate and Eurasia Plate since ca. 55 Ma (de Sigoyer et al., 2000; Garzanti, 2008) and associated crustal thickening, surface uplift, and magmatism. Cenozoic magmatism on the Tibetan plateau shows systematic variations in space and time that are related to Tibetan tectonic evolution (Zhang H. F. et al., 2004; Zhang P. et al., 2004; Zhang Y. et al., 2004; Chung et al., 2005; King et al., 2011; Wang et al., 2012). The magmatism resulting from deeper crustal partial melting is one of the key pieces of evidence for differentiating tectonic processes from central to eastern Tibet (Figure 1). A controversial issue in eastern Tibet is the extent to which uplift has been driven by shortening along surface-breaking faults (Replumaz and Tapponnier, 2003) or by influx of ductile lower crustal material (Royden et al., 1997), which has significant

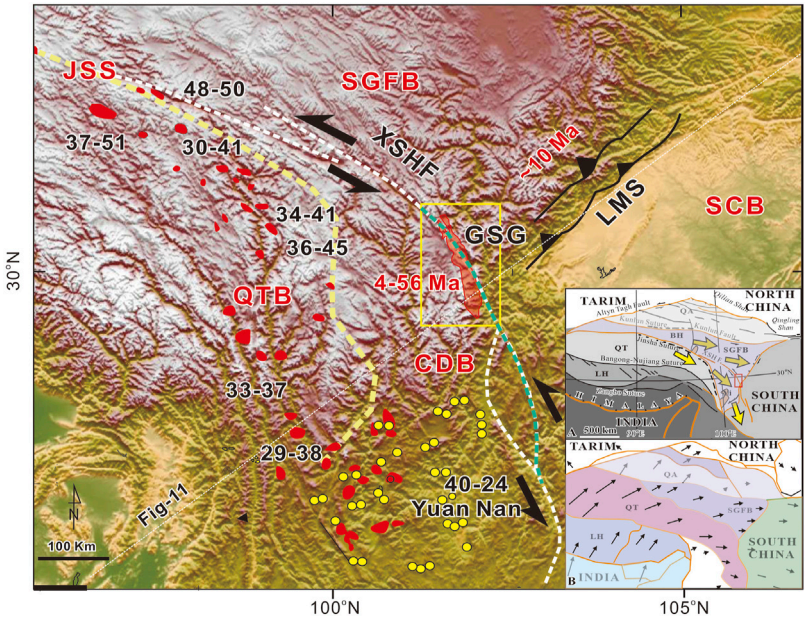

FIGURE 1
Distribution of Cenozoic magmatic events in eastern Tibet. The numbers indicate ages in Ma (data are from Chung et al., 2005; Guo et al., 2005; Spurlin et al., 2005). The solid yellow circles show the 40–24 Ma potassic lamprophyres in southeastern Tibet (Guo et al., 2005). The green dashed line indicates the location of a lithosphere discontinuity (Wang et al., 2010). The inset maps show two different tectonic models. In inert A, the yellow arrows showing the crustal flow directions suggested by geophysical data (Bai et al., 2010; Liu et al., 2014). Rapid exhumation and river incision started from ca. 10 Ma on the hanging wall of the LMS and eastern Tibet (Clark et al., 2005). Inset B shows the deformation (shortening, extrusion, and extensions) are consumed at the boundary of different tectonic blocks. The arrows show the calculated displacement field during 10-5 Ma (Replumaz and Tapponnier, 2003). LMS: Longmenshan fault; SCB: Sichuan Basin, GSG: Gongga Shan granite; QT: Qiangtang block; CDB: Chuan-Dian diamond block; SGFB: Songpan-Garzê fold belt; XSHF: Xianshuihe fault system (white and green dot line); JSS: Jinsha Suture (yellow dot line). Green dash line shows the lithospheric discontinuity from the GSG to ca. latitude 27o-28° (Lei and Zhao, 2016).

implications for our understanding of how continents deform. In the Himalaya and southern Tibet, the channel flow mechanism has been widely accepted as an influence on the uplift of the Tibetan Plateau between the late Oligocene to the Miocene time (Beaumont et al., 2001; Godin et al., 2006). In eastern Tibet, a similar mechanism has been used to model the topography of the eastern margin of the Tibetan Plateau since 10-13 Ma (Clark et al., 2005). The crustal flow requires that the middle to lower crust contain material with reduced viscosity, enabling it to flow laterally in response to pressure/topographic gradients. Even small amounts of partial melt can significantly reduce the strength of continental crust (Rosenberg and Handy, 2005), so the occurrence of crustal melting helps to determine the viability of crustal flow. While geophysical techniques can be used to probe the nature of the crust, such data are indirect and are rarely unequivocal, engendering debate about their interpretation and implications. In addition, geophysical techniques only observe the current state of the crust, providing no information about the temporal evolution of the middle/lower crust. In the products of such melting—leucocratic granite intrusions can provide direct evidence of crustal melting through time.

On the eastern margin of the Tibetan Plateau, the Gongga Shan granite (GSG) provides such an archive of information on Cenozoic crustal melting, opening a time window into the possible tectonic process from the subduction of the Tethyan slab to recent crustal deformation in the eastern Tibet (Figure 1).

The magmatism of the GSG has been previously dated from 12 to 32 Ma (Roger et al., 1995; Liu et al., 2006; Li and Zhang, 2013), and recently Searle et al. (2016) reported a 5 Ma U-Pb age from the GSG. However, these studies primarily focused on a single transect in the central section of the GSG and had relatively few samples over a limited area. Field observations throughout the GSG point to multiple phases of intrusion, including localities where a series of different intrusive episodes can be identified from cross-cutting relationships. To better constrain the entire emplacement history and the spatial distribution of granitoid ages, we conducted a detailed sampling campaign throughout the GSG (Figure 2). In addition to bedrock samples, we collected river sand and granite clasts from several catchments where upstream areas are hard to reach to increase the spatial coverage of our sampling. Our data both confirm the presence of previously recognized phases and identify additional granite ages, significantly extending the temporal range of crustal melting and granite emplacement.

2 Geological background

The GSG is located in the Songpan-Garzê fold belt (SGFB), which is separated from the Qiangtang (QT) block in the southwest by the Jinshajiang Suture (JS) (Burchfiel et al., 1995) (Figure 1). The dominant lithology of the SGFB is the Triassic Songpan-Garzê flysch. Still, the region also contains numerous Mesozoic

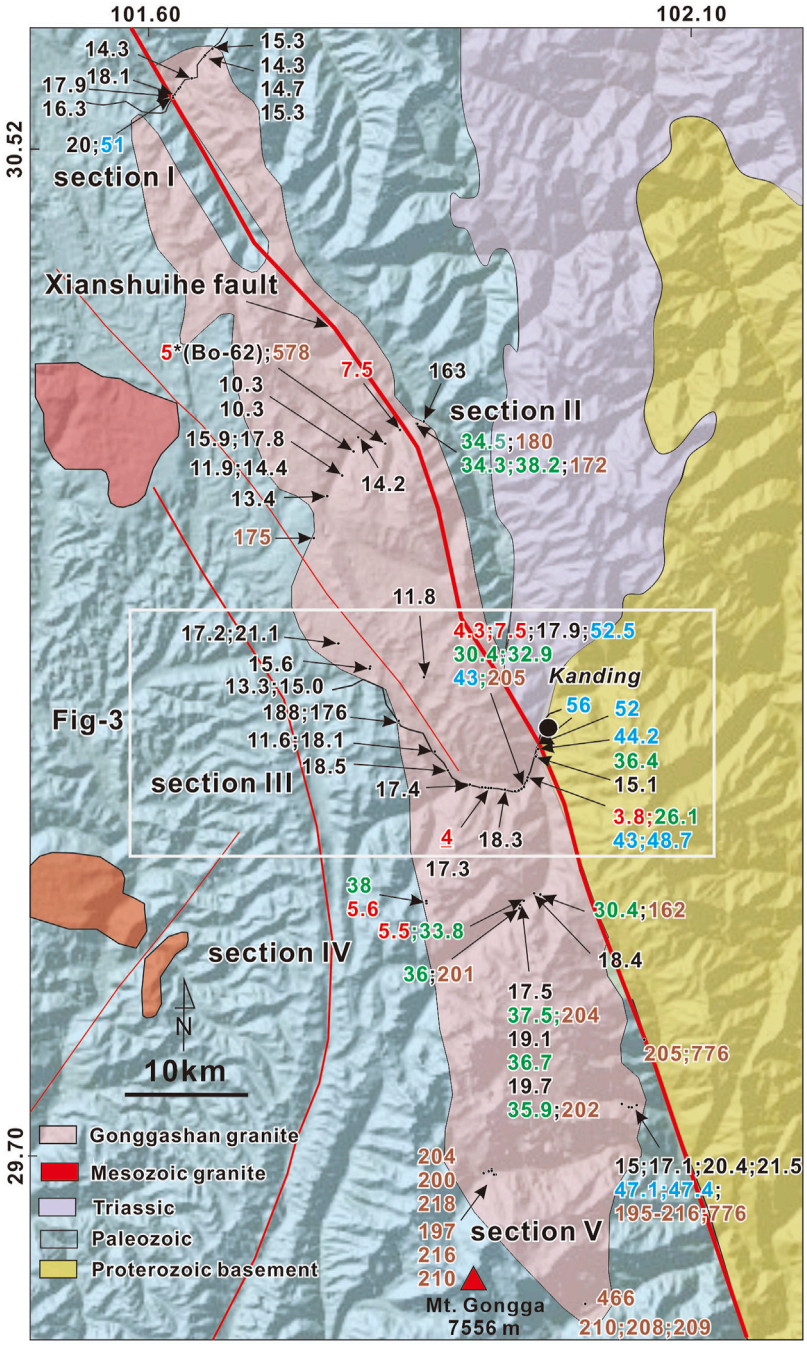

FIGURE 2
Sampling sites and zircon U-Pb ages in the GSG, with ages shown in Ma. The color of the ages indicates different groups of magmatic events. Geological map is modified from Roger et al. (2010). The color of the ages shows four groups of magmatic events (see the text).

intrusions (ranging in age from 105 to 225 Ma) and Neoproterozoic magmatic basement rocks (759–877 Ma) (Roger et al., 2010).

Most of the Cenozoic magmatism in eastern Tibet occurs west of the XSHF. The volcanic and plutonic rocks indicate magmatism at 51–49 and 38–37 Ma and have been attributed to continental subduction with either south-dipping subduction along the Jinsha suture (Roger et al., 2000) or north-dipping subduction along the Banggong-Nujiang suture (Yin and Harrison, 2000; Kapp et al., 2005; Spurlin, et al., 2005). Potassic volcanism, mainly phlogopite-, clinopyroxene- and olivinephyric calc-alkaline (shoshonitic) lamprophyres, was widely developed in SE Tibet (western Sichuan) during the Paleogene (40–24 Ma), and has been attributed to the presence of the palaeo-subducted slab beneath the SE Tibet and the left-lateral strike-slip motions of the Red River fault and reactivation of pre-existing, trans-lithospheric fault systems, which may have triggered melting and provided conduits for magma ascent (Guo et al., 2005).

The GSG is an elongate granitic body oriented along the left-lateral XSHF (Figure 1) (Wang et al., 1998). The southern end of the granite has extremely high topography, including Gongga Shan, a 7,556 m high peak located at the margin of the granite. The timing of GSG formation has long been considered to be 12–15 Ma and 18 Ma (Roger et al., 1995; Liu et al., 2006), but a recent study (Li and Zhang, 2013) identified an earlier phase of zircon growth at 32–27 Ma and Searle et al. (2016) used SIMS to identify an unusually young granite ca. 5 Ma (Figure 2). According to the geochemistry data the 12–18 Ma magma was mainly of crust origin (Roger et al., 1995; Liu et al., 2006).

3 Methods

3.1 LA-ICPMS

We used an Agilent 7500s quadrupole ICP–MS equipped with a New Wave UP213 laser ablation system (LA-ICPMS) at the Department of Earth and Environmental Sciences of the Chung Cheng University, Taiwan, for zircon U-Pb dating. The analysis process for the LA-ICPMS followed Chiu et al. (2009). A secondary zircon standard GJ-1 was used to check the accuracy of the unknowns. (Jackson et al., 2004). Data deduction and common Pb correction were conducted with GLITTER 4.4.2 (GEMOC) software and ComPbCorr, as proposed by Andersen (2002), respectively. Calculation of weighted mean U–Pb ages, probability density curves, as well as the plotting of concordia plots were carried out using Isoplot v. 3.0 (Ludwig, 2008). The detailed analytical method of the LA-ICPMS lab at Chung-Cheng University can be found in Knittel et al. (2014).

3.2 Secondary ion mass spectrometry (SIMS)

Zircon separates, together with zircon standards Plešovice, Penglai and Qinghu, were mounted in epoxy and polished to expose half of the crystals. All zircons were documented with cathodoluminescence (CL) images to reveal their internal textures. Measurements of U, Th and Pb were conducted using the Cameca IMS-1280 SIMS at the Institute of Geology and Geophysics, Chinese Academy of Sciences (IGG-CAS) in Beijing. The O_2^- primary ion beam was accelerated at −13 kV, with an intensity of ca. 10 nA. The aperture illumination mode (Kohler illumination) was used to produce an elliptical spot of about 20 x 30 m in size. Mass resolution was set at ~5,400 (at 10% peak height). A single electron multiplier (EM) was used to measure secondary ion beam intensities by peak jumping sequence. Pb/U calibration was performed relative to the Plešovice standard zircon (Sláma et al., 2008), based on an observed linear relationship between ln (^{206}Pb/^{238}U) and ln ($^{238}U^{16}O_2/^{238}U$) with a slope of 1.3 (Li et al., 2009). U and Th concentration determination of unknowns is calculated against the 91500 standard (Wiedenbeck et al., 1995). Measured compositions were corrected for common Pb using the ^{207}Pb-correction method (Li et al., 2012) with an average present-day crustal composition used for the common Pb (Stacey and Kramers, 1975). Because some samples are quite young, the ^{206}Pb was corrected according to the initial excess or loss of ^{230}Th based on the following equation given by Schärer (1984):

$$\Delta\frac{^{206}Pb}{^{238}U} = \left[\frac{\lambda_{238}}{\lambda_{230}}(f-1) \times \frac{1}{e^{\lambda_{238}t}-1}\right] \times 100\%, \text{ therein } f = \frac{\frac{^{238}Th}{^{238}U}\,zircon}{\frac{^{232}Th}{^{238}U}\,magma}$$

where, λ_{238} and λ_{230} are the decay constant of ^{238}U and ^{230}Th, respectively. Th/U of zircon is the value for the measured zircon area during SIMS analysis, Th/U of magma is the ratio for the host magma estimated by the host rock analyses. Uncertainties on individual analyses in data tables are reported at a 1σ level; mean ages for pooled U/Pb analyses are quoted with 95% confidence interval. Statistical reduction and plotting of the data (including calculate ages, uncertainties, weighted means, and the generation of U–Pb concordia plots) were carried out using the Isoplot/Ex v. 2.49 (Ludwig, 2001).

4 Results

4.1 Zircon U–Pb geochronology

We obtained U-Pb ages (LA-ICPMS and SIMS) for 124 separate samples. (Figures 2, 3, and Supplementary Table S2). The detailed analytical results are listed in the Supplementary Material. Most of the zircon grains are euhedral crystals more than 100 μm in length. Some of the zircons show xenocrystic cores. If a zircon had significantly different core and rim structures, we analyzed both the core and rim to identify the youngest event. The CL images show that most zircon grains have oscillatory zoning, suggesting a magmatic origin (Shore and Fowler, 1996) (Figure 4). The GSG granitoids have varying compositions, including syenogranite, alkali feldspar granite, muscovite granite, monzogranite granodiorite. Part of the mineral compositions of the dated samples are shown in Supplementary Table S2.

Cenozoic zircon U-Pb ages range from ca. 56 Ma to 4 Ma inherited Mesozoic to Proterozoic ages in many samples (Figures 2, 3). To gain an overview of magmatic events in the GSG, we plot the U-Pb ages, including inherited and river sand ages. The inherited ages are defined as zircon ages significantly older than other ages from the same sample. The river sand ages indicate that we obtained consistent ages from detrital zircon sampled from different catchments. In the following, we will describe typical outcrop conditions and each section's zircon U-Pb ages and zircon Th/U ratio.

4.2 Outcrop scale U-Pb results

Figures 5A,B shows the youngest leucogranite outcrops, in which the granodiorite (GO-15) is cut by later-stage granodiorite dike (GO-16) and contains foliated monzogranite Mesozoic xenoliths (GO-18) (Figures 5C, 4I). (location shown in Figure 3) The xenolith (GO-18) is a foliated monzogranite with a concordant age of 235 Ma and many Proterozoic inherited zircons (Figure 5I). We obtained only three Cenozoic zircon grains from GO-16, and two of these grains yielded ages of ca. 3.8 Ma (Figure 5D). Although

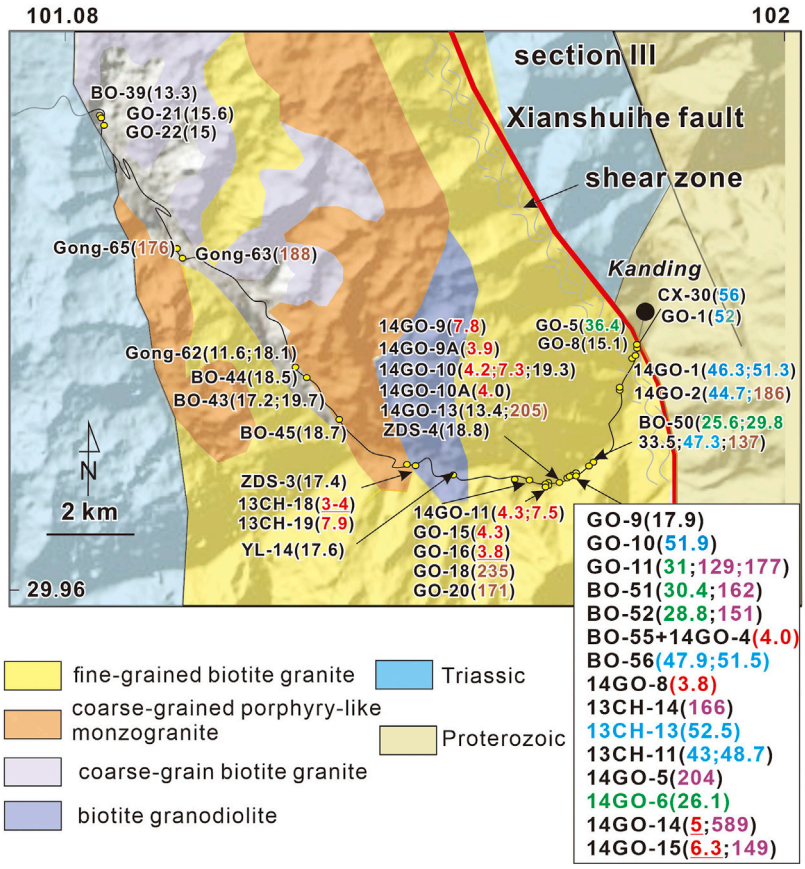

FIGURE 3
Detailed sample locations and zircon U-Pb ages (Ma) for section III. The underlined emplacement ages show the youngest zircon U-Pb age.

GO-15 and GO-16 have a cross-cutting relationship, both samples contain ca. 4 Ma zircons (Figures 5G,H). The grain ages of the GO-15 are more complex, showing from Proterozoic to Cenozoic ages (Figures 5E,F). The youngest grain ages are between 4 and 9 Ma, line up concordantly on the concordia map, and can be separated into two mean ages, 4.3 Ma and 7.5 Ma (Figures 5G,H).

Figure 6A shows another 4 Ma (BO-55) outcrop in which the youngest pegmatite dike (BO-55) cuts older deformed granitoids (location shown in Figure 3). In addition to 4 Ma grain ages, BO-55 also contains Cenozoic to Mesozoic inherited zircon (Figures 6B,C). Sample BO-52 is a migmatitic leucosome with an age of 29 Ma and many Mesozoic inherited zircons (Figures 6D,E). Sample BO-56 has an age of ca. 51 Ma and is from a foliated biotite monzogranite that cuts a Mesozoic foliated biotite monzogranite (14GO-5) (Figures 6F,G).

Samples 14GO-9 and -10 are from two adjacent undeformed granodiorites (location shown in Figure 3). Both samples contain 4 Ma zircons, in addition to inherited zircons of Miocene and Mesozoic to Proterozoic ages (Figure 7). The Cenozoic grain ages can be separated into three groups, ca. 19 Ma, 7.3 Ma, and 4 Ma (Figures 7B–D). The large group of consistent 19 Ma grain ages can be easily distinguished from older and younger groups, indicating an isolated magmatic event (Figure 7C). To confirm the 4 Ma ages, both LA-ICPMS and SIMS analyses were conducted, with consistent results (Figures 7E–G). Although we separate the youngest grain ages into two mean ages, 4 Ma and 7.3 Ma (Figure 7E,G,H), the concordia map shows that all the grain ages from 9–4 Ma line concordantly, indicating the possibility of continuous coherent melting (Figure 7B).

Figure 8A shows the outcrop of alkali feldspar granite where samples BO-64 and -65 were taken. Both samples contain Cenozoic zircons and inherited Mesozoic zircon grains (Figure 8B). The Cenozoic grain ages range from ca. 30–40 Ma (Figures 8C–E) and line up concordantly in the concordia map, indicating a coherent magmatic event (Figure 8C,D).

4.3 Spatial patterns of U-Pb ages

We now describe the patterns of magmatic ages and intrusions in different sections across the GSG. In Section I, magmatic and zircon grain ages range from 14 to 20 Ma (Figures 2, 9A). In this section, we observe dikes of granite cutting the Triassic slate with no apparent contact metamorphism, indicating a shallow granite emplacement. Some granitoids develop foliated or mylonitic structures and the youngest foliated granite is ca. 14 Ma, which gives an upper limit on the timing of deformation. BO-32 and BO-26

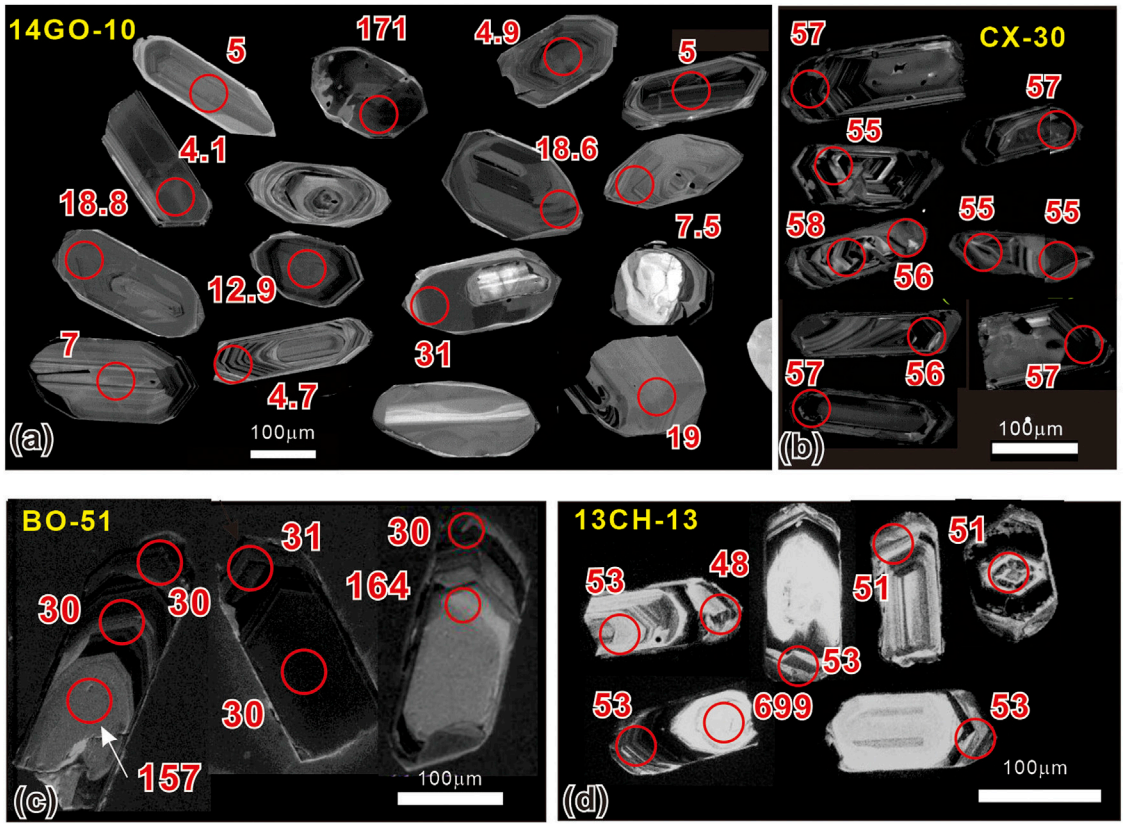

FIGURE 4
(A–D). CL images from samples 14-GO-10, CX-30, BO-51, and 13CH-13. All of these samples show oscillatory zoning, suggesting a magmatic origin. Some grains exhibit a core of inherited zircon but with a Cenozoic rim age.

have average ages of 18 Ma and 14 Ma, typical magmatic ages in section I (Figures 9A,B).

In Section II, we analyzed nine samples and the magmatism ages are much more complex. The youngest age is 5 Ma and there is a small group of ages between 7 and 10 Ma (Figures 2, 9B). Gong-73 is a river sand sample yielding a 7.5 Ma average age, also seen in samples 14GO-10 and GO-15, located 30 km south (Figures 2, 4, 6, 10C). The 10 Ma (Gong 71 and -72) magmatism event is only observed in section II (Figures 2, 8B, 10D). This section also contains a small group of 14-18 Ma ages. Samples BO-64 and -65 indicate magmatism lasting from 30–40 Ma, as described above. According to the grain age spectrum, three main groups can be identified: <10 Ma, 14–18 Ma, 30–40 Ma, and a small group at 47–56 Ma (Figure 2B).

We collected a very dense set of samples along Section III (Figures 3, 9C,D). The Cenozoic spectrum of zircon grain ages suggests the presence of 4 groups: 4–8 Ma, 12–20 Ma, 25–40 Ma, and 43–56 Ma (Figures 2, 9C). A lot of the inherited Mesozoic to Proterozoic zircons are also observed in this section (Figure 9D).

Sample CX-30, located at the eastern end of Section III, is dominated by grains with ages ca. 50–60 Ma, yielding a 56 Ma average age, the oldest Cenozoic magmatic event found in the GSG (Fig-. 2, 3, 9c, and 10c). Most of the grain ages of sample GO-2 are concentrated around ca. 43 Ma, suggesting an isolate magmatism event (Figure 10D). BO-50 yielded a wide grain age distribution mainly from Cenozoic to Mesozoic ages (Figure 10G). The Cenozoic zircon age spectrum can be separated into two groups, ca. 22–40 Ma and 43–52 Ma (Figure 10G). We can further divide the younger Cenozoic group and calculate three average ages (26 Ma, 30M, and 34 Ma); however, considering all grain ages line up concordantly on the concordia map, the magmatism could be ongoing during 22–40 Ma. The older Cenozoic group (43–52 Ma) and the small Mesozoic age group may represent inherited zircons (Figures 10G,H). The outcrop condition is terrible in Section IV, so we collected many granite clasts and river sand to get an overview of possible magmatism ages (Figure 2). The measured ages can be separated into three major groups: 5–10 Ma, 15–20 Ma, and 26–44 Ma, plus a minor group between 47 and 52 Ma. The youngest magmatism age of ca. 5.5 Ma is located in the central and western parts of the GSG (Figure 2).

Section V contains samples from the eastern and western margins of the GSG. In contrast to the other sections, most of the granitoids are Mesozoic rather than Cenozoic in age, and the Cenozoic magmatic events are concentrated around 14 Ma and 44 Ma (Figure 9F).

Overall, from both *in situ* samples and the detrital zircon grain ages, the Cenozoic zircon ages range from 56 Ma to 4 Ma but can be

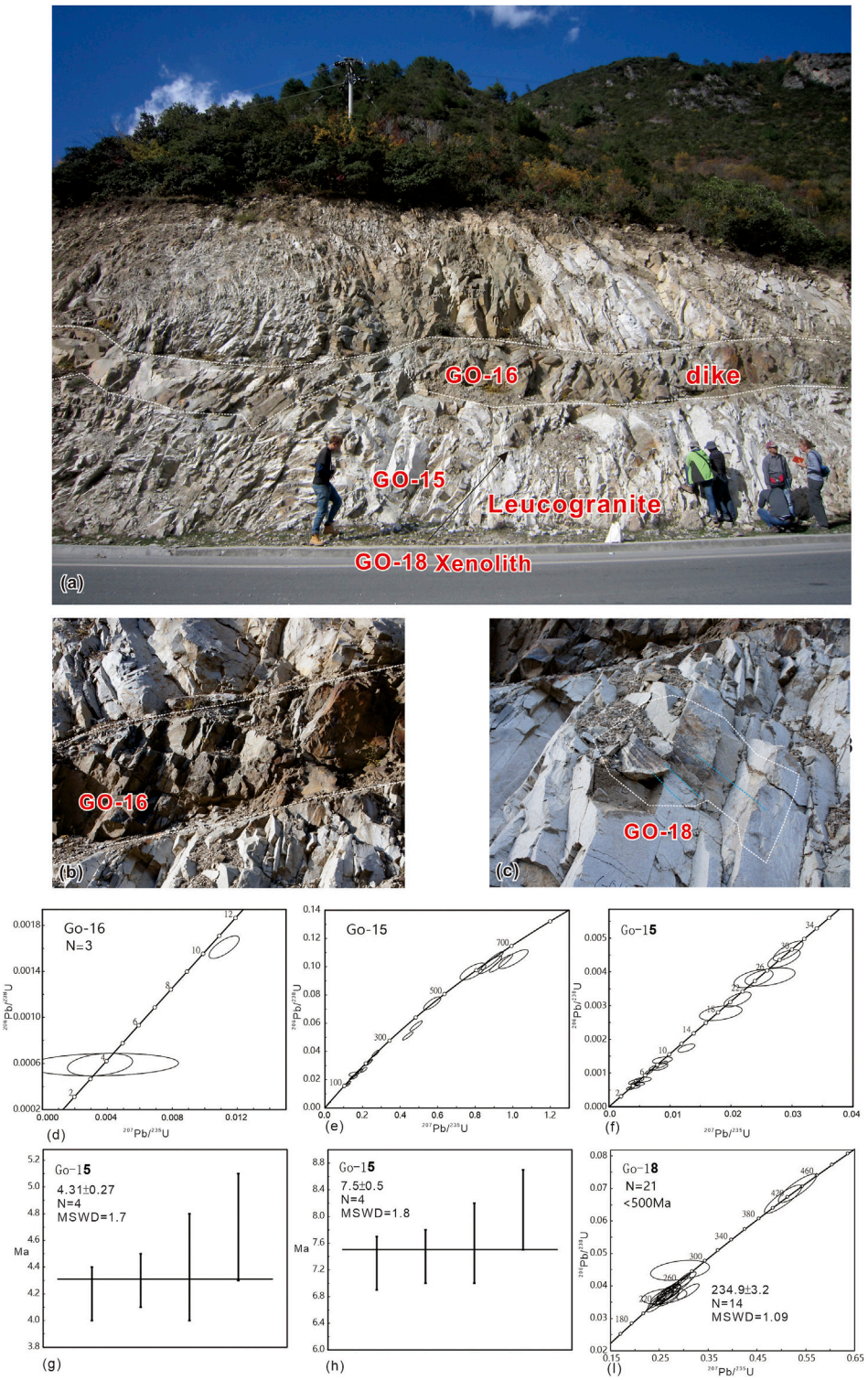

FIGURE 5
(A) Outcrop of the 4 Ma granitoids, with a horizontal mafic dike cutting the leucogranite. **(B)** close-up of the dike. **(C)** Mesozoic xenolith with foliation development (blue color). **(D)** Only three zircon grains have been dated in GO-16; the younger age is ca.3.8 Ma. **(E)** Concordia map for GO-15 leucogranodiorite, which shows Cenozoic to Proterozoic grain ages. The data-point error ellipses are 2σ in the concordia map. **(F)** The Cenozoic grain ages of GO-15, from 4–30 Ma, line concordantly in the condcordia map. **(G, H)** The younger ages of GO-15 can be separated into 4.3 Ma and 7.5 Ma average ages. **(I)** GO-18 is a Mesozoic xenolith that yields a ca.235 Ma average age.

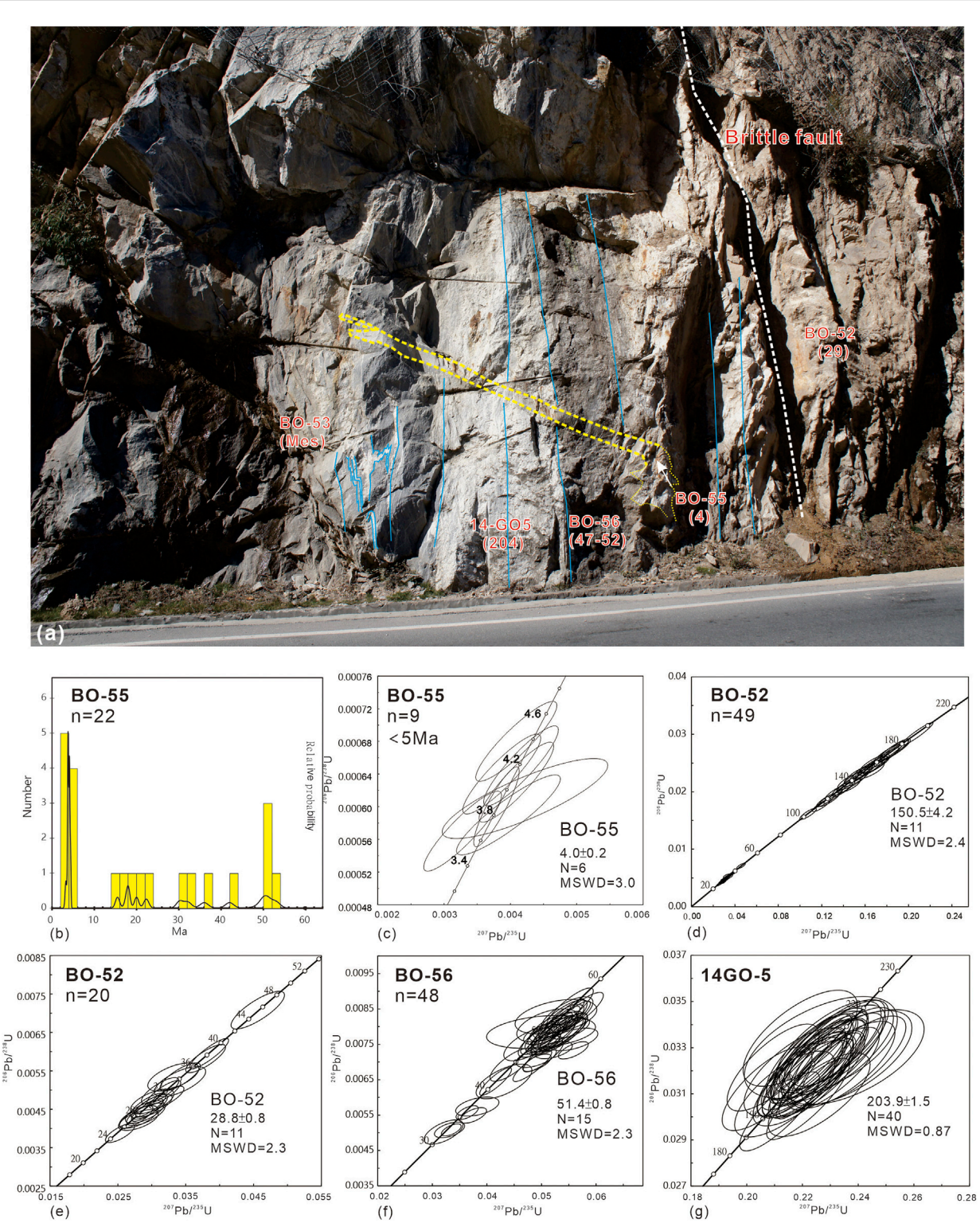

FIGURE 6
(A) Outcrop from Section III, showing a pegmatite dike (yellow) cutting the older granite. The numbers below the sample names indicate the magmatism age. The blue lines are deformed foliation. **(B)** The age spectrum of sample BO-50. In addition to the 4 Ma zircon it also contains many inherited zircons. **(C)** The youngest dike age is ca. 4 Ma (BO-55). The data-point error ellipses are 2σ in the concordia maps. **(D, E)** BO-52 is a 29 Ma migmatitic leucosome with many inherited Mesozoic zircons. **(F)** BO-56 is foliated biotite monzogranite with an age of 51 Ma. **(G)** 14GO-5 is a Mesozoic granitoid with an age of 204 Ma.

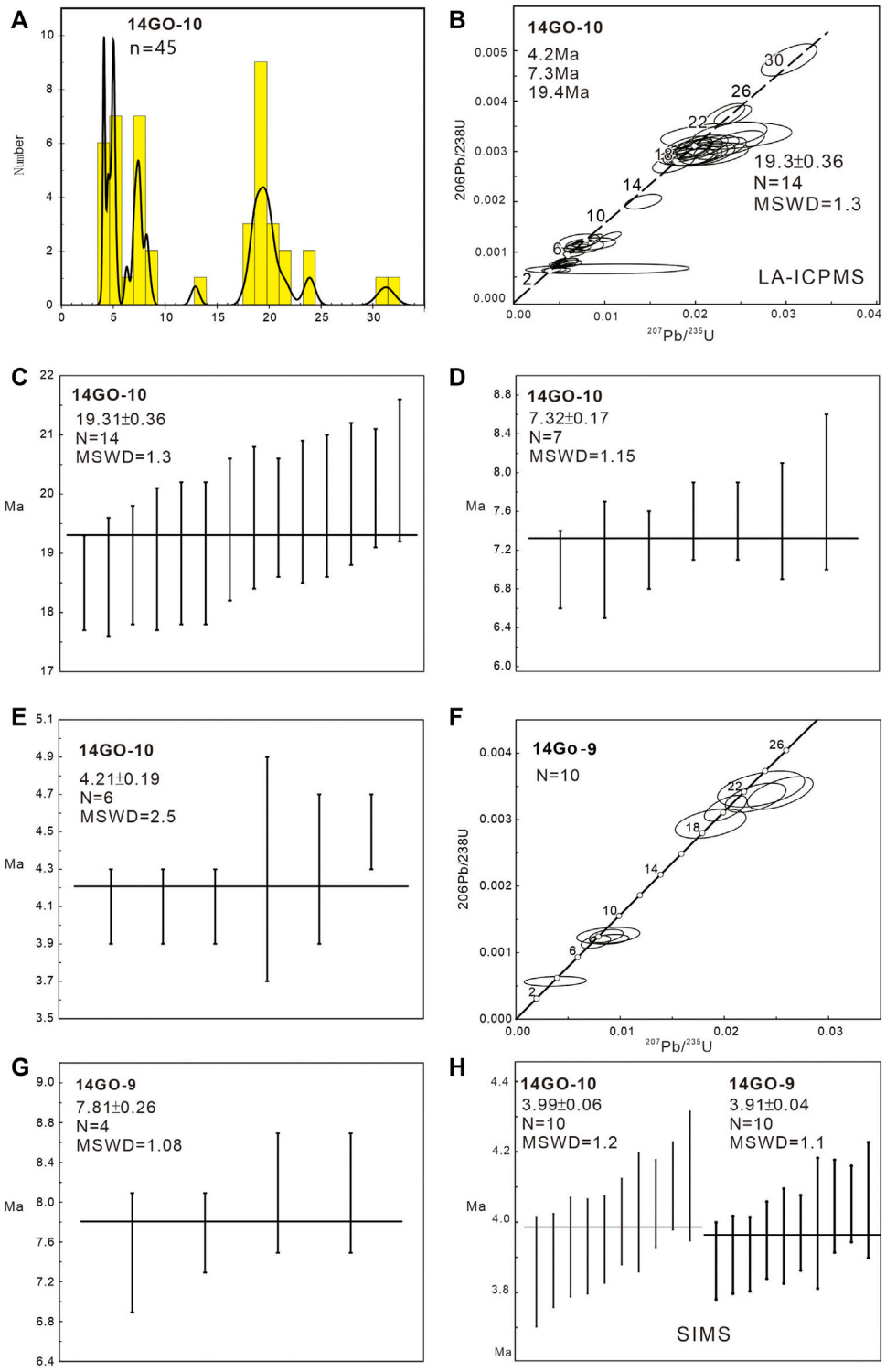

FIGURE 7
(A) Cenozoic age spectrum of sample 14GO-10. **(B–E)** Concordia map and grain age spectrum of the Cenozoic grain ages in 14GO-10, which can be separated into three main groups. The data-point error ellipses are 2σ in the concordia map. **(F, G)** Cenozoic concordia map and younger age of the 14GO-9. **(H)** The two youngest average age is ca. 4 Ma, both in 14GO-10 and 14GO-9, using SIMS analysis.

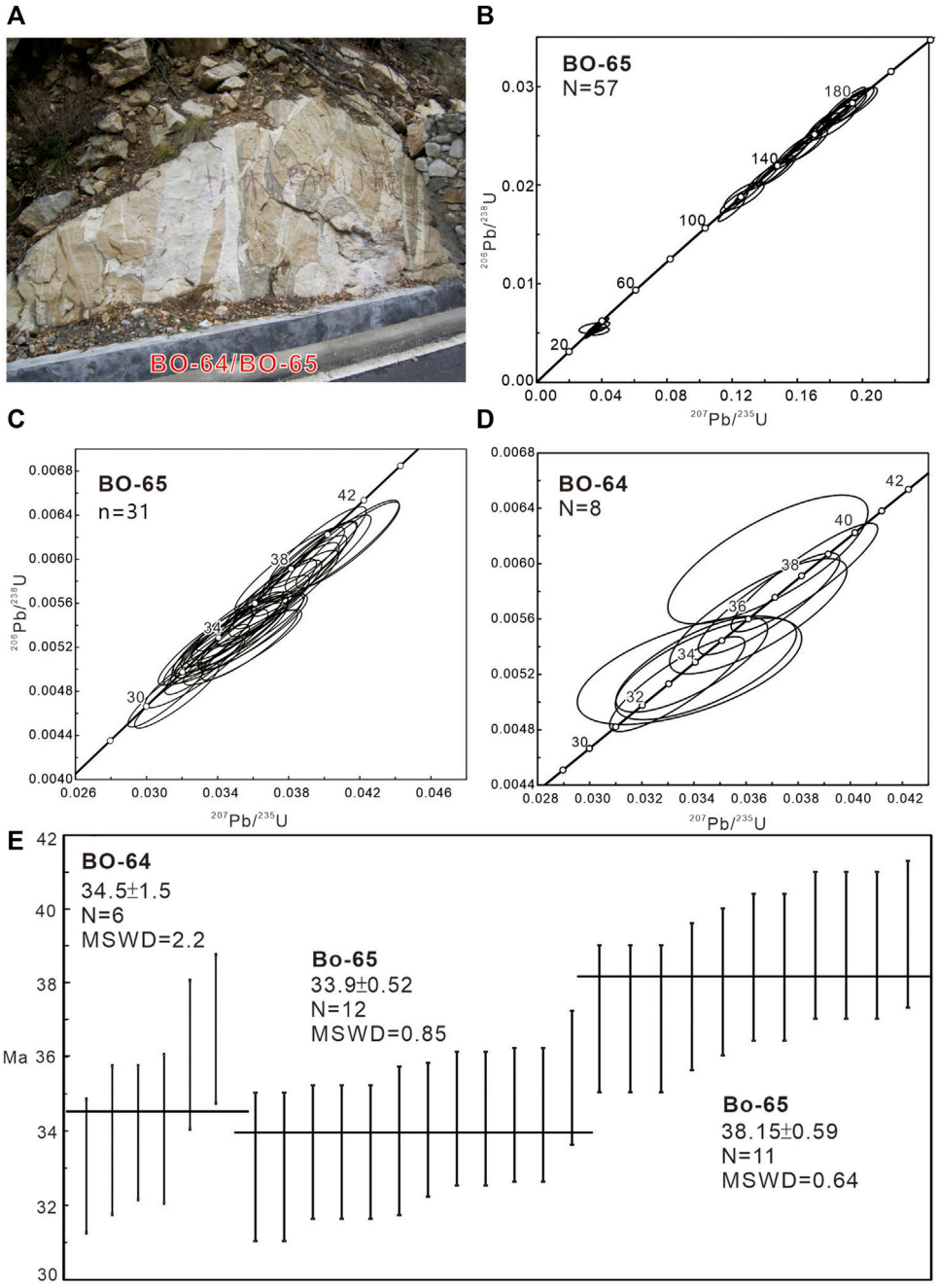

FIGURE 8
(A) Outcrop of the samples BO-64 and BO-65 (alkali feldspar granite). **(B)** Concordia map for BO-65 which shows Cenozoic and Mesozoic C. The data-point error ellipses are 2σ in the concordia maps. **(C, D)** Concordia map for the Cenozoic grain ages of BO-64 and -65; their similar age distributions from 32–40 Ma indicate they are the same event. **(E)** The youngest magmatism in this location is ca. 34 Ma.

separated into four major groups at 4–10 Ma, 12–20 Ma, 25–40 Ma, and 43–56 Ma (Figure 11). Some GSG granitoids are of Mesozoic rather than Cenozoic age, especially in the southern part of the GSG. Most of the older stage Cenozoic granitoids (43–56 Ma) are located on the margin of the GSG (Figure 2). Based on the age distributions, the 12–20 Ma is the dominant magmatic phase in the GSG, and the youngest phase at 10–4 Ma is found scattered throughout the GSG.

Compared to the other groups, the 25–40 Ma granitoids abound with detrital Mesozoic zircon grains (100–170 Ma) (Supplementary Table S1). These Mesozoic ages are consistent with Mesozoic magmatism in the SGFB, with the 235 Ma ages representing the oldest observed Mesozoic magmatism in the region. Paleozoic and Proterozoic ages are also observed in the inherited zircons, ages from 440 to 800 Ma. The numerous inherited Mesozoic to Proterozoic zircons and the presence of zircons that have cores with Mesozoic to Proterozoic ages and rims with Cenozoic age suggest that the source of partial melt included both Mesozoic granite and the Proterozoic basement.

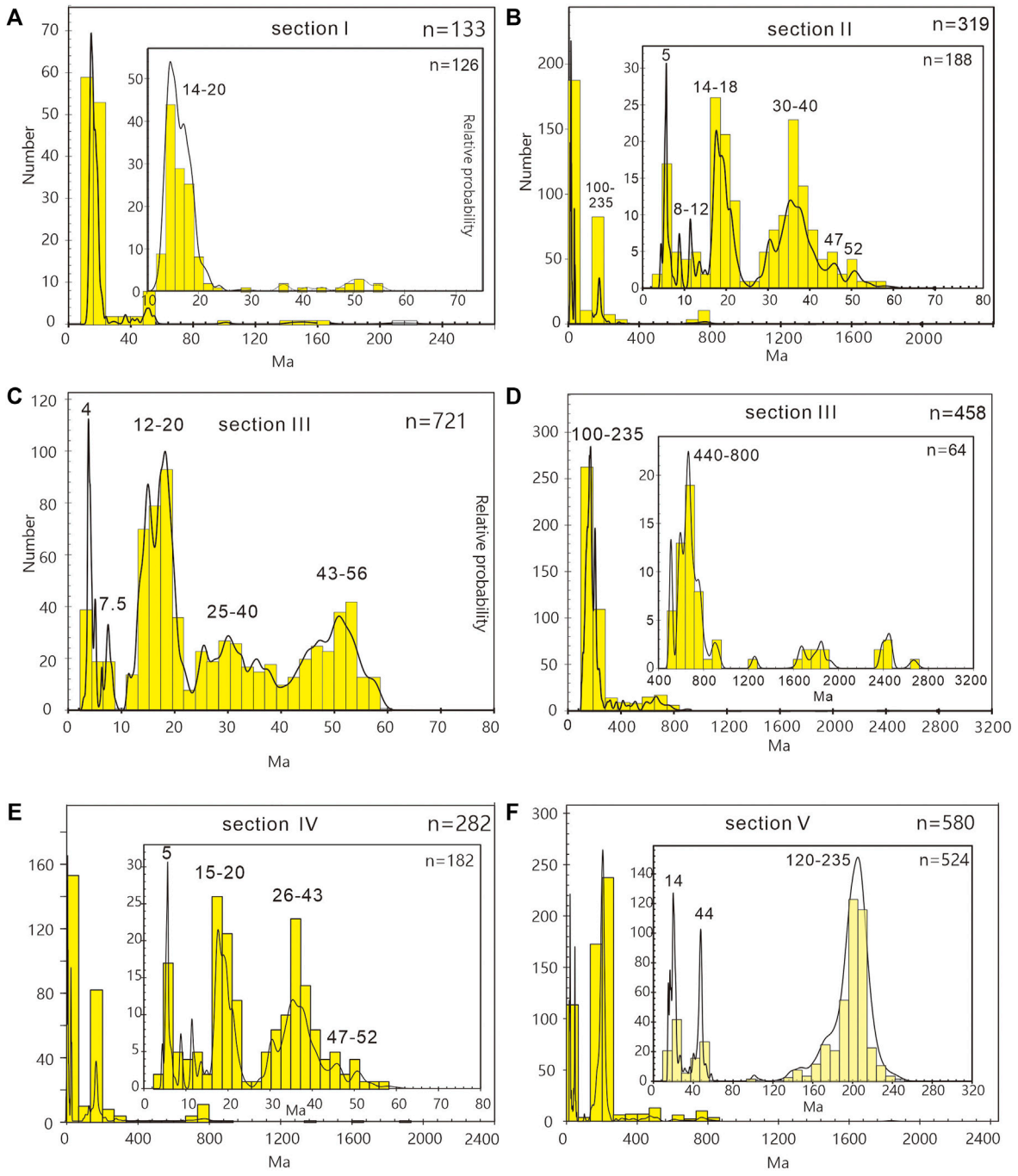

FIGURE 9
Zircon U-Pb grain age spectra for each section. **(A, B)** are Section I and II. **(C, D)** are Section III. **(E, F)** are Section IV and V.

4.4 Zircon Th/U ratios of the GSG

The Th/U ratio of zircon can provide significant clues to the physicochemical environment of zircon growth, which suggests that if we combined the geochronologic ages with Th/U ratios, an understanding of the zircon growth or inheritance mechanism could be derived (Rubatto, 2002; Kirkland et al., 2015). To clarify the characteristics of magmatism events in each stage, we determined Th/U ratios along with U-Pb dates. The results show that the Th/U ratios have varied through time since the Proterozoic (Figure 12). In the Mesozoic (from 235 to 170 Ma), most of the Th/U ratios were greater than 0.1, but there was a significant group of 200–100 Ma ages where the Th/U ratios were lower than 0.1. (Figure 12). From ca. 56 to 40 Ma, the Th/U ratios could be separated into two groups, with one falling above, and one below, ca. 0.1. From ca. 40–25 Ma, most of the Th/U ratios were lower than 0.1. From 20 to 10 Ma, the main group is high than ca. 0.1 and the minor group is below ca. 0.1. From 10 to 4 Ma, most of the ratios were higher than 0.1.

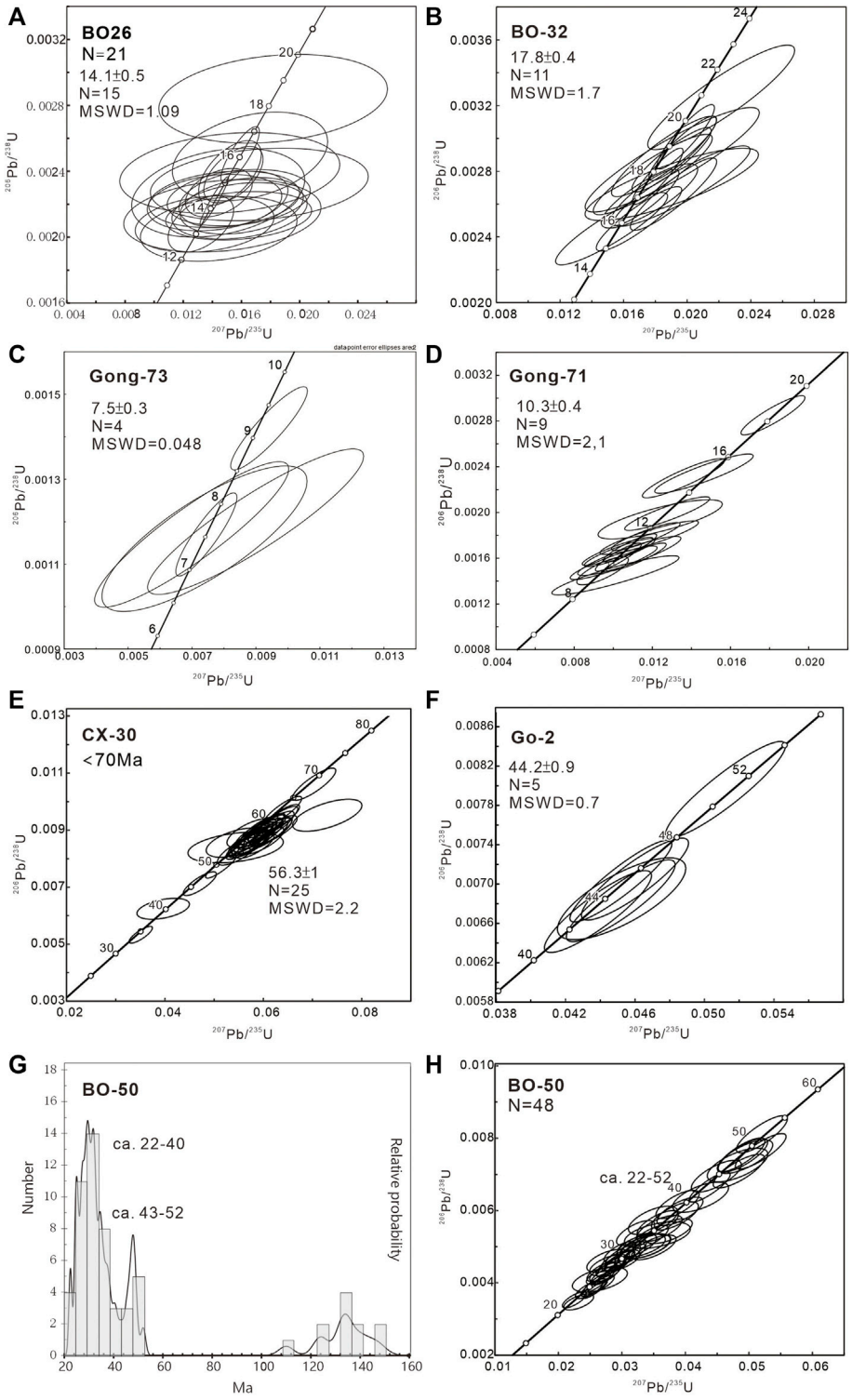

FIGURE 10
Magmatism ages of the GSG. The data-point error ellipses are 2σ in the concordia maps. **(A. B)** BO-26 and -32 are 18 Ma and 14 Ma, respectively, which are the typical magmatism ages in section I. **(C, D)** We obtain magmatism ages of 7.5 (Gong-73) and 10 Ma (Gong-71) in Section II. The 10 Ma event only appears in section II **(E)** CX-30 gives the oldest magmatic age in the GSG. **(F)** Go-2 yields an age of 44 Ma, belonging to the first stage of magmatism. **(G, H)** Concordia map and age spectrum of BO-50 which contains two main groups, Cenozoic and Mesozoic. The Cenozoic grain ages can be separated into two groups, 22–40 Ma and 43–52 Ma. Concordia map of the Cenozoic 1.

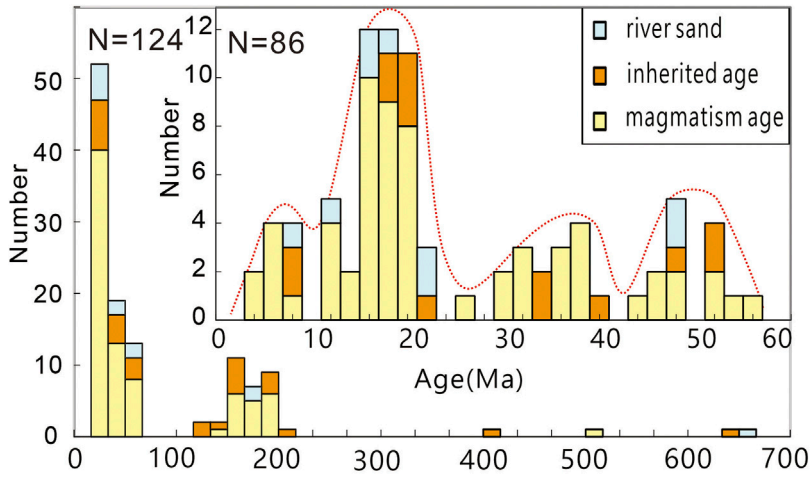

FIGURE 11
Histogram showing the distribution of magmatism ages of the GSG, including river sand, inherited age, and magmatism age.

The Th/U ratio of the Cenozoic zircon grains also shows it can be divided into four groups from 56 Ma to 4 Ma, consistent with four stage magmatism events based on U-Pb zircon ages.

Considering the Th/U ratio also shows two groups higher and lower 0.1 in Mesozoic zircons and lots of the inherited zircon in the Cenozoic granite we infer that the different Th/U ratio in Cenozoic zircon grains could be related to partial melting of the different Mesozoic zircon grains through time but it still needs further studies.

5 Discussions

5.1 Ongoing crustal magmatism events and crustal channel flow in eastern Tibet

Our 4 Ma zircon U-Pb ages provide direct evidence of recent crustal melting under the GSG. Although our data do not constrain the lateral extent of crustal melting in the region, they are consistent with seismic and magnetotelluric data that point to the existence of fluids and/or partial melting in the crust beneath parts of southeastern Tibet (Bai et al., 2010; Wang et al., 2010; Liu et al., 2014) (Figure 13). Figure 13 shows the S-wave velocity structure and VP/VS. ratio of a profile along 30°N which passes through the GSG (Wang et al., 2010). The low S wave velocity zone (2.60–3.40 km/s) in the lower crust suggests that crustal flow might occur locally in the lower crust. The high VP/VS. ratio along the XSHF could be related to partial melting, and the 4 Ma granite provides new evidence that the middle crust has been melting, supporting the crustal channel flow model. In addition, in section III, most of the apatite fission track ages are less than 2 Ma (Xu and Kamp, 2000), indicating rapid exhumation that may be related to ongoing partial melting magma intrusion.

The final stage of magmatism started from ca. 10 Ma that coincides with the rapid exhumation, faulting activity, and river incision starting from ca. 10 Ma in eastern Tibet (Clark et al., 2005; Wang et al., 2012; Tan et al., 2014), which was proposed to be related with crustal channel flow in eastern Tibet (Royden et al., 1997). We, therefore, suggest that the younger (<10 Ma) magmatism might indicate the initial timing of the recent crustal channel flow.

5.2 Stepwise magmatism in eastern Tibet since the India-Asia collision

Eastern Tibet experienced a significant quiescence of magmatism between ~100 and 60 Ma, ended by the onset of stepwise magmatism in the early Cenozoic (Figures 1, 2). The stepwise nature of the magmatism is illustrated by the age distribution, suggesting that the magmatism had different sources and can be separated into four age groups: 4–10 Ma, 12–20 Ma, 25–40 Ma, and 43–56 Ma. Previous studies have suggested that the oldest phase of GSG emplacement was 32–27 Ma (Li and Zhang, 2013). Our new data showing events as old as 56 Ma extend the initiation of granite emplacement by about 20 My. We also suggest this magmatism event lasted from 43–56 Ma (Figure 2). The previously proposed 32-27 Ma magmatic event is the same as our 25–40 Ma event, but our data provide additional evidence to show that the event lasted from ca. 25–40 Ma.

Magmatism of a similar age as our older two magmatic events has been found elsewhere in eastern Tibet, such as potassic magmatism in the Qiangtang block in northeastern Tibet at 50–37 Ma and 40–24 Ma potassic magmatism and lamprophyre dikes west of the Xianshuihe fault in southeastern Tibet (Roger et al., 2000; Guo et al., 2005; Spurlin et al., 2005) (Figure 1). The 50–37 Ma magmatic events in NE Tibet have been interpreted as either northward or southward continental subduction (Roger et al., 2000; Spurlin et al., 2005); Spurlin et al. (2005) argued that northward subduction and rolling back of the India plate resulted in the Eocene magmatism in NE Tibet. Guo et al. (2005) suggested that the 40-24 Ma potassic magmatic events resulted from the subduction and rolling back of the Paleo-Tethyan oceanic crust in SE Tibet. P-wave tomography data show the subducted slab beneath northeastern and southeastern Tibet (Figure 10B) (Li et al., 2008; Lei and Zhao, 2016). Considering that the older stage of magmatism is relatively widespread, and the tomography images show that the slab has been subducted beneath eastern Tibet, we postulate that the older magmatism of the GSG could also be related

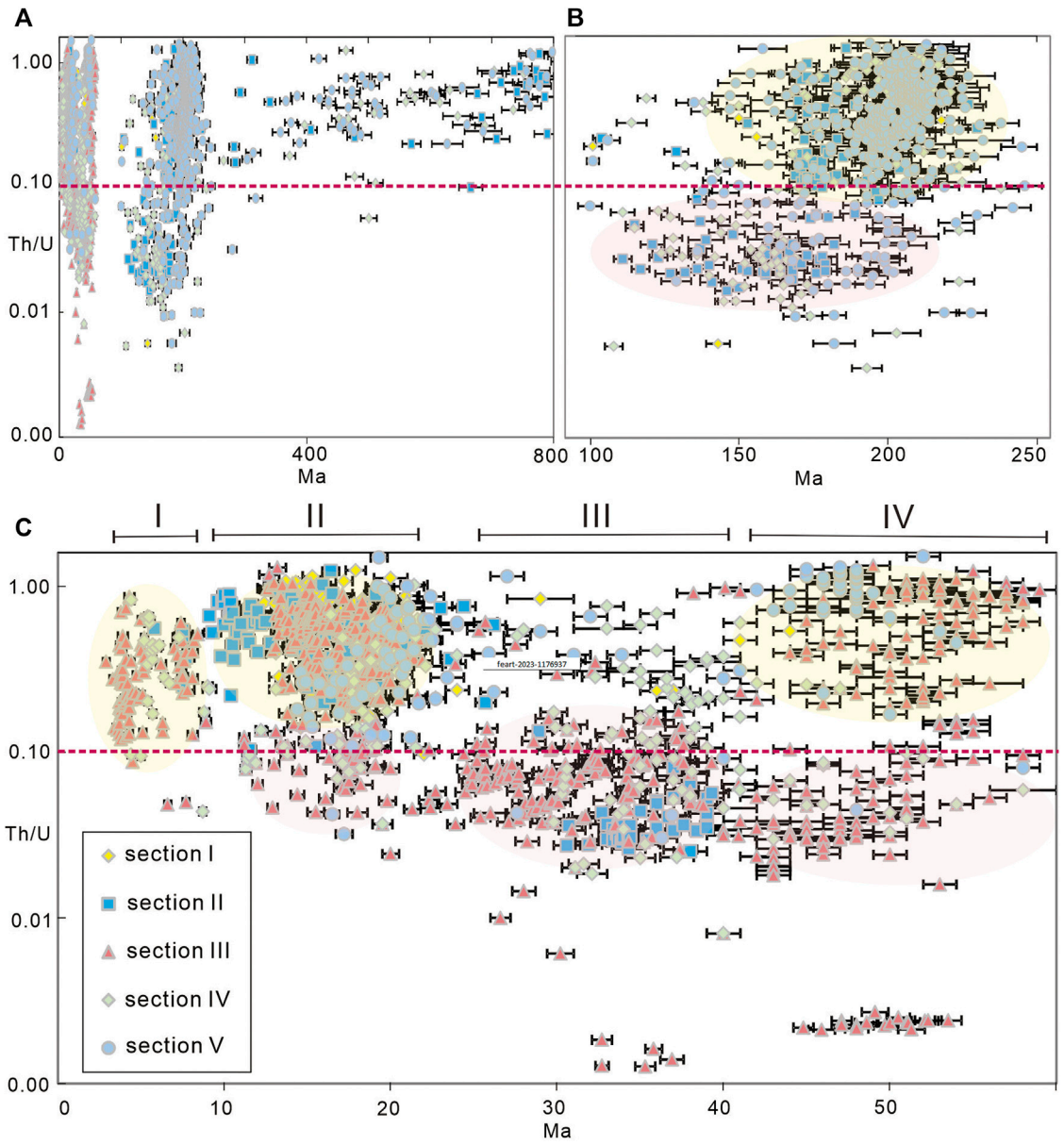

FIGURE 12
Zircon Th/U ratios of the GSG. **(A)** Th/U ratios since the Proterozoic. **(B)** Th/U ratios of Mesozoic zircon grains. **(C)** Th/U ratios of Cenozoic zircon grains.

to slab subduction and rollback processes, but further geochemical studies are needed to confirm the origin of the magma.

Are the 12–20 Ma magmatic events possibly related to crustal channel flow? In central Tibet, 26–13 Ma is proposed to be the timing of large-scale crustal channel flow (e.g., Beaumont et al., 2001; Searle and Godin, 2003). Cook and Royden (2008) used a three-dimensional numerical model of deformation in a viscous crust to show that crustal channel flow could migrate from central Tibet to eastern Tibet with time. The crustal thickness reaches 68 km east of Tibet (Hu et al., 2011), similar to central Tibet, indicating a suitable environment for the development of crustal channel flow. Geochemistry data show that the 12–20 Ma granitoids are peraluminous with a metaluminous tendency, consistent with a crustal melting origin (Roger et al., 1995; Liu et al., 2006). In addition, initial Sr ratios of 0.7084–0.732 and ε(t) of −5.6 to −8.8, combined with REE and rare element data, suggest that the 12–20 Ma granitoids probably derived from partial melting of Proterozoic upper continental greywacke, possibly with a small contribution from a low degree of partial melting of calc-alkaline basaltic volcanic rocks (Roger et al., 1995; Liu et al., 2006). A derivation from the partial melting of continental crust suggests that this magmatism could be linked to crustal channel flow. In addition, the timing of this stage of magmatism (12–20 Ma) is younger than in Central Tibet (26–13 Ma), consistent with the model suggesting that the crustal channel flow will migrate from central to eastern Tibet (Cook and Royden, 2008). Thus, we

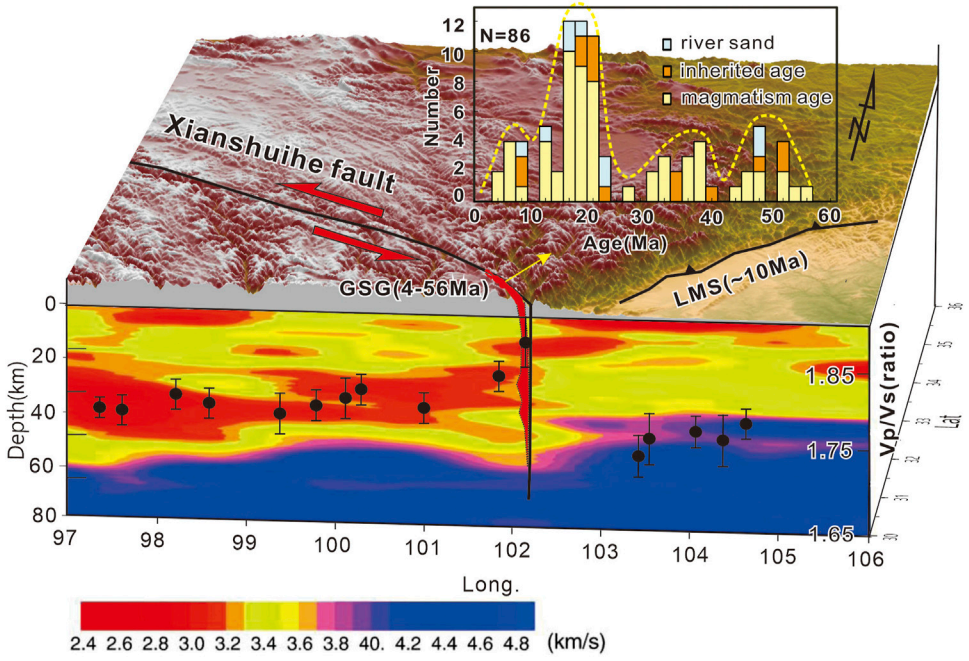

FIGURE 13
Schematic model for the Gongga Shan granite. S-wave velocity structure and VP/VS. ratio of the profile along 30°N, adapted from Wang et al. (2010). The high VP/VS. ratio along the XSHF could be related to partial melting and the Gongga Shan granite extrude to shallow crust along the XSHF.

postulate that the 12-20 Ma magmatism is related to crustal channel flow processes.

6 Conclusion

While the GSG has long been recognized as a Cenozoic feature, our set of zircon U-Pb ages significantly extends the timing of granite formation, pushing the onset of crustal melt in the region back 20 My earlier than previously recognized and strongly suggesting that melting and magmatic zircon formation continues to the present. While the GSG granite occupies only a tiny part of the eastern margin region, it provides a detailed archive of local magmatic processes; the regional extent of this melting requires further study.

The presence of crustal melt during and prior to the period when regional uplift and deformation are thought to have taken place provides new information about the condition of the middle/lower crust that should be considered when considering models of uplift and deformation in the region.

Data availability statement

The original contributions presented in the study are included in the article/Supplementary Material, further inquiries can be directed to the corresponding author.

Author contributions

Y-HL: field works, writing the manuscript; KC: fieldwork, editing manuscript and discussions; X-BT: fieldwork, analysis samples; M-FC: analysis samples; H-YC: analysis samples; Q-LL: analysis samples; JS: analysis samples; X-WX: finical support. All authors contributed to the article and approved the submitted version.

Funding

This project received financial support from the Ministry of Science and Technology, Taiwan, ROC, under Grant MOST 103-2116-M-194-001 and the Special Projects for Basic Research Work of the Institute of Geology, China Earthquake Administration (IGCEA1518), National Natural Science Foundation of China (41302159).

Acknowledgments

Tsai Wen Lien helped to analyze the zircon U-Pb ages. The topography map is drawn by GMT. The manuscript was greatly improved by constructive comments from three reviewers and editor Shuangshuang Chen.

Conflict of interest

The authors declare that the research was conducted in the absence of any commercial or financial relationships that could be construed as a potential conflict of interest.

Publisher's note

All claims expressed in this article are solely those of the authors and do not necessarily represent those of their affiliated organizations, or those of the publisher, the editors and the reviewers. Any product that may be evaluated in this article, or claim that may be made by its manufacturer, is not guaranteed or endorsed by the publisher.

Supplementary material

The Supplementary Material for this article can be found online at: https://www.frontiersin.org/articles/10.3389/feart.2023.1176937/full#supplementary-material

References

Andersen, T. (2002). Correction of common lead in U-Pb analyses that do not report 204Pb. *Chem. Geol.* 192, 59–79. doi:10.1016/s0009-2541(02)00195-x

Bai, D. H., Unsworth, M. J., Meju, M. A., Ma, X. B., Teng, J. W., Kong, X. R., et al. (2010). Crustal deformation of the eastern Tibetan plateau revealed by magnetotelluric imaging. *Nat. Geosci.* 3, 358–362. doi:10.1038/ngeo830

Beaumont, C., Jamieson, R. A., Nguyen, M. H., and Lee, B. (2001). Himalayan tectonics explained by extrusion of a low-viscosity crustal channel coupled to focused surface denudation. *Nature* 414, 738–742. doi:10.1038/414738a

Burchfiel, B. C., Chen, Z., Liu, Y., and Royden, L. H. (1995). Tectonics of the longmen Shan and adjacent regions, Central China. *Int. Geol. Rev.* 37, 661–735. doi:10.1080/00206819509465424

Chiu, H., Chung, S., Wu, F., Liu, D., Liang, Y., Lin, I., et al. (2009). Zircon U-Pb and Hf isotopic constraints from eastern Transhimalayan batholiths on the precollisional magmatic and tectonic evolution in southern Tibet. *Tectonophysics* 477, 3–19. doi:10.1016/j.tecto.2009.02.034

Chung, S. L., Chu, M. F., Zhang, Y. Q., Xie, Y. W., Lo, C. H., Lee, T. Y., et al. (2005). Tibetan tectonic evolution inferred from spatial and temporal variations in post-collisional magmatism. *Earth Sci. Rev.* 68 (3–4), 173–196. doi:10.1016/j.earscirev.2004.05.001

Clark, M. K., House, M. A., Royden, L. H., Whipple, K. X., Burchfield, B. C., Zhang, X., et al. (2005). Late cenozoic uplift of southeastern Tibet. *Geology* 33, 525–528. doi:10.1130/g21265.1

Cook, K. L., and Royden, L. H. (2008). The role of crustal strength variations in shaping orogenic plateaus, with application to Tibet. *J. Geophys. Res. Solid Earth* 113 (B8). doi:10.1029/2007jb005457

de Sigoyer, J., Chavagnac, V., Blichert–Toft, J., Villa, I. M., Luais, B., Guillot, S., et al. (2000). Dating the Indian continental subduction and collisional thickening in the northwest Himalaya: multichronology of the Tso Morari eclogites. *Geology* 28 (6), 487–490. doi:10.1130/0091-7613(2000)028<0487:dticsa>2.3.co;2

Garzanti, E. (2008). Comment on "when and where did India and asia collide?" by jonathan C. Aitchison, jason R. Ali, and aileen M. Davis. *J. Geophys. Res. Solid Earth* 113 (4), B04411. doi:10.1029/2007jb005276

Godin, L., Grujic, D., Law, R. D., Searle, M. P., and Godin, L. (2006). "Channel flow, extrusion, and exhumation in continental collision zones: an introduction," in *Channel flow, ductile extrusion and exhumation in continental collision zones*. Editors R. D. Law and M. P. Searle (London: Geological Society, London, Special Publications), 1–23.

Guo, Z. F., Hertogen, J., Liu, J. Q., Pasteels, P., Boven, A., Punzalan, L., et al. (2005). Potassic magmatism in western sichuan and yunnan provinces, SE Tibet, China: petrological and geochemical constraints on petrogenesis. *J. Petrol.* 46, 33–78. doi:10.1093/petrology/egh061

Hu, J., Xu, X., Yang, H., Wen, L., and Li, G. (2011). S receiver function analysis of the crustal and lithospheric structures beneath eastern Tibet. *Earth Planet. Sci. Lett.* 306, 77–85. doi:10.1016/j.epsl.2011.03.034

Jackson, S. E., Pearson, N. J., Griffin, W. L., and Belousova, E. A. (2004). The application of laser ablation-inductively coupled plasma–mass spectrometry to *in situ* U–Pb zircon geochronology. *Chem. Geol.* 211, 47–69. doi:10.1016/j.chemgeo.2004.06.017

Kapp, P., Yin, A., Harrison, T. M., Ding, L., Deng, X. G., and Zhou, Y. (2005). Cretaceous-Tertiary shortening, basin development, and volcanism in central Tibet. *Geol. Soc. Am. Bull.* 117, 865–878. doi:10.1130/b25595.1

King, J., Harris, N., Argles, T., Parrish, R., and Zhang, H. (2011). Contribution of crustal anatexis to the tectonic evolution of Indian crust beneath southern Tibet. *Geol. Soc. Am. Bull.* 123, 218–239. doi:10.1130/b30085.1

Kirkland, C. L., Smithies, R. H., Taylor, R. J. M., Evans, N., and McDonald, B. (2015). Zircon Th/U ratios in magmatic environs. *Lithos* 212–215, 397–414. doi:10.1016/j.lithos.2014.11.021

Knittel, U., Suzuki, S., Nishizaka, N., Kimura, K., Tsai, W. L., Lu, H. Y., et al. (2014). U–Pb ages of detrital zircons from the sanbagawa belt in western shikoku: additional evidence for the prevalence of late cretaceous protoliths of the sanbagawa metamorphics. *J. Asian Earth Sci.* 96, 148–161. doi:10.1016/j.jseaes.2014.09.001

Lei, J., and Zhao, D. (2016). Teleseismic P-wave tomography and mantle dynamics beneath Eastern Tibet. *Geophys. Geosyst* 17, 1861–1884. doi:10.1002/2016GC006262

Li, C., van der Hilst, R., Meltzer, A. S., and Engdahl, E. R. (2008). Subduction of the Indian lithosphere beneath the Tibetan plateau and Burma. *Earth Planet. Sci. Lett.* 274, 157–168. doi:10.1016/j.epsl.2008.07.016

Li, H. L., and Zhang, Y. Q. (2013). Zircon U–Pb geochronology of the Konggar granitoid and migmatite: constraints on the Oligo-Miocene tectono-thermal evolution of the Xianshuihe fault zone, East Tibet. *Tectonophysics* 606, 127–139. doi:10.1016/j.tecto.2013.07.007

Li, Q. L., Li, X. H., Wu, F. Y., Yin, Q. Z., Ye, H. M., Liu, Y., et al. (2012). *In-situ* SIMS U-Pb dating of phanerozoic apatite with low U and high common Pb. *Gondwana Res.* 21, 745–756. doi:10.1016/j.gr.2011.07.008

Li, X. H., Liu, Y., Li, Q. L., Guo, C. H., and Chamberlain, K. R. (2009). Precise determination of Phanerozoic zircon Pb/Pb age by multi-collector SIMS without external standardization. *Geochem. Geophys. Geosystem* 10, Q04010. doi:10.1029/2009GC002400

Liu, Q. Y., van der Hilst, R. D., Yu, L., Yao, H., Chen, J., Guo, B., et al. (2014). Eastward expansion of the Tibetan Plateau by crustal flow and strain partitioning across faults. *Nat. Geosci.* 7, 361–365. doi:10.1038/ngeo2130

Liu, S. W., Wang, Z. Q., Yan, Q. R., Li, Q. G., Zhang, D. H., and Wang, J. G. (2006). Timing, petrogenesis and geodynamic significance of Zheduoshan granitoids. *Acta Petrol. Sin.* 22 (2), 343–352. doi:10.0000/b21e6aab4ed04f0587c795769ebd83ab

Ludwig, K. R. (2008). *Isoplot 3.70: A geochronological toolkit for microsoft excel*. Berkeley: Berkeley Geochronology Center, Special Publication.

Ludwig, K. R. (2001). *Users manual for Isoplot/Ex rev. 2.49*. Berkeley: Berkeley Geochronology Centre Special Publication, 56.

Replumaz, A., and Tapponnier, P. (2003). Reconstruction of the deformed collision zone between India and Asia by backward motion of lithospheric blocks. *J. Geophys. Res.* 108 (6), 2285. doi:10.1029/2001JB000661

Roger, F., Calassou, S., Lancelot, J., Malavieille, J., Mattauer, M., Xu, Z., et al. (1995). Miocene emplacement and deformation of the Konga Shan granite (Xianshui He fault zone, west Sichuan, China): geodynamic implications. *Earth Planet. Sci. Lett.* 130, 201–216. doi:10.1016/0012-821x(94)00252-t

Roger, F., Jolivet, M., and Malavieille, J. (2010). The tectonic evolution of the songpan-garzê (north Tibet) and adjacent areas from proterozoic to present: a synthesis. *J. Asian Earth Sci.* 39, 254–269. doi:10.1016/j.jseaes.2010.03.008

Roger, F., Tapponnier, P., Arnaud, N., Schärer, U., Maurice, B., Zhiqin, X., et al. (2000). An Eocene magmatic belt across central Tibet: mantle subduction triggered by the Indian collision? *Terra nova.* 12, 102–108. doi:10.1046/j.1365-3121.2000.123282.x

Rosenberg, C., and Handy, M. (2005). Experimental deformation of partially melted granite revisited: implications for the continental crust. *J. Metam. Geol.* 23, 19–28. doi:10.1111/j.1525-1314.2005.00555.x

Royden, L. H., Birchfiel, B. C., King, R. W., Wang, E., Chen, Z., Shen, F., et al. (1997). Surface deformation and lower crustal flow in eastern Tibet. *Science* 276, 788–790. doi:10.1126/science.276.5313.788

Rubatto, D. (2002). Zircon trace element geochemistry; partitioning with garnet and the link between U–Pb ages and metamorphism. *Chem. Geol.* 184, 123–138. doi:10.1016/s0009-2541(01)00355-2

Schärer, U. (1984). The effect of initial 230Th disequilibrium on young U–Pb ages: the makalu case, Himalaya. *Earth Planet. Sci. Lett.* 67, 191–204. doi:10.1016/0012-821x(84)90114-6

Searle, M. P., and Godin, L. (2003). The South Tibetan detachment and the manaslu leucogranite: a structural re-interpretation and restoration of the annapurna–manaslu Himalaya, Nepal. *J. Geol.* 111, 505–523. doi:10.1086/376763

Searle, M. P., Roberts, N. M. W., Chung, S. L., Lee, Y. H., Cook, K. L., Elliott, J. R., et al. (2016). Age and anatomy of the Gongga Shan batholith, eastern Tibetan Plateau, and its relationship to the active Xianshui-he fault. *Geosphere* 12, 948–970. doi:10.1130/GES01244.1

Shore, M., and Fowler, A. D. (1996). Oscillatory zoning in minerals: A common phenomenon. *Can. Mineralogist* 34, 1111–1126.

Sláma, J., Kosler, J., Condon, D. J., Crowley, J. L., Gerdes, A., Hanchar, J. M., et al. (2008). Plešovice zircon — a new natural reference material for U–Pb and Hf isotopic microanalysis. *Chem. Geol.* 249, 1–35. doi:10.1016/j.chemgeo.2007.11.005

Spurlin, M. S., Yin, A., Horton, B. K., Zhou, J. Y., and Wang, J. H. (2005). Structural evolution of the Yushu–Nangqian region and its relationship to syncollisional igneous activity, east-central Tibet. *Geol. Soc. Am. Bull.* 117 (9–10), 1293–1317. doi:10.1130/b25572.1

Stacey, J. S., and Kramers, J. D. (1975). Approximation of terrestrial lead isotope evolution by a two-stage model. *Earth Planet. Sci. Lett.* 26, 207–221. doi:10.1016/0012-821x(75)90088-6

Tan, X. B., Lee, Y. H., Chen, W. Y., Cook, C. L., and Xu, X. W. (2014). Exhumation history and faulting activity of the southern segment of the Longmen Shan, eastern Tibet. *J. Asian Earth Sci.* 81, 91–104. doi:10.1016/j.jseaes.2013.12.002

Wang, C. Y., Hai, L., Paul, G. S., Zhu, L., and Chang, L. (2010). Crustal structure variation along 30°N in the eastern Tibetan Plateau and its tectonic implications. *Earth Planet. Sci. Lett.* 289, 367–376. doi:10.1016/j.epsl.2009.11.026

Wang, E., Burchfiel, B. C., Royden, L. H., Chen, L., Chen, J., Li, W., et al. (1998). *Late cenozoic xianshuihe-xiaojiang, Red River, and dali fault systems of southwestern sichuan and central yunnan, China*. Boulder: Geological Society of America, 108.

Wang, E., Kirby, E., Furlong, K. P., van Soest, M., Xu, G., Shi, X., Kamp, P. J. J., Hodges, K.V., et al. (2012). Two-phase growth of high topography in eastern Tibet during the Cenozoic. *Nat. Geosci.* 5, 640–645. doi:10.1038/ngeo1538

Wiedenbeck, M., Alle, P., Corfu, F., Griffin, W. L., Meier, M., Oberli, F., et al. (1995). Three natural zircon standards for U–Th–Pb, Lu–Hf, trace-element and REE analyses. *Geostand. Newsl.* 19, 1–23. doi:10.1111/j.1751-908x.1995.tb00147.x

Xu, G., and Kamp, P. J. J. (2000). Tectonics and denudation adjacent to the Xianshuihe fault, eastern Tibetan plateau: constraints from fission track thermochronology. *J. Geophys. Res.* 105 (8), 19231–19251. doi:10.1029/2000jb900159

Yin, A., and Harrison, T. M. (2000). Geologic evolution of the Himalayan-Tibetan orogen. *Annu. Rev. Earth Planet. Sci.* 28, 211–280. doi:10.1146/annurev.earth.28.1.211

Zhang, H. F., Harris, N., Parrish, R., Kelley, S., Zhang, L., Rogers, N., et al. (2004a). Causes and consequences of protracted melting of the mid-crust exposed in the North Himalayan antiform. *Earth Planet. Sci. Lett.* 228, 195–212. doi:10.1016/j.epsl.2004.09.031

Zhang, P., Shen, Z., Wang, M., Gan, W., Burgmann, R., Molnar, P., et al. (2004b). Continuous deformation of the Tibetan Plateau from global positioning system data. *Geology* 32, 809–812. doi:10.1130/g20554.1

Zhang, Y., Pham, B., and Eckstein, M. P. (2004c). Evaluation of JPEG 2000 encoder options: human and model observer detection of variable signals in X-ray coronary angiograms. *IEEE Trans. Med. Imaging* 23 (5), 613–632. doi:10.1109/tmi.2004.826359

frontiers | Frontiers in Earth Science

TYPE Original Research
PUBLISHED 28 September 2023
DOI 10.3389/feart.2023.1213958

OPEN ACCESS

EDITED BY
J. Gregory Shellnutt,
National Taiwan Normal University, Taiwan

REVIEWED BY
K. R. Hari,
Pandit Ravishankar Shukla University, India
Thuy Thanh Pham,
National Taiwan University, Taiwan

*CORRESPONDENCE
Yu-Ling Lin,
lulumilin@ntnu.edu.tw
Tung-Yi Lee,
t44001@ntnu.edu.tw

RECEIVED 28 April 2023
ACCEPTED 21 August 2023
PUBLISHED 28 September 2023

CITATION
Lin Y-L, Lee T-Y, Lee H-Y, Iizuka Y, Quek LX and Charusiri P (2023), Zircon U-Pb geochronology of the Lan Sang gneisses and its tectonic implications for the Mae Ping shear zone, NW Thailand. *Front. Earth Sci.* 11:1213958. doi: 10.3389/feart.2023.1213958

Zircon U-Pb geochronology of the Lan Sang gneisses and its tectonic implications for the Mae Ping shear zone, NW Thailand

Yu-Ling Lin[1]*, Tung-Yi Lee[1]*, Hao-Yang Lee[2], Yoshiyuki Iizuka[2], Long Xiang Quek[3] and Punya Charusiri[4]

[1]Department of Earth Sciences, National Taiwan Normal University, Taipei, Taiwan, [2]Institute of Earth Sciences, Academia Sinica, Taipei, Taiwan, [3]Key Laboratory of Computational Geodynamics, College of Earth and Planetary Sciences, College of Earth and Planetary Sciences, University of Chinese Academy of Sciences, Beijing, China, [4]Department of Geology, Faculty of Science, Chulalongkorn University, Bangkok, Thailand

The Mae Ping shear zone (MPSZ), a major shear zone trending NW-SE in Thailand, is responsible for the left-lateral displacement of the N-S Triassic-Jurassic granitoid and gneiss belt. This displacement is postulated to have contributed to Cenozoic extrusion tectonics. Within the Lan Sang National Park, the MPSZ exposes several intensely deformed lithologies, collectively known as the Lan Sang gneisses. These gneisses have attracted considerable attention for their potential to substantiate the extrusion model. However, the timing of the emplacement of the orthogneiss protolith is still debated. Moreover, the origin and distribution of the Eocene syn-shearing granodiorite within this shear zone are not well understood. To shed light on the magmatic history of the MPSZ, this study utilized zircon U-Pb geochronology to systematically investigate the Lan Sang gneisses. Our findings demonstrate that these gneisses can be categorized into paragneiss and orthogneiss groups. Paragneiss samples feature zircons displaying rounded detrital cores ranging from 3,078 to 450 Ma, with metamorphic rim overgrowth of ca. 200 Ma (most Th/U <0.01). This indicates that their Paleozoic sedimentary protoliths experienced high-grade metamorphism during the Triassic-Jurassic Indosinian orogeny. On the other hand, zircon from orthogneiss samples shows that their magmatic protoliths were predominantly emplaced either around ~200 Ma or within 45-32 Ma. The Eocene-Oligocene magmatism likely coincided with the proposed Eocene metamorphism. Since these samples were deformed by left-lateral shearing, the left-lateral motion of the MPSZ probably ended after 32 Ma. Eocene-Oligocene magmatic events have also been identified in granite, mylonite, and gneiss samples from other regions along the Sibumasu terrane, including the Three Pagodas, Klaeng, Ranong, Khlong Marui shear zones, and the Doi Inthanon area. The Eocene-Oligocene magmatism was likely linked with the movement of the shear zones and may be responsible for the regional cooling pattern. The spatial and temporal distribution of the Eocene-Oligocene magmatism within the Sibumasu terrane supports the hypothesis that the inward migration of magmatism in the overriding plate resulted from the shallowing of the Neo-Tethyan slab.

KEYWORDS

Lan Sang gneisses, Mae Ping shear zone, zircon U-Pb geochronology, Sibumasu, Thailand, syn-shearing intrusion

1 Introduction

Numerous studies have focused on the Cenozoic extrusion tectonics induced by the India-Eurasia collision (as shown in Figure 1), with the aim of determining the timing of major shear zones by dating the associated magmatism or metamorphism (Scharer et al., 1994; Wang et al., 1998; Zhang and Schärer, 1999; Searle, 2006; Liang et al., 2007; Chung et al., 2008; Watkinson et al., 2011; Nantasin et al., 2012; Kanjanapayont et al., 2013; Palin et al., 2013; Tang et al., 2013; Liu et al., 2015; Österle et al., 2019; Li et al., 2021). These shear zones include the Ailao Shan-Red River shear zone (AS-RRSZ), the Mae Ping shear zone (MPSZ, also known as the Wang Chao fault zone), the Three Pagodas shear zone (TPSZ), the Klaeng shear zone (KSZ), the Ranong shear zone (RSZ), and the Khlong Marui shear zone (KSZ). It is believed that these shear zones were motivated by the indentation of India into Asia and have accommodated notable deformation. In particular, the MPSZ is thought to have played a crucial role in facilitating the southeastward extrusion of Indochina through its movement (Tapponnier et al., 1982; Peltzer and Tapponnier, 1988; Lacassin et al., 1997).

Previous studies have applied various geochronological methods to the MPSZ and its surrounding area to elucidate its evolution (Ahrendt et al., 1993; Lacassin et al., 1997; Morley et al., 2007; Palin et al., 2013; Österle et al., 2019; Lin et al., 2021). Mineral cooling ages have been obtained to discern the timing of rapid cooling or exhumation potentially linked to the motion of the MPSZ (Ahrendt et al., 1993; Lacassin et al., 1997; Morley et al., 2007; Lin et al., 2021). The rapid cooling during 42-30 Ma was attributed to the left-lateral shearing of the MPSZ, followed by the subsequent cooling between 23 and 18 Ma, probably due to the reversal of right-lateral movement. However, the regional cooling pattern indicates that the strike-slip deformation of the MPSZ did not dominate the cooling history. The exposure of the Lan Sang gneisses is more associated with regional exhumation patterns than the uplift and erosion caused by shearing (Morley et al., 2007). Consequently, Palin et al. (2013) and Österle et al. (2019) endeavored to study metamorphism and magmatism in an effort to achieve a more comprehensive understanding of the MPSZ.

Palin et al. (2013) proposed that the protolith of the Lan Sang orthogneiss was emplaced during the Early Cretaceous based on monazite Th-Pb dates. It was subsequently subjected to an Eocene prograde metamorphism during 45-37 Ma, prior to the ductile shearing of the MPSZ. They concluded that neither metamorphism nor regional cooling was directly related to the shearing of MPSZ. The zircon U-Pb geochronology of Österle et al. (2019) revealed the granitic protolith of an augen gneiss intruded metasedimentary basement during the Late Triassic. They suggested the Eocene metamorphism commenced by ~45 Ma and subsequently led to partial melting of basement gneisses. This metamorphism culminated in the intrusion of granodiorite around 35 Ma, accompanied by contemporaneous ductile shearing along the MPSZ. Their findings are very encouraging since previous zircon U-Pb studies only indicated a Triassic-Jurassic amphibolite facies metamorphism (Ahrendt et al., 1993; Kanjanapayont et al., 2011).

However, further investigation remains essential to ascertain the emplacement timing of the protolith of the Lan Sang orthogneiss and whether it occurred during the Early Cretaceous or the Late Triassic. In fact, not only shearing but also magmatism can contribute to metamorphism or mineral cooling. Therefore, a detailed examination of the interrelationships between the Eocene metamorphism, granodioritic intrusion, regional cooling, and

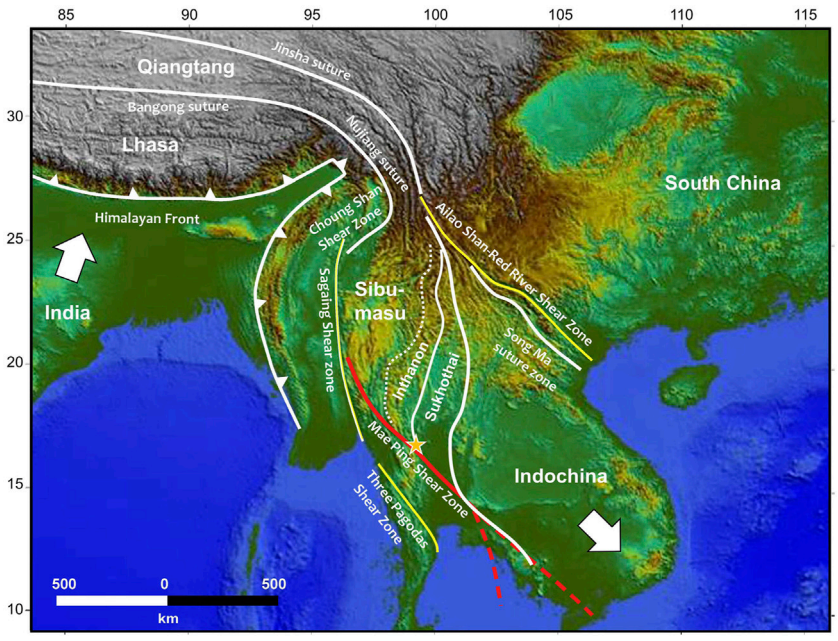

FIGURE 1
DTM map of SE Asia showing the extrusion tectonics based on Leloup et al. (1995), Ueno and Hisada (2001), and Sone et al. (2012). The orange star marks the position of the Lan Sang gneisses within the MPSZ. The left-lateral motion of the MPSZ is thought to have facilitated the extrusion of Indochina.

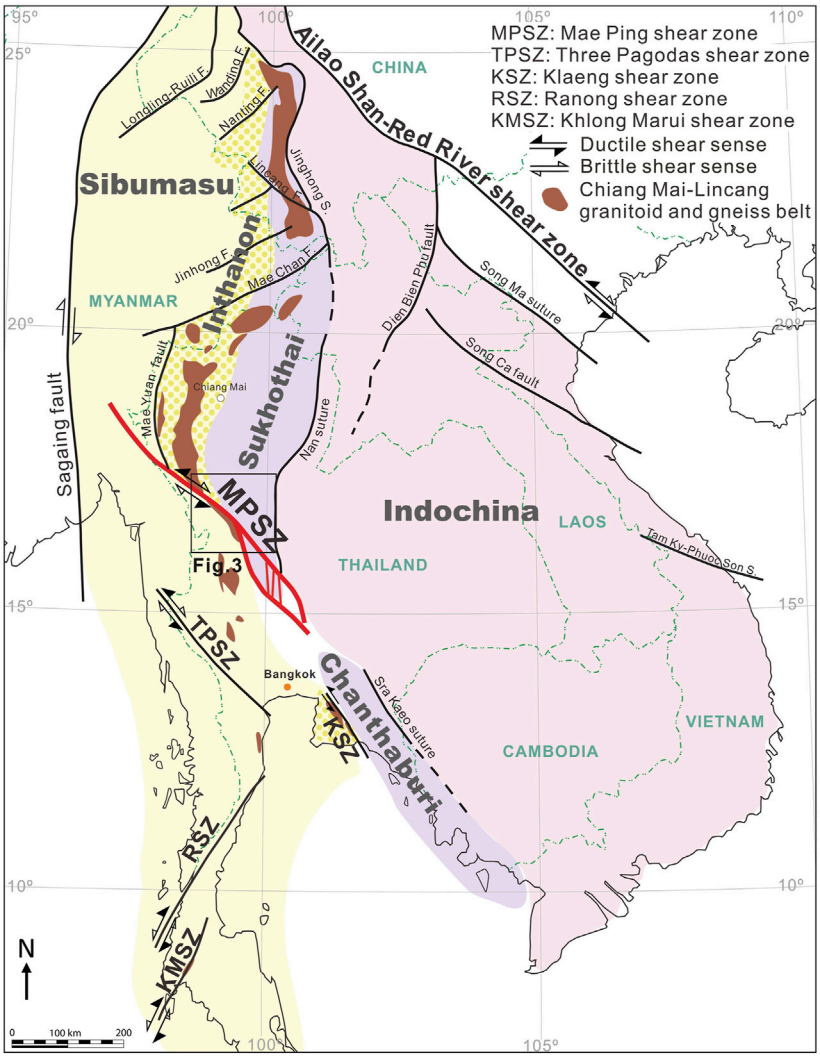

FIGURE 2
Tectonic subdivision map of SE Asia (after Lacassin et al., 1997; Sone et al., 2012; Deng et al., 2014). The MPSZ stretches from the Sibumasu terrane, displacing the Inthanon zone and the Sukhothai arc; however, its southeastward extension is still uncertain.

shearing is necessary for a comprehensive tectonic reconstruction of the MPSZ. In this study, we present new zircon U-Pb geochronology data on the Lan Sang gneisses, aiming to: 1) provide detailed age constraints to elucidate the complex thermal history; 2) offer insights into the spatial and temporal distribution of Eocene magmatism; 3) explore the correlations between magmatism, metamorphism, and shear activity; and 4) propose a tectonic reconstruction of the MPSZ.

2 Geological background

The NW-SE trending MPSZ stretches for approximately 500 km, extending from the Sagaing fault in Myanmar to northern Thailand. However, uncertainties persist about its continuation to the southeast (Morley et al., 2007). It is inferred that the MPSZ has undergone left-lateral deformation for at least 150 km (Lacassin et al., 1997) and possibly up to 300 km (Peltzer and Tapponnier, 1988). Similar to the AR-RRSZ, the MPSZ may also have experienced a later reversal to right-lateral strike-slip motion since the Oligocene or during the Miocene (Polachan et al., 1991; Lacassin et al., 1997). In addition to these uncertainties, the tectonic framework of the MPSZ is complex.

Southeast Asia comprises heterogeneous continental fragments derived from the Gondwana margin and assembled by the closure of Paleo-, Meso-, and Neo-Tethys oceans and back-arc basins (Metcalfe, 2013). In particular, the MPSZ occupies an important position as it encompasses the major tectonic fragments of Southeast Asia, such as the Sibumasu terrane, the Inthanon accretionary zone, the Sukhothai island arc, and the Indochina terrane (Figure 2; Metcalfe, 2011; Sone et al., 2012). The Sibumasu terrane consists of Phanerozoic rocks and a Cambrian-Ordovician crystalline basement that probably formed in a magmatic arc-related regime on the Gondwana India-Australia margin around 502-477 Ma (Lin et al., 2013; Kawakami et al., 2014; Dew et al., 2018). The Indochina terrane is thought to comprise several micro-terranes. Magmatic

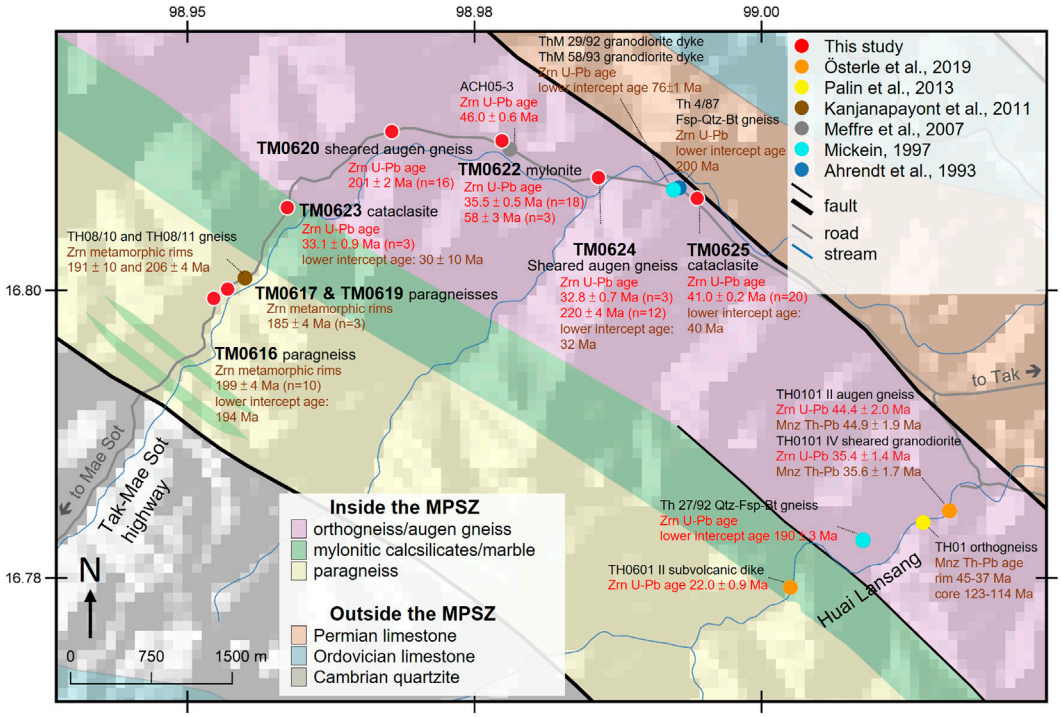

FIGURE 3
Sample location map showing the thermal history of the Lan Sang gneisses by highlighting zircon U-Pb and monazite Th-Pb ages. The simplified geological map (modified from Lacassin et al., 1997; DMR, 1999; Österle et al., 2019) is overlaid with SRTM 90 m DEM data (Jarvis et al., 2008).

and detrital zircon dates indicate that the Indochina terrane underwent two major magmatic events at 480-404 Ma and 300-230 Ma (Khin et al., 2014; Arboit et al., 2016; Wang et al., 2016; Kawaguchi et al., 2021). The Sukhothai arc developed along the margin of Indochina as a result of the Paleo-Tethys ocean subducting beneath Indochina and consists primarily of I-type granitoids of 238-228 Ma (zircon U-Pb ages, Khin et al., 2014; Dew et al., 2018). The Inthanon zone represents a remnant of the Paleo-Tethys accretionary complex that overlies the Sibumasu terrane (Sone et al., 2012).

In addition to the tectonic fragments, the MPSZ has left-laterally displaced the N-S Triassic-Jurassic granitoid and gneiss belt, known as the Chiang Mai-Lincang belt (CM-LB, Figure 2). Therefore, the MPSZ may incorporate magmatic or metamorphic ages originating from the CM-LB. In NW Thailand, the formation of the CM-LB resulted from the collision between the Sibumasu and Indochina terranes, an event commonly referred to as the Indosinian orogeny, following the closure of the Paleo-Tethys (Searle et al., 2012; Palin et al., 2013). This granitoid and gneiss belt has attracted considerable attention because of its tin and tungsten mineralization (Searle et al., 2012). According to the studies of the Doi Inthanon and Doi Suthep areas, this belt should have experienced magmatism and high-grade metamorphism at 221-210 Ma, then upper-amphibolite facies metamorphism at 84-67 Ma, and a late tectonothermal event at 34-24 Ma (Dunning et al., 1995; Macdonald et al., 2010; Gardiner et al., 2016). The MPSZ may contain similar ages.

Due to intense weathering and dense vegetation, only a few suitable outcrops are available to investigate the MPSZ. Within the Lan Sang National Park, the Tak-Mae Sot highway traverses the 5 km-wide MPSZ and exposes outcrops of deformed high-grade paragneiss, orthogneiss, mylonite, cataclasite, calc-silicate, leucogranite, and minor undeformed intrusive rocks (Figure 3). These high-grade and intensely deformed rocks are collectively referred to as the Lan Sang gneisses. In addition to the highway, samples were also collected from Huai Lansang, a stream located ~6 km away from it (Mickein, 1997; Palin et al., 2013; Österle et al., 2019). The exposure of Lan Sang gneisses along these two transects has contributed valuable insights into the tectonic evolution of the MPSZ, although a detailed U-Pb dating study is still lacking.

3 Previous geochronologic constraints for the MPSZ

Zircon U-Pb dating of a feldspar-quartz-biotite gneiss revealed an inherited core age of 1,530 Ma and a discordia lower intercept age of around 200 Ma based on six zircon grains, indicating a Triassic amphibolite facies metamorphism. While biotite yielded K/Ar cooling ages of 32-30 Ma, this may be due to the strong uplift caused by shearing along the MPSZ (Ahrendt et al., 1993). Biotite and K-feldspar $^{40}Ar/^{39}Ar$ ages of Lan Sang gneisses indicated rapid cooling at 30.5 and 23 Ma, which were interpreted as the termination of left-lateral shear and the onset of right-lateral motion due to E-W extension, respectively (Lacassin et al., 1997). Zircon fission track ages of 36-28 Ma indicate exhumation due to the regional uplift, while apatite fission track ages of 25-19 Ma may follow the Late Oligocene-Early Miocene extension (Morley et al., 2007).

TABLE 1 Sample descriptions.

Sample	Lithology	GPS coordinates		Mineral assemblage	Major foliation Dip/Dip Az
Paragneiss samples					
TM0616	Paragneiss	N16.7993	E98.9523	Qz+Pl+Kfs+Ms	62/061
TM0617	Paragneiss	N16.8001	E98.9535	Qz+Pl+Kfs+Ms	79/051
TM0619	Paragneiss	N16.8001	E98.9535	Qz+Pl+Kfs+Bt+Hb	70/061
Orthogneiss samples					
TM0623	Cataclasite	N16.8072	E98.9587	Qz+Pl+Kfs+Bt	34/024
TM0620	Sheared augen gneiss	N16.8138	E98.9678	Qz+Pl+Kfs+Bt	52/059
TM0622	Mylonite	N16.813	E98.9774	Qz+Pl+Kfs+Bt	50/067
TM0624B	Sheared augen gneiss	N16.8098	E98.9858	Biotite rich layer: Qz+Pl+Kfs+Bt+Hb	46/058
				Feldspathic layer: Qz+Pl+Kfs+Bt	
TM0625	Cataclasite	N16.8080	E98.9944	Qz+Pl+Kfs+Bt+Ms	41/042

Metamorphic zircon rims of two Lan Sang gneisses overgrew around 191 ± 10 and 206 ± 4 Ma (Kanjanapayont et al., 2011), suggesting Triassic-Jurassic metamorphism. Monazite U-Th-Pb geochronology on the Lan Sang orthogneiss indicated that its magmatic protolith was likely emplaced at 123-114 Ma, with subsequent metamorphism occurring at 45-37 Ma (Palin et al., 2013). Zircon U-Pb dating suggested the protolith of augen gneiss may have intruded into the metasedimentary rocks at ~235–220 Ma (Österle et al., 2019). Zircons in this augen gneiss exhibit a second age cluster at 45 Ma, whereas zircons in the sheared granodiorite display a dominant age cluster at 35 Ma. Österle et al. (2019) interpreted these findings to indicate that metamorphism likely began around 45 Ma and reached a climax with partial melting and the intrusion of granodiorite at 35 Ma. $^{40}Ar/^{39}Ar$ thermochronology on the leucogranite within the MPSZ, along with careful deformation temperature estimation, suggested that left-lateral shear occurred at least from 42 to 30 Ma (Lin et al., 2021).

4 Methods

4.1 Sampling

Paragneiss, mylonite, cataclasite, and sheared augen gneiss samples were collected from outcrops along the highway in the Lan Sang National Park (Table 1). Samples were collected at intervals of at least every 1 km. The orientation of the major foliation plane in each sample was also measured in the field. Photographs of the outcrops can be found in Figure 3 by Lin et al. (2021). Paragneiss samples were named according to the sedimentary characteristics revealed by zircon U-Pb dating. The nomenclature of other samples is based on their textures from hand specimens, as they were all deformed (Figure 4). In the accompanying text, figures, and tables, samples are arranged according to their geographical locations, from west to east. This is intended to facilitate understanding and comparison of the results. Thin sections of these samples were examined to observe the deformation textures (Figure 5) in order to infer deformation conditions and timing related to the magmatism. Mineral abbreviations in Figure 5 and Table 1 follow Whitney and Evans (2010).

4.2 Zircon U-Pb dating

Zircons were separated from 1-2 kg of samples using magnetic and heavy liquid separation techniques. For each sample, approximately 100–120 zircon grains were mounted, filling the epoxy resin to a depth of ~1 cm. After 24 h of solidification, the mold and the tape were removed from the epoxy discs. The discs were ground using a Struers MD-Piano 500 (Struers, Copenhagen, Denmark) resin-bonded diamond disc until a suitable zircon cross-section was exposed, followed by polishing with 3 μm diamond suspensions. Cathodoluminescence (CL) electron images of zircon grains were taken using a JEOL (Japan Electron Optics Laboratory Co., Ltd.) JSM-6360LV scanning electron microscope (SEM) at the Institute of Earth Sciences, Academia Sinica, Taiwan. These images were used to examine the crystal shapes and internal zoning structures and to select suitable positions for U-Pb isotope analyses.

Zircon U-Pb dating was conducted using an Agilent 7500s quadrupole inductively coupled plasma mass spectrometer (ICP-MS) (Agilent Technologies, Inc., Santa Clara, United States) equipped with a New Wave UP-213 laser ablation system (Electro Scientific Industries, Inc., Portland, United States) at the National Taiwan University (NTU), Taipei, Taiwan. The laser beam was set to a diameter of 35 μm, with a repetition rate of 4 Hz and an energy of 10 J/cm^2. For instrumental drift correction, the GJ-1 zircon served as the primary standard, while the Harvard reference zircon 91,500 and the Australian Mud Tank carbonatite zircon MT were employed as secondary standards for measurement quality monitoring. Analytical procedures and operating conditions followed those outlined in Chiu et al. (2009). The upper and lower intercepts, concordia ages, and plots were calculated and generated using the Excel add-in of the Isoplot 4.15 software (Ludwig, 2008). Of the 366 analyses that underwent common lead correction, 361 of them showed age uncertainty ≤3% at the 1σ level. Age discordance was calculated based on the relative age

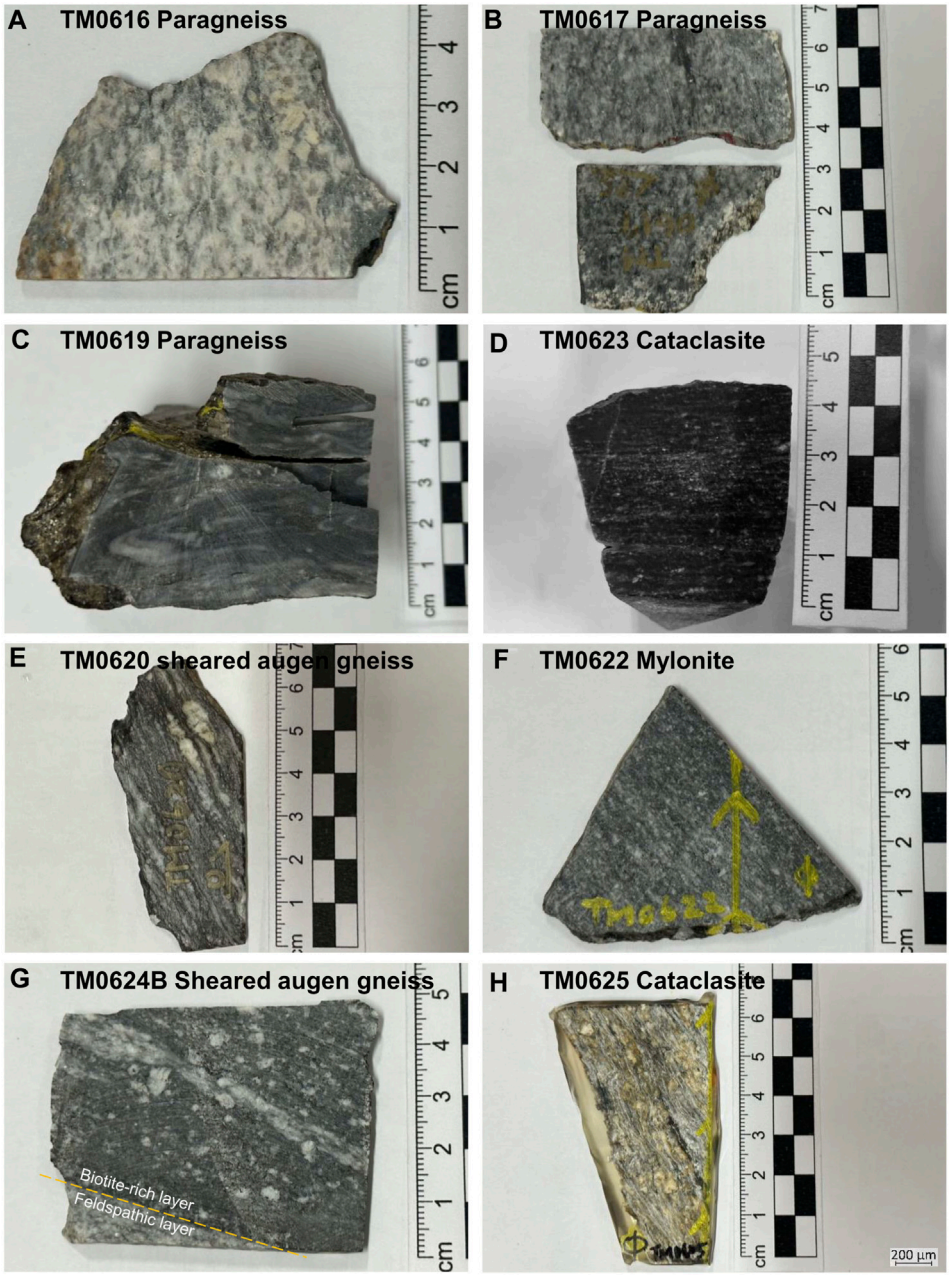

FIGURE 4
Representative photographs of hand specimens taken from samples of the Lan Sang gneisses. **(A–C)** paragneiss samples. **(D–H)** orthogneiss samples.

difference between the $^{207}Pb/^{235}U$ and $^{206}Pb/^{238}U$ ages (for $^{206}Pb/^{238}U$ ages <1,000 Ma) or between the $^{206}Pb/^{238}U$ and $^{207}Pb/^{206}Pb$ ages (for $^{206}Pb/^{238}U$ ages >1,000 Ma). Age spectra for data within 30% discordance were generated using the "detzrcr" software package developed in R (Andersen et al., 2018).

5 Results

All samples exhibit a sheared fabric indicating left-lateral shear sense. The major foliation planes measured at sample locations all dip towards the NE (Table 1), consistent with the findings reported by Lacassin et al. (1997). The paragneiss samples generally have steeper major foliation planes compared to the orthogneiss samples.

5.1 TM0616 feldspathic paragneiss

TM0616 is a muscovite feldspathic paragneiss (Figure 5A). Quartz shows dynamic recrystallization of bulging (BLG), subgrain rotation (SGR), and grain boundary migration (GBM). Sericite is observed both surrounding and embedded within the deformed plagioclase

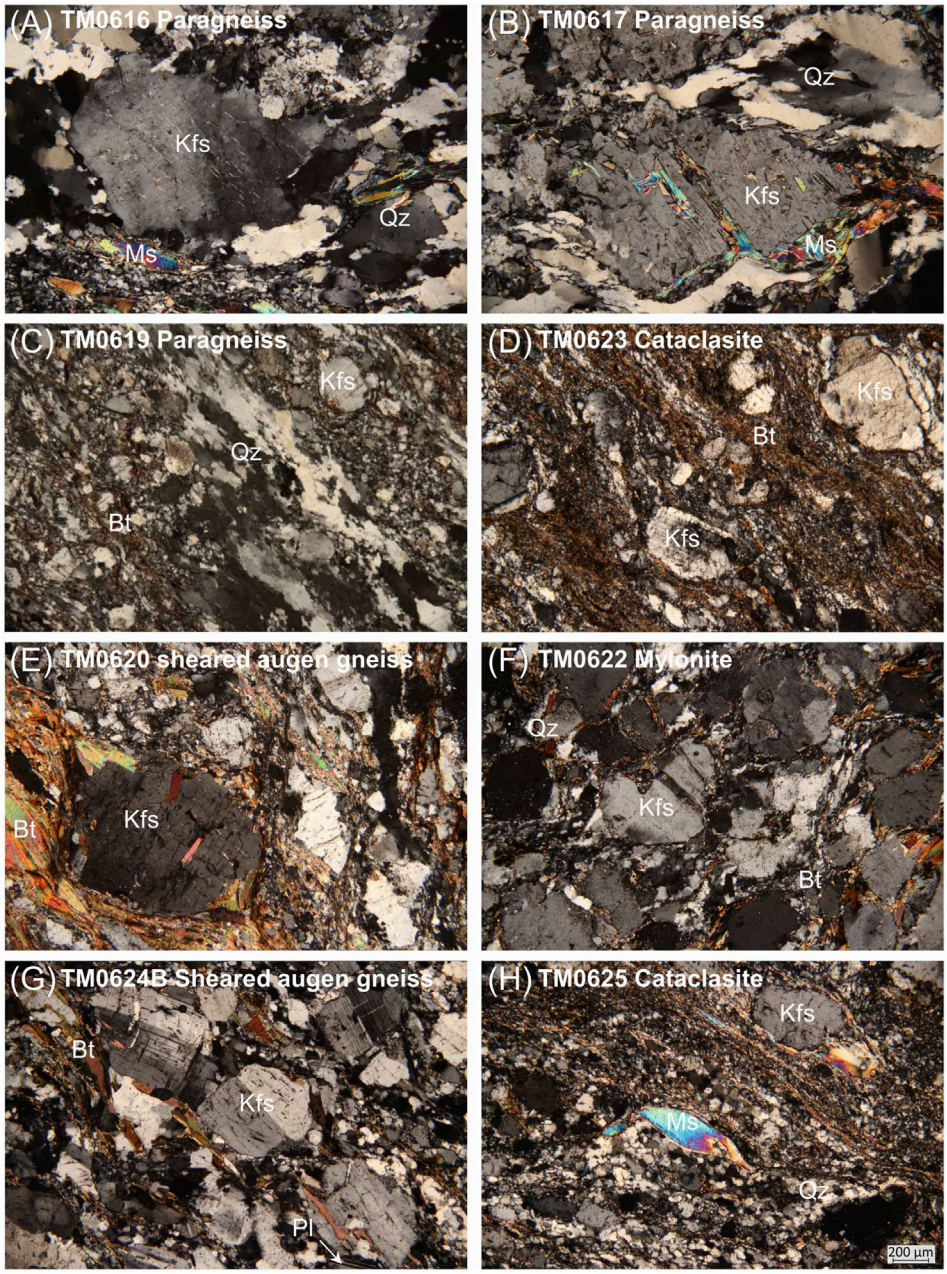

FIGURE 5
Representative photomicrographs of thin sections taken from samples of the Lan Sang gneisses. **(A–C)** paragneiss samples. **(D–H)** orthogneiss samples. All images were viewed under crossed polars at the same magnification. Undulose extinction and grain size reduction in feldspar, quartz, and mica indicate these rocks should have experienced plastic to brittle deformation. Mineral abbreviations follow Whitney and Evans (2010).

porphyroclast, pointing to the alteration of plagioclase through the Na-K exchange reaction. Plagioclase porphyroclasts show deformation twinning. The microstructure of quartz and plagioclase indicates that the deformation temperature could be as high as 600°C (Stipp et al., 2002; Passchier and Trouw, 2005). Fish-shaped muscovite was mainly deformed by grain size reduction.

Zircon grains from TM0616 display short prismatic shapes with lengths of ~200 μm. SEM-CL images reveal that most of the zircons are sub-euhedral and exhibit distinct core-rim structures. The cores are characterized by rounded shapes with bright oscillatory zoning, while the rims appear dull and cloudy without clear zonation (Figure 6). A total of 32 analyses were conducted on this sample, resulting in ages ranging from 2,511 to 191 Ma with a concordia age of 199 ± 4 Ma (Table 2; Figure 7A). Within these analyses, 18 zircon cores yielded ages of 2,511-462 Ma, with an average Th/U ratio of 0.46 (Figures 8A, 9). On the other hand, 14 zircon rim analyses yielded ages of 449, 249, 227, and 202-191 Ma. These rim analyses mostly fell on the concordia curve, although a few of them derived a lower intercept age of 194 ± 8 Ma (Figure 7A). A concordia age of 199 ± 4 Ma was calculated from these rim analyses, which showed an average Th/U ratio of 0.024.

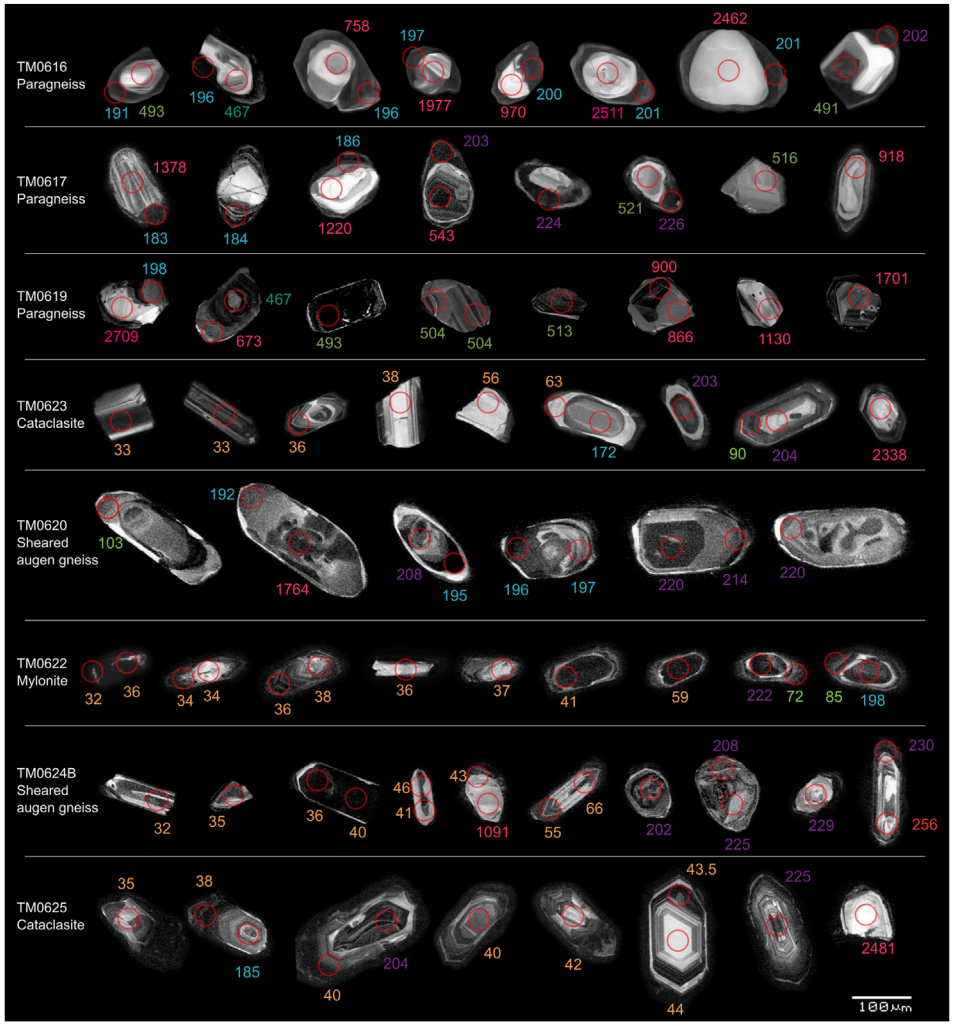

FIGURE 6
Representative zircon SEM cathodoluminescence images. Red circles mark the positions of U-Pb analyses. Ages have been common-lead corrected.

TABLE 2 Summary of zircon U-Pb geochronology data.

Sample	Lithology	Age range (Ma)		Concordia age				Lower intercept age	Age clusters
		min	max	(Ma)	n	MSWD	Th/U	(Ma)	(Ma)
TM0616	Paragneiss	191 ± 4	2,511 ± 24	199 ± 4	10	16	0.024	194 ± 8	198, 468
TM0617	Paragneiss	179 ± 4	2,747 ± 14	185 ± 4	3	1.8	0.004		184, 225, 514, 915
TM0619	Paragneiss	198 ± 5	3,078 ± 14						504, 726, 886, 986
TM0623	Cataclasite	32.6 ± 0.8	2,438 ± 17	33.1 ± 0.9	3	3.5	0.59	30 ± 10	34
TM0620	Sheared augen gneiss	103 ± 2	1764 ± 23	201 ± 2	16	0.24	0.37		194, 208, 214
TM0622	Mylonite	31.6 ± 0.6	924 ± 17	35.5 ± 0.5	18	0.073	0.62		36, 200
				58 ± 3	3	7.8	0.23		
TM0624B	Sheared augen gneiss	32.4 ± 0.6	2,471 ± 17	32.8 ± 0.7	3	4.8	1.11	32 ± 6	33, 41, 211, 219
				220 ± 4	12	0.079	0.57		
TM0625	Cataclasite	34.7 ± 0.9	2,481 ± 22	41.0 ± 0.2	20	3.7	0.27	40 ± 2	41

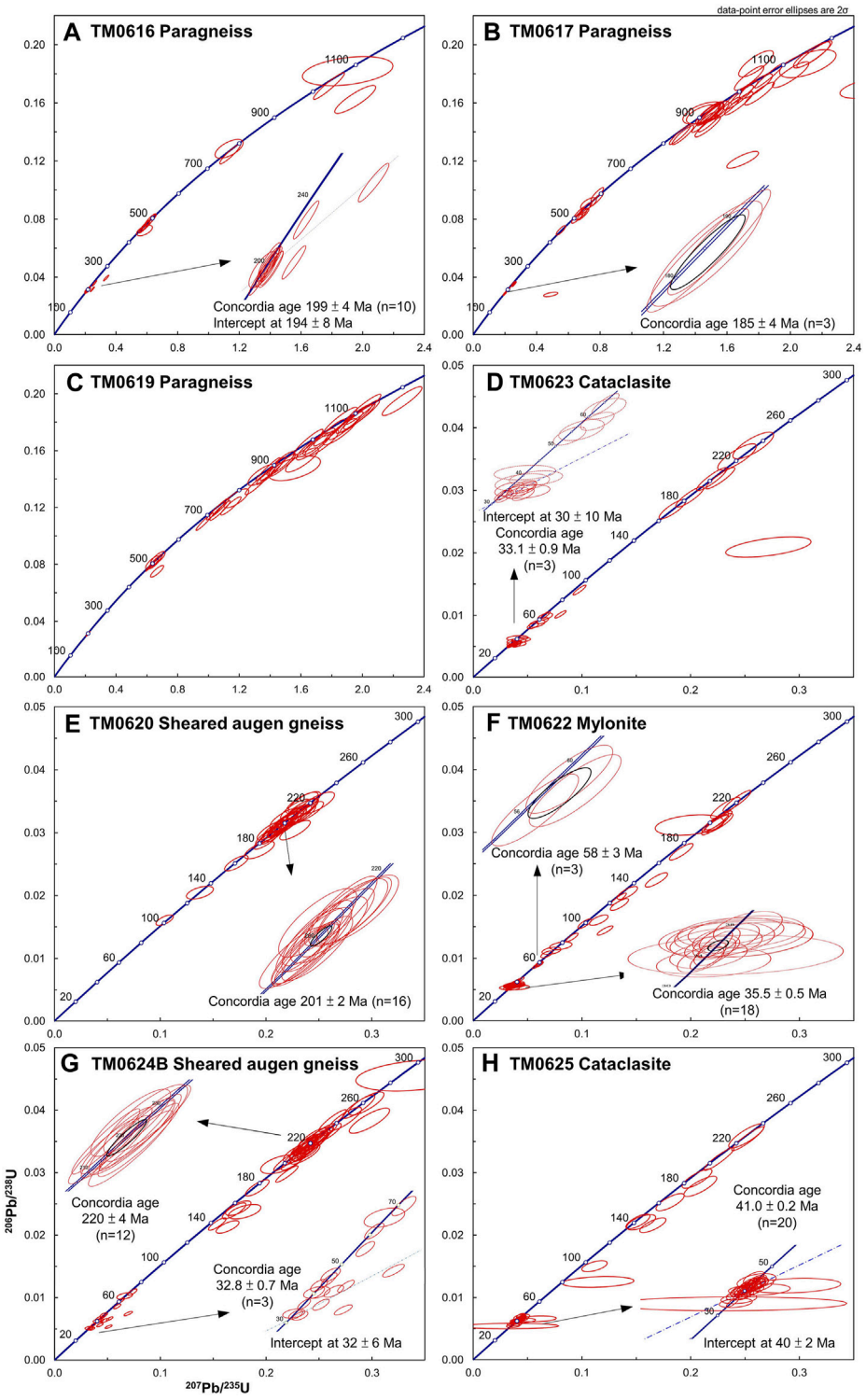

FIGURE 7
Zircon U-Pb concordia plots of the samples in this study. **(A–C)** paragneiss samples. **(D–H)** orthogneiss samples.

5.2 TM0617 paragneiss

In the TM0617 paragneiss, the plagioclase presents a fish-like grain shape coupled with bulging recrystallization, both markers of its ductile deformation (Figure 5B). Additionally, there are some brittle deformation textures present, such as grain size reduction, fractures, and domino structures. Plagioclase and K-feldspar porphyroclasts show alteration by sericite. Muscovite shows undulose extinction, bulging, and brittle deformation characterized by grain size reduction. Quartz shows dynamic recrystallization of BLG, SGR, and GBM.

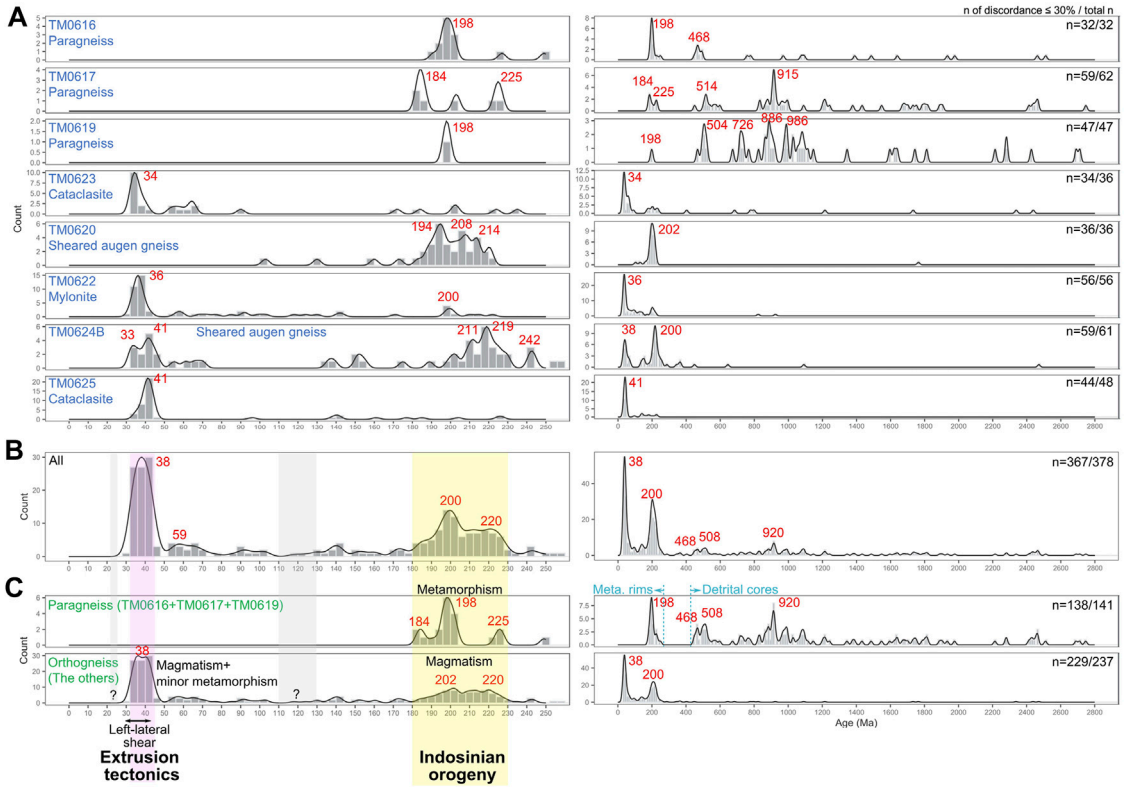

FIGURE 8
Kernel density estimate (KDE) plots of zircon U-Pb age spectra. The left panels are age spectra from 0-250 Ma, and the right panels are age spectra from 0-2,800 Ma **(A)** Age spectra for each sample **(B)** Age spectra of all analyses in this study **(C)** Age spectra for paragneiss and orthogneiss samples, respectively.

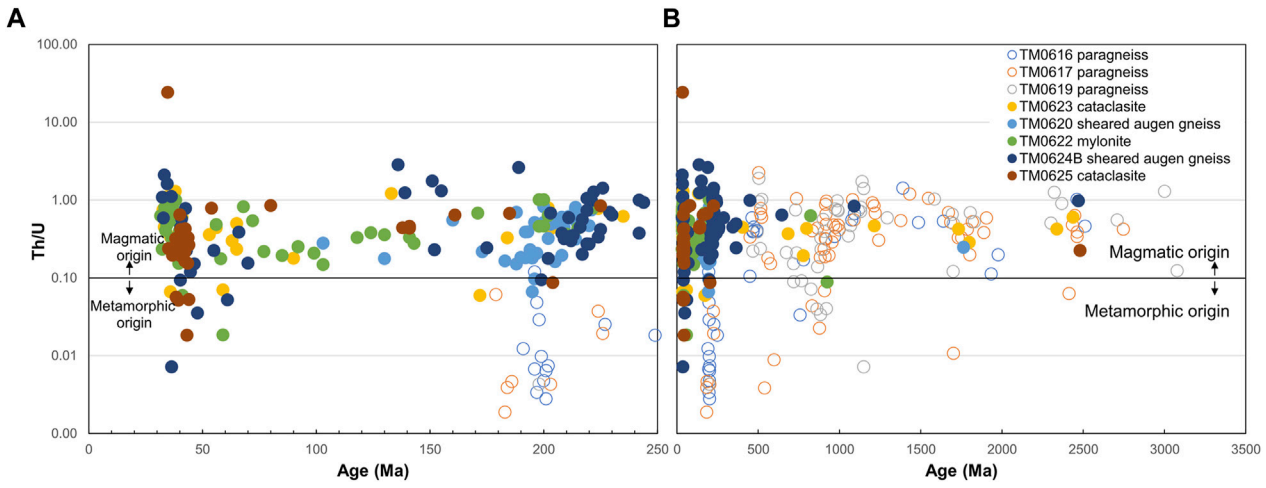

FIGURE 9
Zircon Th/U *versus* inferred ages for all analyses in this study **(A)** 0-250 Ma interval **(B)** 0-3,500 Ma interval. Most paragneiss zircon rims yield Th/U >0.01, indicating their metamorphic origin. The Eocene zircons predominantly have Th/U ratios >0.1, indicating their magmatic origins (Yakymchuk et al., 2018).

Zircons of TM0617 are sub-euhedral and short prismatic with a length of ~150 μm (Figure 6). SEM-CL images demonstrate that most of the zircons have bright and rounded cores with oscillatory zoning, overgrown by a thin layer of dull rims. A total of 62 analyses of 52 zircons yielded ages ranging from 2,747 to 179 Ma, clustered around 915, 514, 225, and 184 Ma (Figures 7B, 8A).

Zircon cores revealed ages of 2,747-450 Ma with an average Th/U ratio of 0.49 (Figure 9). Seven analyses on rims yielded ages of 226-179 Ma, and three of these yielded a concordia age of 185 ± 4 Ma (n=3, average Th/U=0.004).

5.3 TM0619 paragneiss

In the TM0619 paragneiss, quartz exhibits dynamic recrystallization characterized by BLG, SGR, and GBM (Figure 5C). Biotite contains kink bands. Deformation twinning, fish-like grain shape, and boudinage structure reveal ductile to brittle deformation of feldspar. Some myrmekite could be observed around the K-feldspar.

Zircons from sample TM0619 are predominantly rounded to short prismatic, measuring approximately 150 μm in length (Figure 6). SEM-CL images show their distinct oscillatory zoning patterns. A total of 47 analyses were conducted on this sample. Among them, only one analysis on a metamorphic rim was acquired due to the lack of a distinct core-rim structure in the other zircons. The rim age is 198 Ma with a Th/U ratio of 0.004. The remaining 46 analyses yielded U-Pb ages ranging from 3,078 to 467 Ma (Figures 7C, 8A), with the majority exhibiting Th/U ratios >0.1 (Figure 9).

One particular zircon displayed a 467 Ma core with a comparatively older 673 Ma rim. In fact, the core presented a higher age discordance of 10.9% compared to the rim's 2.7%. This could suggest that the core underwent greater Pb loss than the rim. Alternatively, the zircon could have grown during multiple events, which could lead to mixed signals from different generations or perhaps an improper selection of signal intervals during the analysis.

5.4 TM0623 cataclasite

The deformation of TM0623 cataclasite is primarily characterized by grain size reduction (Figure 5D). Feldspar porphyroclasts display deformation twinning, undulose extinction and fractures, indicating a progression of shear from plastic to brittle deformation.

Most zircons in this sample are euhedral to subhedral, long to short prismatic crystals with lengths of ~150 μm. They exhibit clear oscillatory zoning patterns (Figure 6). A total of 36 analyses were conducted on 33 zircon grains, resulting in U-Pb ages ranging from 2,438 to 32.6 Ma. Among these, six analyses yielded ages between 235 and 172 Ma, while another six analyses fell within the 65-53 Ma. Furthermore, 13 analyses yielded ages of 41-32.6 Ma, with a lower intercept age of 29.9 ± 9.6 Ma (Figure 7D). A concordia age of 33.1 ± 0.9 Ma could be calculated from three analyses. Most Eocene ages showed Th/U ratios >0.1 (Figure 9).

Analyses were conducted on both the core and rim of only three grains from this sample. Although some zircon grains showed clear, cloudy overgrowths, these were not sufficiently substantial to allow effective analyses.

5.5 TM0620 sheared augen gneiss

In TM0620 sheared augen gneiss, quartz displays dynamic recrystallization of BLG, SGR, and GBM (Figure 5E). Plagioclase porphyroclast exhibits deformation features such as plagioclase fish and deformation twinning, suggesting a deformation temperature of up to 600 °C. Fractures and grain size reduction of feldspars indicate subsequent brittle deformation. Biotite displays kink bands and grain size reduction. Sericite has formed inside and around the feldspar.

Zircons in this sample exhibit a subhedral, slightly rounded, long prismatic shape with lengths of 200–300 μm. (Figure 6). They share a similar oscillatory zoning pattern, characterized by a darker core, an intermediate cloudy layer, and the brightest thin crust on the SEM-CL images. A total of 36 analyses were performed, resulting in ages ranging from 1764 to 103 Ma. Most of the analyses clustered around 220-188 Ma (n = 30). Among them, 16 analyses yielded a concordia age of 201 ± 2 Ma with an average Th/U ratio of 0.37 (Figure 7E).

Out of 13 zircon grains for which both the core and rim were dated, nine of these grains had similar ages. One core distinctly presented an age of 1764 Ma, indicating its inherited nature, and its associated rim was dated to 192 Ma. Some grains exhibited rim ages older than their respective cores. This discrepancy could be due to the inadequate crosscutting of the zircon grains, resulting in a mixed signal from different generations, or to an improper selection of signal intervals during the analysis.

5.6 TM0622 mylonite

In the TM0622 mylonite, quartz shows dynamic recrystallization of BLG, SGR, and GBM (Figure 5F). Feldspar grains present as elongated and deformed, displaying bulging features. Some feldspar porphyroclasts exhibit boudinage structures. Sericite occurs within and around the feldspar.

Zircons in this mylonite sample are sub-euhedral and short prismatic crystals with a length of ~100 μm (Figure 6). SEM-CL images reveal that they have relatively simpler oscillatory zoning pattern. A total of 56 analyses were performed on 48 zircons, with U-Pb ages ranging mainly from 222 to 31.6 Ma, except for two significantly older ages of 924 and 823 Ma, respectively. Among these analyses, five yielded similar ages between 202 and 198 Ma, and three analyses resulted in ages of ~58 Ma (Figure 7F). A total of 29 analyses yielded ages ranging from 42.9 to 31.6 Ma, with Th/U ratios ranging from 0.15 to 1.00 (averaging 0.6, Figure 9) and a concordia age of 35.5 ± 0.5 Ma (n = 18).

Both core and rim analyses were performed on nine zircon grains for this sample. Four grains yielded similar Eocene-Oligocene ages from both the core and rim. One grain yielded the same age of 200 Ma for its core and rim. The remaining four grains displayed different ages in their core and rim. Their cores yielded Neoproterozoic or Late Triassic-Early Jurassic ages, while their rims were all Late Cretaceous.

5.7 TM0624B sheared augen gneiss

In the TM0624B sheared augen gneiss, quartz shows dynamic recrystallization of grain boundary area reduction (GBAR) to GBM (Figure 5G). Feldspar microstructures include bulging,

deformation twinning, myrmekitization, boudinage brittle deformation, and sericitic alteration.

Zircons in this sample are subhedral crystals with lengths of 100–200 μm (Figure 6). A total of 61 analyses were performed on 49 zircon grains, revealing ages ranging from 2,471 to 32 Ma. The age spectrum exhibited two prominent age clusters of 230–199 Ma and 48–32 Ma (Figure 7G). Of the analyses, 11 yielded a concordia age of 219.6 ± 3.8 Ma, with an average Th/U ratio of 0.57. Additionally, three analyses resulted in a concordia age of 32.8 ± 0.7 Ma with an average Th/U of 1.11. Five discordant analyses yielded a lower intercept age of 32 ± 6 Ma. These Eocene-Oligocene zircons exhibited high Th/U ratios, even exceeding those of the Triassic-Jurassic zircons.

Both core and rim analyses were performed on 12 zircon grains for this sample. Most grains yielded similar ages in both the core and rim, with the exception of two grains. One grain has an age of 1,089 Ma for its core and 43 Ma (Th/U=0.78) for its rim, while the other had ages of 221 and 152 Ma on its core and rim, respectively.

5.8 TM0625 cataclasite

TM0625 cataclasite has a high proportion of fine-grained material, which should result from grain size reduction, possibly due to its proximity to the MPSZ boundary fault (Figure 5H). Quartz displays dynamic recrystallization of GBAR to GBM. The elongated shape of feldspar porphyroclasts, along with undulose extinction and deformation twinning, indicate their plastic deformation. The presence of myrmekitization and sericitic alteration suggest that feldspar experienced deformation at temperatures up to 600°C (Passchier and Trouw, 2005). Biotite exists as fish and fine grains in the matrix, some pristine biotite can be found in the feldspars.

Zircon grains in this sample present as euhedral crystals with a length of ~100–200 μm. They display clear oscillatory zoning patterns on SEM-CL images (Figure 6). A total of 48 analyses were conducted, yielding ages ranging from 2,481 to 34.7 Ma. The majority of the analyses clustered around 45-35 Ma (n=35, Figure 7H). These Eocene zircons resulted in a concordia age of 41.0 ± 0.2 Ma (n=20) with an average Th/U ratio of 0.27.

6 Discussion

This study shows that the Lan Sang gneisses can be clearly divided into two main categories, paragneiss and orthogneiss, based on the geochronological evidence. This discovery reinforces the updated geological cross-section in Figure 4 of Österle et al. (2019). Therefore, we will discuss the formation and thermal history of paragneiss and orthogneiss separately.

6.1 Formation history of paragneisses

6.1.1 Paleozoic sedimentary protolith

Paragneiss samples TM0616, TM0617, and TM0619 were collected from the SW segment of the cross-section. Their zircon grains exhibit a distinct core-rim structure. Most cores have strong oscillatory zoning patterns (Figure 6) with Th/U ratios >0.1 (Figure 9), which may reflect their igneous origin (Belousova et al., 2002; Hoskin and Schaltegger, 2003). However, the rounded outlines (Figure 6) and wide U-Pb age span (3,078-450 Ma, Figures 8A,C) indicate that these cores may have experienced sedimentary processes prior to rim overgrowth. Therefore, these cores are likely to be detrital zircons. The youngest age of these detrital cores can be considered as the maximum depositional age for each corresponding sample (Dickinson and Gehrels, 2009), i.e., 462 Ma for TM0616, 450 Ma for TM0617, and 467 Ma for TM0619. This implies that the protoliths of these paragneisses could be Paleozoic sedimentary rocks.

Moreover, the age cluster of ~508 Ma suggests that the sediments of these paragneiss protoliths primarily came from the Sibumasu terrane rather than the Indochina terrane (Lin et al., 2013; Kawakami et al., 2014; Dew et al., 2018). The age spectrum of detrital zircon cores in this study is also similar to that of Paleozoic sedimentary rocks from the Sibumasu terrane (Dew et al., 2021; Hara et al., 2021). Considering that the MPSZ is flanked by Cambrian quartzite and Permian limestone (Figure 3), it seems reasonable to infer that the protoliths of these paragneisses should be Paleozoic sedimentary rocks around the Sibumasu terrane.

6.1.2 Paragneiss formation in the Triassic-Jurassic metamorphism

On the other hand, zircon rims exhibit dull and cloudy zonation without an oscillatory zoning pattern on the SEM-CL images, very low Th/U ratios (average of 0.02, Figure 9), and a lower intercept age (194 ± 8 Ma of TM0617). These suggest that these zircon rims should be metamorphic overgrowth (Hoskin and Black, 2000; Rubatto, 2002; Blackburn et al., 2011; Rubatto, 2017; Yakymchuk et al., 2018). These zircon rims reveal ages of around 249, 227-183, and 179 Ma (Figure 8C), with the exception of one analysis that yields 449 Ma (Th/U=0.1) in TM0616. This exception may be due to another generation of zircon overgrowth or the mixed core and rim signal. Analyses of 249 and 179 Ma lack repeatable data, and their age discordances (18% and 125%, respectively) are also much greater than others (mostly <4%). These two analyses probably result from the mixed signals of distinct zircon generations and severe Pb loss, respectively. Thus, they should not be considered a representation of the zircon overgrowth.

Similar zircon U-Pb ages of metamorphic zircon rims from two Lan Sang gneiss samples have been reported as 191 ± 10 and 206 ± 4 Ma (Kanjanapayont et al., 2011). These dates are consistent with our ages of 227-183 Ma for the metamorphic zircon rims. The lower intercept ages of approximately 200 Ma revealed by Ahrendt et al. (1993) and by TM0617 paragneiss in this study further substantiate the presence of this metamorphic event.

To summarize, the observed overgrowth rim on the zircons is indicative of metamorphism that occurred between 227 and 183 Ma, consistent with the Indosinian orogeny. This metamorphism is believed to have played a role in the transformation of sedimentary protoliths into paragneiss.

6.2 Thermal history revealed by orthogneiss samples

Orthogneiss samples include TM0623 cataclasite, TM0620 sheared augen gneiss, TM0622 mylonite, TM0624B sheared augen gneiss,

and TM0625 cataclasite. Most of their zircons exhibit euhedral to subhedral shapes with oscillatory zoning and high Th/U ratio (most >0.2, Figure 9), suggesting their igneous origins (Belousova et al., 2002; Hoskin and Schaltegger, 2003). These zircons yield primarily either Triassic-Jurassic or Eocene-Oligocene ages, with a few older ages (Figure 8C). The presence of older ages could be attributed to inherited zircons or mixed ages partially involving inherited zircons. Only the TM0624B sheared augen gneiss sample presents zircons from both age groups.

6.2.1 Triassic-Jurassic magmatism

The age distribution of the TM0624B sheared augen gneiss is similar to that of the TH0101 II augen gneiss sample in Österle et al. (2019), with more Triassic-Jurassic zircons than Eocene-Oligocene zircons. However, the high Th/U ratios and the similarities between the core and rim ages suggest that the Eocene-Oligocene zircons may not have originated from metamorphism. In contrast, these zircons yield a lower intercept age of 32 ± 6 Ma on the concordia plot (Figure 7G), which is often regarded as a metamorphic age, complicating the interpretation. Indeed, there are instances where metamorphic zircons can exhibit Th/U values greater than 0.1. This can occur in recrystallized zircons, zircons grown during high-T metamorphism, or zircons derived from syn-metamorphic, high-T anatectic melts (Schaltegger et al., 1999; Harley et al., 2007; Yakymchuk et al., 2018). Considering the scattered distribution of Eocene-Oligocene dates and a lower intercept on the concordia plot (Figure 7G), the protolith was likely emplaced during the Triassic-Jurassic period (230–199 Ma) and experienced high-T metamorphism, in addition to ductile deformation, by 32 Ma.

Among all samples, the TM0620 sheared augen gneiss is characterized by the largest zircon grain size, and its zircons predominantly exhibit Triassic-Jurassic ages. The protolith of TM0620 should be emplaced between 220 and 188 Ma. The precise timing of its gneiss formation remains unclear due to the absence of metamorphic zircons or a lower intercept age.

Rb-Sr whole rock isochron ages of 219-213 Ma have been reported for Tak granite, east of the MPSZ (Teggin, 1975). Zircon U-Pb dating on augen gneiss of the Lan Sang gneisses revealed that the protolith may have intruded at around 208 Ma (Österle et al., 2019). These ages fit well with magmatic ages of 221-210 Ma for the Chiang Mai-Lincang granitoid and gneiss belt (Dunning et al., 1995; Macdonald et al., 2010; Gardiner et al., 2016). Therefore, it is undoubtedly confirmed that some Lan Sang gneisses had protolith emplacement during the Triassic-Jurassic.

6.2.2 Eocene-Oligocene magmatism

On the other hand, zircons within the TM0623 cataclasite, TM0622 mylonite, and TM0625 cataclasite exhibit predominantly concordant Eocene-Oligocene ages (45-32 Ma) with high Th/U values (Figures 7D,F,H). These zircons also show euhedral to subhedral shapes and clear oscillatory zoning patterns in the SEM-CL images (Figure 6). Thus, these features indicate that these zircons should be of igneous origin (Belousova et al., 2002; Hoskin and Schaltegger, 2003).

Palin et al. (2013) proposed that the event that occurred between 45 and 37 Ma in the MPSZ was a metamorphism, supported by the presence of metamorphic features observed in the dated monazite. Österle et al. (2019) proposed that this metamorphism, initiated at ~45 Ma, culminated in the partial melting of the basement and granodioritic intrusion at ~35 Ma. However, we introduce a new perspective based on our new zircon U-Pb results. The thermal event that occurred at 45 Ma and continued until 32 Ma, was not merely a metamorphic event. Rather, it is indicative of a magmatic event, supported by the spatial distribution of samples containing igneous zircons from 45-32 Ma within the MPSZ (Figure 3).

6.2.3 Eocene-Oligocene metamorphism

Further evidence from the lower intercepts on the concordia of TM0623 and TM0624B (Figures 7D,G) suggests that the associated metamorphism likely terminated at around 32–30 Ma. This extended period of metamorphism may have resulted from cooling due to the cessation of magmatic activity. This corroborates the cooling phase as evidenced by biotite K/Ar ages of 31.9–29.9 Ma, biotite $^{40}Ar/^{39}Ar$ ages of 33-30.6 Ma, K-feldspar $^{40}Ar/^{39}Ar$ ages of 35.4–30.5 Ma, zircon fission track ages of 35.9-28 Ma (Ahrendt et al., 1993; Lacassin et al., 1997; Morley et al., 2007; Lin et al., 2021).

Furthermore, in TM0623, TM0622, and TM0625, K-felspar porphyroclasts have been replaced by muscovite, biotite, or albite, indicating the occurrence of a Na-K exchange reaction. This reaction is known to occur at temperatures of 490°C–750 °C and pressures of 2–13 kbar in peraluminous granitoids (Green and Usdansky, 1986). This observation supports the presence of metamorphism following the Eocene-Oligocene magmatism.

6.3 Possibilities of other magmatic events

Zircon age spectra of paragneisses (TM0616, TM0617, and TM0619) reveal minor age clusters at ~920 Ma and ~508-468 Ma (Figure 8C). These ages are derived from detrital zircon cores, indicating they may provide insight into sedimentary provenance. Prior to the earliest zircon U-Pb dating studies (i.e., Ahrendt et al., 1993; MacDonald et al., 1993; Dunning et al., 1995), it was believed that Thailand had Precambrian basement rocks due to its overlying Cambrian sedimentary rocks (Hansen and Wemmer, 2011). However, subsequent zircon U-Pb dating studies have revealed that most of the crystalline basement rocks in Thailand are of Indosinian age (Dunning et al., 1995; Kawakami et al., 2014; Gardiner et al., 2016; Dew et al., 2018). Only a few outcrops in peninsular Thailand have yielded the oldest magmatic ages of ca. 500 Ma, revealing that the Sibumasu terrane was in a magmatic arc-related regime on the Gondwana India-Australia margin (Lin et al., 2013; Kawakami et al., 2014; Dew et al., 2018). The exact location of the Precambrian basement rock remains unknown, with only clues from inherited and detrital zircon ages (Ahrendt et al., 1993; Watkinson et al., 2011; Cai et al., 2017; Dew et al., 2018; Österle et al., 2019; Dew et al., 2021; Hara et al., 2021). The majority of detrital zircon age spectra obtained from sedimentary and meta-sedimentary rocks in the Sibumasu terrane also exhibit a prominent peak either at 500 Ma or within 1,000-900 Ma (Cai et al., 2017; Dew et al., 2021; Hara et al., 2021). This finding strongly indicates the presence of Neoproterozoic basement rocks in the Sibumasu terrane.

Although the monazite U-Th-Pb geochronology study suggested that the magmatic protolith of the Lan Sang orthogneiss may have been emplaced between 123 and 114 Ma

(Palin et al., 2013), neither the previous zircon U-Pb dating studies (Ahrendt et al., 1993; Kanjanapayont et al., 2011; Österle et al., 2019) nor this study revealed a notable zircon U-Pb age cluster from this period. The two analyses of 123-114 Ma from monazite cores by Palin et al. (2013) probably resulted from a minor metamorphic event or localized intrusion.

This study did not find a date of 22 Ma, an age previously identified from an undeformed subvolcanic dike by Österle et al. (2019). This is likely due to the fact that our samples primarily comprised deformed rocks rather than undeformed ones.

6.4 Relationship between Eocene-Oligocene magmatism and shear activity

The ages obtained from TM0623 cataclasite (41-32.6 Ma), TM0622 mylonite (42.9–31.6 Ma), and TM0625 cataclasite (45-35 Ma), which are mainly from igneous zircons, closely coincide with the proposed shearing duration of 42-30 Ma for the MPSZ (Lin et al., 2021). This suggests that these samples can be syn-shearing intrusions, supporting the findings in Österle et al. (2019).

Magmatism between 45 and 32 Ma appears to slightly precede the left-lateral shearing along the MPSZ between 42 and 30 Ma (Lin et al., 2021). This discrepancy could be attributed to the differences in closure temperatures tied to the respective geochronological methods and to the uncertainty in determining the onset of shearing. Based on calculations and field-based estimates, the closure temperatures for Pb diffusion in zircon of typical size exceed 900 °C (Mezger and Krogstad, 1997; Cherniak and Watson, 2001). Thus, the U-Pb age of igneous zircon usually represents the crystallization age and provides the exact timing of a magmatic event. The closure temperature for Ar diffusion in muscovite ranges from 425°C to 350 °C (Hodges, 1991; Harrison et al., 2009), varying based on grain size, cooling rate, and pressure. When muscovite crystallizes or recrystallizes at a temperature below its closure temperature due to deformation (West and Lux, 1993; Reddy and Potts, 1999), or when it deforms during cooling from a high temperature to beneath its closure temperature (Lin et al., 2021), it can record a deformation age. Consequently, determining the timing of deformation is always challenging, and identifying the precise onset of deformation proves to be even more difficult.

Microstructures in thin sections indicate that the left-lateral shear occurred at high temperatures, likely in excess of 600°C, and persisted into the low-temperature brittle regime characterized by fracturing and cataclasis. This observation is consistent with the estimated deformation temperature range of >600°C to 250°C, derived from the deformation microstructures of various minerals and the recrystallized grain size of quartz in the sheared leucogranite (Lin et al., 2021). Therefore, the onset of the MPSZ is likely to have occurred earlier than 42 Ma, as indicated by the $^{40}Ar/^{39}Ar$ muscovite age with a calculated closure temperature of ~435°C (Lin et al., 2021).

The emplacement of the intrusion has been observed in close spatial and temporal association with shear or fault activity (Pitcher and Bussell, 1977; Neves et al., 1996; Brown and Solar, 1998; Rosenberg, 2004). The development of S-C fabrics within granitoids, which were emplaced in the shear zone, indicates that incompletely solidified plutons can induce strain localization and favor shear zone nucleation due to rheological heterogeneities (Tommasi et al., 1994; Neves et al., 1996; Brown and Solar, 1998). Therefore, the syn-shearing intrusion of TM0623 cataclasite, TM0622 mylonite, and TM0625 cataclasite may have experienced greater strain compared to the country rock. As a result, these samples contain a higher proportion of fine-grained material compared to the other two sheared augen gneiss samples, which were emplaced during the Triassic-Jurassic.

Alternatively, shear heating has been proposed to cause partial melting and metamorphism (Fleitout and Froidevaux, 1980; Leloup and Kienast, 1993). Recent studies show that shear heating can increase temperature by 50°C–200°C (Duretz et al., 2014; Mako and Caddick, 2018). Although the temperature increase caused by shear heating alone may not be sufficient to induce partial melting and metamorphism, it may still contribute to these processes (Strong and Hanmer, 1981). Therefore, the contemporaneous intrusion and shear activity of the MPSZ may not be merely a coincidence.

Our deformed samples show a lack of ages around 22 Ma (Figure 8B), an age previously identified from an undeformed subvolcanic dike by Österle et al. (2019). This suggests that the left-lateral shearing of the MPSZ likely ceased before 22 Ma. Considering the shearing duration of 42-30 Ma as constrained by thermochronology (Lin et al., 2021), it is probable that the cessation of left-lateral shearing within the MPSZ occurred between 30 and 22 Ma.

6.5 Distribution of the Eocene-Oligocene magmatism along the Sibumasu terrane

Apart from the MPSZ, Eocene-Oligocene magmatic events have also been discovered in other areas of the Sibumasu terrane (Figure 10). In the northernmost part of the Sibumasu terrane, the emplacement of the Cangyuan granitoid took place at 45-40 Ma (Deng et al., 2014, and references therein). In northern Thailand, the granitic mylonite of the Doi Suthep core complex has yielded zircon and monazite U-Pb ages of 40 Ma (Macdonald et al., 2010), while a calc-silicate gneiss near the Doi Inthanon metamorphic core complex has shown a zircon age of 27 Ma (Dunning et al., 1995). Moreover, samples of biotite augen gneiss between the Doi Suthep and the Doi Inthanon complexes have revealed zircon and monazite U-Pb ages of 32-26 and 34-24 Ma, respectively. These ages indicate metamorphism and anatexis associated with crustal thickening, which has been used to infer a model for the onset of extension and subsequent development of the Chiang Mai Basin (Gardiner et al., 2016).

Zircon U-Pb dating of orthogneiss and mylonite samples from the TPSZ yields ages of 59-48 Ma (Nantasin et al., 2012). Zircons from a foliated biotite-hornblende granite of the RSZ have been dated, revealing ages of 50–44 Ma (Watkinson et al., 2011). Orthogneisses, mylonitic granite, and pegmatites of the KMSZ have zircon U-Pb ages of 55-46 Ma, which may be linked to an early dextral ductile deformation phase (Kanjanapayont et al., 2012). In southeastern Thailand, magmatic zircon U-Pb ages of 55-43.3 Ma have been obtained from monzogranite and granite samples (Veeravinantanakul et al., 2021; Uchida et al., 2022). Veeravinantanakul et al. (2021) interpreted 43 Ma as the timing of intrusion during the sinistral movement of the KSZ.

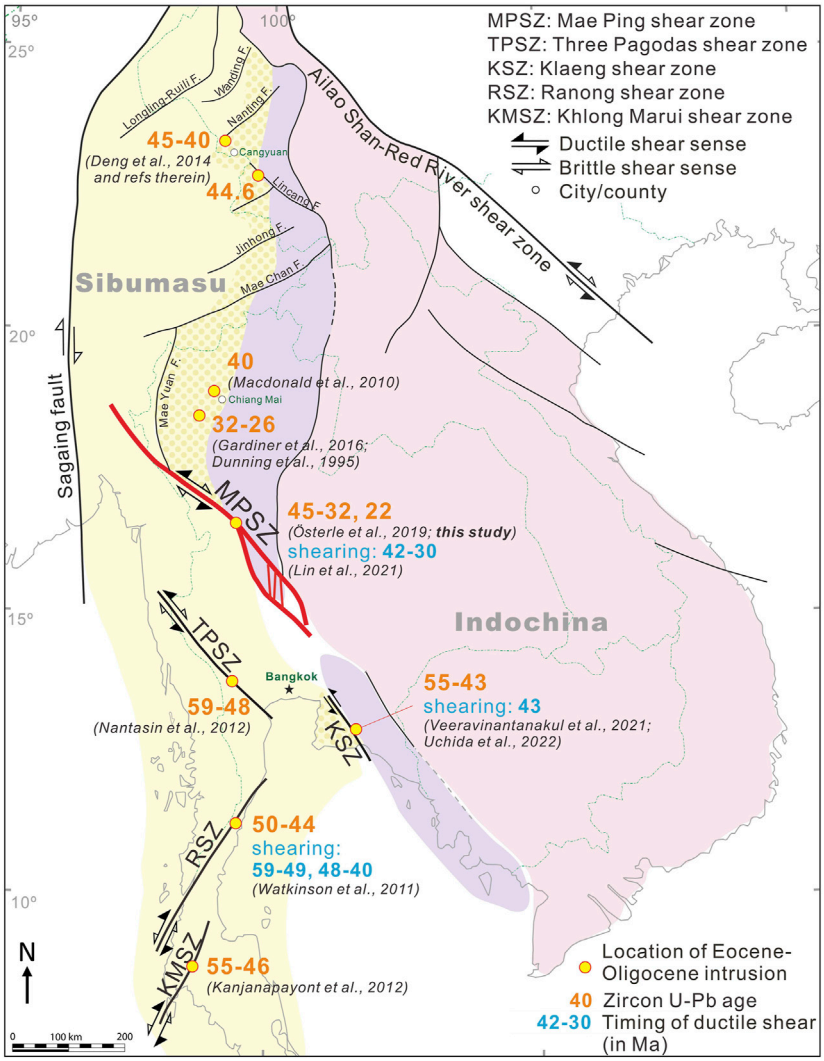

FIGURE 10
Distribution of Eocene-Oligocene intrusions along the Sibumasu terrane. The Eocene-Oligocene intrusions were mainly found within the shear zones or fault zones. Zircon U-Pb ages and the inferred shear durations are from this study and the literature (Dunning et al., 1995; Macdonald et al., 2010; Watkinson et al., 2011; Kanjanapayont et al., 2012; Nantasin et al., 2012; Deng et al., 2014; Gardiner et al., 2016; Österle et al., 2019; Lin et al., 2021; Veeravinantanakul et al., 2021; Uchida et al., 2022).

The prevalence of Eocene-Oligocene magmatism along the Sibumasu terrane may have significantly impacted the regional cooling history. Morley et al. (2007) observed a predominantly N-S trend in the regional cooling patterns of northwestern Thailand as shown by biotite, ZFT, and AFT ages. They proposed that the exposure of the Lan Sang gneisses is more intimately linked with regional exhumation patterns than being solely attributable to strike-slip-induced uplift and erosion (Morley et al., 2007). Palin et al. (2013) also suggested that the strike-slip motion of the MPSZ was not directly responsible for either the metamorphism or regional cooling. The distribution of Eocene-Oligocene magmatism in the Sibumasu terranes (Figure 10) is consistent with the observed N-S trend in the regional cooling pattern (Figure 5 in Morley et al., 2007) and the timing of metamorphism. These findings indicate that Eocene-Oligocene magmatism likely contributed to the contemporaneous metamorphic processes and regional cooling patterns.

The Eocene-Oligocene magmatism in the Sibumasu terrane corresponds well with the period of reduced magmatism (45-30 Ma) in the Neo-Tethyan arc system, which includes Gangdese, West Burma, and Sumatra (Zhang et al., 2019). The reduced magmatism in the Neo-Tethyan arc system and the magmatism in the Sibumasu during the Eocene-Oligocene may not be merely a coincidence. They could be correlated with the tectonic scenario involving the shallowing slab of the Neo Tethys, which would induce magmatism migration from West Burma to the Sibumasu terrane (Zhang et al., 2019).

In addition to the quiescence of arc magmatism and inward migration of magmatism on the overriding plate, shallowing slab or flat subduction may also have resulted in strong compression, leading to crustal thickening, metamorphism, and strike-slip motion on the overriding plate (Kay and Coira, 2009; Lee and King, 2011; Zhang et al., 2019). The inferred shear timing of the MPSZ, RSZ, and KSZ is similar to their corresponding magmatic ages (Figure 10). This can be attributed to the fact that magmatism can soften the lithosphere,

promote strain localization, and favor shear zone nucleation (Neves et al., 1996; Brown and Solar, 1998). One experimental study proposed that the crustal-scale localization of deformation effectively coincides with the onset of melting (Rosenberg and Handy, 2005). It is important to note that magmatism, metamorphism, and deformation may be interconnected or promote each other in the context of convergent tectonic settings, allowing them to occur simultaneously (Hutton and Reavy, 1992; Rosenberg, 2004; Rosenberg and Handy, 2005).

7 Conclusion

This study presents new zircon U-Pb age data, revealing that the magmatic history of the MPSZ was dominated by Triassic-Jurassic and Eocene-Oligocene thermal events. Paragneiss samples with Paleozoic sedimentary protoliths, mainly sourced from the Sibumasu terrane, underwent high-grade metamorphism during the Triassic-Jurassic Indosinian orogeny. The protoliths of the orthogneiss samples were emplaced either during the Triassic-Jurassic or the Eocene-Oligocene. The Eocene-Oligocene thermal event commenced at least at 45 Ma and ceased at 32 Ma. This event, previously recognized as a metamorphism, is now evidenced to be magmatism. Given that all samples were left-laterally sheared, the left-lateral motion of the MPSZ may have ended after the youngest zircon age, i.e., 32 Ma, corroborating previous findings.

Moreover, the Eocene-Oligocene magmatism in the MPSZ was probably not confined to a localized occurrence. Concurrent magmatic activities occurred in various regions within the Sibumasu terrane, i.e., Cangyuan, the Doi Inthanon and Doi Suthep areas, the TPSZ, KSZ, RSZ, and KMSZ. The close temporal and spatial correlation between magmatism and shear zones indicates that the occurrence of magmatism may be associated with shear activity. The Cenozoic regional cooling patterns of northern Thailand now appear to have been influenced by this magmatism. Furthermore, the distribution of Eocene-Oligocene magmatism along the Sibumasu terrane supports the possibility of an inward migration of magmatism within the overriding plate, moving from West Burma towards the Sibumasu terrane, probably due to the slab shallowing of the Neo-Tethyan. This slab shallowing may have induced strain within the Sibumasu. The occurrence of Eocene-Oligocene magmatism may have further weakened the lithosphere, thereby promoting strain concentration along the shear zones. Although metamorphism and regional cooling may not exhibit a direct relationship with shear deformation, these processes may be tectonically interconnected through the presence of magmatism.

Data availability statement

The original contributions presented in the study are included in the article/Supplementary Material, further inquiries can be directed to the corresponding authors.

Author contributions

Y-LL was responsible for data reduction and manuscript writing with support from T-YL. T-YL and PC conducted the field trip and sample collection. Y-LL, H-YL, and YI conducted the experiments. All authors contributed to the article and approved the submitted version.

Funding

This research was supported by grants to Y-LL (MOST 110-2811-M-003-536) and T-YL (MOST 108-2116-M-003-007-MY3) from the Ministry of Science and Technology (now NCST), Taiwan.

Acknowledgments

The authors are grateful to Prof. Meng-Wan Yeh for field work, sample collection, and laboratory equipment. Special thanks to Han-Yi Chiu, Chien-Hui Hung, Jia-Hui Chen, and Yi-Ju Hsin for guidance in zircon target fabrication, LA-ICP-MS operation, and data reduction. The careful review and constructive comments provided by Prof. K. R. Hari and Dr. Thuy Thanh Pham are gratefully acknowledged. The authors thank J. Gregory Shellnutt for editorial assistance.

Conflict of interest

The authors declare that the research was conducted in the absence of any commercial or financial relationship that could be construed as a potential conflict of interest.

The handling editor JGS declared a past co-authorship with the authors TYL, HYL & YL.

Publisher's note

Supplementary material

The Supplementary Material for this article can be found online at: https://www.frontiersin.org/articles/10.3389/feart.2023.1213958/full#supplementary-material

References

Ahrendt, H., Chonglakmani, C., Hansen, B. T., and Helmcke, D. (1993). Geochronological cross section through northern Thailand. *J. Southeast Asian Earth Sci.* 8, 207–217. doi:10.1016/0743-9547(93)90022-h

Andersen, T., Kristoffersen, M., and Elburg, M. A. (2018). Visualizing, interpreting and comparing detrital zircon age and Hf isotope data in basin analysis – A graphical approach. *Basin Res.* 30 (1), 132–147. doi:10.1111/bre.12245

Arboit, F., Collins, A. S., Morley, C. K., King, R., and Amrouch, K. (2016). Detrital zircon analysis of the southwest Indochina terrane, central Thailand: unravelling the indosinian orogeny. *GSA Bull.* 128 (5-6), 1024–1043. doi:10.1130/B31411.1

Belousova, E., Griffin, W., O'Reilly, S. Y., and Fisher, N. (2002). Igneous zircon: trace element composition as an indicator of source rock type. *Contrib. Mineral. Petrol.* 143 (5), 602–622. doi:10.1007/s00410-002-0364-7

Blackburn, T., Bowring, S. A., Schoene, B., Mahan, K., and Dudas, F. (2011). U-Pb thermochronology: creating a temporal record of lithosphere thermal evolution. *Contrib. Mineral. Petrol.* 162 (3), 479–500. doi:10.1007/s00410-011-0607-6

Brown, M., and Solar, G. S. (1998). Shear-zone systems and melts: feedback relations and self-organization in orogenic belts. *J. Struct. Geol.* 20 (2-3), 211–227. doi:10.1016/S0191-8141(97)00068-0

Cai, F., Ding, L., Yao, W., Laskowski, A. K., Xu, Q., Zhang, J. e., et al. (2017). Provenance and tectonic evolution of lower paleozoic–upper mesozoic strata from Sibumasu terrane, Myanmar. *Gondwana Res.* 41, 325–336. doi:10.1016/j.gr.2015.03.005

Cherniak, D. J., and Watson, E. B. (2001). Pb diffusion in zircon. *Chem. Geol.* 172 (1), 5–24. doi:10.1016/S0009-2541(00)00233-3

Chiu, H. Y., Chung, S. L., Wu, F. Y., Liu, D., Liang, Y. H., Lin, I. J., et al. (2009). Zircon U-Pb and Hf isotopic constraints from eastern Transhimalayan batholiths on the precollisional magmatic and tectonic evolution in southern Tibet. *Tectonophysics* 477 (1–2), 3–19. doi:10.1016/j.tecto.2009.02.034

Chung, S. L., Searle, M. P., and Yeh, M. W. (2008). The age of the potassic alkaline igneous rocks along the Ailao Shan–Red River shear zone: implications for the onset age of left-lateral shearing: A discussion. *J. Geol.* 116 (2), 201–204. doi:10.1086/527458

Deng, J., Wang, Q., Li, G., and Santosh, M. (2014). Cenozoic tectono-magmatic and metallogenic processes in the Sanjiang region, southwestern China. *Earth-Science Rev.* 138, 268–299. doi:10.1016/j.earscirev.2014.05.015

Dew, R. E. C., Collins, A. S., Glorie, S., Morley, C. K., Blades, M. L., Nachtergaele, S., et al. (2018). Probing into Thailand's basement: new insights from U–Pb geochronology, Sr, Sm–Nd, Pb and Lu–Hf isotopic systems from granitoids. *Lithos* 320-321, 332–354. doi:10.1016/j.lithos.2018.09.019

Dew, R. E. C., Collins, A. S., Morley, C. K., King, R. C., Evans, N. J., and Glorie, S. (2021). Coupled detrital zircon U–Pb and Hf analysis of the Sibumasu terrane: from Gondwana to northwest Thailand. *J. Asian Earth Sci.* 211, 104709. doi:10.1016/j.jseaes.2021.104709

Dickinson, W. R., and Gehrels, G. E. (2009). Use of U–Pb ages of detrital zircons to infer maximum depositional ages of strata: A test against a Colorado plateau mesozoic database. *Earth Planet. Sci. Lett.* 288 (1), 115–125. doi:10.1016/j.epsl.2009.09.013

DMR (1999). *Geological map of Thailand 1:2,500,000*. Bangkok, Thailand: Geological Survey Division, Department of Mineral Resources.

Dunning, G. R., Macdonald, A. S., and Barr, S. M. (1995). Zircon and monazite U-Pb dating of the Doi inthanon core complex, northern Thailand: implications for extension within the indosinian orogen. *Tectonophysics* 251 (1-4), 197–213. doi:10.1016/0040-1951(95)00037-2

Duretz, T., Schmalholz, S., Podladchikov, Y., and Yuen, D. (2014). Physics-controlled thickness of shear zones caused by viscous heating: implications for crustal shear localization. *Geophys. Res. Lett.* 41, 4904–4911. doi:10.1002/2014GL060438

Fleitout, L., and Froidevaux, C. (1980). Thermal and mechanical evolution of shear zones. *J. Struct. Geol.* 2 (1), 159–164. doi:10.1016/0191-8141(80)90046-2

Gardiner, N. J., Roberts, N. M. W., Morley, C. K., Searle, M. P., and Whitehouse, M. J. (2016). Did Oligocene crustal thickening precede basin development in northern Thailand? A geochronological reassessment of Doi inthanon and Doi Suthep. *Lithos* 240-243, 69–83. doi:10.1016/j.lithos.2015.10.015

Green, N. L., and Usdansky, S. I. (1986). Toward a practical plagioclase-muscovite thermometer. *Am. Mineral.* 71 (9-10), 1109–1117.

Hansen, B. T., and Wemmer, K. (2011). "Age and evolution of the basement rocks in Thailand," in *The Geology of Thailand*. Editors M. F. Ridd, A. J. Barber, and M. J. Crow (London: Geological Society), 19–32.

Hara, H., Tokiwa, T., Kurihara, T., Charoentitirat, T., and Sardsud, A. (2021). Revisiting the tectonic evolution of the Triassic Palaeo-Tethys convergence zone in northern Thailand inferred from detrital zircon U–Pb ages. *Geol. Mag.* 158 (5), 905–929. doi:10.1017/S0016756820001028

Harley, S. L., Kelly, N. M., and Moller, A. (2007). Zircon behaviour and the thermal histories of mountain chains. *Elements* 3 (1), 25–30. doi:10.2113/gselements.3.1.25

Harrison, T. M., Célérier, J., Aikman, A. B., Hermann, J., and Heizler, M. T. (2009). Diffusion of ^{40}Ar in muscovite. *Geochimica Cosmochimica Acta* 73 (4), 1039–1051. doi:10.1016/j.gca.2008.09.038

Hodges, K. V. (1991). Pressure-temperature-time paths. *Annu. Rev. Earth Planet. Sci.* 19 (1), 207–236. doi:10.1146/annurev.ea.19.050191.001231

Hoskin, P. W. O., and Black, L. P. (2000). Metamorphic zircon formation by solid-state recrystallization of protolith igneous zircon. *J. Metamorph. Geol.* 18 (4), 423–439. doi:10.1046/j.1525-1314.2000.00266.x

Hoskin, P. W. O., and Schaltegger, U. (2003). The composition of zircon and igneous and metamorphic petrogenesis. *Rev. Mineral. Geochem.* 53 (1), 27–62. doi:10.2113/0530027

Hutton, D. H. W., and Reavy, R. J. (1992). Strike-slip tectonics and granite petrogenesis. *Tectonics* 11 (5), 960–967. doi:10.1029/92TC00336

Jarvis, A., Reuter, H. I., Nelson, A., and Guevara, E. (2008). *Hole-filled SRTM for the globe version 4.* available from the CGIAR-CSI SRTM 90m Database (http://srtm.csi.cgiar.org).

Kanjanapayont, P., Klötzli, U., Charusiri, P., and Klötzli, E. (2011). "LA-MC-ICP-MS UPb zircon geochronology of the lan Sang and nong yai gneisses, Thailand," in International Conference on Geology, Geotechnology and Mineral Resources of Indochina (GEOINDO 2011).

Kanjanapayont, P., Klötzli, U., Thöni, M., Grasemann, B., and Edwards, M. A. (2012). Rb–Sr, Sm–Nd, and U–Pb geochronology of the rocks within the Khlong Marui shear zone, southern Thailand. *J. Asian Earth Sci.* 56 (0), 263–275. doi:10.1016/j.jseaes.2012.05.029

Kanjanapayont, P., Kieduppatum, P., Klötzli, U., Klötzli, E., and Charusiri, P. (2013). Deformation history and U–Pb zircon geochronology of the high grade metamorphic rocks within the Klaeng fault zone, eastern Thailand. *J. Asian Earth Sci.* 77, 224–233. doi:10.1016/j.jseaes.2013.08.027

Kawaguchi, K., Minh, P., Hieu, P. T., Cuong, T. C., and Das, K. (2021). Evolution of supracrustal rocks of the Indochina block: evidence from new detrital zircon U–Pb ages of the kontum massif, central vietnam. *J. Mineral. Petrol. Sci.* 116 (2), 69–82. doi:10.2465/jmps.200916

Kawakami, T., Nakano, N., Higashino, F., Hokada, T., Osanai, Y., Yuhara, M., et al. (2014). U-Pb zircon and CHIME monazite dating of granitoids and high-grade metamorphic rocks from the Eastern and Peninsular Thailand- A new report of Early Paleozoic granite. *Lithos* 200-201, 64–79. doi:10.1016/j.lithos.2014.04.012

Kay, S. M., and Coira, B. L. (2009). "Shallowing and steepening subduction zones, continental lithospheric loss, magmatism, and crustal flow under the Central Andean Altiplano-Puna Plateau," in *Backbone of the americas: Shallow subduction, plateau uplift, and ridge and terrane collision*. Editors S. M. Kay, V. A. Ramos, and W. R. Dickinson (Geological Society of America).

Khin, Z., Meffre, S., Lai, C.-K., Burrett, C., Santosh, M., Graham, I., et al. (2014). Tectonics and metallogeny of mainland Southeast Asia — a review and contribution. *Gondwana Res.* 26 (1), 5–30. doi:10.1016/j.gr.2013.10.010

Lacassin, R., Maluski, H., Leloup, P. H., Tapponnier, P., Hinthong, C., Siribhakdi, K., et al. (1997). Tertiary diachronic extrusion and deformation of western Indochina: structural and ^{40}Ar/^{39}Ar evidence from NW Thailand. *J. Geophys. Research-Solid Earth* 102 (B5), 10013–10037. doi:10.1029/96jb03831

Lee, C., and King, S. D. (2011). Dynamic buckling of subducting slabs reconciles geological and geophysical observations. *Earth Planet. Sci. Lett.* 312 (3), 360–370. doi:10.1016/j.epsl.2011.10.033

Leloup, P. H., and Kienast, J.-R. (1993). High-temperature metamorphism in a major strike-slip shear zone: the Ailao Shan—red River, people's Republic of China. *Earth Planet. Sci. Lett.* 118 (1), 213–234. doi:10.1016/0012-821X(93)90169-A

Leloup, P. H., Lacassin, R., Tapponnier, P., Schärer, U., Dalai, Z., Xiaohan, L., et al. (1995). The Ailao Shan-Red River shear zone (yunnan, China), tertiary transform boundary of Indochina. *Tectonophysics* 251 (1-4), 3–84. doi:10.1016/0040-1951(95)00070-4

Li, J., Cao, S., Neubauer, F., Cheng, X., Wang, H., and Genser, J. (2021). Structure and spatial-temporal relationships of Eocene-Oligocene potassic magmatism linked to the Ailao Shan-Red River shear zone and post-collisional extension. *Lithos* 396-397, 106203. doi:10.1016/j.lithos.2021.106203

Liang, H. Y., Campbell, I. H., Allen, C. M., Sun, W. D., Yu, H. X., Xie, Y. W., et al. (2007). The age of the potassic alkaline igneous rocks along the Ailao Shan–Red River shear zone: implications for the onset age of left-lateral shearing. *J. Geol.* 115 (2), 231–242. doi:10.1086/510801

Lin, Y. L., Yeh, M. W., Lee, T. Y., Chung, S. L., Iizuka, Y., and Charusiri, P. (2013). First evidence of the Cambrian basement in Upper Peninsula of Thailand and its implication for crustal and tectonic evolution of the Sibumasu terrane. *Gondwana Res.* 24 (3), 1031–1037. doi:10.1016/j.gr.2013.05.014

Lin, Y.-L., Lee, T.-Y., Lo, C.-H., Sherlock, S. C., Iizuka, Y., Usuki, T., et al. (2021). Dating deformation using sheared leucogranite: temporal constraints by 40Ar/39Ar thermochronology for the Mae ping shear zone, NW Thailand. *Contrib. Mineral. Petrol.* 176 (9), 65. doi:10.1007/s00410-021-01822-4

Liu, J., Chen, X., Wu, W., Tang, Y., Tran, M.-D., Nguyen, Q.-L., et al. (2015). New tectono-geochronological constraints on timing of shearing along the Ailao Shan-Red River shear zone: implications for genesis of Ailao Shan gold mineralization. *J. Asian Earth Sci.* 103, 70–86. doi:10.1016/j.jseaes.2014.11.006

Ludwig, K. R. (2008). *User's manual for Isoplot 3.70: A geochronological toolkit for microsoft Excel.*

MacDonald, A. S., Barr, S. M., Dunning, G. R., and Yaowanoiyothin, W. (1993). The Doi inthanon metamorphic core complex in NW Thailand: age and tectonic significance. *J. Southeast Asian Earth Sci.* 8 (1), 117–125. doi:10.1016/0743-9547(93)90013-F

Macdonald, A. S., Barr, S. M., Miller, B. V., Reynolds, P. H., Rhodes, B. P., and Yokart, B. (2010). P-T-t constraints on the development of the Doi Inthanon metamorphic core complex domain and implications for the evolution of the western gneiss belt, northern Thailand. *J. Asian Earth Sci.* 37(1), 82–104. DOI doi:10.1016/j.jseaes.2009.07.010

Mako, C. A., and Caddick, M. J. (2018). Quantifying magnitudes of shear heating in metamorphic systems. *Tectonophysics* 744, 499–517. doi:10.1016/j.tecto.2018.07.003

Metcalfe, I. (2011). Tectonic framework and phanerozoic evolution of sundaland. *Gondwana Res.* 19(1), 3–21. doi:10.1016/j.gr.2010.02.016

Metcalfe, I. (2013). Gondwana dispersion and asian accretion: tectonic and palaeogeographic evolution of eastern Tethys. *J. Asian Earth Sci.* 66, 1–33. doi:10.1016/j.jseaes.2012.12.020

Mezger, K., and Krogstad, E. J. (1997). Interpretation of discordant U-Pb zircon ages: an evaluation. *J. Metamorph. Geol.* 15 (1), 127–140. doi:10.1111/j.1525-1314.1997.00008.x

Mickein, A. (1997). U/Pb-, Rb/Sr-und K/Ar-Untersuchungen zur metamorphen Entwicklung und Alterstellung des "Präkambriums" in NW-Thailand. *Gött. Arb. Zur Geol. Paläontol.* 73, 1–83.

Morley, C. K., Smith, M., Carter, A., Charusiri, P., and Chantraprasert, S. (2007). Evolution of deformation styles at a major restraining bend, constraints from cooling histories, Mae Ping fault zone, western Thailand. *Geol. Soc. Lond. Spec. Publ.* 290, 325–349. doi:10.1144/SP290.12

Nantasin, P., Hauzenberger, C., Liu, X., Krenn, K., Dong, Y., Thöni, M., et al. (2012). Occurrence of the high grade thabsila metamorphic complex within the low grade three Pagodas shear zone, kanchanaburi province, western Thailand: petrology and geochronology. *J. Asian Earth Sci.* 60 (0), 68–87. doi:10.1016/j.jseaes.2012.07.025

Neves, S. P., Vauchez, A., and Archanjo, C. J. (1996). Shear zone-controlled magma emplacement or magma-assisted nucleation of shear zones? Insights from northeast Brazil. *Tectonophysics* 262 (1), 349–364. doi:10.1016/0040-1951(96)00007-8

Österle, J. E., Klötzli, U., Stockli, D. F., Palzer-Khomenko, M., and Kanjanapayont, P. (2019). New age constraints on the Lan Sang gneiss complex, Thailand, and the timing of activity of the Mae Ping shear zone from *in-situ* and depth-profile zircon and monazite U-Th-Pb geochronology. *J. Asian Earth Sci.* 181, 103886. doi:10.1016/j.jseaes.2019.103886

Palin, R. M., Searle, M. P., Morley, C. K., Charusiri, P., Horstwood, M. S. A., and Roberts, N. M. W. (2013). Timing of metamorphism of the Lansang gneiss and implications for left-lateral motion along the Mae Ping (Wang Chao) strike-slip fault, Thailand. *J. Asian Earth Sci.* 76, 120–136. doi:10.1016/j.jseaes.2013.01.021

Passchier, C. W., and Trouw, R. A. J. (2005). *Microtectonics*. Springer.

Peltzer, G., and Tapponnier, P. (1988). Formation and evolution of strike-slip faults, rifts, and basins during the India-Asia collision: an experimental approach. *J. Geophys. Res. Solid Earth* 93 (B12), 15085–15117. doi:10.1029/JB093iB12p15085

Pitcher, W. S., and Bussell, M. A. (1977). Structural control of batholithic emplacement in Peru: a review. *J. Geol. Soc.* 133 (3), 249–255. doi:10.1144/gsjgs.133.3.0249

Polachan, S., Pradidtan, S., Tongtaow, C., Janmaha, S., Intarawijitr, K., and Sangsuwan, C. (1991). Development of cenozoic basins in Thailand. *Mar. Petrol. Geol.* 8 (1), 84–97. doi:10.1016/0264-8172(91)90047-5

Reddy, S. M., and Potts, G. J. (1999). Constraining absolute deformation ages: the relationship between deformation mechanisms and isotope systematics. *J. Struct. Geol.* 21 (8-9), 1255–1265. doi:10.1016/S0191-8141(99)00032-2

Rosenberg, C. L., and Handy, M. R. (2005). Experimental deformation of partially melted granite revisited: implications for the continental crust. *J. Metamorph. Geol.* 23 (1), 19–28. doi:10.1111/j.1525-1314.2005.00555.x

Rosenberg, C. L. (2004). Shear zones and magma ascent: A model based on a review of the tertiary magmatism in the alps. *Tectonics* 23 (3). doi:10.1029/2003TC001526

Rubatto, D. (2002). Zircon trace element geochemistry: partitioning with garnet and the link between U-Pb ages and metamorphism. *Chem. Geol.* 184 (1-2), 123–138. doi:10.1016/s0009-2541(01)00355-2

Rubatto, D. (2017). Zircon: the metamorphic mineral. *Rev. Mineral. Geochem.* 83 (1), 261–295. doi:10.2138/rmg.2017.83.9

Schaltegger, U., Fanning, C. M., Günther, D., Maurin, J. C., Schulmann, K., and Gebauer, D. (1999). Growth, annealing and recrystallization of zircon and preservation of monazite in high-grade metamorphism: conventional and *in-situ* U-Pb isotope, cathodoluminescence and microchemical evidence. *Contributions Mineralogy Petrology* 134 (2), 186–201. doi:10.1007/s004100050478

Scharer, U., Zhang, L. S., and Tapponnier, P. (1994). Duration of strike-slip movements in large shear zones - the Red River belt, China. *Earth Planet. Sci. Lett.* 126 (4), 379–397. doi:10.1016/0012-821x(94)90119-8

Searle, M. P., Whitehouse, M. J., Robb, L. J., Ghani, A. A., Hutchison, C. S., Sone, M., et al. (2012). Tectonic evolution of the sibumasu-indochina terrane collision zone in Thailand and Malaysia: constraints from new U-Pb zircon chronology of SE asian tin granitoids. *J. Geol. Soc.* 169 (4), 489–500. doi:10.1144/0016-76492011-107

Searle, M. P. (2006). Role of the Red River shear zone, yunnan and vietnam, in the continental extrusion of SE Asia. *J. Geol. Soc.* 163 (6), 1025–1036. doi:10.1144/0016-76492005-144

Sone, M., Metcalfe, I., and Chaodumrong, P. (2012). The chanthaburi terrane of southeastern Thailand: stratigraphic confirmation as a disrupted segment of the Sukhothai arc. *J. Asian Earth Sci.* 61, 16–32. doi:10.1016/j.jseaes.2012.08.021

Stipp, M., Stünitz, H., Heilbronner, R., and Schmid, S. M. (2002). The eastern tonale fault zone: a 'natural laboratory' for crystal plastic deformation of quartz over a temperature range from 250 to 700 °C. *J. Struct. Geol.* 24 (12), 1861–1884. doi:10.1016/S0191-8141(02)00035-4

Strong, D. F., and Hanmer, S. K. (1981). The leucogranites of southern Brittany; origin by faulting, frictional heating, fluid flux and fractional melting. *Can. Mineralogist* 19 (1), 163–176.

Tang, Y., Liu, J., Tran, M.-D., Song, Z., Wu, W., Zhang, Z., et al. (2013). Timing of left-lateral shearing along the Ailao Shan-Red River shear zone: constraints from zircon U–Pb ages from granitic rocks in the shear zone along the Ailao Shan range, western yunnan, China. *Int. J. Earth Sci.* 102 (3), 605–626. doi:10.1007/s00531-012-0831-y

Tapponnier, P., Peltzer, G., Ledain, A. Y., Armijo, R., and Cobbold, P. (1982). Propagating extrusion tectonics in Asia - new insights from simple experiments with plasticine. *Geology* 10 (12), 611–616. doi:10.1130/0091-7613(1982)10<611:petian>2.0.co;2

Teggin, D. E. (1975). *The granites of northern Thailand*. Ph.D., Manchester University.

Tommasi, A., Vauchez, A., Femandes, L. A. D., and Porcher, C. C. (1994). Magma-assisted strain localization in an orogen-parallel transcurrent shear zone of southern Brazil. *Tectonics* 13 (2), 421–437. doi:10.1029/93TC03319

Uchida, E., Nagano, S., Niki, S., Yonezu, K., Saitoh, Y., Shin, K.-C., et al. (2022). Geochemical and radiogenic isotopic signatures of granitic rocks in chanthaburi and chachoengsao provinces, southeastern Thailand: implications for origin and evolution. *J. Asian Earth Sci. X* 8, 100111. doi:10.1016/j.jaesx.2022.100111

Ueno, K., and Hisada, K.-i. (2001). The nan-uttaradit-sa kaeo suture as a main paleo-tethyan suture in Thailand: is it real? *Gondwana Res.* 4 (4), 804–806. doi:10.1016/S1342-937X(05)70590-6

Veeravinantanakul, A., Takahashi, R., Agangi, A., Ohba, T., Watanabe, Y., Elburg, M. A., et al. (2021). Zircon Hf-isotope constraints on the formation of metallic mineral deposits in Thailand. *Resour. Geol.* 71 (4), 436–469. doi:10.1111/rge.12276

Wang, P.-L., Lo, C.-H., Lee, T.-Y., Chung, S.-L., Lan, C.-Y., and Yem, N. T. (1998). Thermochronological evidence for the movement of the Ailao Shan–Red River shear zone: A perspective from vietnam. *Geology* 26 (10), 887–890. doi:10.1130/0091-7613(1998)026<0887:Teftmo>2.3.Co;2

Wang, S., Mo, Y., Wang, C., and Ye, P. (2016). Paleotethyan evolution of the Indochina Block as deduced from granites in northern Laos. *Gondwana Res.* 38, 183–196. doi:10.1016/j.gr.2015.11.011

Watkinson, I., Elders, C., Batt, G., Jourdan, F., Hall, R., and McNaughton, N. J. (2011). The timing of strike-slip shear along the Ranong and Khlong Marui faults, Thailand. *J. Geophys. Res. Solid Earth* 116 (B9), B09403. doi:10.1029/2011jb008379

West, D. P., and Lux, D. R. (1993). Dating mylonitic deformation by the 40Ar-39Ar method: an example from the norumbega fault zone, Maine. *Earth Planet. Sci. Lett.* 120 (3), 221–237. doi:10.1016/0012-821X(93)90241-Z

Whitney, D. L., and Evans, B. W. (2010). Abbreviations for names of rock-forming minerals. *Am. Mineral.* 95 (1), 185–187. doi:10.2138/am.2010.3371

Yakymchuk, C., Kirkland, C. L., and Clark, C. (2018). Th/U ratios in metamorphic zircon. *J. Metamorph. Geol.* 36 (6), 715–737. doi:10.1111/jmg.12307

Zhang, L.-S., and Schärer, U. (1999). Age and origin of magmatism along the Cenozoic Red River shear belt, China. *Contributions Mineralogy Petrology* 134 (1), 67–85. doi:10.1007/s004100050469

Zhang, X., Chung, S. L., Lai, Y. M., Ghani, A. A., Murtadha, S., Lee, H. Y., et al. (2019). A 6000-km-long Neo-Tethyan arc system with coherent magmatic flare-ups and lulls in South Asia. *Geology* 47 (6), 573–576. doi:10.1130/g46172.1

frontiers | Frontiers in Earth Science

TYPE Original Research
PUBLISHED 10 October 2023
DOI 10.3389/feart.2023.1213498

OPEN ACCESS

EDITED BY
Claudia Piromallo,
National Institute of Geophysics and Volcanology (INGV), Italy

REVIEWED BY
Stefano Solarino,
Università di Genova, Italy
Luis E. Lara,
Austral University of Chile, Chile

*CORRESPONDENCE
Bor-Shouh Huang,
hwbs@earth.sinica.edu.tw

RECEIVED 28 April 2023
ACCEPTED 19 September 2023
PUBLISHED 10 October 2023

CITATION
Nguyen C-N, Huang B-S, Lee T-Y, Chen P-F, Nguyen VD, Narag I, Bautista BC and Melosantos A (2023), Slab tearing and lithospheric structures in Luzon island, Philippines: constraints from P- and S-wave local earthquake tomography.
Front. Earth Sci. 11:1213498.
doi: 10.3389/feart.2023.1213498

Slab tearing and lithospheric structures in Luzon island, Philippines: constraints from P- and S-wave local earthquake tomography

Cong-Nghia Nguyen[1,2,3], Bor-Shouh Huang[2]*, Tung-Yi Lee[4], Po-Fei Chen[3], Van Duong Nguyen[5,6], Ishmael Narag[7], Bartolome C. Bautista[7] and Arnaldo Melosantos[7]

[1]Taiwan International Graduate Program (TIGP)—Earth System Science Program, Academia Sinica and National Central University, Taipei, Taiwan, [2]Institute of Earth Sciences, Academia Sinica, Taipei, Taiwan, [3]Department of Earth Sciences, National Central University, Taoyuan, Taiwan, [4]Department of Earth Sciences, National Taiwan Normal University, Taipei, Taiwan, [5]Graduate University of Science and Technology (GUST), Vietnam Academy of Science and Technology, Hanoi, Vietnam, [6]Institute of Geophysics, Vietnam Academy of Science and Technology, Hanoi, Vietnam, [7]Department of Science and Technology, Philippine Institute of Volcanology and Seismology, Quezon City, Philippines

Luzon Island is a complex setting of seismicity and magmatism caused by the subduction of the South China Sea lithosphere and the presence of a major strike-slip fault system, the Philippine Fault. Previous studies of the structure of this subduction zone have suggested that a ridge subduction system resulted in a slab tearing along the ridge. On the other hand, the Philippine Fault plays an important role in understanding how major strike-slip faults deform and displace at a continental scale. To constrain the lithospheric geological structure in the area and refine the slab tearing model, we performed a P- and S-wave seismic tomography travel time inversion using local earthquakes. The dataset has been combined from seismic phases reported by the International Seismological Centre and new pickings from six broadband seismic stations in northern Luzon. The three-dimensional P- and S-wave velocity models in Luzon Island were analyzed by applying the LOTOS package with a one-dimensional velocity model obtained from the VELEST program. Our tomographic images indicate contrasting velocity structures across the Philippine Fault to a depth of 60 km. Therefore, we suggest that the Philippine Fault might be a lithospheric structure that displaces both the crust and the upper mantle. The results also indicate regions of low-velocity slab windows from a depth of 40 km, which are interpreted as the sites of slab tearing. Compared with focal mechanisms and earthquake occurrence in this region, we propose that slab tearing extends from the fossil ridge and creates regional kinematic perturbations. The tearing produces shallow upwelling magma to stay in the chambers beneath the crust, which is in contrast to the magmatic system observed in other regions.

KEYWORDS

Luzon, tomography, slab tearing, magmatic system, the Philippine fault

1 Introduction

Subduction zones are the most active tectonic boundaries on Earth's surface, showing great variations of volcanism, earthquakes, arc curvatures, and slab properties (Ruff and Kanamori, 1980; Stern, 2002; Hayes et al., 2018). In some subduction zones, the nature of the subduction process is modified by preexisting fossil ridges, which were spreading centers before subduction (Vogt, 1973; Rosenbaum and Mo, 2011). One of the most controversial characteristics of these structures is the different behaviors of magmatism due to the interaction between the subducting slab, the mantle wedge, and the subducting ridge (Tatsumi, 1989). In some fossil ridge subduction zones, the cessation of volcanism appears and develops a volcanic gap zone. The Nazca and Juan Fernández Ridges were considered examples of volcanic gaps formed by the consumption of fossil ridges possibly by causing a flat slab event (Nur and Benavraham, 1983; Bertin et al., 2022); however, recent studies suggest that the passage of the Juan Fernández might cause a large scale eruption in the future (Bertin et al., 2022). In contrast, volcanism might be enhanced as a result of ridge subduction in some places where slab tearing occurs. A typical example is the enhanced volcanism of the Aleutian Ridges by the formation of a slab window beneath Kamchatka (Levin et al., 2002). The different behaviors of the volcanic systems related to ridge subduction might be explained by the different tectonic responses in each particular region, for example,: flattening of slab dip, subduction rollback, and formation of slab windows (Rosenbaum and Mo, 2011).

The Luzon island arc is a region in which the South China Sea oceanic lithosphere has been consumed along the Manila Trench since the Miocene (Defant et al., 1989). As a result, a system of active earthquakes and volcanoes is well developed (Figure 1A). Compared to other ridge subduction systems in the world, the South China Sea ridge subduction system has been less studied to date. The ridge subduction of the South China Sea along the Manila Trench was first proposed based on the distribution and characteristics of two magmatic systems in North Luzon: the active east volcanic chain and the extinct west volcanic chain (Yang et al., 1996). Further investigation of earthquake distribution and focal mechanism data suggests a change in dip angles of the slab caused by the subduction of an extinct spreading ridge—the Scarborough seamount accreted at North Luzon at 16°N (Bautista et al., 2001; Armada et al., 2020), which is consistent with a change in slab deep angle between latitude 16°N and 17°N observed from earthquake occurrences and the slab model (cross sections BB' and CC' in Figure 1B). Seismic tomographic studies in this region also support the slab tearing model by imaging the large-scale slab geometry and slab window

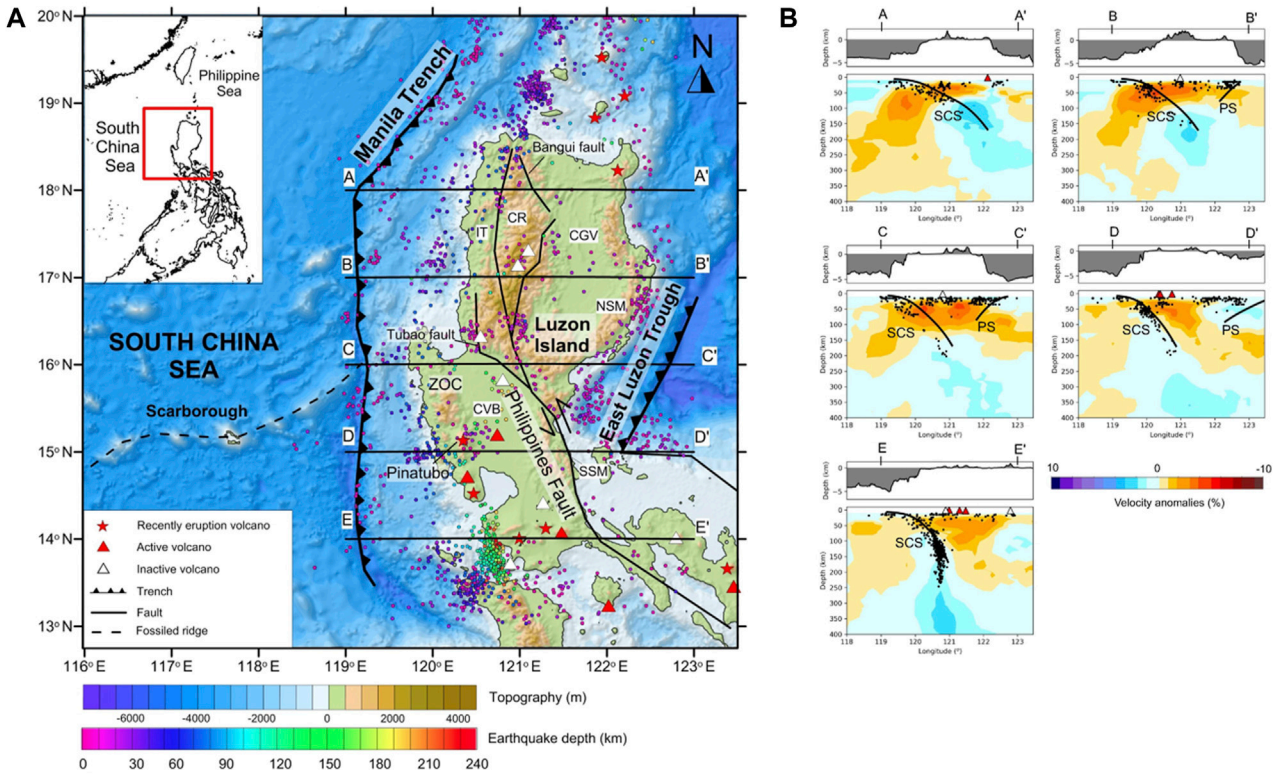

FIGURE 1
(A) Tectonic map of Luzon Island and the surrounding areas. The saw-toothed lines denote trench axes of subduction zones and solid lines denote faults. White triangles denote volacano unrest, red triangles denote active volcanoes, and red stars denote volcanoes with recorded eruptions. The locations of the trenches are modified from Bautista et al. (2001). The bathymetric and topographic data are from Smith and Sandwell (1997), and the location and activities of volcanoes are from Venzke et al. (2002). CVB: Central Valley Basin; CR: Central Cordillera Range; CGV: Cagayan Valley Basin; IT: Ilocos Trough; NSM: North Sierra Madre; SSM: South Sierra Madre; ZOC: Zambales Ophiolite Complex. **(B)** Earthquake distribution from the EHB catalog (Engdahl et al., 1998) in the selected profiles in **(A)** and the P-wave teleseismic tomography model from model UU-P07 (Amaru, 2007). Black lines indicate the surface of the subducting slab with depths from the Slab2 database (Hayes et al., 2018). SCS: South China Sea slab; PS: Philippines Sea slab.

using P-wave travel time seismic tomography (Fan et al., 2015; Fan et al., 2016). The global P-wave seismic tomography also shows possible images of the slab windows at a depth of less than 100 km at latitude 16°N to 18°N (cross sections AA', BB' and CC' in Figure 1B). These studies have provided evidence for a discontinuity of the slab at depths deeper than 100 km at the extension of the fossil ridge. However, the shallow structure at a local scale, particularly the S-wave velocity in the Luzon island, has not been well constrained.

Meanwhile, most previous studies on volcanic systems used geochemical methods to identify the characteristics of lavas and magmatic rocks in the region (Defant et al., 1989; Yumul et al., 2000; Castillo and Newhall, 2004; Jego et al., 2005; Hollings et al., 2011). However, despite various studies in the region, the connection between the ridge subduction structure and volcanic activities is not well resolved.

Another major question is the tectonic role of the Philippine Fault in this area. The Philippine Fault is a major left-lateral strike-slip fault that cuts along the whole Philippine Archipelago and extends from Mindanao to northern Luzon (Barrier et al., 1991; Aurelio, 2000). Previous studies were mostly focused on the present slip and stress regime at the crustal level of the fault (Barrier et al., 1991; Aurelio et al., 1997; Aurelio, 2000; Yu et al., 2013; Hsu et al., 2016), while very few studies have discussed the depth of the fault cut through, which is an important tectonic question considering the massive length of the Philippine Fault.

In this study, we performed a simultaneous P- and S-wave seismic tomography of the crust and upper mantle of Luzon Island from local earthquakes to obtain high-resolution tomographic images of subsurface structures. By using both P- and S-wave velocity models, we obtained independent results, which provided reliable evidence for the same structures. The tomographic results also verified the slab tearing caused by the ridge subduction of the South China Sea and identified the sources of regional magmatism. Based on those findings, we constrained the lithospheric geological structure in the area and refined the slab tearing model. We also observed considerable velocity contrasts at both crustal and upper mantle levels across the Philippine Fault to a depth of 60 km. This allowed us to estimate the depth of the Philippine Fault, which may have cut through the crust and reached the upper mantle.

2 Tectonic settings

Luzon Island is part of the Philippines islands and is made up of assemblages of active and inactive terranes, metamorphosed rocks, sedimentary basins, and ophiolite complexes (Lee and Lawver, 1994). Luzon Island is governed by two subduction zone systems: the South China Sea subduction in the west along the Manila Trench and the Philippines Sea subduction in the east along the East Luzon Trough (Figure 1A). While the depths of earthquakes in the East Luzon Trough are rather shallow, up to 80 km (Defant et al., 1989), a well-defined Wadati—Benioff zone deeper than 200 km was used to construct the geometry of the subducting slab along the Manila Trench (Bautista et al., 2001; Hsu et al., 2012) (Figure 1B). The Scarborough seamount chain is identified as the result of post spreading volcanism in the time period of 13–3 Ma and marked the extinct mid-ocean ridge (Hung et al., 2021). The subduction of this fossil ridge has been proposed to cause a slab tear, evidenced by the change in the South China Sea slab angle (Bautista et al., 2001; Fan et al., 2015). However, the exact location of the slab tear is not well constrained, despite a detailed analysis of the earthquake location that revealed a change in the South China Sea slab angle at approximately 16°N within a depth of 200 km (Bautista et al., 2001), and the P-wave tomographic model showed a significant change in the slab angle at 17°N—17.5°N in a much deeper depth (from 200 km to 700 km) (Fan et al., 2015).

Located between the aforementioned two opposite subduction zones is the major 1300-km left lateral Philippine Fault (Figure 1A). The Philippine Fault is considered a trench-linked strike-slip fault behind a subduction zone—the Philippines Trench, particularly the East Luzon Trough in the North Luzon area, as a consequence of oblique subduction (Fitch, 1972; Aurelio, 2000). In this model, the fault accommodates the parallel convergence of oblique subduction while the perpendicular motion is absorbed along the East Luzon Trough. In the Luzon region, the Philippine Fault has been interpreted as the tectonic boundary separating the Zambales-Angat ophiolites from the Northern Luzon volcanic and Eastern Luzon metamorphic belt (Karig, 1983; Karig et al., 1986). Moreover, the fault is also considered to be the boundary between the preserved remnants of the proto-South China Sea and the proto-Philippine Sea Plate (Yumul et al., 2020). These studies suggest that the Philippines Fault can also be considered as a tectonic boundary separating multiple terranes that made up Luzon Island.

Volcanoes and magmatic systems are well developed on Luzon Island, which is interpreted to be related to the east-dipping subduction along the Manila Trench (Defant et al., 1989), while the slab in the East Luzon Trough is too shallow to generate melts (Hamburger et al., 1983). Intense volcanic eruptions have been observed in the area, most notably the 1991 Pinatubo eruption (Bluth et al., 1992) (location in Figure 1A). The active volcanoes are located in the north and south of Luzon Island (approximately 13°N to 15°N and from 18°N to 20°N), while in the central Luzon region, most of the volcanoes are inactive (Figure 1A) (Venzke et al., 2002).

3 Data and method

3.1 P- and S-wave travel time data

The data used in this study are the P- and S-wave arrival times of regional earthquakes compiled from different sets of data, such as from the International Seismology Centre Bulletin (ISC) from 2000 to 2016 (86 stations) and the six broadband stations operated by the cooperation of the Philippine Institute of Volcanology and Seismology (PHIVOLCS) and Institute of Earth Sciences (IES), Academia Sinica from 2014 to 2016 (Figure 2). The locations and periods of the PHIVOLCS - IES stations are listed in the Supplementary Material (Supplementary Table S1). The events were selected within a maximum distance of 8° from a chosen center point of Luzon island (121°N, 16.5°E) with all depths and magnitudes. The data from the ISC bulletin are the first P- and S-wave arrival times of these earthquakes recorded from stations in Luzon Island and the Taiwan region. We handpicked the first P- and S-wave arrival times from the PHIVOLCS-IES station waveform and then calculated the travel times for each event-station pair. These readings obtained from broadband stations were used to improve

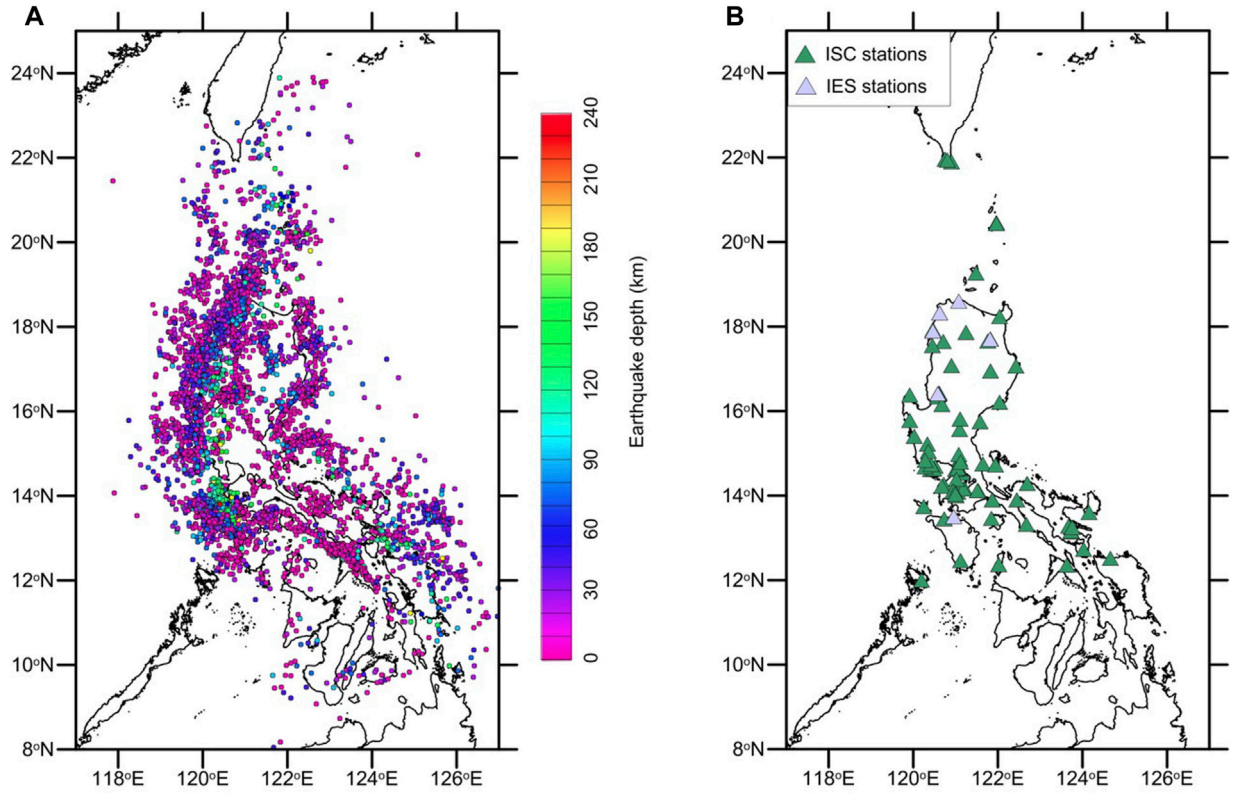

FIGURE 2
Distribution of **(A)** earthquake events and **(B)** seismic stations used in this study. The green triangles indicate stations in the ISC catalog, purple triangles indicate stations of the PHIVOLCS-IES network, and circles indicate earthquakes with colors indicating depth.

the quality of the travel time database, especially the S-wave readings. The two databases were then combined to have a total of 92,950 P-wave readings and 49,087 S-wave readings from 21,134 events.

The ISC catalog data set is large but may contain data errors and poor-quality source locations (Koulakov, 2013). To improve the quality of the data set, we filtered the data using two criteria, namely, choosing only readings with a maximum of 2.0 s of travel time residual and a minimum of eight readings for each event to improve the quality of source relocation. The filtering resulted in a significant reduction of readings and events from the database. The final seismic tomography input included 40,163 P-wave readings and 20,328 S-wave readings from 4,926 events in which there were 1,389 P-wave readings and 1,287 S-wave readings from the PHIVOLCS-IES network, which accounted for 3.13% of the total P-wave readings and 5.75% of the total S-wave readings. The average P- and S-wave readings for each event were 8.15 and 4.12 readings, respectively. These P- and S-wave traveltimes were used to constrain the velocity structure and seismicity distribution of earthquakes in the region. The P-wave and S-wave ray paths of the source receivers are shown in Supplementary Figure S1, S2 for each horizontal section, respectively. The abundance of seismicity from the two subduction zones with a wide range of depths resulted in good coverage of crosscut ray paths. From the coverage of the ray path, we expect the models to be best estimated for the inland region of Luzon Island.

The workflow of this study included: 1) an 1D reference velocity model inversion using the program VELEST (Kissling et al., 1994), and 2) determining the three-dimensional (3D) P- and S-wave velocity models using the Local Tomography Software (LOTOS) (Koulakov, 2009). The results and quality of these velocity structures are herein justified and discussed.

3.2 1D velocity model

In a local tomographic inversion, an appropriate one-dimensional reference velocity model is required and is used as an input for the inversion (Kissling et al., 1994). To define a reliable one-dimensional P-wave velocity model, the VELEST program (Kissling et al., 1994), we first located the earthquake using Hypoinverse (Klein, 2002) to get the maximum azimuthal gap (GAP) and initial travel time residual of each event. We then selected events with GAP <180° and travel time residual <1.0s, which resulted in 526 events. To obtain the best estimation of the average velocity model and test its stability, we used 250 starting P-wave velocity models, in which variations in velocity and depth were added from the base velocity model of CRUST 1.0 (Laske et al., 2013) in the center of the Luzon region. The inversion results in a convergence of the output velocity models from a wide range of inputs, indicating a stable one-dimensional (1D) velocity model for the local structure. Figure 3A shows the results of VELEST inversion,

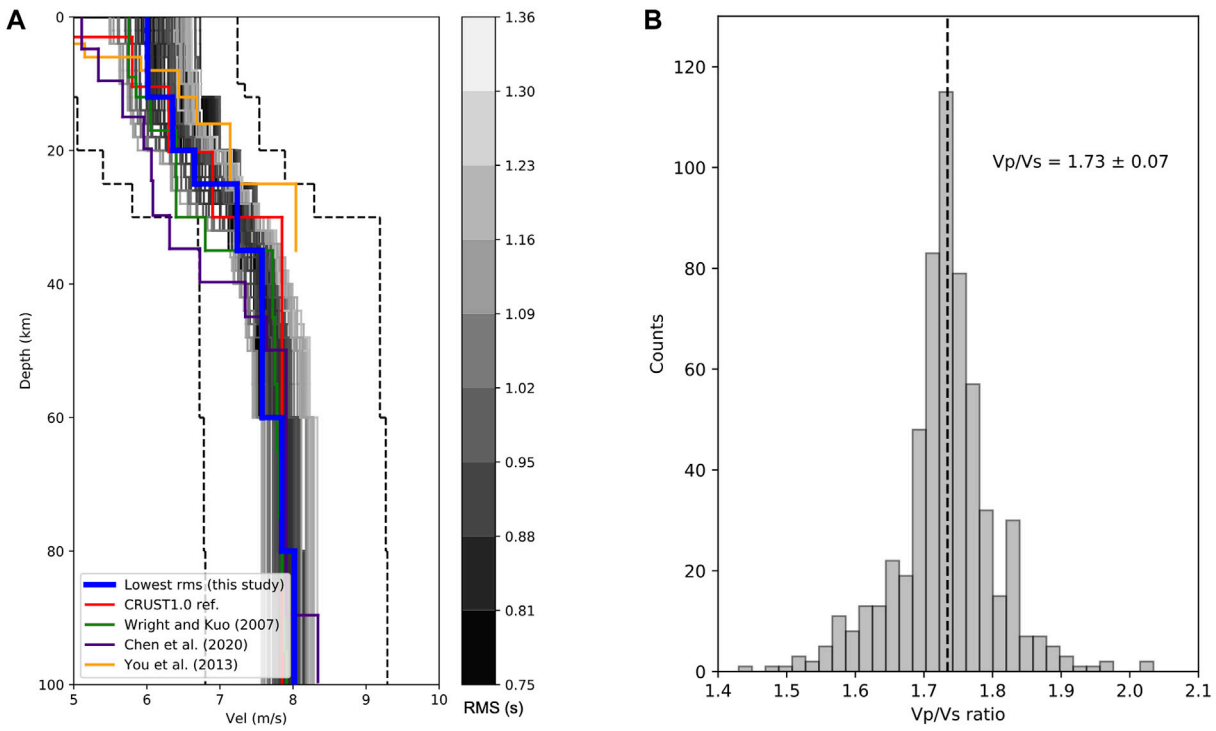

FIGURE 3
(A) 1D velocity model showing results of VELEST inversion (gray line) from a wide range of input velocity models (dash line). The blue line indicates the chosen lowest RMS 1D velocity model. The references model used: CRUST 1.0 (Wright and Kuo, 2007; Laske et al., 2013; You et al., 2013; Chen et al., 2020); **(B)** histogram of the Vp/Vs. ratio of 526 events obtained from a Wadati diagram.

TABLE 1 The starting 1D P-wave velocity model resulted from VELEST for seismic tomographic inversion.

Depth (km)	Velocity (km/s)
0	4.800
10	6.011
20	6.356
25	6.654
30	7.237
35	7.577
60	7.814
80	7.988
150	8.232
200	8.669

in which the grey velocity models are the result of the inversion while the blue indicates the lowest root-mean-square (rms) travel time residual of 0.751 s. In the study area, various 1D velocity models have been obtained from previous studies including a mantle and transition zone seismic velocity model between the Philippines—Taiwan region (Wright and Kuo, 2007), a velocity model for earthquake relocation of Batangas earthquake sequences (Chen et al., 2020), and a velocity model of the Taal volcano (You et al., 2013). We chose the lowest rms model as the starting input for the tomographic inversion and describe the model in Table 1. Compared to these models, our chosen velocity model is most similar to the CRUST 1.0 model and the model from Wright and Kuo (2007), which represents the regional velocity structure. Furthermore, we calculated the Vp/Vs. ratio of each event using the Wadati plot (Wadati and Oki, 1933) for all the abovementioned events used in VELEST. After that, we took the average Vp/Vs. ratios of these events to get a final Vp/Vs. ratio of 1.73 (Figure 3B). Both the P-wave velocity model and the Vp/Vs. ratio were used as inputs in the LOTOS package to obtain the tomographic inversion.

3.3 3D seismic tomography

The 3D seismic tomography inversion was conducted using the LOTOS program for the whole data set (Koulakov, 2009). The LOTOS program is a 3D inversion package designed for local tomography inversion and has been applied to various tectonic settings (Koulakov, 2013; Koulakov et al., 2016; Koulakov et al., 2018; Hua et al., 2019) and different scales, from a small region of a volcano (Koulakov et al., 2016; Koulakov and Vargas, 2018) to a regional area (Raoof et al., 2017).

The input of the program includes a 1D reference model, P- and S-wave traveltimes and locations of selected earthquakes, and seismic stations. The 3D tomographic inversion starts with the initial source location from the inversion of travel time using the input 1-D velocity model. In this step, the source location is calculated based on calculating a goal function that reflects the

probability of the event at a current point (Koulakov and Sobolev, 2006). A grid search method is then applied to get the preliminary locations with the extreme value of the goal function.

In the next step, the tomographic inversion was carried out in several iterations. In each iteration, earthquakes were relocated using a modified bending tracing method based on a previously updated 3D velocity model (Um and Thurber, 1987). This technique searched for a 3D ray path with minimum travel time in the parameterization units, which were the nodes. These nodes were constructed with different basic orientations (e.g., 0°, 22°, 45°, and 66°) and then were averaged to reduce the effect of node distributions on the tomographic results. A large sparse matrix including P- and S velocity anomalies, source parameters, and station corrections were simultaneously inverted using the LSQR algorithm (Paige and Saunders, 1982; Van Der Sluis and Van der Vorst, 1987). The input parameters included the number of iterations, damping parameters, weights, and grid size in horizontal, vertical, and depth dimensions. To get the optimal inversion results, we determined these free parameters by using different synthetic tests. After obtaining the optimal free parameters, we applied the 3D inversion to our data and obtained the tomographic images.

4 Resolution validations of the tomographic image

In seismic tomography inversion, assessing the validity of the inversion is a major challenge and different tests have been proposed that can be grouped into two types: sampling test and synthetic test. The usage and theory of these tests have been discussed in detail in previous studies (Koulakov, 2009; Rawlinson et al., 2014; Rawlinson and Spakman, 2016).

In the sampling test, different subsets of the whole data are used to do the tomographic inversion, then the individual resultant images are compared. There are different statistical resampling techniques used in seismic tomography, for example,: jackknifing, bootstrap (Rawlinson et al., 2014), and the odd/even test (Polat et al., 2016). An odd/even test is a method to divide the data into two-halves, where the two subsets are with odd and even numbers of events. This sampling test can be used to assess the effect of the random noises on the inversions, with a higher degree of differences between two results reflecting a higher level of noise effect and *vice versa* (Polat et al., 2016). We chose this method to test the degree of noise in our data because it is simple and easy to apply.

The synthetic test is another widely used tool in seismic tomography (Koulakov, 2009). In this test, a synthetic pattern of the anomalies is created and the travel times for each source-station pair are then calculated. These calculated travel times are then added noises to replicate the actual random noises in the picking process. In our study, the noise had a predefined average deviation of 0.1s for P-wave travel time and 0.15s for S-wave travel time, because, in reality, the S-wave picks are often less accurate than the P-wave picks. In this process, the synthetic pattern can take the form of an equal space 3D block of positive and negative values (checkerboard test), or an arbitrary form of positive and negative velocity anomalies (Koulakov, 2009). Subsequently, the velocity model and source locations are "forgotten" and then the same inversion processes are applied to the real data, including source locations and velocity model inversion. The resultant images are then compared with the initial models to determine the region that shows good restoration.

In this study, to have a detailed assessment of the quality of inversion, we considered different tests, including the odd-event test and two synthetic tests, namely, the checkerboard resolution test (CRT) and the freeform synthetic test (Koulakov, 2009). By performing these quality tests, we also calibrated the parameters including nodal size, smoothing, damping, and weight of the seismic tomography inversion.

4.1 Checkerboard resolution test

We applied a classic checkerboard resolution test by setting a synthetic model of alternating positive and negative anomalies for horizontal and vertical slices. The amplitude of the anomalies was ±7% with different block sizes of 40 km, 50 km, and 60 km to check the quality of the inverted model for structures with different sizes. In the vertical sections, we created blocks with a depth size of 50 km and defined a change of pattern at a depth of 20 km.

The results of horizontal CRT for a grid size of 50 km are shown in Figures 4, 5, while grid sizes of 40 km and 60 km are shown in Supplementary Figure S3, S4; CRTs for the vertical sections are shown in Supplementary Figure S5.

In general, the P-wave has a higher resolution quality than the S-wave because of the greater number of crosscut ray paths (Supplementary Figure S1, S2). In the horizontal sections, for the most part from depths of 0–50 km, the P-wave checkerboard could be well recovered in the whole region of Luzon Island, while the offshore region of Luzon Island (north of 19°N) was poorly recovered. For the S-wave, most regions of Luzon Island could be well recovered from 10 to 40 km, and poorly recovered in the deeper part.

In the vertical section (Supplementary Figure S5), the checkerboard test could be well recovered in the inland part to the depth of 70 km in most sections. The CRT results indicated that, for most regions of Luzon Island, the tomographic images could be considered reliable with the highest resolution from a depth of 20–50 km, while the deeper parts should be interpreted with caution. After some trial and error runs, we chose the optimal parameters to represent velocity perturbations, which are shown in Supplementary Table S2. We applied these model parameters to all the other quality tests and tomography inversions.

4.2 Odd-even test

In this test, we split real picking data (Figure 2A) into odd and even groups. Each group data was set as independent input data for inversion analysis. While the checkerboard test or freeform synthetic test are used to determine how the structures can be restored, the odd/even test is used to assess the effect of random noise on the tomographic results. If there are major differences between tomographic results from the odd and even datasets, the random noise may have a notable influence on the inversion, and the seismic

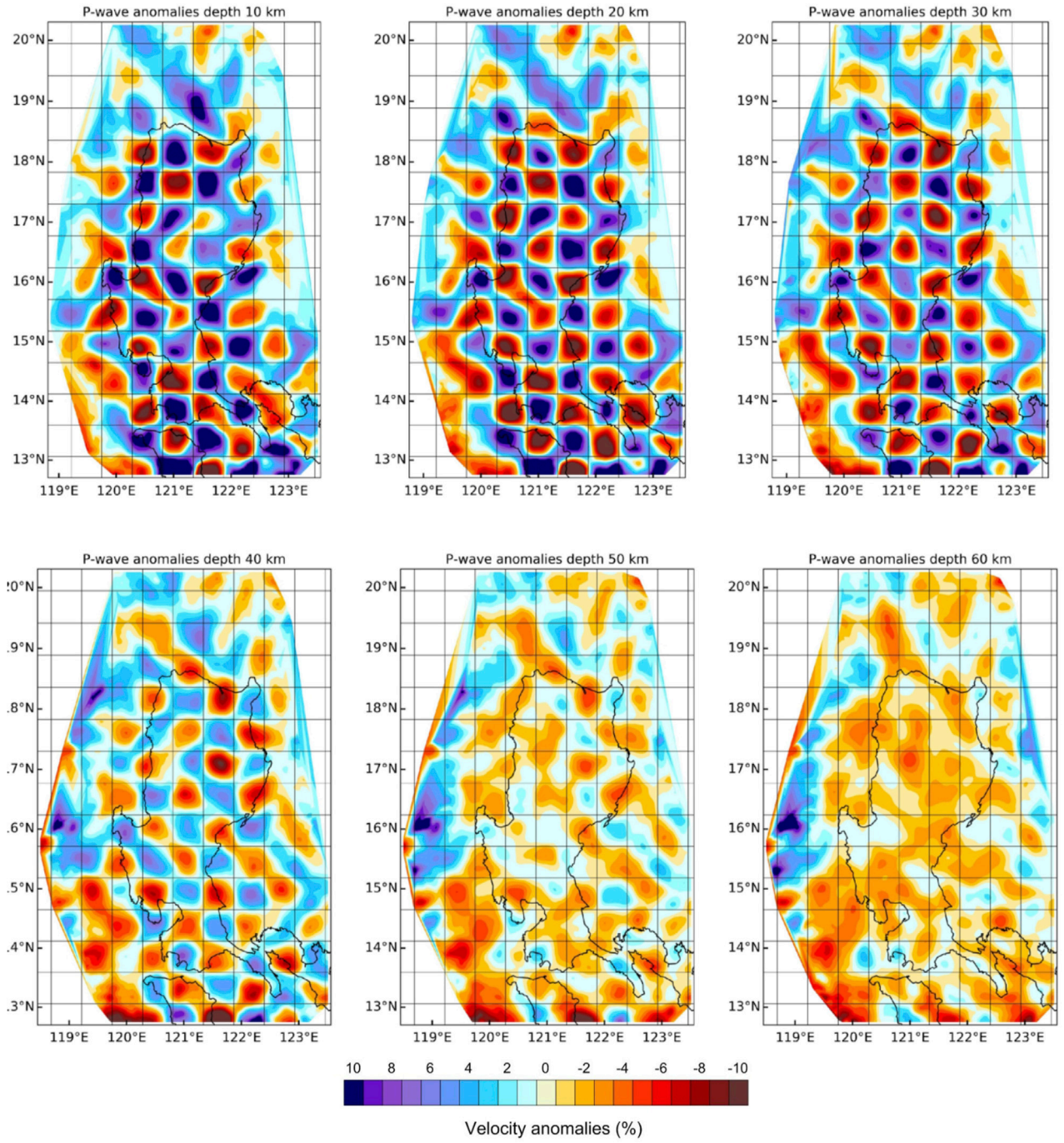

FIGURE 4
Results of the checkerboard resolution test for P-wave at depth layers with a lateral grid interval of 50 km in the longitudinal and latitudinal directions. The layer depth is shown below each map.

tomographic may contain more uncertainties. The results of the odd/even test are shown in Figure 6 and show a horizontal section for P-wave and S-wave. Two layers of each test are presented: one for the shallow layer at 20 km and one for a deeper layer at 40 km. These results from odd/even events were then compared to each other.

For the P-wave results, the models showed a very high correlation for the inland area in both horizontal sections (the left two columns in Figure 6). Most of the structures with different sizes were preserved in odd and even data inversion. However, both the P- and S-wave results showed a lower degree of correlation for regions with less ray path coverage (Supplementary Figure S1, S2). This reflects a higher degree of randomness and requires caution when interpreting the structure there.

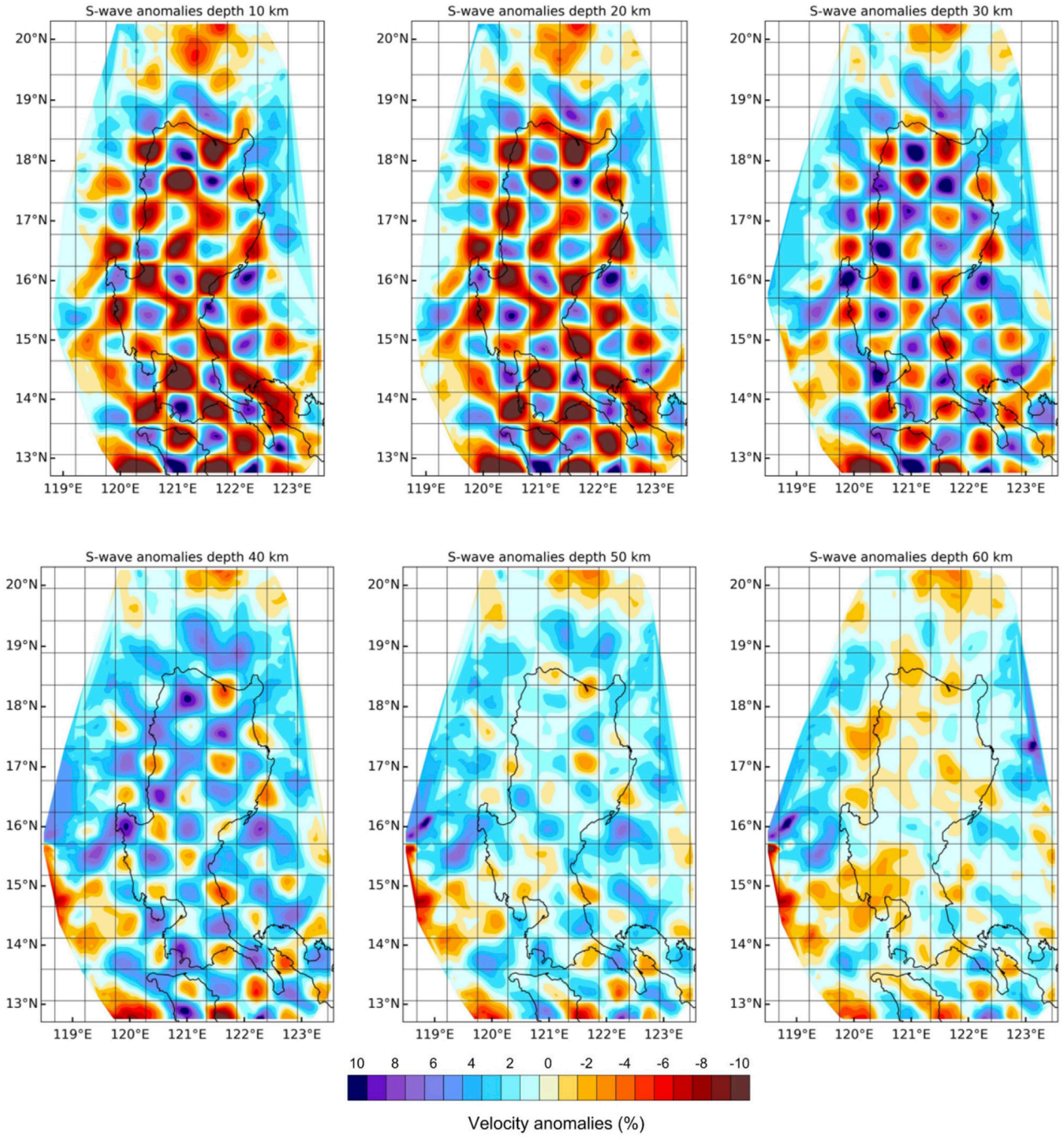

FIGURE 5
Results of the checkerboard resolution test for S-wave at depth layers with a lateral grid interval of 50 km in the longitudinal and latitudinal directions. The layer depth is shown below each map.

4.3 Freeform synthetic test

Finally, we performed a freeform synthetic test in horizontal and vertical sections (assuming the model with 2D variation and the medium was invariant along the third axis, or named as 2.5D model in explosion Geophysics) to verify the quality of the seismic tomography inversion with structures. The horizontal section freeform velocity model of this synthetic test was integrated from the information of the regional tectonic features in Figure 1 and previously reported tomographic images to design the model as shown in Figure 7. The proposed velocity anomalies were ±6% for P-wave and ±8% (higher amplitude) for S-wave to resemble the previous inversion results (Fan et al., 2015; Fan et al., 2016). The horizontal section model was uniformly extended in a vertical direction from the surface to a depth of 100 km. Using the above-defined velocity models, we calculated the travel times for

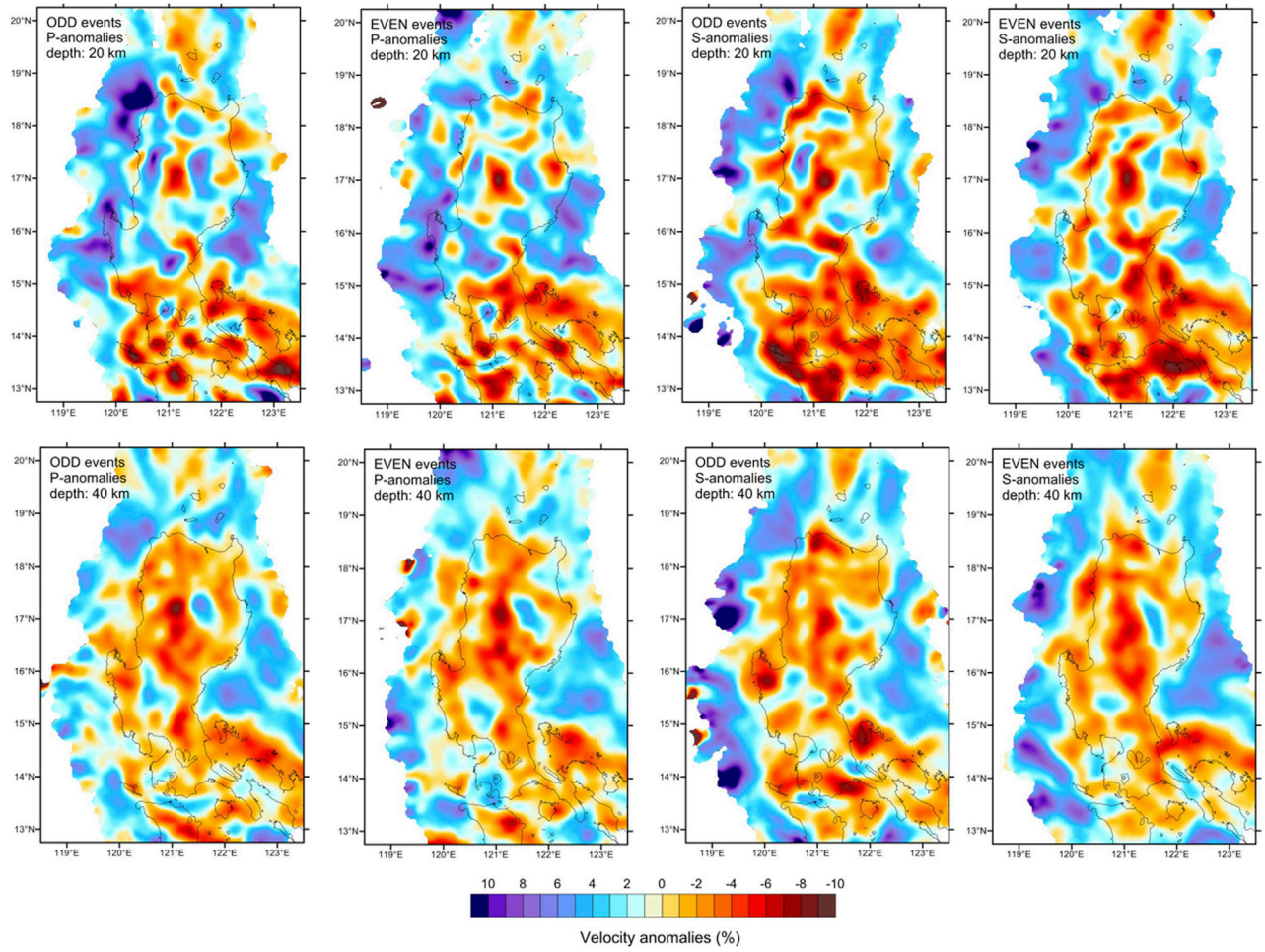

FIGURE 6
Results of the odd/even test in horizontal tomographic images. The data are divided into two subsets based on the number of events and performed independent inversion.

the event-station pair of all selected events as the synthetic input data. Using this synthetic input data and grid design as used in the case of the odd-even test, the results of this test are shown in Figure 7. In the inverted horizontal slices (Figure 7), the structures from the synthetic setup (shown in black lines) were recovered well even at the depth of 60 km, while the areas outside of the initial structures (i.e., 0% anomalies) were overestimated by ±3%. In this study, the vertical section models were arranged to test several candidate subduction zone models that were modified from the previous inversion results (Fan et al., 2015; Fan et al., 2016) of this area as shown in Supplementary Figure S6. The vertical section model extended in the horizontal direction, with the same velocity distribution of the cross section to the entire model. Supplementary Figure S6 also shows the test results of five vertical section models. In the vertical slices, the recovered P- and S-wave velocity structures showed a high correlation with the synthetic model on the vertical sections with minor smearing. The same as with the horizontal slices, the structures from the synthetic setup (shown in black lines) were recovered well above the depth of 60 km. Based on this test, we concluded that the inversion results in the region of interest were reliable enough for geological interpretation. Combined with the CRT test, we concluded that our models are suitable for interpretation with a depth of up to 60 km, with the most reliable horizontal slices from depths of 20–50 km. At a depth deeper than 60 km, the degrees of smearing were higher, thus, these regions should be interpreted with caution.

5 Analyzed results

As stated in the synthetic test, the main model was obtained by inversion of data using five iterations. The tomographic inversion results in P-wave travel time misfit reduced from 0.523s to 0.441s (15.56% reduction) and S-wave travel time misfit reduced from 0.758s to 0.560s (26.1% reduction). The values of the mean residual and their reduction of P- and S-wave during each iteration are presented in Table 2, while Figures 8A,B show histograms of the P- and S-wave travel time misfit before and after the final iteration, respectively. Figure 8C shows the locations of the earthquakes before and after the inversion, which we will discuss in the next section.

The results of seismic tomographic inversion in Luzon Island are presented as horizontal slices of P-wave perturbations (Figure 9) and

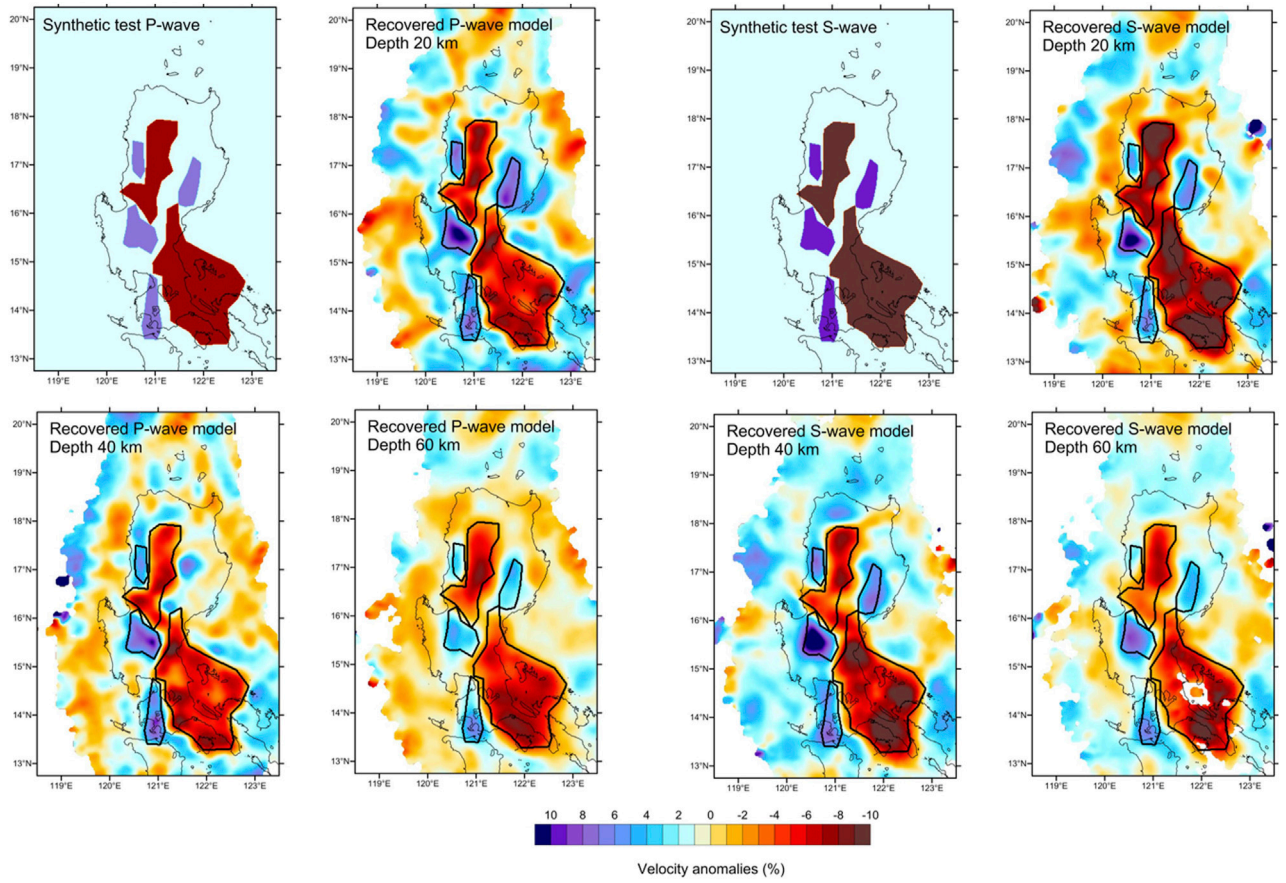

FIGURE 7
Results of the synthetic test with the realistic configuration of patterns in horizontal sections. The proposed velocity structure of the synthetic test referred to the regional tectonic features of Fig.1 to design the model.

TABLE 2 The P-wave and S-wave residuals from tomographic inversion.

Iteration	P rms	P rms reduction	S rms	S rms reduction
1	0.5299	-	0.7619	-
2	0.4679	11.87%	0.6143	19.37%
3	0.4512	14.84%	0.5871	22.93%
4	0.4449	16.03%	0.5716	24.97%
5	0.4421	16.56%	0.5645	25.91%

S-wave perturbations (Figure 10). These images show the velocity anomalies compared with the initial 1D velocity model at the depth of 10 km, 20 km, 30 km, 40 km, 50 km, and 60 km. In P- and S-wave tomographic results, red colors denote the slow velocity anomalies and blue colors indicate high-velocity anomalies. Although the LOTOS program inverts P- and S-wave velocity simultaneously, the link between them is relatively weak and can be considered as independent parameters (Koulakov et al., 2016). Therefore, the high correlations between these results indicate the robustness of tomographic inversion. The Vp/Vs. ratio was also calculated for the vertical cross section by dividing the absolute P-wave velocity by S-wave velocity.

Some seismic velocity zones with high values of anomalies could be noted at the slice of shallow depth of 10 km–30 km, as shown in Figures 9, 10. This higher degree of anomaly level might be due to the presence of the high contrasting velocity structure, e.g., subducting slab and magmatic structures (volcanoes and magma chamber) in the study area. Both the absolute velocity of P- and S-wave were much lower in the shallow depth compared to the deeper depth, therefore, the velocity anomalies at the horizontal slice at 10–30 km were generally higher than at a depth of 40–60 km. As a result, we focused on the structures with higher velocity anomalies in the shallow portion.

In the northern Luzon region, the Central Cordillera Range appeared as a region of mostly high-velocity anomalies, except the eastern region near inactive volcanoes, which appeared as a low-velocity zone at the depth of 10 km (16°N-18°N, Figures 9, 10). However, at depths of 20 km and 30 km, contrasting velocity anomaly patterns in the mountain range across the Philippine Fault could be seen, with the western side appearing as a high-velocity zone while the eastern side showed prominent low-velocity anomalies up to 9%. The Cagayan Valley Basin appeared as a mostly high-velocity zone with some small zones of low-velocity in the north and west. To the east, the North Sierra Madre mountain range was characterized by high-velocity anomalies, while low-velocity zones could be found in the South Sierra Madre. To the south, the

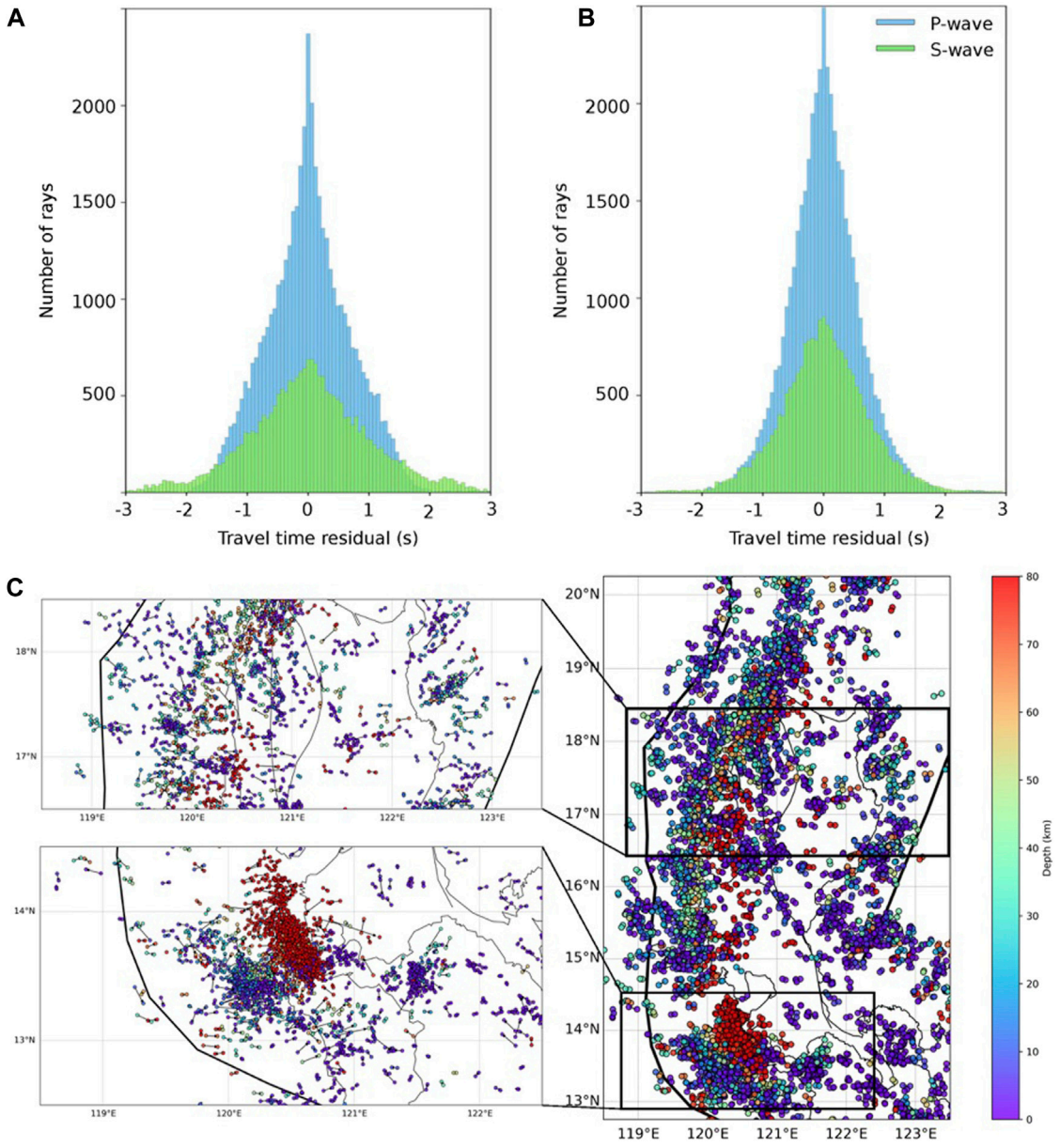

FIGURE 8
Travel time residual histogram **(A)** before and **(B)** after the tomographic inversion. The blue and green bars indicate P-wave and S-wave; **(C)** map showing the earthquake locations change after the inversion, and the arrow indicates points from the original locations to the relocated locations.

Zambales Ophiolite Complex consistently appeared as a high-velocity zone. The Central Valley Basin appeared as a high-velocity zone, which shows a sharp velocity contrast with the northeast Philippine Fault and southeast South Sierra Madre up to a depth of 40 km.

Horizontal P- and S-wave velocity models showed high-velocity anomalies of 8%–10% in the west of Luzon Island from a depth of 10 km up to 60 km (Figures 9, 10). These anomalies were interpreted as the subducting slab of the South China Sea lithosphere, which agrees with the relocated earthquake distribution and reference slab model (gray lines). In the east of Luzon Island, the high-velocity anomalies combined with relocated earthquakes parallel to the East Luzon Trough may represent the subducting Philippines Sea Plate slab.

Low-velocity anomalies of up to 8% of both P- and S-wave could be found in most areas of Luzon Island under both active and inactive volcanoes (Figures 9, 10). These low-velocity anomalies exhibited a very high Vp/Vs. ratio (>1.8), suggesting that these low-velocity regions might indicate the area of magmatic storage. The shallow magmatic storage from seismic tomography images characterized by low velocity, especially low S-wave anomalies, and high Vp/Vs. ratio are quite common in subduction zones settings (Tatsumi et al., 1983; Zhao et al., 2000; Wyss et al., 2001; Husen et al., 2003; Koulakov et al., 2009; Koulakov, 2013; Koulakov

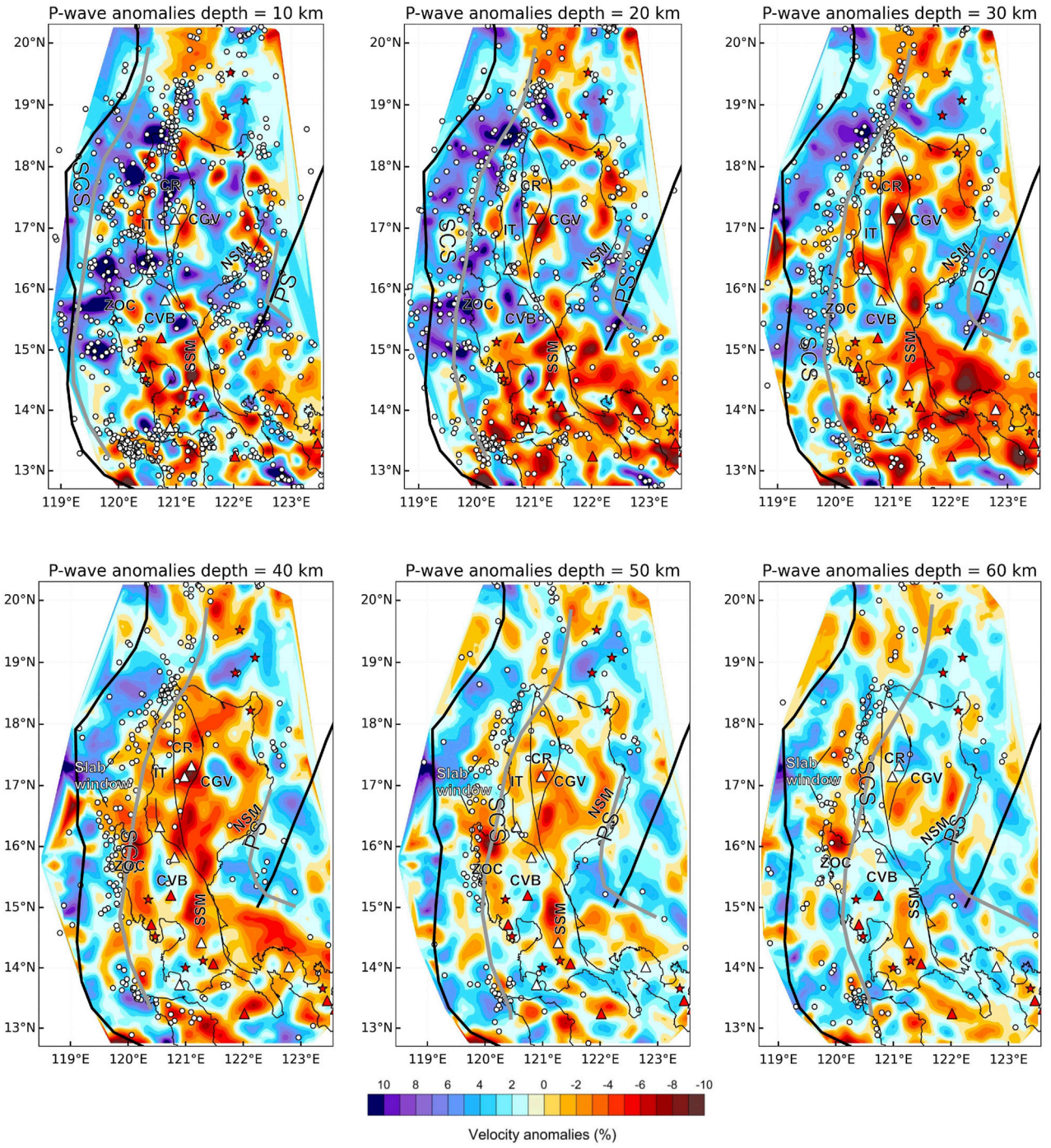

FIGURE 9
Map view of P-wave tomography of different depths. The red and blue colors denote slow and fast velocity perturbations, respectively. Gray lines indicate the subducting slab from the Slab 2 model (Hayes et al., 2018). The symbols and abbreviations are the same as those in Figure 1.

et al., 2016). Figure 11 shows the P, S perturbations, and Vp/Vs. ratio in vertical sections from 14°N to 18°N, while the dots indicate relocated earthquakes. The earthquake locations define a good image of the Wadati-Benioff zone up to a depth of 100 km. The most notable features were the low P- and S-velocity and high Vp/Vs. region, which is interpreted as regions of magma generation and migration. Because S-velocity is more sensitive to fluid, S-velocity has a higher degree of negative anomalies and results in a high Vp/Vs. ratio in this area. The significance of these magma sources will be further discussed in the next section. The high-velocity zones concentrated with earthquakes were interpreted as the subducting slabs. In these images, the South China Sea slab could be well defined based on the high-velocity anomalies and earthquake distributions, while the Philippine Sea Plate resolution was less clear.

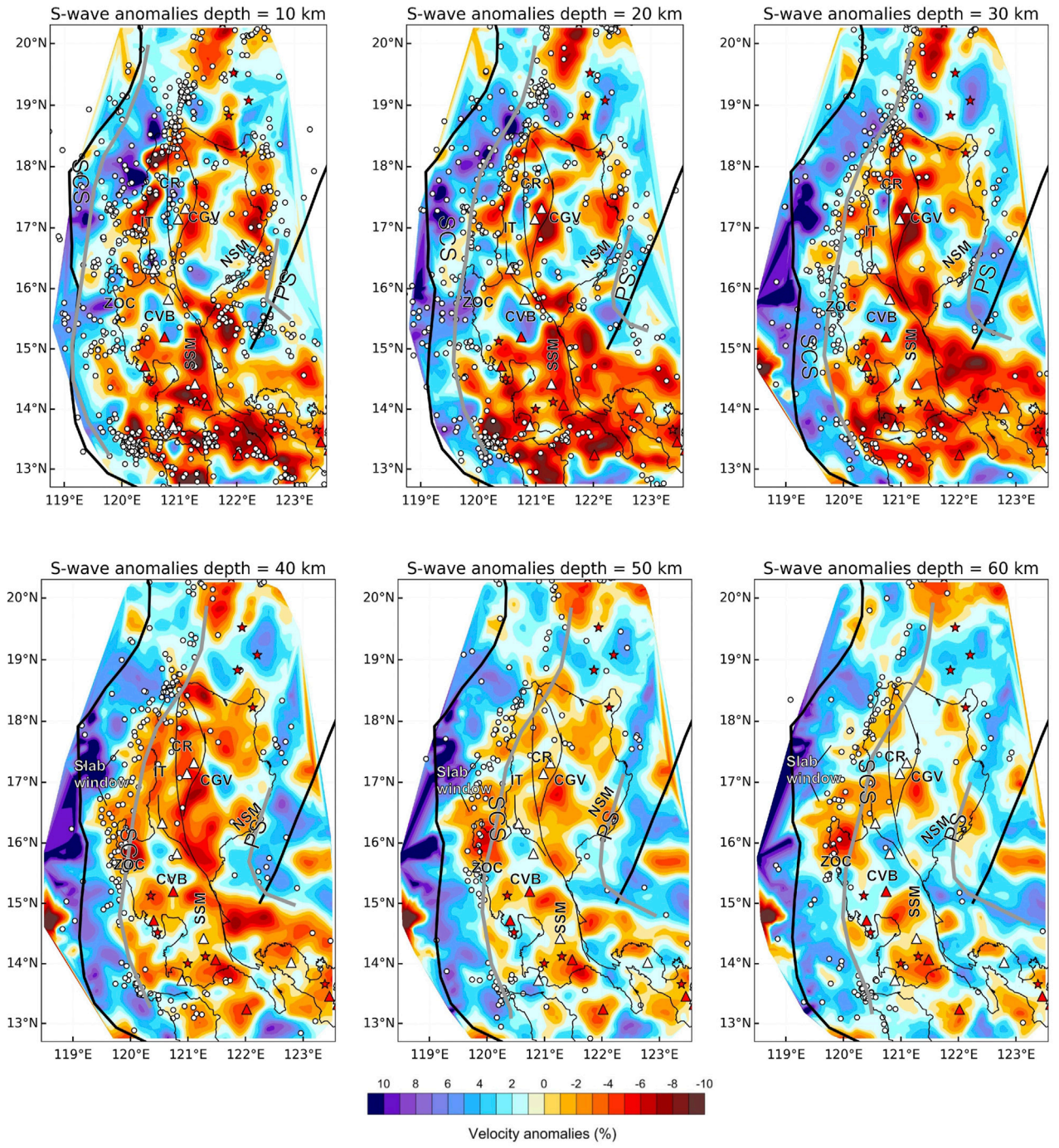

FIGURE 10
Map view of S-wave tomography of different depths. The symbols and abbreviations are the same as those in Figure 9.

6 Discussion

6.1 Comparison with previous studies

Our tomographic results and relocation of earthquakes have provided new images of the velocity structures beneath Luzon Island. Compared with seismic tomographic studies that focused on the regional and global scales of Southeast Asia and the Taiwan region (Bijwaard et al., 1998; Lallemand et al., 2001; Li and van der Hilst, 2010), our results have a higher resolution, making it suitable to study the shallow tectonic structures in detail. Currently, the high-resolution tomographic studies for the North Luzon area only focused on the P-wave structure (Fan et al., 2015; Fan et al., 2016; Fan et al., 2017). Our P-wave velocity structures were consistent with their observations in both horizontal slices at the shallow depth (a depth of less than 100 km) and vertical profiles at 14°N to 18°N. The relocation of earthquakes will increase the quality of the data and can be used to trace the slab geometry of the

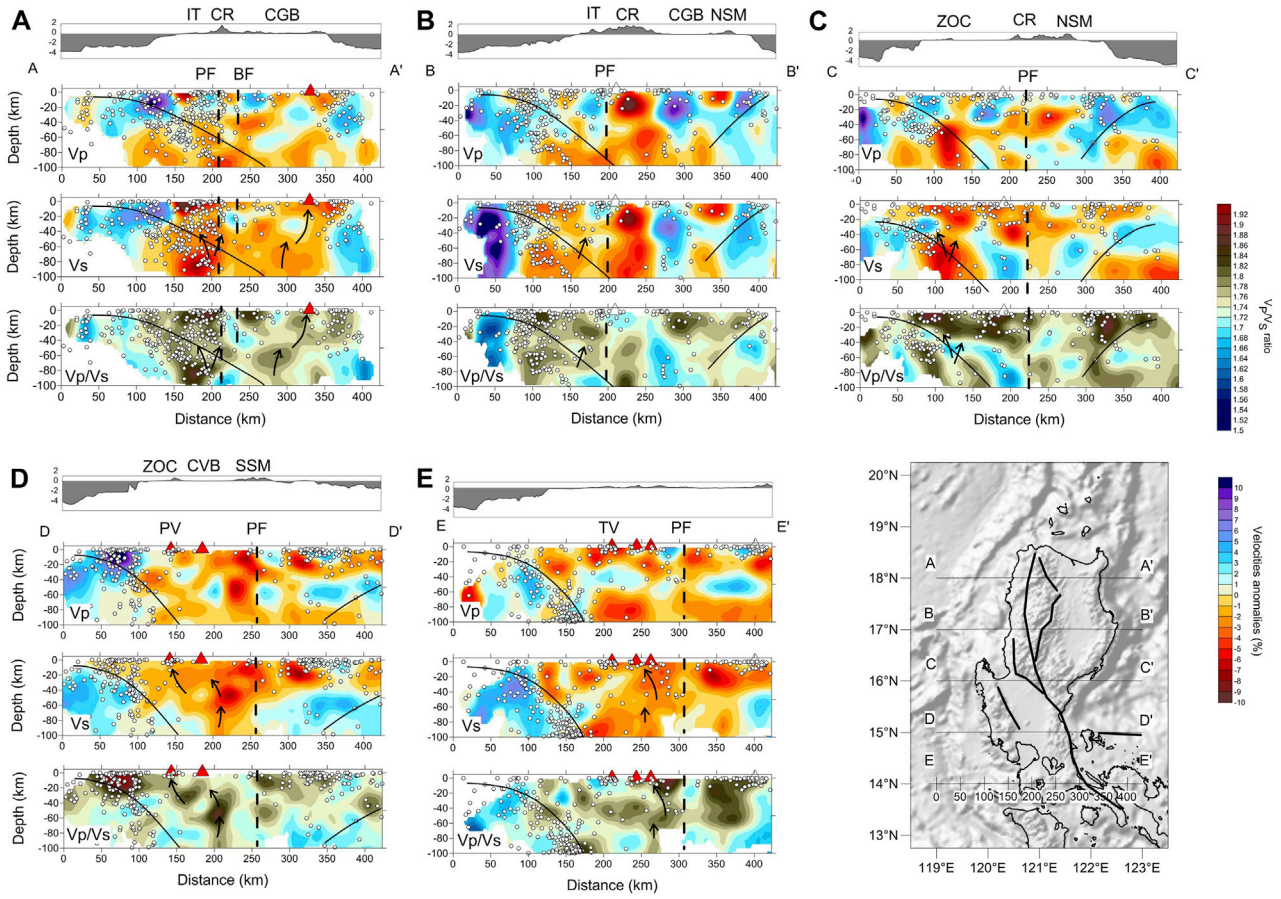

FIGURE 11
P- and S-wave velocity perturbations and Vp/Vs. for selected profiles along 18°N, 17°N, 16°N, 15°N, and 14°N **(A–E)**. The locations of these profiles are in Figure 1. The black arrows indicate the migration path of magmas or melts from the mantle wedge. Red triangles denote the active volcanoes and white triangles denote inactive volcanoes. Dots indicate the locations of the relocated earthquakes. Abbreviations: PF: Philippines Fault; BF: Bangui Fault; PV; Pinatubo volcano; TV: Taal volcano; other abbreviations are the same as Figure 1. See the text for more details.

subducted South China Sea slab (Figures 9–11). In our study, we provide a new P- and S-wave seismic velocity model, which delivers high resolution at shallow depth at a lithospheric scale. The tomographic images are suitable to provide new insights into the lithospheric structures of the study area.

6.2 Accreted terranes in the tomographic images

Different accreted terranes have been proposed as constituting Luzon Island, including ophiolites, continental fragments, and island arc elements (Karig, 1983). However, there is very little seismic evidence of these accreted structures. In both horizontal and vertical tomographic images, we could identify distinguishable velocity anomalies corresponding to the different accreted terranes that constitute Luzon Island. In a subduction zone setting, the observed velocity difference might reflect the geological properties (lithology and metamorphism grade) of the corresponding terranes (Eberhart-Phillips and Reyners, 2001; Kuo-Chen et al., 2012; Raoof et al., 2017).

From our results, we could observe the distinctive velocity anomalies corresponding to the surface geological structures. These showed similarities to the Taiwan region, which previous studies have referred to as the Mindoro-Luzon-Taiwan region (Stephan et al., 1986; Defant et al., 1989). Because our P-wave velocity models showed better quality, we interpreted the structure using mainly the P-wave tomographic images. The low-velocity anomalies under the Cordillera Central and the South Sierra Madre (Figures 9, 10 for horizontal sections and vertical cross sections BB'and DD' in Figures 11B,D) might indicate that low-velocity roots resulted from the thickening of the crust, similar to the Central Range tomographic seismic velocity structure with low-velocity anomalies up to a depth of 54 km (Kuo-Chen et al., 2012). On the other hand, the high-velocity anomalies of the two valleys, namely, the Cagayan Valley Basin and the Central Valley Basin, in depths of 10–30 km, might indicate the metamorphic basement underneath the sedimentary layers (Karig, 1983; Stephan et al., 1986). The Zambales Ophiolite Complex exhibited a distinct high-velocity anomaly zone compared to the volcanic front in the east where active volcanoes are present (Figures 9, 10 and cross sections CC' and DD' in Figures 11C,D).

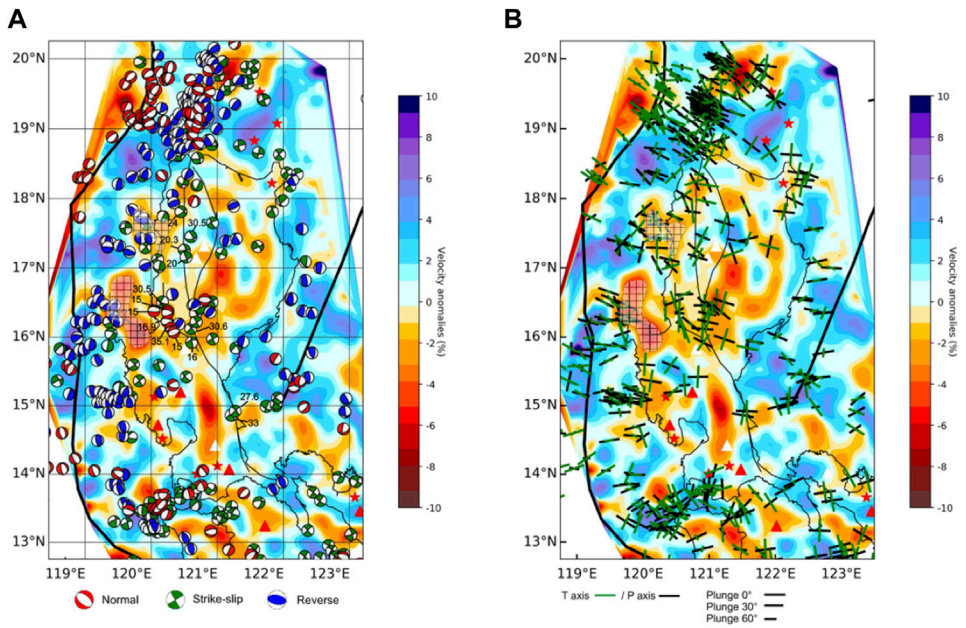

FIGURE 12
(A) Focal mechanism of the shallow earthquake overlying the 50 km depth P-wave anomalies in the study region. The focal mechanisms from earthquakes with hypocenter depths of less than 60 km, combined from NEIC and CMT solutions from 1981 to 2013; numbers indicate the depth in kilometers of selected earthquakes. The oblique stripe denotes the region of suspected slab tearing where earthquakes with normal faulting occur. **(B)** P- and T-axes of the same earthquakes in **(A)**.

6.3 The depth of the Philippine Fault

The contrast in velocity anomalies of the accreted terranes can also be used to trace the fault systems in the area, in which the faults act as boundaries between the surface geological structures, namely, the Philippine Fault separates the Cordillera Central from Ilocos Trough in the north region (from 16°N—18°N) and from Central Valley Basin in the central region (15°N—16°N) (Figures 11A,B), and the Bangui fault separates the Cordillera Central and Cagayan Valley Basins (Figures 9, 10; Figure 11A). In this section, we examine the velocity contrast at the deeper depth to have a first order of estimation for the depth of the Philippine Fault.

In horizontal slices (Figures 9, 10), at the depth of 20 km–40 km, the Philippine Fault was well defined by the contrast velocity anomalies between the structures on two sides of the fault. In addition, the relocated earthquakes aligned clearly along the fault from the depth of 10–40 km, especially at the northern tip of the fault (15.5°N—18.5°N, Figures 9, 10). At the deeper depth, there were a few events aligned along the faults: scattered events at 16°N-18.5°N at 50 km, two events at 16°N, and six events at 18°N at a depth of 60 km (Figures 9, 10). In the vertical sections (Figure 11), it was clearer to see the Philippine Fault from velocity contrast in both P- and S-wave tomography and Vp/Vs. images in different segments of the fault. In all cross sections, we could observe the significant velocity contrast across the Philippine Fault from the surface to at least 60 km, while in cross sections CC' and DD' (Figures 11C,D), the velocity contrast might extend to the depth of 80 km. With the assessment that our tomographic models can be reliable up to 50 km in the horizontal section and up to a maximum of 70 km in the vertical section, we suggest that the observed velocity contrast across the Philippine Fault is reliable to a depth of at least 50 km. This observation of velocity contrast on two sides of the Philippine Fault is consistent with the tomographic images from joint inversion of P-wave local and teleseismic tomography (Fan et al., 2015; Fan et al., 2017).

Figure 12 shows the focal mechanisms of shallow earthquakes (Figure 12A) and their corresponding P- and T-axes with depths of less than 60 km (Figure 12B) overlapping the P-wave velocity anomalies at 40 km. These focal mechanisms corresponding to shallow earthquakes with hypocenter depths of less than 60 km were combined from NEIC (Sipkin, 1994) and CMT solutions (Dziewonski et al., 1981; Ekström et al., 2012) from 1981 to 2013, which contain 133 medium to strong events with the magnitude ranging from 4.7 to 7.7. The strike-slip earthquakes were well distributed along with the major strike-slip fault system with a maximum depth of 33 km, which is consistent with our relocated earthquakes, except for the northern part of the Philippine Fault where earthquakes along the fault were present even at a depth of 40 km (from 17°N to 18°N, Figures 9, 10). Along the fault, most of the earthquakes showed an east-west direction P-axis and a northeast-southwest direction T-axis (Figure 12B), which may imply a relatively homogenous stress pattern. The crustal thickness of the Luzon region was determined to be between 13 and 33 km (Parcutela et al., 2020), which implies that the strike-slip earthquakes related to the Philippine Fault occurred mostly at the crustal level, while at the deeper depth, the displacement was occupied by ductile deformation (Şengör et al., 2019). In other major strike-slip faults, the extension of the fault below the Moho was also revealed by the imaging technique, for example,: the San Andreas fault (Zandt, 1981; Zhu, 2000), North

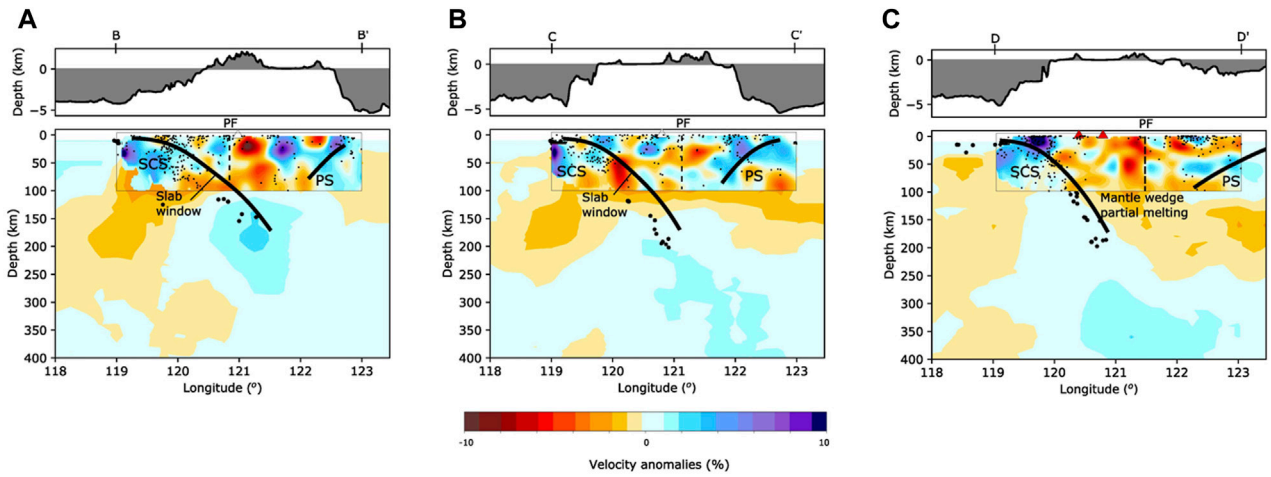

FIGURE 13
Tomographic images of the P-wave velocity model from this study (in the black frame) compared with the global teleseismic model UU-P07 for three profiles at 17°N (BB′-**(A)**), 16°N (CC′-**(B)**), and 15°N (DD′-**(C)**). Black dots indicate the earthquakes, small dots indicate the relocation observed in this study, and big dots indicate data from the EHB catalog. Thick black lines indicate the subduction slab from the Slab 2 model.

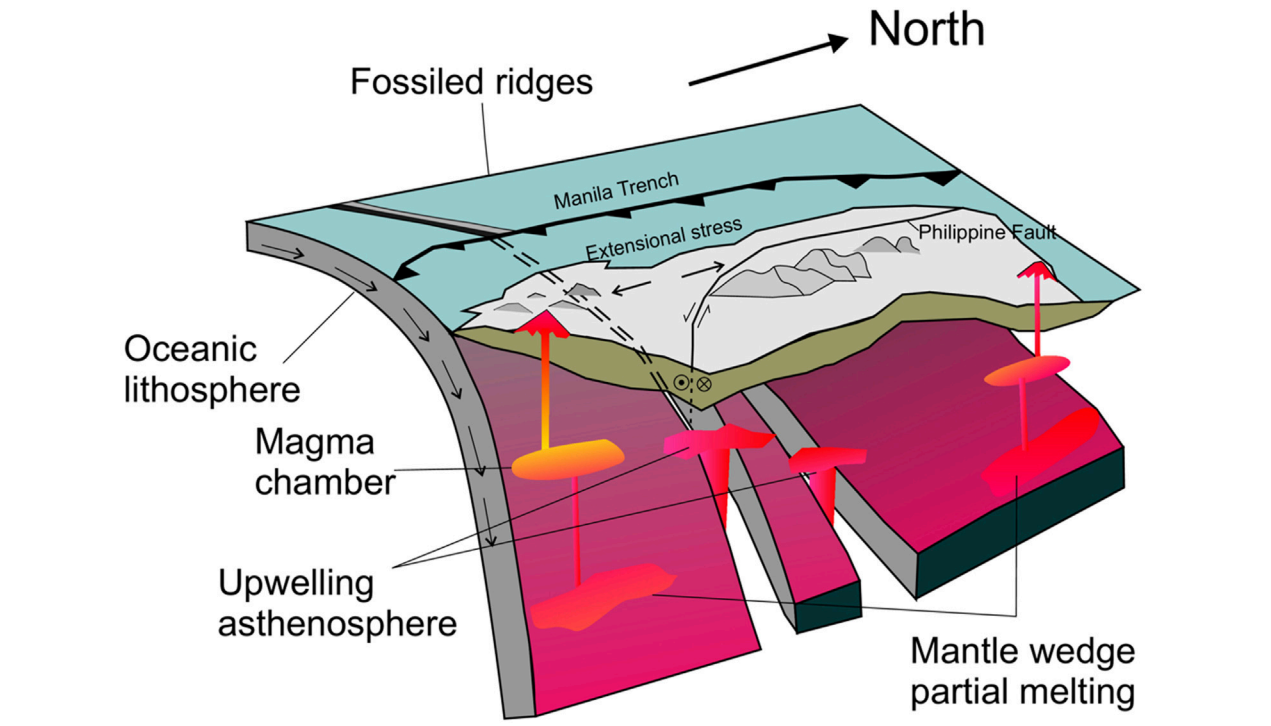

FIGURE 14
Tectonic model of Luzon Island showing the magma formation source from both the mantle wedge melting and asthenosphere upwelling from slab tear sites. The slab tearing occurs in the region where the fossil ridge is subducted. In the central region, the Philippine Fault cuts through the whole crust and offsets the upper mantle.

Anatolian Fault (Papaleo et al., 2017), and Altyn Tagh fault (Jiang et al., 2004). Therefore, from the analysis of earthquakes and heterogeneity of seismic velocity, we suggest that the Philippine Fault is a lithospheric scale structure that cuts through the crust and may offset the upper mantle structure along its displacement.

6.4 Slab tearing locations

The slab tearing along the fossil ridge of the South China Sea in the Manila Trench has been proposed using evidence of geochemistry, seismicity, and seismic tomography (Yang et al.,

1996; Bautista et al., 2001; Fan et al., 2015; Fan et al., 2016). Our results also indicated two major low-velocity regions, high Vp/Vs. at 16°N to 17°N and around 17.5°N (Figures 11A–C and the grid region in Figure 12) that are separated by a thin high-velocity anomaly slab. These low-velocity anomalies were interpreted as results of high-temperature magmas upwelling through the slab tearing and forming a slab window. An abrupt disruption of earthquake continuity can also be noted in profile C-C' at depths of 40–100 km, which may suggest a change in the geodynamic scenario in this area. Examples of a similar seismic gap and low-velocity anomalies resulting from slab tearing caused by ridge subduction can be found in the North Andean margin (Gutscher et al., 1999) and the Italian region (Rosenbaum et al., 2008).

The focal mechanism of the shallow earthquakes also supports our calculation of the place of slab tearing (Figure 12). In general, we observed the normal faulting at the outer trench, which shows an extension regime. On the other hand, thrust faulting is the dominant focal mechanism of the subducting slab. However, abnormal earthquakes, which have east-west strike normal focal mechanisms, are found in the extent of the larger proposed slab tearing region (Figure 12) with depths ranging from 15 km to 35 km. These events have a north-south T-axis and a nearly vertical P-axis, corresponding to a north-south extensional regime at the crustal level. This regime fits with our observation of seismic tearing and mantle upwelling in this region, suggesting that the slab tearing may cause the crust to extend in the northeast-southwest direction, thus producing these normal earthquakes in the lower crust. This pattern may imply a change in crust deformation and stress accumulation induced by ridge subduction and slab tearing.

From these observations of seismic tomography and focal mechanisms, we suggest that the fossil ridge of the South China Sea has been subducting beneath Luzon Island and creating slab-tearing regions at a depth of 40 km.

6.5 Subsurface magmatic feeding systems

To constrain the relationship between the volcanic system and the subduction of the South China Sea slab, S-wave velocity and Vp/Vs. ratio were used to trace the subsurface magmatic chamber and feeding veins because the S-velocity and Vp/Vs. ratio are relatively sensitive to the content of fluids and melts (Koulakov et al., 2016). Large veins of low S-wave velocity and high Vp/Vs. ratio were identified under the active volcanoes and regions of magmatic intrusion, allowing us to trace the ascending magmatic path in vertical images (black arrows on Figure 11). To correlate with the deeper structure, we combined our P-wave tomographic images at a depth of less than 100 km and P-wave global seismic tomography model UU-P07 at a depth deeper than 100 km (Amaru, 2007) for three cross sections, namely, along the 17°N, 16°N, and 15°N sections (Figure 13). The combined images showed a good fit of our model with the global model.

In our seismic tomography images, the slab tearing was identified in two regions, as seen in Figure 12. In the vertical section of these regions, the magmatism from slab tearing could be observed at cross sections AA', BB', and CC' where low-velocity bodies ascended through the slab (Figures 11A–C). This observation fits the deeper structure from the model UU-P07 where low-velocity regions were present underneath the subducting slab (Figures 1B, 11A,B). These low-velocity regions can be interpreted as the ascendant of the asthenosphere to the continental crust (Rosenbaum et al., 2008). In a ridge subduction setting, magma may form and be unable to solidify, thus creating a slab window where magma continues to generate and rise (Thorkelson, 1996).

On the other hand, for the southern region, a deep source of magmatism was identified as the mechanism that feeds magma to the volcanoes. In vertical sections (DD' and EE' cross sections in Figure 11), the low-velocity anomalies fit well with the occurrences of active volcanoes (the Taal and Pinatubo). The magma resulting from the partial melting of the mantle wedge comes from a depth of at least 100 km (Figure 13C) and rises to accumulate in the magma chamber at a depth of 30–50 km before ascending to feed the surface volcanoes. A thermal model suggests the depth of partial melting by dehydration of subducted slab in the island arc system is likely to be deeper than 100 km (Gill, 1981; Tatsumi et al., 1983; Tatsumi, 1989). The deep source magmatism is widely observed from seismic tomography of the island arc region (Zhao et al., 2000; Nakajima et al., 2001; Husen et al., 2003; Koulakov et al., 2016). We interpret this magma source to be the partial melting of the mantle wedge by the dehydration reaction of the slab, ascending to the shallow magma chamber by interconnected magma veins.

The lack of low-velocity regions at a depth deeper than 100 km at the site of slab tearing regions (Figures 13A,B) might indicate an absence of magmatism from partial melting of the mantle wedge. Another observation is that the volcanoes in the regions related to the slab tearing (around 16°N to 18°N) are mostly inactive, in contrast to the very active volcanoes to both the north and south of these regions. In the subduction regions associated with high bathymetric relief, the phenomenon of reduced volcanism is quite common, which might be explained by the absence of a sufficiently deep slab to generate arc volcanism (Rosenbaum and Mo, 2011). This might also apply to the slab tearing region in our study area as the slab tear might cause a lack of deep slab, while the upwelling asthenosphere does not reach the surface. However, to have a more precise explanation of the area's volcanism mechanics, further geophysical and geochemical investigations are needed.

7 Conclusion

In this study, we performed a P- and S-wave travel time seismic tomographic inversion on Luzon Island. The tomographic images resulting from the inversion were used to determine and interpret the major structures at the upper mantle level and crustal level.

Figure 14 summarizes the result of our study and proposes the tectonic model of the Luzon region. We identified the seismic velocity contrast corresponding to the different geological structures, which are separated by the Philippine Fault. The relocated earthquakes from this study combined with the reference focal mechanisms were used to trace the fault in the crust. Medium to large strike-slip earthquakes occurring in the crust may suggest a brittle mechanism. At the upper mantle level, we continued to observe the seismic velocity differences across the fault up to the depth of 60 km, where ductile deformation takes place. From these observations, we conclude

that the Philippine Fault is a lithospheric structure that cuts through the crust and offsets the upper mantle.

The tomographic results confirm the presence of slab-tearing regions extended from the fossil ridges in the northern Luzon region. The observation is supported by the unusual extension regime from the focal mechanism in the suspected area in the crust. This slab tear causes the upwelling of the asthenosphere that ascends through the subducting slab. In addition, it also might create a deep slab absence, and hinder the formation of the magma at the mantle wedge. In regions outside of the slab tearing areas, the mantle wedge partial melting occurs and feeds melt material to the subsurface magma chambers and the active volcanoes.

Data availability statement

The original contributions presented in the study are included in the article/Supplementary Material, further inquiries can be directed to the corresponding author.

Author contributions

C-NN, B-SH, and T-YL initiated the original idea and conceptualized research. P-FC and VN provided comments and discussion. IN, BB, and AM performed the collection of the PHIVOLCS and IES seismic network data used in this study. All co-authors contributed to the interpretation of the results and the manuscript writing led by C-NN, T-YL, and B-SH. All authors contributed to the article and approved the submitted version.

Funding

This study was funded by the Vietnam Academy of Science and Technology (VAST) under grant numbers CT0000.02/22-23 and VAST06.02/23-24, and by the Ministry of Science and Technology in Taiwan under grants MOST 108-2116-M-001-011, MOST 108-2116-M-001-010-MY3, and MOST 109-2119-M-001-011.

Acknowledgments

We appreciate the staff of the Philippine Institute of Volcanology and Seismology, and Academia Sinica for collecting the data used in this study. We thank Ivan Koulakov for helping in running the LOTOS tomographic code. We would like to thank two reviewers for their constructive suggestions and comments.

Conflict of interest

The authors declare that the research was conducted in the absence of any commercial or financial relationships that could be construed as a potential conflict of interest.

Publisher's note

Supplementary material

The Supplementary Material for this article can be found online at: https://www.frontiersin.org/articles/10.3389/feart.2023.1213498/full#supplementary-material

References

Amaru, M. (2007). *Global travel time tomography with 3-D reference models*. Utrecht: Utrecht University.

Armada, L. T., Hsu, S. K., Dimalanta, C. B., Yumul, G. P., Jr, Doo, W. B., and Yeh, Y. C. (2020). Forearc structures and deformation along the Manila Trench. *J. Asian Earth Sci.* X (4), 100036. doi:10.1016/j.jaesx.2020.100036

Aurelio, M. A. (2000). Shear partitioning in the Philippines: constraints from Philippine Fault and global positioning system data. *Isl. Arc* 9, 584–597. doi:10.1111/j.1440-1738.2000.00304.x

Aurelio, M., Barrierj, E., Gaulon, R., and Rangin, C. (1997). Deformation and stress states along the central segmentof the Philippine Fault: implications to wrench fault tectonics. *J. Asian Earth Sci.* 15, 107–119. doi:10.1016/s0743-9547(97)00001-9

Barrier, E., Huchon, P., and Aurelio, M. (1991). Philippine Fault - a key for philippine kinematics. *Geology* 19, 32–35. doi:10.1130/0091-7613(1991)019<0032:pfakfp>2.3.co;2

Bautista, B. C., Bautista, M. L. P., Oike, K., Wu, F. T., and Punongbayan, R. S. (2001). A new insight on the geometry of subducting slabs in northern Luzon, Philippines. *Tectonophysics* 339, 279–310. doi:10.1016/s0040-1951(01)00120-2

Bertin, D., Lindsay, J. M., Cronin, S. J., de Silva, S. L., Connor, C. B., Caffe, P. J., et al. (2022). Probabilistic volcanic hazard assessment of the 22.5–28° S segment of the central volcanic zone of the andes. *Front. Earth Sci.* 10, 875439. doi:10.3389/feart.2022.875439

Bijwaard, H., Spakman, W., and Engdahl, E. R. (1998). Closing the gap between regional and global travel time tomography. *J. Geophys Res-Sol Ea.* 103, 30055–30078. doi:10.1029/98jb02467

Bluth, G. J. S., Doiron, S. D., Schnetzler, C. C., Krueger, A. J., and Walter, L. S. (1992). Global tracking of the So2 clouds from the june, 1991 mount-pinatubo eruptions. *Geophys. Res. Lett.* 19, 151–154. doi:10.1029/91gl02792

Castillo, P. R., and Newhall, C. G. (2004). Geochemical constraints on possible subduction components in lavas of Mayon and Taal Volcanoes, southern Luzon, Philippines. *J. Petrology* 45, 1089–1108. doi:10.1093/petrology/egh005

Chen, P. F., Su, P. L., Olavere, E. A., Solidum, R. U., and Huang, B. S. (2020). Relocation of the April 2017 Batangas, Philippines, earthquake sequence, with tectonic implications. *Terr. Atmos. Ocean. Sci.* 31, 273–282. doi:10.3319/tao.2020.01.31.01

Defant, M. J., Jacques, D., Maury, R. C., Deboer, J., and Joron, J. L. (1989). Geochemistry and tectonic setting of the Luzon arc, Philippines. *Geol. Soc. Am. Bull.* 101, 663–672. doi:10.1130/0016-7606(1989)101<0663:gatsot>2.3.co;2

Dziewonski, A. M., Chou, T. A., and Woodhouse, J. H. (1981). Determination of earthquake source parameters from waveform data for studies of global and regional seismicity. *J. Geophys. Res. Solid Earth* 86 (B4), 2825–2852. doi:10.1029/jb086ib04p02825

Eberhart-Phillips, D., and Reyners, M. (2001). A complex, young subduction zone imaged by three-dimensional seismic velocity, Fiordland, New Zealand. *Geophys. J. Int.* 146, 731–746. doi:10.1046/j.0956-540x.2001.01485.x

Ekström, G., Nettles, M., and Dziewoński, A. M. (2012). The global CMT project 2004–2010: centroid-moment tensors for 13,017 earthquakes. *Phys. Earth Planet. Interiors* 200, 1–9. doi:10.1016/j.pepi.2012.04.002

Engdahl, E. R., van der Hilst, R., and Buland, R. (1998). Global teleseismic earthquake relocation with improved travel times and procedures for depth determination. *Bull. Seismol. Soc. Am.* 88, 722–743. doi:10.1785/bssa0880030722

Fan, J. K., Wu, S. G., and Spence, G. (2015). Tomographic evidence for a slab tear induced by fossil ridge subduction at Manila Trench, South China Sea. *Int. Geol. Rev.* 57, 998–1013. doi:10.1080/00206814.2014.929054

Fan, J. K., Zhao, D. P., and Dong, D. D. (2016). Subduction of a buoyant plateau at the Manila Trench: tomographic evidence and geodynamic implications. *Geochem. Geophys. Geosystems* 17, 571–586. doi:10.1002/2015gc006201

Fan, J. K., Zhao, D. P., Dong, D. D., and Zhang, G. X. (2017). P-wave tomography of subduction zones around the central Philippines and its geodynamic implications. *J. Asian Earth Sci.* 146, 76–89. doi:10.1016/j.jseaes.2017.05.015

Fitch, T. J. (1972). Plate convergence, transcurrent faults, and internal deformation adjacent to southeast Asia and the western Pacific. *J. Geophys. Res.* 77, 4432–4460. doi:10.1029/jb077i023p04432

Gill, J. (1981). *Orogenic andesites and plate tectonics*. Heidelberg: Springer Science & Business Media.

Gutscher, M. A., Malavieille, J., Lallemand, S., and Collot, J. Y. (1999). Tectonic segmentation of the North andean margin: impact of the carnegie ridge collision. *Earth Planet. Sci. Lett.* 168, 255–270. doi:10.1016/s0012-821x(99)00060-6

Hamburger, M. W., Cardwell, R. K., and Isacks, B. L. (1983). "Seismotectonics of the northern Philippine island arc," in *The tectonic and geologic evolution of Southeast asian seas and islands: Part 2* (Washington, D.C: American Geophysical Union), 1–22.

Hayes, G. P., Moore, G. L., Portner, D. E., Hearne, M., Flamme, H., Furtney, M., et al. (2018). Slab2, a comprehensive subduction zone geometry model. *Science* 362, 58–61. doi:10.1126/science.aat4723

Hollings, P., Wolfe, R., Cooke, D. R., and Waters, P. J. (2011). Geochemistry of tertiary igneous rocks of northern Luzon, Philippines: evidence for a back-arc setting for alkalic porphyry copper-gold deposits and a case for slab roll-back? *Econ. Geol.* 106, 1257–1277. doi:10.2113/econgeo.106.8.1257

Hsu, Y. J., Yu, S. B., Loveless, J. P., Bacolcol, T., Solidum, R., Luis, A., et al. (2016). Interseismic deformation and moment deficit along the Manila subduction zone and the Philippine Fault system. *J. Geophys Res-Sol Ea.* 121, 7639–7665. doi:10.1002/2016jb013082

Hsu, Y. J., Yu, S. B., Song, T. R. A., and Bacolcol, T. (2012). Plate coupling along the Manila subduction zone between Taiwan and northern Luzon. *J. Asian Earth Sci.* 51, 98–108. doi:10.1016/j.jseaes.2012.01.005

Hua, Y. J., Zhang, S. X., Li, M. K., Wu, T. F., Zou, C. Y., and Liu, L. (2019). Magma system beneath Tengchong volcanic zone inferred from local earthquake seismic tomography. *J. Volcanol. Geotherm. Res.* 377, 1–16. doi:10.1016/j.jvolgeores.2019.04.002

Hung, T. D., Yang, T., Le, B. M., Yu, Y., Xue, M., Liu, B., et al. (2021). Crustal structure across the extinct mid-ocean ridge in South China sea from OBS receiver functions: insights into the spreading rate and magma supply prior to the Ridge cessation. *Geophys. Res. Lett.* 48 (3), e2020GL089755. doi:10.1029/2020gl089755

Husen, S., Quintero, R., Kissling, E., and Hacker, B. (2003). Subduction-zone structure and magmatic processes beneath Costa Rica constrained by local earthquake tomography and petrological modelling. *Geophys. J. Int.* 155, 11–32. doi:10.1046/j.1365-246x.2003.01984.x

Jego, S., Maury, R. C., Polve, M., Yumul, G. P., Bellon, H., Tamayo, R. A., et al. (2005). Geochemistry of adakites from the Philippines: constraints on their origins. *Resour. Geol.* 55, 163–188. doi:10.1111/j.1751-3928.2005.tb00239.x

Jiang, X. D., Hin, Y., and McNutt, M. K. (2004). Lithospheric deformation beneath the Altyn Tagh and West Kunlun faults from recent gravity surveys. *J. Geophys Res-Sol Ea.* 109. doi:10.1029/2003jb002444

Karig, D. E. (1983). Accreted terranes in the northern part of the philippine Archipelago. *Tectonics* 2, 211–236. doi:10.1029/tc002i002p00211

Karig, D. E., Sarewitz, D. R., and Haeck, G. D. (1986). Role of strike-slip faulting in the evolution of allochthonous terranes in the Philippines. *Geology* 14, 852–855. doi:10.1130/0091-7613(1986)14<852:rosfit>2.0.co;2

Kissling, E., Ellsworth, W. L., Eberhartphillips, D., and Kradolfer, U. (1994). Initial reference models in local earthquake tomography. *J. Geophys Res-Sol Ea.* 99, 19635–19646. doi:10.1029/93jb03138

Koulakov, I. (2009). LOTOS code for local earthquake tomographic inversion: benchmarks for testing tomographic algorithms. *Bull. Seismol. Soc. Am.* 99, 194–214. doi:10.1785/0120080013

Koulakov, I., Smirnov, S. Z., Gladkov, V., Kasatkina, E., West, M., El Khrepy, S., et al. (2018). Causes of volcanic unrest at Mt. Spurr in 2004-2005 inferred from repeated tomography. *Sci. Rep.* 8, 17482. doi:10.1038/s41598-018-35453-w

Koulakov, I., and Sobolev, S. V. (2006). A tomographic image of Indian lithosphere break-off beneath the Pamir-Hindukush region. *Geophys. J. Int.* 164, 425–440. doi:10.1111/j.1365-246x.2005.02841.x

Koulakov, I. (2013). Studying deep sources of volcanism using multiscale seismic tomography. *J. Volcanol. Geotherm. Res.* 257, 205–226. doi:10.1016/j.jvolgeores.2013.03.012

Koulakov, I., and Vargas, C. A. (2018). Evolution of the magma conduit beneath the galeras volcano inferred from repeated seismic tomography. *Geophys. Res. Lett.* 45, 7514–7522. doi:10.1029/2018gl078850

Koulakov, I. Y., Kukarina, E. V., Gordeev, E. I., Chebrov, V. N., and Vernikovsky, V. A. (2016). Magma sources in the mantle wedge beneath the volcanoes of the Klyuchevskoy group and Kizimen based on seismic tomography modeling. *Russ. Geol. Geophys.* 57, 82–94. doi:10.1016/j.rgg.2016.01.006

Koulakov, I., Yudistira, T., Luehr, B.-G., and Wandono, P, (2009). Svelocity and V_P/V_S ratio beneath the Toba caldera complex (Northern Sumatra) from local earthquake tomography. *Geophys. J. Int.* 177, 1121–1139. doi:10.1111/j.1365-246x.2009.04114.x

Kuo-Chen, H., Wu, F. T., and Roecker, S. W. (2012). Three-dimensional P velocity structures of the lithosphere beneath Taiwan from the analysis of TAIGER and related seismic data sets. *J. Geophys. Res. Solid Earth* 117. doi:10.1029/2011jb009108

Lallemand, S., Font, Y., Bijwaard, H., and Kao, H. (2001). New insights on 3-D plates interaction near Taiwan from tomography and tectonic implications. *Tectonophysics* 335, 229–253. doi:10.1016/s0040-1951(01)00071-3

Laske, G., Masters, G., Ma, Z., and Pasyanos, M. (2013). *Update on CRUST1. 0—a 1-degree global model of Earth's crust*. Geophysical Research Abstracts, 2658.

Lee, T. Y., and Lawver, L. A. (1994). Cenozoic Plate reconstruction of the South China sea region. *Tectonophysics* 235, 149–180. doi:10.1016/0040-1951(94)90022-1

Levin, V., Shapiro, N., Park, J., and Ritzwoller, M. (2002). Seismic evidence for catastrophic slab loss beneath Kamchatka. *Nature* 418, 763–767. doi:10.1038/nature00973

Li, C., and van der Hilst, R. D. (2010). Structure of the upper mantle and transition zone beneath Southeast Asia from traveltime tomography. *J. Geophys Res-Sol Ea.* 115, B07308. doi:10.1029/2009jb006882

Nakajima, J., Matsuzawa, T., Hasegawa, A., and Zhao, D. (2001). Three-dimensional structure of $V_{<i>p</i>}$, $V_{<i>s</i>}$, and $V_{<i>p</i>}/V_{<i>s</i>}$ beneath northeastern Japan: implications for arc magmatism and fluids. *J. Geophys. Res. Solid Earth* 106, 21843–21857. doi:10.1029/2000jb000008

Nur, A., and Benavraham, Z. (1983). Volcanic gaps due to oblique consumption of aseismic ridges. *Tectonophysics* 99, 355–362. doi:10.1016/0040-1951(83)90112-9

Parcutela, N. E., Dimalanta, C. B., Armada, L. T., and Yumul, G. P. (2020). PHILCRUST3.0: new constraints in crustal growth rate computations for the Philippine arc. *J. Asian Earth Sci. X* 4, 100032. doi:10.1016/j.jaesx.2020.100032

Paige, C. C., and Saunders, M. A. (1982). Lsqr - an algorithm for sparse linear-equations and sparse least-squares. *Acm Trans. Math. Softw.* 8, 43–71. doi:10.1145/355984.355989

Papaleo, E., Cornwell, D. G., and Rawlinson, N. (2017). Seismic tomography of the North Anatolian Fault: new insights into structural heterogeneity along a continental strike-slip fault. *Geophys. Res. Lett.* 44, 2186–2193. doi:10.1002/2017gl072726

Polat, G., Ozel, N. M., and Koulakov, I. (2016). Investigating P- and S-wave velocity structure beneath the Marmara region (Turkey) and the surrounding area from local earthquake tomography. *Earth Planets Space* 68, 132. doi:10.1186/s40623-016-0503-4

Raoof, J., Mukhopadhyay, S., Koulakov, I., and Kayal, J. R. (2017). 3-D seismic tomography of the lithosphere and its geodynamic implications beneath the northeast India region. *Tectonics* 36, 962–980. doi:10.1002/2016tc004375

Rawlinson, N., Fichtner, A., Sambridge, M., and Young, M. K. (2014). Seismic tomography and the assessment of uncertainty. *Adv. Geophys.* 55, 1–76. doi:10.1016/bs.agph.2014.08.001

Rawlinson, N., and Spakman, W. (2016). On the use of sensitivity tests in seismic tomography. *Geophys. J. Int.* 205, 1221–1243. doi:10.1093/gji/ggw084

Rosenbaum, G., Gasparon, M., Lucente, F. P., Peccerillo, A., and Miller, M. S. (2008). Kinematics of slab tear faults during subduction segmentation and implications for Italian magmatism. *Tectonics* 27, n/a. doi:10.1029/2007tc002143

Rosenbaum, G., and Mo, W. (2011). Tectonic and magmatic responses to the subduction of high bathymetric relief. *Gondwana Res.* 19, 571–582. doi:10.1016/j.gr.2010.10.007

Ruff, L., and Kanamori, H. (1980). Seismicity and the subduction process. *Phys. Earth Planet. Interiors* 23, 240–252. doi:10.1016/0031-9201(80)90117-x

Şengör, A. M. C., Zabcı, C., and Natal'in, B. A. (2019). Continental transform faults: congruence and incongruence with normal plate kinematics. *Transform Plate Boundaries Fract. Zones* 2019, 169–247. doi:10.1016/B978-0-12-812064-4.00009-8

Smith, W. H., and Sandwell, D. T. (1997). Global sea floor topography from satellite altimetry and ship depth soundings. *Science* 277, 1956–1962. doi:10.1126/science.277.5334.1956

Stephan, J. F., Blanchet, R., Rangin, C., Pelletier, B., Letouzey, J., and Muller, C. (1986). Geodynamic evolution of the taiwan Luzon Mindoro belt since the late eocene. *Tectonophysics* 125, 245–268. doi:10.1016/0040-1951(86)90017-x

Stern, R. J. (2002). Subduction zones. *Rev. Geophys.* 40, 3-1–3-38. doi:10.1029/2001RG000108

Tatsumi, Y. (1989). Migration of fluid phases and genesis of basalt magmas in subduction zones. *J. Geophys. Research-Solid Earth Planets* 94, 4697–4707. doi:10.1029/jb094ib04p04697

Tatsumi, Y., Sakuyama, M., Fukuyama, H., and Kushiro, I. (1983). Generation of arc basalt magmas and thermal structure of the mantle wedge in subduction zones. *J. Geophys. Res.* 88, 5815–5825. doi:10.1029/jb088ib07p05815

Thorkelson, D. J. (1996). Subduction of diverging plates and the principles of slab window formation. *Tectonophysics* 255, 47–63. doi:10.1016/0040-1951(95)00106-9

Um, J., and Thurber, C. (1987). A fast algorithm for two-point seismic ray tracing. *Bull. Seismol. Soc. Am.* 77, 972–986. doi:10.1785/bssa0770030972

Van Der Sluis, A., and Van der Vorst, H. (1987). *Numerical solution of large, sparse linear algebraic systems arising from tomographic problems, Seismic tomography*. Dordrecht: Springer, 49–83.

Venzke, E., Wunderman, R., McClelland, L., Simkin, T., Luhr, J., Siebert, L., et al. (2002). Global volcanism, 1968 to the present. Smithsonian Institution. Global Volcanism Program Digital Information Series, GVP-4, Available at: http://www.volcano.si.edu/reports/.

Vogt, P. (1973). Subduction and aseismic ridges. *Nature* 241, 189–191. doi:10.1038/241189a0

Wadati, K., and Oki, S. (1933). On the travel time of earthquake waves.(Part II). *J. Meteorological Soc. Jpn. Ser. II* 11, 14–28. doi:10.2151/jmsj1923.11.1_14

Wright, C., and Kuo, B. Y. (2007). Evidence for an elevated 410 km discontinuity below the Luzon, Philippines region and transition zone properties using seismic stations in Taiwan and earthquake sources to the south. *Earth Planets Space* 59, 523–539. doi:10.1186/bf03352715

Wyss, M., Hasegawa, A., and Nakajima, J. (2001). Source and path of magma for volcanoes in the subduction zone of northeastern Japan. *Geophys. Res. Lett.* 28, 1819–1822. doi:10.1029/2000gl012558

Yang, T. F., Lee, T., Chen, C. H., Cheng, S. N., Knittel, U., Punongbayan, R. S., et al. (1996). A double island arc between Taiwan and Luzon: consequence of ridge subduction. *Tectonophysics* 258, 85–101. doi:10.1016/0040-1951(95)00180-8

You, S. H., Gung, Y., Lin, C. H., Konstantinou, K. I., Chang, T. M., Chang, E. T. Y., et al. (2013). A preliminary seismic study of Taal volcano, Luzon island Philippines. *J. Asian Earth Sci.* 65, 100–106. doi:10.1016/j.jseaes.2012.10.027

Yu, S. B., Hsu, Y. J., Bacolcol, T., Yang, C. C., Tsai, Y. C., and Solidum, R. (2013). Present-day crustal deformation along the philippine Fault in Luzon, Philippines. *J. Asian Earth Sci.* 65, 64–74. doi:10.1016/j.jseaes.2010.12.007

Yumul, G. P., Dimalanta, C., Bellon, H., Faustino, D. V., De Jesus, J. V., Tamayo, R. A., et al. (2000). Adakitic lavas in the central Luzon back-arc region, Philippines: lower crust partial melting products? *Isl. Arc* 9, 499–512. doi:10.1111/j.1440-1738.2000.00297.x

Yumul, G. P., Dimalanta, C. B., Gabo-Ratio, J. A. S., Queaño, K. L., Armada, L. T., Padrones, J. T., et al. (2020). Mesozoic rock suites along western Philippines: exposed proto-South China Sea fragments? *J. Asian Earth Sci. X* 4, 100031. doi:10.1016/j.jaesx.2020.100031

Zandt, G. (1981). Seismic images of the deep-structure of the san-andreas fault system, central coast ranges, California. *J. Geophys. Res.* 86, 5039–5052. doi:10.1029/jb086ib06p05039

Zhao, D. P., Asamori, K., and Iwamori, H. (2000). Seismic structure and magmatism of the young Kyushu subduction zone. *Geophys. Res. Lett.* 27, 2057–2060. doi:10.1029/2000gl011512

Zhu, L. P. (2000). Crustal structure across the San Andreas Fault, southern California from teleseismic converted waves. *Earth Planet. Sci. Lett.* 179, 183–190. doi:10.1016/s0012-821x(00)00101-1

Frontiers in Earth Science

Investigates the processes operating within the major spheres of our planet

Advances our understanding across the earth sciences, providing a theoretical background for better use of our planet's resources and equipping us to face major environmental challenges.

Discover the latest Research Topics

See more →

Frontiers

Avenue du Tribunal-Fédéral 34
1005 Lausanne, Switzerland
frontiersin.org

Contact us

+41 (0)21 510 17 00
frontiersin.org/about/contact